LA-6044-PR
Progress Report

UC-20
Issued: August 1975

C. 3

LASL

Controlled Thermonuclear Research Program

January—December 1974

Compiled by

F. L. Ribe

los alamos
scientific laboratory
of the University of California
LOS ALAMOS, NEW MEXICO 87545

UNITED STATES
ENERGY RESEARCH AND DEVELOPMENT ADMINISTRATION
CONTRACT W-7405-ENG. 36

The four most recent reports in this series, unclassified, are LA-4585-MS, LA-4888-PR, LA-5250-PR, and LA-5656-PR.

In the interest of prompt distribution, this report was not edited by the Technical Information staff.

Printed in the United States of America. Available from
National Technical Information Service
U.S. Department of Commerce
5285 Port Royal Road
Springfield, VA 22151
Price: Printed Copy $7.60 Microfiche $2.25

SUMMARY AND INTRODUCTION

F. L. Ribe and G. A. Sawyer

Since the last Annual Progress Report (LA-5656-PR, July 1974) Scyllac has been rearranged into its final, complete toroidal configuration with 4-meter radius. The equilibrium and $m = 1$ instability properties of the 4-meter-radius sector were found to be unchanged, i.e., plasma confinement was terminated by the $m = 1$ instability with a growth rate $\gamma = 0.7$ MHz at a compression field of 40 kG and an $l = 1,0$ wavelength of 33 cm. The full-torus configuration allowed the toroidal mode structure of the $m = 1$ instability to be measured. It follows the theory with a cutoff minimum wavelength of about 4 meters. No $m = 2$ or higher m instabilities were observed. These results were reported at the 1974 IAEA Fusion Conference in Tokyo.

Since the Tokyo Conference the main attention of the Scyllac group has been to closing the gap between the plasma dynamics of the instabilities and the current risetime (gain-bandwidth) characteristic of the feedback circuit (see Chapter III below). By lengthening the $l = 1,0$ wavelength to 63 cm and decreasing the compression field to 18 kG the growth rate has decreased to 0.3 MHz in accord with theory. The plasma confinement time has been correspondingly increased from 10 to 25 μsec. Improvements in the feedback circuit have decreased its risetime from 1.5 to 1.1 μsec and raised its current capability from 700 to 1100 A. At this writing manipulation of the plasma column by programmed currents in $l = 0$ feedback coils is proceeding to test the theoretical finding that the plasma response will be excessive. $l = 2$ feedback coils are being electrically tested and will probably be used, since they have the virtue of instantaneous plasma response and produce three to four times greater force on the plasma. With the new plasma characteristics, improved circuit response and $l = 2$ coils, we are cautiously optimistic that the next year will see the purpose of Scyllac accomplished—the production of plasmas with staged heating and low compression ratios ($b/a \approx 2.5$) appropriate for wall stabilization of the $m = 1$ mode. Much significant new technology of high-voltage, high-charge capability, low-inductance spark gaps have been developed for this experiment.

A capability of conventional, long linear theta pinches is being restored with the nearing completion of the 5-meter Scylla IV-P experiment.

In the case of the Scylla I-B and I-C experiments, detailed studies of the plasma implosion were completed and the device has been rebuilt for lower-temperature, higher density plasma operation appropriate to heating and scattering experiments using a 100-J, 4×10^{10} W/cm^2 CO_2 laser furnished by Group L-1.

The implosion-heating experiment (Chapter VII) has been in operation for some months after successfully overcoming numerous problems of high-voltage technology. The data are yielding a consistent picture of the implosion process.

In the ZT-1 diffuse toroidal pinch experiment, ion temperatures of 140 eV at confinement times of 10 μsec have been obtained. Detailed studies of magnetic-field structure show that stability is limited by diffusion of the poloidal and toroidal fields. A new configuration (ZT-S) with 50% larger minor radius and more closely matched poloidal and toroidal field risetimes is being set up to lengthen the confinement by raising the field-diffusion times. A parameter study of a Z-pinch fusion reactor has been made.

In the realm of plasma diagnostics HF-laser, side-on holography has been successfully applied to Scyllac, yielding results of primary importance. In addition the basic plasma-beta and coupled-cavity interferometer measurements have been computerized with large savings in data-reduction time. Two-dimensional displays of Thompson scattering data are being developed.

The Experimental Plasma Physics group continued to extend its studies of the electrical resistivity by utilizing the detailed information about the threshold for parametric instabilities or anomalous absorption that was obtained by them in previous years. A particularly important demonstration of these precision measurements is this group's recent observation that intense ac electric fields can produce a fundamental change in the electron-ion collision rate.

The Theoretical Physics Program has continued strong programs in magnetohydrodynamic (MHD) theory including diffuse plasma and field profiles, Vlasov analysis of stability properties of plasmas, and computer modeling of plasmas.

Engineering support of the CTR program includes mechanical design development of specialized electrical components, such as spark gaps, construction of new experiments, and engineering support of the major confinement devices.

Magnetic Energy Transfer and Storage (METS) studies are progressing in the areas of development of superconducting wire, high-current interrupters, and fabrication of a 300-kJ storage coil.

Fusion Technology and Reactor Design have continued in the areas of reactor system studies, neutronics data assessment, and insulator and structural alloy research and development of conceptual design of a Scyllac Fusion Test Reactor (SFTR).

II. SCYLLAC FULL TORUS EXPERIMENTS

E.L. Cantrell, W.R. Ellis, B.L. Freeman, K.B. Freese, H.W. Harris, F.C. Jahoda, R. Kristal, M.D. Machalek, J.R. McConnell, W.E. Quinn, A.S. Rawcliffe, R.E. Siemon

A. Introduction

The main objective of the Scyllac experiment is to study methods of producing stable high-beta plasma equilibria and confinement in a high-beta, stellarator, toroidal geometry. The long range goal is the development of a toroidal fusion reactor based on the theta-pinch principle. Preliminary Scyllac experiments[1] were performed in 5-m (R=2.4 m) and 8-m (R=4.0 m) toroidal sectors to study the plasma equilibrium and stability and their scaling. The 5-m sector experiments, which demonstrated the existence of the high-beta, $\ell = 1,0$ toroidal equilibrium, were completed in 1972. Conversion to the Scyllac full torus with a major radius of 4.0 m began in early 1973 and was completed, including device checkout, in April 1974.

From April to November 1974, experimental confinement studies[2] on the Scyllac full torus were performed without the aid of the planned feedback system. The results on the full torus characterize the confined plasma by the following parameters: $\beta=0.8$; $a=1.0$ cm; $n=2.7\times10^{16}$ cm^{-3}; $T_e=500$ eV; $T_i=0.8$ keV; and $I_z=1.3$ kA. A toroidal helical plasma equilibrium is achieved as predicted by theory.[3,4,5] The stably confined plasma is terminated after 6 to 8 μs by an m=1 unstable motion of the column, whose properties are those of the theoretically predicted[6,7,8] m=1 instability and coincide with the observations on the 8-m sector experiment. Streak photographs give an m=1 instability growth rate of 0.7±0.3 MHz and indicate a toroidal mode structure in agreement with theory. Comparison of the measured plasma parameters and magnetic fields with MHD sharp-boundary theory confirm the plasma equilibrium and instability growth rate and their scaling.

The plasma exhibits an initial 6 to 8 μs stable phase during which equilibrium conditions are achieved. This stable period is consistent with the 8 to 10 μs plasma behavior observed in the studies performed in the toroidal sectors.[1] The equilibrium conditions for force balance along the major radius in the plane of the torus follow the predictions of the MHD theory to within ~5%. The unstable m=1 plasma motion follows the predictions of both the old-ordering[6,7] and Freidberg's generalized theory[8] to within 15% both in absolute value and the relative scaling of the growth rate from the 5- and 8-m sector experiments. Furthermore, conditions in both the sectors and the torus satisfied Freidberg's stabilization criterion for m=2 modes.[9] These studies provide no indication of higher order poloidal mode structure than m=1, supporting experimentally the validity of the finite gyroradius stabilization criteria.

Experimental evidence gives a strong indication that the unstable plasma motion lies in the plane of the torus. Theory predicts a toroidal mode structure for the m=1 instability with a cut-off at a minimum wavelength which is dependent on the major radius and the bending of the magnetic field lines. An analysis of the mode structure in Scyllac gives further credence to the theoretically predicted scaling of the absolute magnitude of the m=1 instability growth rates. Measurements of the toroidal mode numbers have been made up to 5, and the measurements reveal the theoretically expected fall-off of the unstable displacement amplitude past n=3. Theory also predicts that the maximum unstable mode number, n, which can exist in the Scyllac torus is 6.

Toroidal currents exhibiting peak values as high as 1.3 kA have been observed in the Scyllac discharges. Currents of this magnitude exceed the Kruskal-Shafranov limit for Scyllac, but apparently do not influence the plasma stability on the available time scales. This conclusion is based on the experimental observations that the unstable plasma motion is predominantly planar, whereas kink modes would produce plasma motion out of the plane, and the observed growth rates are a factor of 5 greater than the predicted values of the Kruskal-Shafranov kink-mode growth rates, whereas the measured values agree quite well with the theoretical m=1 growth rate. In addition, no observable difference in the plasma behavior results when the net toroidal current is reduced to zero or even reversed by an externally induced counter current.

The major divergence of the observed plasma behavior from theoretical predictions is in the period of quiescent equilibrium in the initial stages of the discharge. Sharp-boundary MHD theory of an overcompressed toroidally-structured $\ell = 1$ or $\ell = 0$ plasma predicts the onset of the instability at the initiation of the discharge. The dispersion relation,[5] derived in sharp-boundary theory, and even the generalized treatment of Freidberg[8] for overcompressed plasmas, shows that destabilizing terms due to the helical and bumpy plasma distortions dominate the wall-stabilization term. According to MHD predictions, the plasma should move toward the walls immediately with the e-folding time exhibited in the experiments. This experimental observation of stable plasma confinement, although not completely understood, gives an encouraging indication that high-beta toroidal equilibrium can be achieved and maintained.

The Scyllac full torus experiments, including a brief summary of the theory, the experimental arrangements, and the results, are presented below. The preparations for the feedback stabilization of the m = 1 instability on Scyllac are presented in Section III.

B. Summary of Scyllac Theory

The fundamental idea behind Scyllac is to bend a theta pinch into a toroidal configuration as nearly similar to a linear theta pinch as possible, in order to retain the advantages of the straight geometry, i.e., neutral stability and a proven method of plasma heating, while eliminating particle end loss. In Scyllac a high-β toroidal equilibrium is achieved by superimposing a small $\ell = 1$ helical field and a small $\ell = 0$ axisymmetric bumpy field on the main toroidal theta-pinch field,[3,4,5,6,7] where ℓ describes the perturbation fields which vary as sine ($\ell\theta$ - hz). This $\ell = 1,0$ configuration has the advantage that to leading order in the helical field quantities the plasma column is stable to the m = 1 mode, which has an exp(imθ) dependence. In the theoretical sharp-boundary model, the equilibrium is described by a constant-pressure plasma contained by currents flowing only on its surface.

1. Equilibrium. In the Scyllac torus the combination of plasma pressure and the gradient of the main compression field B_0 results in the outward toroidal drift force per unit length of the plasma column given by

$$F_R = \beta B_0^2/4R, \qquad (1)$$

where R is the major radius, a is the plasma radius and β is the ratio of plasma pressure to the external magnetic-field pressure. The super-position of the small $\ell = 1$ and $\ell = 0$ fields on the main theta-pinch field produces first-order distortions in the plasma surface of the form

$$r = a[1 + \delta_1 \cos(\theta - hz) - \delta_0 \cos hz], \qquad (2)$$

where $h = 2\pi/\lambda$ is the common $\ell = 1$ and $\ell = 0$ wavenumber, z is the toroidal coordinate and θ is the azimuthal coordinate. Figure II-1 shows a perspective view of the plasma column in its helically shifted equilibrium position, together with the right-handed coordinate system used.

The plasma column distortions δ_1 and δ_0 are related to the applied fields by

$$\delta_1 = \frac{I_1'(\varepsilon)}{\varepsilon}\left[\frac{2B_{\ell=1}/B_0}{1+\varepsilon\beta I_1(\varepsilon)K_1'(\varepsilon)}\right] \approx \frac{B_{\ell=1}/B_0}{\varepsilon(1-\beta/2)}\ , \qquad (3)$$

and

$$\delta_0 = \frac{I_0'(\varepsilon)}{\varepsilon}\left[\frac{B_{\ell=0}/B_0}{1+\varepsilon\beta I_0(\varepsilon)K_0'(\varepsilon)}\right] \approx \frac{B_{\ell=0}/B_0}{2(1-\beta)} \qquad (4)$$

where I and K are the modified Bessel functions and $\epsilon = ha$. The applied field ratios, $B_{\ell=1}/B_0$ and $B_{=0}/B_0$, are defined as coefficients in the expression for the vacuum magnetic field,

$$\bar{B}/B_0 = \hat{e}_z\left(1 - \frac{r}{R}\cos\theta\right) + \nabla\phi \qquad (5)$$

where $\hat{e}_z$ is a unit vector in the direction of the minor toroidal axis, and ϕ is the vacuum magnetic scalar potential:

$$\phi = (B_{=1}/B_0)\,[2I_1(hr)/h]\,\sin(\theta - hz) + (B_{=0}/B_0)\,[I_0(hr)/h]\,\sin hz + (B_v/B_0)r\,\sin\theta + (B_{1,2}/B_0)[I_1(2hr)/h]\sin(\theta - 2hz). \qquad (6)$$

The two small components, B_v, and $B_{1,2}$ (B_v is a vertical field, perpendicular to the plasma of the torus, and $B_{1,2}$ is a helical field with twice the periodicity of the main $\ell = 1$ field) are required theoretically,[3] to produce vacuum flux surfaces which are centered on the torus minor axis. Their theoretical amplitude is

$$B_v/B_0 = B_{1,2}/B_0 = B_{\ell=1}B_{\ell=0}/4B_0^2. \qquad (7)$$

The asymmetry in the sum of the impressed plasma excursions δ_1 and δ_0 results in the Z-independent equilibrating force

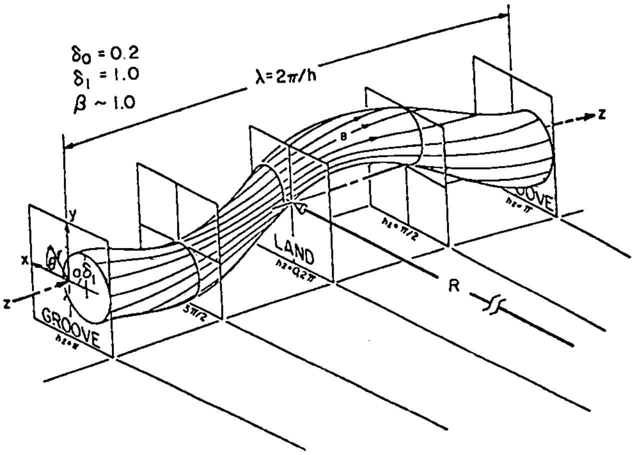

Fig. II-1
Perspective view of the =1 helical and =0 bumpy, high-β plasma column in the Scyllac toroidal equilibrium configuration.

$$F_{1,0} = h^2 a^3 \beta B_o^2 [1 + (1 - \beta) I_o(\varepsilon)/I_1'(\varepsilon)] \delta_1 \delta_o / 8 \qquad (8)$$

Equating the outward toroidal force F_r to the $F_{1,0}$ force gives the toroidal equilibrium condition,

$$\delta_1 \delta_0 = 2/h^2 aR\,[1 + (1 - \beta) I_o(\epsilon)/I'_1(\epsilon)] \approx 2/(3 - 2\beta) h^2 aR. \qquad (9)$$

The amplitudes of the $\ell = 1,0$ equilibrium fields, $B_{\ell=1} B_o$ and $B_{\ell=0}/B_o$, are determined by this equilibrium relation. Figure II-2 shows graphs of the $F_{1,0}/F_R$ force ratio, from Eqs. (8) and (1), as a function of the plasma β for various plasma radii.

2. Stability. Although MHD theory shows that the leading order $m=1$ destabilizing term vanishes for the $\ell = 1,0$ equilibrium system, higher order terms indicate the plasma column is unstable to displacements of the form $\xi(n) = \xi_0 \exp i(m\theta - nz/R)$.[5] The instability growth rate $\gamma(n)$ is given by[4]

$$\gamma^2(n) = \gamma^2(o) - v_A^2 (2-\beta) n^2/R^2, \qquad (10)$$

Alfvén speed, and the growth rate $\gamma(o)$ of the fundamental mode is given by[4,8]

$$\gamma^2(o) = h^2 v_A^2 \left[-\beta^2 \left(\frac{a}{b}\right)^4 \delta_1^2 + \frac{\beta(4-3\beta)(2-\beta)}{8(1-\beta)} h^2 a^2 \delta_1^2 + \frac{\beta(3-2\beta)(1-\beta)}{(2-\beta)} \delta_o^2 \right] . \qquad (11)$$

The first term in Eq. (11) is a dipole wall-stabilization term due to the induced $\ell = 1$ plasma currents. However, because of the strong fourth-power dependence on the ratio of plasma radius to wall, a/b, this term is negligible in the present Scyllac experiments. The second term in Eq. (11) represents a weak instability driven by the $\ell = 1$ field and the last term an instability driven by the $\ell = 0$ field.

The highest unstable mode, which has the minimum toroidal wavelength, is given by the maximum n value in Eq. (10) for which $\gamma(n)$ is real. Setting $\gamma(n) = 0$ gives

$$n_{max} = \frac{R}{(2-\beta)^{1/2}} \frac{\gamma(o)}{v_A} . \qquad (12)$$

C. Experimental Arrangement. The Scyllac torus has a major radius of 4.0 m and a circumference of 25.13 m. The compression coil, whose inner surface is shaped to generate the $\ell = 1$ helical and $\ell = 0$ bumpy equilibrium fields, has an average bore of 14.2 cm. The toroidal quartz discharge tube has an inside diameter of 88 mm. The primary energy storage system consists of a 10.5-MJ capacitor bank of 3,150 1.85-μF, 60-kV capacitors. The energy storage system and the compression coil are divided into 15 independent sections termed racks. The fifteen energy storage racks are symmetrically arranged around the central torus and are tangent to the walls of the experimental area at four points. A three-level platform structure fills the central core of the torus. The upper or coil level is situated 7.6 m above the basement floor and 1.3 m below the horizontal plane of the torus. A photograph of the torus is shown in Fig. II-3.

Each rack of the Scyllac energy storage system feeds a single collector plate assembly which in turn feeds a 1.67-m arc-length of the toroidal compression coil termed a coil-sector. Each of the fifteen collector plates are cabled with 1,260 coaxial load cables from the 210 capacitor-spark gap units of the main bank in one rack and with 24 cables from the two 0.7-μF capacitors of the preionization bank. Figure II-4 shows a plan view of the torus with its collector plate current feeds and the various diagnostic viewing slots in the coil-sectors.

1. Parameters of the Scyllac Torus. The electrical and mechanical parameters of the Scyllac full torus are listed in Table I. These are discussed further in Section XI.

$$\frac{F_{1,0}}{F_R}=\frac{R}{a}\,I_1'(\epsilon)I_0'(\epsilon)\left[1+(1-\beta)\,I_0(\epsilon)/I_1'(\epsilon)\right]\left[1/\{1+\epsilon\beta I_1(\epsilon)K_1'(\epsilon)\}\right]\left[1/\{1+\epsilon\beta I_0(\epsilon)K_0'(\epsilon)\}\right]\frac{B_{\ell=0}B_{\ell=1}}{B_0^2}$$

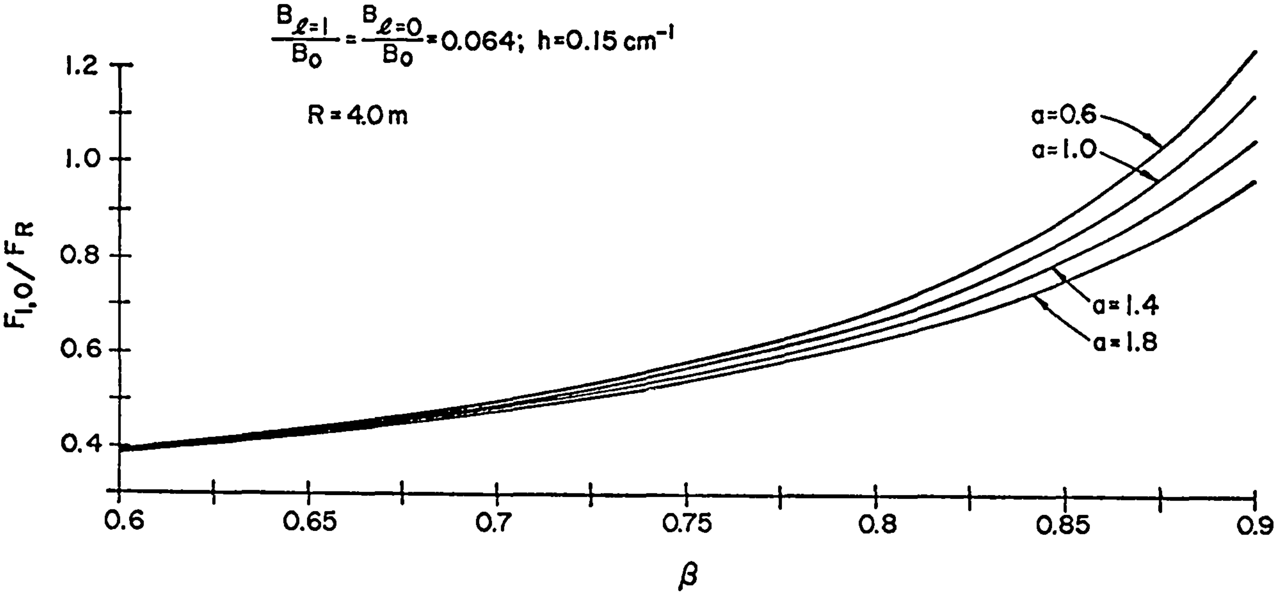

Fig. II-2
Ratio of the $F_{1,0}$ equilibrium force to the outward toroidal force F_R as a function of the plasma β for various plasma radii a and the indicated Scyllac parameters.

2. Scyllac Control and Monitor Systems. The Scyllac control system includes the monitoring of the various bank voltages during the charge phase by the Scyllac computer which has an abort control over the overall system.

A spark-gap monitor system based on magnetic probes is used to monitor the firing times of the main bank start gaps, the crowbar trigger gaps, and the crowbar' gaps. This function assists in the maintenance and trouble-shooting of the 6800 spark gap switches in the Scyllac energy storage system.

3. $\ell=1,0$ Toroidal Equilibrium Fields. The experiments on the 8-m toroidal sector resulted in a choice of 41.9 cm for the $\ell=1$ and $\ell=0$ wavelength and equilibrium plasma column excursions of $\delta_1=0.71$ and $\delta_0=0.21$ for the full torus. The magnitudes of the $\ell=1$ helical and the $\ell=0$ bumpy fields were determined through the toroidal equilibrium condition, Eq. (9), and the expressions for the plasma distortions, Eqs. (3) and (4), to be: $(B_{\ell=1}/B_0) = (B_{\ell=0}/B_0 = 0.064$ and $(B_v/B_0) = B_{1,2}/B_0) = 0.001024$.

4. $\ell=1,0$ Shaped Compression Coil. The compression coil, whose inner surface was shaped to generate the $\ell=1$ and $\ell=0$ equilibrium fields, was designed by calculating the shape of the magnetic flux surfaces for the required vacuum fields given by Eqs. (5) and (6). Figure II-5 shows plots of the flux surfaces at four z positions: hz=0, center of a land region where B_z is a maximum; hz=π/2, between a land and groove region; hz=π, center of a groove region where B_z is a minimum; and hz=3π/2, between a groove and land region. The annular cross-hatched areas of Fig. II-5 indicate the location of the quartz discharge tube. The outer flux surfaces give the coil-bore cross sections at the indicated Z positions.

Figure II-5 shows that the inner flux surfaces are circular in cross section and as a set are centered about the minor axis of the torus. The helical shift of the flux surfaces about the minor axis is produced by the $\ell=1$ field. Magnetic probe results obtained on the toroidal minor axis in the shaped compression coil show that the $\ell=1$ and $\ell=0$ fields are in agreement with the design values.

5. Toroidal Discharge Tube and Pump-Out Ports. The discharge tube for the 8-m diameter torus consisted of 10 quartz tube sections, each with an arc length of 2.5 m. These quartz sections were joined by O-ring seals to short ceramic sections of 99% alumina, which had an oval shaped pump-out

TABLE II-I

SCYLLAC FULL TORUS PARAMETERS

PARAMETER	VALUE
Preionization Bank	
Bank capacitance	21 μF
Bank operating voltage	50 kV
Bank energy storage	26 kJ
Ringing frequency	400 kHz
Peak current	2.4 MA
Maximum magnetic field	1.2 kG
Primary Bank	
Bank capacitance	5828 μF
Bank voltage	60 kV
Bank energy storage	10.5 MJ
Normal operating voltage range	40-55 kV
Major radius	4.0 m
Torus circumference	25.13 m
Average coil bore radius	7.1 cm
Discharge tube wall radius	4.4 cm
Source inductance	0.17 nH
Coil inductance	0.80 nH
Transfer efficiency	0.82
Rise time	3.6 μs
L/R decay time	250 μs
Peak current (at 50 kV)	110 MA
Maximum magnetic field (at 50 kV)	55 kG
Azimuthal electric field (at 4.4 cm and 50 kV)	0.57 kV/cm
$\ell=1,0$ wavelength	41.89 cm
$\ell=1,0$ wavenumber	0.15 cm^{-1}
No. of $\ell=1,0$ wavelengths	60
$B_{\ell=1}/B_o = B_{\ell=0}/B_o$	0.064
$B_v/B_o = B_{1,2}/B_o$	0.001024

stub extending downward through the compression coil as shown in Fig. II-6. The wall of the cylindrical portion of the ceramic section was semi-continuous, being perforated with 10, 5-mm diameter holes above the pump-out stub. The objective in the design of the pump-out ports was to achieve sufficient pumping speed while minimizing perturbations in the magnetic field and in the initial plasma sheath formation.

The ceramic pump-out stubs terminated in a 9-cm diameter ceramic tube after partial penetration through the compression coil wall. The cylindrical ceramic tubes, which had a metal valve near the center of their 1-m length, provided appropriate voltage insulation. These tubes connected into a common toroidal manifold below the torus.

6. Magnetic Field Variations Between Coil-Rack Sections. In the toroidal geometry, it is important that the plasma have the same properties all around the torus, other than for variations within $\ell = 1,0$ wavelengths, in order to satisfy the requirements for toroidal plasma equilibrium. Since the parameters of the plasma are dependent on both the implosion and compression phases of the discharge, there has been concern about possible variations in the magnitude and waveforms of the magnetic field between coil sections.

The Scyllac energy storage system is divided into fifteen capacitor racks. As mentioned above, each rack feeds a single collector-plate assembly which in turn drives a 1.67-m arc length of the 25-m compression coil. The racks are independent of each other except for conducting ties near the compression coil which have relatively high inductance and a common trigger source. Bank voltage variations were largely eliminated by connecting the charging supply systems together through 2-kΩ resistors to give an RC time of 0.4 s between adjacent capacitor racks.

Field variations of ~0.5% can result from variations in the resistance of the liquid resistors used to isolate various sections of the capacitor bank. Variations in the crowbar trigger system and in the crowbar spark gaps can also produce significant differences in the magnetic field during the crowbarred phase of the discharge.

7. Magnetic Field Measurements. Magnetic field measurements were made around the torus to determine if significant field variations existed from coil-sector to coil-sector. This was accomplished after the power supplies were connected together as described above.

Measurements were made with a standard B_z probe, RC integrator, and oscilloscope. The standard probe was moved from coil-sector to coil-sector while fixed probes were maintained to record shot-to-shot variations. To assure reproducibility, the output of the standard probe versus penetration depth into the coil was investigated. It was found the probe could

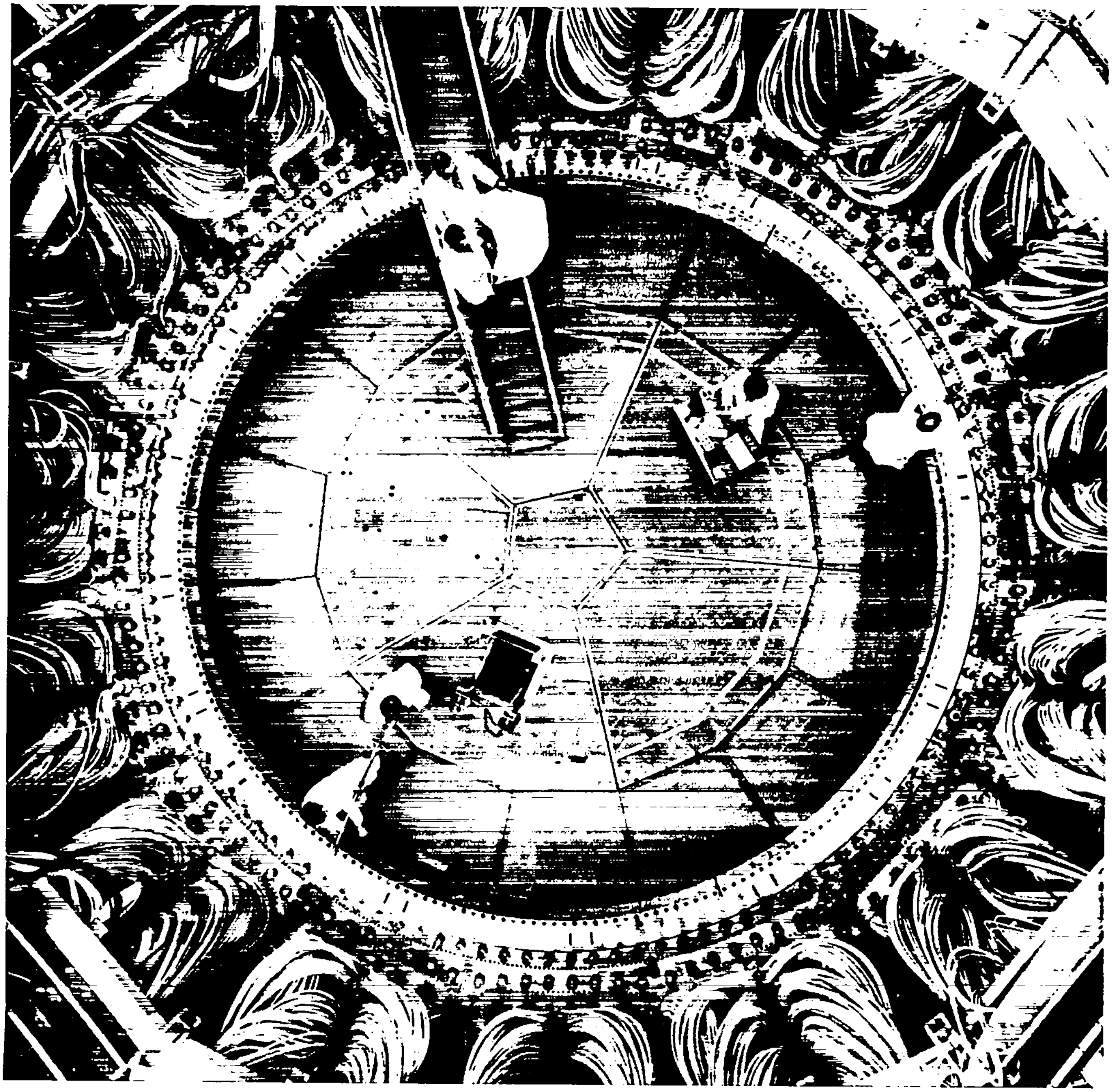

Fig. II-3
Photograph of the Scyllac full torus.

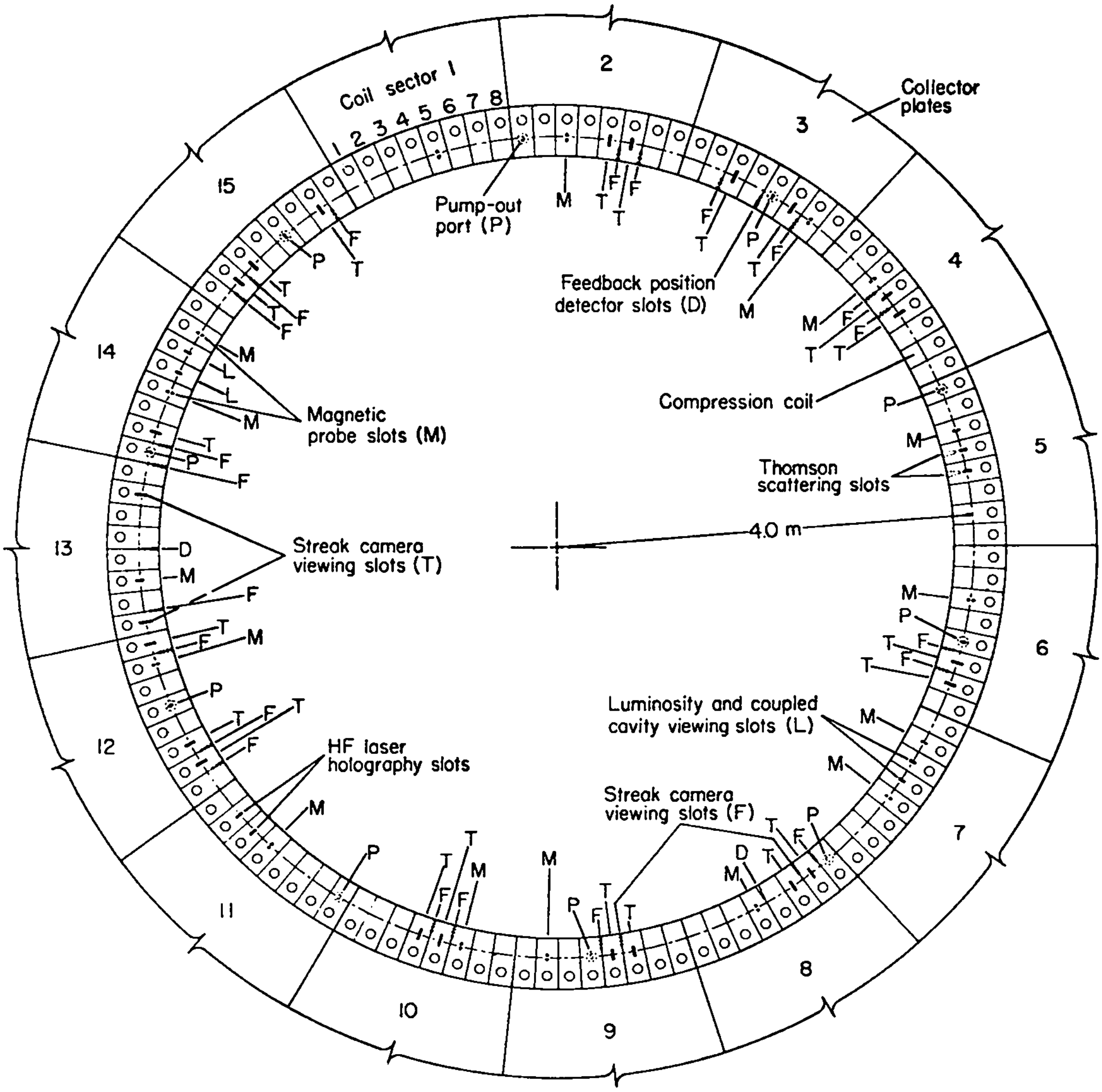

Fig. II-4

Plan view of the Scyllac torus showing the various diagnostic viewing slots, the vacuum pump-out ports and the collector plate current feeds.

be moved 6.5 mm with no measurable change in the groove regions in which measurements were made. Position was easily maintained within 2 mm for all measurements.

Comparative measurements of B_z were made at peak field and also in the crowbarred phase, 3.6 μs and 7 μs respectively, after firing the main bank. The results are shown in Fig. II-7 as a plot of $[B_z - (B_z)_{av}]/(B_z)_{av}$ as a function of coil-sector number. The variations at peak field time are larger than expected and are observed to further increase during the crowbarred phase.

The probe was positioned in one coil for 21 shots to obtain data on shot-to-shot variations resulting in $\pm 1\%$ at peak field and $\pm 2\%$ at 7 μs. The ratio of fields for each coil at peak field and at crowbar time should be the same for all coils, but it ranges from 0.77 to 0.84. The magnitude of the variations between coil-sectors, at peak field, with the power supplies connected together and with relatively large inductive ties between collector plates, suggests that in the coil-sectors with lower fields a fraction of the crowbar gaps are firing early and/or some of the start gaps are not triggering. The largest variations during

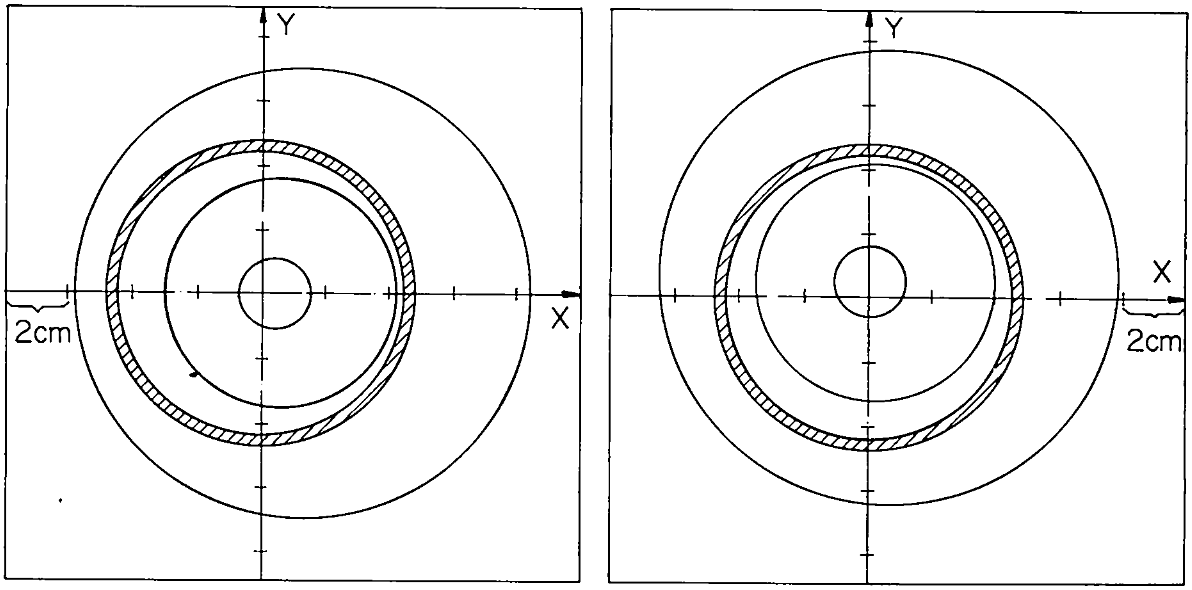

hz = 0 (Land)

hz = $\pi/2$

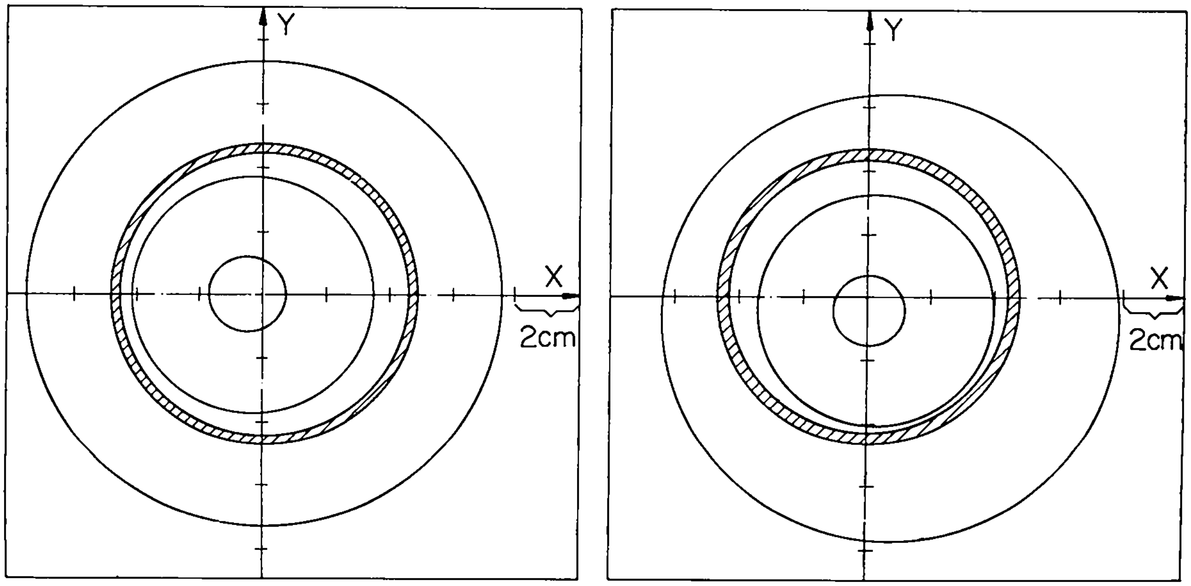

hz = π (Groove)

hz = $\frac{3\pi}{2}$

Fig. II-5

Plots of the vacuum magnetic flux surfaces generated by the shaped inner surface of the compression coil at four toroidal z positions. The annular cross-hatched areas indicated the discharge tube.

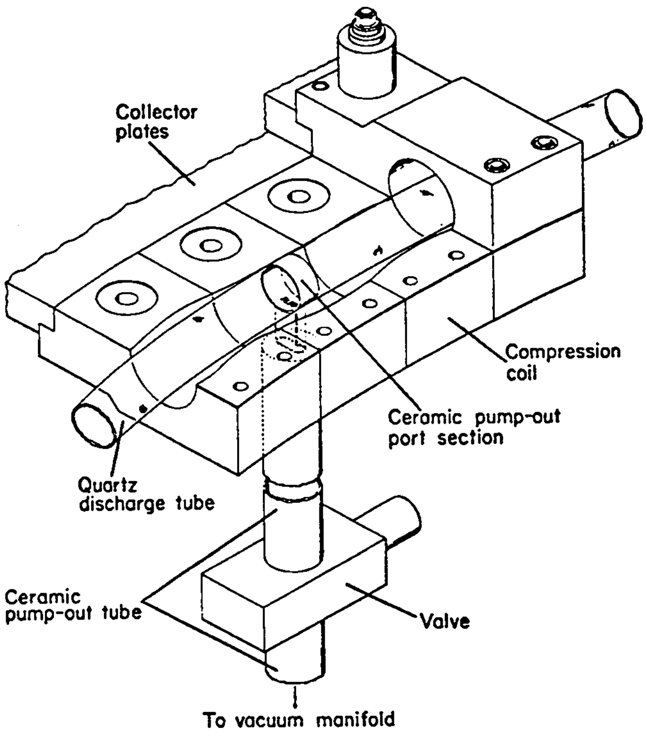

Fig. II-6
Perspective view of the discharge tube and vacuum pump-out port in the Scyllac compression coil.

the crow-barred phase occurred in the older capacitor racks (which have many more discharges on the gaps), indicating those gaps might be firing improperly due to wear. Data were not taken in coil-sectors 7 and 14 as excluded flux measurements were being made there.

8. Driven I_z-Current Arrangement. Two different arrangements have been used to induce an I_z current in the plasma column: (a) a single-turn loop around the inner face of the compression coil (~24-m circumference) was driven by a 14-μF, 10-kV capacitor to induce a plasma current of ~1.5 kA with a risetime of 15 μs; and (b) a fast-rising $I_z(\tau/4 \sim 2\ \mu s)$ was produced by breaking the single-turn loop into five sections and driving these in a parallel arrangement with a 1.85-μF, 60-kV capacitor. The fast I_z had a variable amplitude of 1 to 2 kA. Effective coupling of the I_z flux to the toroidal plasma column required the removal of electrical conducting ties between collector plates near the compression coil. New conducting ties were installed between collector plates approximately one meter back from the compression coil, which allowed an area of approximately 320 cm^2 between collector plates for coupling of the driven-I_z flux around the plasma column.

9. Plasma Diagnostic Apparatus. Figure II-4 shows a plan view of the torus with its various diagnostic viewing slots. The following measurements are being used to study the high-β toroidal plasma: (a) As many as seven high-speed streak cameras are used to record the transverse motions of the plasma column at various locations around the torus; (b) A coupled-cavity He-Ne laser interferometer is used to measure the time-history of the plasma electron density integrated along a chord of the plasma cross section. This diagnostic, which has a fully automated data acquisition system, is also used routinely for determining preionization levels during machine operation; (c) A ten-channel luminosity experiment provides self-luminous profiles of the plasma column. These luminosity profiles give the plasma radius and, in conjunction with the coupled-cavity interferometer data, give absolute density profiles; (d) A balanced magnetic loop and probe arrangement measures the magnetic flux excluded by the plasma column. Combined with the relative density profiles from the luminosity measurement, the excluded flux can be expressed in terms of the plasma β; (e) Scintillation and silver-foil activation counters measure the neutron emissions; and (f) Thomson scattering of laser light is used to determine the plasma electron temperature with a unique three-grating polychrometer.

Additional new diagnostics on the full torus include: (a) A side-on holographic interferometer gives spatially and time resolved absolute plasma electron density profiles. Radiation at 2.87 μm from a hydrogen-fluoride laser is used as the interferometer light source in order to maximize sensitivity with a wavelength transmittable through the quartz discharge tube; (b) Net toroidal currents are measured with an 81-turn Rogowski coil mounted around the quartz tube inside the theta-pinch compression coil. An extraneous component of B_z pickup is nulled-out in vacuum using a differencing circuit of the excluded flux, loop-probe type and a small B_z probe; and (c) A fast, 360° optical system on the torus main axis images eleven top coil slits in grooves, almost uniformly distributed around the torus, onto a single image-converter framing camera. This arrangement provides a determination, at one instant in time, of the toroidal mode structure of gross plasma column displacement away from the discharge tube axis.

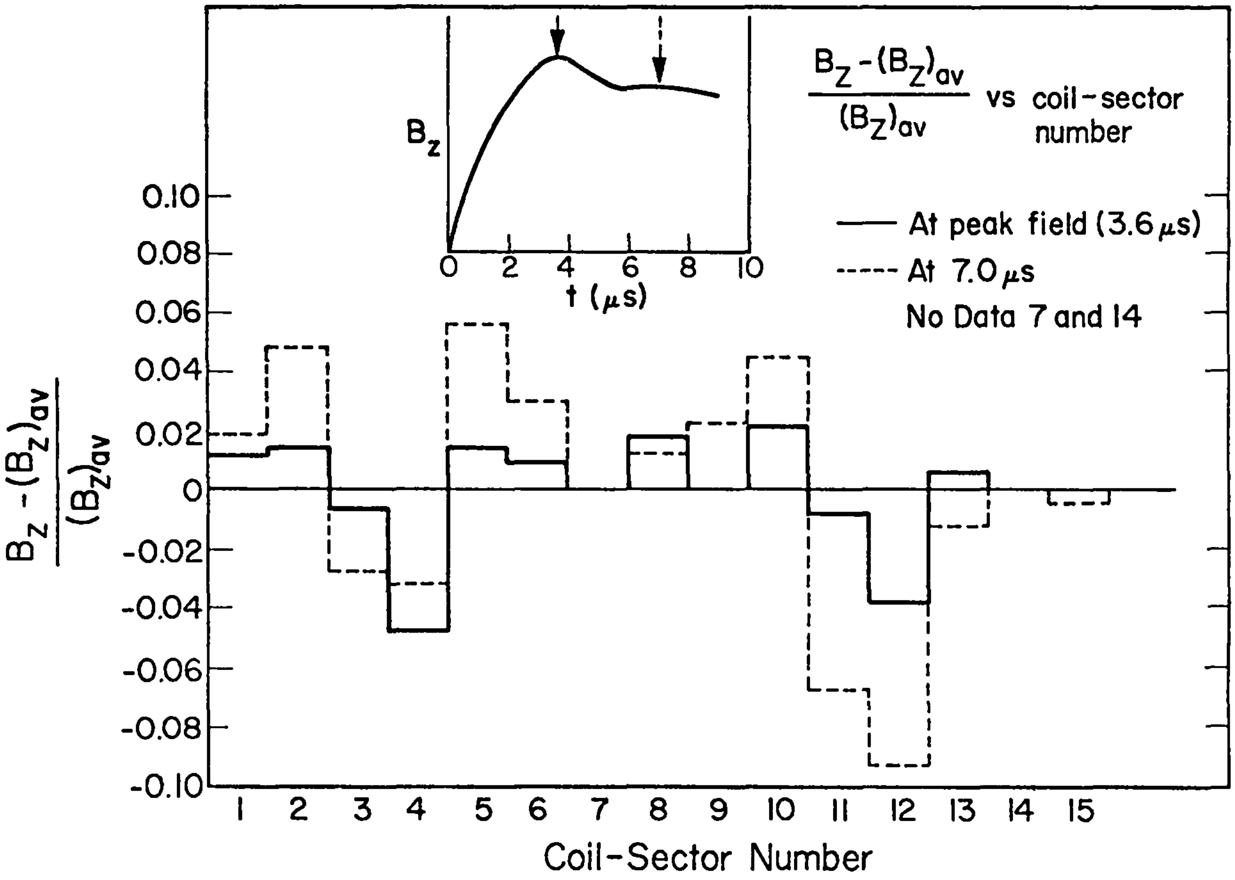

Fig. II-7
Graphs of magnetic field variations around the torus as a function of coil-sector number at peak field time (3.6 μs) and during the crowbar phase (7.0 μs).

D. Plasma Measurements and Parameters.

The plasma parameters in the Scyllac full torus experiment with the bank operating at 40 kV ($B_0 \approx 40$ kG) are summarized in Table II-2.

The plasma radius was determined from the luminosity profiles (*cf.* section E2) and confirmed by absolute profile measurements in the groove regions with the side-on, HF-laser, holographic interferometer (*cf.* Sections II-F-5 and IX-B-1). The plasma beta on axis was determined from the combined excluded flux and luminosity profile measurements (*cf.* Section II-E-2). The plasma density was derived independently from (a) the coupled-cavity interferometer measurements (*cf.* Sec. IX-C-3) and (b) the side-on HF interferometer measurements (*cf.* Sections II-F-5 and IX-B-1). The total plasma temperature ($T = T_e + T_i$) was calculated from pressure balance using the plasma beta, density, and magnetic field measurements.

TABLE II-2

FULL-TORUS PLASMA PARAMETERS

Radius (a)	~1.0 cm
Beta (β)	~0.8
Density (n)	2.5–2.8×10^{16} cm^{-3}
Temperature (T)	1.2–1.4 keV
T_e	0.5–0.6 keV
T_i	0.7–0.8 keV
Neutron emissions	~10^5/cm
δ_1	~0.71
δ_o	~0.16
I_z	1.0–1.5 kA
γ(o)	0.7 ± 0.3 MHz

The electron temperature was determined from 90° Thomson scattering (*cf.* Section II-F-3) and the ion temperature is inferred from $T_i = T - T_e$. The neutron emissions were measured by the Ag activation counters.

The δ_l and δ_0 values in the table were calculated from Eqs. (3) and (4) using measured values of β and a, and design values of $B_{\ell=1}/B_0$ and $B_{\ell=0}/B_0$ (Table II-1). The luminosity profile data, by contrast, provided a direct measurement of δ_0 : $\delta_0 = (a_G - a_L)/(a_G + a_L) \approx 0.22$ (see Fig. II-9).

The axial current I_z was measured by the Rogowski loop (*cf.* Section II-F-4). The m = 1 growth rate was determined by fitting an exponential curve to the plasma column trajectories from the streak photographs.

1. Plasma Beta Measurements. Measurements of the plasma "beta parameters" (excluded flux and external magnetic field from the loop-probe system and plasma radius from the luminosity apparatus) have been made, and these data have been combined to yield the plasma beta on axis[1] as a function of time in the Scyllac full torus experiments. In order to compare measurements with theory, the beta parameters should be measured in both land and groove positions (axial positions of maximum and minimum magnetic field, respectively, *cf.* Fig. II-1). In contrast to the sector experiments, however, which required measurements to be made essentially in one restricted place, namely near the center of the sector, in the full torus there were 60 nominally identical $\ell = 1,0$ wavelengths available for study. In order for plasma measurements at one or two locations to be valid for "global" equilibrium studies involving the entire plasma ring, it was necessary to establish that land positions around the torus were indistinguishable from one another, and similarly for grooves.

In order to test this hypothesis, simultaneous measurements of the beta parameters were made on roughly diametrically-opposite sides of the torus, in racks 7 and 14 (see Fig. II-4). Typical results for the "raw data" are shown in Fig. II-8, all obtained in this case from a groove in rack 7. Data from four nominally identical discharges (12-15 mtorr D_2 filling pressure and 40-kV charging voltage) taken close together in time have been superimposed in Fig. II-8 to illustrate normal shot-to-shot data scatter. The reproducibility of the data is seen to be good, allowing meaningful coverages to be obtained. Figure II-9 compares average data curves derived in this fashion from land and groove positions in racks 7 and 14. Data curves derived from Fig. II-8 appear in Fig. II-9 as the solid curves labeled "G". A series of such data sets have been analyzed, and they reveal the following general characteristics: (a) there is little or no systematic difference between equivalent positions on opposite sides of the torus; (b) land positions and groove positions on opposite sides of the torus are equally reproducible in this regard, within experimental error; (c) land data differs from groove data in significant and characteristic ways, these differences being much larger than either shot-to-shot variations in a given location, or opposite effects in a given location. Data from racks 7 and 14, such as represented in Fig. II-9, have therefore been used with confidence to analyze the characteristics of the plasma equilibrium in the Scyllac full torus. Further discussion of these parameters is given in Sec. II-E-2.

2. HF Interferometry

a. Measurements. A technique has been developed for side-on holographic interferometry of Scyllac at 2.9-μm wavelength using an HF laser. The method is described in Section IX-B. The background or reference fringe pattern is arranged with straight fringes perpendicular to the plasma column with the laser beam passing through the plasma perpendicular to the plane of the torus.

A typical data interferogram is shown in Fig. II-10. The several fringes shown provide a redundant measurement of the electron density profile. This results from the fact that the viewing slit in the compression coil (1.5-cm width) is only a small fraction (4%) of the $\ell = 1,0$ wavelength (41.9 cm), and the variation in plasma position and profile is therefore negligible across the slit width. Averaging the nominally identical fringes together helps to improve the fringe resolution.

An analysis of the fringe data vs position is also shown in Fig. II-10. The solid line, labeled "data", is a free-hand average of several fringes. The peak fringe shift is ~0.8, corresponding to a particle area density of 6×10^{16} cm^{-2} and a peak number density on axis of 3×10^{16} cm^{-3}.

For comparison a Gaussian profile is also shown, with the same peak and 1/e point as the data curve. The data appear to be somewhat less diffuse than Gaussian, although the Gaussian fit is everywhere better than 0.1 fringe. In either case, the plasma radius (1/e point) is about 1 cm (at 3.1 μs in a groove region). A comparison of plasma radius determined from holographic profiles (e.g., Fig. II-10) and from conventional luminosity profiles (e.g., Fig. II-9) has been made. Agreement in 1/e point obtained by the two methods (at the time of the holographic exposure) is better than 5%.

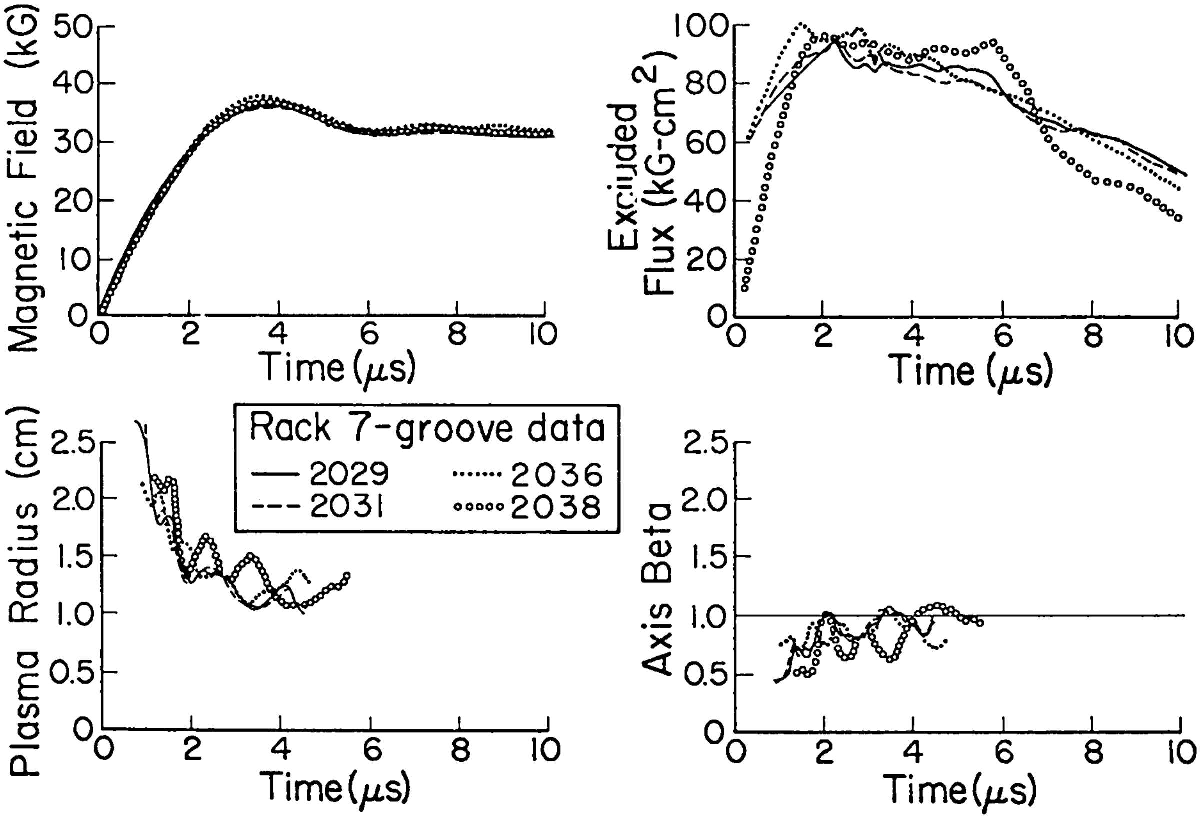

Fig. II-8
Observed time variations of the magnetic field, excluded magnetic flux, plasma radius from luminosity profiles, and computed plasma β on axis in a groove region of coil-sector No. 7.

For the analysis of the luminosity data, a Gaussian profile is nearly always assumed. Inversion to radial coordinates then yields a Gaussian of the same radius. Figure II-11 shows the result of fitting both a Gaussian and a $\beta=1$ rigid-rotor profile to the Abel-inverted side-on interferometry data. It appears that a high-β rigid-rotor profile is a better fit to the data than a Gaussian for the conditions of this discharge (Groove Region, 3.1 μs). No data were obtained in a land position due to the lack of an appropriate viewing window (see Section IX-B).

b. Line Density Analysis. The plasma line density results from integrating over the density profile. Comparison of the side-on interferometry data with the initial deuterium filling density indicates that most of the plasma resides in a groove region. This observation is supported by the "enhanced" δ_0 measurements derived from the luminosity radius (*cf.* Sec. II-D). The measured line density from the data curve in Fig. II-10, for example, is $\sim 1.2\times 10^{17}\text{cm}^{-1}$. The expected line density can also be computed from the known filling density. If we assume a plasma density n which is uniform in z and a plasma radius given by $r=a(1-\delta_0 \cos hz)$ [Eq. (2)], the average line density $\bar{N}$ over a complete wavelength should be

$$\bar{N}=n\pi a^2(1+\delta_0^2/2) \qquad (13)$$

whereas the line density N_G in a groove should be

$$N_G=n\pi a^2\,(1+\delta_0)^2. \qquad (14)$$

Equating $\bar{N}$ to $n_0\pi b^2$ where n_0 is the atom filling density and b is the tube radius, gives,

$$N_G\;=n_0\pi b^2(1+\delta_0)^2/(1+\delta_0^2/2). \qquad (15)$$

Using the luminosity-measured δ_0 of 0.22 and a filling pressure of 15 mtorr ($n_0=1.1\times 10^{15}\ \text{cm}^{-3}$), Eq. (15) gives $N_G=9.7\times 10^{16}\text{cm}^{-1}$, vs the measured value of $\sim 1.2\times 10^{17}\text{cm}^{-1}$ from Fig. II-10. Thus the observed line density in a groove is ~25% larger than a uniform plasma density would imply. A 25% excess of particles in a groove would imply a ~60% deficit

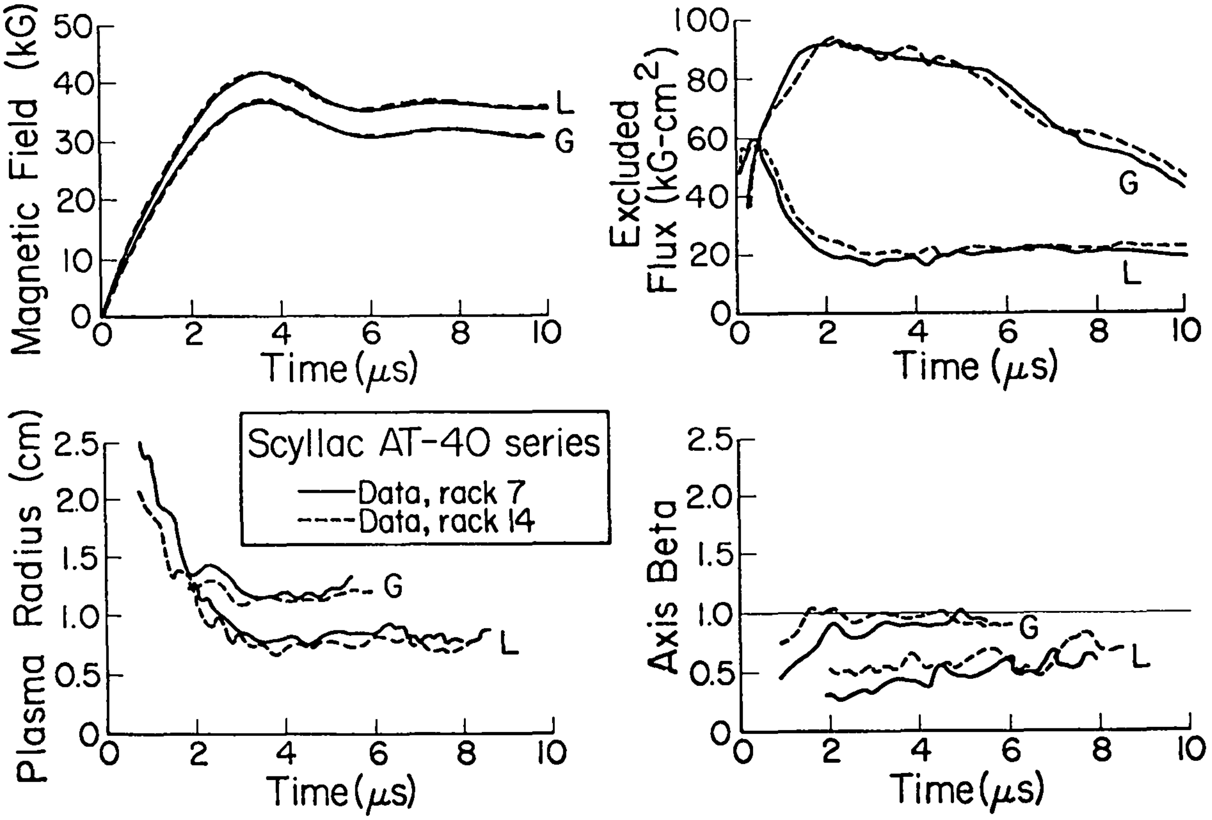

Fig. II-9

Observed time variations of the magnetic field, excluded magnetic flux, plasma radius from luminosity profiles, and computed plasma β on axis in groove and land regions of coil-sector Nos. 7 and 14.

of particles in a land due to the ratio of areas, $(1+\delta_0)^2/(1-\delta_0)^2$, corresponding to a density differential of a factor of ~3. As mentioned above, no line density measurements in a land position were made. If such a large density gradient does exist, it could create transient longitudinal particle flows possibly affecting both the plasma equilibrium and stability. In fact the comparison of the plasma β data with theory (Section II-E-2) indicates that an axial pressure readjustment occurs between land and groove regions, which corresponds to a net transfer of energy density from grooves to lands during the first few microseconds of the discharge.

3. Electron Temperature. The electron temperature was measured by Thomson scattering using a special polychrometer to reject stray light.[10] A 10-J, 30-ns Q-switched ruby laser beam was passed side-on through the 8-mm-diameter quartz discharge tube without special entrance and exit ports and focused at the center of the plasma column. The plasma luminosity was comparable in intensity to the scattered signal, and fluctuations in the luminosity were the limiting noise sources in the experiment. Seven channels recorded the intensity of the Thomson-scattered laser light. The spectral width of each channel was made progressively wider as the separation from the incident wavelength increased. The fitting of the data to a Gaussian, taking into account the spectral widths of the detector channels and corrections for relativistic effects, gave plasma electron temperatures in the range of 500 to 600 eV, with T_e having the same value in land and groove positions within experimental error. Measurements were made at the time of peak field.

4. Integrated Neutron Measurements. Fifteen LASL Ag activation detectors[11] were installed on the Scyllac torus and calibrated with a known source, PuBe (2.23×10^6n/sec), *in situ*. These detectors use Victoreen 1B85 Thyrode counter tubes for the active element in the electronic circuit.

Integrated neutron-yield information was obtained for each of the fifteen Scyllac coil-sectors on

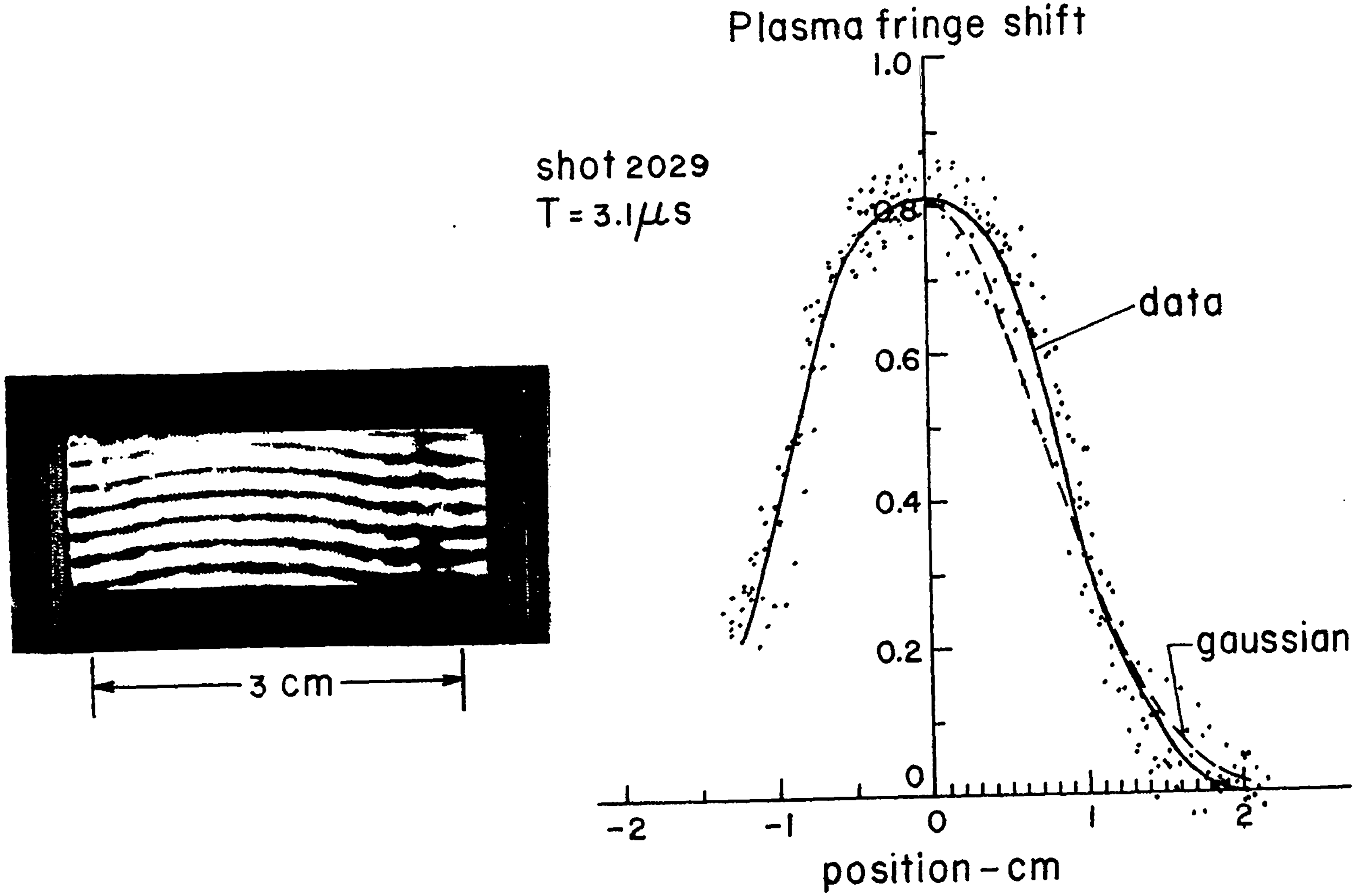

Fig. II-10
Left, side-on HF laser holographic interferogram (λ= 2.87 μm), Δ=100 ns) of plasma offset from tube center in a groove region. Each fringe yields a nominally identical profile. Right, averaged plasma profile, indicating ~0.1 fringe (∫ndl= 7×10^{15} cm^{-2} resolution.

Inverted profile

Gaussian fit

Rigid Rotor fit,
beta=1

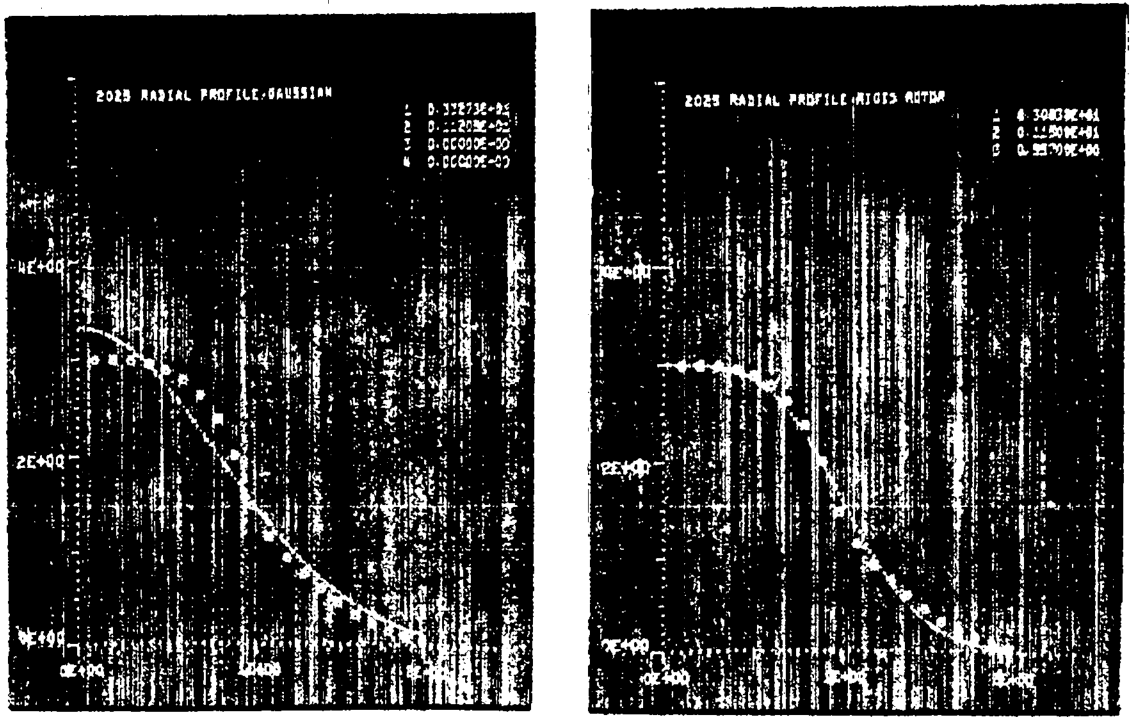

Fig. II-11
Plots of the best fits of a Gaussian (left) and a $\beta = 1$ *rigid rotor profile (right) to the Abel-inverted side-on interferometry data of Fig. II-10.*

each discharge. An average of 1.33×10^7 neutrons per detector was measured in a series of thirty-five 40-kV discharges. It is estimated that each detector observed approximately one meter of the plasma column, implying a neutron yield of $\sim1.3\times10^5$ n/cm. Even though the various detectors around the torus had different relative locations with respect to lands and grooves, no differences in neutron yield due to this geometric effect were observed, probably due to the relatively long length of plasma column being observed. Average results from three different series of discharges, thirty-five discharges at bank voltage of 40 kV, eight discharges at 45 kV, and eight discharges at 40 kV after the 45-kV series, are displayed in Fig. II-12. In all three series, coil-sectors 5 and 3 were consistently the highest neutron-producing racks. On the average, coil-sectors 11 through 15 produced lower yields than coil-sectors 1 through 10. In the 45-kV series, the smallest variation in yield around the torus was observed.

E. Plasma Equilibrium and Stability

In the experiments on the full torus the $\ell = 1$ and $\ell = 0$ equilibrium fields were generated by shaping the inner surface of the compression coil. The plasma equilibrium was achieved by adjusting the initial deuterium filling pressure to give a balance between the $F_{1,0}$ force [Eq. (8)] and the outward toroidal force F_R[Eq. (1)] through their β dependence, as shown in Fig. II-2. With the main energy-storage bank operating at 40 kV [B_0=40 kG], the plasma equilibrium was achieved with a deuterium filling pressure in the range of 9 to 14 mtorr. It was observed experimentally that the force ratio $F_{1,0}/F_R$ decreases with increasing filling pressure in the range of 8 to 100 mtorr. Since $F_{1,0}/F_R$ increases with β (Fig. II-2), this implies that β decreases with increasing pressure over this range.

1. Transverse Plasma Motions. The streak photographs of Fig. II-13 show transverse plasma motions in the full torus. The top views show the plasma motions in the plane of the torus in two groove regions as indicated. The front views show the motion in the vertical plane between land and groove regions. Figure II-14 compares streak photographs taken in the full torus with those of the 8-m sector. In both the sector and the full torus, the plasma forms a well defined column, comes into an equilibrium position, and the stable confinement is terminated by an m=1 sideward motion of the column to the wall. The terminating motion generally occurs in the horizontal plane of the torus. The general plasma behavior is similar to the behavior in previous sector experiments except that the observed m=1 motions appear to have a toroidal mode structure, i.e., a Fourier decomposition into various wavelengths (k > 0) around the torus.

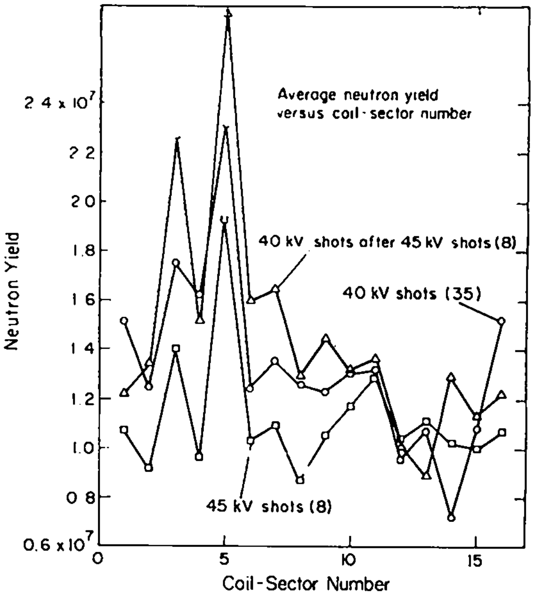

Fig. II-12
Average neutron yields from Ag activation counters around the torus for the indicated bank voltages as a function of toroidal position or coil-sector.

The streak photographs of Fig. II-15 show variations in the terminating m=1 motion of the plasma column. Discharge 2224 shows the plasma going outward in the plane of the torus at various circumferential locations, while discharge 2226 shows the column going outward in two regions (141° and 174°) and inward at another (273°). Such streak camera observations suggest that the m=1 plasma motion has a toroidal mode structure.

The streak photographs show that when the plasma beta is approximately that required for equilibrium, i.e., when the plasma column is in approximate equilibrium, the terminating m=1 motion usually carries the plasma to the inside wall at some locations and to the outside wall at others. This plasma behavior indicates that m=1 instability, which is predicted by MHD theory, is occurring and terminating the discharge rather than a loss of equilibrium. When the plasma β is slightly below that required for equilibrium, the plasma strikes the outer wall at many points and if the β is too high for equilibrium the plasma hits the inner wall at many points.

The streak photographs in the full torus show that: (a) The plasma forms a well defined column and comes into a helical equilibrium position; (b)

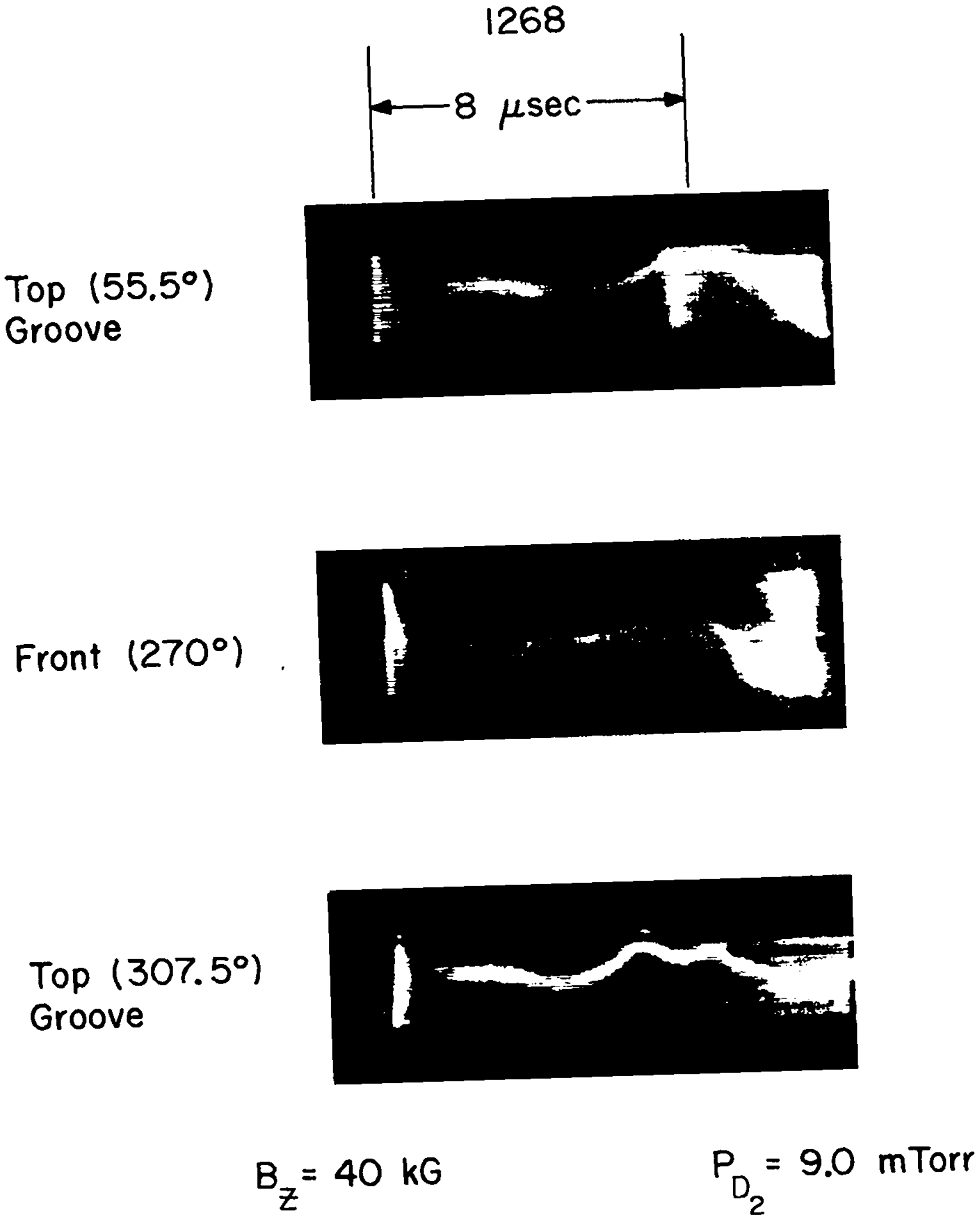

Fig. II-13
Streak photographs of the full-torus plasma, showing the plasma motion in the plane of the torus (upper and lower photographs) and perpendicular to the toroidal plane at the indicated toroidal angle.

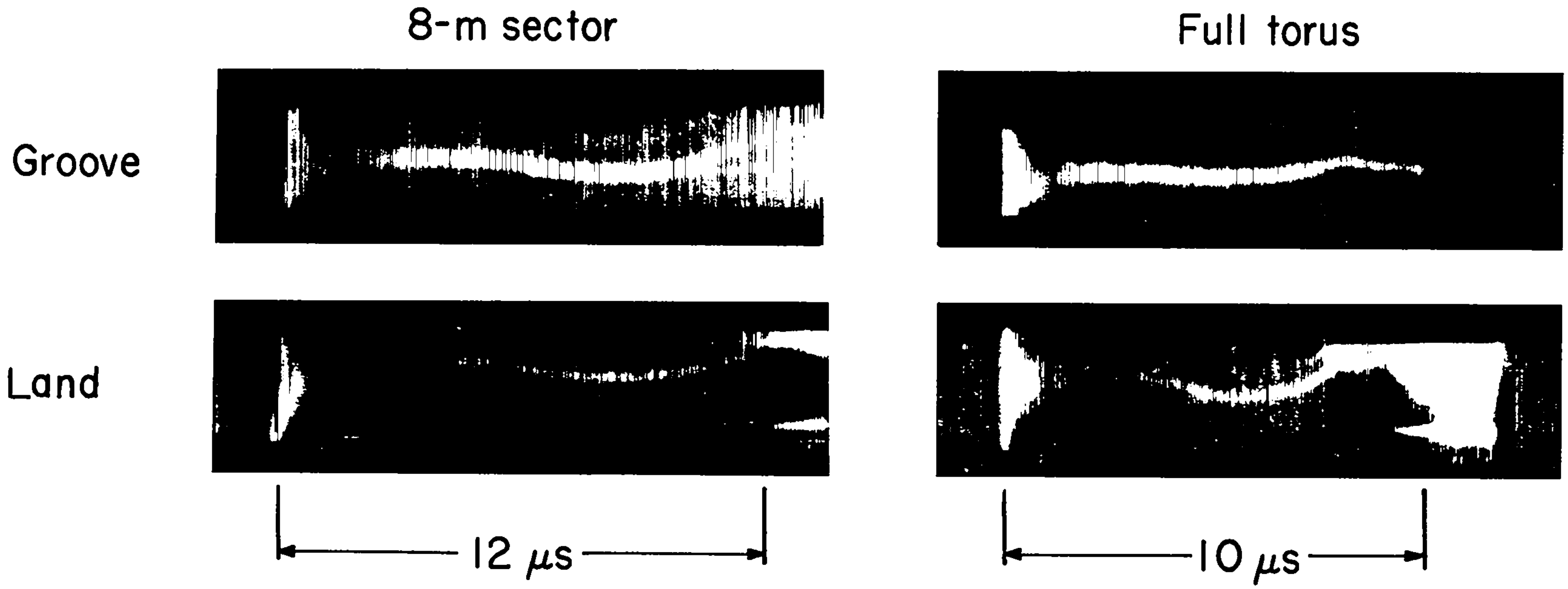

Fig. II-14
Streak photographs comparing plasma motion in the 8-m sector and full-torus experiments. G, groove region, and L, land region, showing motion in torus plane. F, front, halfway between L and G, showing motion perpendicular to the plane of the torus.

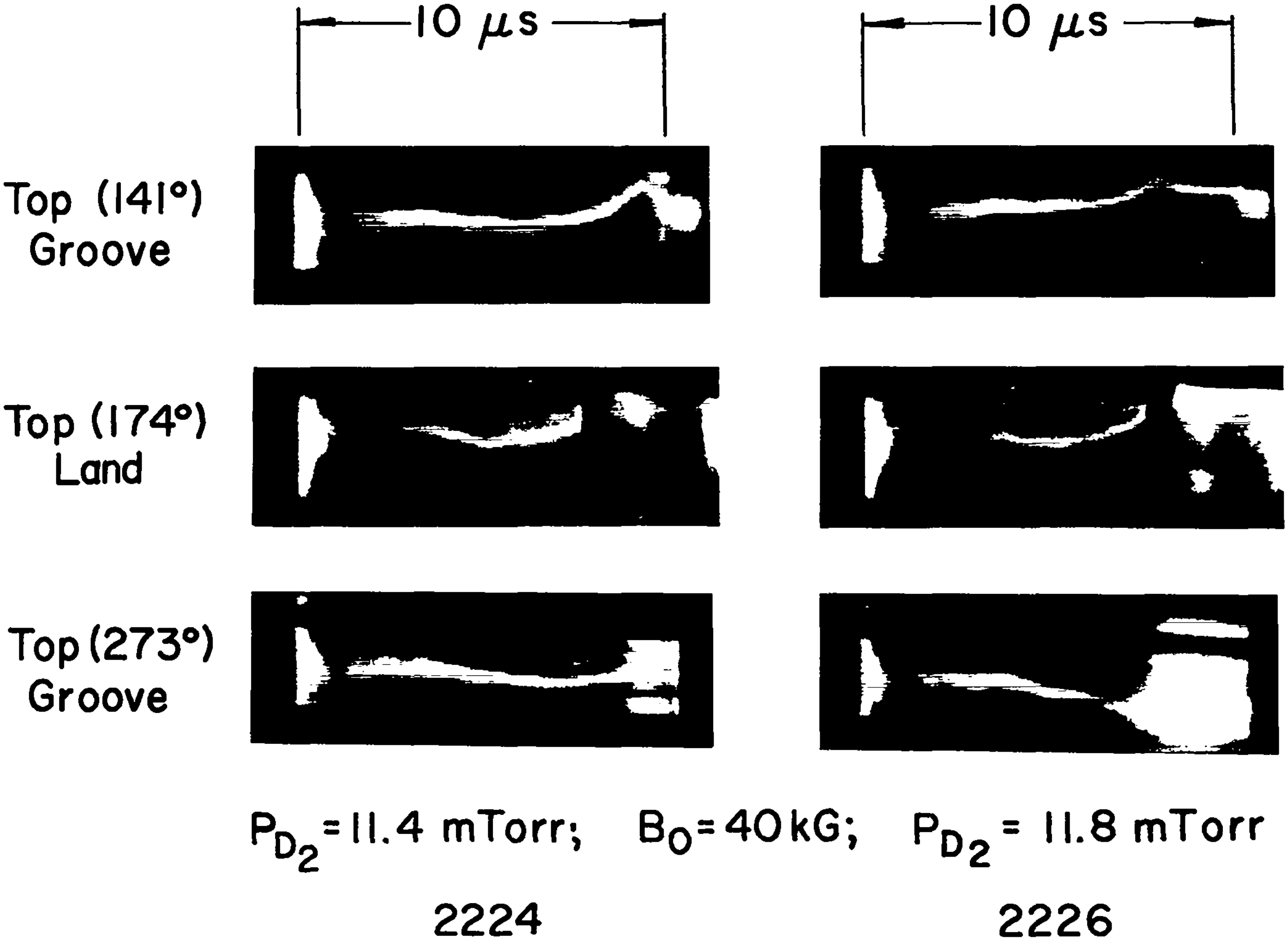

Fig. II-15
Streak photographs comparing plasma motions in the plane of the torus at the indicated toroidal locations on two separate discharges (2224 and 2226).

The stable confined plasma period of 6 to 8 μs is terminated by an m=1 sideward motion of the column; (c) The m=1 motion is predominantly in the plane of the torus; (d) The plasma observations indicate that the m=1 motion has a toroidal mode structure; (e) The plasma confinement times are 6 to 10 μs; and (f) Assuming the m=1 motion is an instability, the fitting of an exponential to the m=1 trajectories give an experimental growth rate of 0.7±0.3 MHz, in agreement with the predictions of MHD sharp-boundary theory [Eq. (11) gives $\gamma(o)=0.705$MHz].

2. Comparison of the ℓ=1,0 Plasma Equilibrium with Theory. In addition to the use of streak photographs, plasma equilibrium and force balance have been studied parametrically in the full torus by means of the measured plasma beta, plasma radius, and external magnetic field as discussed in Sec. II-D-1. Typical time variations of these parameters have been plotted in Fig. II-9. In order to compare experimental measurements in lands and grooves to the predictions of sharp-boundary theory, it is convenient to define the average, or unperturbed, measured radius as

$$\langle a\rangle_{meas} = \frac{\bar{a}_L + \bar{a}_G}{2} \tag{16}$$

where a_L and a_G are themselves averages over several nominally identical discharges in lands and grooves, respectively. This quantity is plotted as the top set of curves in Fig. II-16 for both the 8-m sector and full-torus experiments. The error bars give the standard deviation from the mean due to shot-to-shot data scatter.

The middle set of curves in Fig. II-16 relate to the toroidal, or horizontal-plane, force balance. According to sharp-boundary theory (see, e.g., Fig. II-1), for each value of the plasma radius a there corresponds a unique value of beta for which $F_R = F_{1,0}$. The theoretical beta curve in Fig. II-16 is derived assuming $F_R=F_{1,0}$ and $a=\langle a\rangle_{meas}$ from the experiment. The actual measured beta curve, shown for comparison, is labeled $\langle\beta\rangle_{meas}$, and is defined analogous to Eq. (16).

The lower set of curves in Fig. II-16 refers to axial pressure equilibrium along the plasma column. The condition that nkT be independent of axial position leads to the requirement that

$$\frac{\beta_L}{\beta_G} = \left(\frac{B_G}{B_L}\right)^2 . \tag{17}$$

The measured field ratio, $(B_G/B_L)^2_{meas}$, is seen to agree with the vacuum design value, $(B_G/B_L)^2_{design(VAC)}$, within a few percent. The experimental beta ratio is also close to the magnetic field ratio for times greater than 4 - 6 μs, indicating that 4 - 6 μs is the time required for axial pressure readjustment to take place. The direction of change in both the 8-m sector experiment and the full torus is to increase beta in a land relative to beta in a groove during the period of pressure readjustment.

The average plasma betas measured in the various toroidal sectors and full torus experiments can be compared in a different way with the theoretical values required for toroidal equilibrium. Using the expressions for the plasma excursions δ_1 and δ_0 [Eqs. (3) and (4)], in the ℓ = 1,0 equilibrium relation [Eq. (9)] gives a relationship between the ℓ = 1,0 wavenumber, the torus major radius, the equilibrium fields, and the plasma beta, as

$$hR\,\frac{B_{\ell=1}B_{\ell=0}}{B_o^2} = \frac{2(2-\beta)(1-\beta)}{(3-2\beta)} \tag{18}$$

or

$$\beta = \frac{1}{2}\left\{3 - hR\,\frac{B_{\ell=1}B_{\ell=0}}{B_o^2} - \left[hR\,\frac{B_{\ell=1}B_{\ell=0}}{B_o^2} + 1\right]^{1/2}\right\} . \tag{19}$$

This relationship is plotted in Fig. II-17. The solid curve gives the theoretical value of the plasma β required for toroidal equilibrium as a function of the quantity $hR\,B_{\ell=1}\,B_{\ell=0}/B_o^2$. In this approximation the equilibrium beta value is independent of plasma radius.

With the equilibrium fields generated by the shaped inner surface of the compression coil, the quantity $hR\,B_{\ell=1}\,B_{\ell=0}/B_o^2$ is fixed for a given experiment as indicated by the vertical dashed lines of Fig. II-17. The experimental points for the average measured plasma beta are plotted together with error bars to indicate the observed shot-to-shot spread (note the suppressed zero). It can be seen that theory and experiment agree quite well for all three basic Scyllac configurations studied to date.

These results confirm quantitatively that the same basic type of ℓ=1,0 equilibrium has been successfully achieved in the closed torus as was earlier achieved in the open-ended toroidal sector

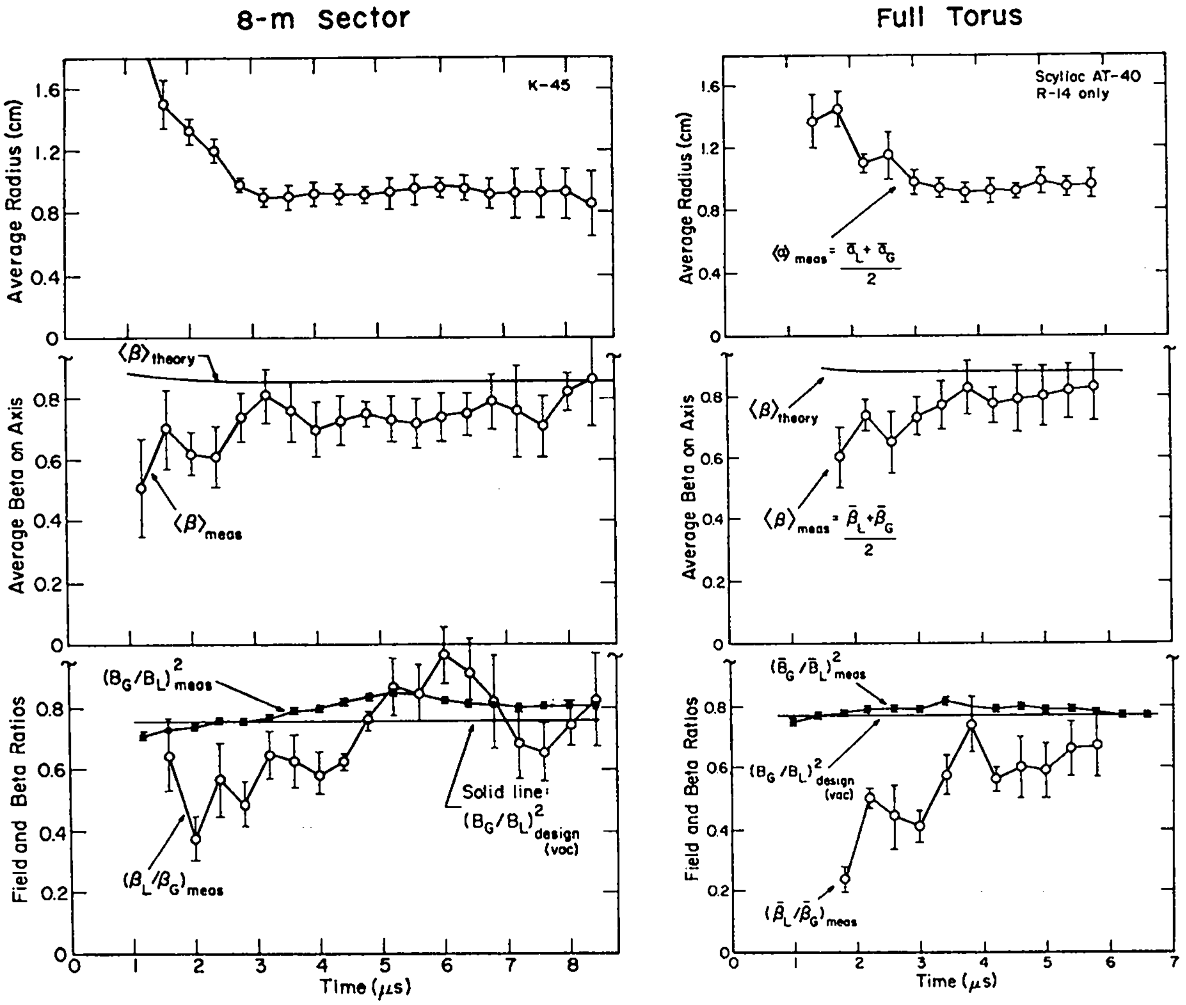

Fig. II-16

Graphs of measured and theoretical parameters as functions of time describing the Scyllac plasma equilibrium in the 8-m sector and full torus experiments. Data points are averaged over four or more discharges.

devices. The $\ell = 1,0$ plasma equilibrium and its scaling have been verified according to sharp boundary theory, and the equilibrium plasma and magnetic field parameters agree with sharp boundary theoretical predictions to within 10%.

3. Toroidal I_zCurrent. A net toroidal plasma current of 1-1.5 kA peak amplitude has been measured in the Scyllac torus by means of a nulled Rogoswki coil (*cf.* Section II-C-8) mounted around the discharge tube in a groove region. The lower oscilloscope trace of Fig. II-18 (1796) shows the waveform of the I_z displayed with the main toroidal field (upper trace). The current rises in two stages, ~50% in the first few hundred ns during the plasma implosion phase, and the remainder in the following ~3.5 μs during the risetime of the main compression field. The direction of the toroidal current is opposite to the main field and can be interpreted as resulting from changes in the magnetic flux of the main field which link the helical plasma column.

The I_z current exceeds the Kruskal-Shafranov limiting current of approximately 500 A for 40 kG and one-cm radius, indicating instability to current-driven kink modes. However the streak photographs show little evidence of plasma motion out of the toroidal plane and the theoretical growth rate is 0.1 to 0.2 MHz which is smaller than the observed m = 1 growth rate [γ(o) = 0.7±0.3 MHz].

Similar I_z currents were observed previously in the plasma experiments with ℓ = 1 fields in the linear 3-m Scylla IV-3 device when electrodes were placed at the ends of the discharge tube and a current return was connected externally.[12]. With a linear ℓ

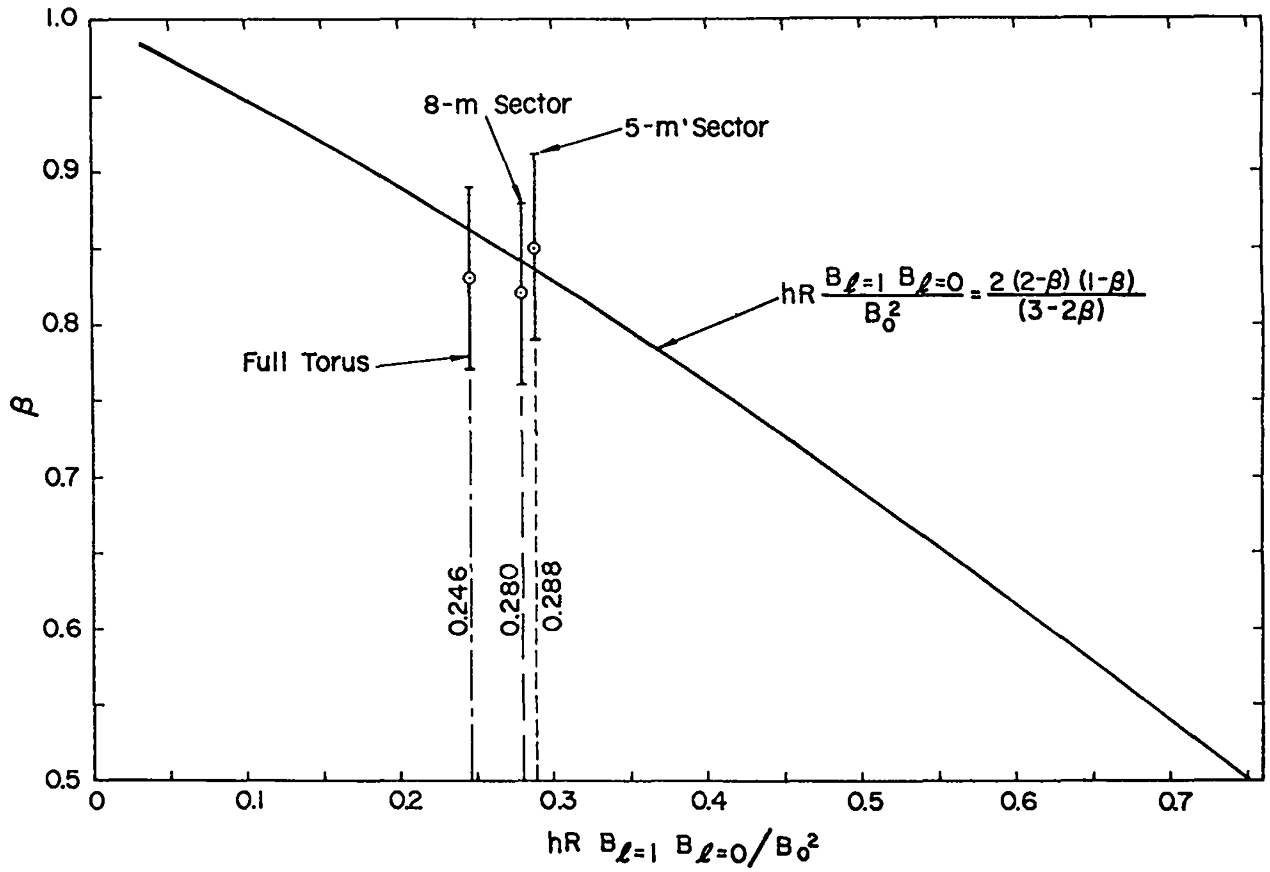

Fig. II-17

Comparison of the measured plasma beta required experimentally for toroidal plasma equilibrium (experimental points) with that predicted by sharp-boundary theory (solid line).

= 1 shaped compression coil ($B_{\ell=1}/B_0 = 0.11$), the I_z current was ~ 1 kA with a risetime comparable to the main B_0 field and in a direction opposite to that of the B_0 field, as in the present torus experiments. With driven $\ell = 1$ windings in Scylla IV-3 ($B_{\ell=1}/B_0 \approx 0.067$), I_z was smaller (~100-300 A) and parallel to B_0. Also, in the latter case, the magnitude of I_z decreased with increasing delay of the $\ell = 1$ fields relative to the main field.

A slowly rising axial current ($\tau/4 \sim 15$ μs) was induced in the full-torus plasma by a single-turn, capacitor-driven loop mounted on the inner face of the toroidal compression coil (R~3.8 m). This externally driven I_z was applied to the preionized plasma such that its maximum was achieved at the time the main compression field was applied. This current had a variable amplitude of 0.8-1.5 kA and was applied either opposing or aiding I_z. With the applied axial current opposed to I_z a reduction of approximately one-third in the amplitude of I_z was observed. However, with the driven current aiding I_z the amplitude of the net axial current remained approximately constant during the rise of the main magnetic field. These results with the applied slow I_z indicate a tendency for the plasma to carry a constant current.

A fast rising $I_z(\tau/4 \sim 2$ μs) was induced in the plasma by breaking the single primary loop into parallel sections and driving them with a low capacity, high-voltage capacitor. The fast I_z was usually applied 0.3-0.6 μs after the application of the main compression field, i.e., near the end of the implosion phase of the discharge. Figure II-18 shows the results with a fast-rising current: the lower left oscillogram shows an axial current of ~1.1 kA generated in the plasma in the absence of an applied i_z; the lower right oscillogram shows the successful cancellation of the net axial current by the applied I_z; the upper left oscillogram shows the applied I_z waveform in the primary circuit; and the upper right oscillogram shows the approximately nulled-out B_z pickup in the 81-turn Rogowski coil on a vacuum shot in the absence of plasma.

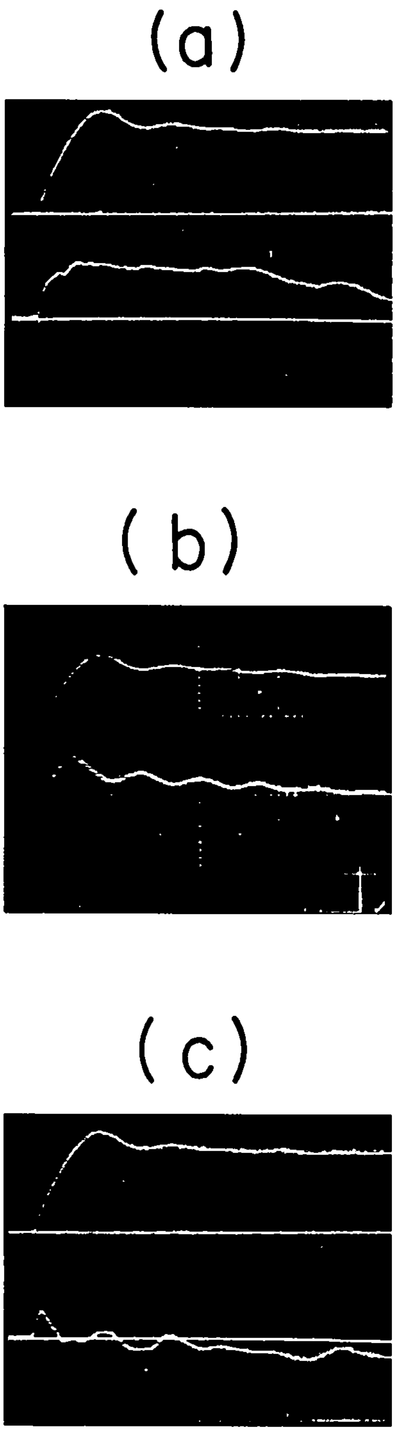

Fig. II-18
Top trace, axial magnetic field (2 μs/div). Bottom trace, axial current (0.7 kA/div): (a) typical I_z *current generated in torus with* (I_z) *applied = 0; (b)* I_z *current applied in primary* I_z *circuit; and (c) net* I_z *plasma current with an applied* I_z.

The cancellation of the net I_z did not have a noticeable effect on the plasma behavior. Obviously, inducing a cancelling current cannot guarantee that toroidal currents are not distributed in such a manner as to produce a zero net toroidal current and locally violate the Kruskal-Shafranov limit. However, the fact that the plasma behavior is the same whether or not it is under the influence of an opposing current, coupled with the observed planar plasma motion and growth rate, shows that the instability is not a kink mode.

4. Toroidal Mode Structure

a. Introduction. Sharp boundary MHD theory predicts a growth rate for the m=1 instability given by

$$\gamma^2(n)=\gamma^2(0) - v_A^2(2-\beta)n^2/R^2$$

where v_A is the Alfvén velocity, and R is the torus major radius. The axial mode number, n, is defined by the number of wavelengths around the torus, and $\gamma(0)$, Eq. (11), the growth rate for an infinite wavelength, is calculated to be 0.7 MHz for the Scyllac torus parameters.

Streak cameras initially indicated the existence of a toroidal mode structure. In order to determine the plasma structure more precisely at one instant of time, a 360° framing camera system was devised that eventually had 11 viewing slits distributed almost uniformly around the circumference.[13] Randomness of phase between modes caused non-reproducibility of the plasma motion from discharge to discharge, and required (2n+1) simultaneous data points to measure n harmonics (a constant displacement term for zero order, and displacement and phase for each n>0).

b. Experimental Arrangement. The experimental arrangement is indicated in Fig. II-19. A single image-converter framing camera located at the geometrical center of the torus had 11 horizontal viewing slits, almost uniformily spread in angle over 360°, imaged on its photocathode. The light from each slit was relayed by two plane mirrors, one directly above the slit, and the second a member of a multi-facet pyramid structure also centered on the toroidal axis, to a Cassegranian telescope (f/1.8, focal length 41 cm), which imaged the slits at 10:1 reduction in an approximately circular array onto the 2.5-cm diameter photocathode.

In order to measure the plasma location within each slit, the slit ends had to be well defined in the

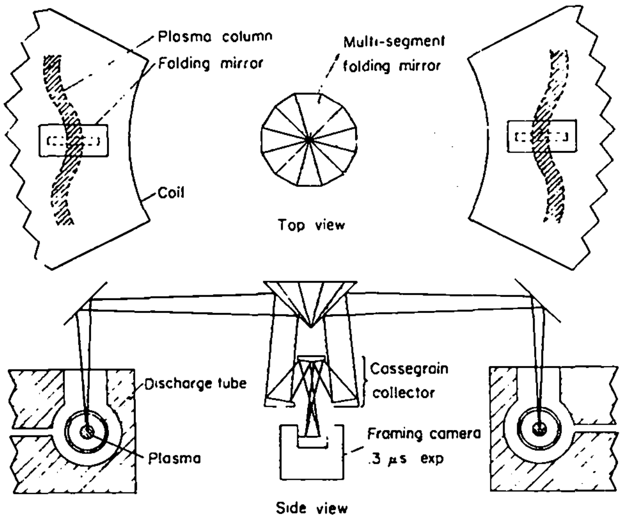

Fig. II-19
Schematic of 360° framing camera arrangement on Scyllac. The plasma is viewed simultaneously at eleven different circumferential locations in the toroidal plane.

image. This was accomplished by a separate long-time exposure of reflecting tape on the slit ends illuminated by individual flood lamps.

An example of the raw data is shown on the left of Fig. II-20. The circular arrangement is the somewhat arbitrary result of the alignment procedure, and while it evokes a mental image of the toroidal geometry, in fact, the images are inverted, so that the ends nearest the center are actually toward the outside, and the large aspect ratio of the torus is completely distorted.

c. *Data Analysis.* Numerical values of the plasma displacement from the discharge tube axis at each angular position were obtained with the Graf-Pen digitizer under the control of a computer program which then proceeded to a curve fitting routine. The analytical form of the fitting function was chosen to be

$$d = a_0 + \sum_{\ell=1}^{n} \left(a_\ell \cos \ell\phi + b_\ell \sin \ell\phi \right) . \qquad (21)$$

The inputs are the 11 values of displacement d at the 11 different angular positions ϕ and, for a specified $n \leq 4$, the $(2n+1)$ a and b coefficients were determined in a least-squares fit with $2(5-n)$ degrees of freedom. The results were displayed in terms of a mode amplitude, $(a_\ell + b_\ell)^{1/2}$, and a mode phase angle, $\tan^{-1}(b_\ell / a_\ell)$. Also computed was the weighted variance of the fit, i.e., the square root of the sum of the squares of the deviations of the data points from the curve divided by the number of degrees of freedom. Figure II-21 illustrates a succession of curves with an increasing number of modes, n, fitted to the data of one particular discharge. Over a collection of 15 such discharges, the weighted variance was a minimum either at $n=3$ or $n=4$, with almost the same number of times for each. This means that three modes fit the data pretty well, with the 4th harmonic generally of smaller amplitude aiding the fit by a small amount. On the other hand, using only 2 harmonics, the fit was definitely worse. It should also be noted that using 5 harmonics forced an exact fit to the 11 data points, and was therefore statistically meaningless, since the curve was forced to pass precisely through the data points, which themselves were determined with less than absolute precision. It is significant, nonetheless, that when 5 harmonics were fitted, the amplitude of the 5th harmonic on average was only slightly larger than the 4th, and smaller than the first three, in support of the conclusion that there is a rapid fall-off in amplitude with increasing mode number.

As a consequence of the above results, a fitting procedure including all mode numbers $n=0$ to $n=4$ was selected as the best representation of the data. The tabulated chi-square distribution of 2 degrees of freedom fit the distribution obtained from the sums of squares of the deviations if the experimental accuracy σ was chosen to be 0.35 cm. Repeated readings of the data indicated that this relatively large uncertainty was not unreasonable. The phase anglesf the modes appeared to be randomly distributed, and the relative amplitudes also varied from discharge-to-discharge. In consequence, the plasma column assumed a different shape every discharge, as illustrated by comparing the 4-harmonics case in Fig. II-21 with the right side of Fig. II-20. This is just what would be expected for a superposition of several instability modes, and all further inferences must be of a statistical nature.

The amplitudes of the various modes, $n=0$ through $n=4$, were averaged over 15 discharges and are plotted in the lower half of Fig. II-22. We use the calculated growth rate of 0.7 MHz for the $n=0$ mode and the relative growth rates for the other n numbers, as indicated by the upper half of Fig. II-22, as well as the actual time, $t=4.6$ μs, when the framing pictures were obtained. The relative displacements of the various modes were then calculated on the "white noise" assumption of equal initial amplitudes. The absolute scale value was determined by fitting to the observed data point for $n=1$. This set the coefficient of the growing exponential $x = x_0 e^{\gamma t}$ at $x_0 = 0.023$ cm. The resultant

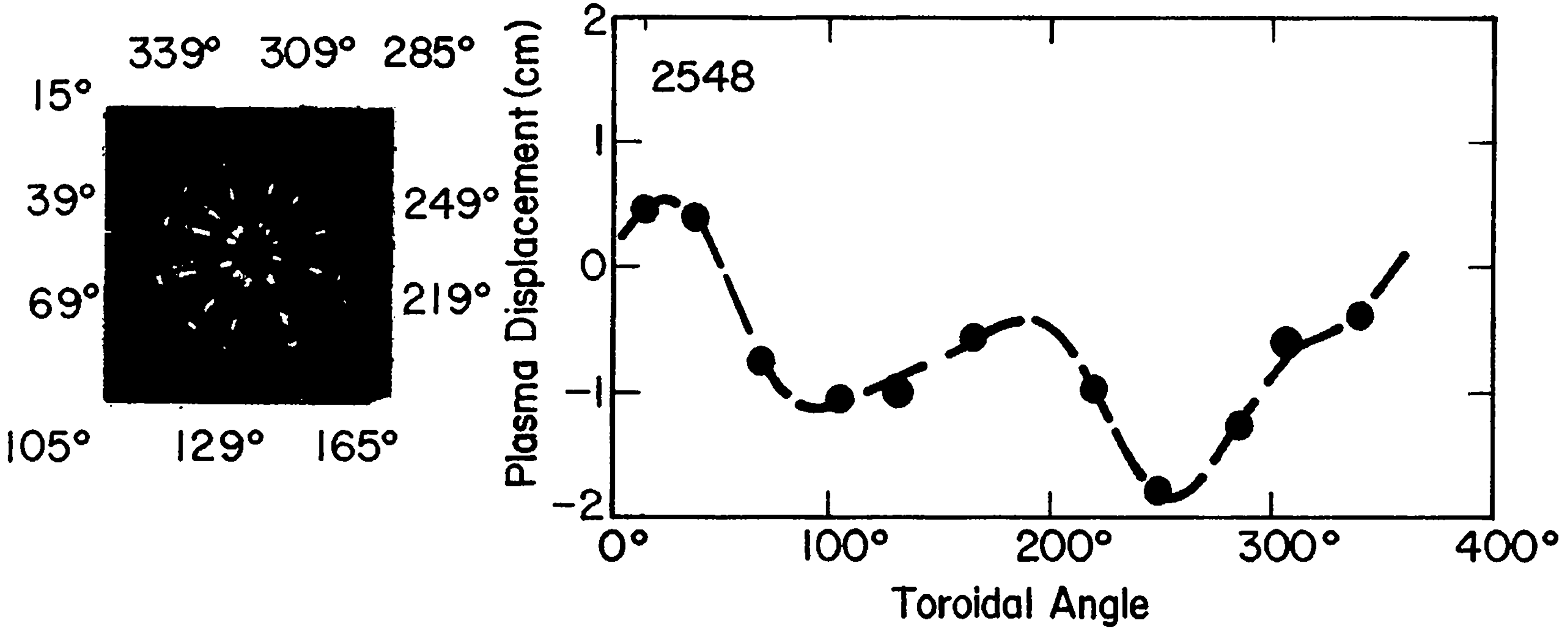

Fig. II-20
Framing camera photograph (left) and radial plasma displacement as a function of toroidal angle with least-squares best fit curve using four harmonics (right).

calculated displacements are plotted as crosses in the lower half of Fig. II-22 and are connected by the solid line.

The scale was not fitted to n=0 because this is a somewhat special case which is only a constant shift term in position vs angle and can be confused with small errors in setting up the correct equilibrium conditions due, for instance, to slightly incorrect initial fill pressure. There should, in fact, be an initial 6-mm inward equilibrium shift since all the viewing slits were in groove locations, and using this or some other value instead of the discharge tube center would slightly change the observed value for n=0.

d. Conclusions. The data presented here are entirely consistent with sharp boundary calculations for the expected m=1 instability modes. *A priori*, instability might be expected to develop with equal likelihood in the vertical plane. Streak camera pictures, however, indicate much less vertical than horizontal motion. This could well be explained by slight force imbalances in the horizontal plane providing the initial set from which the instability grows primarily in the toroidal plane. These could arise from variations in the magnetic field around the torus (*cf.* Fig. II-7). We must then distinguish instability motion resulting from an initial set, due to force imbalance, from the total motion being the result of the longer term action of this force imbalance.

Simple arguments can be evolved to show that a force imbalance of only 2% can establish the initial set of 0.02 cm in about 0.4 μs, i.e., a time short compared to when the position determination was made, so that the instability calculation can actually be applied from essentially t=0. On the other hand, the same 2% force imbalance continuing to act in the absence of instability would give a trajectory which is too slow to explain the observed limit on plasma confinement. This reinforces our interpretation of the data.

This argument breaks down if the force imbalance is assumed appreciably larger. A significant experiment would have been to measure at two instants of time, during the same discharge, to determine whether the separate n modes grow at different rates. Neither the available light level nor the experimental schedule permitted such a measurement.

(e) The experiments confirm further the scaling of the toroidal equilibrium from the previous toroidal sector experiments (R=2.4 m and 4.0 m) to the full torus.

(f) The unstable m=1 plasma motion follows the predictions of both the old-ordering and Freidberg's generalized theory to within 15%, both in absolute value and in the relative scaling of the growth rate from the previous sector experiments.

(g) Measurements of the toroidal mode structure of the m=1 instability show the existence of at least five toroidal modes (theory predicts a maximum of six) and confirm the theoretically expected fall-off of the unstable displacement amplitude past n=3. These measurements give further credence to the theoretically predicted scaling of the absolute magnitude of the m=1 instability growth rates.

(h) These experiments provide no indication of higher order poloidal instability modes than m=1, supporting experimentally the validity of the finite gyroradius stabilization criteria.[8]

(i) The major divergence of the observed plasma behavior from theoretical predictions is the period of quiescent equilibrium in the initial stages of the discharge. Recent Nihon University experiments,[14] indicate that the time variation of the plasma radii between the minima and maxima of the ℓ=0 field regions in Scyllac is providing dynamic stabilization of the m=1 instability according to the Haas-Wesson theory.[15]

References

1. W.R. Ellis, F.C. Jahoda, R. Kristal, W.E. Quinn, F.L. Ribe, G.A. Sawyer and R.E. Siemon, "Plasma Equilibrium and Stability in the Scyllac Toroidal Sector Experiments," Nuclear Fusion **14,** 841 (1974).

2. E.L. Cantrell, W.R. Ellis, H.W. Harris, F.C. Jahoda, R. Kristal, M.D. Machalek, J.R. McConnell, W.E. Quinn, F.L. Ribe, G.A. Sawyer, F.T. Seibel, and R.E. Siemon, "Plasma Experiments in the Scyllac Toroidal Theta Pinch," Fifth IAEA Conf. on Plasma Phys. and Controlled Nuclear Fusion, Tokyo, Japan, Nov. 1974, Paper CN-33/E1-2.

3. F.L. Ribe, "Free-Boundary Solution for High-Beta Stellarators of Large Aspect Ratio," Los Alamos Scientific Laboratory Report, LA-4098 (1969).

4. F.L. Ribe and M.N. Rosenbluth, "Feedback Stabilization of a High-β, Sharp-Boundaried Plasma Column with Helical Fields," Phys. Fluids **13,** 2572 (1970).

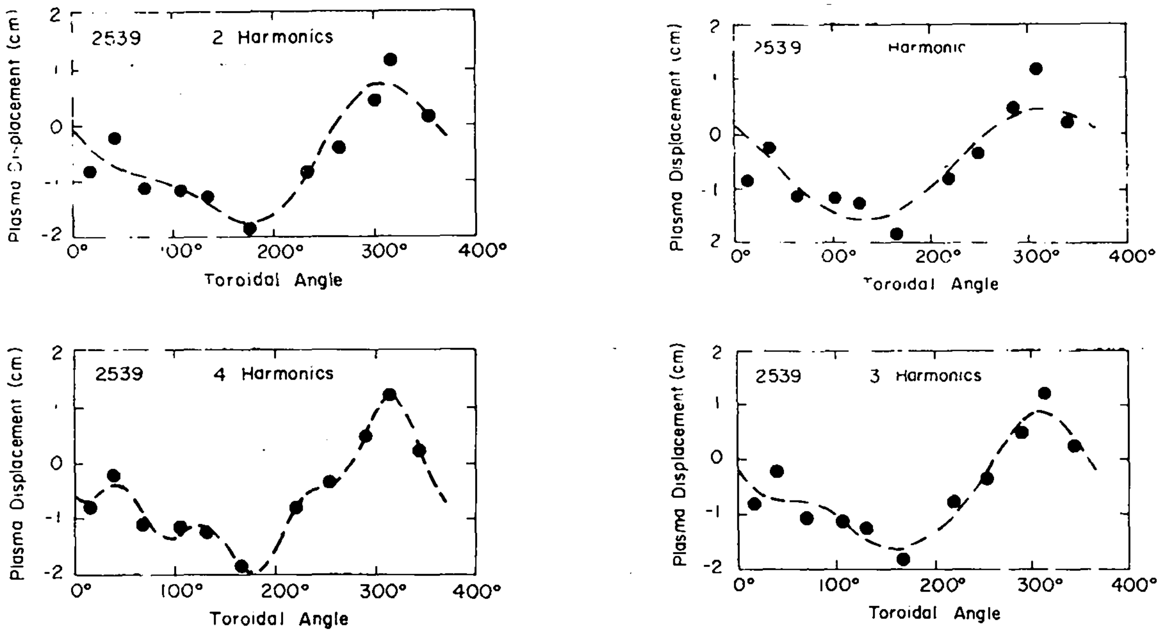

Fig. II-21
Radial plasma displacement versus toroidal angle for one discharge successively fitted with an increasing number of harmonic terms.

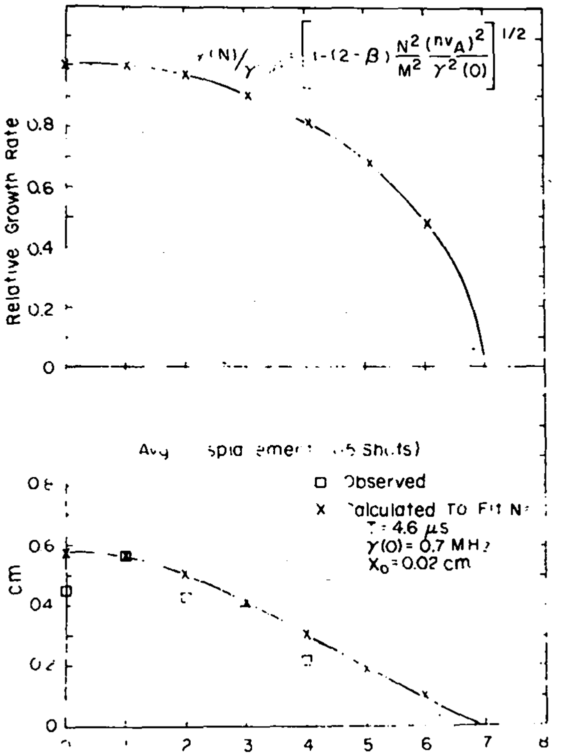

Fig. II-22
Spectrum of theoretical growth rate (upper) and average displacement as a function of toroidal mode number (lower).

F. Conclusions

Plasma experiments on the Scyllac full torus have shown the following:

(a) The theta-pinch plasma heating by "shock" implosion and subsequent adiabatic compression is unaffected by the toroidal curvature and the presence of the $\ell=1$ and $\ell=0$ equilibrium fields during the implosion.

(b) The plasma column takes up a helical, bumpy toroidal shape and comes into an equilibrium position as predicted by theory, and remains stably confined for 6 to 8 μs.

(c) The period of stable confinement is terminated by an $m=1$ unstable motion of the plasma column, whose properties are those of the theoretically predicted $m=1$ instability and coincide with the observations on the 8-m sector experiment. The unstable motion usually develops in the plane of the torus.

(d) Measurements of the magnetic field, plasma beta, plasma radius, and relative density profile confirm in detail the theoretical predictions of a high-β toroidal equilibrium for the Scyllac plasma.

5. J.P. Freidberg, "Survey of Scyllac Theory," Plasma Physics and Controlled Nuclear Fusion Research (Proc. 4th Int. Conf., Madison, 1971) IAEA, Vienna, **3,** 215 (1971).

6. M.N. Rosenbluth, J.L. Johnson, J.M. Greene, and K.E. Weimer, "Stability Limitations for Stellerators with Sharp Surfaces," Phys. Fluids **12,** 726 (1969).

7. H. Grad and H. Weitzner, "Critical β from Stellarator and Scyllac Expansions," Phys. Fluids **12,** 1725 (1969).

8. J.P. Freidberg, "Stability of the Straight $\ell = 1$ Scyllac Configuration," Phys. Fluids **14,** 2454 (1971).

9. J.P. Freidberg, "Vlasov-Fluid Model for Studying Gross Stability of High-β Plasmas," Phys. Fluids **15,** 1102 (1972).

10. R.E. Siemon, "Polychrometer with Extreme Rejection of Stray Light," Appl. Optics **13,** 697 (1974).

11. R.J. Lanter and D.E. Bannerman, "The Silver Counter, A Detector for Bursts of Neutrons," Los Alamos Scientific Laboratory Report LA-3498-C (July 1966).

12. K.S. Thomas, C.R. Harder, W.E. Quinn, and R.E. Siemon, "Helical Field Experiments on a Three-Meter Theta Pinch," Phys. Fluids **15,** 1658 (1972).

13. F.C. Jahoda, R. Kristal and W.E. Quinn, "Toroidal Mode Structure in the Scyllac Full Torus," Los Alamos Scientific Laboratory Report LA-5853-MS (1975).

14. T. Itagaki, T. Karakizawa, K. Suito, S. Shiina, J. Jodoroki, "Stability and Toroidal Equilibrium Conditions of Theta-Pinch Plasma in a Multiple-Mirror Field," Fifth IAEA Conf. on Plasma Phys. and Controlled Nuclear Fusion, Tokyo, Japan, Nov. 1974, Paper CN-33/E7-3.

15. J.A. Wesson and F.A. Haas, "Dynamic Stabilization of the Theta Pinch," Phys. Fluids **12,** 1271 (1969).

III. FEEDBACK STABILIZATION OF SCYLLAC

D.L. Call, K.J. Kutac, G. Miller, W.E. Quinn

A. Introduction

The Scyllac full torus experiment as well as the previous sector and $\ell = 1$ linear experiments indicate that the observed $m = 1$ plasma motion is due to the instability predicted by sharp-boundary MHD theory. The growth rate γ from the MHD theory (for long wavelength modes) is given by

$$\gamma = hv_A \left[-\beta^2 \left(\frac{a}{b}\right)^4 \delta_1^2 + \frac{\beta(4-3\beta)(2-\beta)}{8(1-\beta)} h^2 a^2 \delta_1^2 + \frac{\beta(3-2\beta)(1-\beta)}{(2-\beta)} \delta_o^2 \right]^{1/2} \quad (1)$$

Two methods of stabilization have been proposed, feedback[1] and wall stabilization.[2] Since in the present Scyllac experiments the ratio a/b of plasma to wall radius is too small (~0.1) for wall stabilization, feedback control has been chosen for plasma stabilization.

The results from the toroidal sectors and the full torus have established the relationship between the required specifications of the feedback system and the plasma parameters. An assessment of the feedback system based on this knowledge showed that the time response of the existing feedback amplifier system is insufficient to control the unstable motion in the Scyllac torus. Modeling studies indicate that $\gamma\tau \leq 0.5$ ($\gamma\tau$ is the product of instability growth rate and the feedback delay-risetime) is required for controlling the instability, while Scyllac has $\gamma\tau \approx 1$. These considerations have led to a re-evaluation of the plasma regime in which the initial feedback experiments will be conducted. In order to reduce the instability growth rates to values which are compatible with the response time of the present feedback system, the main compression field will be reduced to ~15 kG and plasma parameters derated accordingly. Feedback studies utilizing the derated plasma will be carried out in a new series of 120°, 8-m sector experiments. The objective of these experiments is to clearly establish the principles of feedback stabilization in Scyllac.

The derated plasma parameters will allow a relatively long end-loss time in which the feedback system should be able to demonstrate control of the plasma instabilities, provided other end effects are absent. The derated parameters will be in a plasma regime which will yield additional information on the Freidberg criterion for the finite-Larmor-radius (FLR) stabilization of the $m \geq 2$ modes. In the derated plasma regime, the criterion for the $m=2$ may be violated. Hence, there is a possibility for comparing the theoretical predictions for the FLR criterion and the $m=2$ growth rates with experiment.

The preparation for feedback stabilization experiments on the derated Scyllac sector are described below. The selection of the derated plasma parameters and the capabilities of the feedback system are also discussed. A detailed analysis of the feedback loop with the conditions expected in the Scyllac feedback experiment has been carried out and projects a generally favorable result.

B. Experimental Arrangement.

In the MHD feedback stabilization system[2,3,4,5] for Scyllac, the feedback force is generated by small controllable $=0$ field which produces a plasma perturbation

$$\delta_o^{FB} = -B_{\ell=0}^{FB}/2B_o(1 - \beta) \quad (2)$$

This plasma perturbation produces a feedback restoring force

$$F_{1,0}^{FB} = \beta(3-2\beta)B_o^2 h^2 a^3 \delta_1 \delta_0^{FB}/8 \quad (3)$$

in opposition to the $m=1$ destabilizing force,

$$F_\gamma = \pi a^2 \rho\, \gamma^2 \xi \quad , \quad (4)$$

where ρ is the mass density of the plasma column and ξ the displacement from its equilibrium position.

Equating the feedback force to the destabilizing force gives the $\ell=0$ feedback field required for plasma stabilization,

$$B^{FB}_{\ell=0} = \frac{4(1-\beta)}{\beta(3-2\beta)} \; \frac{\gamma^2 \xi B_o}{h^2 a v_A^2 \delta_1} \tag{5}$$

The feedback field is produced by four $\ell=0$ feedback coils per $\ell=1,0$ wavelength inside the main compression coil with alternate pairs connected in opposition to the feedback power amplifiers.

The feedback stabilization system, shown schematically in Fig. III-1, consists of four basic components: (a) the plasma position detectors, silicon quad-cell photodiodes designed to detect plasma motion up to 1 cm away from the equilibrium position; (b) signal processing units, which produce an output proportional to the sum of plasma position and velocity with separate position and velocity gain controls (the principal "knobs" of the feedback system); (c) power amplifier modules, each of which consists of three separate stages of amplification ending in the push-pull operation of two ML-8618 power vacuum tubes operating at 35-kV plate voltage; and (d) $\ell=0$ feedback coils driven by the power module output transformer.

Initial feedback plans for Scyllac used 60 feedback modules with each module driving two pairs of $\ell=0$ feedback coils (one module per $\ell=1,0$ wavelength). It was planned to remachine the compression coil to a mean inner radius of 8 cm, corresponding to a compression field of approximately 35 kG with a clearance of 2 cm between the feedback coils and compression coil inner surface. Modeling measurements showed that the feedback modules could generate a feedback field of 230 G in this configuration. More important, the total time delay, τ_{FB}, from optical position detector to the feedback coils in a realistic mock-up was found to be 2.1 μs. A large fraction of the 2.1 μs was the L/R risetime ($\sim$1.2 μs) of the output current from the feedback modules, arising because two pairs of feedback coils were driven by each module. This arrangement was planned in order that the available 60 modules would cover the 60 $\ell=1,0$ wavelengths of the 25-m circumference.

In order to feedback stabilize we must simultaneously have sufficient $B^{FB}_{\ell=0}$ to restore the plasma from reasonable displacement (approximately one cm) and a growth rate small enough to be followed after the risetime delay of the feedback system ($\gamma\tau_{FB} \leq 0.5$). The full torus experiments (*cf.* Sec. II) with a growth rate of 0.7×10^6 sec^{-1} require a feedback field of 620 G with a risetime of 0.7 μs to meet these criteria in contrast to the feedback capability of $B^{FB}_{\ell=0}$ = 230 G and τ_{FB} = 2.1 μs given above.

In order to accomodate the capability of the feedback system, it was decided to reduce the plasma parameters. To achieve $\gamma\tau_{FB} = 0.5$ and to reduce the required feedback field, the Alfvén speed will be reduced by lowering the main toroidal field to 15 kG. With the milder implosion-compression conditions it is estimated that the plasma β will be lowered to approximately 0.65.

In order to reduce τ_{FB}, the output inductance will be halved by using each module to drive only a single pair of feedback coils, which requires 2 modules per $\ell=1,0$ wavelength. This decreases the L/R risetime to 0.6 μs and the overall delay τ_{FB} to 1.5 μs (*cf.* Fig. III-2). The feedback field $B^{FB}_{\ell=0}$ will be increased by enlarging the clearance between the $\ell=0$ coils and the compression coil wall from the previously planned 2 cm to 6 cm, thereby reducing image currents effects. Figure III-3 is a photograph of the new sector compression coil with an average diameter of 24 cm. The inner surface of the coil is shaped to generate the $\ell=1$ helical and $\ell=0$ bumpy equilibrium fields.

Since the device and plasma parameters are being considerably changed to accomodate the feedback capability, the initial feedback experiments on Scyllac will be carried out in an 8-m sector (120°) using Racks 6 through 10.

C. Parameters of the Derated Sector with Feedback

1. Scaling of Scyllac to Lower Magnetic Fields.

Simple scaling of the plasma temperature in the implosion phase and subsequent compression and neglecting inertia and expansion effects following the implosion give

$$T \propto \frac{m^{1/4} E_\theta^{1/2} B_o}{n_o^{3/4}} , \tag{6}$$

where n_o is the initial filling density and m the ion mass. Using this temperature scaling, conservation of particles and the plasma beta relation gives a plasma radius scaling,

$$a \propto n_o^{1/8} m^{1/8} b_t \frac{E_\theta^{1/4}}{\beta^{1/2} B_o^{1/2}} \tag{7}$$

where b_t is the discharge tube radius.

The plasma density scaling is derived from the beta relation using the temperature scaling,

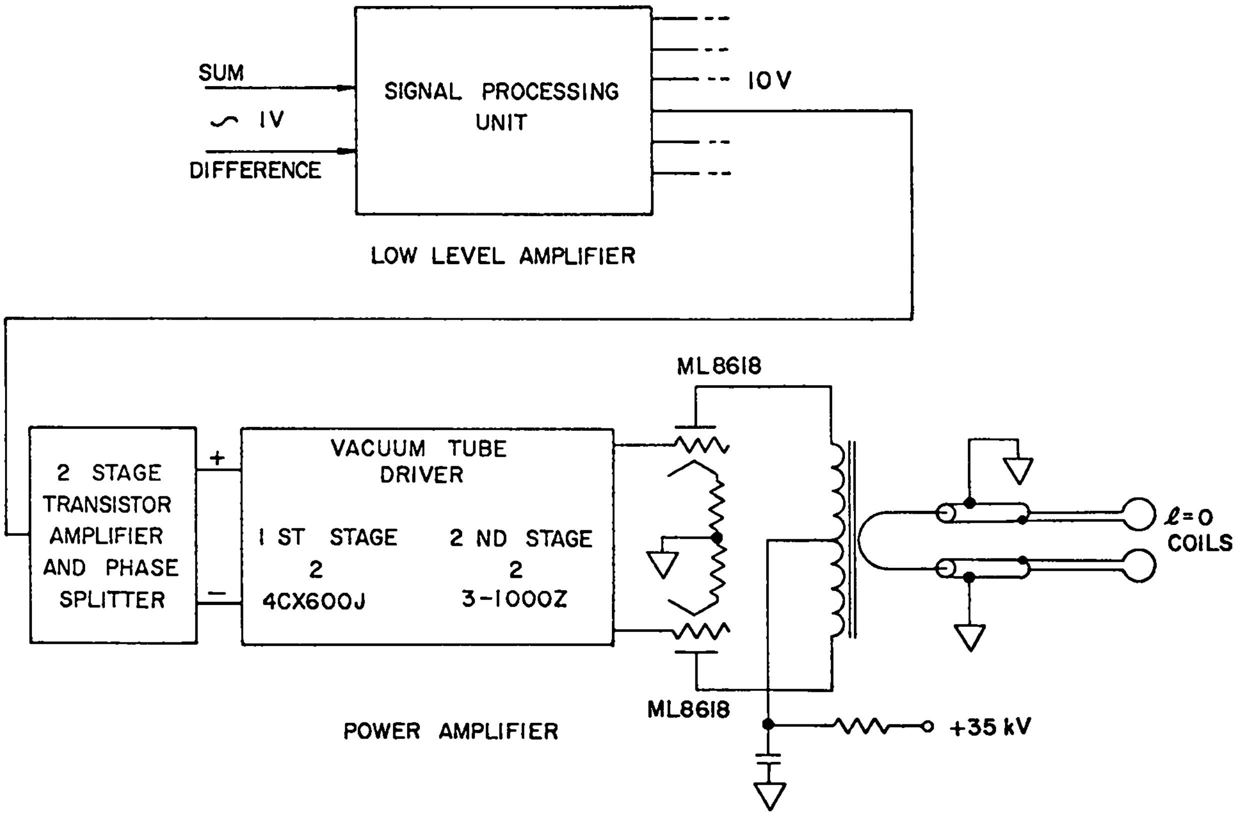

FEEDBACK AMPLIFIER AND LOGIC SYSTEM

Fig. III-1
Schematic of feedback stabilization system.

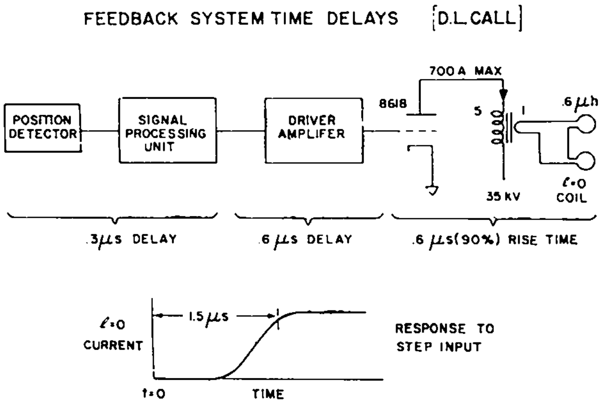

Fig. III-2
Block diagram (upper) of feedback system showing the system time delays and the feedback output current response (lower) to a step input at t=0.

$$n \propto \frac{n_o^{3/4}\beta B_o}{m^{1/4}E_\theta^{1/2}} \quad . \tag{8}$$

The Alfvén speed scaling is obtained by using the density scaling,

$$v_A \propto \frac{E_\theta^{1/4}B_o^{1/2}}{n_o^{3/8}m^{3/8}\beta^{1/2}} \quad . \tag{9}$$

Using these scalings and assuming the initial filling density remains constant the parameters in Table III-1 for a field of 15 kG have been scaled from the listed parameters in the present torus experiments.

2. Feedback Parameters. The growth rate γ and the required feedback field $B^{FB}_{\ell=0}$ can be minimized with respect to the $\ell=1,0$ wavelength

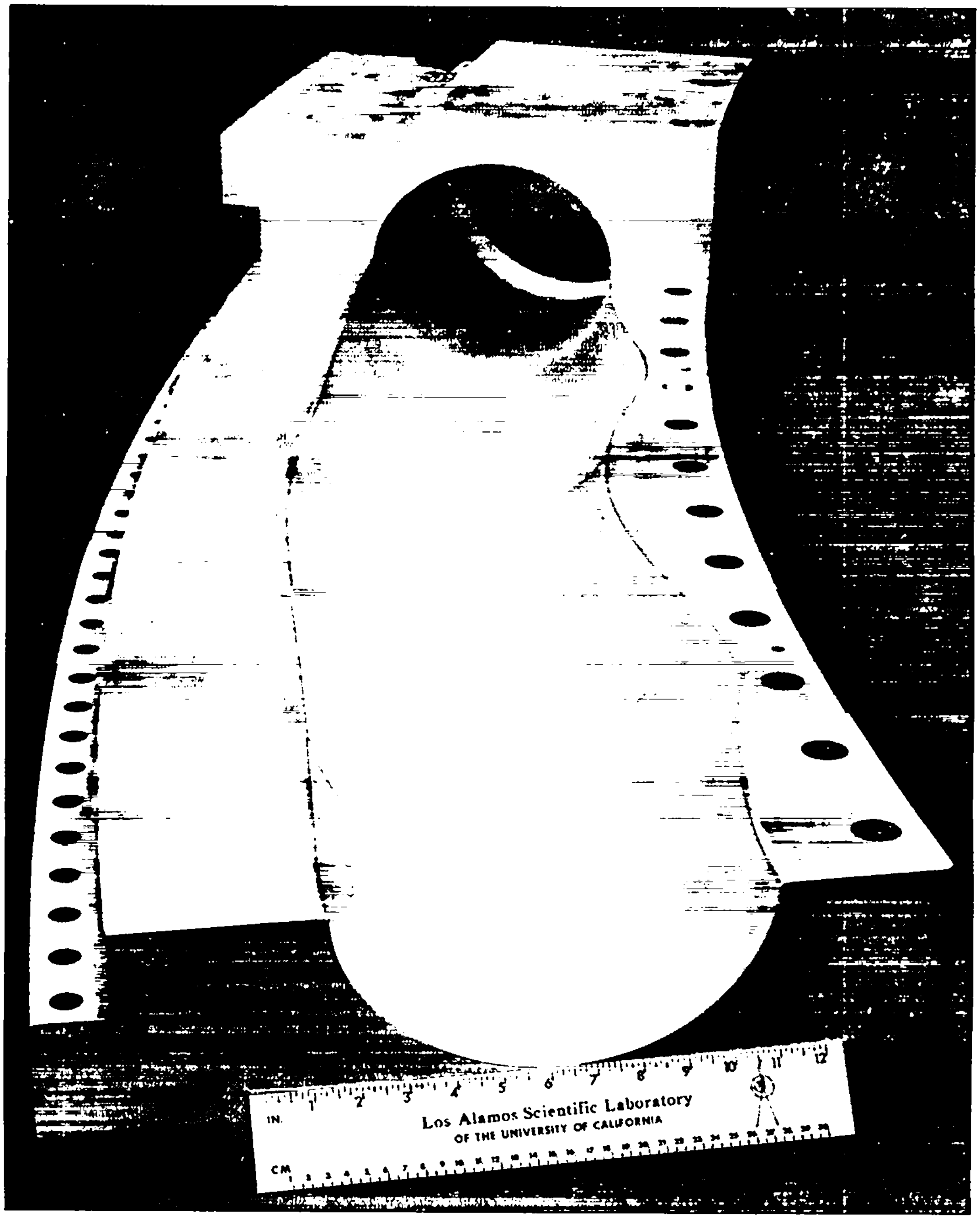

Fig. III-3
A photograph of a section of the shaped compression coil for the derated sector.

TABLE III-1

SCYLLAC PARAMETERS

Parameter	Full Torus Experiment	Sector Feedback Experiment
B_o (kG)	40	15
E_θ (v/cm)	445	170
$\tau/4$ (μs)	3.7	3.5
β	0.8	0.65
a (CM)	1.0	1.42
$n(cm^{-3})$	2.7×10^{16}	1.33×10^{16}
T (eV)	1177	272
v_A (cm/sec)	37.55×10^{6}	20.04×10^{6}
$\lambda_{1,0}$ (cm)	41.89	62.83
$h(cm^{-1})$	0.15	0.10
δ_1	0.71	0.98
δ_o	0.16	0.21
$\gamma(\mu s^{-1})$	0.705	0.318
$\gamma\tau_{FB}$	1.1 - 1.5	0.48
B_{FB} (G) (ξ=1.0 cm)	620	342

$\lambda_{1,0}=2\pi/h$, where h is the $\ell=1,0$ wavenumber. Freidberg has done a theoretical optimization to minimize γ which gives an optimum wavenumber,

$$h_{(\min\gamma)} = \left[\frac{(4-3\beta)(3-2\beta)(2-\beta)^2}{16(1-\beta)^2}\right]^{-1/6} \left[Ra^2\delta_1^2\right]^{-1/3} . \tag{10}$$

It is convenient to express γ, Eq. (1), and $B^{FB}_{\ell=0}$, Eq. (5), in terms of the $\ell=1$ helical equilibrium field, $B_1 \equiv B_{\ell=1}/B_o$ using $\delta_1 = 2B_1/ha(1-\beta)$ and the equilibrium relation, $\delta_o = 2/(3-2\beta)h^2aR\delta_1$, to obtain

$$\gamma = v_A\left[\frac{\beta(4-3\beta)}{2(1-\beta)(2-\beta)}\, h^2B_1^2 + \frac{\beta(1-\beta)(2-\beta)}{(3-2\beta)}\, \frac{1}{R^2B_1^2}\right]^{1/2} , \tag{11}$$

where the wall-stabilization term has been neglected, and

$$B^{FB}_{\ell=0} = \left[\frac{(4-3\beta)}{(3-2\beta)}\, hB_1 + \frac{2(1-\beta)^2(2-\beta)^2}{(3-2\beta)^2}\, \frac{1}{hR^2B_1^3}\right]\xi B_o . \tag{12}$$

The growth rate γ, Eq. (11), is plotted as a function of β for $h=0.10\ cm^{-1}$ and $B_1 = 0.09459$ in Fig. III-4 and as a function of B_1 for $\beta = 0.65$ in Fig. III-5 for Alfvén velocities in the range of 1.5 to 3.5×10^{7} cm/s.

The feedback field $B^{FB}_{\ell=0}$, Eq. (12), required for stabilization of the m=1 mode is plotted as a function of β for $h=0.10\ cm^{-1}$ and $B_1=0.09459$ in Fig. III-6 and as a function of B_1 for $\beta=0.65$ for ξB_o values in the range of 10 to 30 kG-cm in Fig. III-7.

Minimization of the required feedback field, Eq. (12) [which is proportional to γ^2, Eq. (11)] with respect to B_1 gives

$$h\left(\min B^{FB}_{\ell=0}\right) = \left[\frac{2(1-\beta)^2(2-\beta)^2}{(3-2\beta)(4-3\beta)}\right]^{1/2} \frac{1}{RB_1^2} . \tag{13}$$

The optimum values of h from Eq. (10) and Eq. (13) for $\beta\sim0.65$ and $B_1\sim0.09$ are in the vicinity of 0.1, which corresponds to an $\ell=1,0$ wavelength of 62.8 cm. Practical considerations such as an integral number of $\ell=1,0$ wavelengths around the torus and the machining of the inner surface of the coil lead to a choice of $\lambda_{1,0}=62.83185$ cm and a corresponding $h=0.10\ cm^{-1}$. This choice consists of 3 coil sections per wavelength.

Taking $h=0.10\ cm^{-1}$, the optimum B_1 field can be determined from Eqs. (10) and (13) for h, which minimizes γ and $B^{FB}_{\ell=0}$, respectively. Table III-2 lists the resulting feedback parameters for a B_o field of 15 kG.

The parameters in the first row of Table III-2, i.e., with $\beta=0.65$ and $B_1=0.09459$, have been selected for the sector experiments. The $\beta=0.7$ and $B_1 = 0.08774$ case is a better selection from a feedback point of view, however, there is some question about making a plasma β of 0.7 with the reduced E_θ and B_o. Secondly there is concern about the separation of the helical plasma from the discharge tube wall, which would be smaller with $\delta_1=1.08$.

The selected parameters are listed in Table III-1 with the Scyllac full-torus parameters.

D. Analysis of the Feedback Loop

The Scyllac experiment has shown the m=1 growth rate and toroidal mode structure to be

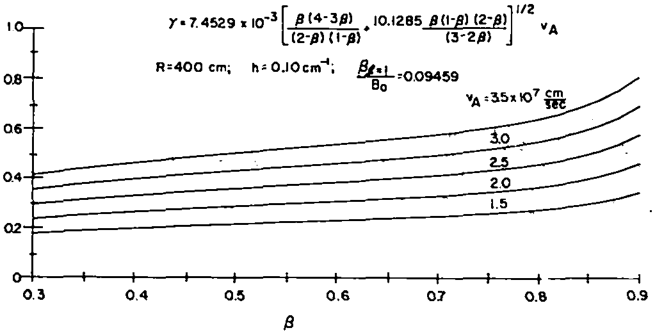

Fig. III-4
Graphs of the m=1 growth rate as a function of the plasma β for various Aflvén speeds.

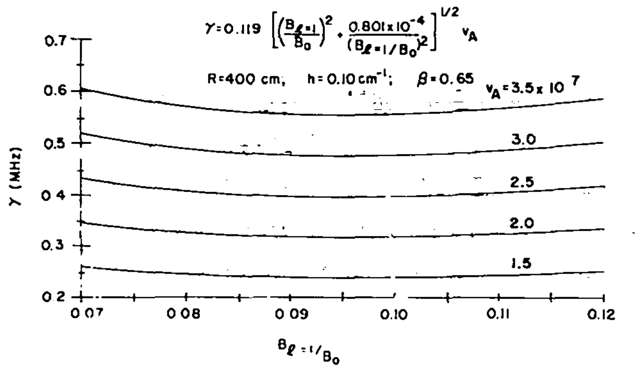

Fig. III-5
Plots of the m=1 growth rate as a function of the ℓ=1 field for the indicated Alfvé speeds.

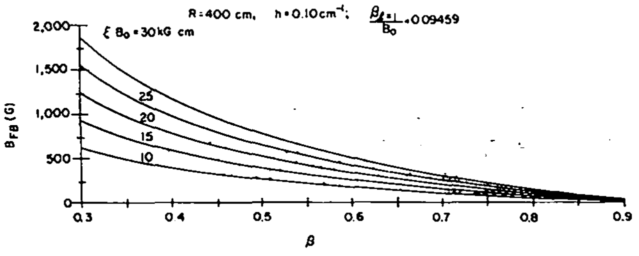

Fig. III-6
Graphs of the feedback field required for stabilization of the m=1 instability as a function of the plasma β for the indicated values of ξ B₀.

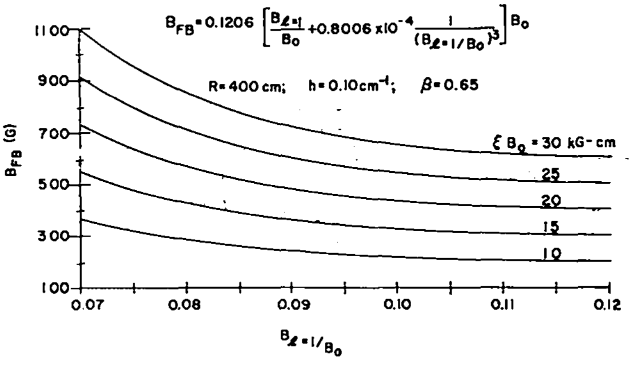

Fig. III-7
Plots of the feedback field required for stabilization of the m=1 instability as a function of the ℓ=1 helical equilibrium field for the indicated values of ξ B₀.

generally in line with those predicted by sharp boundary MHD theory. Also in the past year a less marginal configuration of the feedback system has been decided upon, and the relevant parameters measured. With these updated inputs analysis of the feedback loop has been carried out taking into account delay and risetime of the feedback controlled ℓ=0 field, plasma dynamics, toroidal mode structure, and feedback amplifier saturation and threshold characteristics. The result is a generally favorable prognosis for the upcoming Scyllac feedback experiment, although a previously ignored additional delay, the time for plasma axial flow, reduces the capability of the system.

1. **Feedback Model.** As a starting point the simplest case of m=1, n=0 plasma motion (rigid sideways motion) will be considered. With a linear position and velocity control algorithm[6] The equation of motion is

$$\ddot{\xi}(t) = \gamma^2\xi(t) - F_{max}\left(\alpha\xi(t-\tau) + \beta\dot{\xi}(t-\tau)\right) , \quad (14)$$

where ξ is the plasma displacement from its equilibrium position, γ^2 the growth rate squared of the unstable m=1, n=0 plasma displacement from sharp boundary MHD theory, τ the time delay in the feedback system, and F_{max} the maximum feedback $F_{1,0}$ "force" corresponding to the maximum ℓ=0 field produced by the feedback system. Under the conditions expected for the Scyllac feedback experiment, γ= 0.33 μs^{-1}, τ=1.5 μs, and F_{max}=.11 cm μs^{-2}, the latter for a maximum ℓ=0 field of 350 G.

TABLE III-2

OPTIMIZED FEEDBACK PARAMETERS FOR B_o = 15 kG

h	β	a (cm)	B_1	γ (MHz)	B_{FB} (G)	δ_1	δ_o
$h_{\min B^{FB}_{\ell=0}}$	0.65	1.42	0.09459	0.318	342	0.986	0.210
$h_{(\min \gamma)}$	0.65	1.42	0.07955	0.329	432	0.829	0.250
$h_{\min B^{FB}_{\ell=0}}$	0,7	1.37	0.08774	0.317	313	1.079	0.211
$h_{(\min \gamma)}$	0.7	1.37	0.07478	0.330	386	0.92	0.248

The position and velocity gains are α and β with $1/\alpha$ and $1/\beta$ the plasma displacement and velocity that produce maximum (saturated) output of the feedback amplifier.

2. Frequency Response Analysis. Neglecting saturation Eq. (14) is a linear equation with solutions of the form $e^{-i\omega t}$. The frequencies ω are roots of the following equation obtained by expressing $\xi(t)$ in terms of its Fourier components,

$$-(\omega/\gamma)^2 = 1 - \xi_{max}(\alpha - i\omega\beta)\, e^{i\omega\tau} \quad , \qquad (15)$$

where ξ_{max} is F_{max}/γ^2, the plasma displacement that leads to an unstable force equal to the maximum feedback force.

With the assumption of small time delay ($\omega\tau \ll 1$) Eq. 15 is quadratic and the two roots are

$$\omega = i\gamma \frac{-\gamma\xi_{max}(\beta-\alpha\tau) \pm \sqrt{\gamma^2\xi^2_{max}(\beta-\alpha\tau)^2-4(\alpha\xi_{max}-1)(1-\beta\xi_{max}\gamma^2\tau)}}{2(1-\beta\xi_{max}\gamma^2\tau)} \,. \qquad (16)$$

To avoid a positive imaginary part of ω, the following conditions are seen to be necessary

$$\alpha > 1/\xi_{max} \quad , \qquad (17)$$

$$1/(\xi_{max}\gamma^2\tau) > \beta > \alpha\tau \quad . \qquad (18)$$

This indicates that velocity control ($\beta \neq 0$) is essential when time delay is present.

In the general case Eq. (15) has more than two roots so that there are more than two linearly independent solutions of Eq. (14) and the motion is not specified by the initial position and velocity alone.

a. $\gamma\tau$ **Limitation.** The transcendental equation, Eq. (15) has well defined roots even when time delay is not small. It seems to be the case that as $\gamma\tau \to 1$, it is impossible to keep these roots out of the upper half of the complex ω plane by adjusting the gains α and β. This is illustrated in Fig. III-8 which shows the variation in growth rate produced by varying the gains from 0 to some final values, keeping velocity gain β proportional to position gain α. By suitably choosing the ratio of β to α it is possible to make the locus of roots barely dip into the lower half plane for $\gamma\tau = 1$, but this appears to be very close to the upper limit of time delays where this is possible.

b. Amplifier Frequency Response. The amplifier response is approximated by a pure delay τ and the frequency response function is thus $e^{i\omega\tau}$. A more realistic assumption is that the response is characterized partly by a delay τ_d and partly by an L/R risetime. In that case the response would be $\exp(i\omega\tau_d)/(1-i\omega L/R)$. The consequence of substituting into Eq. (15) such a response function, consistent with measurements of amplifier performance, namely with τ_d = 0.9 μs, L=15 μH, and R=50Ω, is generally to improve the stability of the system. This is as might be expected because the effective time delay in this case would seem to be somewhat less.

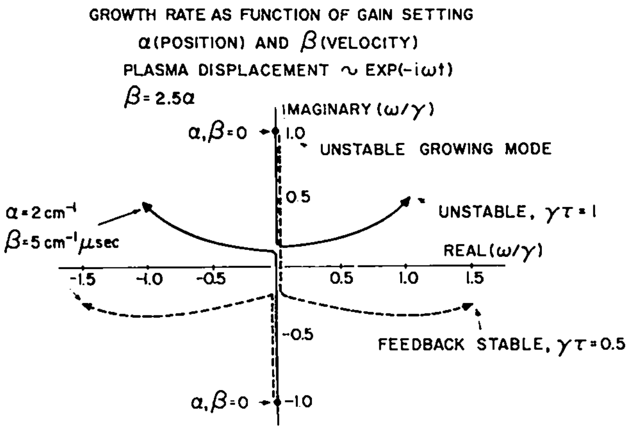

Fig. III-8

Plots of the m=1 growth rate as a function of the position (α) and velocity (β) gains of the feedback system with $\beta = 2.5\ \alpha$ for the indicated $\gamma\tau$ values.

c. Plasma Dynamics. In deriving the feedback equation of motion Eq. (14) it is assumed that the time scale is such that δ_0 takes on an equilibrium value, with negligible delay, corresponding to the applied feedback $\ell = 0$ field. This assumption will now be examined more closely.

The feedback $F_{1,0}$ force in the case of non-equilibrium is given by[7]

$$F = \bar{F}\,\frac{\left[\bar{\delta}_1\delta_0(2-\beta)-2(1-\beta)\bar{\delta}_0\left(\bar{\delta}_1(2-\beta)-\delta_1\right)\right]}{\bar{\delta}_0\bar{\delta}_1\beta(3-2\beta)}\,, \tag{19}$$

where the bars denote equilibrium values. In the case of high β, with $\delta_1 = \bar{\delta}_1$, this means that the force is roughly proportional to δ_0.

Using sharp boundary MHD theory[8] it can be shown that the plasma response as a function of frequency ω to an applied $\ell = 0$ field is

$$\delta_\omega = \frac{B_\omega^{(\ell=0)}}{B_o}\ \frac{1}{2(1-\beta)}\ \frac{(hc)^2-\omega^2}{(hc)^2}\ \frac{(hv_o)^2}{(hv_o)^2-\omega^2} \tag{20}$$

where δ_ω is the Fourier component of $\delta_0(t)$, h is the wavenumber of the applied field, c is the sound velocity given by $c = \sqrt{\gamma\beta/2}\,v_A$, and v_0 is the group velocity of an m=0 disturbance, given by

$$v_o = v_A\sqrt{\frac{(1-\beta)\gamma\beta}{\gamma\beta+2(1-\beta)}} \tag{21}$$

for β not too near 0 or 1. In both limiting cases $\omega \to 0$ (equilibrium response) and $\omega \to \infty$ (instantaneous response) Eq. (20) can be derived from elementary considerations, constant pressure along the column in the former case, and local adiabatic compression or expansion in the latter case.

The consequences of inserting the frequency response function obtained from Eq. (19) and Eq. (20) into Eq. (15) are that new weakly damped or growing oscillation frequencies are obtained, related to the natural frequency $\omega = hv_0$. However because the bounciness, due to the lack of any damping, of the plasma described by Eq. (20) seems unphysical, we concluude only that plasma dynamics may be responsible for an additional delay.

This delay is equal to the propagation time over a quarter wavelength, $\pi/(2h)$, at the velocity v_0, which is roughly the thermal velocity. For the conditions of the feedback experiment the numerical value is $\tau_p = 1.6\ \mu s$, or $\gamma\tau_p \cong 0.5$.

The ratio of instantaneous response to equilibrium response from Eq. (20) is given by $(1-\beta)/(\gamma\beta/2+1-\beta)$. For the expected β of the feedback experiment ($\beta = .65$) this is about 0.4. Thus a fair fraction of the feedback force is applied without any delay.

3. Integration of the Equations of Motion. A more straightforward approach to Eq. (14) is to integrate it numerically to obtain the plasma displacement as a function of time and check that the motion remains within the confines of the discharge tube. This method has the advantage that toroidal mode structure and nonlinear effects may be included. The disadvantage is that only a pure time delay can be assumed.

a. Toroidal Modes. It appears that the plasma instability in the Scyllac torus is characterized by a number of modes along the toroidal axis, generally consistent with sharp boundary MHD theory, which predicts the following relation between growth rate and n,

$$\gamma_n^2 = \gamma_{n=0}^2 - (2-\beta)\left(\frac{n}{R}\right)^2 v_A^2\ , \tag{22}$$

where R is the major radius of the torus. The feedback system is thus faced with the task of stabilizing a plasma displacement which is a function of toroidal angle ϕ as well as time,

$$\xi(\phi,t) = \sum_{n=0}^{\infty}\left[a_n(t)\cos n\phi + b_n(t)\sin n\phi\right]\ . \tag{23}$$

The generalization of the equation of motion, Eq. (14) for higher n modes is a physically reasonable extension of the $F_{1,0}$ body force concept. The n^{th} Fourier component of the feedback force considered as a function of ϕ is assumed to act on the n^{th} mode amplitude together with the unstable force e.g., $\ddot{a}_n = \gamma_n^2 a_n - F_n$.

Two slightly different feedback algorithms were considered, both generalizations of the linear position and velocity control given by Eq. (14). In the first, each position detector station was used to drive equally the power amplifiers and $\ell = 0$ coils nearest to it. In the refined algorithm, illustrated in Fig. III-9, the position detector signals are interpolated between stations, as might be accomplished with simple voltage divider networks. In the numerical work the following parameters were assumed:

$\gamma_{n=0} = .33\,\mu s^{-1}$

$\tau = 1.5\,\mu s$

$\xi_{max} = 1.0$ cm

$n_{max} = 5$

where n_{max} refers to the maximum unstable n value. The series given by Eq. (23) was truncated at n = 7 neglecting the effect of higher order stable modes.

The differential equation of motion was integrated for various choices of gains, α and β, and initial conditions. In Fig. III-10 are shown the plasma position versus time trajectories at one point on the torus (ϕ=0) calculated for various gain settings. The damping effect of velocity gain is illustrated. The initial conditions are a uniform (n=0) 3-mm displacement at t = 0 and each a_n and b_n having a random initial velocity in the range ± 0.05 cm/μs. The refined feedback algorithm illustrated in Fig. III-9 is used; however, only a small difference is caused by use of the simpler algorithm.

The range of gain settings that stabilized the motion with the initial conditions as stated was approximately $2 < \alpha < 5$, $3 < \beta < 20$, and $1.5 < \alpha < \beta$,

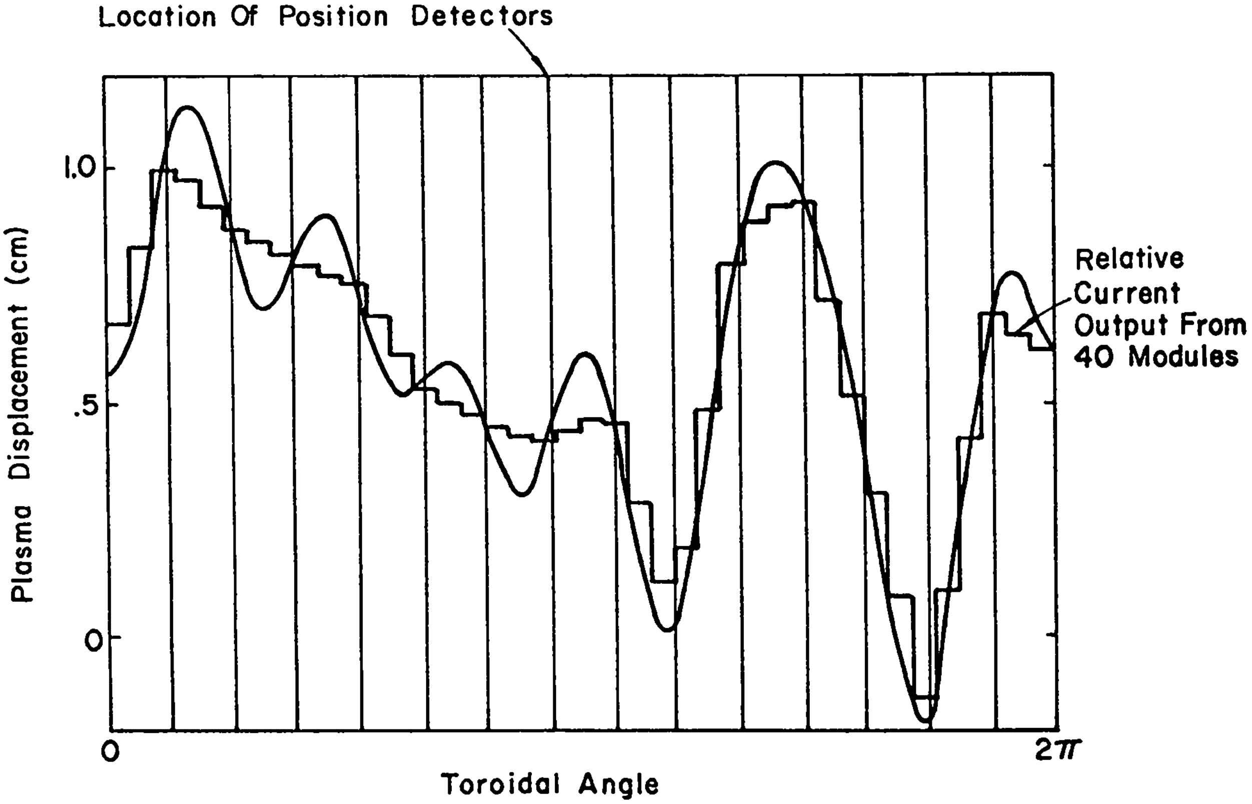

Fig. III-9
Computer simulation of the plasma position and the feedback output current as a function of toroidal angle with multiple position detectors.

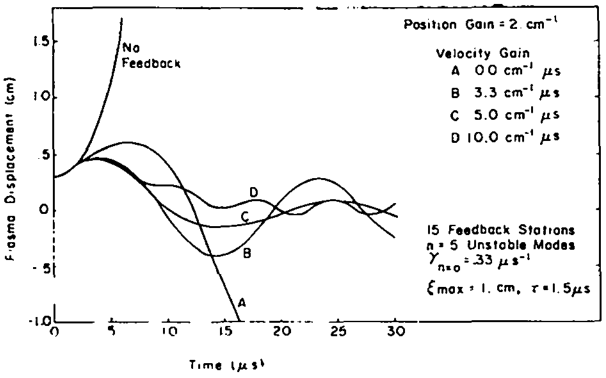

Fig. III-10
Graphs of the plasma position versus time trajectories at a fixed toroidal position ($\phi=0$) for various velocity gain settings.

in qualitative agreement with the gain limitations given by Eq. (17). This range is comparable to that obtained when only one mode was allowed with the initial velocity increased to compensate for fewer degrees of freedom.

The number of feedback stations required for $n_{max} = 5$ is greater than ten so that the distance between detector stations is less than the smallest unstable half-wavelength. The computer studies indicated that 15 stations was a workable number. A configuration with 11 or 12 stations was unable to hold the plasma with the same initial conditions.

b. Amplifier Non-Linearity. Feedback amplifier saturation was included in the computations leading to Fig. III-10. The split phase design of the amplifiers seems to result in an unavoidable threshold type non-linearity as well. This is illustrated in Fig. III-11. A 20% threshold, that illustrated in the figure, was incorporated into the computer calculation with surprisingly little deleterious effect. The range of gain settings for stability quoted above was only slightly diminished. Thresholds of 30 — 40%, however, led to loss of stability.

4. Conclusions. Feedback stabilization of the $m = 1$ instability looks feasible on the basis of these modeling exercises. Realistic time delays, toroidal mode structure (with a sufficient number of position detector stations), and amplifier nonlinearity are all surmountable obstacles. The time required for axial flow of the plasma is a significant additional delay and may be a serious problem if the estimates of its magnitude are correct.

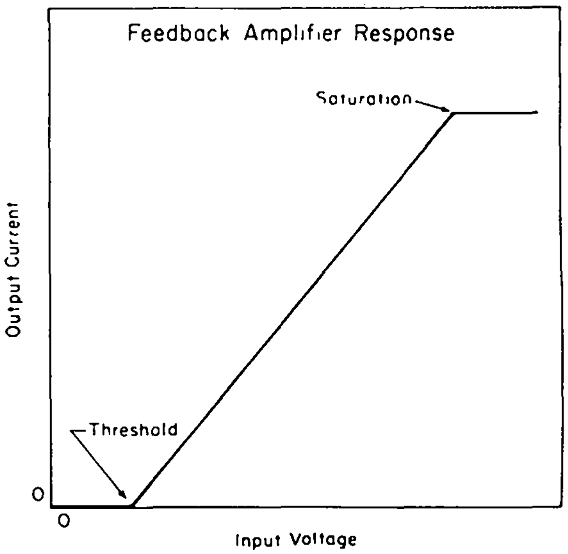

Fig. III-11
Measured output current response of the feedback amplifier system as a function of input voltage.

E. Status of the Feedback Stabilization Experiments

Following the Scyllac full torus experiments, which were completed in late November 1974, the modification of a 120° sector (8.4-m arc length) of the torus and the installation of the feedback components were begun. The Scyllac compression coils were bored out and their inner surfaces machined to the new design of the $\ell = 1$ and $\ell = 0$ equilibrium fields as given in Table III-1. The sector bank has been modified to operate at one-half capacity for the derated experiments. The assembly of the compression coils with the discharge tube and the device check out should be completed by mid-February 1975. The initial experiments will determine the derated plasma behavior and parameters in the absence of the $\ell = 0$ feedback coils, which will be installed in March 1975.

References

1. F.L. Ribe and M.N. Rosenbluth, "Feedback Stabilization of a High-β, Sharp-Boundaried Plasma Column with Helical Fields," Phys. Fluids 13, 2571 (1970).

2. J.P. Freidberg, "Stability of the Straight =1 Scyllac Configuration," Phys. Fluids 14, 2454 (1971).

3. "Annual Progress Report LASL Controlled Thermonuclear Research Program," Los Alamos Scientific Laboratory Report, LA-5656-PR (July, 1974).

4. R.F. Gribble, S.C. Burnett, and C.R. Harder, "Feedback Stabilization of an $\ell=1$ Theta-Pinch Plasma Column," Proc. Second Topical Conf. on Pulsed, High-Beta Plasmas, Garching, W. Germany, July 1972, p. 229, Garching Report IPP-1/127 (1972).

5. W.R. Ellis, R.F. Gribble, and C.R. Harder, "Preliminary $\ell_{1,0}$ Feedback Force Experiments on Scylla IV-3," Los Alamos Scientific Laboratory Report LA-5788-MS (November 1974).

6. K.I. Thomassen, "Feedback Systems on Linear θ Pinches with Helical Fields," Los Alamos Scientific Laboratory Report LA-4598-MS.

7. G. Miller, "Motion of a Plasma Column in a Perturbing Magnetic Field," Phys. Fluids, to be published.

IV. STAGED THETA PINCH PROGRAM

K. Thomas, W. Borkenhagen, D. Call. R. Dike, J. Downing, R.Gribble, C. Hammer, A. Jacobson, R. Kewish, R. Linford, E. Little, M. McKinstry, A. Rawcliffe, G. Sherwood, T. Zaugg

A. Introduction

Previous theta pinches have performed initial implosion heating of the ions and subsequent adiabatic compression with a single capacitor bank power supply. Projected theta pinch feasibility experiments and fusion reactors, however, will require separation of the two functions to achieve greater implosion heating and less adiabatic compression. The Staged Theta Pinch (STP) program is designed to study the technological and physics problems associated with separating the two functions.

The principal experiment in the program is the 4.5-m-long linear STP. It will use a relatively low energy, high-voltage capacitor bank to produce the theta pinch plasma. A lower voltage, higher energy capacitor bank will be used to contain the plasma and provide a variable amount of adiabatic compression. The experiment will be capable of producing high temperature plasmas with a much larger ratio of plasma radius to discharge tube radius than is possible in conventional theta pinches. Plasma experiments will study the effect of magnetic field amplitude and time history on plasma formation, the properties of the plasma formed, and later, the effect of helical magnetic fields on plasma stability. If the ratio of plasma radius to coil radius can be made large enough, the effect of plasma stabilization by image currents in the coil walls will be observable.

In addition, two smaller experiments were constructed to support the main program. The first, the 0.9 m long STP prototype, was operated from May to October 1974. It was used to obtain experience in the design and operation of high voltage experiments and to conduct initial studies of the effect of time varying magnetic fields on plasma behavior. The experiment was operated in the corner of the STP experimental area and was closed down to allow completion of the 4.5 m experiment. The Resonant Heating Experiment was constructed in another area during the last four months of 1974. It uses components of the same design as the new components used in the 4.5 m STP experiment as well as parts from the 0.9 m STP prototype. This experiment will be useds to test new circuits and components for possible use on the 4.5 m STP.

B. Resonant Heating Concept

Resonant heating is the name given to a new method of implosion heating which involves the "tuning" of a simple circuit to the plasma dynamics resulting in a "fat" plasma, i.e., a plasma with a relatively large ratio of plasma radius to implosion coil radius. This process could be used in future theta pinch feasibility experiments where it would be followed by an adiabatic compression. Because the resonant heating creates a hot fat plasma, the adiabatic compression can raise the plasma to thermonuclear temperatures without making the plasma radius too small for wall stabilization as mentioned in Section A.

Other implosion heating methods have been proposed for producing fat plasmas. Freidberg, Morse, and Ribe[1] presented three concepts indicated in Fig. IV-1 which was taken from their paper.* No specific circuits were proposed to produce these precise waveforms, but the plasma dynamics were analyzed for each case. Since the free expansion case appeared most promising, R. Gribble designed a circuit which simulates the field behavior in Fig. IV-1b. The resulting circuit, shown in Fig. IV-4, is being used in the STP experiment described in Section C.

The resonant heating process theoretically produces plasma parameters very similar to those resulting from the STP circuit. The advantage of resonant heating is the efficiency and simplicity of

---

*The paper[1] contains an error in the calculation of the relative size of the two pulses of implosion field for the "free expansion" case, but the numerical factor has been corrected in Fig. IV-1b.

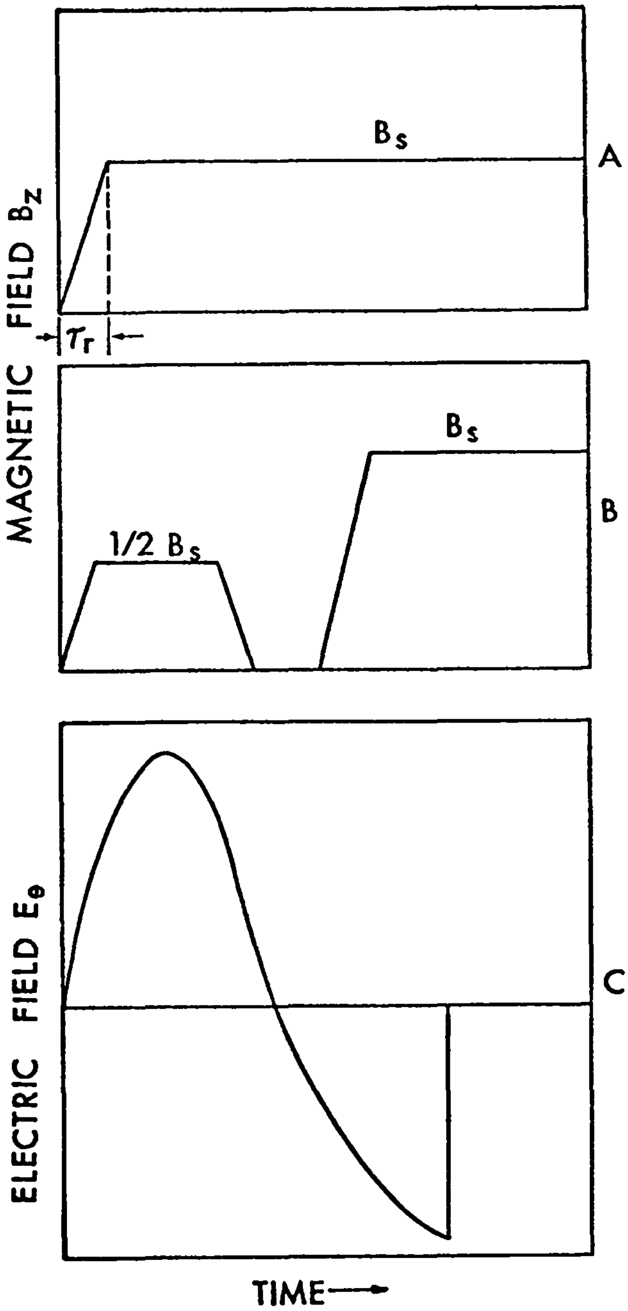

Fig. IV-1
Driving fields assumed by Freidberg, Morse, and Ribe[1] for (a) simple implosion heating, (b) free-expansion heating and (c) programmed E_θ heating of a theta-pinch plasma.

the circuit shown in Fig. IV-2a. The circuit is topologically the same as the circuits used in present theta pinches such as Scyllac, but the component sizes are chosen so that the peak field is reached before the time t_c at minimum radius as shown in Figs. IV-2a and IV-2c. This allows the field to decay to a specified value at t_c when the crowbar switch is closed. The B-field value at t_i is chosen so that the field at t_e is barely sufficient to prevent the expanding plasma from touching the wall. Following t_e the oscillations of the field and the plasma radius decay as shown schematically in Fig. IV-2. The field decays exponentially on a much longer time scale, which would allow the slowly rising compression field of future experiments to take over. Since this simple crowbar is sufficient, the power crowbar used in the STP experiment appears to be unnecessary in these future experiments.

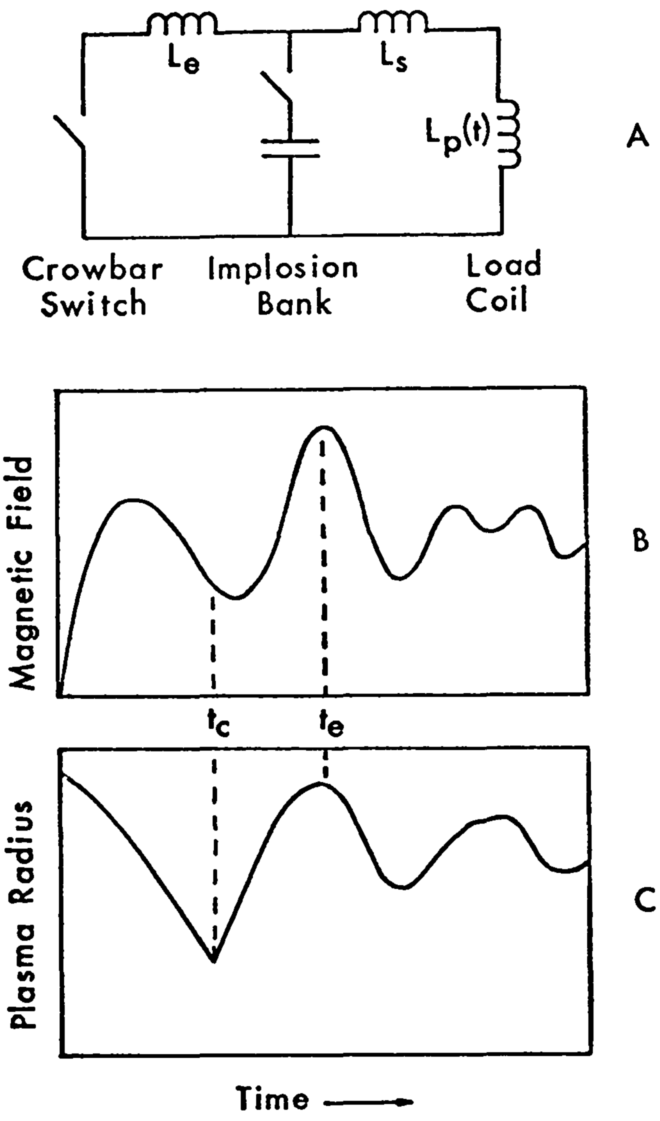

Fig. IV-2
Resonant heating circuit showing the temporal behavior of the B-field and the plasma.

The field profile of the resonant heating system (Fig. IV-1b) is somewhat similar to the free-expansion case in Fig. IV-2b since the plasma is allowed to reexpand against a field which is less than the initial implosion field. This feature reduces the work done by the expanding plasma on the field. In the STP circuit, this field programming is accomplished by properly tuning the resonant frequencies of the two circuit loops containing the implosion banks, and by closing the switches at the appropriate times. In the resonant heating case, the natural resonance of the imploding and expanding plasma is used as the second "resonant loop" thus necessitating only one properly tuned implosion bank.

The actual design of the circuit and numerical comparison with the STP circuit requires the use of a model for the plasma dynamics which strongly affects the circuit behavior through the load inductance L_p. Several analytic and numerical simulation codes are being used at the present time.* Preliminary results indicate that the plasma characteristics are similar for the STP and resonant heating circuits, as previously mentioned, but the efficiency of transfer of stored capacitor energy to plasma energy is about 3 times higher for the resonant heating circuit than for the STP circuit. This efficiency and simplicity makes the resonant system easier and less costly to build and operate.

In addition to the theoretical comparisons now being worked on, a Resonant Heating Experiment (RHX) described in Section E is being constructed so that experimental results can be compared with STP and the theoretical models.

C. 4.5 m STP

1. Description. The layout of the STP experiment in the old Scylla IV experimental area is shown in Fig. 3. The staging bank, which is the Scylla IV 50 kV main bank, is located on a platform above the high voltage implosion circuit. The start switches for the staging bank have been moved down to the collector plate in order to isolate the load cables from the high voltage circuit. This necessitated the replacement of the start switch in the Scylla IV capacitor gaps with a shorting column. The crowbar system was left intact. The high voltage gaps are connected directly into the collector plates.

The circuit design is shown in Fig. IV-4. The 22.5-cm-i.d. compression coil is fed from both sides and Fig. IV-4 represents a 0.9-m-long section. There are five such sections on each side of the machine. The opposite sides will operate at different electrical polarities, which requires the insulating of the electrical components from ground potential. The high voltage (125 kV) part of the circuit is divided into two parts with independent trigger systems.

Figures IV-5 and IV-6 are photographs of the experiment as it existed in mid-December 1974. Figure IV-5 is an end view of the coil and implosion circuit part of the experiment and Fig. IV-6 is a top view of the same area.

2. Construction. Engineering design of the STP was started during the summer of 1973 and construction started in August of that year. The platform and capacitor racks were installed during January 1974. The staging bank capacitors were installed in February 1974. Assembly of the Pulse Forming Network (PFN) charging Marxes was completed by August 1974. The installation of the PFN gaps, capacitors and collector plates was completed by October 1974. Construction of the experiment should be complete by late January 1975. Preliminary electrical checkout of the new trigger systems started in December 1974.

3. Engineering. The STP has a 4.5-m-long load coil and collector plate system. The collector plate system consists of five individual assemblies at each of two feed points. It is arranged so that a fault in the collector plate insulation can be repaired without disassembling the entire collector plate.

The discharge tube consists of two 2.75-m-long quartz sections, with 21-cm o.d. The sections are jointed together using a nylon-Pyrex slip joint, Fig. IV-7. This joint is similar to the one used to join the Scyllac torus.

The experiment is designed so that energy is fed from two 125-kV capacitor banks to the load coil through two feedpoints, one positive and the other negative. The electric field around the discharge tube is approximately 2 kV/cm. The system consists of a number of energy storage banks shown in Table IV-7-I.

The trigger system for the preionization and crowbar is identical to that used in Scyllac. The preionization has a master gap for each polarity. The crowbar trigger consists of two masters for each polarity, which are completely independent. In the event of a single fault, this design will ensure the operation of the crowbar system and thus prevent the breakage of the discharge tube.

---

*The principal models and codes have been developed by F. Freidberg, R. Gribble, R. Linford, C. Nielson, and T. Oliphant.

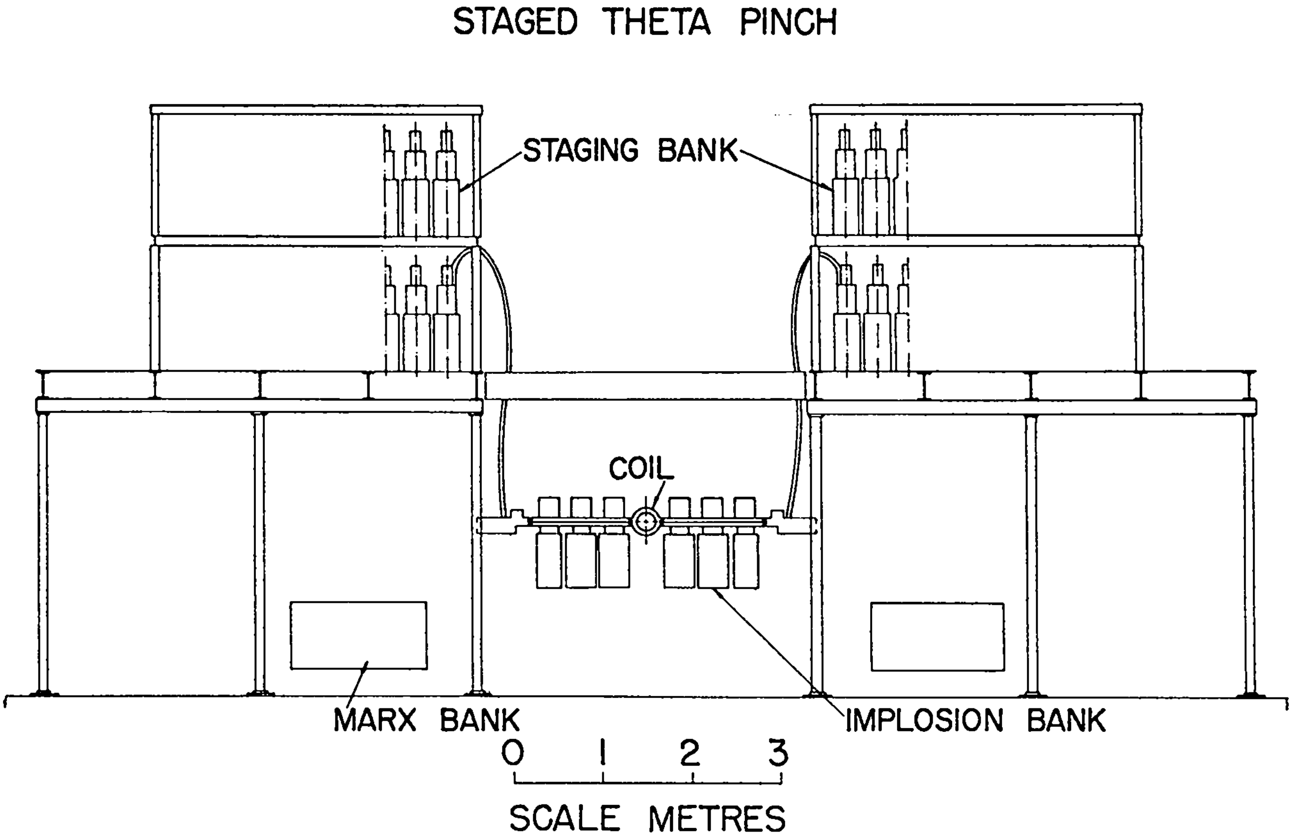

Fig. IV-3

Layout of Staged Theta-Pinch experiment.

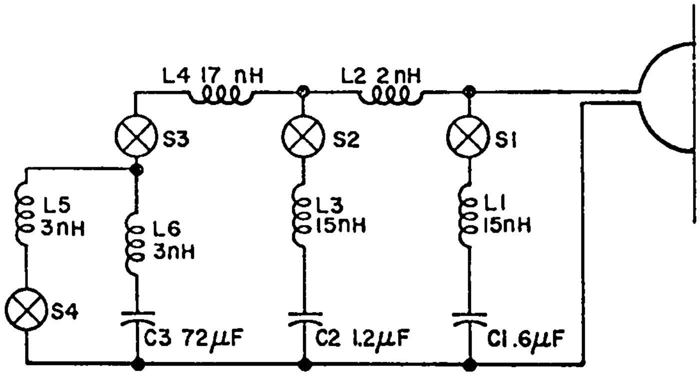

Fig. IV-4

Circuit diagram of 0.9 m section of Staged Theta-Pinch experiment.

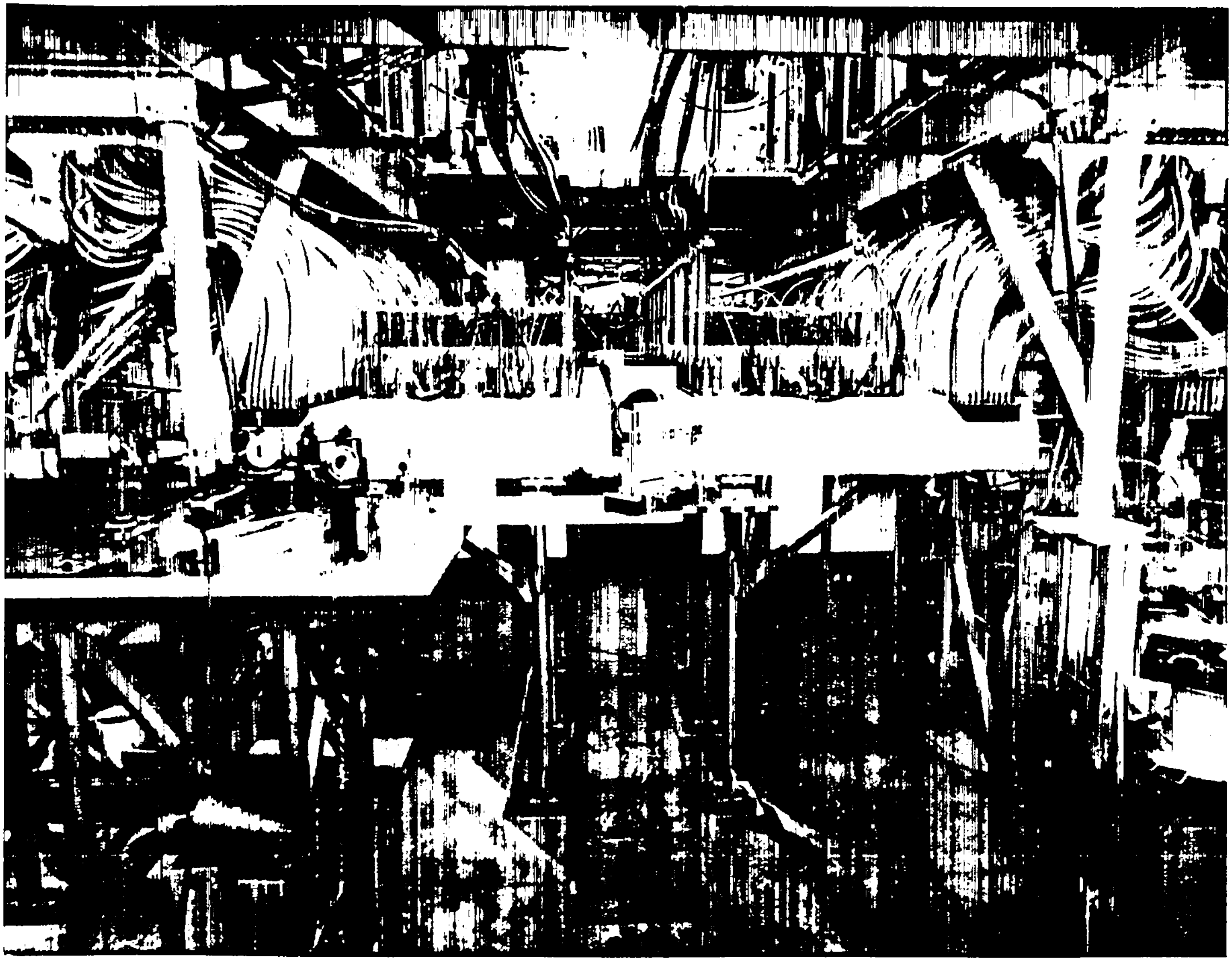

Fig. IV-5

End view of coil and implosion circuit part of Staged Theta-Pinch experiment.

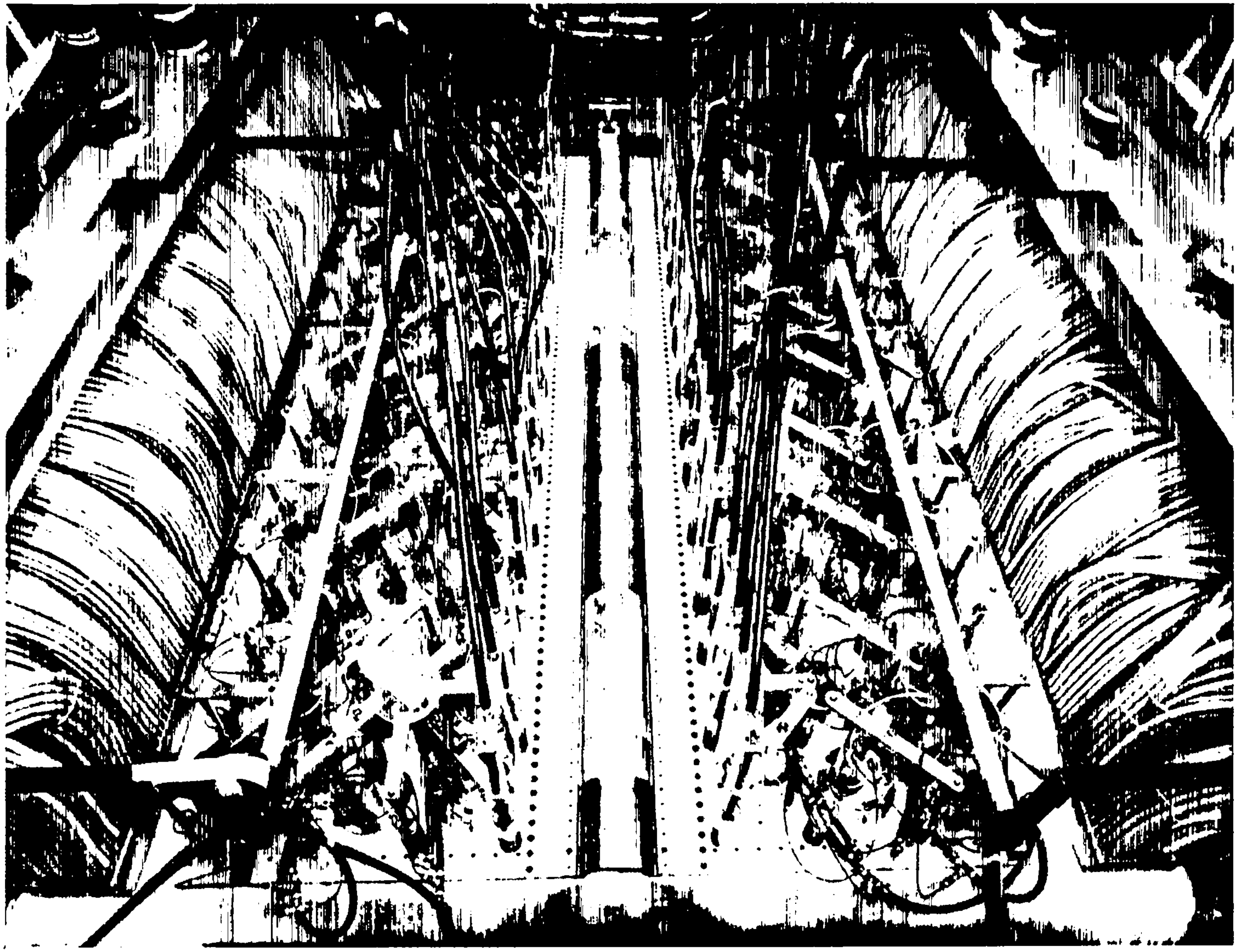

Fig. IV-6

Top view of coil and implosion circuit part of Staged Theta-Pinch experiment.

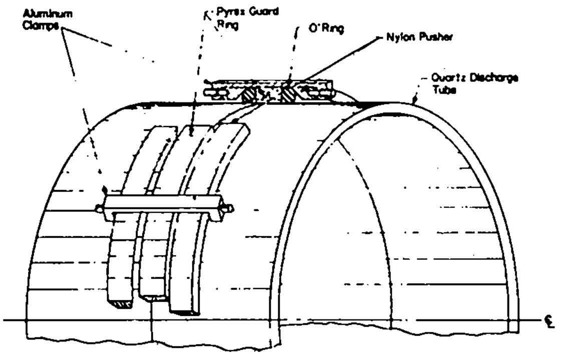

Fig. IV-7
Vacuum joint used to connect two sections of discharge tube in Staged Theta-Pinch experiment.

The trigger system for PFN 1, PFN 2, and the staging bank are all basically the same and consist of a master which in turn triggers sub-masters (two) which in turn trigger the main gaps (15 PFN or 20 staging gaps). These systems use RG-19 source and trigger cable; the source cables are pulse charged to 200 kV by a small trigger Marx unit.

The STP experiment uses two completely new spark gaps. The PFN gap is shown in Fig. IV-8. It is a 125 kV field distortion gap with fast biasing characteristics so that half the PFN capacitors may be fired without prefiring the other gaps. The staging rail gap (Fig. IV-9) is also a field distortion gap with the same fast biasing characteristics. In addition it is capable of handling the large amounts of energy from the staging bank. Both of these gaps must multichannel to operate correctly. In order that they multichannel, it is necessary that they receive a very-fast (10-15 kV/ns), very- high-voltage (200 kV) trigger voltage. Producing this type of a trigger voltage in a large system is very difficult, and may be the largest engineering problem in the future operation of the experiment.

D. 0.9 m STP Prototype

The 0.9 m STP Prototype operated with plasma from June to October 1974. The experiment had a 22-cm-i.d. compression coil with a 20-cm-i.d. quartz discharge tube. Each of the two feed points was driven by a capacitor bank consisting of three 125 kV capacitors, each capacitor having its own spark gap. The spark gaps used were modified Scyllac gaps. Because of the high inductance of the spark gaps the transfer efficiency without plasma was only about 40%. (The new gaps to be used on the 4.5 m experiment will lower the source inductance by a factor of almost two.) The experiment was operated initially with 0.2 μF capacitors. With these capacitors the magnetic field waveform without plasma was a slightly damped L-C discharge with a half period of 0.6 μs. With plasma the magnetic field waveform in the first half cycle was a slightly distorted sine wave

TABLE IV-I

SUMMARY OF STAGED THETA-PINCH ENERGY STORAGE BANKS

Bank	Type Capacitor	Number	Stored Energy (kJ)
P.I.	0.7 μF/75 kV	10	20
PFN #1	0.2 μF/125 kV	30	47
PFN #2	0.4 μF/125 kV	30	94
Staging Bank	2 μF/50 kV	320	800
Crowbar (Staging Bank)	0.7 μF/75 kV	32	63
Maxi-Marx Assemblies* (To charge PFN system)	15 μF/20 kV	80	240
TOTAL		502	1264

*These assemblies consist of eight capacitors connected in a Marx configuration with a voltage output of 160 kV maximum.

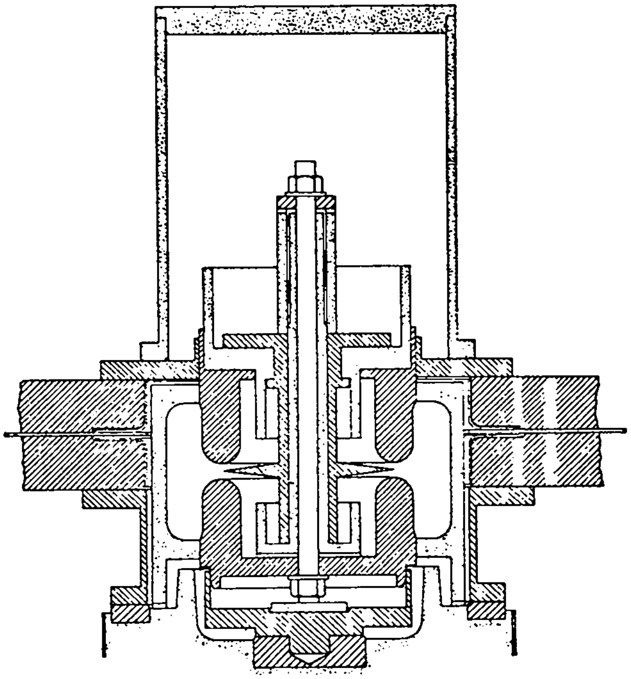

Fig. IV-8

PFN spark gap.

with a half period of 0.5 μs. Because of the higher source impedance the dL/dt term due to the imploding plasma did not cause as large a change in the magnetic field waveform as had been observed in the Scylla 1B experiment. Because of this fact, the implosion velocities in the 0.9 m experiment and in Scylla 1B were similar, allowing a close comparison of the results of the two experiments.

The 0.9 m experiment was first operated with 0.2 μF capacitors up to a voltage of 95 kV. The capacitors were then changed to 0.4 μF. This increased the time of the first half period with plasma to 0.8 μsec. When the main bank was charged to 125 kV, operating conditions were close to those desired for optimum magnetic field programming, i.e., the maximum of the magnetic field occurred slightly before the time of maximum plasma compression ($\sim$ 650 ns).

Preionization of the plasma was accomplished by a Z-pinch discharge. The preionization bank was initially a 0.7 μF capacitor. This was later increased to 1.5 μF to determine the effect of increased preionization levels on plasma performance.

Plasma diagnostics consisted of an excluded flux apparatus, an internal magnetic probe inserted axially and an end-on streak camera.

The results of the plasma studies were:

a. Two different plasma regimes were observed. The initial conditions for the two cases differed only in initial fill density or in the size of the preionization bank. The difference in plasma behavior was probably a result of different preionization levels. Similar results have been observed in Scylla 1B. For low preionization levels rapid magnetic field penetration occurs and a plasma with a relatively low $\beta(\beta<0.6)$ is formed. At higher preionization levels magnetic field penetration is about a factor of 2 slower and a high-$\beta(\beta\approx1)$ plasma is created.

b. During the implosion two luminous rings are observed. Figure IV-10 shows end-on streak camera pictures for four different plasma conditions. Of the four cases shown, the case with 8 mtorr fill and 0.5 kJ preionization capacitor had rapid magnetic field penetration. The other cases correspond to slower field penetration.

c. During the initial implosion, magnetic field gradients extend all the way to the discharge tube wall. Similar results were obtained in Scylla 1B showing that the field gradients existed even in the region where the plasma density was below the sensitivity limit of the holographic interferometer ($\sim$3 $\times$ 10^{14} cm^{-3}). Figure IV-11 shows magnetic field profiles for the case of 123 kV main bank voltage, 13 mtorr initial fill. Figure IV-11a is the external magnetic field. Figures IV-11B, IV-11c, and IV-11d show B_z vs radius for different times after main discharge initiation.

The magnetic field just inside the discharge tube wall is the same as the external magnetic field until approximately halfway through the second quarter cycle. At this time a strong breakdown at the wall (discussed below) occurs. This greatly reduces the rate at which flux can diffuse into or out of the region inside the discharge tube. Because of this effect the expansion of the plasma after the initial implosion compresses the magnetic flux outside the main plasma column against the discharge tube wall. This leads to a magnetic field time history at a point 0.5 cm inside the discharge tube which is similar to the time history desired for optimum magnetic field programming; the magnetic field external to the main plasma column decreases as the plasma expands after its initial maximum compression and then rises again to prevent the plasma column from contacting the discharge tube wall. This effect is shown in Figs. IV-11c and IV-11d. Although the plasma is still in the dynamic phase, the pressure profiles at the later times in Fig. IV-11d show that if

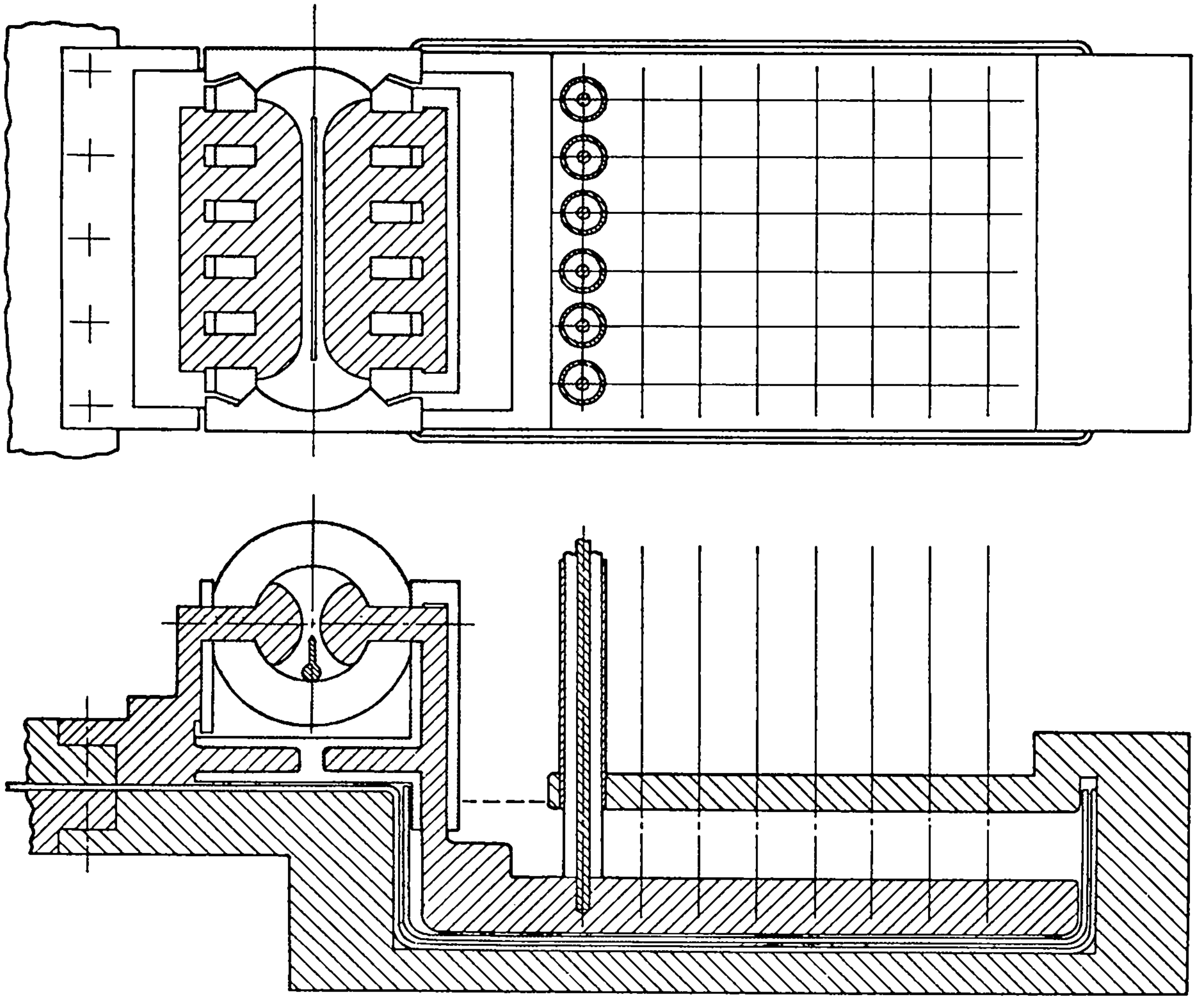

Fig. IV-9

Staging rail spark gap.

the field near the wall could be held constant the plasma would probably settle down to a radius of about 7 cm.

d. Secondary breakdown at the quartz discharge tube wall occurs about 600-700 ns after discharge initiation. The cause of the formation of the current sheath at the wall is unknown. The process may start at the time when the plasma is in contact with the discharge tube and take some time to develop, or it may be due to low density plasma being carried to the wall because of the decrease of magnetic flux inside the discharge tube.

The above results were presented, along with implosion studies on other experiments in the paper "Implosion Heating Studies in the Scylla 1B, Implosion Heating, and Staged Theta Pinch Experiments," by R. F. Gribble *et al.* presented at the Fifth Conference on Plasma Physics and Controlled Nuclear Fusion Research, Tokyo, Japan, November 11-15, 1974.

The plasma results obtained on the 0.9 m experiment lead to several conclusions. First, the mode of magnetic field programming where the magnetic field in the first half cycle is in the opposite direction from the magnetic field at later times will not work due to the large amount of magnetic flux locked into the plasma column. Secondly, a better understanding of the origin and parameters of the low density plasma which causes the magnetic pressure gradients outside the main plasma column is needed. Also more information should be obtained on the causes of wall breakdown and its dependence on discharge tube material.

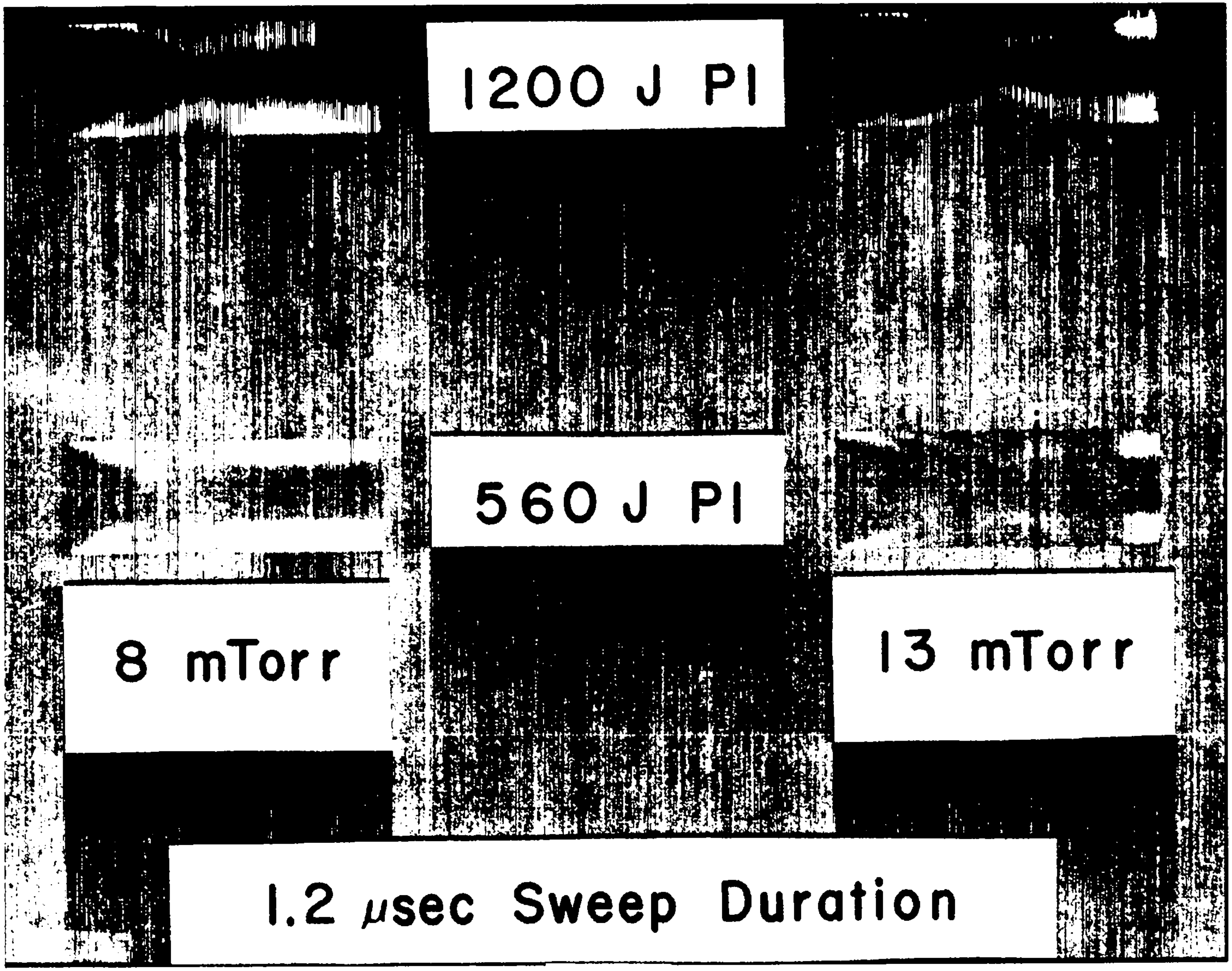

Fig. IV-10
End-on streak pictures of plasma in 0.9 m STP prototype.

E. 0.9 m Resonant Heating Experiment

The 0.9 m Resonant Heating Experiment (RHX) was designed and constructed during the last four months of 1974. In its initial configuration it is the same as a 0.9 m PFN section of the STP experiment. After initial checkout and operation, it will be converted to a configuration where each side of the experiment will have four 0.2 μF capacitors with PFN gaps. The other two gaps will be converted to crowbar gaps to study the resonant heating concepts outlined in Section B. Later it will be used to test new components such as new spark gaps and end-fed implosion coils which will be needed for future experiments on the STP experiment.

References

1. F.P. Friedberg, R.L. Morse, and F.L. Ribe, "Staged Theta Pinches with Implosion Heating," Technology of Controlled Thermonuclear Fusion Experiments and Engineering Aspects of Fusion Reactors, Austin, TX, (1974), USAEC Report CONF 721111.

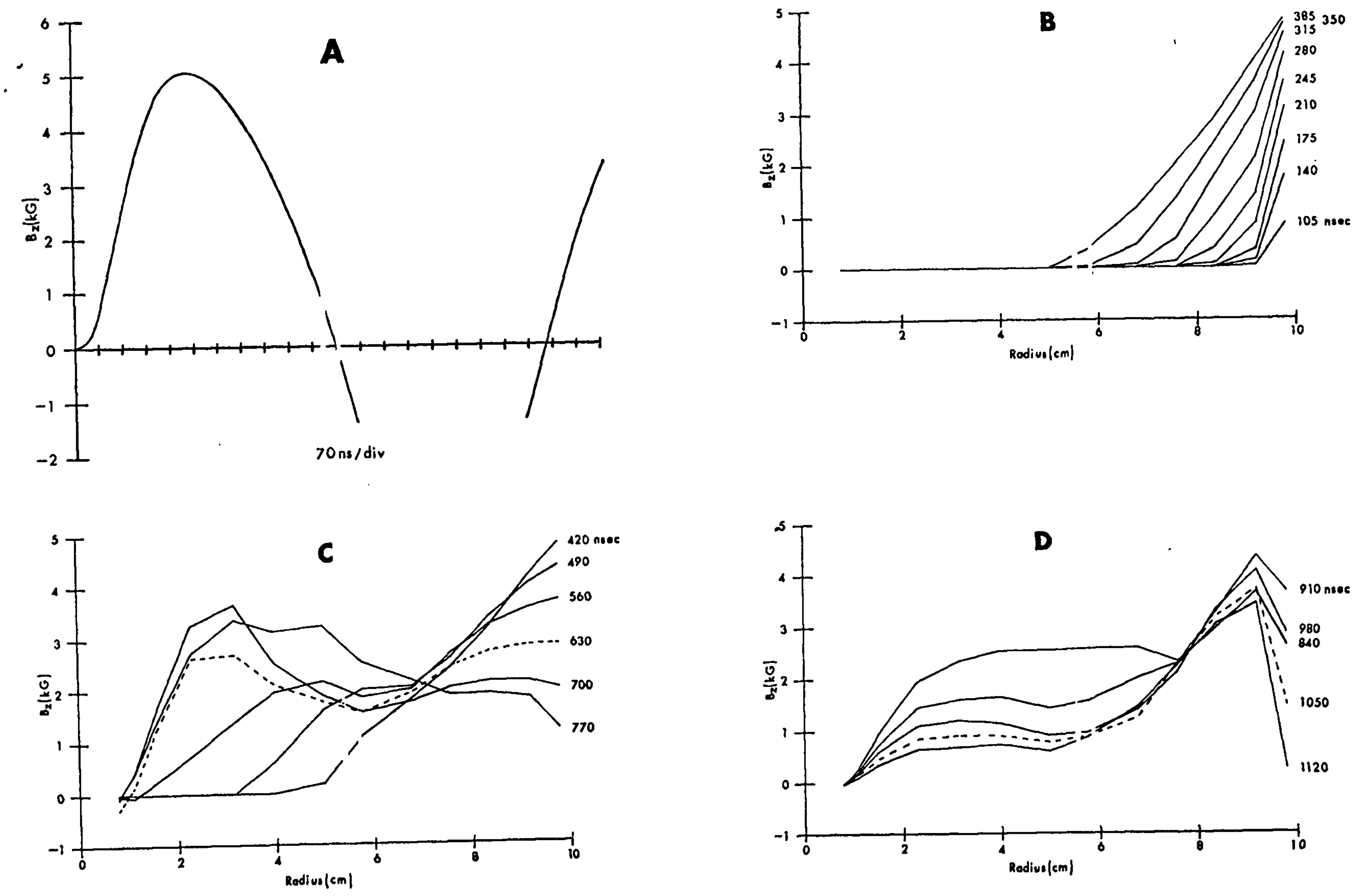

Magnetic field measurements in 0.9 m STP prototype.

A. External magnetic field vs time.

B. B_z vs radius for 105-385 ns after discharge initiation.

C. B_z vs radius for 420-770 ns.

V. SCYLLA IV-P THETA PINCH

W.E. Quinn, A.G. Bailey, G.I. Chandler, L.D. Hansborough, J.W. Lillberg, M.D. Machalek, F.T. Seibel

A. Introduction

Scylla IV-P is a flexible, linear experiment to support the toroidal Scyllac experiments and to investigate high-density, linear theta-pinch concepts. The Scylla IV-P device was proposed[1,2] and approved in FY 1974. It is a conventional linear theta pinch with a 5-m length that is energized by a 60-kV, 2-MJ capacitor bank of the Scyllac type. The design, fabrication, procurement and construction of Scylla IV-P began in early FY 1975 and is scheduled for completion in August 1975.

Linear theta pinches have demonstrated stable plasma confinement and intense heating throughout the history of their exploration. In the mid-1960s, the Scylla IV experiment at LASL routinely produced ion heating to thermonuclear ignition temperatures in a straight theta-pinch geometry. In the linear systems the limiting factor on confinement is the loss of plasma from the ends of the theta pinch and not MHD stability or radial diffusion. However, the particle losses through the ends at conventional densities (a few times 10^{16}cm^{-3}) would require a theta pinch of several kilometers length to achieve economical fusion power production.

The application of uranium or thorium blankets surrounding the plasma for the purpose of breeding fissionable materials gives impetus to the application of linear theta pinches as neutron sources for hybrid fusion-fission.[3] Therefore a compelling reason for pursuing high-density, linear theta-pinch research to larger systems is to breed fuel and provide power in combination with fission reactors. The linear theta pinch with its established plasma heating and stability properties may provide such a fusion-fission hybrid system on a time scale comparable to that of the first fusion test reactors. The Scylla IV-P linear theta-pinch program stems from approximately 20 years of world-wide research on theta-pinch systems. It is a test bed for longer, denser systems aimed at a fusion-fission hybrid system. There are two approaches to the linear fusion-fission hybrid system: (a) a theta-pinch shock-heating and compression system; and (b) a combination of laser heating and compression.[4] The basic physics problems relevant to both approaches are being addressed in the Scylla IV-P device and in laser heating experiments of plasmas with magnetic confinement. The Scylla IC experiment described in Section VI addresses the question of laser heating of dense theta-pinch plasmas.

The experiments planned for Scylla IV-P include the following: (a) Experiments to measure end effects including end-loss rates and associated phenomena such as "area waves", the variation of the plasma beta with time and axial position, end shorting effects, and electron thermal conduction. These experiments will assist in quantitative interpretation of end effects; (b) Investigation of the wall-stabilization phenomenon is planned by means of an injection experiment.[5] In the injection procedure a theta-pinch coil is energized with quasi-steady helical magnetic fields which will ultimately contain a wall-stabilized helical column. Two adjacent linear theta-pinch coils are operated in such a way that their final pulsed field is of the same magnitude as the quasi-steady helical field. The axial pressure gradient created in their plasmas should drive plasma from each end into the helical region. The diameter of the region into which plasma is injected can be made small enough to permit wall stabilization. Fluid codes are now being developed to predict the plasma behavior; (c) "Variable-epsilon" experiments are planned to study the $\ell = 1$ and $\ell = 0$ scaling, and $m = 1$ growth rates relevant to the Scyllac toroidal configuration. An important aspect of these experiments will be the investigation of the finite-Larmor-radius (FLR) stabilization of $m \geq 2$ modes; (d) The application of the linear theta pinch to high plasma densities (1-5$\times10^{17}$cm^{-3}) and high magnetic fields (200-300 kG) will be investigated.[6] These include high-density plasma formation and heating, particle and thermal-conduction end loss, and other end effects (line-tying, end shorting, the "wobble" effect, impurities, etc.). These experiments will provide important information for the linear fusion-fission hybrid reactor; (e) Various end-stoppering techniques, such as multiple mirrors, cusps, etc., will be investigated to reduce the end-loss rates; (f) The sustained theta pinch may also be investigated providing studies indicate its feasibility. A constant dc magnetic field is generated by an outer coil and an inner pulsed coil is energized to bring the dc field to zero in the plasma region to allow the initial plasma production and shock heating; (g) Laser-heating experiments will be performed using a 1-kJ CO_2 laser furnished by the LASL Laser Division; and (h) The device will also be used in the development of plasma diagnostic techniques.

B. Experimental Arrangement

The Scylla IV-P device is being constructed in the Pit room, which has a floor area of 256 square meters and a ceiling height of 8 m. The 5-m long compression coil will be energized by a 60-kV, 2-MJ capacitor bank of the Scyllac type. Figure V-1 shows an elevation view of the device. The arrangement of the energy storage system is unique in that the capacitor-spark gap units are arranged in clusters on a three level platform structure rather than in conventional racks. This will provide for more convenient access to the bank. The collector plates and compression coil are situated on the middle or experimental platform level. Another feature of the device is a computer control system.

C. Construction Status

Scylla IV-P is approaching its period of maximum activity relative to component assembly and installation. The skilled crafts have now essentially completed their work of modification of utilities and installation of new steel support structures in the Pit.

The PRIME computer and its attendant hardware have been set up in the Scyllac area. The system has been debugged and at present software development is proceeding. As soon as the new screened room has been erected and wired for power, the computer will be moved to the Pit.

The following items are in progress in early 1975: Collector plate fabrication, coil machining, cable dressing, vacuum system assembly, shorting ball assembly, trigger system construction,, and cable tray installation.

Delivery of load capacitors is essentially complete, with less than two dozen yet to be delivered. These final units should be shipped along with replacements for defective units discovered during testing.

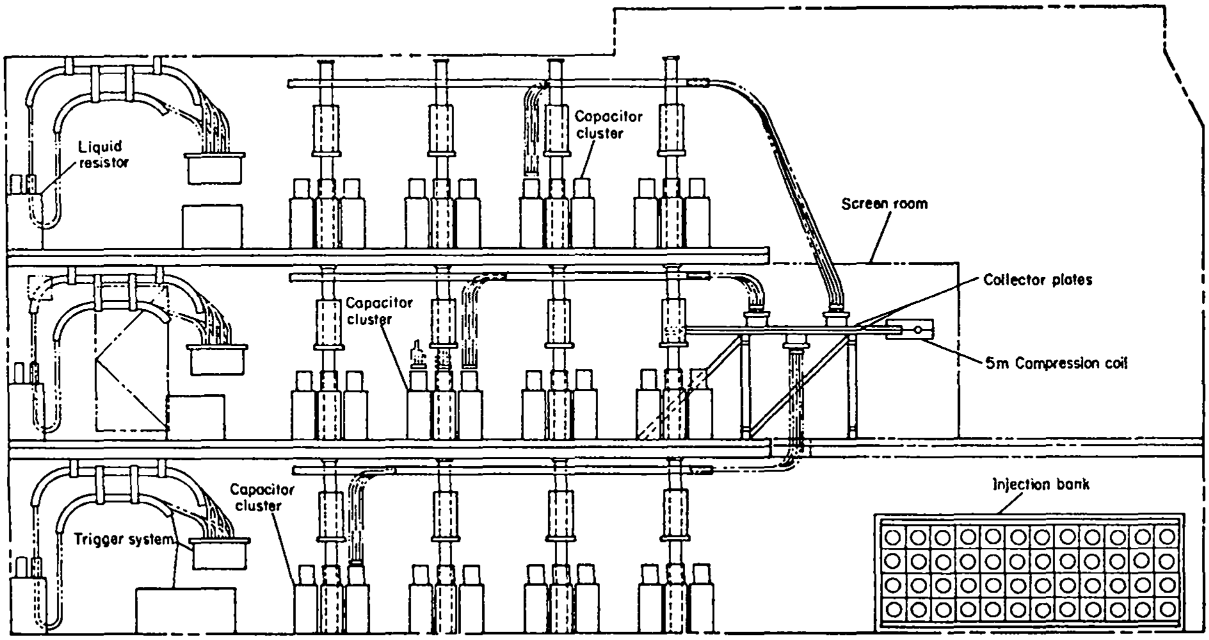

Fig. V-1

Elevation View of Scylla IV-P Experimental Area.

Spark gap components have been steadily arriving and presently enough components are available to assemble about 400 gaps. Considerable subassembly work on spark-gap components has been completed. Actual, complete assembly of spark gaps has been postponed until spring 1975, at which time several new technicians are to be available for work.

Scylla IV-P is now in an excellent position to proceed at full speed toward assembly. Barring any failure to receive the necessary additional funds and manpower, completion of the capacitor bank system for Scylla IV-P by mid-summer 1975 at present appears to be a very realistic goal.

References 1. W.R. Ellis, W.B. Riesenfeld, and G.A. Sawyer, "Proposal for the Construction of a Scylla IV-P Confinement Studies Theta Pinch," Los Alamos Scientific Laboratory Report LA-5474-P (December 1973).

2. W.R. Ellis, J.P. Freidberg, and W.E. Quinn, "Supplement to the Proposal for the Construction of a Scylla IV-P Confinement Studies Theta Pinch," Los Alamos Scientific Laboratory Report LA-5474-P, Suppl. (May 1974).

3. G.E. Bosler, D.J. Dudziak, and W.R. Ellis, "A Preliminary Appraisal of a Fusion-Fission Hybrid Reactor Based on the Linear Theta Pinch," Proc. Ninth Intersociety Energy Conversion Engineering Conference (IECEC), San Francisco (August 1974).

4. W.R. Ellis and G.A. Sawyer, "Sealing Laws for the Linear Theta Pinch I: A Comparison of Magnetic and Laser Heating," Los Alamos Scientific Laboratory Report LA-5434-MS (October 1973).

5. B.M. Marder and R.E. Siemon, "A Long Confinement Experiment (LCE) Proposal," Los Alamos Scientific Laboratory Report LA-5399-P (September 1973).

6. W.R. Ellis, "CTR Applications of the High-Density Linear Theta Pinch," Nuclear Fusion **15**, (1975).

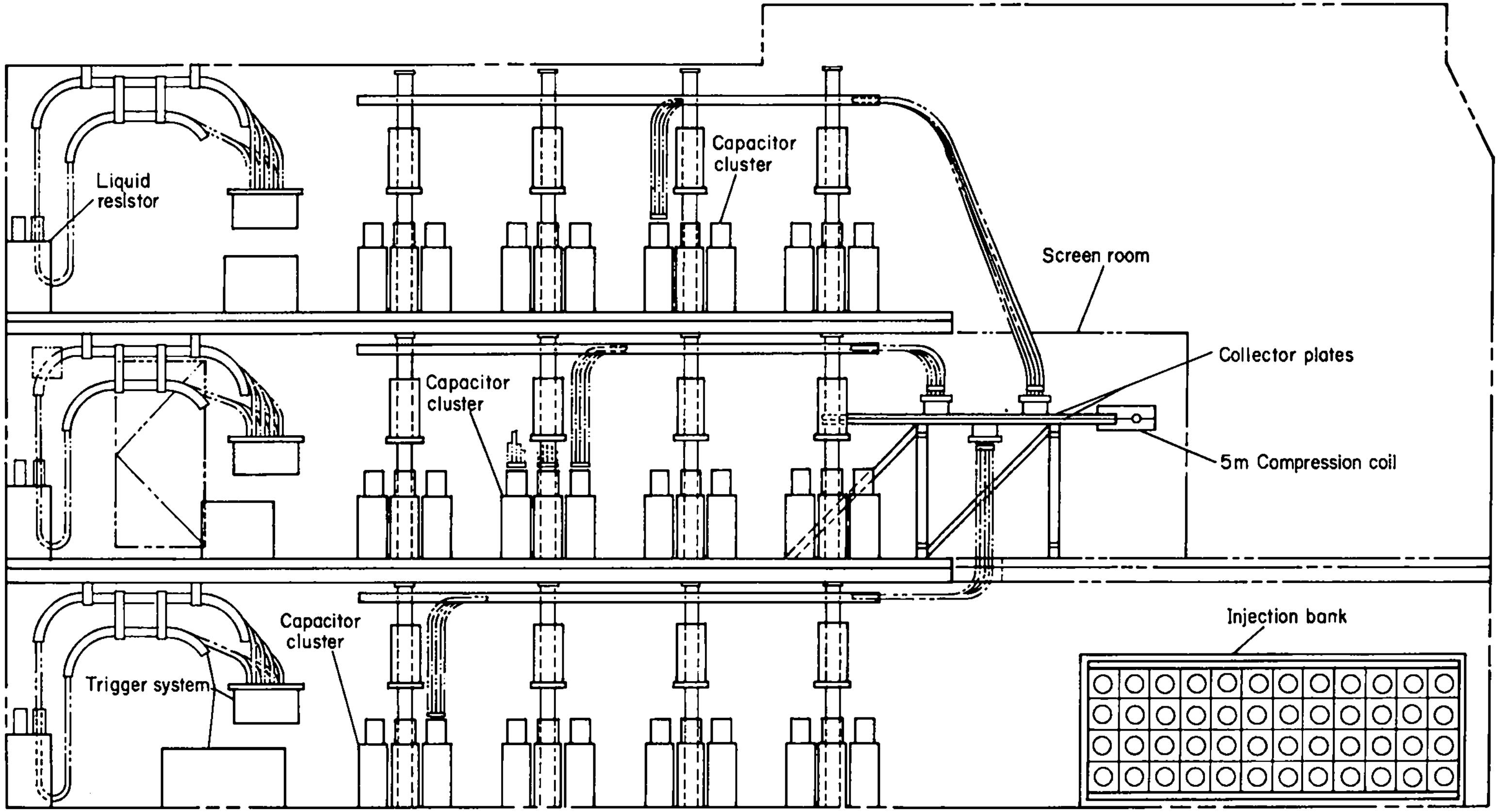

Scylla IV-P Elevation View

VI. SCYLLA I-B/C

K.F. McKenna, K.B. Freese, F.C. Jahoda, T.M. York, E.L. Zimmermann

A. Implosion Heating Experiments in Scylla I-B

1. Introduction. Future toroidal theta-pinch devices will use fast implosion heating in order to generate high-β thermonuclear plasmas of low compression ratio (ratio of coil radius to plasma radius). Theory[1] predicts that such plasmas can be wall stabilized against the $m=1$ instability. The object of the Scylla I-B implosion heating experiment was to study the implosion process over a range of E_θ's and initial fill densities characteristic of past and present Scylla type theta pinches.

2. Apparatus. The Scylla I-B θ-pinch apparatus is described in the 1973 annual report.[2] Fifty-four 0.7 μF capacitors provided a maximum energy storage of 106 kJ at a charging voltage of 75 kV. The 100-cm long, 22-cm-diameter compression coil consisted of two half-turn sections, each section being fed by half the capacitor bank. Main bank operation from 40 kV to 70 kV generated vacuum E_θ's from about 0.7 kV/cm to 1.2 kV/cm at the inner wall of the 20-cm i.d. discharge tube and corresponding peak crowbarred compression fields of approximately 9.5 kG and 17 kG were obtained 1.25 μs after main bank initiation.

3. Diagnostics. The principal plasma diagnostics consisted of magnetic field probes, a laser interferometer and a plasma luminosity detector. The magnetic field probe contained three identical ten-turn B_z coils with a 2-cm separation between coils. The 0.16-cm-diameter coils were mounted within a sealed 0.65-cm-diameter alumina tube and inserted radially through the discharge tube wall at an axial position 7 cm from the tube center. Radial surveys were made in 1-cm increments from the discharge tube axis, $r=0$ cm, to the tube wall, $r=10$ cm. The field probe yielded spatially- and time-resolved magnetic field profiles. Excluded flux measurements were made with a diamagnetic loop-probe system of standard design.

The imploding-plasma electron density distribution was measured by means of 5-ns pulsed holographic ruby-laser interferometer. A double pass, modified Michelson end-on system was used, giving an interferometer sensitivity of $\approx 3\times10^{14}\text{cm}^{-3}$. One interferogram was obtained per plasma discharge.

End-on photographs of the imploding plasma self-luminosity were made with a Beckman Whitley image-converter camera. The framing camera had an exposure time of 10-ns and a spectral response of 3500Å-6500Å.

The preionized plasma density distribution was studied using a 3.4-μm He-Ne laser interferometer operating in the coupled cavity mode. The time resolved measurements were made end-on, with the laser beam parallel to the tube axis. Data were collected in 1-cm radial increments.

4. Preionization Studies. Preionization of the 10-mtorr D_2 fill gas was accomplished with a single capacitor discharge through the compression coil. Three different PI capacitors were used to generate the initial plasma; 1.8 μF, 0.7 μF and 0.25 μF capacitors charged to 55 kV. The total fractional ionization produced for each PI system was obtained by numerical integration of the radial electron density profiles[3] obtained from the coupled cavity interferometer data. At the time of main bank initiation the percent ionization of the fill gas was $\approx$60% with the 1.8 μF capacitor, $\approx$15% with the 0.7 μF unit, and $\leq$5% for the 0.25 μF unit.

Internal magnetic field probe data taken during the preionization discharge[3] indicated that after gas breakdown the external ringing magnetic field was effectively shielded from radial positions $r \leq 6$ cm. Within this radius the direction (negative field refers to B_z opposite to the direction of the main compression field) and magnitude of the slowly decaying and spatially uniform trapped PI field was $\leq$50 G with the 1.8 μF PI capacitor, ≤ -60 G with the 0.7 μF capacitor and $\leq$50 G for the 0.25 μF unit, at the time of main bank discharge.

5. Implosion Density and Magnetic Field Profiles. The general characteristics of the magnetic field implosion were found to be dependent on the degree of initial fill gas preionization. At low preionization levels, $\leq$ 5% ($<5\times10^{13}$ cm^{-3} for the 10-mtorr fill pressure), rapid penetration of the main magnetic field was observed from the reduced magnetic field profiles[3] and a magnetic piston sheath of definable thickness could not be identified. At preionization levels above 15% ($>10^{-14}$ cm^{-3}) the magnetic field penetration rate was about a factor of two slower, and a piston sheath thickness of about 2 cm was observed at 40 kV main bank voltage. In the latter case, compression of the initial (−60 G) trapped preionization field was observed on axis. In the following only the results obtained with the high preionization level (15%, 0.7 μF PI capacitor) will be discussed.

Scylla I-B implosion phase results for operation at 40 kV main bank voltage, 10 mtorr initial fill pressure and preionnization level $\approx 10^{14}$ cm^{-3} have been published.[4] Figures IV-1 and VI-2 present results for 55 kV main bank voltage. Figure VI-1 shows end-on interferograms taken at six different times during the implosion. The entire 20 cm diam of the discharge tube was illuminated by the laser light. The tip of the magnetic field probe, seen in the interferograms, was located 5 cm from the discharge tube axis. At early times during the implosion ($t \leq$ 200 ns, Fig. VI-1) a relatively smooth density distribution is observed. At later times a well defined structure develops. Macroscopic flute like instabilities can be seen on the trailing edge of the density distribution. Interferograms obtained at higher, 70 kV, and lower, 40 kV, main bank charging voltages display an identical density structure during the implosion phase, with the inward radial velocity of the plasma being greater at higher bank voltages.

Interferograms of the compressed plasma column were also taken.[3] Spatial integration of the reduced plasma column density profiles $n_e(r)$ indicated that all of the initial fill gas was swept up by the magnetic piston field. Although only 15% of the fill gas was ionized at the time of main bank discharge, the remaining neutral particles were ionized and swept up during the implosion process. Total sweep up was indicated at all operating voltages.

Profiles of $n_e(r)$ and $B_z(r)$ at various times during the implosion, derived from the interferograms (Fig. VI-1) and internal magnetic field probe data obtained at 55 kV main bank voltage,[5] are presented in Fig. VI-2. The implosion is characterized by an initial period, 100-150 ns, of fast penetration of the external magnetic field, implying a plasma resistivity during this time which is greater than classical. The plasma resistivity drops rapidly with time as indicated by the fact that the −60 G trapped preionization field is compressed by the imploding plasma. Halfway through the implosion ($t \approx 200$ nsec) the plasma density front begins to separate and accelerate away from the magnetic piston field. The front attains a maximum velocity of about 3.5×10^7 cm/s, nearly 1.8 times as large as the magnetic piston velocity. The density front collapses on the discharge tube axis at $t \approx 410$ ns. The piston field decelerates during the formation of the plasma column and is finally stopped by the kinetic pressure of the $\beta \approx 1$ compressed plasma at about 500 ns. After a few radial oscillations the plasma column settled to a mean 1/e radius of 4.5 cm with a peak density of about 5×10^{15} cm^{-3} and attained an average compressed-plasma kinetic temperature ($T_e + T_i$) of approximately 0.8 keV, as determined from pressure balance.

The implosion phase results presented for 55 kV main bank voltage are characteristic of those obtained over the entire range of operating voltages, only the time scale of the implosion event and final column temperature changes, the implosion being more rapid and final temperatures greater at higher initial E_θ's.

During the implosion, magnetic field gradients are observed in the region external to the imploding plasma density distribution, indicating the presence of a low density ($<3 \times 10^{14}$ cm−3, the holographic interferometer sensitivity) high temperature plasma. The magnetic field gradients, being nearly negligible at 40 kV main bank voltage, increase significantly with increasing operating voltage.[5] Very similar behavior has been observed in the Garching high voltage, fast magnetic compression θ-pinch,[6] operating with an initial preionization density $n_0 \approx 2 \times 10^{13}$ cm^{-3} (in Scylla I-B $n_0 \approx 1 \times 10^{14}$ cm^{-3}). In the Garching experiment the external field gradients are believed to be supported by an observed low density plasma halo, $n_e \sim 0.5 \times 10^{14}$ cm^{-3}, caused by flute instabilities which develop during the implosion. Flute-like instabilities, discussed below, have also been identified during the Scylla I-B implosion. However, the existence of a low density plasma region surrounding the plasma column in the Scylla I-B experiment could not be measured due to the sensitivity limitation of the interferometer. It should be noted that the external magnetic field gradients indicated from the magnetic field probe data at the higher main bank voltages could possibly result from inaccuracies in the probe measurements resulting from probe interactions with the hostile plasma environment.

6. Plasma Implosion with Applied Bias Field. The implosion process was studied with a reversed bias field applied. At the time of main bank initiation the bias field had a magnitude of −400 G (opposite to direction of the main magnetic field). With the bias field, data were collected at 40 kV main bank voltage and 10 mtorr D_2 fill pressure.

Holographic interferograms taken with and without the applied bias field are shown in Fig. VI-3. The main bank voltage and fill pressure are the same in both interferograms. The structure of the imploding plasma is significantly altered by the introduction of the bias field. With no applied bias field (Fig. VI-3a) the fully developed density profiles (plasma at mid-radius) are characterized by (a) an

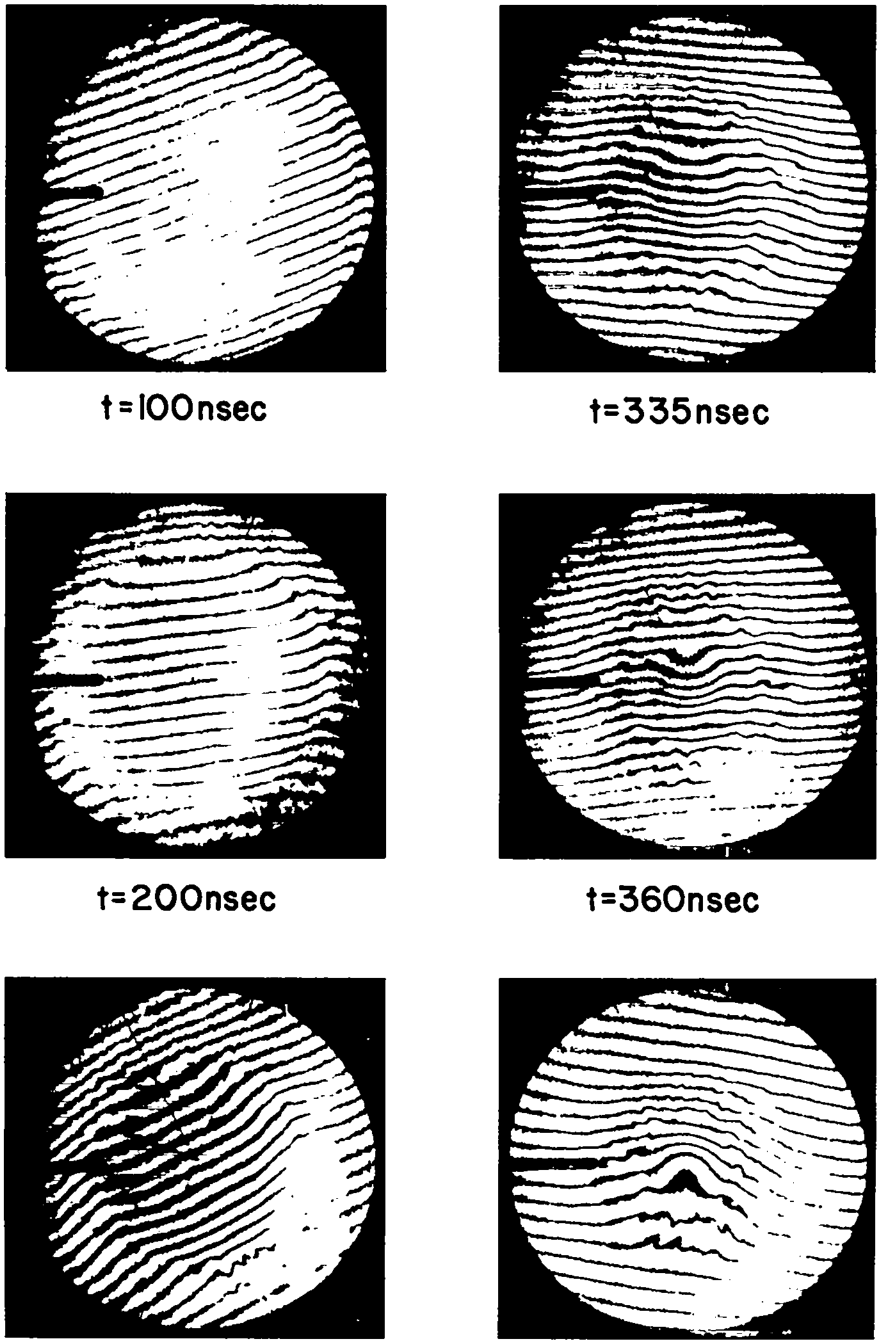

t=100nsec

t=335nsec

t=200nsec

t=360nsec

t=275nsec

t=410nsec

55kV Main Bank Voltage, 10mTorr D_2 Fill Pressure

Fig. VI-1

Plasma implosion interferograms.

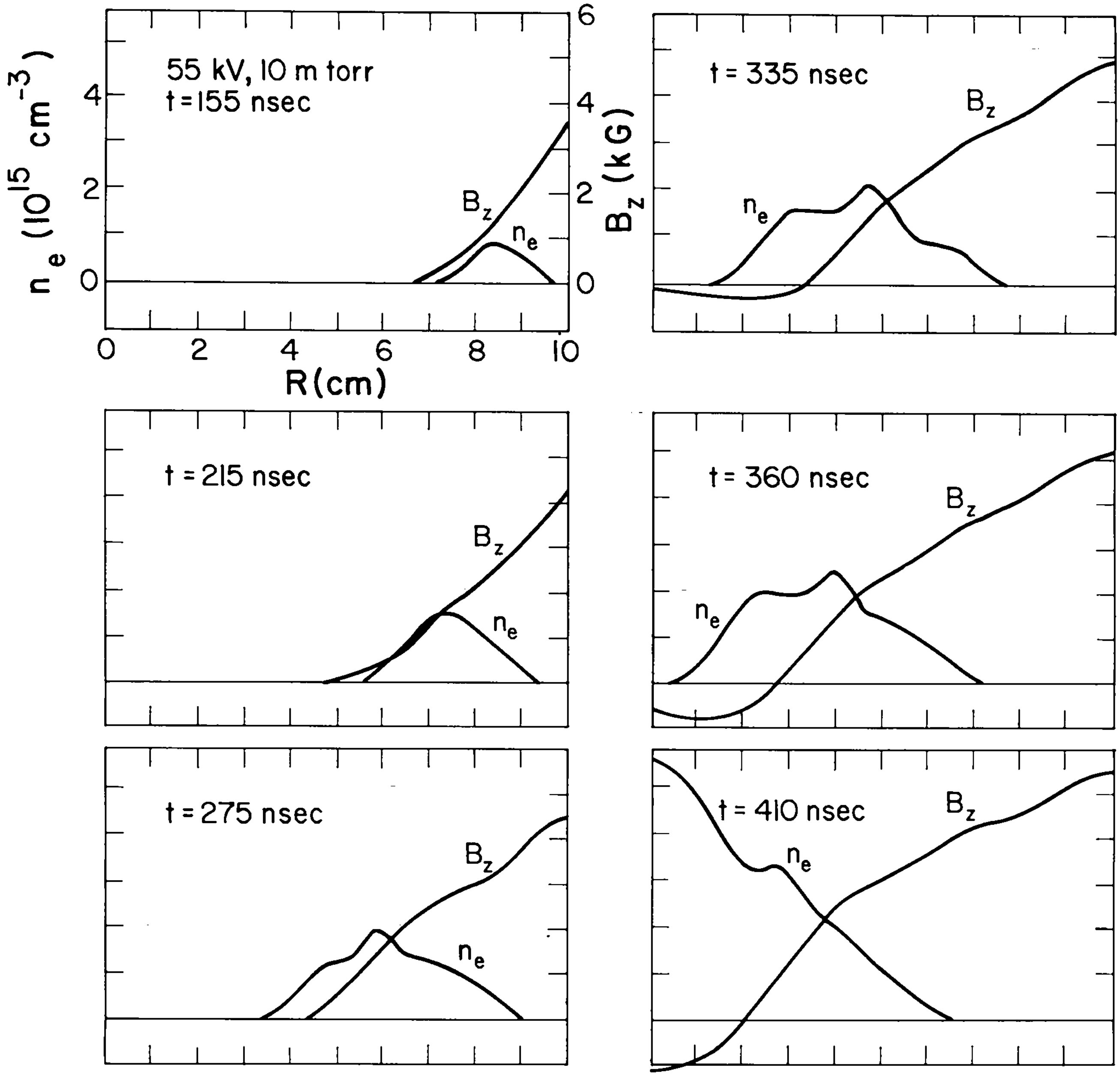

Fig. VI-2

Implosion profiles of $n_e(r)$ and $B_z(r)$ at fixed times, reduced from interferograms and magnetic field probe data obtained at 55 kV main bank voltage.

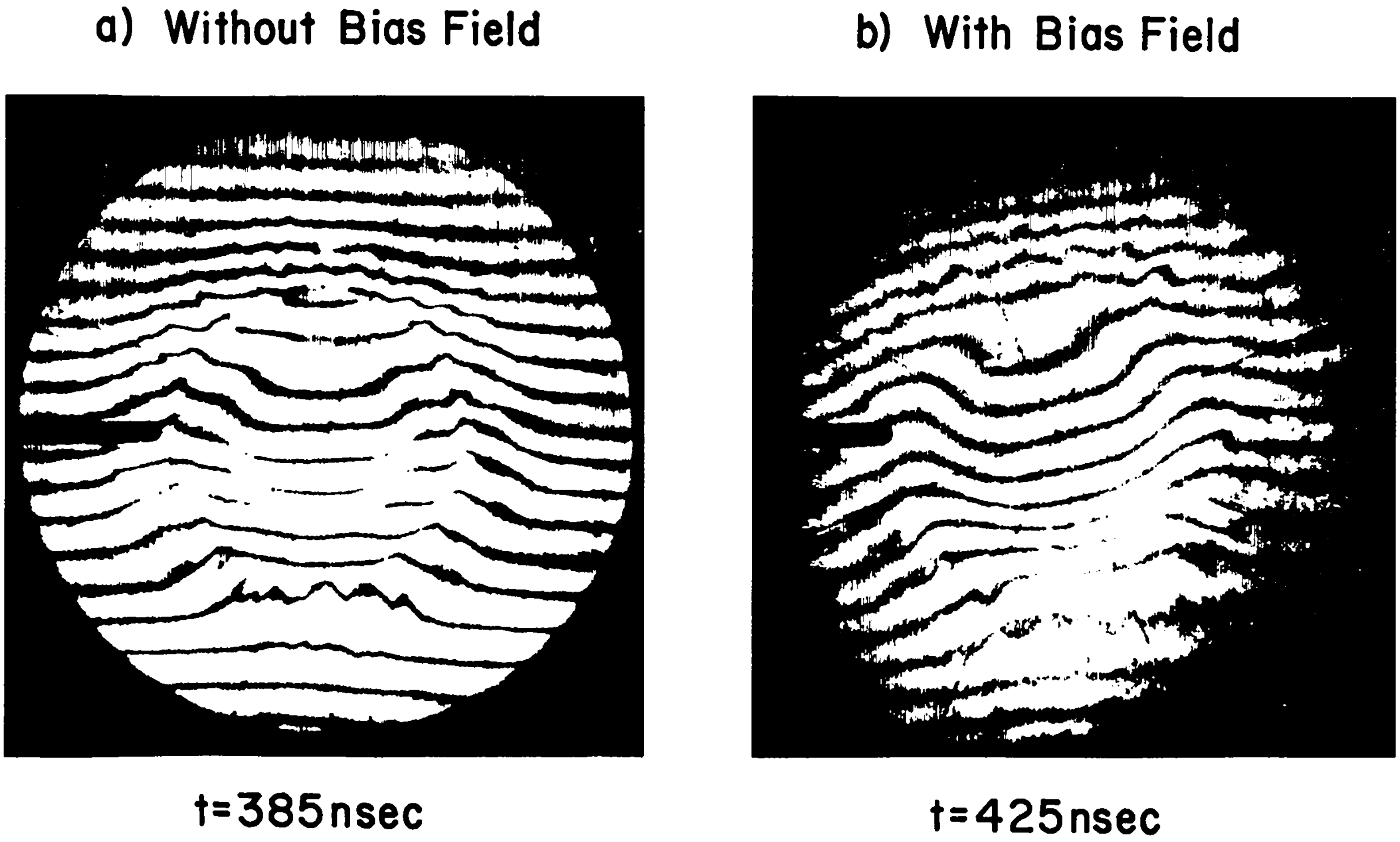

a) Without Bias Field

b) With Bias Field

t=385nsec

t=425nsec

Fig. VI-3

Implosion interferograms taken with and without an applied bias field.

initial density rise and plateau, interpreted as a shock region containing plasma moving ahead of the magnetic piston field, (b) a density peak corresponding to the magnetic piston region and (c) a region of electron density decay which supports flute-like macroinstabilities. Conversely, in the presence of the bias field (Fig. VI-3b) a relatively smooth density profile is observed for the entire duration of the implosion event. The development of flute-like instabilities on the trailing edge of the imploding density distribution is not affected by the bias field as can be seen from inspections of Figs. VI-3a and VI-3b. In addition to altering the imploding plasma structure, the bias field also increased the time required for the plasma to arrive at the discharge tube axis, an expected result. The pinch time with the applied bias field is about 525 ns compared to 435 ns without the bias field.

At the termination of the implosion a "density well" is observed on axis in the bias field case. The density minimum is attributed to trapping of the reverse bias field during the implosion. The density minimum on axis persists for the duration of the experiment, ~1500 ns, indicating that the compressed trapped field is not annihilated within the plasma column, a result substantiated from the internal magnetic field probe measurements.[5] Spatial integration of the plasma column density profiles indicated, as in the case without applied bias field, that all the initial fill gas was swept up during the implosion.

7. Imploding Plasma Self-Luminosity Patterns. In weakly compressed (a/b~1/3) high-β plasmas at low θ-pinch fill densities $n_o \leq 10^{14}$ cm^{-3}, Rayleigh-Taylor flute instabilities which surround the implosion-heated plasma column and extend to the discharge tube wall have been identified photographically. The question of the existence of such macroinstabilities disrupting the stabilization of confined plasmas in planned,[8] higher density ($n_o \sim 10^{15}$cm^{-3}), wall stabilization experiments has been posed.[7] In Scylla I-B the evolution of these instabilities was observed, both photographically and by interferometer density measurements. The flutes only occupy a fraction of the plasma self-luminosity pattern. Details of the total self-luminosity patterns have been directly associated with the dominant structural features of the transient plasma density and magnetic field distribution.

The time development of the plasma self-luminosity, obtained with a 10-ns exposure time end-on framing camera is shown in Fig. VI-4. The photographs were taken at 40 kV main bank voltage and 10 mtorr fill pressure and are typical of those obtained at higher operating voltages. The tip of the magnetic field probe, visible in some of the photographs, was located 5 cm from the discharge tube axis. Immediately after discharge initiation a single uniformly luminous structure, indicative of current sheath formation, is observed near the discharge tube wall. As the current sheath accelerates radially inward, striations in the outer luminous boundary appear. These striations indicate the growth of Rayleigh-Taylor flute-like instabilities,[9] generated during the inward acceleration of the plasma-magnetic field interface. For an incompressible fluid the growth time for the flutes is given by $\tau = (gk)^{-1/2}$, where g is the interface acceleration and k the wave number ($k=2\pi/\lambda$, where λ is the wavelength). This formulation is extended to the present case only to indicate expected order of magnitude values. At t≈175 ns the instability m number (total number of striations), determined from the luminosity photographs and laser interferograms, discussed below, is approximately 90 at a mean radius r=9 cm, yielding a wavelength $\lambda=2\pi r/m$ of 0.63 cm. Estimating the interface acceleration from the trajectory of the density profile peak to be about 7×10^{13} cm/s^2, the predicted growth time is then ~40 ns. This is within an order of magnitude of the observed time of appearance of the striations, about 150 ns after discharge initiation. The instability wavelength increases linearly with time attaining a maximum value of 1.2 cm at t≈500 ns.

As the implosion progesses a structureless inner luminous front develops and moves ahead of the striated region, the front being separated from the striations by a relatively dim ring (t=210 ns, Fig. VI-4). The dim ring moves inward with the magnetic piston velocity, while the inner luminous front travels inward at the velocity of the imploding plasma density front. Approximately 100 ns after the luminous front collapses on the discharge tube axis, the striations in the outer luminous region can no longer be photographically observed.

The evolution of the flute instabilities was also observable from end-on interferograms. Figure VI-5 shows interferograms taken during the implosion (t=325 ns) and after formation of the plasma column (t=640 ns) for 40 kV main bank voltage and 10 mtorr fill pressure. The flutes appear as ripples on the trailing edge of the density distribution (t=325 ns, Fig. VI-5). The time varying instability wavelengths obtained from the interferograms are identical to those determined from the luminosity photographs.

Of major significance here is the fact that the instability disappears ($n_e<3\times10^{14}$ cm^{-3}, the interferometer sensitivity) after the plasma column is formed. This is seen from inspection of the interferogram taken t=640 ns, Fig. VI-5. As previously noted this occurs about 100 ns after collapse of the luminous front onto the discharge tube axis. Such

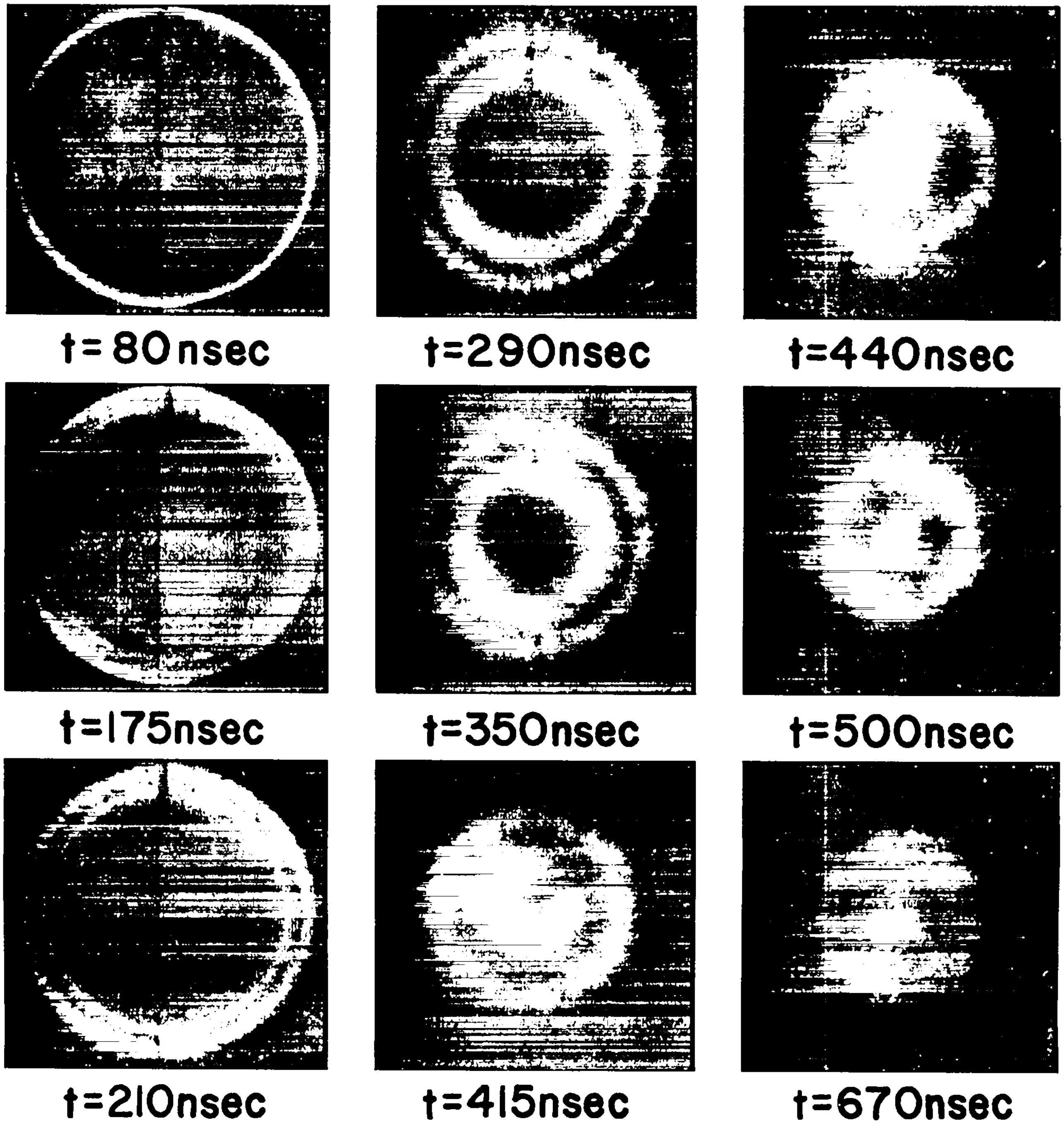

t=80nsec t=290nsec t=440nsec

t=175nsec t=350nsec t=500nsec

t=210nsec t=415nsec t=670nsec

Fig. VI-4

Time sequence of framing camera photographs taken during the plasma implosion.

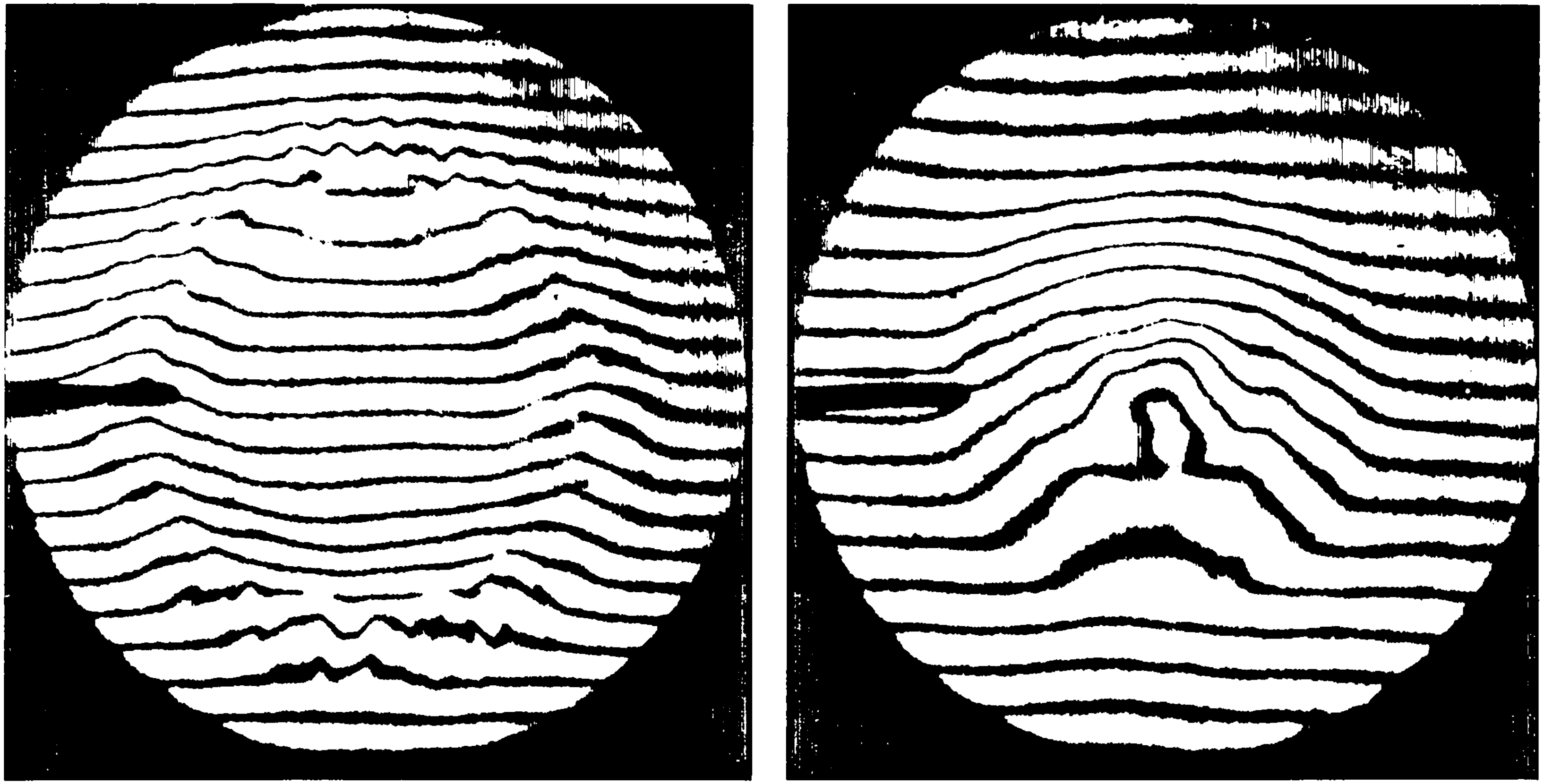

t=325nsec

t=640nsec

Fig. VI-5

Interferograms of plasma discharge during and after the implosion phase.

behavior indicates the interaction of either a reflected shock wave with the region of instability, or radially imploding deuterons passing through the center of the tube and interacting with the piston field. The exact mechanism causing the flute disappearance is unknown. In either case, the experimental results demonstrate that macroscopic flute instabilities do not surround the implosion-heated plasma in 10^{15} cm^{-3} fill density θ-pinches. Accordingly, such instabilities would not be expected to influence the stability of the plasma column in planned wall stabilization experiments.[8]

Figure VI-6 shows profiles of $n_e(r)$ and $B_z(r)$ at t=385 ns derived from the interferograms and magnetic-field-probe records obtained at 40 kV main bank voltage. The reduced data illustrate the structure of the plasma halfway through the implosion, where initial effects (rapid field diffusion and piston sheath formation) no longer dominate the flow and the general characteristics of the imploding plasma are fully developed. Also shown in Fig. VI-6 are the boundaries of the self-luminous regions, obtained from reduction of many luminosity photographs. Region I corresponds to the boundaries of the inner uniform luminous front and is identified with the plasma which travels ahead of the piston field and interacts with the partially ionized background gas. The dim ring, region II, coincides with the magnetic piston, defined by the maximum B_z gradient and corresponding to the electron density peak. Region III identifies the trailing edge of the detectable electron density profile where the flute instabilities generated during the early stage of the implosion are observed.

The ions in the plasma front interact with the neutral background through charge exchange with a cross section $\sigma \approx 2\times10^{-15}$ cm^{-2}. For the neutral density of $\sim 6\times10^{14}$ cm^{-3}, the ion mean-free path is ~0.8 cm, indicative of some collisional processes in the ~2-cm-thick plasma front region. The ionization cross section is about 6×10^{-17} cm^{-2} and with an electron density of $\sim 1\times10^{15}$, the ionization time is on the order of 50 ns. In the plasma frame a neutral travels ~1.6 cm during the 50-ns time interval, indicating significant ionization phenomena in the piston, which could account for the density increase in this region.

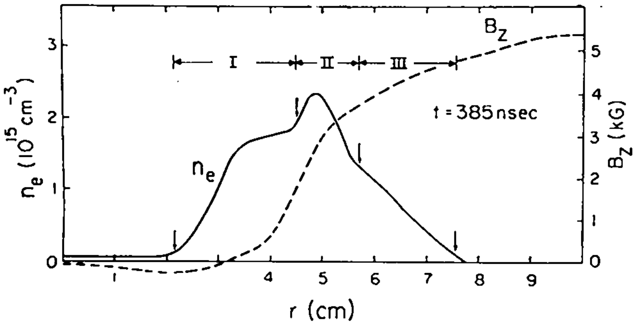

Fig. VI-6

Profiles of $n_e(r)$ and $B_z(r)$ and the plasma self luminosity boundaries half-way through the implosion.

From the known framing camera and film spectral sensitivity, phototube gain, and geometry of the optical setup the power density of the emitted plasma self-luminosity was determined within an accuracy of about a factor of two. A comparison of the measured power density with that predicted for Bremsstrahlung emission ($P_B \propto n_e^2 T_e^{-1/2}$), over the spectral range of the phototube, indicated that the radiation observed from region I could result solely from continuum emission, assuming a reasonable electron temperature on the order of 25 eV.[10] To support this result, various light filters were used in order to identify the spectral distribution of the emitted radiation. Results of the filter studies again demonstrated that Bremsstrahlung radiation could account for the observed emission. From these results it can thus be inferred that the dim ring (region II) identifies a region of rapid electron heating, probably turbulent, in which the electron temperature increases significantly, decreasing the intenstiy of the continuum radiation. Such rapid electron heating in the magnetic piston region agrees with previous experimental results.[6,10]

B. Plasma Experiments in Scylla I-C

1. Introduction. The Scylla I-C theta pinch is being used in conjunction with a CO_2 cold cathode laser, supplied by the L-1 group of the Laser Research and Technology Division, to study the interaction of axially directed long wavelength laser light (10.5 μm) with the dense ($n_e \geq 10^{17}$ cm^{-3}) theta pinch plasma column. Initially, the experimental investigation will be directed toward studying (a) containment or diffraction of the laser beam as it traverses the meter-long plasma column, (b) heating of the plasma column by laser energy absorption and (c) instability induced anomalous backscatter of the incident laser light.

Construction of the CO_2 laser has been completed and electrical testing of the laser power supply system is in progress. Operation with plasma of the Scylla I-C theta pinch began in July 1974. The electrical characteristics of Scylla I-C and the properties of the theta-pinch generated dense plasma are discussed below.

2. Experimental Arrangement. A schematic of the Scylla I-C linear θ-pinch is shown in Fig. VI-7. Scylla I-C has a maximum capacitor energy storage of 175 kJ at 60-kV main bank voltage. Fifty-four 1.8-μF capacitors feed the 100-cm long, 10.5-cm diameter single turn compression coil. Main bank operation at 40 kV generates a vacuum E_θ of 0.26 kV/cm at the inner wall of the 3.6-cm i.d. quartz discharge tube and a peak crowbarred compression field of 33 kG is obtained 2.0 μs after discharge initiation. Plasma experiments, conducted at 40-kV main bank voltages, have been carried out over a range of fill pressure, P_o, from 100-mtorr to 500-mtorr D_2.

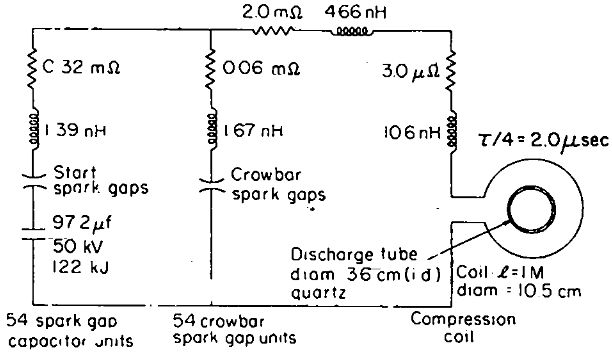

Fig. VI-7
Scylla I-C theta pinch schematic.

3. Preionization Studies. Gas preionization is acomplished with a specially designed Z-pinch preionizer. The Z-pinch system consists of a 0.7-μF, 75-kV capacitor, a crowbar spark gap modified to accommodate five varistors, eight RG-14/59 load cables, and the Z-pinch electrodes. A schematic of the Z-pinch is shown in Fig. VI-8a. The current waveform generated by this system, at a capacitor voltage of 60 kV, is presented in Fig. VI-8b. A side-on streak camera photograph of the preionized plasma for 100-mtorr fill pressure is presented in Fig. VI-8c. A sufficiently rapid rising current, of ~18-kA peak, is supplied to the static fill gas to cause pinching of the plasma under the $j_z B_\theta$ force interaction. At the termination of the pinch the plasma expands and uniformly fills the discharge tube.

The density of the preionization plasma was measured by means of a 30 ns pulsed holographic ruby laser interferometer. A single pass end-on system with a sensitivity of $\sim 1 \times 10^{14}$ cm^{-3} was used. A typical preionization plasma interferogram, obtained with 100 mtorr fill pressure, is presented in Fig. VI-9. Spatial integration of the reduced density profiles $n_e(r)$ indicated that for the 100 mtorr fill pressure case, 50% of the fill gas was ionized by the time the pinched plasma column had expanded to discharge tube wall. With 500 mtorr fill pressure, about 20% of the gas was ionized at this time.

4. Main Discharge Luminosity Measurements. Side-on streak photographs of the main discharge plasma were taken at the coil midplane. Figure VI-10 shows typical streak pictures obtained with $P_0 = 100$ mtorr. These streaks are characteristic of those taken at higher fill pressures.[11]

The dynamics of the plasma during the implosion and plasma column formation phase can be observed in Fig. VI-11a. The initial radial shock wave and subsequent plasma oscillations can be clearly identified. The radial oscillations damp out approximately 1 μs after termination of the implosion. The quiescent plasma column is highly stable and reproducible for a period of approximately 9 μs, Figs. VI-10b and VI-10c. The compressed column breaks up into filaments ($m = 2$) after this time, probably as a result of classical Rayleigh-Taylor flute-like instabilities characteristic of high-density θ-pinch operation.[12]

5. Plasma Density Measurements. The time and spatial evolution of the main discharge plasma density distribution was determined using a 30-ns pulsed holographic ruby laser interferometer. A limited number of interferograms were taken with the laser beam transverse to the plasma column. In order to obtain details of the plasma density distribution near the column axis, the majority of the interferograms were taken with the laser beam parallel to the tube axis.

Figure VI-11 presents a sequence of end-on interferograms obtained with an initial fill pressure of 100 mtorr. The plasma column formation phase ($t = 0.7$ μs, Fig. VI-11) is dominated by high m-number ($m > 6$) flutes, with some of the flutes extending from the plasma column to the discharge tube wall. At later times, $t \geq 1.4$ μs, the flutes disappear and a well confined high density plasma column is observed for several microseconds. The beginning of the plasma column break up and filamentation ($m = 2$) is evidenced at $t = 10$ μs.

Figure VI-12a presents a plasma column interferogram obtained at 300 mtorr fill pressure and is typical of the high fill pressure data. The plasma electron density profile, derived from the interferogram of Fig. VI-12a is shown in Fig. VI-12b. The density profile is non-Gaussian and exhibits a

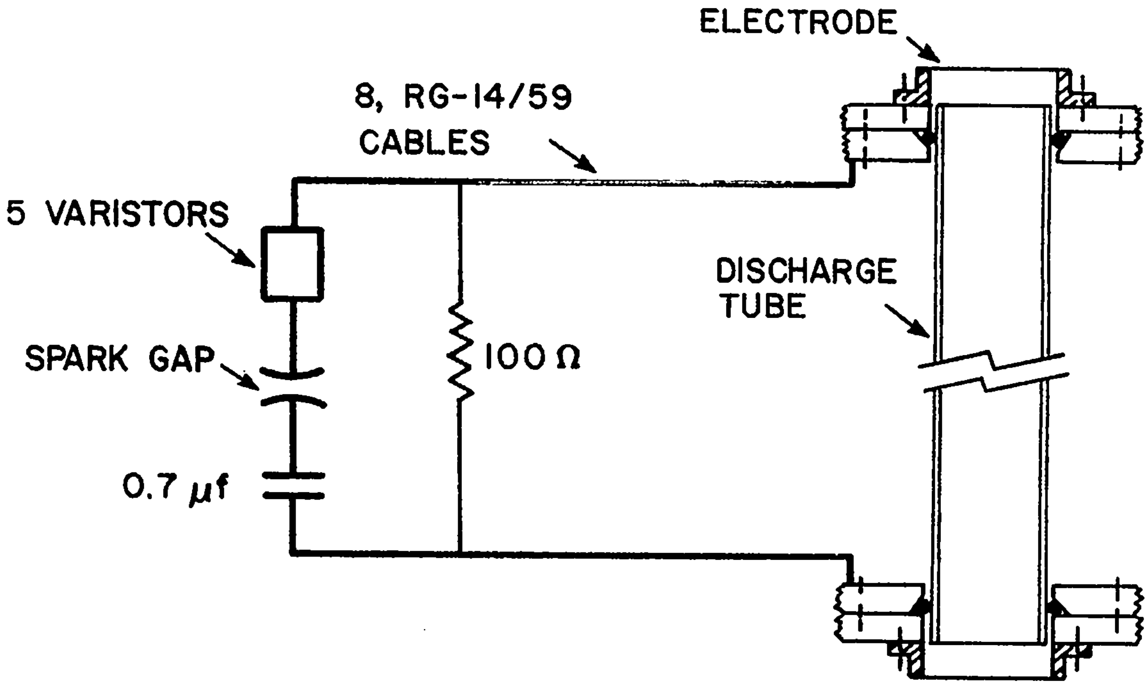

a) Z-PINCH CIRCUIT SCHEMATIC

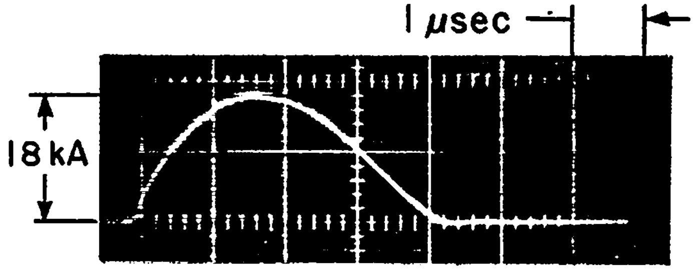

b) CURRENT WAVEFORM

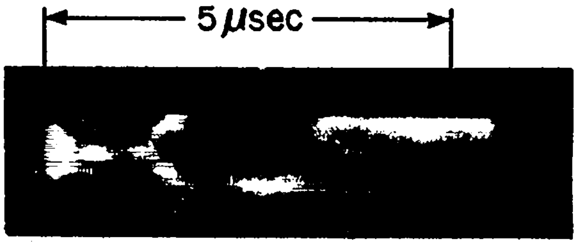

c) STREAK PHOTOGRAPH

Fig. VI-8

Z-pinch preionization system.

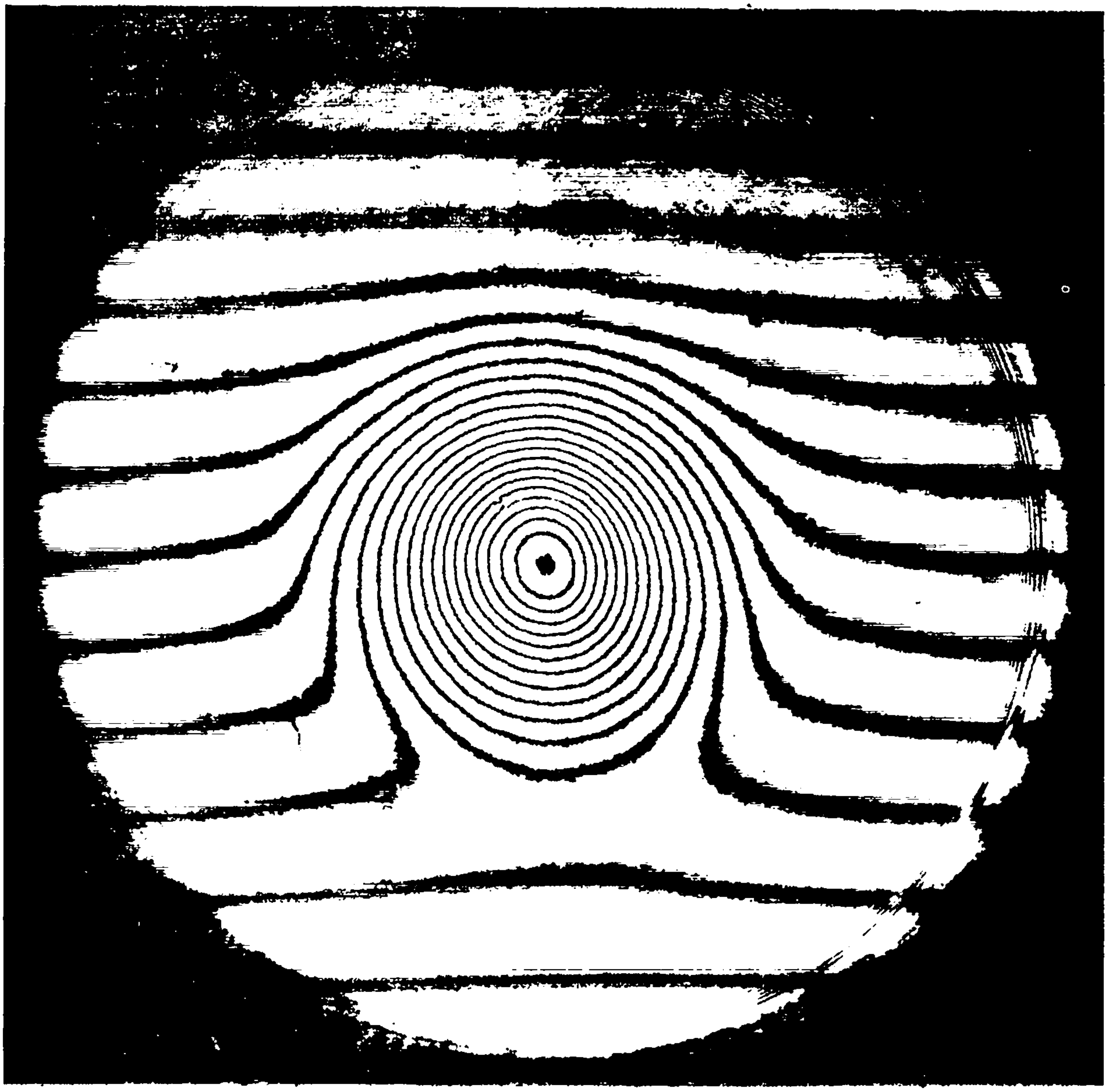

Fig. VI-9

Interferogram of preionization plasma obtained with 100 mtorr fill pressure.

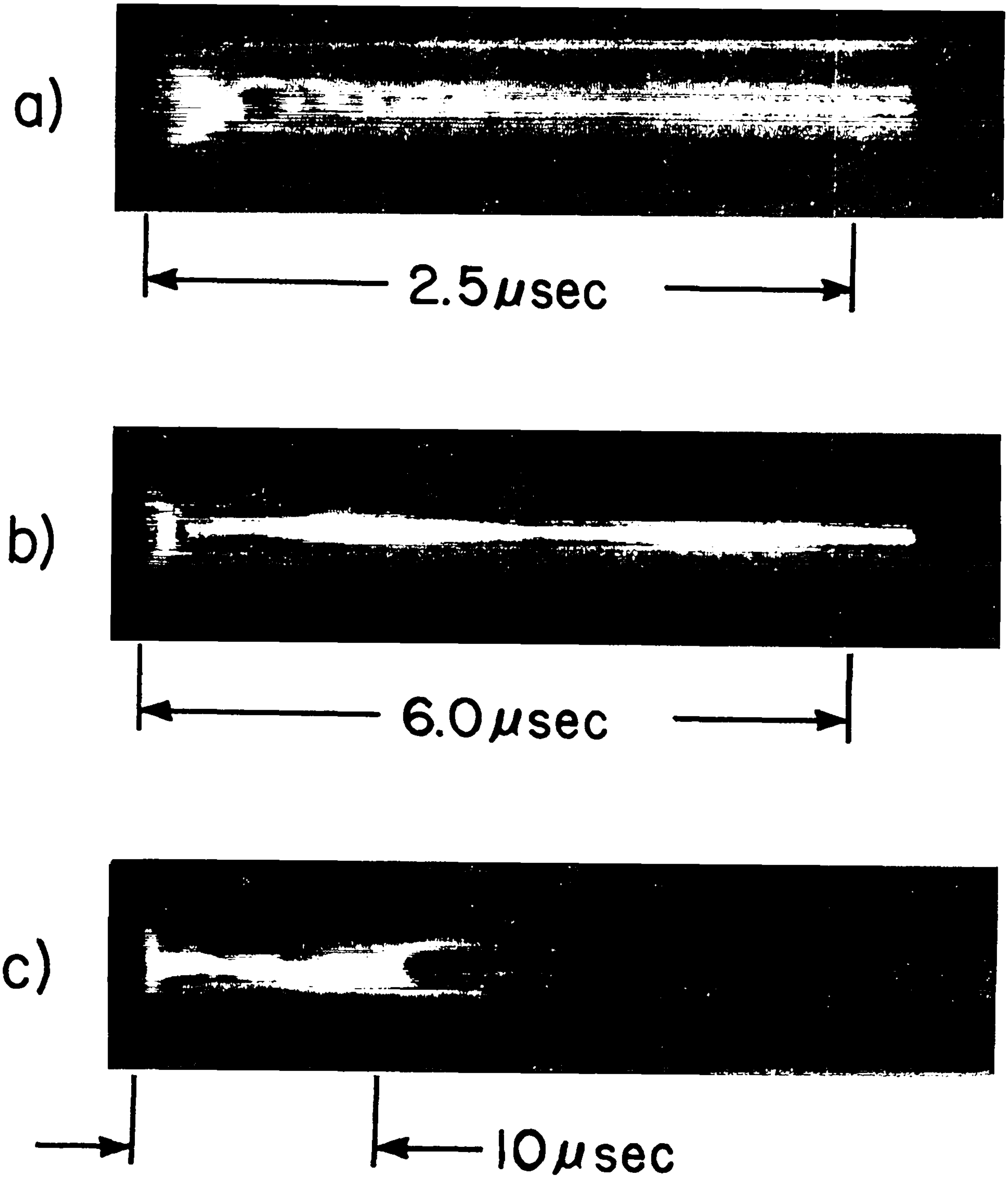

Fig. VI-10

Streak photographs of the main plasma discharge obtained at 100 mtorr fill pressure.

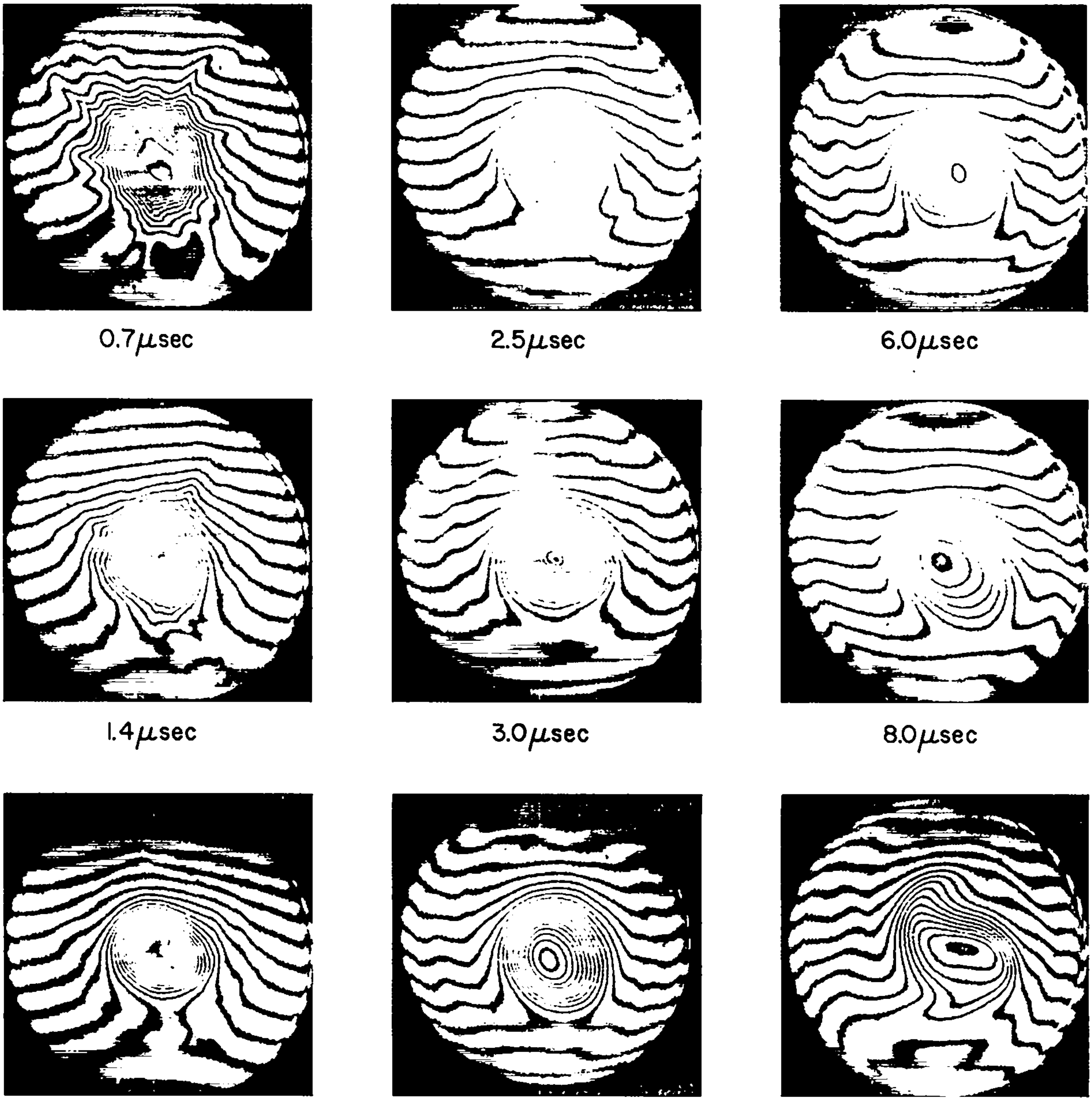

0.7μsec

2.5μsec

6.0μsec

1.4μsec

3.0μsec

8.0μsec

2.0μsec

4.0μsec

10.0μsec

Fig. VI-11

Time sequence of plasma column interferograms obtained at 100 mtorr fill pressure.

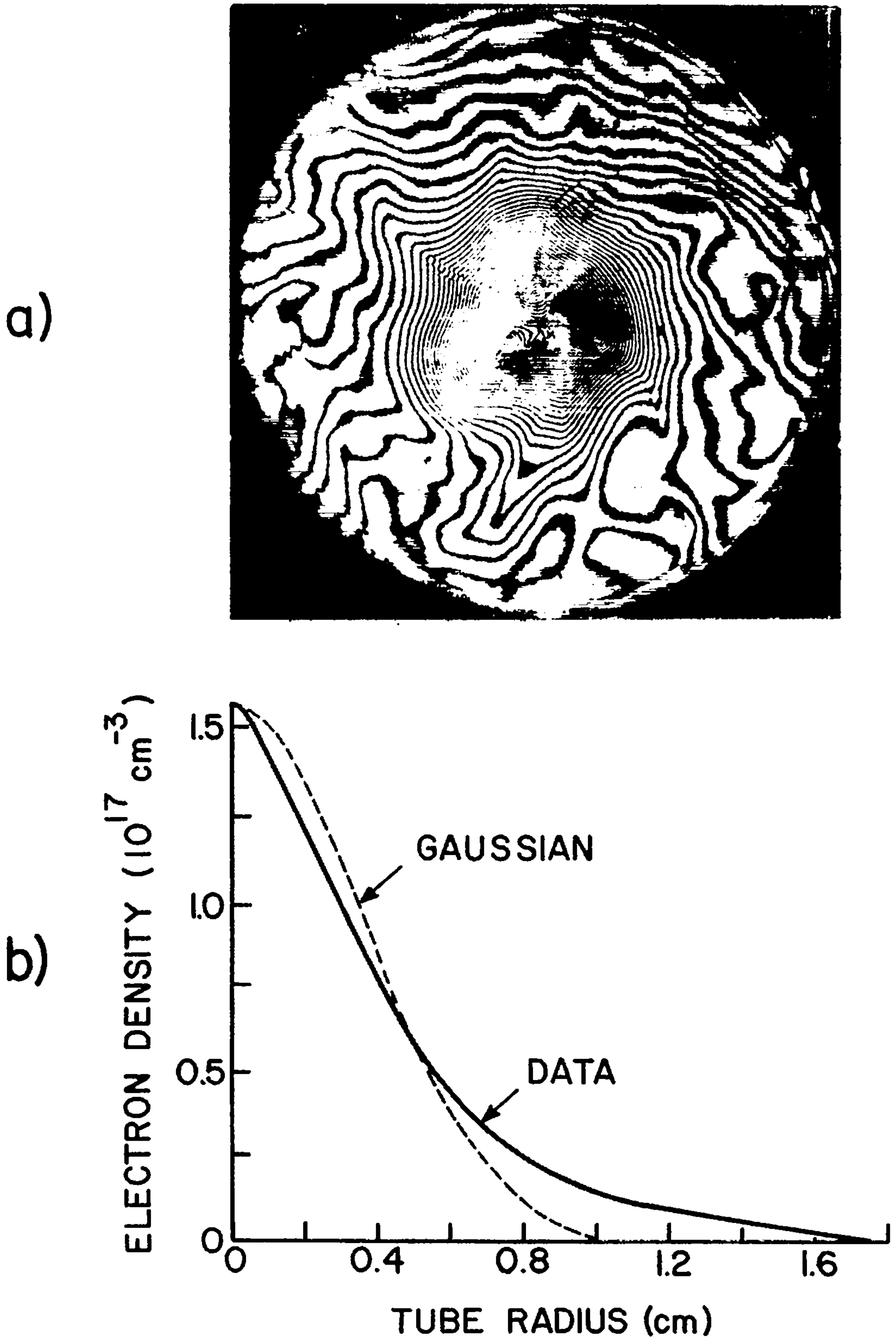

Fig. VI-12

Plasma column interferogram and reduced density profile for $p_o=300$ *mtorr,* $t=2.7\ \mu s$.

long tail which, at high fill pressure, extends to the discharge tube wall ($r=1.8$ cm). Extracting an exact plasma density profile from the interferograms taken at fill pressures greater than 300 mtorr is difficult due to the large number of closely spaced fringes. At $P_0=500$ mtorr the total number of fringes was ≈77 at maximum compression, $t=2.0$ μs. The peak density on axis could be estimated from simple fringe counting and the peak density determined from the end-on interferograms at 500 mtorr fill agreed within 20% with the values derived from the side-on interferograms.

From analysis of many interferograms, the average plasma density at maximum compression, $t=2.0$ μs, was estimated to be 1.05×10^{17} cm^{-3} at $P_0=100$ mtorr, 1.45×10^{17} cm^{-3} at $P_0=250$ mtorr, and 2.33×10^{17} cm^{-3} at 500 mtorr fill. Spatial integration over the reduced density profiles, obtained at 100 mtorr and 250 mtorr fill, indicated that 100% of the fill gas was ionized and contained within the observable plasma density distribution at the time of maximum compression; approximately 70% ionization was indicated from both end-on and side-on data at $P_0=500$ mtorr.

6. Excluded Flux Measurements. The effective radius r_{eff} at which magnetic flux is excluded from the compressed plasma was determined from standard differential magnetic loop probe measurements. The excluded flux data, when appropriately combined with the known plasma density distribution, is used to determine the plasma β (ratio of plasma pressure to magnetic field pressure). From the β measurement an estimate of the plasma kinetic temperature can be made.

The excluded flux radius derived from the loop probe data is presented in Fig. VI-13 for the 100 mtorr fill pressure case. The implosion phase, damped oscillation phase and quiescent plasma column phase observed in the streak photographs of Fig. VI-10, can also be identified from the excluded flux data of Fig. VI-13. Of primary interest to the CO_2 laser-plasma interaction experiment is the quiescent plasma column period immediately following the damped plasma oscillation phase. During this period the plasma density is maximum, the plasma column is well defined and the end losses minimal. From Fig. VI-13 it can be seen that r_{eff} remains relatively constant at a minimum value of 0.22 cm for a period of approximately 1 μs centered about the time of maximum compression, $t=2.0$ μs. It is during this time interval that the CO_2 laser beam will be fired. The excluded flux data of Fig. VI-13 is typical of that obtained at higher fill pressures, where a period of constant r_{eff} of at least 1-μs duration is also observed. The minimum value of r_{eff} is almost insensitive to fill pressure, changing only 15% between 100 mtorr fill (0.22 cm) and 500 mtorr fill (0.19 cm).

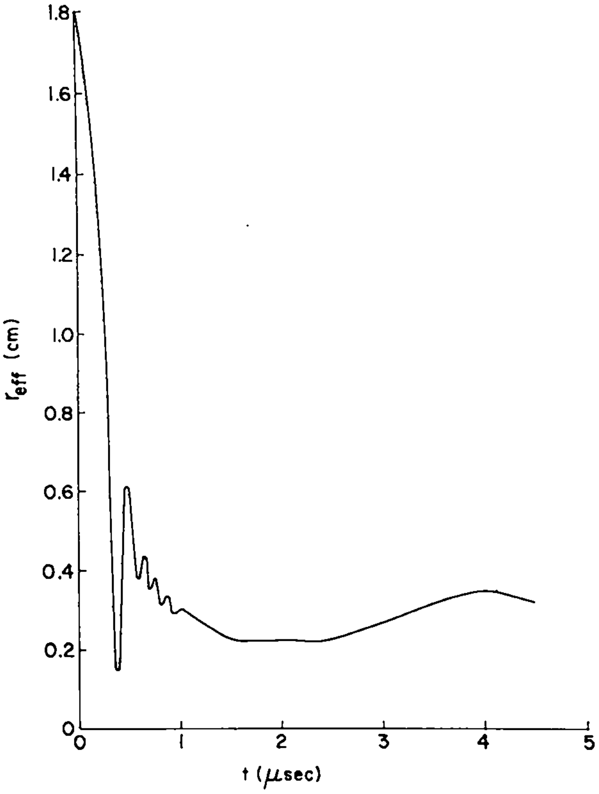

Fig. VI-13
Excluded flux radius obtained at 100 mtorr fill pressure.

7. Determination of Plasma β. From the definitions of excluded flux and the pressure balance equation it can be shown[13] that the area of excluded flux πr_{eff}^2 is related to the plasma β through the expression

$$\pi r_{eff}^2 = \int_0^\infty \left[1-\sqrt{1-\beta(r)}\right]2\pi r\,dr \qquad (1)$$

Assuming that the plasma temperature is independent of radius, pressure balance yields

$$\beta(r) = \frac{n(r)}{n_A}\beta_A \qquad (2)$$

where n_A and β_A are the plasma density and β on axis. For a Gaussian density distribution, substitution of Eq. (2) into Eq. (1) yields an exact solution for β_A as a function of r_{eff} and the 1/e plasma radius.

For a non-Gaussian profile such as shown in Fig. VI-12b, $n(r)/n_A$ must be determined graphically and the result substituted into Eq. (1) which can then be numerically integrated to determine β_A.

For the Scylla I-C density profiles at maximum compression, t=2.0 μs, the β_A determined by numerical techniques were; $\beta_A=0.45$ with $P_o=100$ mtorr and $\beta_A=0.33$ with $P_o=250$ mtorr. The value of β_A obtained assuming a Gaussian profile (Fig. 12b) and calculating the 1/e radius using the peak density value were; $\beta_A=0.63$ for 100 mtorr fill and $\beta_A=0.37$ for 250 mtorr fill. The difference between the β_A determined numerically and that calculated assuming a Gaussian profile decreases as the fill pressure increases, being ~29% at 100 mtorr and 11% at 250 mtorr. The convergence of the β_A values generated by the two techniques indicates that the density profiles more closely approximate a Gaussian shape as the fill pressure is increased. Assuming that the profile at $P_o=500$ mtorr is Gaussian, the calculated β_A is then ≈0.17.

8. Determination of Plasma Electron Temperature. The compressed plasma temperature is determined from the measured values of plasma density on axis n_A, the measured external magnetic field B_z, and the calculated values of β_A. From pressure balance,

$$\beta_A \frac{B_z^2}{8\pi} = n_A k(T_e+T_i) \qquad (3)$$

In the high density plasma column the thermal equilibration time between electrons and ions is small (≪ 1 μs) so that $k(T_e+T_i) \approx 2kT_e$. The plasma electron temperature can then be determined directly from Eq. (3).

Figure VI-14 summarizes the Scylla I-C plasma parameters n_A, T_e and β_A obtained at maximum compression over the investigated range of fill pressure, P_o, from 100 mtorr to 500 mtorr. The error bars displayed on the plasma density data reflect the assumed uncertainty in the data reduction and indicate the error associated with the calculated value of T_e and β_A.

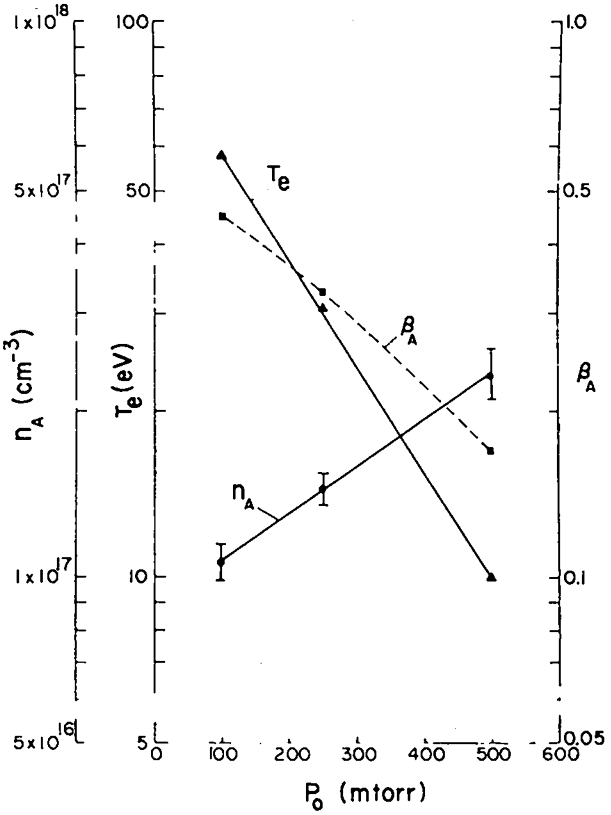

Fig. VI-14

Scylla I-C plasma parameters at the time of maximum compression, t=2.0 μs.

C. Laser-Plasma Interaction in Scylla I-C

1. Introduction. The concept of heating high density magnetically confined plasma with long wavelength laser light is of considerable interest for fusion applications. The Scylla I-C experiment was initiated in order to investigate the interaction of a 10 μm CO_2 laser beam with a high density ($n_e \geq 10^{17}$ cm^{-3}) θ-pinch plasma column. Initial experiments will be directed toward the investigation of (a) channeling of the laser beam along the large aspect ratio (L/D ≃100) plasma column, (b)plasma heating by laser energy absorption and, (c) anomalous backscatter of laser light.

The properties of the dense plasma column generated in Scylla I-C have been discussed in the previous section. Final electrical testing of the CO_2 laser system is currently in progress. The design characteristics of the CO_2 laser and a discussion of the expected results of the laser-plasma interaction, based on preliminary analysis, is given below.

2. CO_2 Laser Parameters. The CO_2 cold cathode laser was designed and constructed by the L-1 group of the Laser Research and Technology Division. A modification of the A-3 amplifier[14] of the LASL CO_2 laser system was chosen as a source for the 50-100 J requirement of the laser-plasma interaction experiment. A photograph of the completed laser system of the Scylla I-C experiment is shown in Fig. VI-15. The CO_2 laser design characteristics are given in Table VI-I.

TABLE VI-1

CO_2 Laser Parameters

Optical aperature	$50\ \text{cm}^2$
Laser length	100 cm
Beam diameter	8 cm
Short pulse output	80±20 J in 60 ns (2×10^9W, peak)
Focusing mirror radius of curvature	R=6m for post-pinch heating R=8m for laser preheating
Focused beam diameter	2 mm
Laser power density	$4\times10^{10}\ \text{W/cm}^2$ (nominal average)

The 8-cm diameter beam will be focused onto the end of the plasma column by one of two possible spherical reflecting mirrors. A mirror with radius of curvature, R=6 m, will focus the beam to a ~2-mm spot at the near end of the plasma column. This mirror is intended for heating of the compressed plasma column. A second mirror with a radius of curvature of 8 m will be available for future experiments where laser heating of the preionized plasma, followed by main field compression, will be investigated. The R=8 m mirror would focus the beam at the far end of the plasma column.

3. Laser Heating of the Plasma Column. The plasma column generated in the Scylla I-C theta pinch has a density maximum on axis. A fundamental objective of the present experiment is to determine if the laser beam will "drill" a hole into this density maximum and channel down the entire length of the plasma column. Channeling of the beam will be considered in a later section. For the discussion given below it will be assumed that the incident laser beam does remain contained within the compressed plasma column.

In the fully ionized plasma column the energy of the incident CO_2 laser light is absorbed through the process of inverse bremsstrahlung by which the electrons are accelerated in the electric field of the focused light. The plasma ions are heated as a result of subsequent electron-ion collisions. For CO_2 laser radiation, the inverse bremsstrahlung power absorption length in an underdense plasma ($n_e \ll n_{ec}$, $n_{ec} = 10^{19}\ \text{cm}^{-3}$) can be expressed as

$$\ell_{ab} = \frac{1.03\times10^{35}(T_e)^{3/2}}{n_e^2\ \ell n(1.39\ T_e)^{3/2}}\left(1-\frac{n_e}{10^{19}}\right)^{1/2}\ \text{cm} \qquad (4)$$

where T_e is in eV and n_e in cm^{-3}. This length represents the distance at which the power in the CO_2 laser beam, traversing a uniform plasma of temperature T_e and density n_e, will be reduced to 1/e (37%) of its initial value. The absorption length is plotted in Fig. VI-16 for the experimentally determined plasma parameters of the Scylla I-C theta pinch.

The rate of energy absorption by the electron population as a result of the inverse bremsstrahlung mechanism, assuming that the electron-ion thermalization time t_{eq} is greater than the laser pulse width t_ℓ and neglecting thermal heat conduction losses, can be written as[15]

$$\frac{3}{2} N_o k \frac{\partial T_e}{\partial t} = W/\ell_{ab} \qquad (5)$$

where N_o is the particle line density (N_o=fill density × discharge tube area) and W is the CO_2 laser power. Neglecting scattering and emission, the spatial rate of change of the incident laser power is given by

$$\frac{dW}{dz} = -W/\ell_{ab} \qquad (6)$$

where z=0 defines the vacuum-plasma interface at the end of the plasma column.

For the case of constant absorption length ℓ_{ab}, Eq. (6) can be integrated directly yielding the classical exponential decay in laser power along the beam

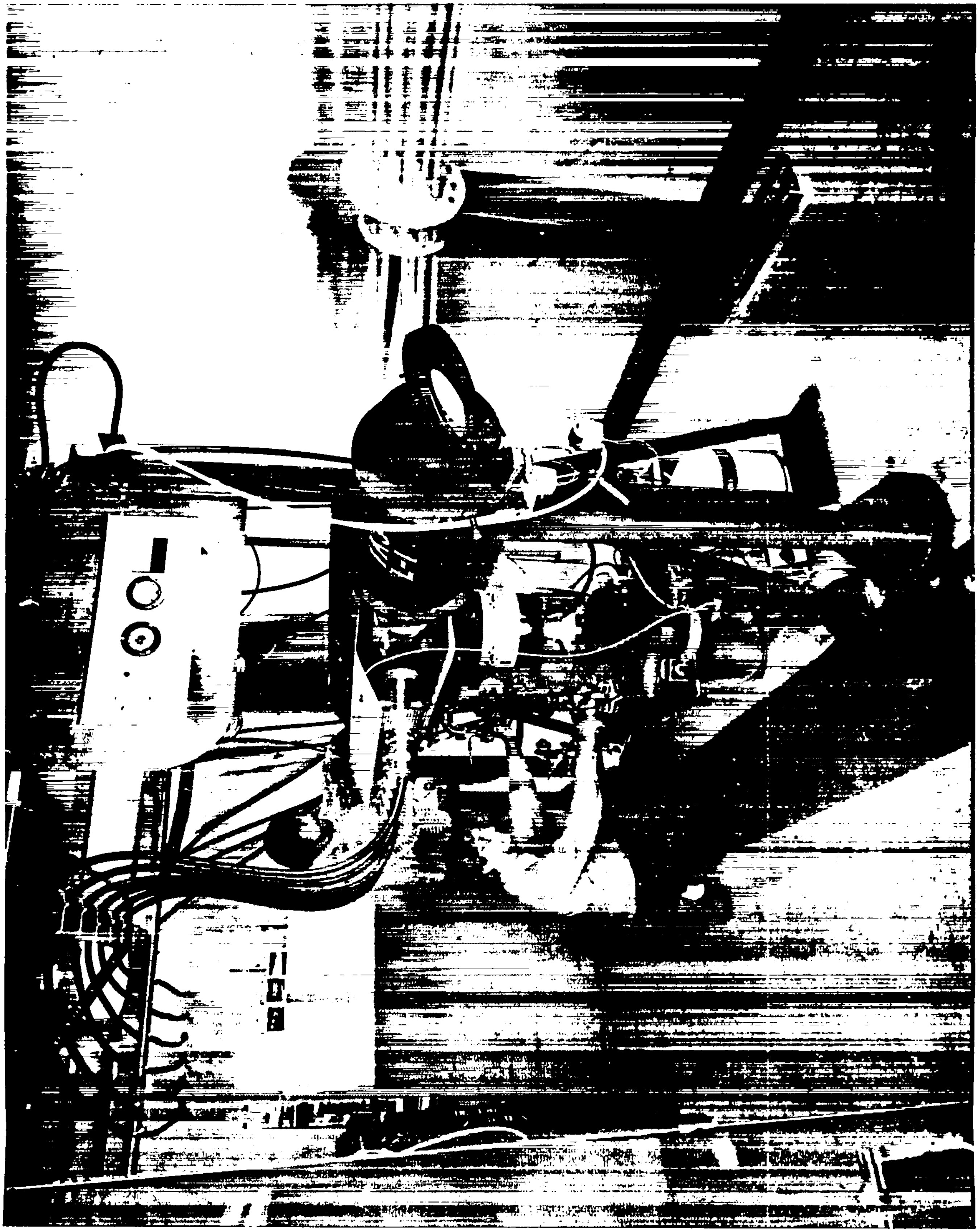

Fig. VI-15

CO_2 laser constructed for the Scylla I-C laser-plasma interaction experiment.

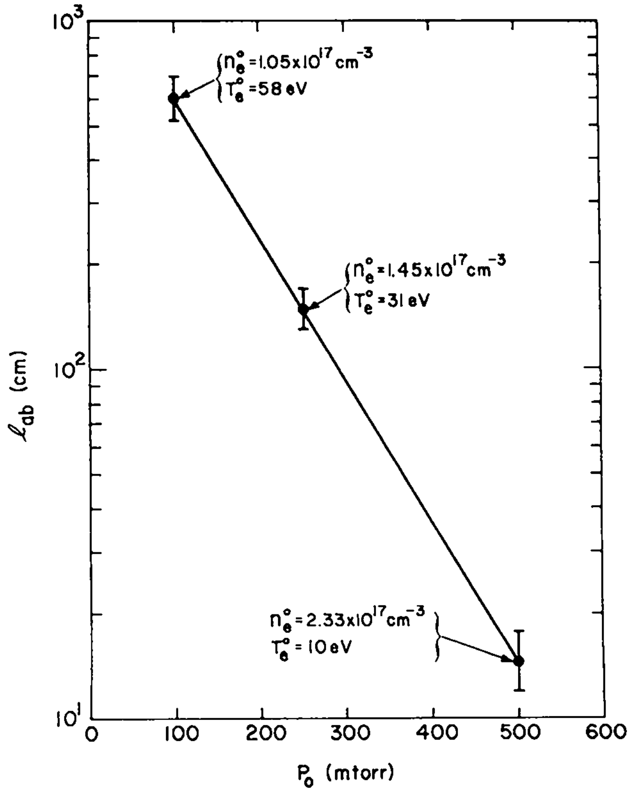

Fig. VI-16

CO_2 laser beam absorption length for the experimentally determined plasma parameters in the Scylla I-C theta pinch.

path. Substituting this solution for W(z) into Eq. (5), the change in electron temperature can be obtained by integrating Eq. (5) over the duration of the laser pulse. This procedure provides an approximate value for the laser induced change in electron temperature when the absorbed laser energy results in only a small perturbation on the total plasma energy.

When the absorbed laser energy becomes a significant fraction of the initial plasma energy, nonlinear absorption, referred to as "bleaching", results. Since $\ell_{ab} \sim T_e^{3/2}$, local laser heating of the electron plasma continually increases the absorption length over the laser pulse duration, rendering the plasma increasingly more transparent to the incident radiation. In this case Eqs. (5) and (6) must be solved with ℓ_{ab} as a function of the local electron temperature and density.

For nonlinear absorption, the governing equations can be simplified by considering only the electron temperature change at the laser input end (z=0) of the plasma column. In this case W in Eq. (5) can be replaced by W_0, the incident laser power. From Eq. (4) the absorption length can be approximated as,

$$\ell_{ab} \simeq 1.7\times10^{34}\,\frac{(T_e)^{3/2}}{n_e^2} \qquad (7)$$

where $\ell n(1.39T_e)^{3/2} = \ell n\,\Lambda$ has been taken as 6.

As the electron temperature increases the local plasma expands. Assuming that pressure balance is maintained and that β does not vary significantly during the expansion, the electron density can be written as

$$n_e = 2.5\times10^{10}\,\frac{\beta B^2}{\left(T_e + T_i^o\right)} \qquad (8)$$

where T_i^o is the plasma ion temperature prior to laser heating in eV and B is in gauss. The laser beam is assumed to expand at the same rate as the local plasma.

Substituting Eqs. (7) and (8) into (5) with $W=W_o$ yields,

$$\frac{\partial T_e}{\partial t} = 1.5\times10^5\left(\frac{E_o}{N_o}\right)(\beta B^2)^2(T_e)^{-3/2}(T_e+T_i^o)^{-2} \qquad (9)$$

where E_o(J) is the total laser energy. Integrating the above equation over the laser pulse width t_ℓ and neglecting any changes in the ion temperature gives,

$$\frac{1}{9}(T_e)^{9/2} + \frac{1}{7}(T_e^o)^{7/2}(T_i^o) + \frac{1}{5}(T_e)^{5/2}(T_i^o)^2$$

$$= 0.45\,(T_e^o)^{9/2} + 1.5\times10^5\,(\beta B^2)^2\left(\frac{E_o}{N_o}\right) \qquad (10)$$

where T_e^o is the plasma electron-temperature prior to laser heating.

For the Scylla I-C experiment where B=33 kG (at peak compression, t=2.0 μs) and E_0=80 J, the expected electron temperatures at the laser input end of the plasma column calculated from Eq. (10) and the final heated region density, estimated from Eq. (8), are given in Table VI-II.

From a more detailed analysis of the nonlinear laser absorption process[16] it can be shown that, for the measured Scylla I-C plasma parameters and CO_2 laser energy, the laser induced electron temperatures at the laser beam exit end of the plasma column are within 10% of the values calculated for the input end, indicating a relatively uniform heating of the entire plasma column.

In the above analysis only electron heating was considered, the electron-ion thermalization time was assumed to be long compared to the laser pulse width, $t_\ell \approx 60$ ns. From Spitzer[17] the thermalization time between the laser heated electrons and the

TABLE VI-II

Initial plasma temperature, plasma temperature increase after laser heating and final heated plasma density as a function of initial fill pressure

P_o (mtorr)	T_e (eV)	ΔT_e (eV)	h_e (10^{17} cm^{-3})
100	66	8	1.02
250	42	11	1.19
500	28	18	1.22

plasma ions is ≈425 nsec at $P_0=100$ mtorr and $t_{eq} \simeq 110$ ns at 500 mtorr. Thus, the ion temperature significantly lags the electron temperature over the time scale of the laser pulse.

A possible energy loss mechanism, not included in the simple analysis presented above, is radial heat conduction. Since $\omega_{ci}\, t_{ci} < 1$ (ω_{ci} is the ion cyclotron frequency, t_{ci} the ion-ion collision time) in the Scylla I-C plasma, transverse heat conduction is performed mainly by the electrons. The characteristic distance for radial heat diffusion $L = \sqrt{D_\perp t}$, where $D_\perp$ is the cross field thermal diffusivity[5] is determined to be approximately 0.013 cm, which is nearly an order of magnitude less than the radius (>0.1 cm) of the heated plasma region. Accordingly, radial heat losses during the laser heating time are insignificant. Since the plasma column is expected to be heated relatively uniformly along its length, axial heat conduction is unimportant.

4. Laser Beam Refraction-Channeling and Self-Focusing. In the theoretical study of laser heating of confined plasmas, it has been proposed that density gradients within the plasma would refract the laser beam toward regions of lower density[18] (higher index of refraction). If the incident laser light is directed along the cylindrical plasma column axis, as in the present case, then a density minimum on axis (dn/dr) > 0 should result in channeling of the beam down the column axis, and possible beam self-focusing. Conversely, the laser beam would be expected to refract away from the axis, and thus out of the plasma column, if the plasma density has an on-axis maximum. Experimentally, it has been established[19] that channeling of the laser beam does result when the plasma has a density minimum on axis, and for low power density laser beams (~10^7W/cm^2), refraction of the beam out of the plasma has been observed[19] for the case of an on-axis density maximum. However, Hoffman[20] has found that a laser beam of sufficient power density (~10^{10} W/cm^2) can create and maintain an on-axis density minimum (and thus channel) even if a density maximum is initially present on axis of the confined plasma column. It would thus appear that a laser power density "self-channeling" threshold exists, above which the laser beam will "drill" its own density minimum through the plasma regardless of the on-axis density conditions. It might be expected that such a threshold would coincide with the initiation of the "bleaching" phenomena discussed earlier. It should be noted that in Hoffman's experiment[20,21] the plasma column length was an order of magnitude smaller (10 cm) than the column produced in Scylla 1-C (100 cm). Accordingly, the investigation of beam channeling in the present experiment, and the possible identification of a "self-channeling" threshold, is of primary interest.

Assuming that the laser beam forms its own density minimum during the early stages of the laser pulse (an assumption consistent with the bleaching process), the refraction of the laser beam within the confined plasma column can then be determined from calculated light ray trajectories. From such an analysis,[16] with dn/dr >0, converging diffraction of the incident laser light is indicated. Further, the analysis[16] predicts that at sufficiently large axial positions, point focusing of the channeling laser beam will occur. The axial position, $_{fp}$ at which all of the internal laser beam is focused to a point can be obtained from the calculated ray trajectories. (It should be noted that total focusing of the laser beam will not occur since, in any real plasma, the density gradient (dn/dr) goes to zero as r → 0). For the Scylla I-C plasma parameters it can be shown[4] that $\ell_{fp} \ll \ell_{ab}$ under all experimental conditions. Thus, if the laser beam does form its own density minimum local "hot spots," beam filamentation and the necessarily inherent nonlinearities associated with intense heating of very small plasma volumes, might be expected to occur. Such phenomena could represent a serious problem for the present 100-cm long plasma column heating experiment and for future fusion applications. These effects will be investigated in detail in the present experiment.

5. Laser Light Scattering Instabilities. The irradiation of plasma with laser light of sufficient power level can cause "laser driven instabilities" to occur which result in anomalous absorption[22] or backscatter[23] of the laser light. Anomalous absorption instabilities are effective for laser radiation near the plasma frequency or twice the plasma frequency. In the Scylla I-C experiment $\omega_o \ll \omega_{pe}$ (ω_o is the CO_2 laser light frequency and ω_{pe} the plasma frequency) and thus anomalous absorption instabilities will not be important. However laser light scattering instabilities, which occur in underdense plasmas, could result in the reflection of a significant fraction of the incident laser radiation.

The set of coupled wave equations which describe the evolution of the scattering instabilities are obtained by combining the fluid equations for ions and electrons with Maxwell's equations. It can be shown[23] that the solution of this set of equations is completely described in terms of three waves excited by the incident laser light. Two of the excited waves are electromagnetic, the backscattered wave and a forward traveling nonresonant wave. The forward scattered "Stokes" wave, not being in resonance, can be neglected. The remaining excited wave is electrostatic, being either an ion wave, Brillouin scattering, or an electron plasma wave, Raman scattering.

The power density thresholds for the scattering instabilities are obtained from balancing the wave growth rate with the damping rate. For the Raman and Brillouin instabilities the linear thresholds can be written as,[23]

$$I(\mathrm{Raman}) > \frac{\gamma_p \nu_{ei}}{\omega_o \omega_{pe}} n_e m_e c^3 \tag{11}$$

$$I(\mathrm{Brillouin}) > 4 \frac{\gamma_\ell \nu_{ei}}{\omega_s \omega_{pe}^2} v_e^2 k_o n_e m_e c^2 \tag{12}$$

where $\gamma_p = (\gamma \quad + \nu_{ei})$ is the damping rate for the electron wave, γ the Landau damping rate, ν_{ei} the electron-ion collision frequency, ω_{pe} the plasma frequency, ω_s the ion wave frequency, ω_o and k_o the incident light frequency and wave number, respectively and v_e is the electron thermal velocity.

In the Scylla I-C experiment the CO_2 laser power density is expected to be $I \approx 4 \times 10^{10}$ W/cm^2. The instability thresholds for the plasma parameters at p_o =250 mtorr (Fig. VI-2) are I(Raman)≈I(Brillouin)≈ 3×10^8 W/cm^2. Accordingly, strong backscatter of the incident laser light could be expected in the present experiment.

References

1. J.P. Freidberg and B.M. Marder, "Stability of Two-Dimensional Magnetohydrodynamic Equilibria," Phys. Fluids **16**, 247 (1973).

2. M.J. Katz, compiler, Progress Report LASL Controlled Thermonuclear Research Program, Los Alamos Scientific Laboratory Report, LA-5656-PR (July 1974).

3. K.F. McKenna, R. Kristal, F. Jahoda, R. Gribble, K. Thomas, E. Zimmermann, F. Seibel, S. Linzey, R. Deaton, R. Amsden, J. Smith, CTR-3 Quarterly Report, July-September 1973.

4. K.F. McKenna, R. Kristal and K.S. Thomas, "Measurements of Plasma Density Distribution and Current-Sheath Structure in the Implosion Phase of a Theta-Pinch Discharge," Phys. Rev. Lett. **32**, 409 (1974).

5. K.F. McKenna, E. Zimmermann, S. Linzey, port, January-March 1974.

6. F. Söldner, "Investigation of Fast Magnetic Plasma Compression as a Method for Generating High Temperature with Weak Compression," Max-Planck-Institut für Plasmaphysik Garching bei München Report IPP-1/141, 1974.

7. M. Keilhacker, M. Kornherr, H. Niedermeyer, F. Sölder, and K.H. Steuer, "Flute Instabilities during Fast Magnetic Compression of Collisionless β=1 Plasmas," Phys. Rev. Lett. **32**, 1044 (1974).

8. F.L. Ribe, ed., "Proposed Experiments on Heating, Staging, and Stabilization of Theta Pinches," Los Alamos Scientific Laboratory report LA-5026-P, (1972).

9. T.S. Green and G.B.F. Niblett, "Rayleigh-Taylor Instabilities of a Magnetically Accelerated Plasma," Nucl. Fusion **1**, 42 (1960).

10. M. Keilhacker, M. Kornherr and K.H. Steuer, "Observation of Collissionless Plasma Heating by Strong Shock Waves," Z. Physik **223**, 385 (1969).

11. K.F. McKenna, E.L. Zimmermann, S. Linzey, R. Kristal CTR-3 Quarterly Report, July-September 1974.

12. H.A.B. Bodin, T.S. Green, G.B.F. Niblett, N.J. Peacock, J.M.P. Quinn, J.A. Reynolds, "The Influence of Trapped Field on the Characteristics of a Magnetically Compressed Plasma," Nucl. Fusion, **2**, 521 (1961).

13. W.R. Ellis, J.P. Freidberg, R.E. Siemon, E.L. Zimmermann, in Progress Report LASL Controlled Thermonuclear Research Program, Los Alamos Scientific Laboratory Report LA-5250-PR, 38 (1972).

14. W.H. Reichelt, E.E. Stark and E.O. Swickard, "Gigawatt Pulses from a 3 Atmosphere CO_2 Electron Beam Controlled Laser," Los Alamos Scientific Laboratory internal report (1973).

15. A.L. Hoffman, "Laser Heating of Magnetically Confined Plasmas for X-Ray Production," Mathematical Sciences Northwest, Inc., Report MSNW74-118-1 (1974).

16. T.M. York and K.F. McKenna, "Laser-Plasma Interactions in the Scylla 1-C Experiment: Preliminary Analysis," Los Alamos Scientific Laboratory report LA-5957-MS (1975).

17. L. Spitzer, *Physics of Fully Ionized Gases,* 2nd Ed. Interscience Pub., New York (1962).

18. L.C. Steinhauer and H.G. Ahlstrom, "Propagation of Coherent Radiation in a Cylindrical Plasma Column," Phys. Fluids, **14**, 1109 (1971).

19. N.A. Amherd and G.C. Vlases, "CO_2 Laser Heating of a Small θ-Pinch," Proc. 2nd APS Topical Conf. on Pulsed High-β Plasmas, Garching, Paper G4, July 1972.

20. A.L. Hoffman, Mathematical Sciences Northwest, Inc., personal communication, 1975.

21. A.L. Hoffman, "Strong Axial Laser Heating of a Theta-Pinch Plasma," Appl. Phys. Lett., **23**, 693 (1973).

22. E. Fabre and C. Steng, "CO_2-Laser-Beam Absorption by a Dense Plasma," Phys. Rev. Lett.,**32** , 823 (1974).

23. D.W. Forslund, J.M. Kindel and E.L. Lindman, "The Theory of Stimulated Scattering Processes in Laser Irradiated Plasmas, I," submitted to Phys. Fluids (1974).

VII. IMPLOSION HEATING EXPERIMENT

J.E. Hammel, I. Henins, T.R. Jarboe, J. Marshall,
A.R. Sherwood

A. Introduction

The Implosion Heating Experiment (IHX) was completed toward the end of this year and now is in routine operation, although not yet at full design level. IHX has two basic purposes, one scientific and the other technological. Its scientific purpose is the study of the implosion process, the initial heating mechanism in fast theta pinches. It is hoped in the future to develop theta pinches with enhanced implosion heating and, in order to do this intelligently, more must be known about the physics of the process, and the requirements and effects of the preionization process preceding it. The technical objective is the development of high voltage technology. This has been necessary in order to build IHX, and is expected to be applicable to future machines. The technical objective has now been largely accomplished; IHX is in operation, and some elements of the technology developed have been incorporated in the Staging Experiment, now nearing completion. A general view of the experiment is shown in Fig. VII-1.

In order to facilitate the study of the implosion process, IHX is designed as a relatively short (one meter) linear theta pinch of unusually large diameter (40 cm). The coil is long enough so that the implosion process at the center should be unaffected by the ends. The large diameter gives enhanced space and time for diagnostics. One object of IHX is to extend the implosion to larger velocities thus requiring more driving magnetic field strength during the implosion than has been customary. A large implosion field strength at standard theta pinch filling density (10^{15}cm^{-3}) with faster implosion implies a more rapid flow of magnetic flux into the discharge tube and therefore a larger azimuthal electric field strength. IHX is designed to achieve a field of 2 kV/cm, approximately twice the value used in previous LASL theta pinches. All of this requires a large total voltage applied around the tube, 250 kV during the implosion. Systems resembling IHX have been built in the past for the so-called collisionless shock experiments. The voltage around the tube in some of them exceeded the requirement for this experiment, but was applied to a much lower density plasma. Here at standard LASL theta pinch density, the plasma appears as an inconveniently low impedance (0.3 Ω) and in order to achieve 250 kV actually applied during the implosion, a very low impedance generator is required. The generators of the various collisionless shock experiments have all had impedances amounting to several ohms. The effective impedance of IHX is approximately 0.3 Ω, equal to the plasma impedance, and thus a total emf of 500 kV is required in the circuit.

After considering a number of different types of generators it was decided to use pulse forming networks (PFN's) built up out of capacitors and inductances. The final system drives the coil at four feed slots, the PFN capacitors being fast Marx charged to 125 kV, so as to add up to a total of 500 kV. The PFN's are connected to the feed slots through field distortion rail gaps, and the switching is done near Marx current maximum so as to add transfer capacitor characteristics to the system. The charging current, since it is already flowing at switching time, can be added to the load current, and need not build up in the capacitor inductances. Thus a larger current and faster rise are produced than would be possible if the PFN's were slow charged. The PFN capacitors are modified Scyllac preionization capacitors, having substantially smaller capacity (0.2 and 0.4 μF instead of 0.7 μF as in the original). This allows the ringing frequency of the capacitors to be considerably higher, and makes a fast risetime possible. The PFN circuit was designed, with the help of computer modeling, to have a fast rise to 800 kA, followed by nearly constant current for about 500 ns. A model had to be assumed for the plasma in order to do this, since the plasma has a large effect on the waveform. The plasma was assumed to be surrounded by a thin inward moving current sheath, originating at the wall and reflecting ions by an elastic bounce process, so that the deuterons move radially inward ahead of the sheath at twice its speed. No accounting was taken of the same particles interacting more than once with the sheath. This produces a small error during current rise, but a very large effect when deuterons from the other side meet the sheath at about one-third its initial radius. For purposes of computation the plasma

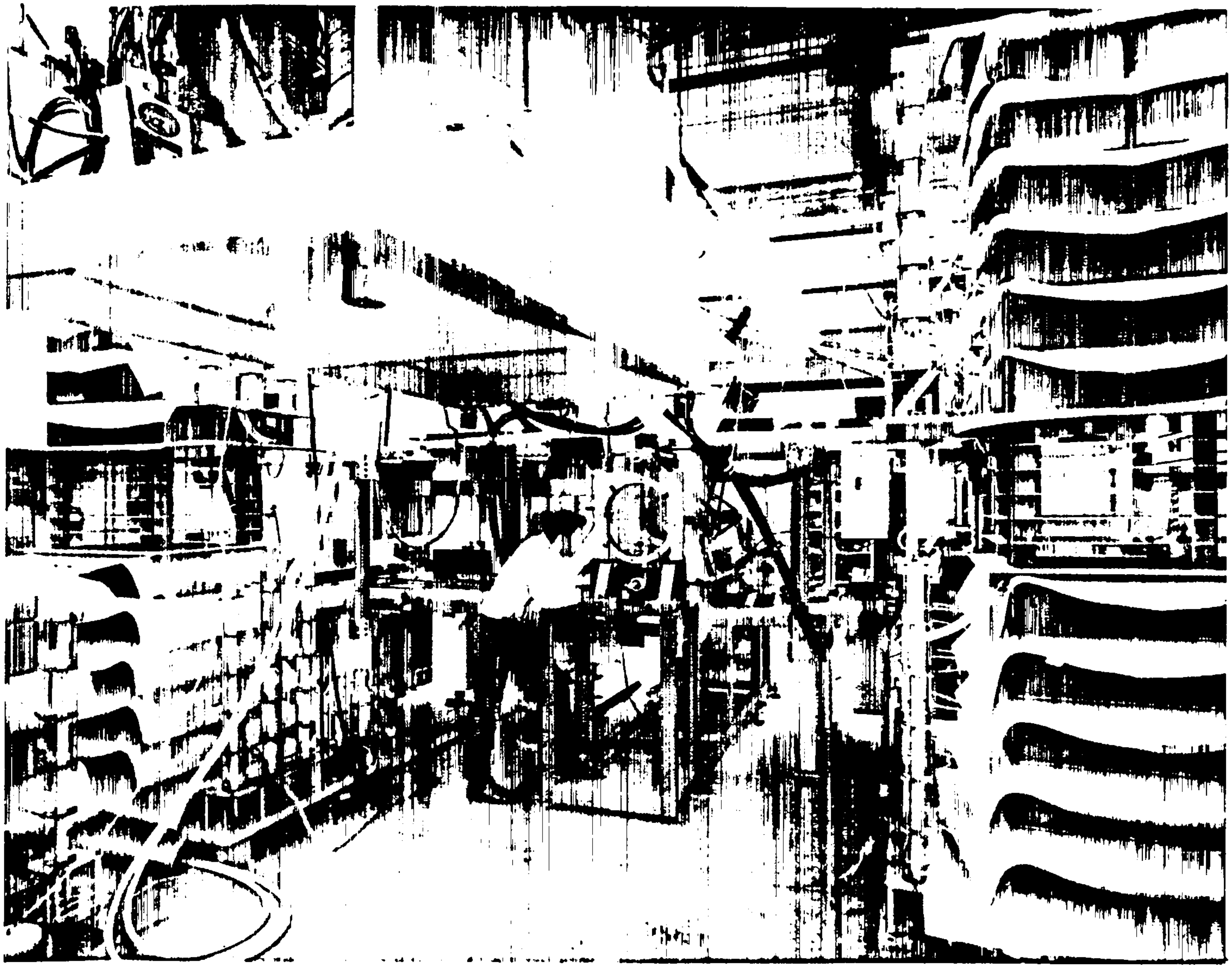

Fig. VII-1

A General View of the Implosion Heating Experiment (IHX) was assumed to stop its motion at that time. The final circuit design is shown in Fig. VII-2.

In order to design the PFN circuit it was necessary to know the circuit parameters of its various components. These included the pinch itself, with its connections. The capacitor headers were developed to use silicone rubber voltage gaskets, the original capacitor insulators having been cut down so as to allow smaller inductance. The capacitors were assumed to have internal inductances equal to the Scyllac preionization prototype. The coil connection design depended on the development of adequate surface flashover protection, as did the cable connections from the Marx generators to the PFN's. The rail gaps were commerical from Physics International, having been adapted from a design intended to be used at higher voltage and lower current under water. It turned out that reliable voltage hold off against flashover at Los Alamos altitude required the addition of conducting plastic to the rail gaps for voltage grading. The preionization system was designed to use four standard Scyllac preionization capacitors, each with a spark gap, feeding one of the four feed slots through two 50 Ω cables in parallel for inductive isolation.

B. Final Construction and Initial Operation

It had been planned to bring IHX into preliminary operation early in 1974 with two feed slots instead of four, the idea being that the less complicated system would be easier to operate, and that valuable experience would be obtained for operation of the full system. This plan was dropped when it began to be apparent that the two-feed-slot system would be radically different in symmetry, requiring special arrangements for triggering, diagnostics and grounding. In addition, operation of a half system would interfere seriously with construction and would delay completion of the full machine. Accordingly construction of the second pair of PFN's was continued in place.

1. Capacitor Failures. The second pair of PFN's, being on the other side of the coil from the first, had to have negative high voltage on the bottom side instead of the top. It was desired however to operate the capacitors right side up on both sides because of problems of bubbles in the impregnating oil. This meant that these PFN capacitors had to be positively charged instead of negatively, as were

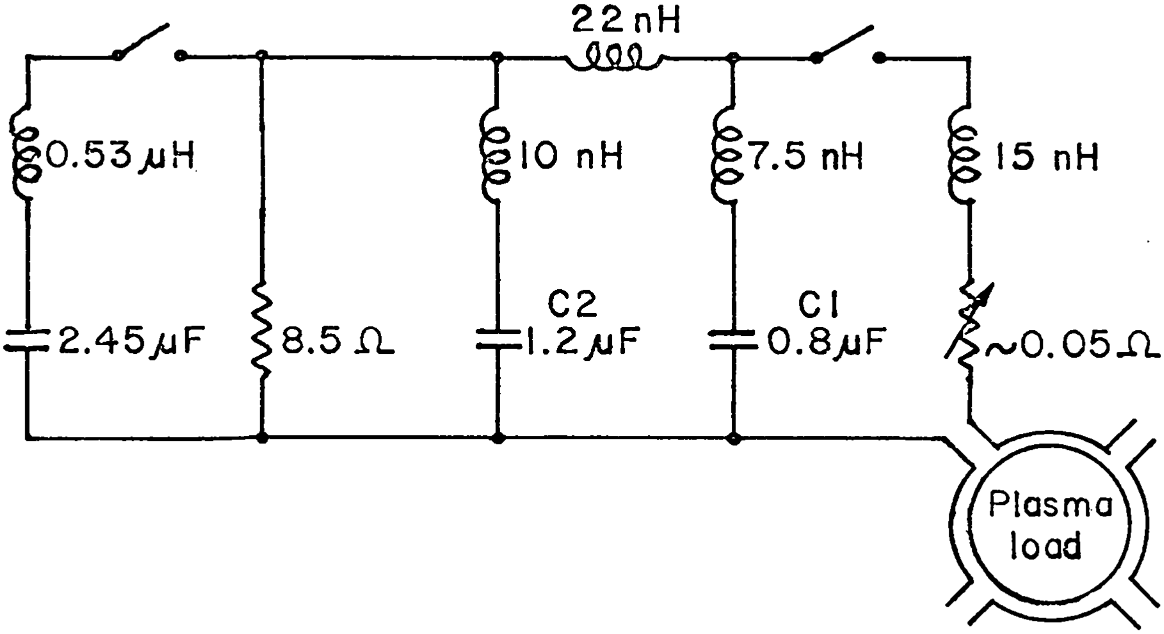

Fig. VII-2

The IHX electrical circuit for one feed slot. The parameters given here are representative of those obtained from the computer by matching the observed voltage and current waveforms. Some of these values are somewhat different from the original design, but they probably represent closer to what has actually been achieved.

those in the first two PFN's. In fact, what was done was to ground the capacitor terminals and charge the cans to negative high voltage. When the positively charged PFN's were tested, a number of capacitors failed on first charge. Apparently the capacitors had a polarity dependent failure mode. Postmortem investigation showed that failure was in the same place in all capacitors, across the surface of the insulating paper where it was folded at the top, near the terminal. Fortunately a second batch of capacitors had been procured from a competing manufacturer and these have given no trouble of this sort. Capacitors from both manufacturers had gas bubbles at the top. The failure appears to have something to do with the precise way in which the paper is folded. The capacitors, of the type which failed on positive charge, have given no trouble in long operation on negative charge.

2. First Operation. IHX was finally completed and brought into initial operation in May 1974. Almost immediately difficulty was encountered with the main switch rail gaps. The difficulty was the result of a complex of small problems which led to mechanical failure of the acrylic plastic gap envelopes. The gaps were adapted by the manufacturer from a switch built for service under water at ~400 kV with much less charge transfer. SF_6gas had been used at ~15 bars pressure. SF does not perform well at low enough pressure to break down at 125 kV, but it was found that N_2 behaved quite well. Air did not produce good multichannel breakdown so it could not be used. N_2 led to surface contamination and single channel untriggered surface breakdown. This made it necessary to clean the gaps, and this turned out to be time consuming, particularly in readjusting the electrode positions. Additional troubles were initiated by cross talk in trigger systems aggravated by the very complicated circuit. One typical trouble was failure of one of the preionization (PI) gaps to fire when triggered. Since all four PI capacitors and gaps were effectively in series, this tended to put 400 kV across one of the coil feed slots, and therefore across one of the rail gaps. The rail gap would then break down single channel, and break down in the same channel again when the voltage came up on the PFN's. Enough energy might thus be dissipated locally to cause mechanical failure of the gap. This particular cause of single channel breakdown has been circumvented by connecting all four PI capacitors in parallel, using one rail gap to switch them on to the coil through four pairs of 50 Ω cables as before.

3. New Spark Gap Gas Mixture. At this point news came from Physics International that better gap behavior might be obtained with a different gas, 92% Ar, 8% SF_6. The mixture has breakdown characteristics resembling N_2, but presumably has chemical behavior like SF_6. In any case it does not produce insulator surface contamination resulting in spark gap flashover. The new gas mixture came after a decision had been made to abandon the commercial gap, however.

4. Failure of Commercial Gaps. Single channel breakdowns at high energy resulted in the fracture of the plastic envelopes of several of the commercial rail gaps. It is probable that under ideal conditions the gaps could have been made to work. It appeared, however, that ideal conditions might be a long time coming, and that to get the machine running reliably, it would be advisable to have a more robust main switch, which would be easier to service if that were necessary. Two simultaneous programs were initiated for the development of such a switch. One involved the use of solid dielectric switches, and the other was to build rail gaps capable of high energy single channel operation without damage. The solid dielectric switch was the less attractive alternative, but appeared at the time to be the more nearly certain of success. Its disadvantages were the time required for replacing switches on every shot and the large amount of material which would be used up. The rail gap alternative turned out to be not too difficult, so the solid dielectric switch development was dropped.

5. New Rail Gap. A cross section of the new rail gap is shown in Fig. VII-3. In some of its features it resembles the rail gaps developed by Linford *et al.*, for staging gaps. It differs from the commercial gap in having much heavier, stronger electrodes, a much stronger plastic envelope with much larger internal volume, better access for maintenance of the interior, and more accessible terminals for making circuit connections. It has been modified from the original design by the addition of acrylic flashover shields glued to the top of the switch. These were added when it was found that under unusual, but not vanishingly rare circumstances a flashover could occur between trigger electrode terminal and the more distant main electrode terminal along the surface of the lid to a bolt head and from the bolt under the edge of the lid and round the side of the switch to the terminal. The discharge under the edge of the lid tended to crack it although no lid was ruined beyond use, since they are made of polycarbonate plastic. In order to maintain accurate electrode spacing the lids are keyed into slots machined in the switch envelope.

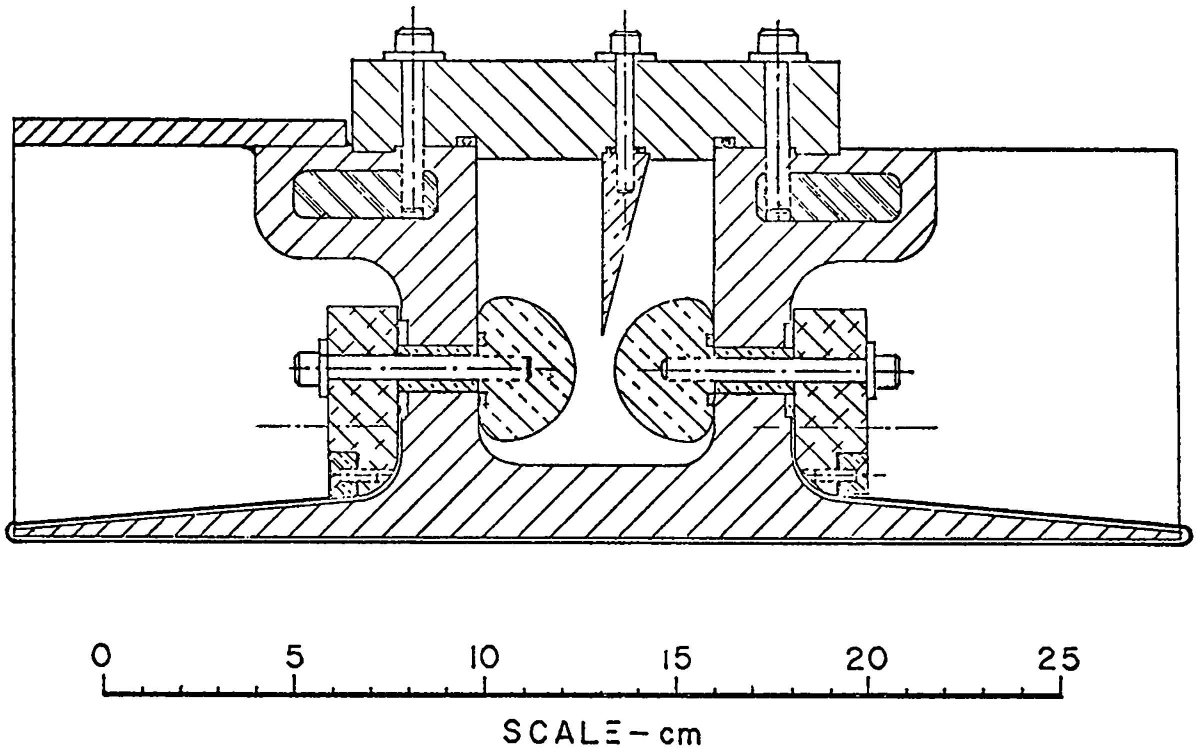

Fig. VII-3
A cross section of the new rail gap switch body of of fiber glass reinforced epoxy. The electrodes are approximately 40 cm long.

6. **Optical Trigger Links.** Problems were also encountered with cross talk in the trigger systems. These were caused partly by the difficulty of maintaining a simply connected electrical system in a complicated circuit in a limited space. Inevitably, it seems, ground loops develop. Different amounts of return flux from the coil, threading through the different loops, cause currents to flow in cable braids, and produce extraneous emf's. This problem has been attacked frontally in IHX by the development of optically triggered high voltage pulsers. The master timer is in the screen room where it triggers solid state injection lasers in the near infra red. The light pulses from these are transmitted through fiber optics to electrically isolated high voltage pulsers at the required places around the machine.

7. **Routine Operation.** The new rail gaps were completed, the optical trigger system installed, and the machine put back into operation in November 1974. Since then IHX has been in operation, so far at reduced current, and data are being taken on the implosion. The reduced level at which the machine is being operated, (~0.6 T instead of the design value of 1.0 T) is matched by a reduced filling density, so as to produce the design implosion velocity. This allows the current waveform to take approximately its design shape, with a fast rise followed by nearly constant current for about 500 ns. Operation at reduced current allows the development of diagnostics and debugging of the control system under conditions where component failures are less likely and less destructive than at design current. A good fraction of the failures encountered until now have been associated with control system or trigger system malfunction. As the systems are improved the chance of failures decreases and operation at high voltages becomes less hazardous.

C. Diagnostics

The diagnostics in use until now include magnetic probes, image converter photography, both framing and streak, fractional fringe interferometry, flux measurements including excluded flux and of course voltage and current measurements. Problems remain in several of these diagnostics, mostly associated with the high implosion velocity, the complicated circuit, the high voltage and the large tube diameter. As a result no completely consistent picture has yet been obtained of magnetic field and plasma density as a function of time and radius.

1. **Probes.** The only probes used so far have been magnetic probes consisting of small coils enclosed in fused quartz or ceramic envelopes. Plans are being made for electric probing in the near future for the measurement of radial ambipolar and azimuthal inductive electric fields. Magnetic probes have yielded questionable results in previous LASL theta pinches, because of the energetic plasma surrounding them, which tends to destroy probes and to ablate the probe surface, producing a secondary local plasma and thus a locally reduced magnetic field. Preliminary results are that these problems are still with us, but that probe surfaces tend to clean up after many discharges. Some indication of the accuracy of probe measurements can be obtained by integrating the results over the area of the discharge tube and comparing it with flux measurements (see below). If nothing else the probes appear to give a correct qualitative picture of the motion of the magnetic piston during the implosion. Results till now are that the current sheath is about 2 cm thick with a velocity roughly what would be expected from the bounce model. A large part of the current sheath thickness appears to be built in during the first rise of the coil current, and may be associated more with degree of preionization than with plasma resistivity. Azimuthal inductive electric field measurements with double probes may give a valuable alternative measurement of magnetic fields. Such probes have given physically believable results in the past under much more severe plasma energy flux conditions in gun plasmas. They measure the radial flow of magnetic flux (V×B), and with velocity information obtained from other measurements can give values for B. Radial electric fields are expected during the implosion, because the current driving the plasma inward is carried mostly by electrons. The electrons are then driven ahead of the ions, producing partial charge separation and electric fields such as to drag the ions along. These probing programs are only beginning, but are expected to consume a considerable part of the effort during the next year.

2. **Image Converter Photography.** The information available so far from image converter photography is incomplete and primarily qualitative. Partly this is because no image converter camera is available full time. Streak photography of the preionization phase fits well with probe measurements, giving a general picture of the preionization process discussed below. The picture is dominated by a series of luminous fronts moving inward from the wall on every successive current excursion. The main implosion shows a luminous front coming in at about sheath velocity, but no dark space behind it, as would be expected with a plasma-free magnetic piston. Photography with the camera off axis shows high luminosity near the wall beyond the ends of the coil. This is presumably due to plasma flowing out through the ends of the coil along field lines during the implosion. Whether all of the luminosity outside of the current sheath is due to this is not known as yet.

3. **Flux Measurements.** Excluded flux measurements have become a standard diagnostic on most theta pinches at LASL. They are performed by comparing the total flux inside the tube with a flux obtained by multiplying the magnetic field just inside the coil by the area of the tube. The difference of the two is the flux excluded by the plasma. The total flux is the time integral of the voltage around the tube obtained with a wire loop. The subtraction of the two fluxes is done automatically by a resistor network. In the case of IHX the flux measurement is much more difficult than in standard theta pinches because of the high voltage. The wire loop would have to be insulated for ~500 kV, and it would have to be between the coil and the tube, a place where there is not overmuch room. The solution of this problem which has been applied to IHX is to replace the wire loop around the tube with a resistive loop connected around the tube, a small portion being tapped off to provide the signal. The resistive loop is made of fine resistance wire glued to the glass of the tube in a zigzag pattern to provide enough length. The resistive loop has performed well functionally in that no high voltage arcs have occurred in its neighborhood. Problems remain however which appear to be associated with the RC behavior of the loop-coil system and the effects of one rail gap firing slightly out of synchronism with the others. There is not yet a reliable comparison of the flux measurement with the probe measurement although preliminary comparisons have supported the view that the probes indicate a lower magnetic field than is actually there.

4. **Fractional Fringe Interferometry.** A fractional fringe interferometer is used to obtain a time-resolved measurement of electron density along a line parallel to, and at various distances from, the axis of IHX. It uses the red light from a He Ne laser (6328Å) arranged in approximately a Mach-Zehnder interferometer configuration, one beam passing once through the plasma and being then combined with a reference beam passing outside the coil. The light is

detected by a PIN diode and displayed on an oscilloscope. A discriminator, on the output of the detector, fires the machine when the detector output is halfway between extrema. Fringes are passing by relatively slowly all of the time, of course, because of room vibrations or because of the motion of a driven mirror in the interferometer. An auxiliary measurement gives the voltage difference between extrema, and, by comparing the observed signal during a shot with this, the phase shift introduced by the plasma can be calculated. Room vibrations are much slower than the effect of the plasma, and produce only a slight error over the time from preionization to the end of implosion. Various difficulties with the system such as electrical noise, plasma light and subtle effects of frequency response in the electronics have prevented the accumulation of interferometer data which can be reliably correlated with other diagnostics. These difficulties are much less severe in the preionization phase than in the implosion, so that relatively trustworthy results have been obtained for the preionization electron density.

D. Preionization

The preionization system uses four Scyllac preionization capacitors in parallel (2.8 μF altogether) switched into cables which provide inductive isolation from the coil feed slots. Each feed slot is fed by two 50 Ω cables in parallel. This circuit has a natural frequency of ~ 200 kHz but the actual behavior of the system is strongly affected by the charging system of the capacitors. The capacitors are pulse charged by means of a Marx generator to a potential of up to 125 kV. Slow charging is avoided because the capacitors are rated to only 70 kV dc, although, because of pecularities of the Scyllac circuit, they may be exposed there to pulses of up to 120 kV, and were so designed. The Marx generator and the connection cables are inductive, giving the charging system a ringing frequency of ~100 kHz. The resulting closely coupled systems then produce a complicated waveform for the preionization current in the coil, with successive current peaks varying considerably in amplitude. Typically the first half cycle of preionization current fills the volume of the coil with magnetic field as though there were no gas present but produces a small amount of ionization. As the magnetic flux flows out at the end of the first half cycle, it carries plasma with it, depositing it on the surface of the discharge tube, and finally accumulating enough plasma there to amount to a crowbar current. This traps magnetic field inside the plasma, and this magnetic field from the first half cycle of the PI discharge remains inside the plasma until implosion time, gradually diminishing because of resistive diffusion, and/or because of outward plasma motion. The ionization of the gas during the PI discharge is the result of a series of magnetosonic waves propagating inward from the wall, one starting each time the magnitude of the field at the wall exceeds the magnetic field inside the plasma appreciably. These waves can be observed with magnetic probes and with image converter streak photographs, where they appear as inward moving luminescence. The preionization discharge is followed ~40 μs later by the main implosion, at which time the ionization is about 25% in the outer half of the discharge tube, falling off to lower values at the center. Occasionally there is a shot on which the preionization is lower than usual, such that the implosion current waveform is noticeably affected, having a more or less sinusoidal shape instead of the usual more or less square wave. The reasons for this are not well understood. Increase of preionization voltage raises the ionization fraction rapidly. The general subject of preionization, its mechanism and its effects, will be studied during the coming year.

E. Implosion

As mentioned above there is as yet no internally consistent picture of the main implosion. The diagnostics are plagued by a set of difficulties which lead to inaccuracies in each measurement. Probes are strongly affected by plasma bombardment. Interferometry suffers from the necessity of looking through plasma which is escaping from the ends of the coil. Side-on interferometry has not yet been tried because of high voltage problems, but has its difficulties too. The general features of the implosion are roughly as expected from the bounce model. The current sheath is about 2 cm thick, with the thickness determined during initial formation. Strong luminescence appears on the wall beyond the ends of the coil rather early during the implosion, presumably because of plasma flowing outward along field lines. A strong crowbar effect is found on the wall at the end of the flat-topped current pulse which traps magnetic flux inside the tube. This is accompanied by strong luminescence on the wall near the middle of the coil. The study of implosion phenomena is being carried out intensively, initially at less than design values of density (5×10^{14} instead of 10^{15} cm^{-3}) magnetic field (~0.6 T instead of 1.0 T) and E_θ (~1.2 kV/cm instead of 2 kV/cm). These numbers will be pushed up after sufficient data have been collected to give a more or less complete picture at initial conditions, and after system shakedown and debugging.

VIII. THE Z-PINCH PROGRAM

D.A. Baker, L.C. Burkhardt, J.N. DiMarco, P. R. Forman, A. Haberstich, R.B. Howell, H.J. Karr, J.A. Phillips, A.E. Schofield

A. Summary

The past year has been spent studying the characteristics of the toroidal reversed field Z-pinch experiment ZT-1 between 10^{10} A/s and 2×10^{11} A/s.

In this derated mode of operation improved stability is obtained with reversed field programming. A pinch which would normally strike the wall in 2-3 μs without reversed field, contacts the wall between 10 and 15 μs, when appropriate reversed field programming is used. Best results are obtained when the reversed field is programmed early in the discharge. The discharge exhibits fast poloidal field diffusion and loses part of its positive toroidal flux so that an initially favorable profile will diffuse to an unstable one having a fast growth rate. The studies on ZT-1 have been concentrated in two major areas: (a) the physics of setting up stable profiles and (b) the processes involved in the loss of stable configurations.

Detailed studies of the pitch of the field lines and the poloidal flux surfaces from magnetic probe data show that the setting up of given pitch profiles in the pinch, assuming a perfectly conducting plasma, is not a viable technique. As the field diffusion proceeds the loss of positive toroidal flux and the shortening of the pitch of the field lines in the neighborhood of the magnetic axis lead to very unstable profiles.

In order to decrease the field diffusion time, steps were taken to increase the electron temperature by increasing the preionization currents. Thomson scattering data showed that these measures were able to increase the interior T_e value before the main compression from $\sim$1 eV to at most 8 eV. Although the rate of poloidal field diffusion was slowed for early times in the pinch, T_e after $\sim$3 μs was $\sim$20 eV and was nearly the same as previously obtained so that little was gained in the long time diffusion and stable times.

Measurements of the electron density indicate that the plasma has a hollow profile and is well confined away from the walls. Integration of the density profiles indicates that essentially all of the filling gas is brought into the pinched column and that the contribution of gas from the walls is small.

A parameter study of ion temperature for various values of toroidal bias field, peak current, rate of change of current, and filling pressure has been made. At the lower toroidal bias fields the mean T_i values range up to $\sim$140 eV for 90 kA peak current. As one might expect, the higher temperatures are achieved at the higher compression ratios which locate the plasma farther from the wall and are harder to stabilize. The lengthy optimization of stable times has not been done at these higher temperatures. The exact nature of the ion heating mechanisms is not known. The T_i values increase both with I and dI/dt. Strong shock fronts were looked for but not observed.

A combination of numerical linear MHD stability analyses of magnetic field data with the results of a one dimensional time dependent MHD computer code has proven to be a powerful tool in determining the nature of the unstable modes expected as the plasma profiles evolve due to diffusion. These analyses give evidence that the anomalous resistivity is indeed responsible for the loss of a portion of the initially trapped toroidal flux and lead to narrower unstable profiles. Calculations indicate that the plasma has an anisotropic conductivity, nearly classical near the pinch center but anomalously high at the larger radii.

Studies have continued on the restrictions for setting up stable equilibria that are imposed by the requirements of global energy and pressure balance. The concern is that for very fast rising currents the pressure due to compression and diffusion heating may become too large for the poloidal field to contain without first having plasma-wall contact. Further calculations indicate that if the full diffusion of the toroidal current to a uniform current channel can be prevented for containment times of interest, then the requirements for equilibrium can be established without the requirement of energy losses or plasma pressure at the walls.

The above studies point to the need of a larger bore discharge tube in order to increase diffusion and stability times. The ZT-S device, which involves a modification of ZT-1 to replace the 10 cm diameter tube with a 15 cm diameter one, is planned to come on line in a few months. ZT-S should give information on the scaling of diffusion and ion temperature with size.

Preliminary Z-pinch fusion reactor calculations have been made and indicate that the lower limits on burning time are critically dependent upon the neutron damage at the first wall.

Experiments on the peaking capacitor circuit using a constant inductance load have reached dI/dt values of 3×10^{12} A/s with ~40 nh inductance in the load circuit. If favorable results can be obtained with the varying inductance of a linear Z-pinch this circuit will be used to energize a larger device, ZT-P. This would eliminate the need of fuses to obtain fast rising currents.

B. Modes of Machine Operation

The Z-pinch experiment has been operated in three modes: the fast (fuse) mode, the intermediate (resistor) mode, and the slow mode. Each gives a different range of the amplitude and rise time of the toroidal current. The different modes may be explained by referring to Fig. VIII-1. The toroidal current is inductively coupled into the plasma from a coaxial aluminum primary that is divided into quadrants. Each quadrant is energized by a pair of parallel feed plates connected to the power supply, as indicated in the figure. In order to prevent electrical imbalance the storage inductor L_s is common to each quadrant. However, in the equivalent circuits of Fig. VIII-1 it is represented as an inductance per quadrant. The highest currents and shortest rise times are obtained with the fuse circuit. The fuses open near the time of peak current and the transfer switches close, resulting in a high voltage pulse of up to 70 kV per quadrant.

The intermediate mode which involves lower currents and lower rates of rise is obtained by removing the fuse and replacing the transfer switch with a series resistance R_s, as shown in Fig. VIII-1. This resistance is made large compared to the remaining circuit impedance to give an overdamped current waveform. The value of R_s and L_s can be varied to control both the rise time and the peak current.

The slow mode is obtained by shorting the series resistor; a slow rate of rise, governed by the natural period of the circuit, is then obtained.

Typical rates of rise, magnitudes of the toroidal current and corresponding electron and ion temperatures for these three modes of operation with plasma densities of $\sim 3 \times 10^{15}$ are shown in Table VIII-I.

Results obtained from the slow and fast modes have been previously reported. This report will expand on the intermediate mode.

The intermediate mode is broken down into categories called Derate 1 through 5, which progress through increasing I_z and dI/dt. The electron and ion temperature, and formation of a stable plasma are investigated over as wide a parameter range as possible.

Table VIII-II summarizes the Derate operation. The parameter values in Table VIII-II reflect the initial stage of operation with the circuit and are not the maximum attainable values.

C. Formation of Reversed Field Profiles

The formation and time evolution of the reversed field profiles in ZT-1 were investigated by varying the rate of change of the reversing field and its timing with respect to the start of the I_z current. The experiment was set up to operate in the mode "Derate 4", with a gas filling of 20% He, 80% D_2 at ~40 mtorr. The maximum rate of change of the poloidal magnetic field was 4.7×10^5 T/s.

The rate of reversal of the toroidal magnetic field was controlled by the initial voltage on the reversed field capacitor bank. The rate of change of the toroidal magnetic field depends on the plasma being present; with no plasma, 12 kV on the reverse bank is equivalent to 0.6×10^5 T/s. With plasma, a rate of change of 1.3×10^5 T/s was measured.

All data presented were obtained from magnetic field probes which are inserted into the plasma at 1 cm intervals; five probes measured B_θ and an additional five probes measured B_z. From these magnetic field profiles the motion of flux tubes and the time behavior of the pitch of the magnetic field lines were obtained. Figure VIII-2 shows the flux tubes for the reversed field pinch. The motion of the poloidal and toroidal flux tubes with respect to one another can be seen from the plots. This nullifies one concept of pitch programming based on the idea of the flux tubes being "locked" to the plasma.

The evolution of constant values of the pitch is shown in Fig. VIII-3. The value of pitch is specified for each curve and the dashed lines to the right represent the location of the ceramic discharge tube. The pitch can be seen to disappear on axis, an effect that can only result from diffusion of the magnetic field.

These data are combined with data from the other discharge conditions and replotted to show the time behavior of values of constant pitch as presented in Figs. VIII-4, VIII-5 and VIII-6.

Figure VIII-7 shows a comparison of the toroidal flux measured with a flux loop with the integral of the toroidal magnetic field measured with probes.

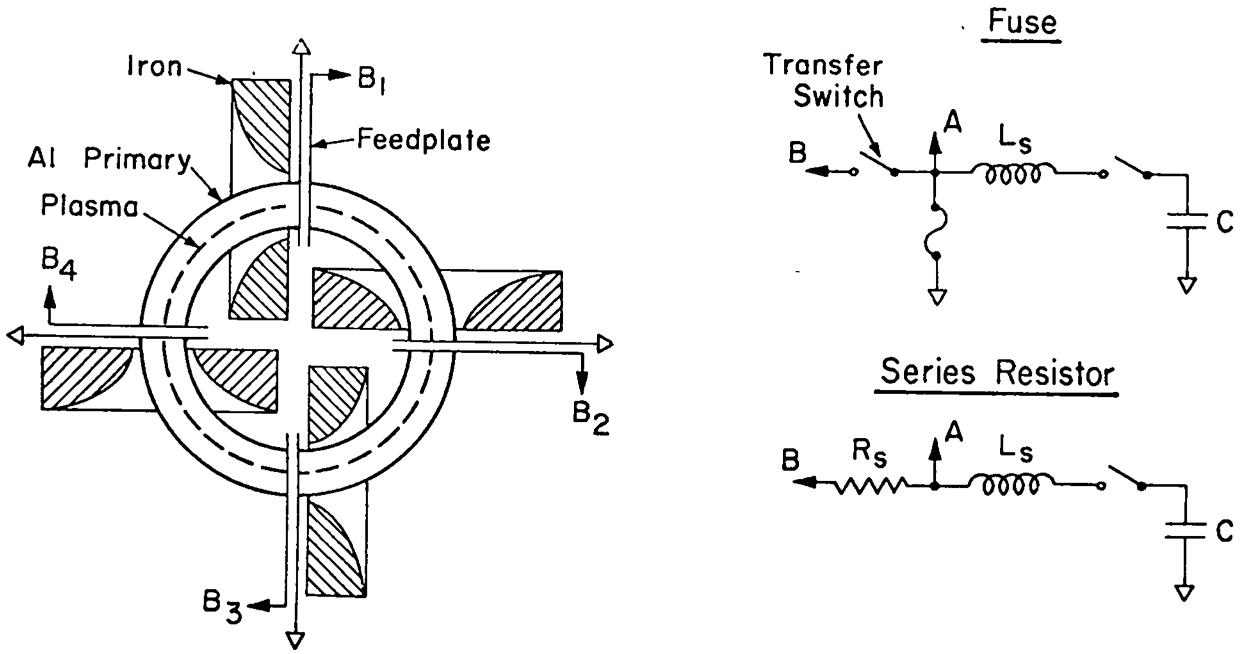

Fig. VIII-1
Diagram showing the four quadrant feed point arrangement in ZT-1 and the circuits used to obtain fast and intermediate rise times by means of fuses and series resistors, respectively.

TABLE VIII-I

MODES OF ZT-1 OPERATION

Mode of Operation	$\dot{I}$ (A/s)	$\dot{I}$ (kA)	T_e (eV)	T_i (eV)
Slow	2×10^{10}	130	~15	$\leq$ 60
Intermediate (Resistor)	2×10^{11}	120	~20	$\leq$ 80
Fast (Fuse)	1.5×10^{12}	200	~40	~800

TABLE VIII-II

DERATE MODES

	Per Quadrant				
Derate Mode	Resistance Ω	Capacitance μF	Inductance μH	$\dot{I}_z$ $\times 10^{11}$ A/s	I_z kA
1	0.45	150	280	0.6	40
2	0.45	150	140	1.2	40
3	0.355	150	140	1.2	60
4	0.2	150	140	1.2	75
5[a]	0.094	45	~200	2.0	110

[a] Derate #5 uses a modification of the fuse circuit, in that, the fuse is replaced by a resistor designed to heat up but not vaporize.

Back bias	+ 50 kV
Main marx charging voltage	- 72 kV
Total voltage swing during shot	122 kV
Maximum $\dot{V}$ in peaking charge circuit	8×10^{11} V/s
Average $\dot{V}$ during peaking capacitor charge cycle	2.4×10^{11} V/s
Input charging circuit current	80.3 kA
Output current into inductive load	227 kA
Maximum $\dot{I}$	2.8×10^{12} A/sec
Percentage of voltage appearing across the inductive load coil	25%
Total inductance of load circuit	~40 nH

The flux loop is a loop of wire placed on the outside of the aluminum primary. Circled data points represent the positive flux in the discharge. A paramagnetic effect can be seen at ~1 μs when $B_z=0$ at the wall of the discharge tube. Annihilation of the positive flux with time is noted here as well as in Fig. VIII-2, but when the crowbar is applied the annihilation stops, and in some cases at high forward bias field, the positive flux increases in time.

Some conclusions based on this investigation are as follows: (a) Pitch programming by assuming that flux tubes move with the plasma cannot be applied to the present mode of operation; (b) Pitch values longer than 0.1 m are unaffected by programming and must be set up by initial conditions; (c) Pitch values shorter than 0.1 m can be modified by programming; (d) Diffusion of the magnetic field results in a continued evolution of the pitch profile, so that even if a stable profile can be achieved by the combination of initial conditions and programming, the profile eventually evolves to one having values of pitch on the axis approximately equal to the diameter of the discharge tube; (e) The loss of positive B_z flux results in an overcompression of the pinch; (f) For favorable programming, the rates of change of the poloidal and toroidal magnetic field must be comparable, at least within a factor of approximately four.

One way to reduce the rate of diffusion by increasing the initial electron temperature is considered in section D.

D. Experiments to Increase the Electron Temperature During the Preionization Phase of ZT-1

This work was motivated by the results obtained from the programming experiments which showed that the pinch becomes unstable as the magnetic

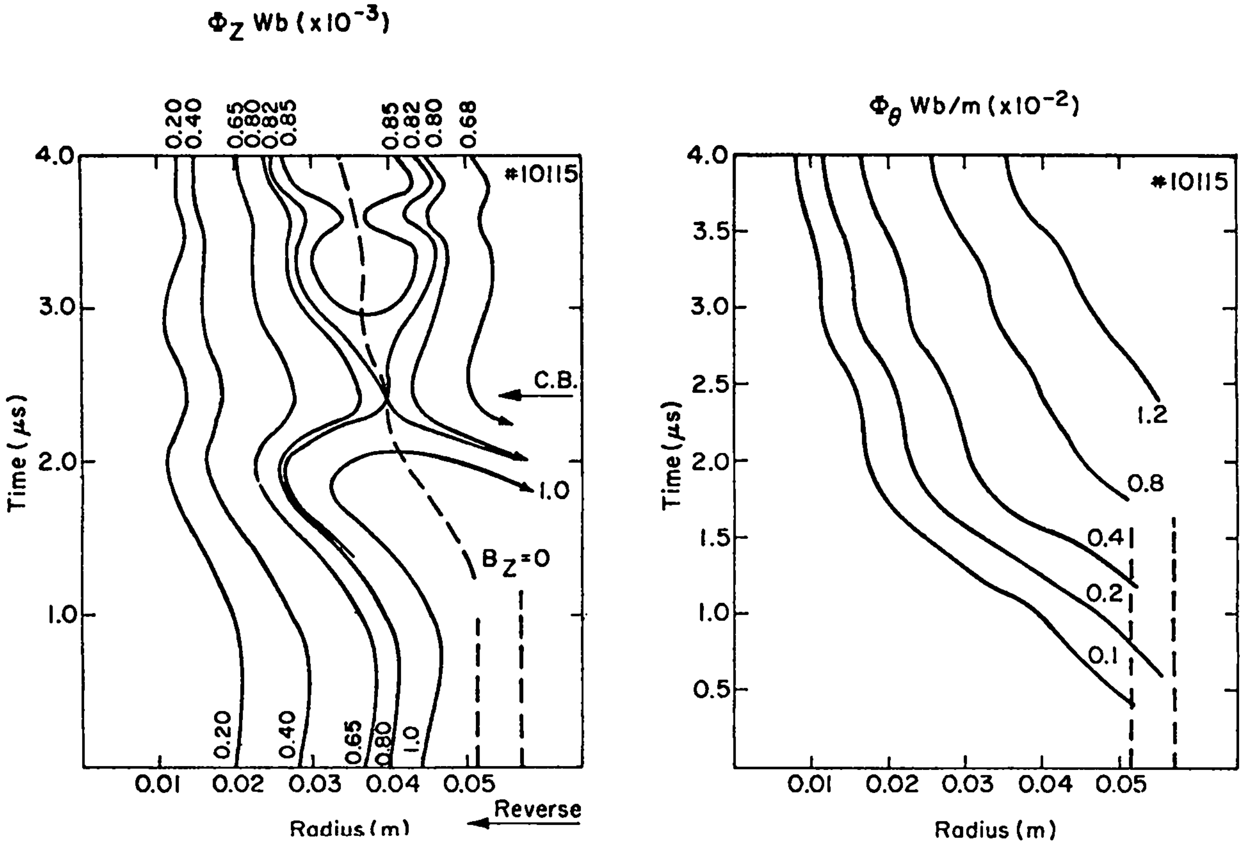

Fig. VIII-2

Radial time dependence of toroidal and poloidal flux tubes for a reversed field pinch. The magnitude of each flux tube is shown on the plot.

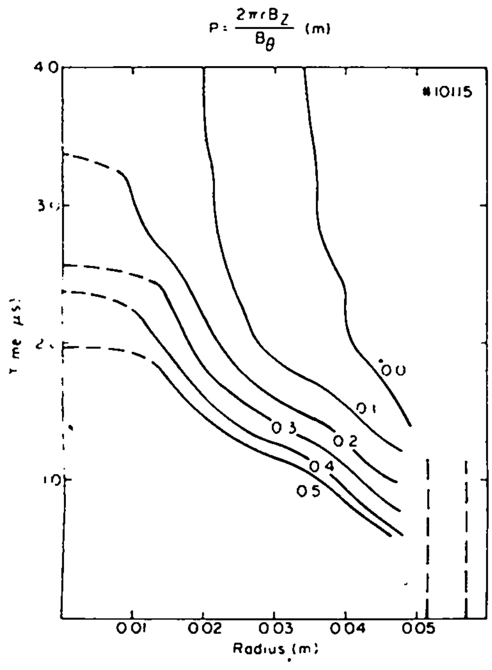

Fig. VIII-3

Radial time dependence of specified values of the pitch for a reversed field pinch. The value of pitch is specified for each curve.

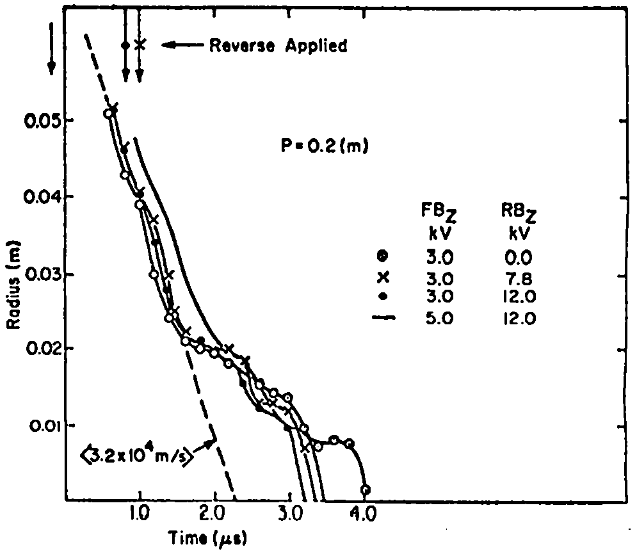

Fig. VIII-4

Radial time dependence for a pitch value of 0.2 m, under different conditions of rate of toroidal field reversal and the time at which the reverse field is applied.

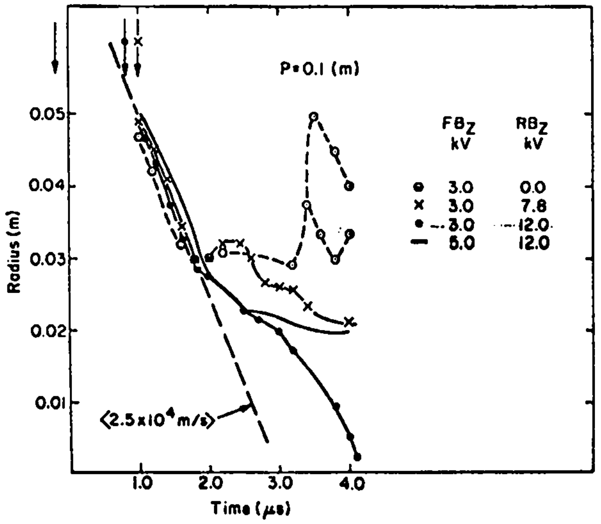

Fig. VIII-5
Radial time dependence for a pitch value of 0.1 m, under different conditions of rate of toroidal field reversal and the time at which the reverse field is applied.

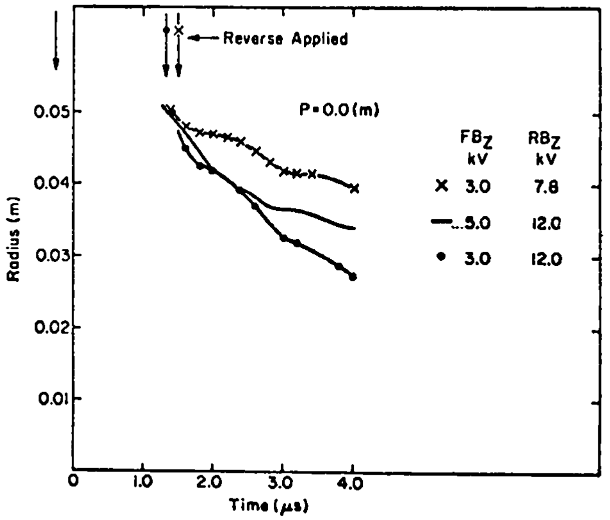

Fig. VIII-6
Radial time dependence for a pitch value of zero, under different conditions of rate of toroidal field reversal and the time at which the reverse field is applied.

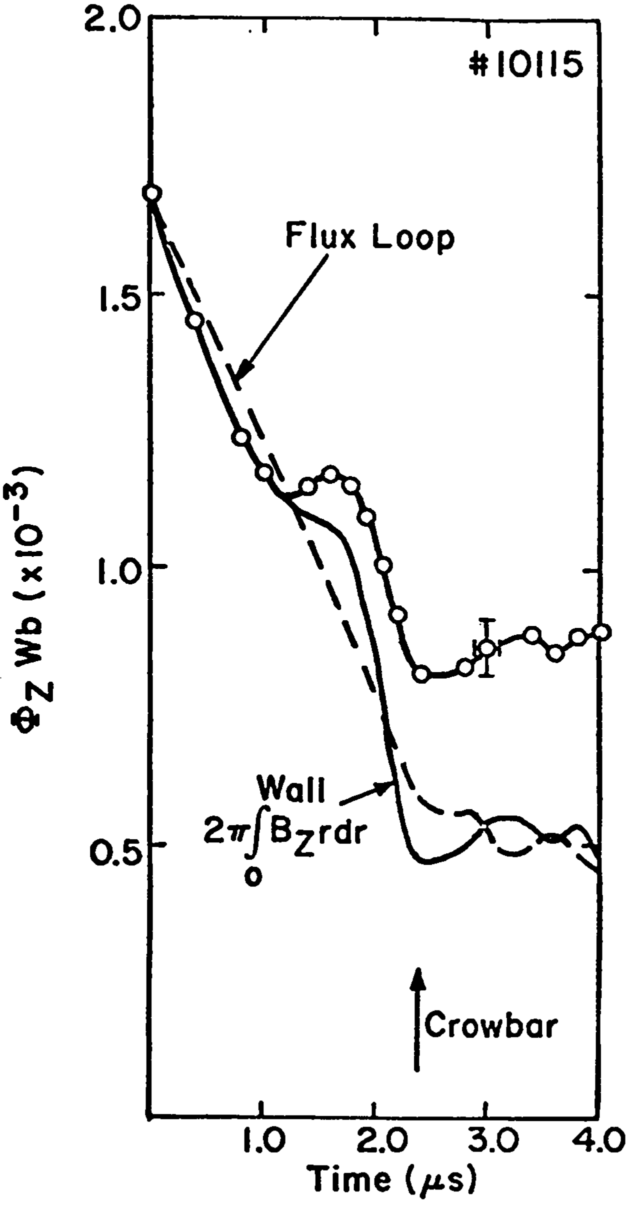

Fig. VIII-7
Time dependence of the toroidal flux for a reversed field pinch.

fields diffuse in time. If the time scale for diffusion could be changed by increasing the conductivity, extended stable periods should result.

Four approaches were tried in the attempt to increase the initial electron temperature using existing systems. The first approach was to increase the voltage on the preionization bank. This was limited to about 12 kV by prefiring of the main bank switches. The second approach was to match the impedance of the preionization bank to the Z-pinch by transformer coupling through the fast magnetic core.

A third approach was to increase the preionization bank from its present 60 μF to 150 μF total capacitance. The fourth technique was called screw pinch preionization (SPP). The timing of the I_z preionization bank was adjusted as early as possible during the rise time of the toroidal B_z magnetic field. In this way energy from the B_z bank was also coupled into the plasma. The two banks could not be fired simultaneously because a finite B_z is required (~60 mT) before ionization of the 20% He, 80% D_2 gas mix will take place. This technique is to be contrasted with the standard mode of preionization (SMP), where the preionization timing was adjusted so that the variation of the B_z field during the preionization was reduced to a minimum of approximately 5%.

Electron temperature was measured by Thomson scattering at a position 1 cm from the axis of the discharge tube. The polychromator's limit of resolution was ~1 eV. The density was obtained from a coupled-cavity interferometer using a He-Ne gas laser.

Sine-cosine coils were used to detect the onset of an instability during the preionization period. The coils respond to a displacement of the centroid of the I_z current from the axis of the discharge tube.

All of the results reported here are obtained with 40 mtorr of 20% He, 80% D_2 gas mix and the toroidal bias field is 0.15 T.

The time dependence of the plasma current and electron temperature are shown in Figs. VIII-8 and VIII-9.

The SPP mode gives a substantial improvement in electron temperature and it appears that temperatures of ~4.6 eV can be achieved with small toroidal shift as determined from the sine-cosine coil. Higher temperatures can be achieved; however, the sine-cosine coil indicates that a helical distribution of current is established. Driving more current to achieve still higher temperature produces a kink instability. Figure VIII-10 shows the line density obtained from the coupled-cavity interferometer compared to the initial filling line density. This general behavior is the same for all conditions investigated; higher power inputs result in the peak occurring earlier. These data are interpreted as indicating the 100% ionization is achieved.

The effect of increasing the initial electron temperature on the poloidal field diffusion is shown in Fig. VIII-11. A faster diffusion rate of the main pinch current is observed for the case of a low initial electron temperature. However, for times greater than ~3 μs the electron temperature for both trials is approximately the same at ~20 eV, so that further diffusion of the magnetic fields proceeds at nearly the same rate and the stable times are essentially unchanged.

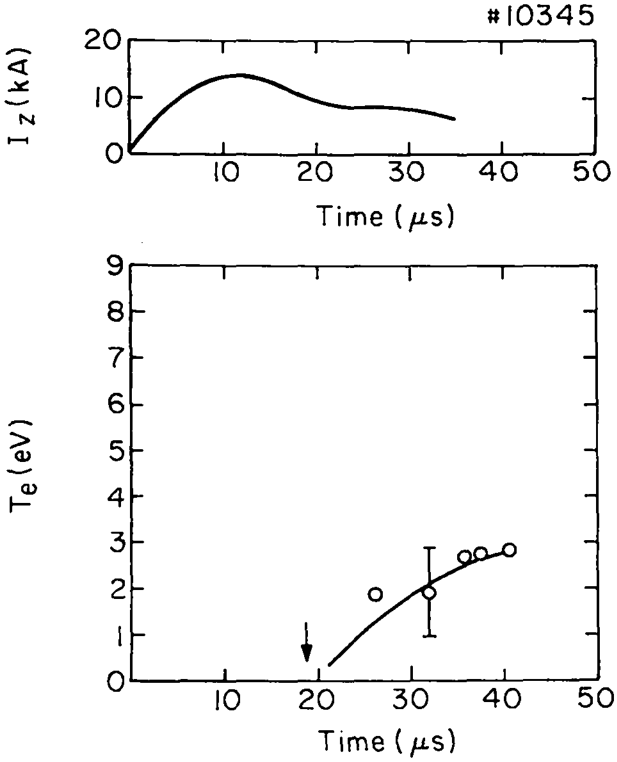

Fig. VIII-8
Toroidal current and electron temperature vs time for the SMP with a 60 μF capacitor bank.

E. Plasma Density

The coupled-cavity interferometry technique has been used to measure the electron line density across chords of the toroidal discharge region. An Abel inversion of the fringe shift data for a set of chords gives the radial density profile. The resulting distributions of electron density at five different times after pinch current onset are shown in Fig. VIII-12. The results indicate the existence of a minimum in density on the axis of the pinch. The dotted line represents the symmetry axis of the density distribution which agrees with the toroidal shift obtained from equilibrium calculations.[1] After 8 μs the column becomes unstable.

Integrations of the density profiles yield essenially constant values for the total number of electrons present during the stable period of the discharge. The value agrees within ~15% of that deduced assuming full ionization of the initial filling gas. One concludes that essentially all of the initial gas is brought into the pinched column and that the contribution due to gas from the wall is small.

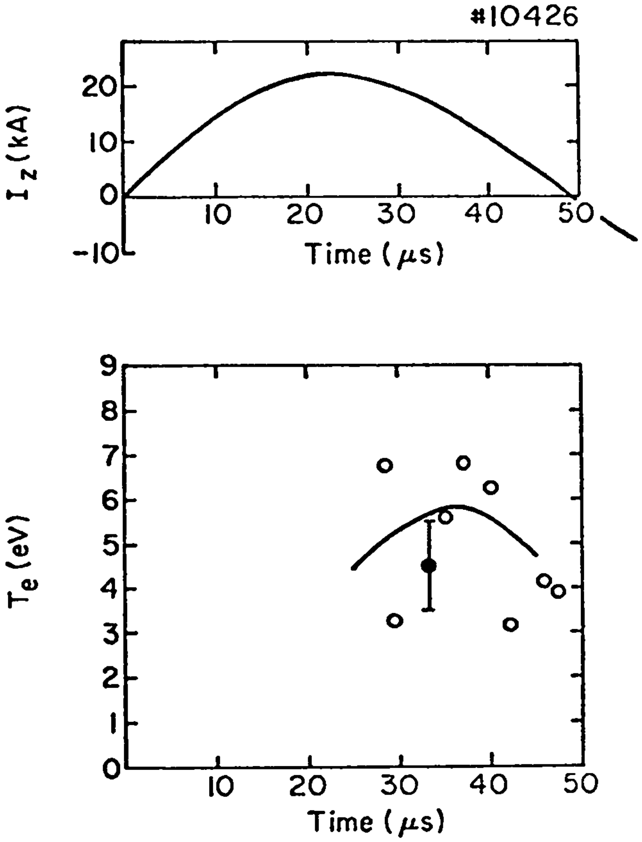

Fig. VIII-9
Toroidal current and electron temperature vs time for SPP with a 60 μF capacitor bank and transformer coupling.

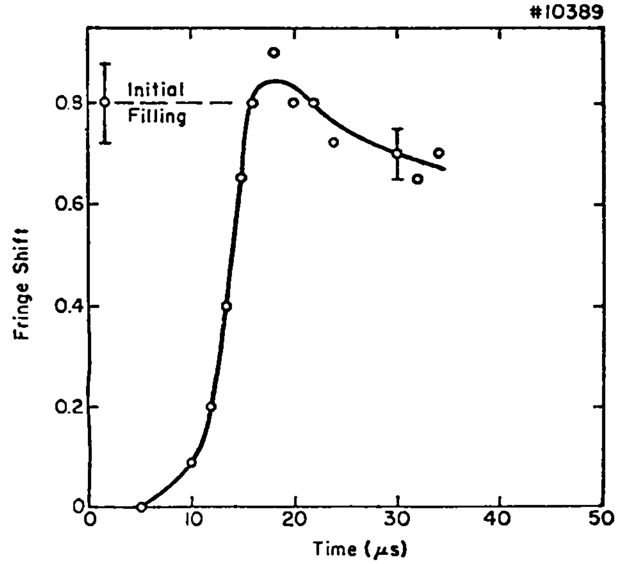

Fig. VIII-10
Typical electron line density (in terms of interferometer fringe shift) vs time. Initial filling refers to a calculation that assumes 100% uniform ionization across the discharge tube.

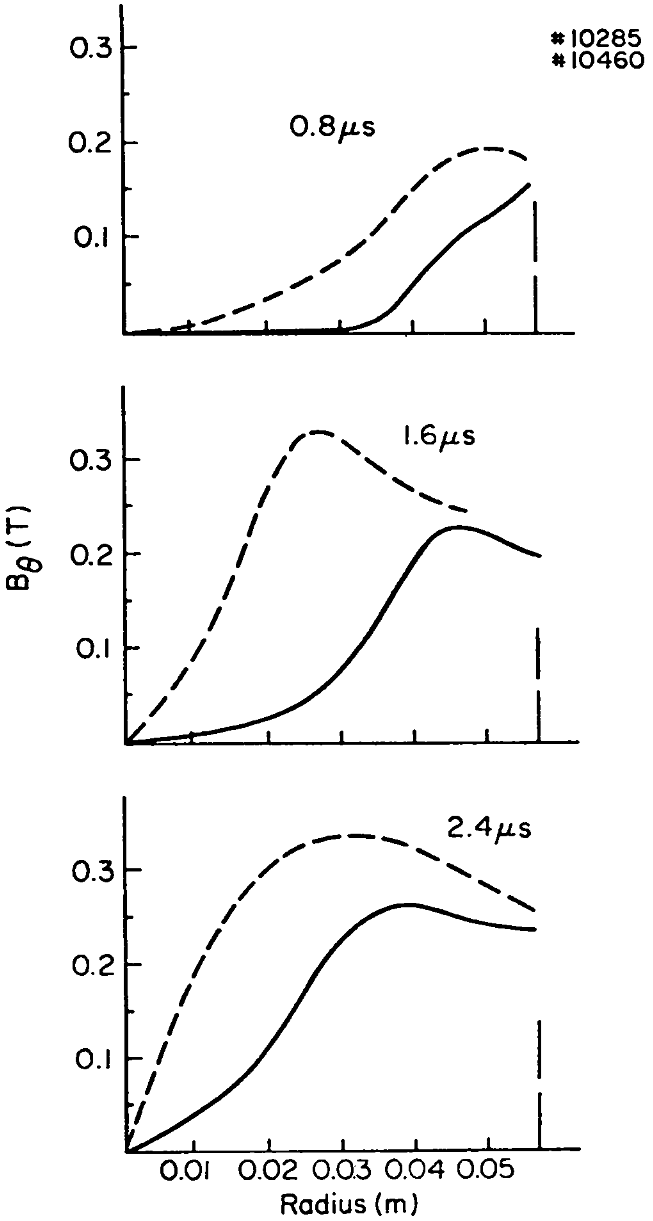

Fig. VIII-11
Poloidal magnetic field profiles of the main pinch current at three times, comparing the low preionization case (dashed curve) to a high preionization case (solid curve).

F. Plasma Ion Temperature

To obtain the plasma ion temperature, measurements were made of the Doppler broadening of spectral lines from impurity ions added in known amounts to the plasma. The results reported here were obtained with the HeII 468.6 nm line with a 20% He and 80% D_2 mixture. The addition of helium to the deuterium filling did not observably alter the

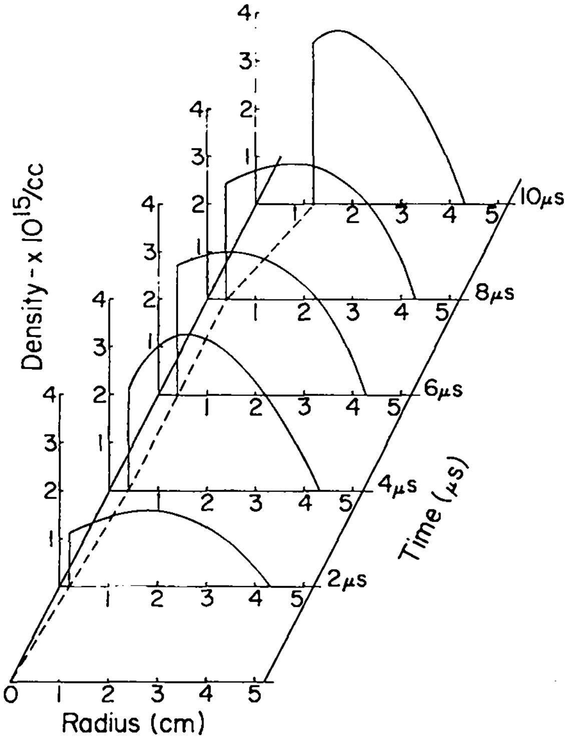

Fig. VIII-12
Electron density profiles obtained from interferometer measurements.

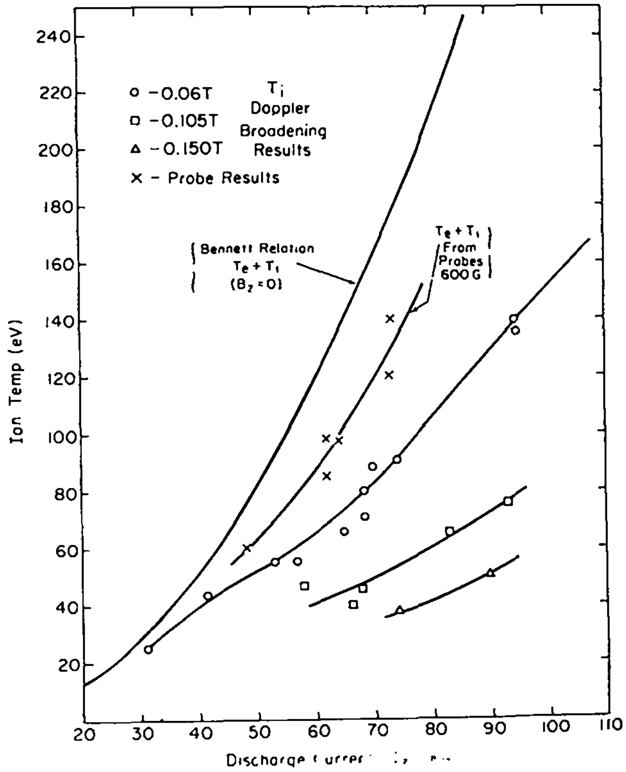

Fig. VIII-13
Temperature in ZT-1 as a function oo current with the initial toroidal bias field as a parameter.

plasma dynamics as indicated by magnetic probe and electron temperature measurements. The spectral line broadening was determined with a seven channel polychromator. Since the recent addition of Biomation analog to digital converters and connections to the SDS Sigma II computer, the signals are fed directly to the computer for analysis.

The ion temperature obtained with the ZT-1 system depends on several parameters — the main ones being discharge current, current rise time, stabilizing magnetic field, and gas filling pressure. In the fuse mode of operation ion temperatures of ~1 keV have been observed. To facilitate observations of the plasma stability behavior, the system has been operated in a derated or intermediate mode during the last year with the current and current rise time reduced by a series resistor.

The increase in ion temperature with discharge current in the derated mode is shown in Fig. VIII-13. The measured values of ion temperature increase monotonically with current up to 130 eV at ~95 kA with a stabilizing toroidal bias field B_{zo} of 0.06 T. The ion temperature is reduced with increasing stabilizing fields as shown in Fig. VIII-13. The sum of ion and electron temperatures predicted by the classic Bennett relation (for a zero bias field) is also shown in the figure along with values of $T_e + T_i$ obtained from magnetic field probe measurements at 0.06 T.

To obtain the results shown in Fig. VIII-14, five derated modes of increasing current and current rise time were used so that the increase in T_i shown is the result of both increasing I_z and dI/dt. Figure VIII-14 shows the increase in T_i with I_z for constant values of the parameter θ_0 (where $\theta_0 = B_{\theta wall}/B_{zo}$). These results show that both I_z and dI/dt are important factors in determining the ion temperature.

Measurements of the ion temperature distribution over the cross section of the plasma column were made through small holes in the metal primary and a quartz window in the ceramic discharge tube. The holes defined parallel chords through the plasma. Results indicate that T_i is somewhat lower on the axis of the pinch. The mean value of T_i is found to be higher than the T_e obtained from Thomson scattering 1 cm from the tube axis.

The precise mechanism for the ion heating is not presently known. For the intermediate mode of operation, a search was made for the existence of a shock using a figure eight magnetic field probe. (See

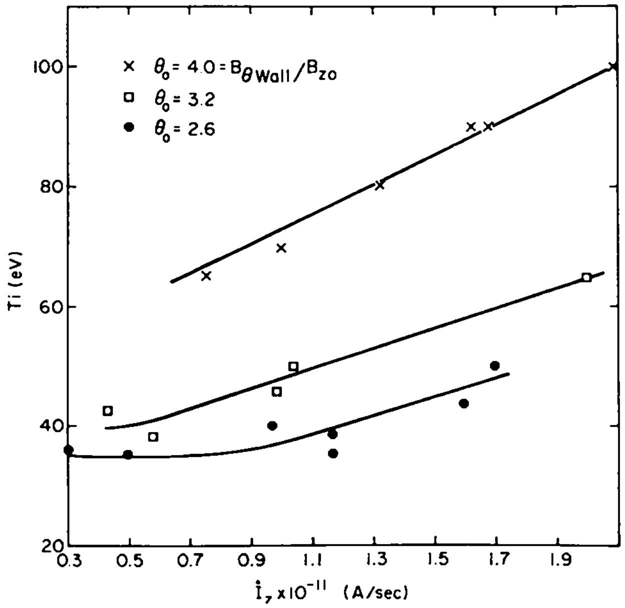

Fig. VIII-14
Dependence of ion temperature on the rate of rise of current with the compression factor θ_0 *as a parameter.*

Sec. G.) No strong shocks were observed. Also preliminary measurements made of the Doppler broadening of radiation from high Z impurity ions do not show the mass dependence that would be expected if the ions had a common velocity distribution rather than an equal thermal energy distribution. Calculations made with a time dependent MHD code suggest that a large anomalous resistivity or viscosity may explain the observed temperatures.

G. Field Gradient Measurement

The gradient $\partial B_z/\partial r$ of the axial magnetic field has been measured as a function of time and radius by means of two differential magnetic probes. The probes were inserted in a 6.5 mm outer diameter ceramic tube which was mounted across a minor diameter of the discharge tube. The spatial resolution of the probes was of the order of 6 mm. The purpose of the measurement was to see whether there was a shock present during the imploding phase of the pinch. The experiment was run in the Derate 4 mode of operation (see Sec. B), at 75% D_2, 25% H_e filling pressures of 10 and 30 mtorr.

A shock should manifest itself by a compression of the initial B_z bias field and, therefore, by the inward motion of a positive gradient $\partial B_z/\partial r$. Figure VIII-15 shows one-dimensional MHD simulations of the pinch at a filling pressure of 30 mtorr. Figure VIII-15(a) is calculated with an anomalous perpendicular resistivity of the form $\mu_\perp = 1.25$ B/(ne). The result is essentially an anomalous shock driven by an anomalous pinch. Figure VIII-15(b) is obtained with a quasi-classical resistivity of the form $\mu_\perp = \mu_s\, n_o/n$, where μ_s is the Spitzer resistivity at 4 eV, n_o is the initial and n the instantaneous local electron density. This version produces a classical shock with an anomalous pinch effect.

The measurement at 30 mtorr indicates that if the B_z field gradient extends over a distance greater than the spatial resolution of the probes, it must be no greater than 1.2 T/m. If, on the other hand, the B_z front is very steep, then the change in magnetic field does not exceed 0.0034 T. Thus, the result of the experiment is closest to the theoretical result of Fig. VIII-15(a) obtained with the anomalous resistivity. The measurement at 10 mtorr gave a similar result.

An alternate explanation for the weakness of the B_z front might be an anomalously high viscosity or a combination of high resistivity and viscosity. There also remains the possibility that the differential probes are being shielded by the plasma and do not see the true gradient of the magnetic field.

H. MHD Stability and Diffusion

1. **MHD Stability.** Magnetic field profiles have been measured and analyzed for MHD stability under the following Derate 4 (see Sec. B) discharge conditions. The filling gas was 40 or 120 mtorr of 80% D_2, 20% He. The preionization (PI) current was set at 13 or 22 kA. The experiment was run without B_z reversal, or with prompt or delayed B_z reversal.

The results are stability diagrams such as those shown in Fig. VIII-16. These plots are completely computer produced, under the assumptions of cylindrical symmetry, ideal incompressible MHD, and equilibrium. Only the fastest growing m=1 modes are considered. The lines crossing the diagram horizontally are unstable axial wavenumbers k_z. Five of the unstable k_z's are analyzed for normal modes. The width and location of these modes are indicated by heavy horizontal bars and their growth times are shown on the right hand side of the diagram. The remaining curve in the diagram is the locus of $-1/P$, where P is the pitch length rB_z/B_θ.

The stability diagrams in Figs. VIII-16(a) and VIII-16(b) have been obtained at 3 and 5 μs respectively, at 40 mtorr, low PI, and delayed B_z reversal. Unstable modes are concentrated at the edge of the plasma column, that is in the region of steepest pressure gradient. As time goes on, this region gradually shifts toward the axis of the discharge and the calculated growth times become shorter. This

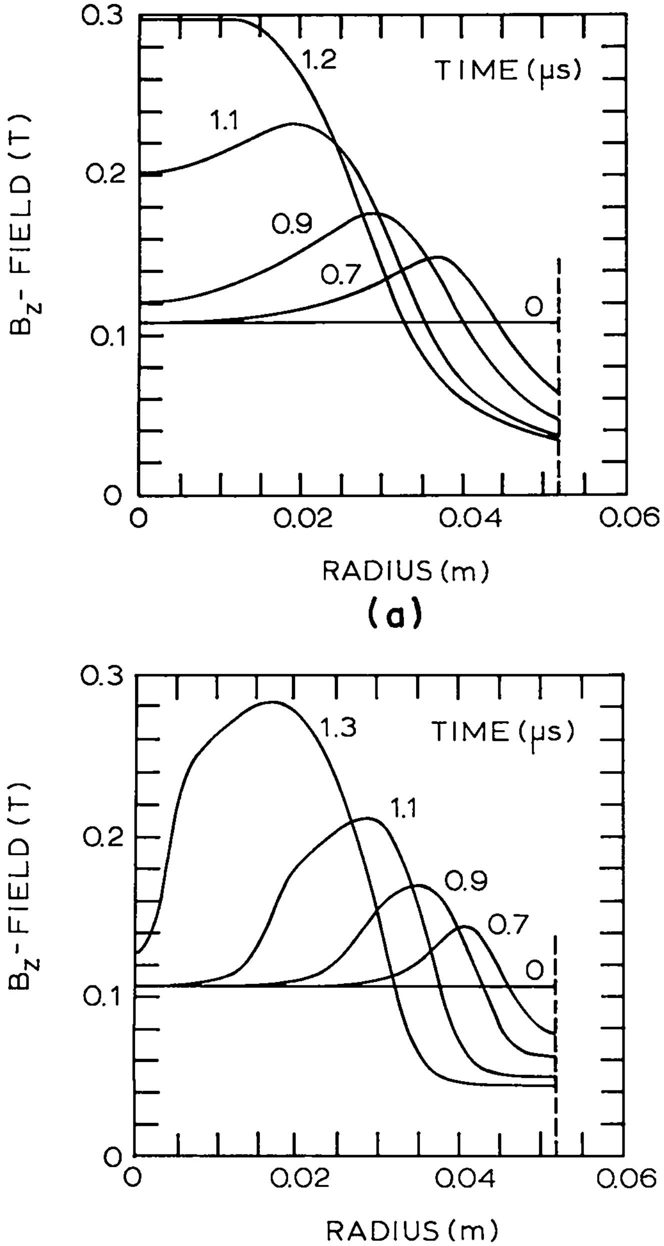

(a)

(b)

Fig. VIII-15
One-dimensional MHD simulation of the implosion phase of (a) an anomalous 30 mtorr discharge (b) a quasi-classical 30 mtorr discharge.

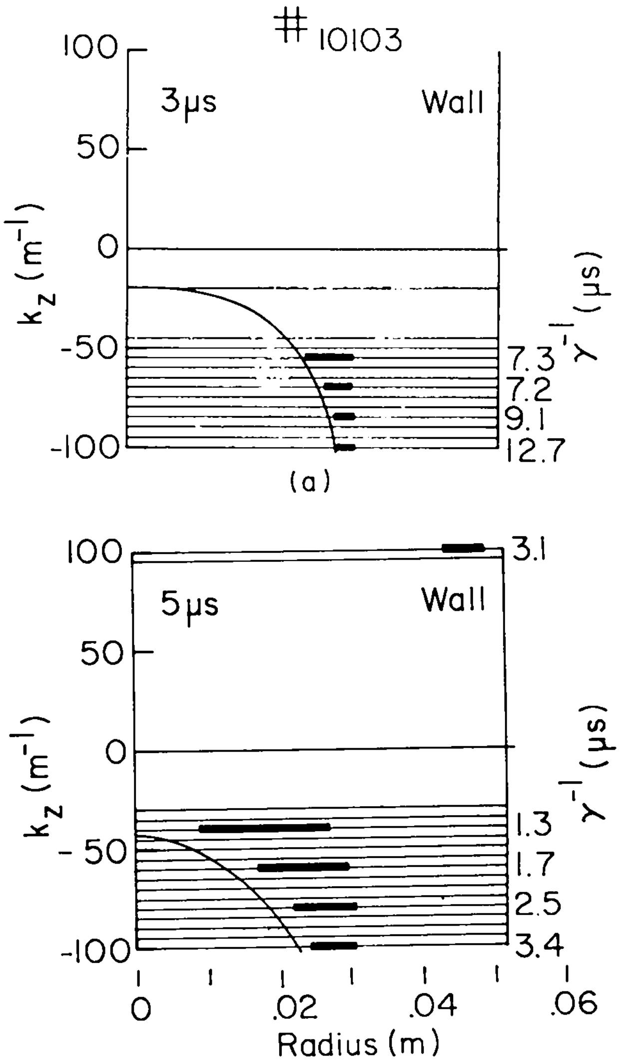

(a)

(b)

Fig. VIII-16
Stability diagram of a 40 mtorr discharge with low PI and delayed B_z reversal, k_z is the axial wave number, and γ^{-1} the growth time of the unstable m=1 modes.

behavior correlates with a gradual loss of the trapped positive B_z flux in the central region of the pinch and with a slow increase of the axial current density. Both effects appear to be due to diffusion.

The trend of the calculated growth times and of the loss of trapped B_z flux is shown in Figs. VIII-17(a) and VIII-17(b), respectively. Growth times and trapped fluxes are plotted for three 40 mtorr, low PI discharges: without B_z reversal, with prompt reversal and with delayed reversal. Delaying the reversal by about 2 μs reduces the loss of trapped flux and improves the stability of the pinch. The

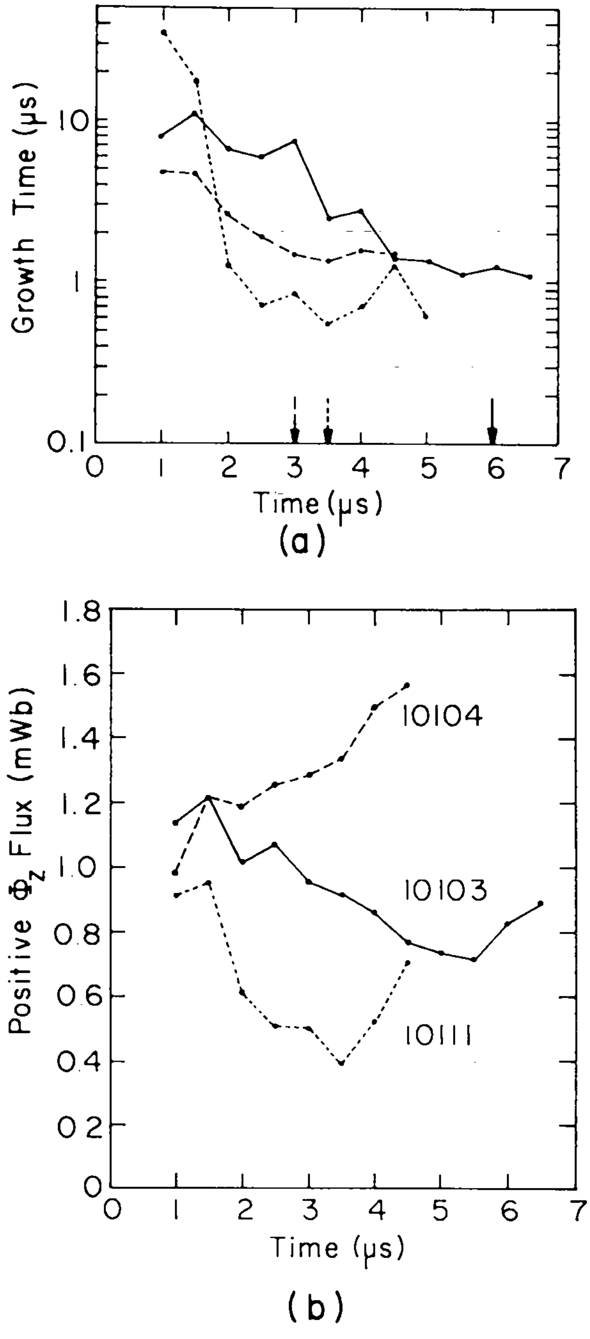

Fig. VIII-17

Growth time of the fastest m=1 modes and trapped B_z flux as functions of time for three 40 mtorr, low PI discharges: without B_z reversal (dashed line), with prompt reversal (dotted line), and with delayed reversal (solid line).

arrows indicate the earliest time at which the discharge is observed to go unstable. The instability becomes visible 1-2 e-folding times after having been predicted by the analysis.

The magnetic field profiles at 120 mtorr, and low PI give calculated growth times which are roughly 10 times longer than the 40 mtorr low PI results. Increasing the PI current tends to eliminate the instabilities at the edge of the plasma column while creating some unstable axial modes. These modes could be fortuitous, since they are caused by a narrow central peak in the calculated pressure profiles. They are not visible on the streak photographs. The higher PI current clearly reduces the loss of trapped B_z flux, and the observed stable times exceed 8 μs.

The 40 mtorr, high PI discharges show some slight improvements on their low PI counterparts. The calculated growth times are increased by approximately a factor of 2 and the loss of B_z flux is only very slight with delayed reversal. The shortest observed stable times are of the order of 6 μs.

2. Diffusion. The preceeding results indicate fairly good initial MHD stability followed by a gradual deterioration of the stability conditions in the Derate 4 mode of operation. This late behavior has been tentatively attributed to diffusion.

To test this hypothesis, the magnetic field profiles measured at 3 μs in the 40 mtorr, low PI, delayed reversal case have been entered as initial conditions in our one-dimensional hydromagnetic code. The code was then run for 2 μs discharge time, and the resulting profiles compared with the profiles measured at 5 μs. The initial radial dependences of the ion and electron temperatures were assumed to be parabolic, with $T_i=T_e=20$ eV on axis, and $T_i=T_e=10$ eV at the wall. The initial density profile followed from pressure balance. The expression for the electrical resistivity tensor was varied until the calculated profiles agreed with the profiles measured at 5 μs. Finally, the calculated magnetic field profiles were analyzed for stability, as if they had been measured on the experiment.

The resulting stability diagram at 5 μs is shown in Fig. VIII-18. It is seen to be almost identical to that obtained experimentally in Fig. VIII-16(b). The comparison shows that the slow change in the stability of the pinch can be interpreted on the basis of a simple MHD model; that is diffusion, heating and plasma motion.

The value of the electrical resistivity necessary to duplicate the experiment is essentially classical on axis with a 100-fold exponential increase toward the wall of the discharge tube. A comparison of the measured parallel and perpendicular curent densities at the intermediate time of 4 μs shows that the parallel current is much larger than the perpendicular current over most of the interior of the discharge. If the increased resistivity toward the wall is

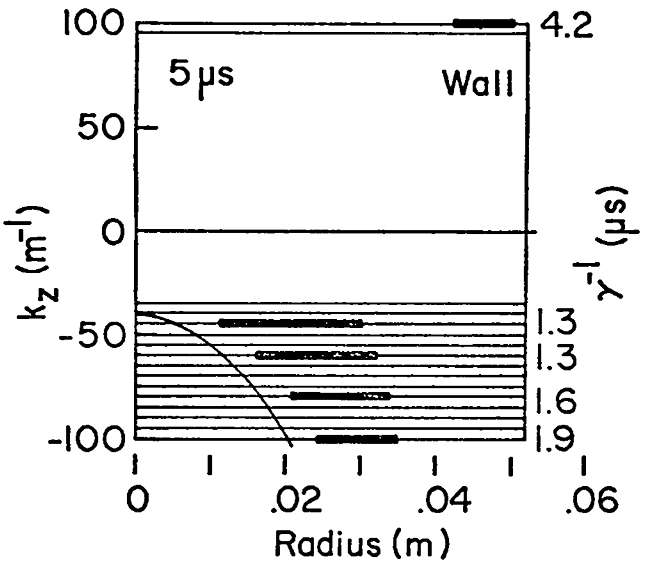

Fig. VIII-18
Stability diagram of the discharge shown in Fig. VIII-16(a) following a 2 µs simulation with the one-dimensional MHD code.

the result of some anomalous effect, and if this effect is related to a threshold in the electron drift velocity, it appears, therefore, that this threshold must be related to the perpendicular component of the electron drift velocity rather than to the parallel component. An accurate measurement of the electron density profile, and if possible of the electron temperature profile, would help clarify this point.

I. Calculation of Parallel Plasma Resistivity

The parallel plasma resistivity can be calculated from the time varying signals of B_z and B_θ measured at several radial positions. The limitations of this calculation are that a given B_θ signal can range over several decades in the time duration of the implosion and thus cannot be properly measured from one oscilloscope trace. There are also inherent errors in the amplitude and timing of the measured signals. However, measurements have been made of the parallel resistivity at five radial probe positions as a function of time. The measured values of the parallel resistivity on the outside region of the discharge tube (greater than 2.6 cm from center) are between 2.5×10^{-4} ohm-m and 5.0×10^{-4} ohm-m for times between 0.4 and 0.9 µs into the discharge. The values in the inside region are considered highly inaccurate because the B_θ field is below the resolution of the digitizing apparatus.

J. Plasma Resistivity from MHD

Using the MHD code, the parallel and perpendicular resistivities have been calculated between zero and 1.6 µs for shot number 11678. Radial heat transport was included in the calculation. The thermal conductivity was assumed to scale from its classical value by the ratio $\eta_{\parallel}/\eta_{\parallel\text{class}}$. These are analyzed to find what part can be described by classical resistivity and what part can be described by anomalous resistivity. The radial profiles of resistivity which give the correct magnetic field profiles in the MHD code from 0 to 0.9 µs are shown in Fig. VIII-19 and profiles from 1.0 to 1.3 µs as are shown in Fig. VIII-20. The inner region corresponds to a classical parallel resistivity of 5 eV which fits well with the measured electron temperature of 6 eV. Assuming no other losses than thermal heat conduction, it is found that a perpendicular resistivity of

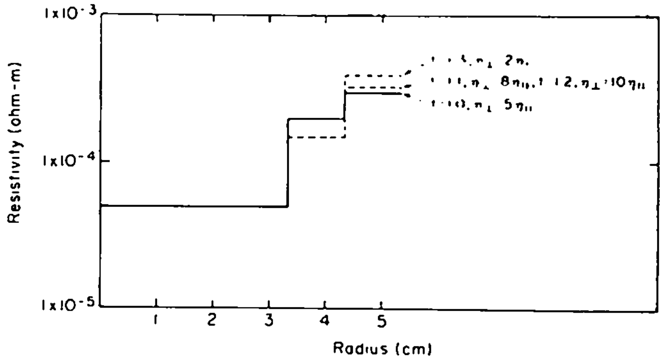

Fig. VIII-19
Radial resistivity profiles for the time interval up to 0.9 µs after the onset of the main pinch current. $\eta_{\parallel}$ and $\eta_{\perp}$ are the parallel and perpendicular resistivities.

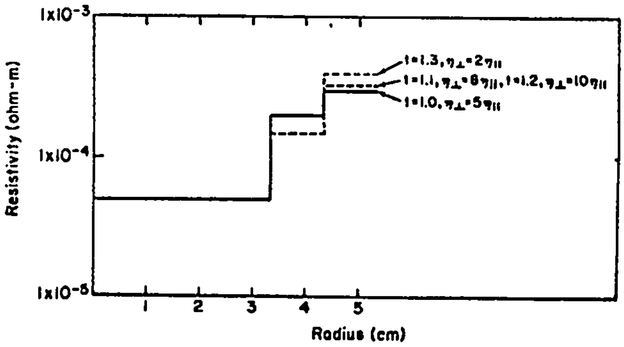

Fig. VIII-20
Radial resistivity profiles for the time interval 1.0 to 1.3 µs.

five times larger than the parallel is required in the outside region. It corresponds to an effective collision frequency of 0.2 to 0.3 ω_{pi}.If the other losses are negligible, the outside region has to be anomalous. Another interpretation is that T_e is reduced in the outer region of the pinch. Radial electron temperature profiles are required to resolve these questions. The anomalous resistivity which may be present is related to the various processes such as turbulence which may be taking place in the plasma. These processes may in turn be responsible for the high ion temperature that we observe.

K. Energy and Pressure Balance Calculations

The previous work[2,3] has shown that for fast rising currents (i.e. rise time ≪ field diffusion and plasma compression times) equilibrium pressure balance can be reached, after the current has diffused to a uniform column, only with losses or kinetic pressure at the wall. This consideration becomes particularly important for short rise times with fast diffusion where radiation and ionization losses during the pinch formation may become low and wall contact may be required before equilibrium is attainable. Even if the equilibrium is accessible the combined diffusion and compression heating may give rise to poloidal beta values too high to be compatible with MHD stability. The present experiments are directed at determining the optimum rise times and currents for attaining stable profiles with T_i as high as possible. Since diffusion rates and losses are not predictable the conditions must be established experimentally.

More recent calculations (to be published) indicate that if a pinch can be formed in which the current layer does not diffuse to the axis in confinement times of interest, the above limitations implied by global energy and pressure balance can be relaxed. Thus the current layer scaling with minor diameter becomes important. If, as has been evidenced by earlier Perhapsatron experiments, the diffusion of the poloidal field occurs at a slower rate, the heating due to poloidal field diffusion will be reduced, resulting in lower beta values and making the achievement of stable profiles easier.

L. Transfer Capacitor Prototype Circuit

In the past year, the size of the peaking capacitor has been increased a factor of four to 0.32 μF. The value of dI/dt has increased from 1.5×10^{12} to 3×10^{12}. More than 1000 shots have been fired in the high-energy, high voltage mode, extending the life test of the components. The header insulation has held off routinely, +40 kV and then was reversed to −100 kV. Triggering has not been in the self-triggered bootstrap mode, as before, but initiated with a (−) 90 kV fast rising pulse derived from shorting a length of coaxial cable charged to (+) 45 kV. With a voltage on the Marx bank charging circuit of the order of 80 kV, trigger delay times of about 30 ns are observed, with jitter being less than ±30 ns.

The limitations inherent in the field distortion gap are being studied in terms of trigger jitter and delay time. The requirements of switching several peaking capacitor sources into one load will be unusually stringent.

The fast-rising peaking capacitor currents are about 2.5×10^5 A and modifications are in progress to provide more current in the Marx charging circuit to give the desired approximation to a constant current source having a fast rise with a relatively flat top of 10 μs. Components for this phase are in the assembly stage. After the psuedo square wave-shape is proven with the aluminum inductive load, a plasma will be substituted as the dynamic, pinching load.

When this phase is successful, the peaking capacitor circuit should be able to replace the inductive storage system which is switched by explosive switches on ZT-1 type toroidal pinch experiments. The convenience of the peaking capacitor method will increase the rep-rate and hence improve the data acquisition rate.

During the interval of this report, typical of the 1748 shots, are the conditions tabulated here:

Back bias	+ 50 kV
Main marx charging voltage	− 72 kV
Total voltage swing during shot	122 kV
Maximum V in peaking charge circuit	8×10^{11} V/s
Average $\dot{V}$ during peaking capacitor charge cycle	2.4×10^{11} V/s
Input charging circuit current	80.3 kA
Output current into inductive load	227 kA
Maximum $\dot{I}$	2.8×10^{12} A/sec
Percentage of voltage appearing across the inductive load coil	25%
Total inductance of load circuit	~40 nH

M. Z Pinch Fusion Reactor Studies

Elementary calculations have been made to study the nature of a toroidal reversed-field Z-pinch fusion reactor. The main constraint considered is that the device must produce more electrical power than it consumes. To simplify the calculations, idealized field distributions are assumed. The reversed toroidal field configuration and limited radial compression features of a stable reversed field pinch are retained. The energy losses associated with maintaining the appropriate currents, both within the plasma and in the external windings, are assumed to correspond to those of copper windings at room temperature. All the energies are recovered with a thermal-conversion efficiency. No direct conversion of plasma energy to electrical energy is assumed.

The basic energy balance equation considered is

$$\epsilon(W_n+W_e+W_b+W_p+W_{br})=M(W_p+W_e+W_b+W_{br})$$

where

ϵ is the thermodynamic efficiency with which the heat energy is converted to electrical energy

W_n is the energy from nuclear fusion reactions

W_e is the resistive loss in the conductors which establish and maintain the appropriate fields

W_b is the total magnetic field energy

W_p is the plasma energy

W_{br} is the energy lost by the plasma due to bremsstrahlung radiation

M is a multiplication factor.

All quantities are considered per unit length around the major circumference. These quantities are then expressed (in MKS units) in terms of the following variables: the total toroidal current I_ϕ as deduced from the generalized Bennet relation,[3] the poloidal beta β_θ, the time of burn τ_B, the radius of the conducting wall R_w, the compression ratio k, i.e., the radius of the wall divided by the radius of the plasma, and δ_p and δ_f which are the thicknesses of the primary and reversed field windings (*cf.* Fig. VIII-21). These substitutions lead to

$$W_n = 7.7 \times 10^{-21} \frac{\beta_\theta^2 I_\phi^4 K^2}{R_w^2} \tau_B$$

where an ion temperature of 10 keV has been assumed and the extra energy due to the lithium reactions in the blanket has been included.

$$W_e = \frac{3.4\times10^{-8} I^2}{2\pi R_w}\left[\frac{1}{\delta_p} + \frac{2-\beta_\partial}{K^2\delta_f}\right]\tau_B$$

$$W_b = \frac{10^{-7} I^2}{2}\left[2\left(\ln K + \frac{1}{4}\right) + \left(2-\beta_\theta\right)\left(1+\frac{1}{K^2}-\frac{1}{K^4}\right)\right]$$

$$W_p = 7.5 \times 10^{-8} \beta_\theta I^2$$

$$W_{br} = 7.1 \times 10^{-23} \frac{\beta_\theta I^4 K^2 \tau_B}{R_w^2}$$

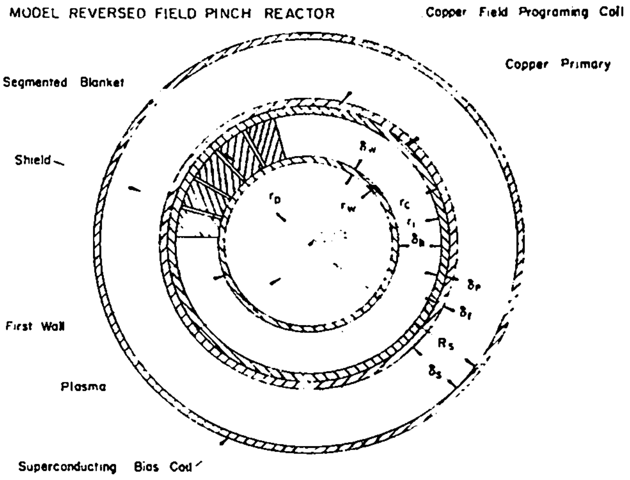

Fig. VIII-21
Cross-section of a reversed-field Z-pinch reactor.

The energy balance equation then gives a relation between I_ϕ, R_w, and τ_b for values K, β_θ, δ_p, δ_f and ϵ/M. The field energy formula for W_b is based on a uniform current sharp boundary pinch.

Shown as solid lines in Fig. VIII-22 are plots of I_ϕ versus R_w for two values of the burn time τ_B (1 s and 10 s). The following values for the adjustable parameters were assumed

$$\beta_\theta=0.5,\ K=2.5,\ M=10,\ \epsilon=0.4,\ \delta_p=\delta_f=0.1\ \mathrm{m}$$

These values of β_θ and K are chosen to be consistent with the requirements of plasma stability. The value of $\epsilon=0.4$ represents a typical thermal efficiency and an M of 10 yields a circulating-power fraction = 1/M of 10%. Also plotted on this graph are two curves labeled A=20 and A=10 where A is the aspect ratio of the torus R_m/R_w where R_m is the mean major radius. These curves are a result of the requirement that the area inside the torus is sufficient to provide the volt-sec to drive the toroidal current. It is assumed that the flux is supplied by a magnetic core, which itself has a packing fraction f_1 of 0.85. The fraction f_2 of the area which is available for iron is assumed to be 0.75.

The flux in the core is given by

$$\phi_c=\pi(R_m-R_w)^2 f_1 f_2 B_s$$

where B_s is the saturation magnetic field. This equation and the curves of Fig. VIII-22 are for no back biasing of the iron. The flux needed to establish the current in the plasma is

$$\phi_p=4\pi\times10^{-7} R_m(\ln K+1/2)I_\phi$$

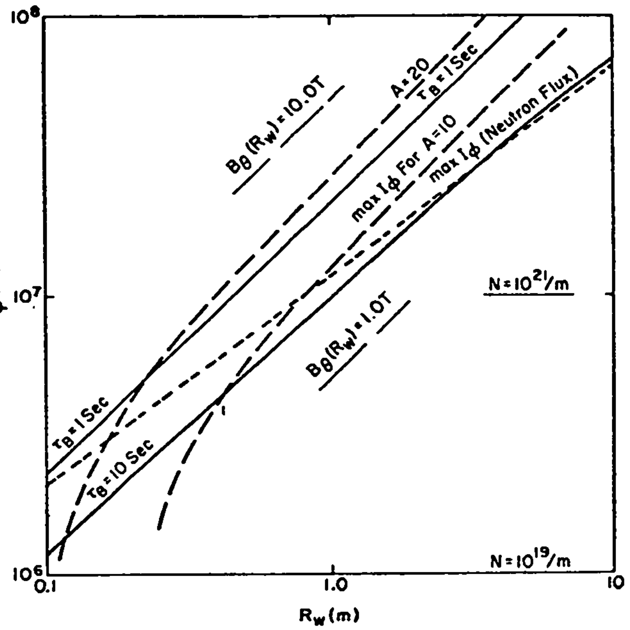

Fig. VIII-22

Solution of the energy equation (solid lines) for two burn times (1 and 10 s). Assumed parameters are $\beta=0.5$, $K=2.5$, $\epsilon=0.4$, $M=10$. These lines represent upper limits. Also shown are volt-second constraints on the aspect ratio (bold-dashed lines) and a first wall constraint due to total neutron fluence.

the requirement then is

$$4\pi\times10^{-7}\, R_m\, (\ell n\ K+1/2) I_\phi \leq Pi\, (R_m-R_s)^2\, f_1 f_2\, l\, B_s$$

The curves of Fig. VIII-22 use a value of $B_s=1.2$ T. The loss of poloidal flux due to plasma resistance is assumed small enough to be handled with the safety factor provided by the use of back biasing of the iron.

The limitation of I_ϕ due to neutron bombardment of the first wall has also been plotted on Fig. VIII-22. It is assumed that the total allowable number of neutrons incident on the first wall of the device is $3\times10^{21}/cm^2$. A duty cycle of 0.1 is assumed for the reactor and the requirement is made that the first wall last for two years. With $\beta_\theta=0.5$ and $K=2.5$, and these assumptions the curve labeled Max I_ϕ (neutron flux) results.

These simple considerations indicate that a crucial constraint on the maximum current and hence on the minimum burning time of a Z-pinch reactor, with a given first wall diameter, is imposed by the limited lifetime of the first wall as a result of neutron damage. For the neutron fluence of 3×10^{21} cm^{-2} assumed here, a reactor with a first wall radius of ~12 cm would have a minimum burning time of ~3 s, an aspect ratio of ≥20, a current of ~4 MA and a density of $n_e\approx2.5\times10^{15}$ cm^{-3}. A larger bore wall with a minor radius of ~1 m would have a minimum burning time of ~7 s, an aspect ratio of ≥10, a current of 10 MA and $n\approx3\times10^{14}$ cm^{-3}. A whole spectrum of reactor sizes is possible, but with the constraints imposed here, a burning time of tens of milliseconds could only be achieved with a small bore (few cm) high density device. To achieve such short burning times with larger bore reactors requires either a more neutron-damage resistant first wall or a more frequent replacement of the first wall than once every two years. Since a large range of reactor sizes is admitted by the above analysis, it is evident that the actual size of a working reactor depends primarily upon the physics and scaling of confinement time and field diffusion.

References

1. D.A. Baker, L.C. Burkhardt, J.N. DiMarco, P.R. Forman, A. Haberstich, H.J. Karr, L.W. Mann, J.A. Phillips, and A.E. Schofield, "Z-Pinch Experiments with Schock Heating," Proc. Fourth Int. Conf. Plasma Phys. and Controlled Nuclear Fusion, Madison 1971, Vol. I (IAEA, Vienna, 1971) 203.

2. M.J. Katz (Compiler) LASL Controlled Thermonuclear Research Program, Los Alamos Scientific Laboratory Report LA-5656-PR, (July 1974), p. 120.

3. D.A. Baker and J.A. Phillips, "Pressure Balance Limitations in Z-Pinches with Diffusion Heating," Phys. Rev. Lett. **32**, (February 1974) 202.

IX. PLASMA DIAGNOSTICS

F.C. Jahoda, R.C. Amsden, G.I. Chandler, A. DeSilva, W.R. Ellis, K.B. Freese, P.R. Forman, R. Kristal, J.W. Lillberg, F.T. Seibel, R.E. Siemon

A. Summary

The primary responsibility of the Diagnostics and Computer Applications Group is to aid the toroidal and linear theta-pinch experiments in all aspects of plasma measurements. Some diagnostic support is given other CTR groups, particularly in automated data processing functions.

Side-on holographic interferograms with a hydrogen fluoride laser ($\lambda = 2.9$ μm) have given detailed spatial density profiles in a groove location on Scyllac, overcoming the sensitivity limitation of ruby laser holography. Preparations are underway to utilize two of the output wavelengths from the same laser for simultaneous interferograms at adjacent land and groove locations in order to quantify axial flow measurements (Section B).

A 360° multiple-slit framing camera (11 viewing slits) has shown that the Scyllac toroidal mode structure is consistent in a statistical sense with the $m = 1$ instability predictions of the sharp-boundary model. The first few modes of finite wavelength around the torus have growth rates comparable to the $k = 0$ mode, and the developed plasma mode structure approaches a cutoff at the theoretical value given by magnetic field line-bending effects (Section C).

During the past year, all diagnostic measurements on Scyllac with analog electronic signal output (i.e., suitable for oscilloscope display) have been fully automated. Analyzed results in graphical form on a TV screen are available to the machine operator upon push-button command. In particular, this includes preionization density vs time from the coupled cavity laser interferometer, electron temperature from ruby laser scattering, and, most significantly, β vs time from the combination of plasma luminosity and excluded magnetic flux (Section D-3). The computer also performs various monitoring functions during the charge cycle and has abort control upon fault indication (Section D-2).

Through time sharing of our second Sigma 2 computer, the Z-Pinch Experiment, the Staged Theta Pinch Experiment, and the Basic Plasma Physics Group have all been given computerized data acquisition capability with access to on-line analysis programs (Section D-1).

Computer control of all operational functions on Scylla IV-P, except hard-wire fail-safes for personnel safety and equipment protection, is being implemented (Section D-2).

The start-gap and crowbar-gap monitoring system, which was adequate on the previous sector experiments, has never worked satisfactorily in the more extreme noise environment of the full torus operation. Great effort has gone into understanding the source of noise, and curative measures are being explored (Section E).

Development of spatially resolved Thomson scattering measurements of T_e with a digitally controlled S.I.T. tube television camera is well along (Section F).

A plasma motion simulator was built by acousto-optic deflection modulation of a laser beam to enable complete check-out of the feedback system (Section G).

Some further infrared laser developments, either achieved, in progress, or contemplated are outlined (Section H).

B. HF Laser Side-On Holographic Interferometry

1. Introduction. With side-on interferometry at the ruby laser wavelength of 0.694 μm, only ~1/4 fringe shift maximum would result through the Scyllac plasma. Since the sensitivity limit of holographic interferometry is ~1/10 fringe, the ruby wavelength is insufficient to give a spatial distribution with adequate resolution. While sensitivity scales linearly with wavelength, the 10.6 μm CO_2 laser wavelength is not transmitted by the quartz discharge tube. A hydrogen fluoride laser holographic interferometer operating at 2.9 μm has therefore been developed. A preliminary report of the laser and interferometer design appeared in the last Annual Report, LA-5656-PR, p. 49.

Good interferograms at 2.9 μm have been obtained on the Scyllac full torus. Measurements were made in a groove region of the coil which directly yield the plasma fringe profile. Integration of the fringe profile gives plasma line density, and inversion of the data from the cylindrical observation geometry to radial coordinates gives local plasma electron density. The Scyllac results are given in Section II-D.

2. Method. The layout on the machine is shown in Fig. IX-1. The laser beam comes up through the floor to the diagnostic level. All subsequent beam handling is done by elements mounted on a single vertical base plate in close proximity to the Scyllac compression coil. The beam is first filtered to select a single wavelength out of the several emitted by the laser. Line selection is accomplished with a grating, lens, and pinhole combination. Either of 2 strong lines near 2.9 μm may be used. These are the most intense lines available that are transmitted by quartz between the absorption band at 2.7 μm and the IR cutoff at ~3.6 μm.

After the single wavelength beam passes the pinhole, it is allowed to expand to the size needed to cover the plasma before being collected by a lens. This lens also converges the beam to compensate for the diverging lens effect of the discharge tube. After the lens, a beamsplitter directs part of the beam to the reference arm of the interferometer. From this point on, scene and reference beams pass through nominally identical optical paths. The imaging lenses give about a 6:1 reduction in size of the plasma image on the 200Å thick bismuth film detector. This reduction is needed in order to have enough energy density for evaporation of the bismuth. The reference arm also contains a piece of discharge tube to help equalize the two patterns on the bismuth film. The beams are incident on the detector plate from opposite sides.

Reference fringes are introduced by tilting the bismuth plate between the first and second exposure. The direction of tilt is about an axis parallel to the torus major radius vector passing through the point of observation. In this way, the reference fringes are produced perpendicular to the plasma axis and parallel to the long direction of the slit. In the presence of a diffuse plasma column, the fringes are distorted by the total phase contribution ($\propto \int n d\ell$) along the various chords through the plasma.

The quality of the interferograms was found to be strongly affected by the optical quality of the discharge tube. In fact, it was necessary to replace a small section (~6 cm) of the standard Scyllac tube with a more highly polished cylindrical section to obtain the data shown below. The O-ring seal used only permitted this change in a groove region where the coil bore was large. For future experiments, two such sections have been fused into the toroidal tube in adjacent land and groove regions.

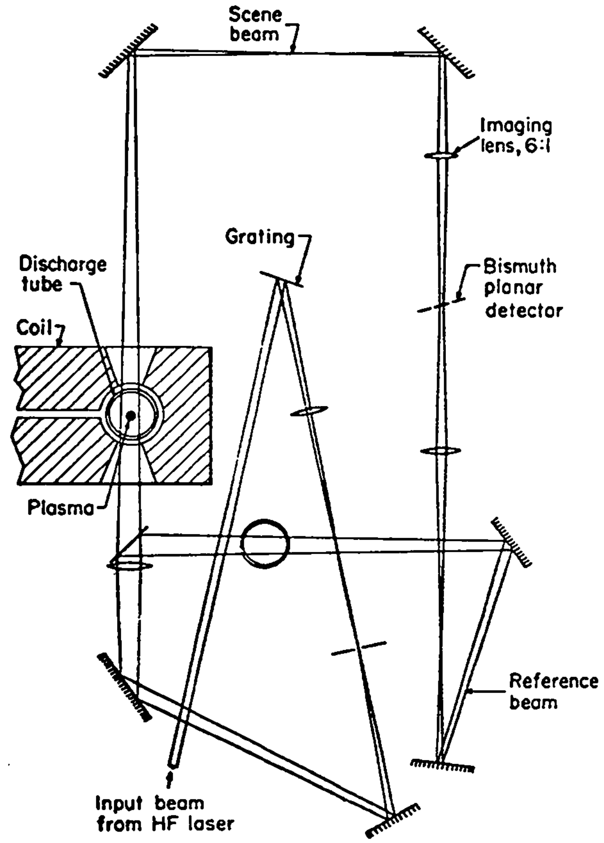

Fig. IX-1
Layout of HF holographic interferometer on Scyllac coil.

Further details on the system may be found elsewhere.[1]

3. Results. Results are discussed in Sec. II-D along with other Scyllac data. Figure IX-2 shows a typical interferogram and the density profile derived from it. For comparison a Gaussian profile is shown. The experimental profile is somewhat less diffuse than Gaussian although the Gaussian is everywhere better than 0.1 fringe. A detailed analysis of the profile and comparison with luminosity data has been made.

4. Plans. The questions raised by the high line density in the grooves (Sec. II-D) point out the need for simultaneous side-on interferometry in adjacent land and groove regions. A system for doing this is presently being assembled for Scyllac. Essentially two interferometers are required. In order to use the

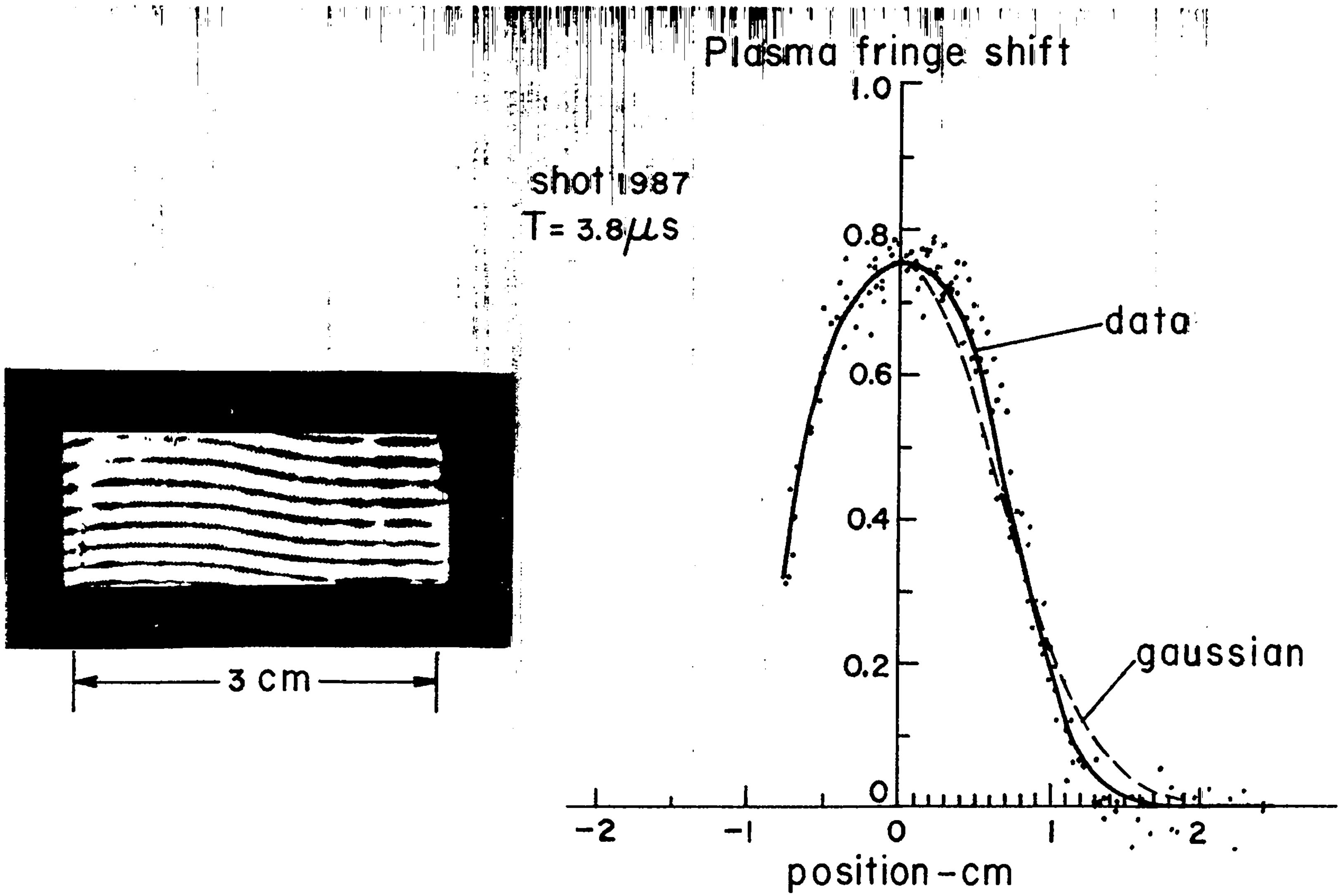

Fig. IX-2
HF laser interferogram of Scyllac discharge.

one laser source and not suffer a loss of laser energy in the double measurement, we are planning to use two of the wavelengths emitted by the HF system, one at each location.

The land and groove measurements will also permit determination of δ_0 and δ_1. Further, this technique could be used to measure particle end loss rate in sector experiments.

A higher energy amplifier section for the laser is under development.

C. Toroidal Mode Structure Framing Camera

A special framing camera with a 360° field of view has been developed. The optical system, located on the torus main axis, images 11 top slits, almost uniformly distributed around the torus, onto a single image-converter framing camera. This camera permits precise determination, at one instant of time, of the toroidal mode stucture of the Scyllac plasma column.

The toroidal mode structure framing camera and its use on Scyllac are described in Sec. II-4. In the future, it is planned to incorporate micro-channel plate image intensification to permit image beam splitting after the telescope lens in order to obtain more than one exposure per discharge. This should also allow more viewing slits.

D. Automated Data Processing and Computer Control

1. Data Acquisition

a. Scyllac. Direct data acquisition by computer with the submicrosecond time resolution required by pulsed high density experiments is limited by the capability of buffered A/D conversion between the data accumulation rate and the Scyllac Sigma 2 computer acceptance rate.

There are currently 64 Biomation 610 transient recorders in use on Scyllac, with 256 sequential 100 ns (minimum) 6-bit time bins each. In early 1975, 32 more units will be installed. Besides recording plasma diagnostic physics data, these are widely used for monitoring bank voltage waveforms, trigger signals, feedback module operational parameters, etc., that can then be called for display on a TV console or for hardcopy reproduction. One special Biomation (10 ns sample time, 8 bit × 2048 words) records data from the coupled cavity interferometer. Eight gated integrators store Thomson scattering data.

Shot number, date and time, digital pressure gauge reading, and shot type, e.g., main bank or preionization, are logged for use by analysis programs. Data from individual shots are archived on the disk (capacity ~100 shots) until removed to magnetic tape storage.

The multiplexed A/D conversion of stored charge on ~6000 capacitors for the gap monitor system has been described previously (LA-5656-PR, p. 53).

b. Other experiments. The Z-Pinch, Staged Theta Pinch, and Basic Plasma Physics experiments have all been put on-line for data acquisition on a multiplexed basis on the second CTR Sigma 2 computer. The first two experiments use Biomation transient recorders while the third experiment has its own highly multiplexed A/D converter (Phoenix Data System). Light coupling units were installed at both ends of the lines between the computer and the Z-Pinch to prevent ground loops between experimental areas.

All three experiments are equipped with keyboards which allow command and data entry to on-line analysis programs.

2. Computer Control Functions

a. Scyllac. While Scyllac remains under the control of hardwired relay logic for most functions, the high speed response of the computer has been utilized in the design of a protection scheme to prevent a full-bank discharge subsequent to a pre-fired or otherwise disabled crowbar circuit. This involves physically inhibiting the clock in the Scyllac timing circuit during the charge cycle, thus preventing any premature firing due to noise transients into the circuit. When "charge complete" has been reached and the charging circuits are quiescent, the clock is restored and the trigger input is enabled. If at any time any crowbar voltage falls below a preset value, the trigger input is disabled. If the timer has not been triggered, then the relay logic is activated to discharge the bank through dump resistors.

b. Scylla IV-P. The Scylla IV-P experiment will be completely computer controlled, except for hardwired "fail-safe" interlocks for personnel safety and equipment protection. This is to be a learning experience for large future experiments. A Prime 300 computer has been delivered. Interfacing will be done with CAMAC components for purposes of future standardization. System design is proceeding rapidly.

3. Data Processing (Scyllac). A push-button panel at the Scyllac control console currently offers a selection of data analysis programs. A brief description of four of these follows:

a. Luminosity. The 10 channel side-on plasma luminosity recorded on Biomations is a quantitative analog of a streak camera picture. Each channel is normalized to a strobe light calibration pulse at the start of the charge cycle. The data are assembled into intensity vs position plots (least square Gaussian fits) at discrete time intervals; plasma radius, position, and profile information can be displayed in a variety of graphical forms. These data are also one input to the on-line beta analysis.

b. Laser Scattering. The outputs of the 7 channel polychrometer and a laser monitor pulse are stored on a LeCroy Model 227 gated integrator; a 100 ns wide gate pulse is synchronized to the 40 ns laser pulse. Read-out through an A/D converter (Fifth Dimension) follows a computer command approximately 5 ms after the shot. A least square fitting procedure of a Gaussian distribution to the channel signals results in a display of the best fit and the associated electron temperature with error estimation with 45 seconds.

c. Coupled Cavity Interferometer. The time history of density integrated along a 3.4 μm He-Ne CW laser line-of-sight is obtained from phase shifts due to plasma changes. The plasma effects are superimposed on an externally generated periodic modulation. The output waveform is sampled by the fast Biomation transient recorder every 10 ns over a 20 μs period. The software programming picks out the extrema of the ~0.5 μs modulation cycle and plots integrated density vs time. Digital noise is ~1/25 of a cycle $(\Delta \int \ell \sim 10^{15} \mathrm{cm}^{-2})$. By assuming uniformity across the tube and using the digitally monitored filling pressure, the preionization level as a function of time is obtained and plotted. To obtain absolute density after compression by the main bank discharge, the relative density profile from luminosity is required.

d. Plasma Beta. By combining the luminosity relative density profiles with the measurement of the total magnetic flux excluded from the plasma, it is possible to calculate the plasma beta, as described in the 1972 Annual Report, LA-5250-PR, pp. 37-40. During most of the Scyllac torus operation, luminosity was recorded on-line with Biomations, and excluded flux oscilloscope traces were manually digitized with the Graf-Pen. The analysis required considerable interactive computing with qualitative judgements of data required from the operator, and thus was very time consuming. By modifying the excluded flux measurement to also be amenable to Biomation recording and considerably increasing the software sophistication, this procedure is now also automated to give results within three minutes after a shot.

Results of the new program, as displayed on the CRT consoles are shown in Fig. IX-3. The output beta plot also alerts the operator to fault conditions on signal levels and calibrations that should be corrected for acquiring better data on subsequent shots. The results are identical with the older means of analysis.

4. Programming. The computer code that traces flux surfaces for fields with specified on-axis components has been converted to run interactively under LTSS (a time sharing system) on a remote terminal for more rapid Scyllac coil design. After repeated iterations achieve a design that fulfills the physical constraints, a more precise calculation produces coordinates to drive a numerically controlled milling machine to produce the templates of non-circular cross section used on the boring lathe for the coil manufacture.

Programming aid was given to several groups for file handling and data analysis, and a User's Handbook for the Sigma 2 was written.

E. Gap Monitor Maintenance

The same spark gap monitor system which was adequate for the sector experiments has been very unreliable in the hostile noise environment of the Scyllac full torus operation. Two major failure modes are evident:

(a) Catastrophic failure of electrical components due to overvoltages on signal cables.

(b) System failures due to induced voltages which cause the timing circuits to operate incorrectly.

Most of the first class of failures have been eliminated by improving the components in susceptible circuits. The second class has required considerable time and effort to locate the mechanisms by which stray electromagnetic energy can penetrate the gap monitor system, and to conceive and test curative measures.

We now believe the primary fault is the gap monitor screen rooms, which are a single-wall galvanized steel enclosure electrically continuous with the outer Scyllac screen room. These enclosures have been found to be ineffective shields when the ground arcs which occur during Scyllac discharges are simulated by discharging a spark gap nearby. We are investigating ways of improving the shielding, either by modifying the present enclosures (especially the doors) or by constructing double-shielded enclosures.

PLASMA PARAMETERS vs. TIME

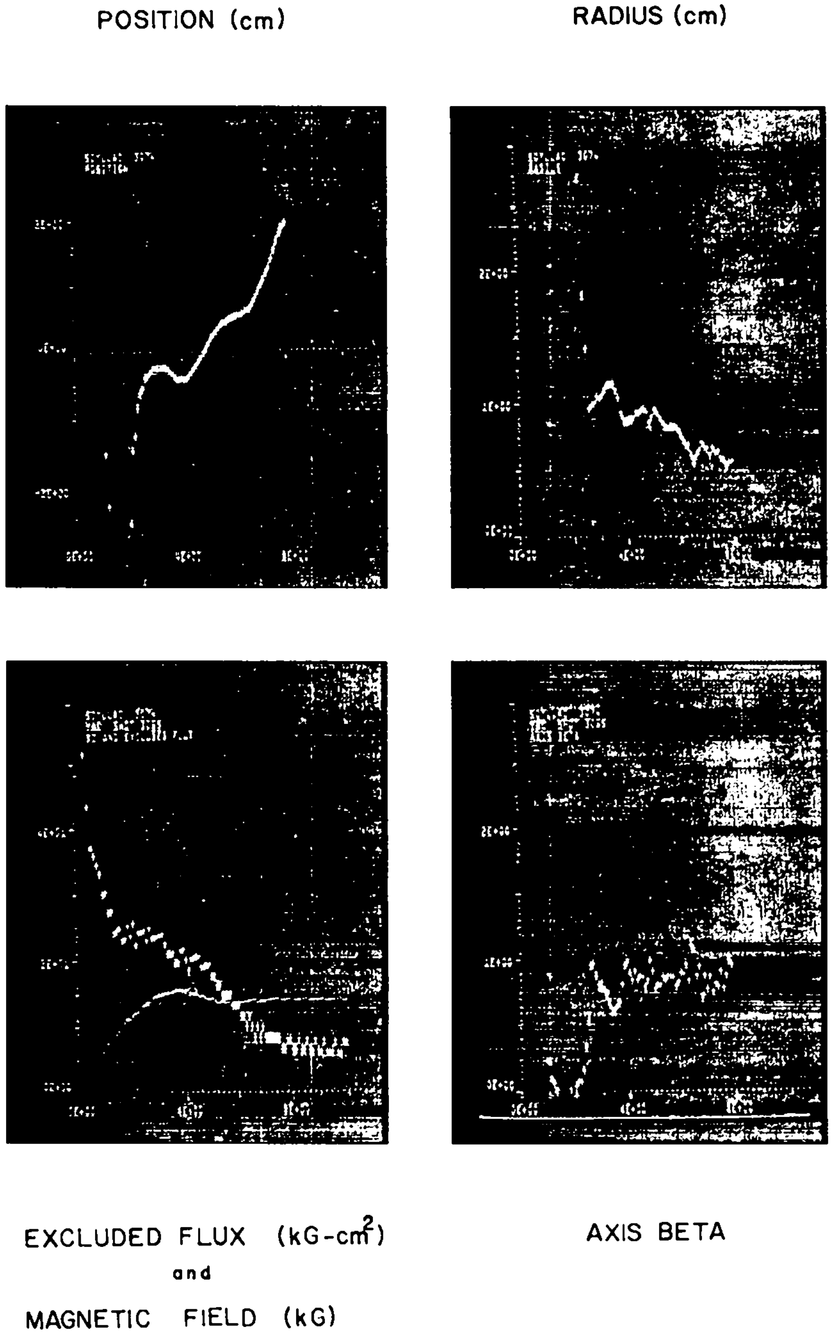

Fig. IX-3
Plasma position and radius from luminosity (top), excluded flux and magnetic field from probes (bottom, left), and derived axis beta (bottom, right) vs time.

In conjunction with modifying the gap monitor screen rooms, considerable effort is being expended to develop an EMI/RFI testing capability. This is intended to produce a permanent capability for periodically checking out various existing and future shielded enclosures.

F. Development of Spatially Resolved Thomson Scattering

The Thomson scattering measurement used on both the Scyllac sector (LA-5656-PR, p. 16, p.46) and the Scyllac full torus is capable of measuring the electron temperature in only one small volume element centered on the axis. Considerable progress has been made toward a simultaneous measurement at several radial locations within one cross-section.

The incident laser beam used in the Scyllac Thomson scattering experiment propagates side-on through the radial pressure distribution of the plasma column as shown in Fig. IX-4. By forming an image of the scattering volume on the entrance slit of a stigmatic polychrometer, one obtains a two-dimensional distribution of the scattered light intensity at the output focal plane of the polychrometer with wavelength dispersion along one dimension, and radial position along the other dimension.

Sensitive television camera tubes such as RCA S.I.T. (silicon intensifier target) tubes are capable of measuring the space resolved intensity of the scattered light. The system being developed consists of a three-grating polychrometer and an Optical Data Digitizer, a digitally controlled television camera.

The principles by which a three-grating instrument rejects stray laser light with very high contrast ratio have been described elsewhere.[2] The new polychrometer is shown in Fig. IX-5. The first two stages are high quality, but conventional, plane ruled gratings with 600 grooves per mm. The collimating optics are telescope objectives. In the third stage, a special design holographic grating is used with several advantages: (a) stray light is minimized, (b) no collimation optics are required, (c) a demagnified spectrum of large solid angle illumination, well matched to the S.I.T. tube, is created. Construction of the polychrometer is complete and the measured efficiency is 8-15% over the entire visible spectrum. The rejection ratio for 6943Å has not yet been measured, but is expected to be better than 10^{-10}.

The Optical Data Digitizer, ODD, was obtained from EMR Photoelectric of Princeton, New Jersey. It consists of an RCA 4826 S.I.T. television camera tube and the necessary electronics to operate the tube and to produce digital data.

The ODD will be controlled by a minicomputer which is presently being procured. It will include a central processor with 16K words (16 bits), a high-speed teletype, and a floppy disk auxiliary storage medium. The disk will permit program development during the checkout and calibration of the detector. In actual use on Scyllac, we will probably need only the ODD and central processor connected directly to our Sigma 2.

The heart of the system is the RCA camera tube which is basically the same as the better known 4804 S.I.T. tube, except that it has a special electrode to

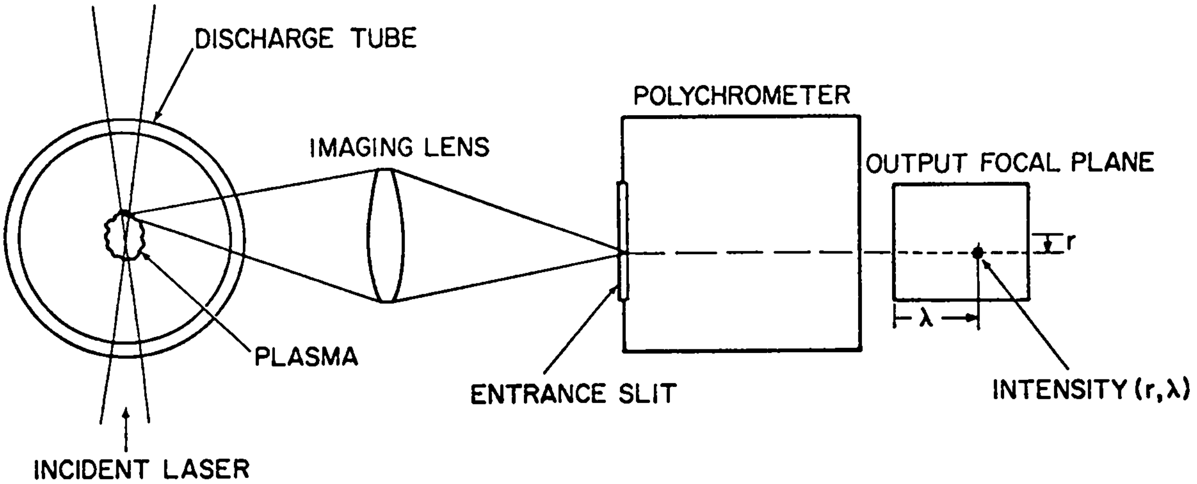

Fig. IX-4
Layout for spatially resolved laser scattering measurement of electron temperature on Scyllac.

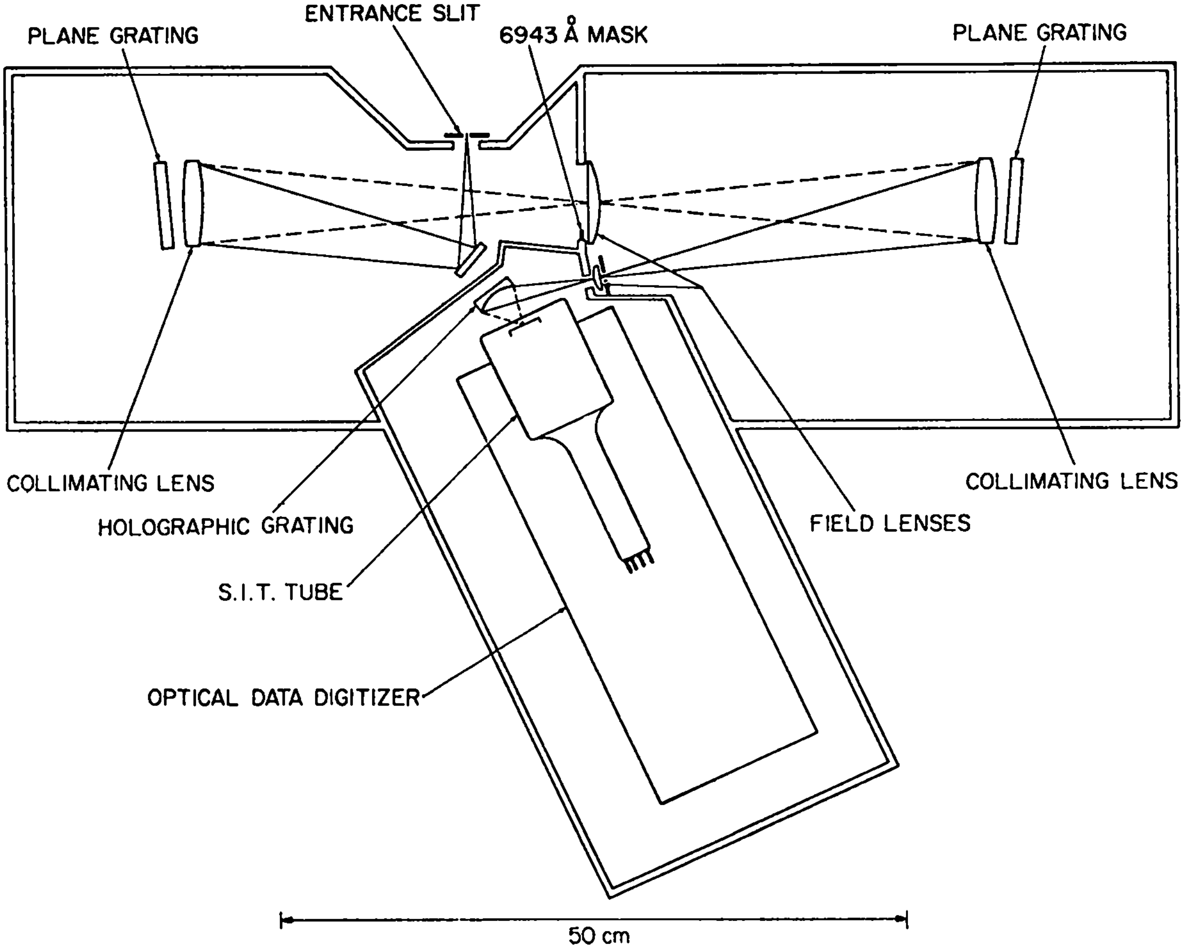

Fig. IX-5
Schematic of three-stage polychrometer and digitally controlled television camera for spatially resolved laser scattering experiment.

permit on-off gating of the tube response. The S.I.T. tube consists of an S-20 cathode, followed by an electrostatic imaging section which relays a high-velocity electron image to a silicon diode array. The accelerated electrons from the cathode generate many carriers in the silicon target due to an impact ionization process. This electron image is held by the target until read from the back side by a low energy electron beam.

The system of ODD and control computer will be used in the following sequence:

(1) S.I.T. tube is prepared by an erase procedure.
(2) S.I.T. tube is gated on for 100 ns in synchronization with the laser pulse.
(3) Control computer begins a cycle (~30 μs/data point) in which:
  (a) Computer sends x-y address to ODD.
  (b) ODD returns an 8-bit intensity word for the location on the silicon target.
  (c) Repeat of (a) and (b) for an array of probably 64×64 points.
(4) Computer subtracts background and applies various correction factors.
(5) Digital data is available for processing.

Operation of the ODD has been delayed because of difficulty in obtaining the minicomputer for control. Lacking the computer, a controller with fewer functions has been designed for initial use, and will soon be operational.

Special gating of the S.I.T. tube is required for Thomson scattering applications, and a 500 volt, 100 ns pulser has been developed for this purpose.

G. Plasma Motion Simulator For Feedback

An optical system has been designed to simulate the plasma motion for routine testing of the Scyllac feedback system. The system is shown schematically in Fig. IX-6, along with position detectors and θ-pinch coil. The beam from a 4 MW He-Ne laser (~1 mrad divergence, 1 mm diameter) is focused inside an acousto-optic deflector (Isomet Model 1206). A ten-power microscope objective at the output magnifies both the deflection and the beam divergence. The beam is split into two separate beams, which are then incident on semi-diffuse screens mounted at ±45° from horizontal at the simulated plasma position. System parameters ar designed so that the spot size (~2 cm diameter) approximates the plasma size, and the deflection (up to ~2 cm, depending on frequency) simulates the plasma motion. The semi-diffuse screens are acrylic plastic that has been lightly sand blasted; they are just diffuse enough so that the laser beam at the position detector overfills the lens for all deflections.

The acousto-optic cell is driven by a frequency modulated rf source (Isomet Model D-100) through an rf switch (AEL Model 500-1392-11). The system functions as follows: A master trigger generates two gates with independent start times and pulse widths. One gate closes the rf switch, starting the acoustic wave in the deflector. This, in turn, initiates Bragg diffraction in the crystal, and the diffracted light is used as the source for the rest of the system. The light seen by the position detector is therefore gated on, simulating the sudden turn-on of light emitted by the plasma.

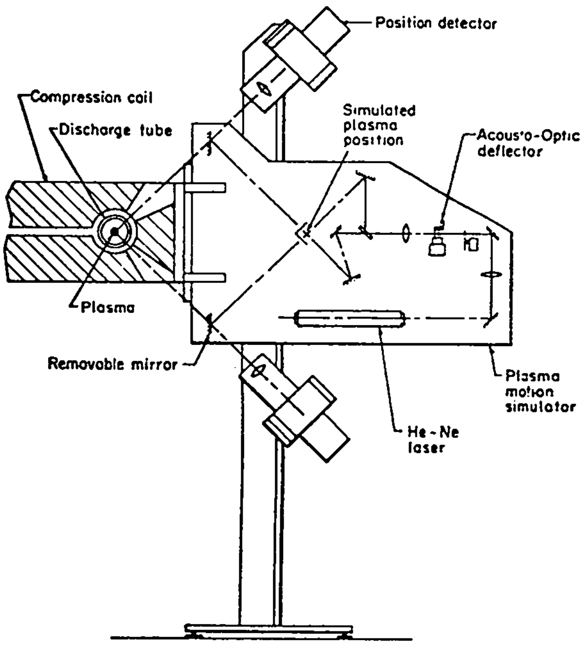

Fig. IX-6
Schematic of plasma motion simulator for feedback system checkout.

The second gate turns on a tone burst generator (Wavetek Model 164). This provides a video signal (useful range up to ~2 MHz) which frequency modulates the rf driver. With the rf switch closed, a modulation of the acoustic wavelength in the deflector results. This, in turn, produces modulation of the direction of the diffracted light, which causes the spots on the target screen to oscillate. This simulates small amplitude (~1 plasma diameter) motion of the plasma column. The timing of the tone burst is independent of the rf switch gate. Typically, it starts some microseconds after the soundwave gate in order to simulate plasma motion after a quiescent period.

The tone burst generator also has a variable DC offset. This remains on continuously, and is used to position the rf source carrier frequency in the center of the allowed Bragg diffraction range.

Figure IX-7 shows a typical position detector response to sine wave deflection at 250 kHz. The sum signal modulation visible in Fig. IX-7 is due to the image of the light spot moving slightly off the position detector on each swing of the beam. Maximum slew rate obtainable is ~1 beam diameter/μs.

Further details of the system may be found elsewhere.[3]

H. Infrared Laser Developments

1. Interferometric Measurement of Pulsed Laser Beam Profiles. In various plasma diagnostic applications involving lasers, it is useful to be able to determine the laser beam profile. This is particularly true, for example, in the case of pulsed infrared interferometry. Since direct photography is not possible at these wavelengths, we have developed a new technique using bismuth films.

Spatial resolution can easily exceed 100 ℓp/mm, and the entire profile is recorded on one laser pulse. Figure IX-8 shows a comparison of a visible (ruby) laser profile obtained by the new method (left) and by conventional photography (right). Qualitative information is obtainable merely from visual examination of the fringe width modulation, and precise profiles are obtained by fringe width measurement across the exposed area.

2. CO_2 TEA Lasers. The great sensitivity of CO_2 holographic interferometry might well be useful in the study of the linear theta pinches currently under construction by the Staged Theta Pinch and Implosion Heating groups. In addition, CO_2

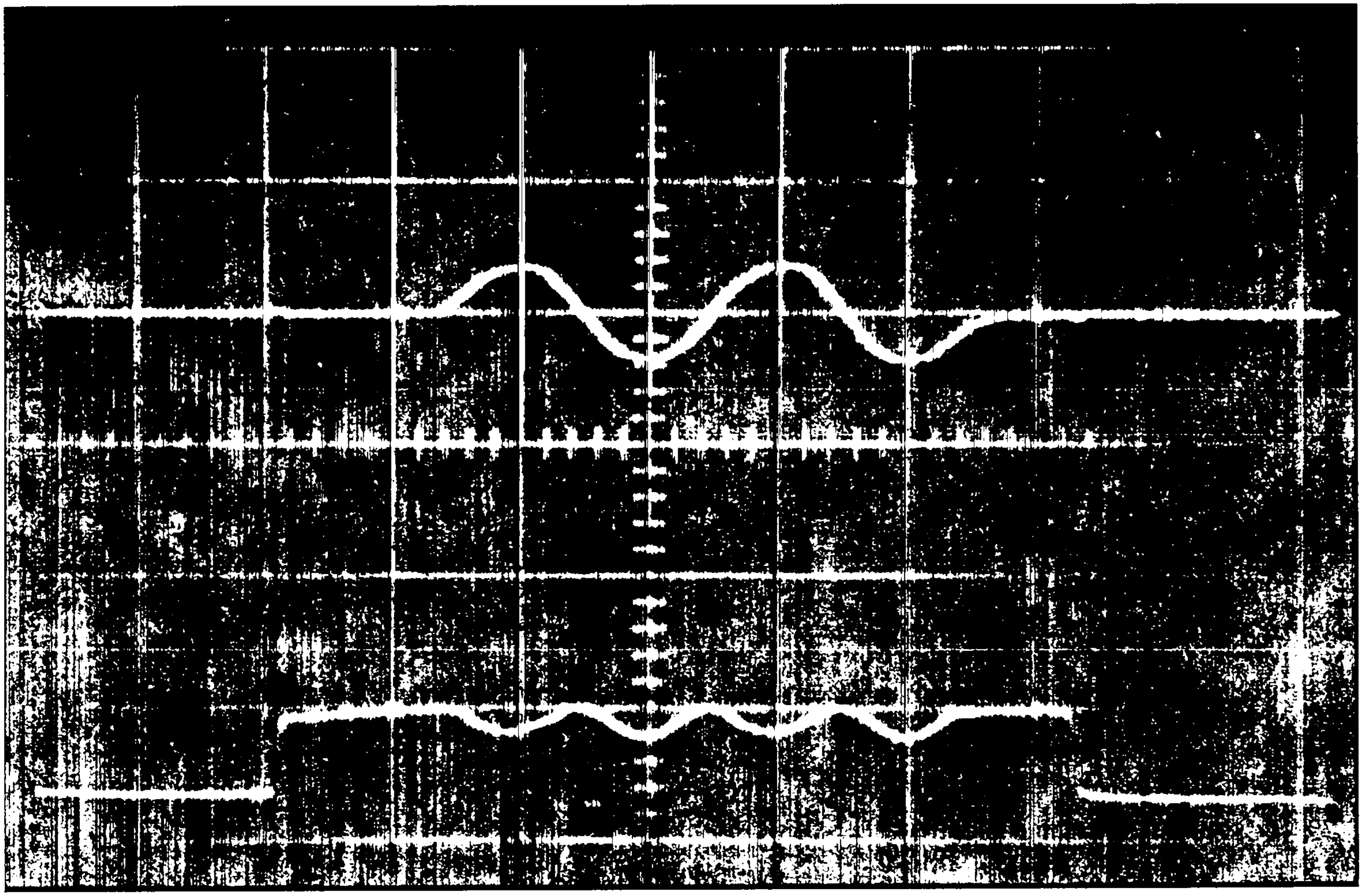

Fig. IX-7

Position detector difference signal in response to simulated 250 kHz sinusoidal plasma motion (top). Position detector sum signal (bottom) exhibits some modulation due to beam wandering off detector.

interferometry of the linear transfer capacitor Z-pinch of CTR-2 should prove to be an important diagnostic. Because all of these experiments have such rapid implosions, investigations of techniques to make CO_2 holograms with short exposure times (~5 ns) have been started. Short (1-2 ns) CO_2 pulses have been reported by various groups using mode locking. This scheme is not too attractive because it is complicated by the need to select one pulse from a train of pulses, and apparatus which would have sufficient energy for holography would be rather large. One of the requirements of a successful diagnostic is that it is reasonably easy to take the diagnostic equipment to the experiment.

Because of this, an alternate scheme called cavity dumping is being tried. A schematic drawing of such a laser is shown in Fig. IX-9. The method relies on switching out the energy within the cavity during one transit time. This leads to a longer duration pulse than mode locking, but it should be sufficiently short for our purposes. By applying an electric field of about 15 kV/cm, the CdTe crystal rotates the plane of polarization of the energy within the cavity. The germanium polarizer, which before rotation was essentially transparent, now appears as a front surface 78% reflecting mirror.

Preliminary tests, using our existing CO_2 TEA laser, indicate that the small aperture of the CdTe crystal within the laser cavity seriously reduces the output power of the laser. Two approaches are being pursued to correct this situation. A simple off-axis mirror telescope is being constructed to match the crystal size with the active volume size of the laser, and a laser amplifier is being designed.

A second use for a cavity dumped laser is possible. If one considers a homodyne CO_2 scattering experiment to observe collective scattering from the ion feature of a plasma, the laser pulse shape is critical.[4] The information from such an experiment is obtained by Fourier analyzing the pulse obtained from mixing radiation which is scattered by the plasma with unscattered radiation. If the unscattered pulse itself has a high harmonic content, the signal will be obscured. Since gain switchd CO_2

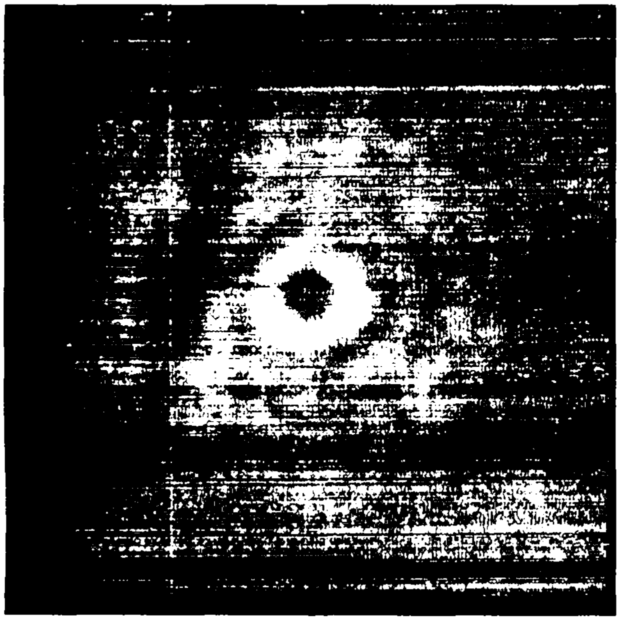

Fig. IX-8
Comparison of ruby laser beam intensity profile from fringe modulation (top) and conventional photography (bottom). Fringe method is equally applicable for infrared lasers.

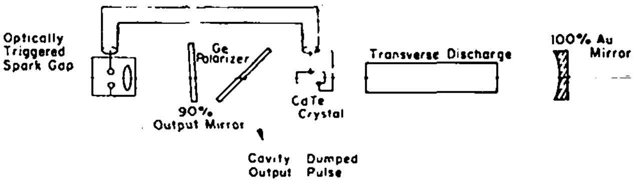

Fig. IX-9
Provisional design of cavity-dumped CO_2 laser.

TEA lasers tend to suffer from this, an attempt at feedback control of the CdTe voltage will be made in order to eliminate the sharp initial spike of the gain switched pulse. Such control would be analogous to that achieved with a ruby laser by Lovberg, *et al.* [5]

3. Ion Temperature Measurement on Scyllac. The use on Scyllac, in separate contexts, of (a) an HF laser, and (b) a three-stage polychrometer that allows scattering experiments through the discharge tube walls, raises the possibility that their combination might yield an ion temperature measurement at a modest forward scattering angle such that the scattering parameter α is about unity for the longer wavelength. A LAMS report is in preparation which concludes that such an experiment is feasible, but experimentaly difficult. Signal to noise ratios for available detectors are very favorable. The problems center on a weak dependence of the spectral width on T_i for $\alpha \sim 1$, and a cumbersome calibration when the absence of vacuum ports prevents the use of Rayleigh scattering.

References

1. R. Kristal, "Pulsed HF Laser Holographic Interferometry," Applied Optics, **14**, 628 (1975).

2. R.E. Siemon, "Polychrometer with Extreme Rejection of Stray Light," Applied Optics, **13**, 697 (1974).

3. R. Kristal, "Acousto-Optic Plasma Position Simulator," submitted to Rev. Sci. Inst.

4. A. Gondhalekar and F. Keilmann, "Proposal of a New Scheme Using Extreme Forward Light Scattering for Ion Temperature Measurement in Stellerator and Tokamak Plasmas," Institute of Plasma Physics report IPP 2/202, IPP IV/26, Garching, West Germany, Aug. 1971.

5. R. Lovberg, E. Wooding and M.L. Yeoman, "Pulse Stretching and Shape Control by Compound in a Q-Switched Ruby Laser," IEEE J. Quantum Electronics **QE-11** 17 (1975).

X. EXPERIMENTAL PLASMA PHYSICS

H. Dreicer, M.E. Banton, J.H. Brownell, R.F. Ellis, J.C. Ingraham, and B.L. Wright*

A. Summary

During the past year the LASL Plasma Physics Research program continued to be devoted to the study of the plasma ac electrical resistivity and plasma heating produced by the application of high frequency electromagnetic radiation to fully ionized plasmas. At the start of 1974 the status of our work could be summarized as follows: By utilizing a steady state contact ionized quiescent plasma column and a high Q microwave resonator we had determined the threshold for anomalous microwave absorption as a function of density.[1,2,3] The density range was large enough to separate threshold regions controlled by Landau damping from those controlled by collisional damping. Although the measured threshold electric field is a strong function of density, good agreement was obtained with the threshold predicted by ac parametric instability theory over a wide density range.

In very weak microwave fields, far below the anomalous absorption threshold, our measurement of the ac electrical resistivity was also in excellent agreement with the theoretical Ohm's law value computed in this weak field limit by Dawson and Oberman.[4] Encouraged by these excellent results in two widely differing limits of operation we pressed on in several new directions. One of these, a study of the influence that intense ac electric fields have on the electron-ion collision rate, yields important deviations from the weak field Ohm's law resistivity when the driving field becomes strong. We are dealing here with a *decreasing* resistivity brought about by the effect of the external driving field on the Debye-screened electron-ion Rutherford cross section, and not with Ohmic heating effects.

To observe this phenomenon clearly, it was necessary to measure absorption in strong driving fields without ohmically heating the electrons. Moreover it was necessary to use large electric fields without inducing anomalous absorption due to parametric instabilities. The successful resolution of these problems was largely based upon the experience gained in the earlier measurements of absorption and threshold.[1,2,3] An account of this work was published[5,6] by J.H. Brownell, H. Dreicer, R.F. Ellis, and J.C. Ingraham during 1974 and is described in some detail below (Sec. B).

Another area into which we directed renewed attention was the anomalous absorption above threshold. Our goal was to determine the most important factors that enhance the resistivity and study them under controlled conditions. This required extensions of the microwave technology we used in the past, and these were developed by H. Dreicer, J.C. Ingraham, and B. Wright. By the end of 1974 plasma experiments began, but no results are available yet.

A third study carried out during the past year, principally by J.H. Brownell, involves an experimental search for the anomalous absorption threshold on a new magnetized plasma column characterized by $T_e/T_i \gg 1$. The techniques used successfully by us earlier to make observations on our $T_e/T_i \approx 1$ (Q-machine) plasma have so far failed to disclose a clear-cut anomalous absorption and spectral decay threshold, although there is preliminary evidence for both. There is presently only one published observation of anomalous absorption near the electron plasma frequency in a plasma system other than a Q-machine. This is the observation of the Lebedev group[7] made above threshold on a spark-plug plasma source for which the value of T_e/T_i was uncertain, but probably larger than unity. It is conceivable that systems in which ion acoustic waves are not strongly damped (i.e., $T_e/T_i \gg 1$), show a quite different anomalous absorption behavior than systems in which ion acoustic waves are strongly damped. Theory provides little guidance on this matter, and this emphasizes the importance of this experimental study.

We are using a dispenser-cathode helium discharge which unfortunately suffers from a larger level of density fluctuations than the Q-machine plasma column used previously in our laboratory. This may be responsible for the difficulties encountered so far. Steps are being taken to reduce the noise level and to continue the search for anomalous absorption threshold.

All of our microwave absorption and electron heating work is carried out with short microwave pulses in order to limit electron heating and perturbation of other plasma parameters, i.e., plasma potential and density, to controlled levels. During the past year J.C. Ingraham carried out a theoretical investigation of such perturbing effects for the experimental conditions we encounter in our work. He computed plasma potential and plasma density changes of the magnitude observed in our experiments. Of particular importance is application of these methods to our earlier measurements, above threshold, of the hot electron tail distribution and the fraction of anomalously absorbed power that it carried. Ingraham's results indicate that our earlier interpretations[2] were accurate, except for experiments carried out at the lowest densities. In this case it appears that we may have underestimated the fraction of anomalously absorbed power that appears in a hot electron tail.

Our fruitful two-year collaboration with R.F. Ellis ended in July when he left LASL to join the faculty of Dartmouth College. M. Banton, who joined the group during the past year, assumed responsibility for our on-line data acquisition and data analysis and is presently studying anomalous absorption above threshold.

The Q-machine isotope separation proposal made several years ago by Hashmi and Van Oordt[8] was subjected to a critical appraisal during the past year by H. Dreicer. This work will be published during 1975.

B. Influence of Intense ac Electric Fields on the Electron-Ion Collision Rate in a Plasma

Current interest in the heating of several plasma configurations[9,10] to thermonuclear temperatures centers on efficient absorption of electromagnetic energy by plasma particles. In these cases the time-dependent absorption goes hand in hand with other important transport processes, such as heat flow and electron-ion energy equilibration. Although such particle heating is well known to influence other classical transport processes indirectly through their temperature dependence, it is generally not recognized that the application of intense electromagnetic heating fields may also directly modify classical transport parameters on a time scale that is much shorter than the heating time, without generating plasma instabilities. This effect arises when the electromagnetic field is intense enough to produce significant modifications in the hyperbolic orbits traversed during Coulomb encounters and thus occurs as soon as these fields begin to oscillate. Several theoretical treatments[11,12] predict such an orbit-modification-electric-field effect for the classical ac electrical resistivity or, equivalently, the classical inverse bremsstrahlung absorption rate.[13,14] We report the first experimental observation of this effect. Our measurements of inverse bremsstrahlung absorption yield an electric-field-dependent electron-ion momentum-transfer collision rate which can also be used to estimate the dependence of other transport parameters upon the strength of applied ac fields. On the basis of these observations we conclude that the application of intense electromagnetic heating fields to a long magnetized plasma column[10] could significantly reduce absorption and equilibration rates and could significantly increase the electron-thermal conduction loss to the column ends compared to the generally accepted values that apply only in the absence of an electromagnetic field. In the case of the laser-illuminated DT pellet experiment,[9] increased heat flow could occur in the pellet's low-density plasma ablation cloud, and this would reduce the requirements for symmetric laser illumination imposed by the need for a high-compression spherical implosion.[15]

Our experiment measures microwave absorption by a magnetized 110-150 cm long potassium plasma column contact-ionized on a single hot plate at 2250 K. The plasma[2] is fully ionized, has a nearly trapezoidal density profile n(r)/n(0) with a mean diameter of 2.5 cm, and electron cyclotron-to electron plasma-frequency ratio $\omega_{ce}/\omega_{po} \approx 6\text{-}10$. Microwaves are stored in an 8.6 cm long cylindrical TM_{010} cavity that is coaxial with the plasma column, resonates near $\omega/2\pi = 2$ GHz, and has a loaded Q of 21,000 without plasma. The measured change in Q due to plasma, expressed as $\Delta(1/Q)$, is independent of applied magnetic field B and is given by[16]

$$\Delta(1/Q) = \frac{\int \left[\frac{\omega_{po}^2 n(r)}{\omega^2 n(0)}\right] \left[\frac{\nu_{ei}(E,T) n(r)}{\omega n(0)} E^2 dV\right]}{\left[\int E^2 dV\right]} \qquad (1)$$

Here ω_{po} is the electron plasma frequency at r = 0, E is the microwave electric field, and ν_{ei}E,T)isthe electric-field- and temperature-dependent electron-ion-momentum-transfer collision rate at r = 0. Equation (1) applies when $\nu_{ei} \ll \omega$, and $\vec{E}$ is parallel to $\vec{B}$, two situations that prevail in our experiment. To measure Q, a fast microwave switch is used to interrupt the microwave power incident on the resonator and the initial decay rate of the transmitted power is determined. Measurements of $\Delta(1/Q)$ are made as a function of the two most relevant parameters accessible in our experiment. These are the microwave pulse length τ_p and microwave electric field strength E which play the following roles.

Electric field. E displaces the plasma electrons to the oscillation amplitude $\delta = eE/(m\omega^2) = v_E/\omega$ which may also be expressed in terms of the Debye length λ_D and the electron thermal speed $[v_T = \sqrt{2kT/m}]$ as $\delta = \sqrt{2}\,\lambda_D(v_E/v_T)\,(\omega_p/\omega)$. Consideration of Debye-shielded binary-encounter dynamics suggests that modifications in ν_{ei} will be produced if δ exceeds $\sim 0.1\lambda_D$ during the typical electron-ion encounter duration $\omega_p{}^{-1}$. These requirements are satisfied by $(v_E/v_T)\,(\omega_p/\omega) \geq 0.1$ and $\omega \gtrsim \omega_p$, or upon combining these, by $v_E/v_T \gtrsim 0.1$.

Pulse length. The need to separate the effect of Ohmic heating (i.e., temperature changes) on ν_{ei} (E,T) from the orbit-modification effect dictates the use of short pulse lengths. In weak electric fields, with heat conduction ignored, Ohmic heating raises the electron temperature T at the rate

$$\nu_h \equiv (1/T)(dT/dt) = (2/3)(v_e/v_T)^2\nu_{ei}(0,T) \qquad (2)$$

where $\nu_{ei}(0,T)$ is a function of ω/ω_p.[4] Near $\omega = \omega_p$ we have $\nu_{ei}(0,T) = \sqrt{\pi}nZe^4\ln\Lambda/[3\,(2m)^{1/2}(kT)^{3/2}]$. Use of microwave measuring pulses, whose duration τ_p exceeds $\nu_h{}^{-1}$, might therefore produce temporal changes in ν_{ei} that could mask the more fundamental-orbit modification effect. In our experiment $\Delta(1/Q)$ is measured with microwave pulses in the range $0.2 < \tau_p < 30\ \mu s$, which, depending upon E, gives $\tau_p \leq \nu_h{}^{-1}$ as well as $\tau_p \geq \nu_h{}^{-1}$. A typical pulse shape is shown in Fig. X-1. The duration τ_Q required for measurement of Q is approximately 0.1 μs. During τ_Q, E varies at most by 5%. Orbit modification may also be masked by anomalous absorption, which causes a marked decrease in resonator Q when E is large enough to excite ac parametric instabilities during the time τ_p. The threshold for these instabilities measured by us on the same plasma with a $\tau_p \approx 5\ \mu s$ is described elsewhere.[2] Even though instability growth-rate limitations cause the apparent threshold to increase as τ_p is shortened, the threshold for $\tau_p \approx 5\ \mu s$ serves as the most conservative boundary for a clear separation of effects. The foregoing considerations led us to study the range $0.55 \leq (\omega_{po}/\omega)^2 \leq 0.65$ where the density is still large enough to give measurable classical absorption below threshold, and yet the density is not so large as to preclude a reasonable search range in v_E/v_T without exceeding the threshold at $v_E/v_T \simeq 0.75$.

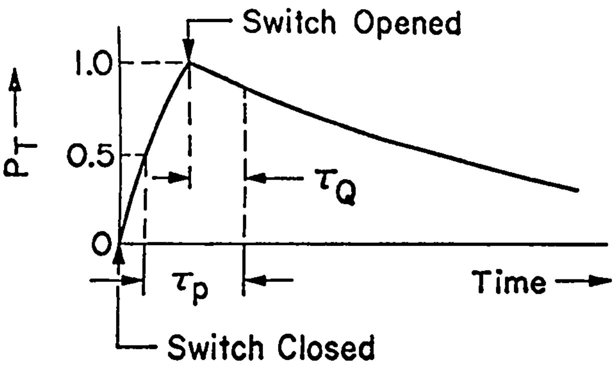

Fig. X-1
Power transmitted through a resonator as a function of time for a typical short pulse.

Figure X-2 shows the values of $<\nu_{ei}>$ (dots clustered about dashed line) deduced from $\Delta(1/Q)$ measurements as a function of τ_p at $v_E/v_T = 0.37$. The brackets on ν_{ei} indicate that it is the average value measured during τ_Q. The normalization $\nu_{ei}(T_0)$ is the value of ν_{ei} deduced from $\Delta(1/Q)$ measurements at $v_E/v_T = 0.0035$. [In such a weak field Ohmic heating is absent for the pulse lengths used and, as shown in Fig. X-3, the theoretical value of $\Delta(1/Q)$ (solid line), based upon the local application of $\nu_{ei}(0,T)$[4] to our trapezoidal density profile, is in excellent agreement with our observed $\Delta(1/Q)$ (dots) for a wide range of $(\omega_{po}/\omega)^2$ at the measured hot-plate temperature $T_0 = 2250$ K].

The strong-field data in Fig. X-2 clearly indicate that $<\nu_{ei}(E,T)>/\nu_{ei}(T_0)$ approaches ~0.55 rather than unity as τ_p tends to zero. This limiting behavior cannot be explained by a temperature increase and the usual $T^{-3/2}$ temperature dependence of $\nu_{ei}(0,T)$, because the amount of Ohmic heating for small τ_p is insufficient. According to Eq. (2) the initial heating rate for Fig. X-2 conditions is $\nu_h = (1.5\mu s^{-1}$. A more careful calculation of electron heating without orbit modification was obtained by computer solution of the energy equation

$$\frac{3}{2}\,nk\frac{\partial T}{\partial t} - \frac{\partial}{\partial x}\left(K_0(T)\,\frac{\partial T}{\partial x}\right) = \frac{\omega_p^2\,\nu_{ei}(0,T)}{\omega^2 + \nu_{ei}^2(0,T)}\;\frac{E^2(x,t)}{8\pi} \qquad (3)$$

which is valid during the relatively long period ($>0.1\mu s$) after application of the microwave pulse before ion-response motions manifest themselves in our experiment. The classical thermal conductivity[17] $K_0(T) = 0.96k(kT)^{5/2}/(e^4\ln\Lambda\sqrt{m}\ )$ without orbit modification was used in this calculation. Orbit modification of $K_0(T)$ would have increased the heat flow only over the 5-7% plasma length occupied by the microwave resonator, and would have resulted in an even smaller computed temperature increase.

From T(x,t) evaluated for the interval τ_Q at the resonator location we have computed $\nu_{ei}(0,T)/\nu_{ei}(T_0) = (T_0/T)^{3/2}$, the theoretical comparison (top solid line) shown in Fig. X-2. This result shows that

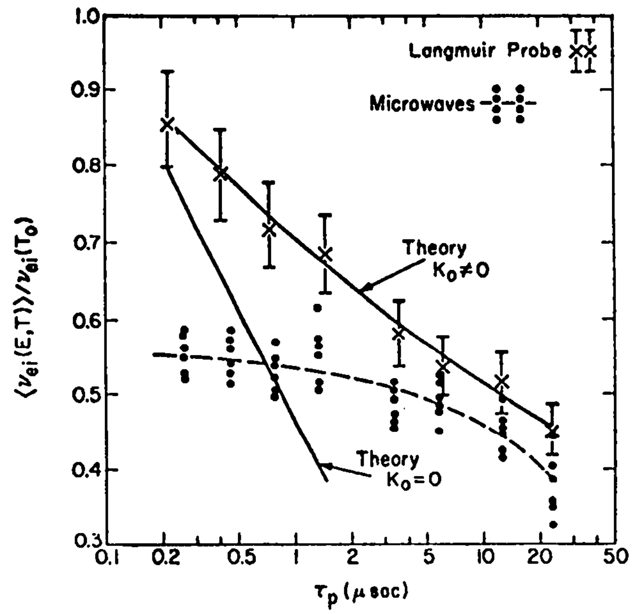

Fig. X-2
Normalized collizion rate as a function of pulse length for $(\omega_p/\omega)^2 = 0.6$ *and* $v_E/v_T = 0.37$.

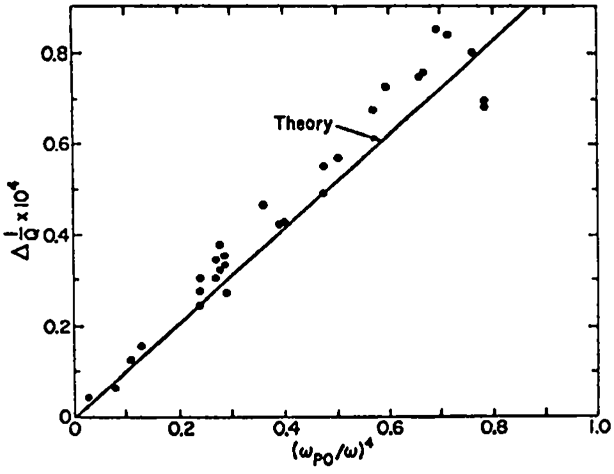

Fig. X-3
$\Delta(1/Q)$ *as a function of* $(\omega_p/\omega)^4$ *for* $v_E/v_T = 0.0035$.

Ohmic heating cannot account for the appreciable decrease in $<\nu_{ei}>/\nu_{ei}(T_0)$ measured for $\tau_p \le 1.0$ μs. Even with heat flow neglected in Eq. (3) (i.e., $K_0 = 0$) we come to the same conclusion for small τ_p (see lower solid line), and this is because the time constant for thermal diffusion is considerably larger than 1 μs. A more consistent calculation which utilizes $\nu_{ei}(E,T)$ in place of $\nu_{ei}(0,T)$ in Eq. (3) results in even less Ohmic heating as discussed below.

These conclusions were subjected to an independent experimental check by measuring T with Langmuir probes. The measurement was made outside of the resonator to avoid interference with the microwave fields. Equation (3) was then used to extrapolate T to the resonator location at the time of the $\Delta(1/Q)$ measurement. The resulting values of $(T_0/T)^{3/2}$, represented by crosses (with error bars) in Fig.X-2, approach unity for small τ_p. This again supports the view that $<\nu_{ei}>/\nu_{ei}(T_0)$ approaches 0.55 as τ_p tends to zero, because $<\nu_{ei}>$ is a function of E and not because of heating.

The further decrease in $<\nu_{ei}>/\nu_{ei}(T_0)$ shown in Fig. X-2 for $\tau_p > 1$ μs is complicated, because Ohmic heating and orbit modification are occurring simultaneously. To minimize Ohmic heating our study of the electric field dependence of $\nu_{ei}(E,T)$ has therefore been carried out with the shortest practical pulses, i.e., $\tau_p = 0.2$-0.4 μs. The result for $0.55 \le (\omega_p/\omega)^2 \le 0.65$ is shown in Fig. X-4 (black dots). For the smallest field shown, E = 10 V/cm ($v_E/v_T = 0.06$), we find $<\nu_{ei}(E,T)>/\nu_{ei}(T_0) \approx 1.0$ as expected. As E increases to E = 150 V/cm ($v_E/v_T = 0.74$), $<\nu_{ei}(E,T)>/\nu_{ei}(T_0)$ falls to about 0.4. In such strong fields there is a small increase in T/T_0 due to Ohmic heating even for the short pulses used by us. We compute this increase by substituting $\nu_{ei}(E,T)$ for

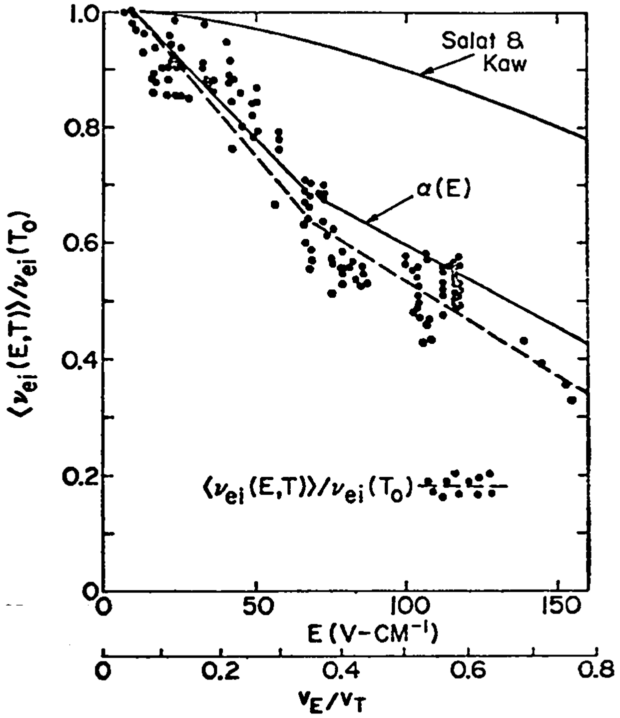

Fig. X-4
Normalized collision rate as a function of E and v_E/v_T *for short pulses and* $(\omega_p/\omega)^2 = 0.6$.

$\nu_{ei}(0,T)$ in Eq. (3) and by assuming $\nu_{ei}(E,T) = \alpha(E)\nu_{ei}(0,T)$. To compute T and α (E) from our observed value of (ν_{ei}) we utilize Eq. (3) in an iterative computational procedure based on $\alpha^{(n)}(E) = \nu_{ei}(E,T)/\nu_{ei}(T_0)\ (T^{(n)}/T_0)^{3/2}$. This scheme converges adequately for n = 3 or 4 and results in the α(E) curve shown in Fig. X-4. The dashed line in this figure provided the starting values for the iteration. In agreement with our Langmuir-probe measurements we find the temperature correction to be small and this supports the evidence that the orbit modification effect has been observed with $\alpha(E) < 1$. In the range $0 \leq E \leq 150\ \mathrm{V\ cm}^{-1}$, the empirical relation $\alpha\ (E) = (1 + 2v_E^2/v_T^2)^{-3/2}$, which is obtained by substituting $kT + mv_E^2$ for kT in $\nu_{ei}(0,T)$, is in good agreement with the α(E) values deduced from the measurements. The α (E) values computed by Salat and Kaw[11] in the absence of magnetic field are shown in Fig. X-4 for comparison. Their predicted $1 - \alpha$ values are only 10-30% of our observed $1 - \alpha$. A recent numerical re-evaluation of the Salat and Kaw result by Wright[11] reduces this difference somewhat, but still leaves a very significant discrepancy between theory and experiment. Although we have observed no dependence of $<\nu_{ei}(0,T)>$ on magnetic field we have not yet experimentally ruled out the possibility that a dependence of α on B can explain this discrepancy.

Our measurements are supported by the following: (a) We check the time dependence of electron density n and the possibility of E field enhancement in the plasma by monitoring the cavity resonant frequency during τ_p as a function of E. No appreciable frequency shift is observed, and this rules out the possibility that the ν_{ei} reduction observed as E increases is actually because of a sudden reduction in n or an enhancement of E inside of the plasma. (b) Magnitudes of E are deduced from separate measurements of Q and the microwave cavity power absorbed, and by using the microwave electric field distributions predicted by a computer solution for the actual resonator filled with a plasma column.

We have observed an electric field-dependent, electron-ion collision rate for $v_E/v_T \leq 0.74$ by carefully avoiding masking effects due to Ohmic heating and ac parametric instabilities (for $v_E/v_T > 0.74$ this effect is expected to become even stronger). Our observations have application to all classical transport processes produced by electron-ion encounters in the presence of intense electromagnetic fields.

*Present address: Department of Physics, Dartmouth College.

References

1. H. Dreicer, D.B. Henderson, and J.C. Ingraham, "Anomalous Microwave Absorption Near the Plasma Frequency," Phys. Rev. Lett. 26, 1616 (1971).

2. H. Dreicer, R.F. Ellis, and J.C. Ingraham, "Hot Electron Production and Anomalous Microwave Absorption Near the Plasma Frequency," Phys. Rev. Letters **31**, 426 (1973).

3. H. Dreicer, R.F. Ellis, and J.C. Ingraham, "Anomalous Microwave Absorption Near the Plasma Frequency," Proceedings of the Fifth European Conference on Cont. Fusion and Plasma Physics, Grenoble 1971, **1**, 120 & **2**, 242.

4. J.M. Dawson and C.R. Oberman, "High-Frequency Conductivity and the Emission and Absorption Coefficients of a Fully-Ionized Plasma," Phys. Fluids **5**, 517 (1961).

5. J.H. Brownell, H. Dreicer, R.F. Ellis, and J.C. Ingraham, "Influence of Intense AC Electric Fields on the Electron-Ion Collision Rate in a Plasma," Phys. Rev. Letters, **33**, 1210 (1974).

6. J.H. Brownell, H. Dreicer, R.F. Ellis, and J.C. Ingraham, "Hot Electron Production, Anomalous Absorption and Effect of Intense Electromagnetic Fields on Inverse Bremsstrahlung Absorption Near the Electron Plasma Frequency," Paper CN-33/H-4-2, Proceedings of the Fifth International Conference on Plasma Physics and Controlled Nuclear Fusion Research, (Tokyo, Japan November 11-15, 1974).

7. I.R. Gekker and O.V. Sizukhin, "Anomalous Absorption of a Powerful Electromagnetic Wave in a Collisionless Plasma," Pisma Zh. Eksp. Teor. Fis. **9**, 408 (1969). [JETP Lett. **9**, 243 (1969)].

8. M. Hashmi and A.J. Van Der Houven Van Oordt "Production and Application of a Uranium Plasma in a Q-Device," Proceedings of 3rd International Conference on Quiescent Plasmas, p. 27, Elsinore, Denmark 1971.

9. J.S. Clark, H.N. Fisher, and R.J. Mason, "Laser-Driven Implosion of Spherical DT Targets to Thermonuclear Burn Conditions," Phys. Rev. Letters **30**, 89 (1973).

10. J.M. Dawson, A. Hertzberg, R.E. Kidder, G.C. Vlases, H.G. Ahlstrom, and L.C. Steinhauer, "Long-Wavelength, High-Powered Lasers for Controlled

Thermonuclear Fusion," in *Proceedings of the Fourth International Conference on Plasma Physics and Controlled Nuclear Fusion Research, Madison, Wisconsin, 1971* (International Atomic Energy Agency, Vienna, Austria, 1972), Vol. 1, p. 673.

11. A. Salat and P.K. Kaw, "Nonlinear High-Frequency Plasma Conductivity," Phys. Fluids **12** , 342 (1969); T.P. Wright, "Nonlinear High-Frequency Conductivity of a Fully-Ionized Plasma," Bull. Amer. Phys. Soc. **18** , 1303 (1973), and private communication.

12. V.P. Silin, "Nonlinear High Frequency Plasma Conductivity," Zh. Eksp. Teor. Fiz. **47** , 2254 (1965) [Sov. Phys. JETP **20**, 1510 (1965)].

13. S. Rand, "Inverse Bremsstrahlung with High-Intensity Radiation Fields," Phys. Rev. **136**, B231 (1964); G.J. Pert, "Inverse Bremsstrahlung Absorption in Large Radiation Fields During Binary Collisions-Classical Theory," J. Phys. A: Gen. Phys. **5**, 506 (1972), and "Inverse Bremsstrahlung Absorption in Large Radiation Fields During Binary Collisions - Born Approximation," *Op. Cit.* **5**, 1221 (1972).

14. H.A. Bethe, "Note on Inverse Bremsstralung in a Strong Electromagnetic Field," Los Alamos Scientific Laboratory Report LA-5031-MS (1972).

15. D.B. Henderson and R.L. Morse, "Symmetry of Laser-Driven Implosions," Phys. Rev. Lett., **32**, 355 (1974).

16. S.J. Buchsbaum, L. Mower, and S.C. Brown, "Interaction Between Cold Plasmas and Guilded Electromagnetic Waves," Phys. Fluids **3**, 355 (1974).

17. L. Spitzer, *Physics of Fully Ionized Gases* (Interscience, New York, 1962), Chap. V.

XI. THEORETICAL PHYSICS PROGRAM

W.B. Riesenfeld, D.A. Baker, D. Barnes, G. Berge, J. Brackbill, B.L. Buzbee, R.C. Davidson, D.A. D'Ippolito, J.P. Freidberg, R. Gerwin, N.T. Gladd, J.P. Goedbloed, D.W. Hewett, H.R. Lewis, L.W. Mann, M. Menzel, C.W. Nielson, J.M. Ogden, A. Sgro, M. Stein, K.R. Symon, L. Turner, D. Winske

A. General Summary

During the reporting year the LASL CTR theory group has continued to increase its efforts in the field of magnetohydrodynamics (MHD) theory as applied to the equilibrium and stability of complex toroidal confinement systems such as Scyllac and high-beta tokamaks. The analyses have become more sophisticated as they have been extended to treat diffuse plasma and field profiles and the detailed radial mode structure for such systems. The Computer Applications program has had a major impact in this area, with the development of a useful three-dimensional MHD numerical code which follows the time evolution of magnetically confined plasma columns in realistic and interesting geometries. To complement these efforts, fundamental studies have been undertaken of the general mode spectrum of toroidal ideal MHD systems.

The second field which has seen concentrated efforts is the area of Vlasov analysis and numerical computation. Much work was done to map out and analyze high-beta electromagnetic microinstabilities acting in theta and Z-pinch implosion sheaths, and to refine several formulations of the so-called hybrid plasma model, in which the ions are treated kinetically through the Vlasov equations while the electrons are considered to form a charge neutralizing MHD or drift fluid. This work is needed for gaining a better quantitative understanding of the stability properties of high-beta confinement systems, as well as for a better understanding of the dynamics of implosion heating. Much progress has been made in the Vlasov analysis and computation of spatially inhomogeneous equilibria.

In a third area of work, the numerical Computer Applications program has made significant contributions to the experimental programs by modeling the dynamics of Z-pinches and theta pinches using various physical models for the plasma. The one-dimensional hybrid Z-pinch model, in particular, has yielded remarkably detailed correlation with experimental results, so that tests of the assumptions underlying the model could be carried out, and permitting quantitative predictions of the results of future Z-pinch discharge. A computer modeling program has also been written for the so-called Injection Experiment, in which a highly heated and compressed theta pinch plasma is transferred into an $\ell = 1$ confinement sector designed to test the concept of wall stabilization.

Finally, considerable effort has been expended on scaling studies of the feedback, wall stabilization, and staging requirements of Scyllac-like confinement systems. This work not only has immediate application to present experiments, but also has direct relevance to the planning for, and design of, future high-beta confinement devices up to and including a possible Fusion Test Reactor.

As was the case in the past, the present report on the theoretical program covers work done during the entire reporting year, but emphasizes results obtained during the final quarter.

B. Summary of Scyllac MHD Theory

During the past year the MHD Scyllac theory has been concentrated in four areas. The first concerns studies of the $m=1$ stability in a diffuse $= 1$ system. This problem has obvious importance, because the $m=1$ mode is the most dangerous mode experimentally. Secondly, a large effort was initiated to study nonlinear 3-D diffuse equilibria in a toroidal Scyllac configuration. Essentially all equilibrium calculations to date have been calculated from sharp boundary models, and it is our goal to obtain more realistic answers for diffuse profiles. A third area of investigation was a study of the $m=1$ stability in a modified Scyllac configuration. In this system equal amplitude $\ell = +1$ and $\ell = -1$ fields are superimposed providing a closed line geometry. It was hoped that this configuration would have more favorable stability properties than the pure $\ell = 1$ system. Finally, we have continued our studies of scaling laws as applied to the design of Scyllac experiments. By taking into account the proper constraints, it has been possible to find the optimum design of feedback experiments and staging experiments, using the existing Scyllac facility. Listed below is a brief status report on each of these investigations.

1. m=1 Stability. In the m=1 calculation we examine the stability of a diffuse $\ell = 1$ system using the old ordering expansion, since this theory appears to give rise to the most dangerous modes. Growth rates and eigenfunctions are calculated for a wide range of parameters.

The main result obtained is that the gross m=1 mode for a diffuse $\ell = 1$ system can be wall stabilized, with the wall at a realistic distance from the plasma. At wall distances corresponding to instability there is a pronounced decrease in the growth rate compared to the sharp boundary model especially for higher values of β. The critical wall radius below which the gross mode is stabilized is close to that predicted by the sharp boundary model except for high and low values of β. It is easier to fulfill the requirements for a diffuse system.

For monotonic pressure profiles, two new classes of modes are found. One is localized on the inside of the plasma and the other on the outside. In general their growth rates are quite small. The exterior mode can be wall stabilized but the interior mode is present for any monotonic profile. A further study suggests that flat profiles (i.e., zero θ pinch current) on the outside could eliminate the external unstable modes.

2. Toroidal Equilibrium. A substantial effort has been undertaken to numerically compute 3-D diffuse toroidal equilibrium. At this point, there are no final results, but substantial progress has been made both in code development and in formulating a well defined program.

A 3-D nonlinear ideal MHD code has been developed. Versions of the code exist for the straight screw pinch, linear θ pinch and toroidal Scyllac geometries.

The plan to compute 3-D equilibria is as follows. The first step is to test a pure toroidal θ pinch for which it is well known that there are no equilibria. This is important as a benchmark to see how the code reacts if an equilibrium does not exist. Next a longitudinal current will be added. This configuration does of course have diffuse equilibria, although they are quite unstable. This is important to test how well the code can suppress MHD instabilities arising from the noise level of the computation. Finally, a helical section of the full torus will be studied to examine Scyllac equilibria. We hope to get realistic answers for diffuse profiles as well as addressing the more fundamental question of the existence of 3-D MHD equilibria.

3. Closed Line Scyllac Configuration. We have considered the stability of a sharp boundary, circular cross section closed line Scyllac configuration against m=1 perturbations. The configuration consists of a large finite β,θ pinch field, moderate size $\ell = +1$ and $\ell = -1$ helical fields with exactly equal amplitudes and small $\ell = 0$ field for toroidal equilibrium.

The motivation for studying the $\ell = \pm 1$ configuration arose out of proposed feedback experiments on Scyllac. The nature of the limitation on the feedback system is such that any reduction in growth rate leads to an effective improvement in the feedback response time. Since the existing feedback system is projected to operate at its technological limit any improvement in growth rate represents a substantial gain in feedback performance.

The idea that the closed line configuration might have a lower growth rate than the pure $\ell = 1$ system can be described as follows. For a given $\ell = 0$ field, the condition for toroidal equilibrium depends linearly upon the amplitude of the $\ell = 1$ field. Since the closed line configuration has both $\ell = \pm 1$, each corresponding field need be only half as large as that of a pure $\ell = 1$ system, for equilibrium. On the other hand, the m=1 stability (i.e., ω^2) depends quadratically on the $\ell = 1$ amplitude. Thus, if the $\ell = \pm 1$ contributions to ω^2 simply added algebraically then the growth rate would be reduced by $1/\sqrt{2}$.

We have investigated the stability of m=1, k=0 perturbations in a closed line Scyllac configuration and compared it with the pure $\ell = 1$ system. The closed line system is unstable to a vertical m=1 displacement (i.e., perpendicular to the helical distortions) with growth rate on the order $1/\epsilon$ times larger than that of pure $\ell = 1$ system. We conclude that the pure $\ell = 1$ system has more favorable stability properties than the closed line configuration.

4. Scaling Laws. Much of the work on scaling laws was devoted to optimizing the design of feedback and staged experiments in the existing Scyllac facility. For both feedback and staging it turns out that the optimum design requires maximizing both the major radius R and helical distortion δ_1. In the present Scyllac building the largest possible R is about 12.5 m. The largest possible δ_1 is by and large a matter of faith and courage. In our calculations we take $\delta_1 = 1$.

For the feedback experiment, which is far from being wall stabilized, we fix R and δ_1 and minimize the m=1 growth rate, subject to the constraint of toroidal equilibrium by varying δ_0, h and a. The results indicate that a should be as large as possible. In the staging experiment, we again fix R and δ_1 as above. We then minimize the ratio of plasma to wall ratio a/b, required to make m=1 neutrally stable subject to the constraint of toroidal equilibrium. In this case we vary δ_0, ha, and b. It turns out that the optimum design has b as small as possible. This is set from shock heating requirements at about b=11 cm.

The results for the optimum design are given below for each case.

Feedback Design

$$\frac{\delta_o}{\delta_1} = \left(\frac{2g_1}{g_o f_o}\right)^{1/3} \left(\frac{a}{R\delta_1^2}\right)^{1/3}$$

$$ha = \left(\frac{g_o}{2g_1 f_o^2}\right)^{1/6} \left(\frac{a}{R\delta_1^2}\right)^{1/3}$$

$$\gamma^2 = \frac{3}{2}\,\frac{\delta_1^2 v_a^2}{a^2} \left(\frac{2g_1 g_o^2}{f_o^4}\right)^{1/32} \left(\frac{a}{R\delta_1^2}\right)^{4/3}$$

Staging Design

$$\frac{a}{b} = \left(\frac{27}{4}\;\frac{g_o g_1^2}{\beta^3 f_o^2}\right)^{1/10} \left(\frac{b}{R\delta_1^2}\right)^{1/5}$$

$$\frac{\delta_o}{\delta_1} = \left(\frac{g_1}{2g_o f_o}\right)^{1/3} \left(\frac{a}{b}\right)^{1/3} \left(\frac{b}{R\delta_1^2}\right)^{1/3}$$

$$ha = \left(\frac{1}{f_o}\;\frac{a}{b}\;\frac{b}{\delta_o \delta_1 R}\right)^{1/2}$$

Here the f's and g's are function of β given by

$g_1 = \beta(4-3\beta)(2-\beta/8(1-\beta)$

$g_0 = \beta(3-2\beta)(1-\beta)/(2-\beta)$

$f_0 = (3-2\beta)/2$

One goal of our diffuse equilibrium and stability calculations will be to obtain more accurate values of g_0, g_1, and f_0 to be used in the scaling calculations.

C. Diffuse $\ell = 1$ and Stability (MHD)

The diffuse $\ell = 1$ calculation started last year has essentially been completed. The main results were presented at the IAEA Tokyo meeting (Nov. 1974), and a more complete paper to be published is on the way.

The calculation is based on an expansion in δ (measure of the helical shift), and with arbitrary ha; h = helical pitch number, a = plasma radius. The computational part of the problem was made difficult because of the presence of an accumulation point for the spectrum of ω at $\omega = 0$. Associated with this there was the existence of local m = 1 modes, localized on both the outside and at the axis of the plasma column. Also in some parameter regions it was very difficult to separate the local m = 1 modes from the global m = 1 mode. However, this problem has now been solved in sufficient detail to provide an overall understanding. In this connection a study was made of the possible effects on the local modes from changing the zero order pressure profile.

The effect of finite k_z (wave number in the axial direction) was studied and it has been demonstrated by numerical examples that for finite, but small k_z there exist a critical wall-radius beyond which the plasma column is stable. This is because the accumulation point $\omega = 0$ for $k_z = 0$ is shifted toward the stable side by taking $k_z \neq 0$. Thus a reasonably small but finite k_z can effectively remove the local unstable m = 1 modes, without having any noticeable effect on the gross m = 1 mode, which is wall stabilized in good agreement with sharp boundary theory.

The numerical computation of this problem was done by having a finite density (of a few percent of density on axis) extending to the wall. Another approach would be to solve the same problem with a vacuum region outside the plasma and this way one would also expect to eliminate the external local modes. Work on this problem was started, and first the proper boundary conditions had to be derived. It turned out that this was more difficult than anticipated. This derivation is completed, but the result is quite complicated to apply and the problem has not yet been pursued further. Instead some effort has been made to look into the possibility of analyzing a combined $\ell = 0$, $\ell = 1$ diffuse system by expansion in δ and for arbitrary ha. Some progress has been made on this problem and it is currently being studied, because of its great significance to the Scyllac program.

D. The Continuous Spectrum of Ideal Magnetohydrodynamics in Toroidal Geometry

The continuous spectrum of ideal MHD arises as a result of spatial inhomogeneities, in much the same way as the continuous spectrum in the Vlasov description results from inhomogeneities in velocity place. Thus, in ideal MHD two continua of δ-functions are found analogous to the van Kampen modes in the Vlasov picture. These continua are relatively independent of geometry effects like curvature (which affects the discrete spectrum) and, therefore, play a central role in the understanding of the structure of the spectrum. In the diffuse linear pinch the slow and Alfvén continua are sandwiched between Sturmian and anti-Sturmian discrete spectra clustering at the continua. Both continua consist of modes localized in a particular magnetic surface, but polarized parallel to the magnetic field for the slow modes and perpendicular for the Alfvén modes.

In axially symmetric toroidal systems it is much harder to distinguish the discrete subspectra, but one can find the continua cluster points analytically. The singular continuum modes are again localized on particular magnetic surfaces but the polarization is no longer purely parallel or perpendicular. The reason is that the magnetic field is not constant on a magnetic surface so that the waves propagate neither along field-lines nor along goedesics. As a result, the Alfvén and slow continua are coupled giving rise to oblique propagation for both continuum modes. This complicates the spectral problem considerably, especially as regards stability because the coupling is strong near the origin $\omega^2=0$.

Curvature effects determine whether the tip of a continuum is a cluster point of localized modes. Thus, the Mercier criterion turns out to be just a special case for modes that are localized around rational surfaces.

E. Equilibrium and Stability of High-Beta Diffuse Tokamaks

The limitations on β as regards equilibrium and stability of tokamaks are investigated. The regime of interest is obtained for $\beta \sim \epsilon$ and $B_{pol}/B_{tor} \sim \epsilon$, where ϵ is the inverse aspect ratio. The shift δ of the magnetic axis away from the center of the tube is then of order unity so that the equilibrium is essentially two-dimensional. (In the usual low-β tokamak order where $\beta \sim \epsilon^2$, the shift $\delta \sim \epsilon$ so that one-dimensional approximations are possible). After Fourier decomposing modes in the ignorable angle ϕ the stability analysis also becomes two-dimensional, so that the basic problem consists of calculating equilibria accurately enough that it makes sense to do a spectral analysis of the stability. This problem is solved in the following manner.

The nonlinear equilibrium equation for the flux function ψ is solved for exponential pressure profiles, exploiting a conformal mapping to a polar coordinate system $\acute{r}$, θ in which the magnetic axis is at the center $\acute{r} = 0$ and the plasma boundary at the circle $\acute{r} = 1$. Both equilibrium and stability are then solved in this coordinate system so that no accuracy is lost in converting from one coordinate system to another. This transformation makes the low-β equilibrium trivially concentric circles to leading order, whereas high-β equilibria can be accurately represented by an extremely rapidly converging Fourier-series in the angle θ This Fourier representation of the equilibrium is also a very convenient one for the stability analysis as part of it can now be done analytically.

Limits on the equilibrium typically arise from the appearance of a second magnetic axis and bifurcated solutions when δ becomes too large (this occurs at about $\delta \approx 0.4$). This limit fixes a critical value of β depending on the safety factor q. From the stability analysis similar limitations on β arise so that one can then optimize parameters so as to obtain the maximum possible β as far as ideal MHD equilibria and stability are concerned.

F. Three Dimensional Computational Magnetohydrodynamics

A numerical algorithm for solving the fully nonlinear, time dependent equations of ideal MHD has been developed this year. This algorithm employs an implicit algorithm to obtain time advanced accelerations. Hence, the usual Courant stability condition is relaxed and the time step is not limited by high signal speeds which are not of physical interest. The difference equations are formulated for an arbitrary three dimensional computational mesh. Numerical diffusion is minimized by the use of an arbitrary Lagrangian-Eulerian (ALE) mesh in which almost Lagrangian zoning diminishes convection between cells.

Because of the arbitrary shape of the computational zones, boundary conditions appropriate to general configurations are easily implemented. A subroutine permits the representation of a conducting wall of specified shape by the definition of a single function. In toroidal geometries, periodic boundary conditions are imposed in the axial direction in such a way that a toroidal sector of specified length may be represented. Thus, for example, a single period of a helical Scyllac equilibrium may be studied.

A number of computations have been performed in straight axisymmetric configurations as well as in toroidal geometry. A truncation error in the computation of acceleration at the boundary has been observed in these initial toroidal computations. This effect is due to the toroidal curvature and has been understood and corrected for the case of isotropic stress. The general case of anisotropic stress due to a magnetic field is currently under investigation and it is expected that soon this effect will be understood analytically and eliminated from the computation.

The implicit phase of the computation includes all coupling terms in the equations determining the time advanced magnetic field and the time advanced pressure for each cell. This eliminates cases in which the relative magnitudes of the various propagation speeds of Alfvén and magneto-acoustic waves would otherwise cause convergence difficulties in the iteration. The present scheme converges efficiently for the entire range of signal speeds of interest.

The computation mesh is rezoned by the application of a smoothing algorithm. The algorithm gives the minimal adjustments to the grid which are often sufficient to prevent negative volume cells without introducing appreciable relative motion of the grid and fluid. When minimal adjustment is not sufficient, as in turbulent flow, the algorithm allows the smooth transition to an Eulerian mode. This gives the ALE code the full range of applicability of an Eulerian computation with a reduction in computational diffusion when the flow is resolved by a Lagrangian mesh. The smoothing algorithm may also be used to generate an initial computation mesh for a problem with an arbitrarily shaped boundary. When the position of boundary vertices is specified, the algorithm will give a distribution of vertices interior to the boundary with the desired properties.

Calculations have indicated a number of key features of the algorithm. For the rotating theta pinch in an axisymmetric geometry, good agreement with linearly predicted growth rates has been observed. More importantly, even very unstable modes were not excited by numerical noise. Hence, it is possible to find unstable equilibria with the algorithm and focus attention on those modes found experimentally to be most troublesome.

Preliminary results from toroidal calculations indicate that if no equilibrium close to the initial state exists, the code will provide a clear indication of this by following the motion of the plasma to the conducting boundary. By solving the initial value problem in this way, the problems of equilibrium and stability may be decoupled.

All computations to date have indicated that numerical diffusion is small enough that reasonable physical problems may be represented with the relatively coarse grids that must be used in three dimensions.

Plans for the coming year include computations to study the nonlinear evolution of internal kink modes in noncircular cross section axisymmetric devices. Various two dimensional toroidal configurations will be studied in which an equilibrium is possible or not possible and in which the equilibrium, if it exists, is stable or not. These computations will demonstrate the separation of equilibrium and stability questions. Finally, the toroidal code will be used to examine the three dimensional Scyllac configuration.

G. A One Dimensional Hybrid Simulation of the Biased Z Pinch Implosion

We have commenced a program to calculate pinch implosions in which non-thermal effects (such as reflected ion streams) are important. Ideally, one would wish to treat both electrons and ions by the Vlasov formalism; however, the speed and storage capabilities of the current generation of computing machines does not allow this. A workable alternative is the hybrid approach, which consists of treating the ions by the Vlasov formalism and the electrons as a fluid while assuming charge neutrality and neglecting variations on the electron time scale. This may be rationalized, in the case of the Fuse mode of the ZT-1 experiment, by noting that a typical Fokker-Plank relaxation time for the ions is $\sim 30\mu s$, for the electrons is $\sim 0.01\mu s$, while the implosion time is $\sim 1\mu s$; and that the Debye length is $\sim 10^{-4}$ cm while a cell is $\sim 10^{-2}$ cm. We have written such a hybrid code in one spatial dimension (r) and we present a description of the code along with some illustrative results.

The ions reside in a four dimensional phase space $(V_r,V_\theta V_z,r)$. The Vlasov equation for ions in such a space is solved by the particle simulation technique.[1] Knowing the ion distribution function we may find the average density and average radial velocity of the ions as a function of position, which by charge neutrality determine the electron density and radial velocity.

The momentum equation for the fluid electrons may be written as

$$m_e n\left(\frac{d\vec{V}_e}{dt}\right) = -en\left(\vec{E}+\vec{V}_e \times \vec{B}/c\right) - \mathrm{grad}\,p_e + en\sigma^{-1}\cdot\vec{J}$$

Consistent with our neglect of variations on the electron time scale we set the left hand side to zero. $\mathrm{Div}\bar{B}(r)=0$ implied $B_r(r)=0$, and in the $\hat{\theta}$ and $\hat{z}$ directions $\mathrm{grad}p_e(r)=0$, so that the $\hat{\theta}$ and $\hat{z}$ components of the momentum equation reduce to field diffusion equations which we solve by introducing the vector potential.[2] The conductivity along the field is allowed to differ from that perpendicular to the field, so that we construct a conductivity tensor σ.[2] The boundary magnetic field may be specified as a function of time.

Finally, the electron heat equation, which includes compressive heating, Joule heating and heat conduction may be used to solve for p_e while the r component of the electron momentum equation may be used to solve for E_r.

This approach requires an electrical conductivity and a thermal conductivity to be specified. It is here that the non-Maxwellian aspects of the electrons, their interaction with the ions, and turbulence enter the formalism. One may use coefficients derived from the theory of plasma turbulence or from the nonlinear evolution of a given instability or one may find by trial and error coefficients that allow the results of a given experiment to be reproduced, and then inquire into which processes give rise to such a coefficient.

In the results presented below, we have set the thermal conductivity to 0 and have chosen a collision frequency ν (where $\sigma=e^2n/me\nu$) similar to the one suggested by Chodura. In principle, we take ν to be ν_s, the value given by Spitzer,[3] if $V_d<f\,c_s$, where V_d is the electron drift velocity, and $c_s = (\gamma kT_e/m_i)^{1/2}$ and $\nu=C\omega_{pi}$ if $V_d \geq f\,c_s$. However, in order to avoid numerical problems resulting from a sudden switch ν, we use

$$\nu = \max\left[C\,\omega_{pi}\left(1-e^{-V_d/fC_s}\right),\ \nu_s\right]$$

in the code. The formalism requires $\sigma_\parallel$ and $\sigma_\perp$, and to get these we substitute $V_{d\parallel}$ and $V_{d\perp}$ into the above equation. Furthermore $C_\parallel$ and $C_\perp$, as well as $f_\parallel$ and $f_\perp$, may differ.

In Fig. XI-1 is shown experimental field profiles for the ZT-1 derated shot 10115 and calculated profiles assuming $C_\parallel=C_\perp=1.0$, $f_\parallel=f_\perp=3.0$. As can be seen, the agreement is acceptable. In particular the code reproduces the principal features of the field evolution, namely considerable diffusion in the B_θ profile together with a B_z profile which shows considerable compression and which does not diffuse away. During the implosion, $\nu = \nu_s$ near the center while in the sheath region (where H_θ is large) v/v_s may be as high as 10^5 and $v_\parallel/v_\perp$ may be as high as 5. Evidently turbulence enhances the collision frequency in the sheath region. This conclusion is reinforced by Fig. XI-2, which gives field profiles for 10115 calculated assuming $C_\parallel = C_\perp = 0$ ($v = v_s$ everywhere).

In Fig. XI-3 are shown experimental field profiles for the ZT-1 shot 11678 and calculated profiles assuming the same collsion frequency as before ($C_\parallel=C_\perp=1.0$, $f_\parallel=f_\perp=3.0$). Again, the agreement is acceptable. That the data from both shots can be matched by using the same conductivity may be significant. If this turns out to be a general feature of the hybrid calculations, this approach will be useful in predicting the results of future shots.

H. A Code for Modeling the θ-Pinch Implosion Including the External Circuit

As a guide both for designing implosion heating circuitry and for interpreting the data from the experiments, we have written a code IMPLOD which is now in active use.

The plasma model is a one-dimensional hybrid model similar to that described by Sgro in the previous section (G). Some simplification in the treatment of electron pressure is made to guarantee numerical stability. The circuit is defined in the loop current formulation by specifying the nonzero elements of the inductance, resistance, and susceptance matrices. A simple but accurate time-advance algorithm makes this circuit code considerably faster than library network codes. However, the simple code is somewhat more cumbersome to use for very complicated circuits.

The interaction of the circuit and the plasma involves a special feature which deserves further discussion. Because of the complex electrical properties of a coil containing dynamic plasma, no simple

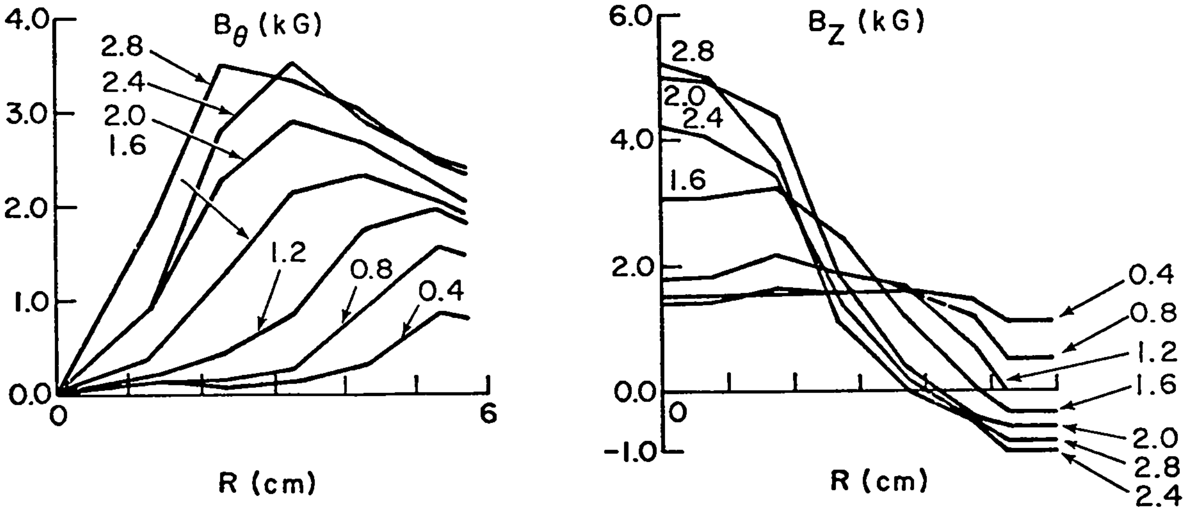

Experiment

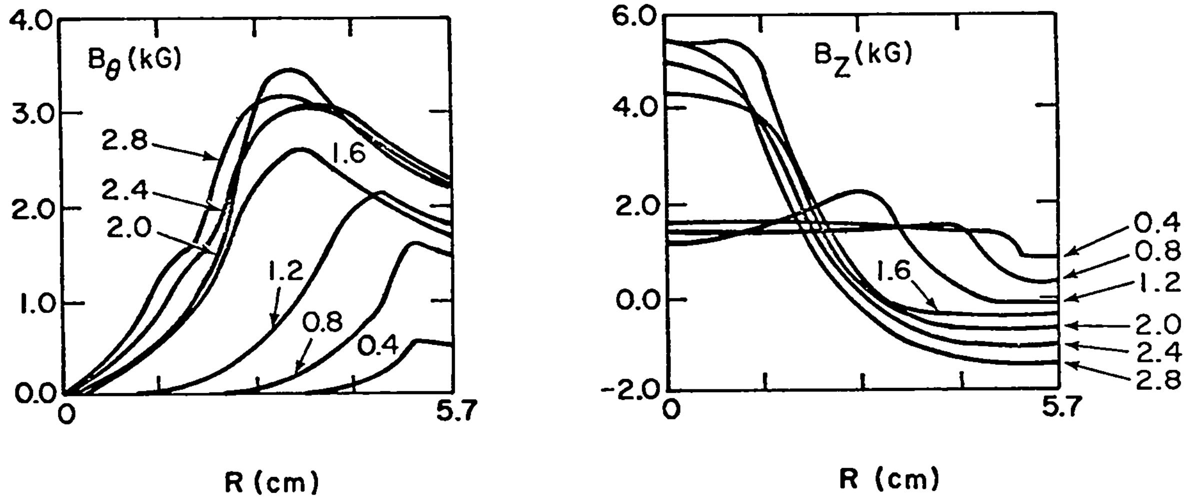

Theory

Fig. XI-1
Comparison of theoretical and experimental magnetic field profile for ZT-1 shot 10115.

decoupling of the circuit and plasma is possible. The boundary condition on the plasma is related to the circuit through Ampere's law for I_p,

$$I_p \;\alpha\; \frac{1}{r}\frac{\partial}{\partial r}\left(r\,\frac{\partial A_\theta}{\partial r}\right)\Bigg|_{r\,=\,\mathrm{RMAX}}$$

and through Faraday's law for V_p,V_p α $\partial(rA_\theta)/\partial t|_{r=\mathrm{RMAX}}$. At any time step of the computation one has N loop equations for the circuit plus the boundary value problem for the magnetic field in the plasma. By proceeding as far as possible with elimination on the circuit equations one can reduce the set of circuit equations to $\alpha I_p+\beta B_p=\gamma$ even though the numerical values of the current and voltage through the plasma coil are not yet known. However, since a *mixed* boundary condition on A_θ produces a well-posed boundary value problem for A_θ, the field diffusion equation can be solved before numerically knowing either the current or voltage in the coil. This having been done, back substitution leads to values for all circuit currents and voltages. Thus a completely self-consistent solution is obtained without iteration.

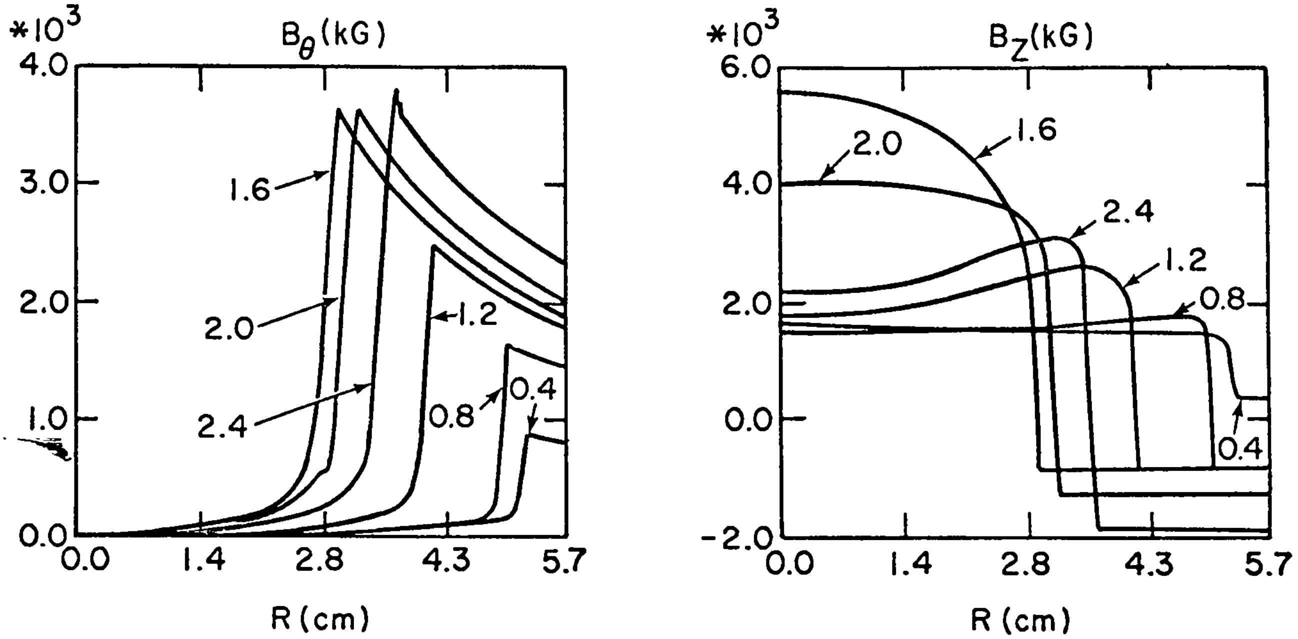

Fig. XI-2
Field profiles for the same shot as Fig. 1, assuming no turbulent enhancement of the conductivity in the sheath region.

This code is being used by R. Linford to study proposed implosion heating circuitry and by T. Jarboe to correlate data in the implosion heating experiment.

I. The Darwin Model for Plasma Simulation

Two-dimensional particle simulation is one of the few techniques available for studying the properties of microscopic plasma turbulence. In high-β pinches magnetic fields and steep gradients complicate this turbulence beyond the capability of simple electrostatic models. Fully electromagnetic simulation codes, while fairly simple to write, must follow all processes on the lightwave time scale. Not only is this inefficient for nonrelativistic plasmas, but the bremsstrahlung is artificially enhanced due to the relatively small number of simulation particles.

The correct nonrelativistic treatment consists of neglecting the transverse displacement current in Maxwell's equations while keeping the time derivative of the electrostatic field. This was first demonstrated by C.G. Darwin[4] and is called the Darwin model. One-dimensional simulation codes for this model have existed for some time, but two-dimensional forms, essential for studying most significant problems, have presented difficulties. The source of these difficulties is the fact that the reduced model has no retardation, that is, it is an instantaneous-action-at-a-distance model. Any attempt to implement this with a numerical model having only local interactions is bound to be numerically unstable. By formulating the Maxwell-Lorentz equations in a somewhat complicated but totally elliptic form we have obtained a completely stable numerical model.

This two-dimensional code is now being used to study the nonlinear properties of electromagnetic streaming instabilities in highly inhomogeneous plasmas.

J. Numerical Simulation of the Proposed Injection Experiment

A two-dimensional MHD code for the axisymmetric geometries is being used to simulate the proposed plasma injection experiment.[5] Several numerical algorithms have been developed to make the existing code applicable to this experiment, including developing a method for applying time-dependent boundary conditions, and a method for the construction of a suitable mesh for a domain with sharp corners and an unfavorable ratio of length to diameter. The first method was described in a previous quarterly progress report. The second is an adaptation of an algorithm for generating body-fitted coordinates developed by Thompson, *et al.* [6]

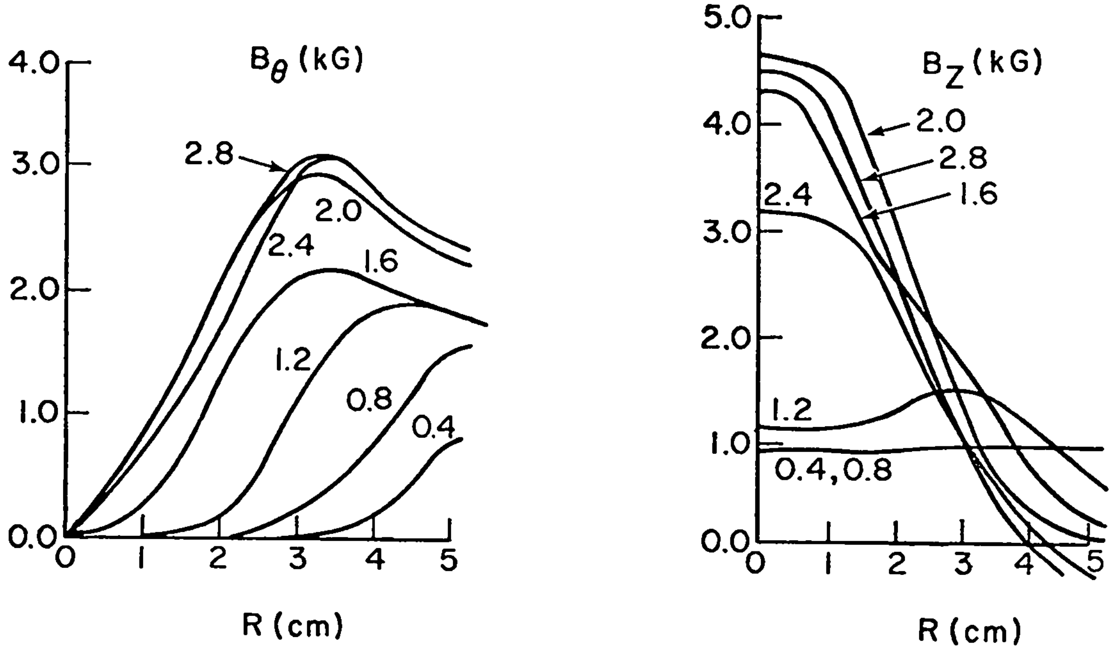

Experiment

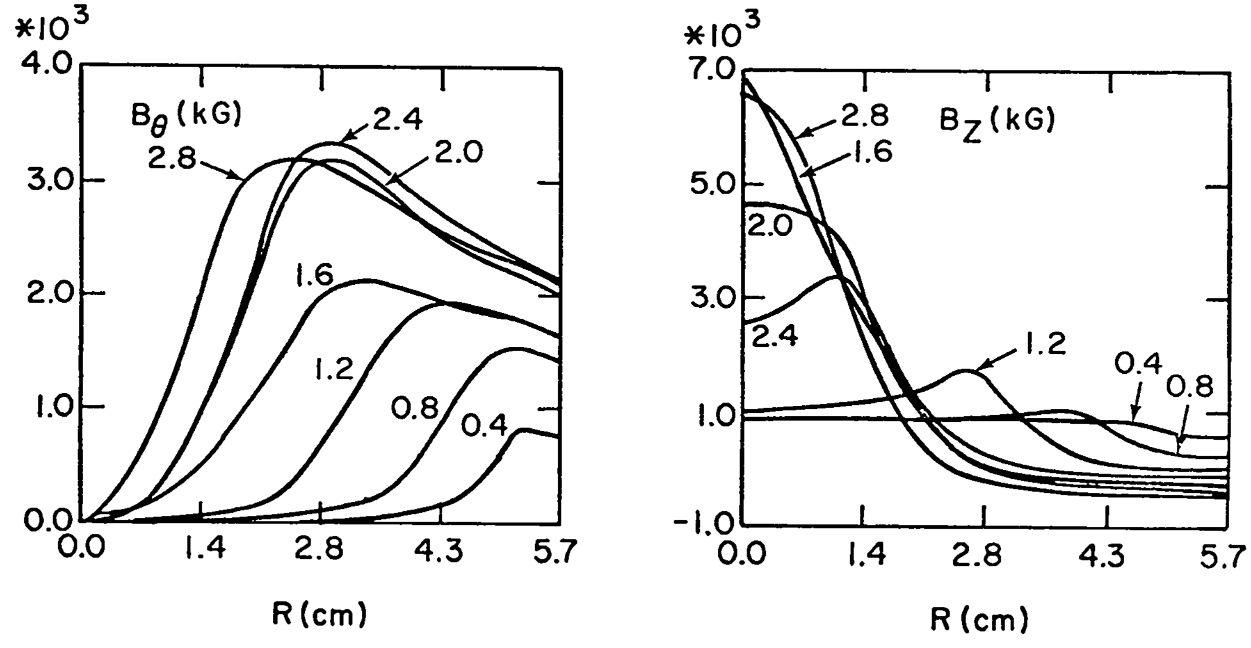

Theory

Fig. XI-3
Comparison of theoretical and experimental profiles for ZT-1 shot 11678. The curves are labeled in microseconds.

With this algorithm, only the location of points on the boundary need be specified. The solution of a quasi-linear differential equation then gives a distribution of vertices interior to the boundary which is suitable for an MHD calculation. That is, the cells are convex and smoothly varying in size as can be seen in the mesh for the injection experiment shown in Fig. XI-4. This algorithm is general in its application, and will be useful in the future in shortening the set up time for new problems with new geometries.

K. Inhomogeneous Vlasov Equilibria

Inhomogeneous magnetized Vlasov equilibria which correspond to the situation found in the sheath region of theta pinches have been constructed numerically using a hermite transformed Vlasov equation. The primary aim of this work is to find initial states for 2-D PIC simulations of the microinstabilities which occur in the sheath region and are responsible for the observed anomalous resistivity. It is advantageous to initialize these simulations with inhomogeneous equilibria so that the detailed structure of the instabilities will not be masked by larger dynamical effects resulting from a nonequilibrium initial state.

The basic procedure for generating equilibria by this new method is to choose a density profile for the ions, which are assumed to be Maxwellian and, therefore, elecrostatically confined. Electron and ion temperature profiles in x (which corresponds to the radial direction in a theta pinch) are assumed constant. The electric field required to confine the ions may now be calculated from the ion Vlasov equation. The electron density is then computed from Poisson's equation, the magnetic field from the electron pressure balance equation, the current from Ampere's law, and higher y (i.e., θ) velocity moments may then be calculcated recursively from the Hermite transformed Vlasov equation.

Several new features of this type of equilibria have been discovered. The first is that if the ion density outside of the sheath region is too small, electrostatic confinement of the ions by a charge neutral sheath is not possible. The second feature is that the temperature of the electrons in the y direction (T_y) is not equal to that in the x directicn (T_x). In the region just inside of the current sheath T_y is significantly less than T_x, and the effect becomes more pronounced the narrower the sheath. Since one requires T_y to be greater than zero always, one obtains a restriction on the minimum sheath width and the maximum current allowable.

A generalized version of the equilibria generating procedure allowing arbitrary T_x profiles is presently being pursued. Preliminary results indicate that simulation runs initialized with the new equilibria exhibit elecromagnetic instabilities, which may be related to the Weibel instability.[7] Figure XI-5 shows (a) the initial densities, (b) the magnetic field (B_z), and (c) the electron temperature profiles as a function of x. The ion temperature is ten times the electron temperature at $x=0$; they are equal at large x. The contour plot (d) of B_z in the x-y plane, taken from a PIC simulation run at time $t=80\ \omega_{pe}^{-1}$, shows definite wave structure, indicative of an electromagnetic instability.

L. Vlasov-Fluid Research

1. Sharp Boundary Pinches. During the first quarter, extensive analytical investigations were performed in an attempt to apply the Freidberg Vlasov-fluid model of hot pinches to sharp-boundary-pinch stability. A significant result of this work can be stated as follows. In the uniform region of a near-theta pinch, to leading order in ion gyroradius to radial scale length, (r_L/a), the ideal-MHD equations are valid provided the ratio of specific heats, γ, is replaced by $\gamma_{eff.} \equiv -2\ (\omega/k_z v_i)\ Z(\omega/k_z v_i)$, where the perturbation has complex frequency ω, real wave-vector k with magnetic field projection $k_z \equiv k.B/|B|$, where v is the ion thermal speed and Z is the plasma dispersion function. Moreover, the corrections to this result, of order $(r_L/a)^0$, have been shown to be of order $(r_L/a)^2$ in the uniform magnetoplasma region. Thus, γ_{eff} contains the kinetic effects of free particle motion along field lines. It was then decided that further analytical effort on hot pinch stability would be better spent on the more realistic diffuse pinches.

2. Diffuse Pinches. During the second quarter, a near-theta diffuse pinch of Gaussian density profile with self-consistent equilibrium electric and magnetic fields was considered. The deviations from a straight theta-pinch were assumed small, but otherwise arbitrary. The stability of this pinch including the full effects of the gradient-B particle drifts. A trial-function dispersion relation was derived and solved numerically. The growth rate of the $m=1$ mode was found to be given by its ideal-MHD expression (the δW expression) to within 1/2%, over the large parameter range that was investigated. Because of the finite-Larmor-radius ordering that was used in this work, it became necessary to know

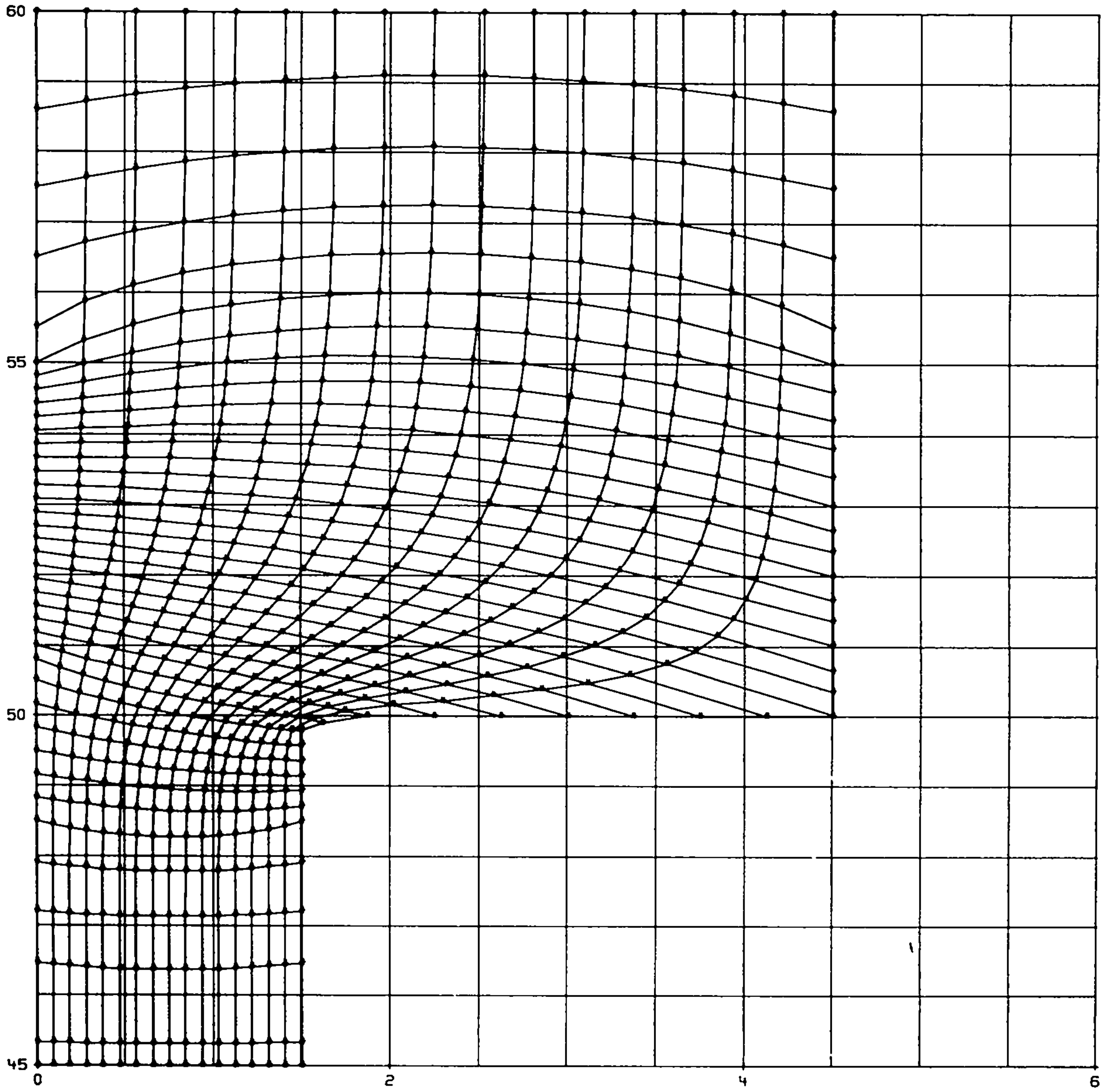

Fig. XI-4
Graph showing part of the computation mesh in the vicinity of the reentrant corner.

that there were no order $(r_L/a)^2$ contributions to the usual particle drift velocity expressions of order $(r_L/a)^1$. This can be inferred from a particle-orbit review article by Ira Bernstein, for the case of low-beta plasmas (i.e., gradient-B drifts small compared to E×B drifts). It remains to be demonstrated in general for high-beta plasmas. However, R. Gerwin has made some progress in this direction by examining the orbit equations within the context of a gradient-B slab geometry. It was indeed found that the leading correction to the usual gradient-B drift was of order $(r_L/a)^3$.

3. Model Generalization. During the third quarter, the Freidberg Vlasov-fluid model of hot-ion pinches was extended to include finite electron temperature. A lengthy analysis produced a rather simple final result. Leaf Turner then performed a small (r_L/a) expansion on these new equations, for a uniform magnetoplasma, and found that the MHD-type behavior of pinch stability is again characterized by a certain γ_{eff}, which is a generalization of that described above. The new Vlasov-fluid equation now encompasses a much more complicated mode structure that includes ion-acoustic waves.

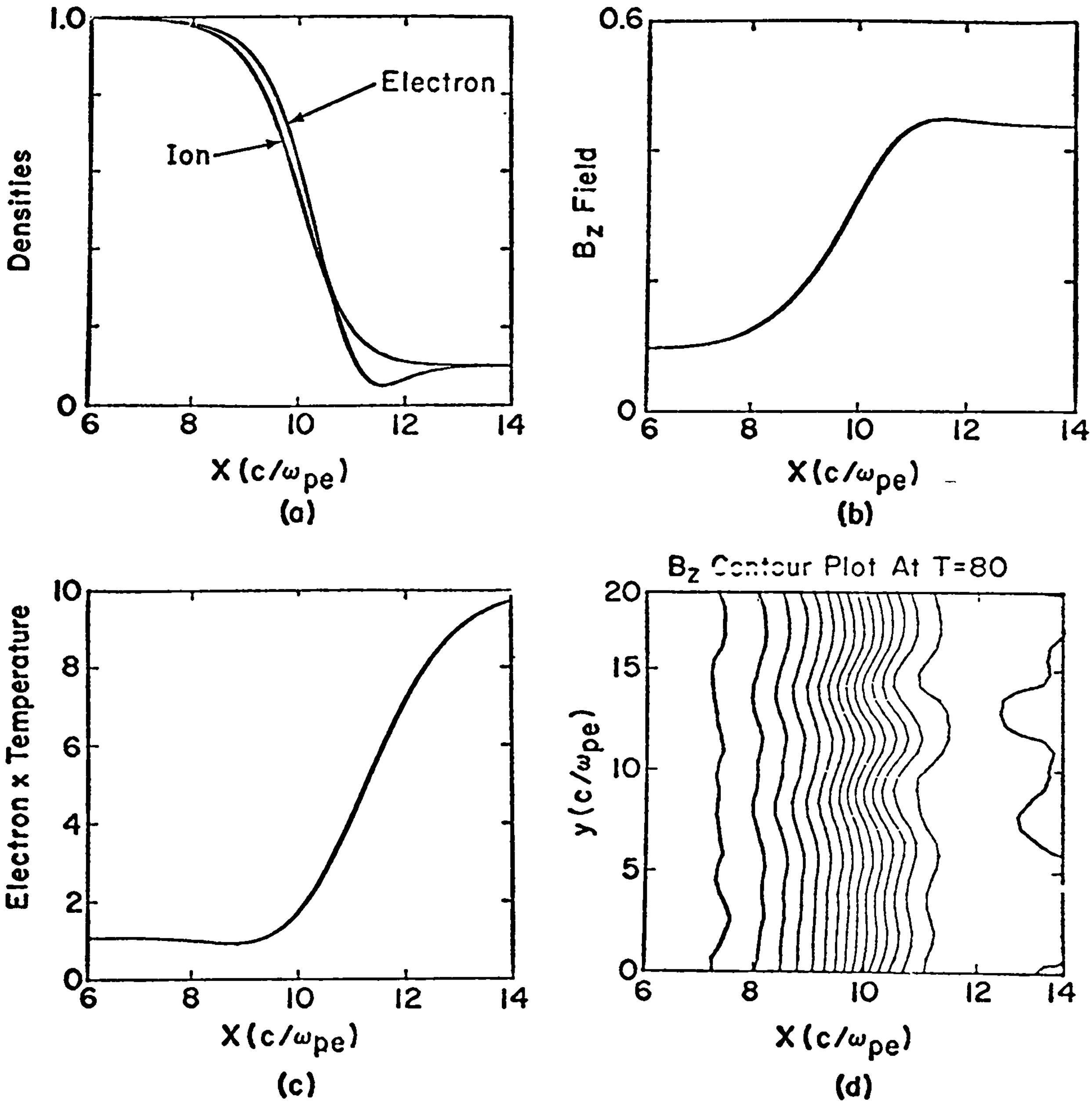

Fig. XI-5
Profiles of the initial densities, z-component of the magnetic field and electron temperature, and a contour plot of B_z *at* $t = 80\,\omega^{-1}_{pe}$.

M. Equilibrium and Microinstabilities in ZT-1

During the third and fourth quarters, R. Gerwin and Leaf Turner constructed a nonresistive model of the ZT-1 equilibrium that allows for a reversal in the toroidal magnetic field, and a pressure profile that can be either full or depressed on axis. The purpose of this model is to furnish electron-drift drift velocity profiles for application to current-driven microinstabilities that may be a source of anomalous resistivity and concommitant undesirable diffusion of the ZT-1 profiles. A code has been written that quickly furnishes these velocity profiles in a straight geometry.

The model equilibrium predicts a total toroidal current that is in reasonably good agreement with observation, both for the fuse- and intermediate-modes of ZT-1 operation. It further predicts that the component of drift velocity parallel to the total magnetic field is of the order of the ion-thermal speed, v_i, whereas the component of drift velocity perpendicular to the field is small against v_i in the core of the pinch, but rises to the order of v_i in the periphery of the pinch (densities ~ 10% to 30% of the density on axis). These drift velocities appear to be in qualitative agreement with the code of Baker and Mann that includes the exact toroidal geometry. The consequences of these properties for microinstabilities will now be discussed.

R. Gerwin spent most of the fourth quarter extending the review of microinstabilities to include inhomogeneous equilibria with self-consistent drifts, thus enlarging the work of the previous quarter on uniform magneto-plasmas with relative electron-ion drifts when $T_e \ll T_i$ as in ZT-1. The modes important for anomalous resistivity (fine-grained against MHD space and time scales) all prove to require either (a) parallel drifts $u_{\parallel}$ larger than the electron thermal speed, v_e, or (b) perpendicular drifts $u_{\perp}$ not *too* much smaller than the ion thermal speed v_i. In view of our equilibrium studies, only the latter possibility appears to be relevant to ZT-1.

Of all the modes examined, those of the electron-acoustic type appear to be the most dangerous, for the following reasons. First, they do not depend upon gyro-resonance for their existence, and thus are not subject to low saturation level of turbulence due to gyro-resonance-broadening. Second, they seem to have the largest growth rates of any microinstability available to the present ZT-1 parameter regime, at positions in the profile where $u_{\perp} \rightarrow v_i$. As mentioned earlier, this condition is attained in the periphery of the pinch. (Many other modes, such as the ion and electron cyclotron drift instabilities, can also be driven by $u_{\perp} > v_i$.) R.C. Davidson and N.T. Gladd have examined a $k_{\parallel}=0$ drift-wave instability (the hot-ion version of the lower hybrid-drift instability) that has a growth rate which scales exactly like the standard electron acoustic instability but is a factor of two larger. Thus, the particular mode appears to be very relevant to ZT-1.

The anomalous resistivity associated with the hot-ion lower-hybrid drift instability has been calculated and is characterized by an effective electron-momentum-transfer collision frequency of the form

$$\nu_{eff} \approx \sqrt{\pi/8}\,(u_{\perp}/v_i)^2\,(1 + \omega_{pe}^2/\omega_{ce}^2)^{1/2}\,\omega_{pi} \qquad (1)$$

where ωp and ωc are species plasma- and gyro-frequencies respectively. In the periphery of ZT-1 this amounts to $\nu eff \sim \omega pi$ in order of magnitude, and is thus similar to an effective collison frequency employed by Sgro in his computer studies. However, it scales differently than ωpi.

The broad-brushstroke picture that suggests itself for ZT-1 now seems to run as follows. In the pinch periphery, microinstabilities probably of the electron-acoustic type are driven by $u_{\perp} \leq v_i$. It is important to note that in this part of the profile, toroidal field reversal occurs. Hence $u_{\perp}$ is largely in the toroidal direction in this region, and the microinstabilities it drives will be associated primarily with toroidal resistivity and concommitant diffusion of the poloidal magnetic field. In this connection, it is also important to note that the wave-vector k corresponding to maximum growth rate has no component along B, and hence k is along the toroidal direction near the reversal point of the toroidal field.

Thus, the unwanted diffusion of poloidal field is driven by $u_{\perp}$ in the periphery. Since u scales like a diamagnetic velocity and hence like $|\nabla n/n|$, its magnitude should be reduced (other quantities remaining equal) when the minor radius is scaled up as planned. This should then reduce the anomalous resistivity as represented by the expression for ν_{eff}, and, in fact, one predicts $\nu_{eff} \sim$ (minor radius)$^{-2}$.

One can expect that the reduced diffusion of poloidal field in the periphery of the pinch due to scaling up the minor radius will also have a beneficial effect on the interior of the pinch.

N. Microinstability Properties of High Density Pinches

The movement toward implementation of the staging concept[8] as a means of achieving wall stabilization of the Los Alamos high-beta toroidal confinement device, Scyllac, has provided strong motivation for understanding the microprocesses which occur in various high-density pinch implosions. In particular, the turbulence associated with the existence of microinstabilities in implosion sheath manifests itself, macroscopically, as an anomalous resistivity which strongly affects the way in which magnetic fields interpenetrate the plasma. Since to scale up staging from current experiments[9] to reactor-like devices will probably require knowledge about the scaling of anomalous transport coefficients, it is desirable to understand the microinstability picture as well as possible. This report relates some of the theoretical steps taken in the past year to understand the microinstabilities characteristic of high density ($\omega_{pe}/\Omega_e \gg 1$), hot ion ($T_e/T_i \leq 1$) theta-pinch and Z-pinch implosions.

1. Linear Theory. The anomalous resistivity and other anomalous transport coefficients which are required as input to macroscopic fluid-numerical codes and other theoretical devices used to model the macroscopic behavior of high-density pinches are the consequence of nonlinear plasma theories. A general characteristic of nonlinear plasma theories is that their predictions depend quite strongly on the linear properties of the instabilities which are most important in the plasma under consideration. Therefore, to have confidence in calculated anomalous transport coefficients it is necessary to have a firm base of knowledge about the linear stability theory of high-density pinch implosion sheaths. To this end a dispersion relation was derived from the Vlasov-Maxwell equations which has provisions for both finite-beta effects and the effects of gradients in density, temperature, and magnetic field.

The dispersion relation was applied to study the instabilities thought to be most important in typical high-density pinch implosions, namely the lower-hybrid-drift instability[10] and the modified-two-stream instability.[11] Although these instabilities have been previously examined in the literature, the published analyses were deficient in one way or another as they related to application in high density pinch experiments. For example the detailed study of the modified-two-stream instability[12] showed that the maximum growth rate for the instability occurred in a regime where the electrons required a kinetic description, but restricted itself to a homogeneous $\beta=0$ plasma model. Subsequent analysis of the effects of finite beta[13] on this mode was again restricted to a homogeneous plasma with the electrons described by fluid theory and thus the most rapidly growing modes were not treated. Similar gaps exist in the published analyses of the lower-hybrid-drift instability.[10,14]

An important question which was initially addressed with the more general dispersion relation was the question of the relative importance of the lower-hybrid-drift instability and the modified-two-stream instability. The lower-hybrid-drift instability is characteristically a flute mode ($\underline{k}.\underline{B}=0$) with maximum growth occurring for $k_\perp \rho_e \sim 1$. The modified two-stream instability experiences maximum growth at somewhat longer wavelength ($k_\perp \rho_e \ll 1$) and at a particular oblique angle of propagation to the magnetic field ($k_\parallel/k_\perp \neq 0$). It was found that for almost all situations typical of high-density pinch implosions that it is the lower-hybrid-drift instability which has the largest growth rate. Furthermore it was found that the effects of finite β on this dominant instability manifest themselves primarily through the magnetic field gradients necssarily implied by finite β rather than through coupling of the electrostatic lower-hybrid-drift mode to various electromagnetic modes. In this context it was also found that the effect of finite β is generally destabilizing but not strongly so. The statements above constitute only a brief summary of the work performed. For details the reader is directed to Ref. 15.

An interesting aspect of the dispersion relation derived in Ref. 8 is that it is sufficiently general to allow application to real experimental profiles of density, temperature, and magnetic field. In particular, the well diagnosed collisionless shock experiment of Keilhacker, Kornherr, and Steuer[16] was chosen and the instability characteristics [frequency(ω_r), maximum growth rate (γ), and growth maximizing wave number ($k_{y\ max}\rho_e$)] were calculated as a function of position within the implosion sheath (see Fig. XI-6). In the figure the density profile is superimposed for reference. Again, for details the reader is referred to Ref. 8. From this type of analysis some conclusions about the spatial structure of microturbulence within implosion sheaths, to the extent that it can be so described by a local linear Vlasov theory, may be drawn. Possible points of observational interest for this experiment are the differences in the microturbulence characteristics in the shock region [1-2] and the piston region [3-4].

The general dispersion relation was not expressible in closed form when all detailed effects were included and so a significant portion of the analysis required numerical solution of the dispersion relation. Furthermore, comparison of the general dispersion relation with previously published results required, in general, numerical computation. For these reasons a numerical code (ANLYZ) was developed which allows for the numerical solution of general dispersion relations and the processing of solution related information by a number of techniques. The code is interactive and is designed to run on the LTSS (CDC 7600) system available at Los Alamos. Intentions are to extend the capability of the code to include interactive graphics as soon as the hardware becomes available. The code itself is independent of the particular dispersion relation which is to be analyzed and thus has general plasma physics applications.

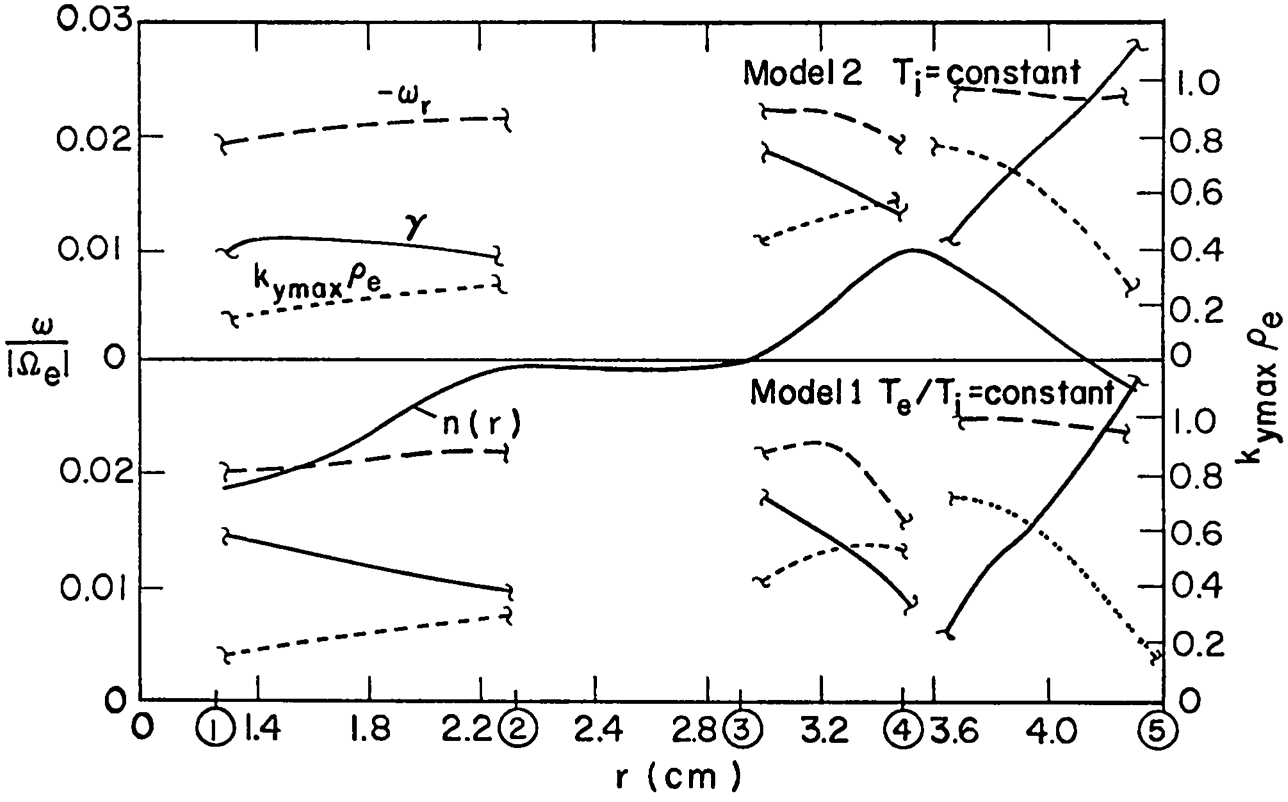

Fig. XI-6

Dependence of instability properties (frequency, growth rate, and growth maximizing wavenumber) on position within an experimental implosion sheath.

2. Nonlinear Theory. The discovery of the general dominance of the lower-hybrid drift instability over the modified-two-stream instability strongly suggests that the calculation of anomalous transport coefficients associated with microturbulence due to the lower-hybrid-drift instability is of paramount importance in understanding the macroscopic characteristics of high-density pinch implosions. Quasilinear theory was applied to study the nonlinear development of the lower-hybrid-drift instability and the anomalous heating rates and resistivity due to this mode were calculated in a regime ($V_E \leq 3V_{thi}$) heretofore not explored theoretically. Also, upper bounds for the effective collision frequencies for the various anomalous processes were obtained using the thermodynamic method of Fowler[17] to obtain an upper bound on the unstable fluctuation energy. It was found that intense plasma heating can occur when the cross-field electron E×B velocity (V_E) is comparable with the ion thermal velocity (V_{thi}) as well as in the large drift velocity regime ($V_E \gg V_{thi}$) previously discussed by Liewer and Krall.[18] This result is imortant in understanding the experimental observation that in the late stages of theta-pinch implosions the plasma is hotter than is predicted by existing theoretical estimates and fluid-numerical studies. Furthermore the quasilinear analysis indicates substantial anomalous resistivity when $V_E = v_{thi}$, a result which is in keeping with the observation of enhanced broadening of profiles during the late stages of implosion. Details of the results summarized above may be found in Ref. 19.

In addition to its relevance to the late stages of theta-pinch implosions, the theory appears to have application to ZT-1. ZT-1.[20] A recent survey by Gerwin[21] of the instabilities which could contribute to anomalous resistivity in Z-pinches reaches the conclusion that the hot ion ($\omega/kV_{thi} \leq 1$) version of the lower-hybrid-drift instability is probably the most important instability. In the limiting case $V_E \leq V_{thi}$ analytic expressions for the anomalous resistivity have been obtained and preliminary comparisons of the theoretically predicted resistivity with measured resistivity in ZT-1[22] are very encouraging.[23]

O. Electromagnetic Ion Cyclotron Instability Driven by Ion Energy Anisotropy in High-Beta Plasmas

Low frequency ($\omega \approx \omega_{ci} = eB_o/m_ic$) transverse electromagnetic perturbations propagating parallel to a confining magnetic field $B_o$êp07~z are shown to exhibit instability in the presence of ion energy anisotropy with $T_{i\perp} > T_{i\parallel}$. The characteristic maximum growth rate for $T_{i\perp} \gg T_{i\parallel}$ is $\gamma_m \approx (\beta_{i\perp}/2)^{1/2}\omega_{ci}$, where $\beta_{i\perp} = 8\pi n_i T_{\perp\perp}/B^2_o$, and the wavelengths corresponding to instability are of order c/ω_{pi}, where ω_{pi} is the ion plasma frequency. Within the context of a quasilinear model, it was shown that the characteristic time scale for energy isotropization through nonlinear response of the ions to the instability is several γ^{-1}_M. Since $\gamma^{-1}_M \ll \tau_{ii}$ (the ion-ion binary collision time) in typical high-density pinch experiments, this instability appears to provide a viable collective mechanism for ion energy isotropization during the implosion or post-implosion phases of these experiments. [The mirror instability is sometimes invoked in this regard. However, the corresponding (MHD) growth time predicted by theory is much longer than the characteristic growth time for the instability considered here.] It is also found that the instability persists in the limit of weakly magnetized ions ($|\omega + i\gamma| \gg |\omega_{ci}|$, $k^2_z r^2_{Li} \gg 1$) and strongly magnetized electrons ($|\omega + i\gamma| \ll |\omega_{ce}|$, $k^2_z r^2_{Le} \ll 1$) provided the local $\beta_{i\perp} \gg 1$.

P. A Hybrid-Kinetic Model for High-Beta Plasmas

A hybrid-kinetic model for describing collisionless, high-β plasmas has been developed and preliminary applications made to the equilibrium and stability properties of linear pinches. The model is applicable to high-β plasmas in which the characteristic ion Larmor radius is comparable to the macroscopic $\sim \epsilon \ll 1$).The ions are described by the exact Vlasov equation, with no assumption that the ion gyroradius is small. A drift-kinetic description is employed for the electrons, assuming $\omega/\omega_{ce} \sim r_{Le}/L \sim \epsilon$ and $V_E/V_{the} \leq 1$, where V_E is the E×B drift velocity. In this model, the electrons behave as a fluid perpendicular to the field lines but exhibit kinetic behavior along the field lines. The description is applicable in general magnetic field configurations and on time scales relevant to both the implosion and post-implosion phases of high-beta pinch experiments.

The hybrid-kinetic model is an important extension of and supplement to existing theories.[24,25,26] The particle distribution functions and the electromagnetic fields are calculated self-consistently to first order in ϵ. To lowest order the *electron* drift-kinetic description is identical to the guiding-center formalism of Grad.[24] However the inclusion of first-order electron inertial effects,[25] together with the fully kinetic treatment of the ions, allows the application of the present work to experiments (high-beta, implosion and post-implosion time scales) and instabilities (.e.g, lower-hybrid drift) where the earlier theory[24] is invalid. The hybrid-kinetic description is closely related to the Vlasov-fluid model of Freidberg.[26] However, the treatment of the electrons in the present work includes physical effects (.e.g, finite electron temperature and parallel kinetic behavior) that are absent in the Vlasov-fluid model,[26] as well as physical effects (e.g., electron inertia) that are important on the relatively fast time scale $\omega_{ci} \leq \omega_{ce}$. It is hoped that this model will lead to a better understanding of the implosion and post-implosion phases of current high-beta experiments.

Linear Analysis of Inhomogeneous Vlasov Equilibria

1. Introduction. Study of inhomogeneous equilibria of collisionless plasmas is important for understanding the stability properties of hot experimental plasmas produced in θ- and Z-pinch devices; these experimental plasmas are, of course, always inhomogeneous and of finite extent. Because most of the theory for high-β plasmas is based on linearized treatments of the ideal MHD model, a major objective of studies based on collisionless or hybrid models is to assess the modifications of linearized MHD predictions by finite gyroradius effects.

For several years a program has been underway to develop effective means for studying the linearized behavior of perturbations of inhomogeneous equilibria in which at least one of the plasma components obeys the Vlasov equation. A formulation has been developed that is amenable to numerical evaluation, as it must in order to be applicable in a useful way to actual experimental devices, and practical techniques for the numerical evaluation have been developed. During the past year intensive work has been carried out employing these techniques in the application of the Vlasov-fluid model to the sharp-boundary screw pinch. It has turned out that difficulties encountered over a year ago in this work were due to imperfect understanding of how the Vlasov-fluid model itself is to be expressed when applying it to a plasma with a sharp boundary; no problem has been found with the general method of studying linearized behavior about inhomogeneous equilibria. The question of how a sharp boundary should be treated within the framework of the Vlasov-fluid model has been resolved, and the numerical studies will recommence.

Work on the sharp-boundary screw pinch has led to involvement with the MACSYMA symbolic manipulation computing system, to calculation of compressible MHD growth rates for a sharp-boundary screw pinch, and to the formulation of a two-fluid model for this problem. The method for studying the properties of inhomogeneous equilibria that is being used with the Vlasov-fluid model has been extended to cover rather general situations, and is being applied to one-dimensional, electrostatic equilibria. In addition, a similar formulation has been made for the two-dimensional guiding-center model.

Some of the basic numerical methods being used were introduced as part of a different, but closely related, computational scheme for studying the linear properties of a homogeneous, one-dimensional, single-species equilibrium where the equilibrium velocity distribution was arbitrary.[27] However, attempts to generalize that scheme to include inhomogeneous electrostatic equilibria were unsuccessful. It appeared to be impossible to preserve certain quite useful formal aspects of the scheme. Despite this failure, it turned out to be possible to develop a similar scheme which could be used to implement the Vlasov-fluid model, which treats collisionless ions and massless electrons in a low frequency approximation.[28-30]

The scheme for applying the Vlasov-fluid model required a realization that expansion of functions of position and velocity in terms of eigenfunctions of the unperturbed Liouville operator is very useful; it required development of effective numerical methods for solving a type of very large eigenvalue problem;[30,31] and it required an extension to more than one dimension of a previously developed method of choosing and evaluating matrix elements. The method of evaluating matrix elements in more than one dimension amounts to a general method of approximating multiple integrals over arbitrary domains. These developments allowed extension of the scheme to include inhomogeneous electrostatic equilibria and other, more general, situations.

2. Small Ion-Gyroradius Limit of the Vlasov-Fluid Model Applied to a Sharp-Boundary Screw Pinch. The numerical computations for sharp-boundary screw pinches that were discussed in the previous Annual Progress Report[31] indicated a need to understand the small ion-gyroradius limit of the Vlasov-fluid model as applied to a sharp-boundary screw pinch, and an intense effort was made to obtain an analytical understanding of the small ion gyroradius limit with the help of the MACSYMA symbolic computation system at the Massachusetts Institute of Technology. A different but parallel effort was undertaken by R.A. Gerwin. The original motivation for the analytical work was to provide a firm basis for checking the computer code and to determine optimal boundary conditions on the expansion functions for the perturbed vector potential at the sharp boundary. In fact, conditions that were used for the numerical computations were incorrect and that the basic equations must be modified somewhat because of the presence of a sharp boundary. The correct boundary conditions and form of the equations are now known, and thus much of the original motivation for the analytical small gyroradius work is no longer applicable. Nevertheless, it is still of interest to obtain analytical results on the nature of the eigenfrequency spectrum for small gyroradius, and so the small gyroradius approximation will be carried to a conclusion.

The approach being followed with the small gyroradius calculation parallels the formulation used for the numerical computations and makes no approximation other than small ion gyroradius. The calculation focuses on the elements of the matrix that determine the natural eigenfrequencies of the system by the condition that its determinant vanish. For the analytical evaluation of the matrix elements, an infinite series was summed in closed form and the matrix elements were thereby reduced to five-fold integrals. In order to perform the integrations, the integrands must be simplified considerably. This can be done by means of an approximation valid for small ion gyroradii. This approximation is being carried out and the integrals are being performed with the aid of the MACSYMA symbolic computation system at the Massachusetts Institute of Technology. The matrix elements are being evaluated to zeroth, first, and second order in the ion gyroradius for arbitrary ω/ω_c, k, r_0, and m, where ω_c is the cyclotron frequency, r_0 is the equilibrium plasma radius, and the θ and z dependence of perturbations is given by $\exp[i(m\theta + kz)]$.

This calculation has turned out to be quite ambitious, even with the aid of MACSYMA. When it is finished, the results should be useful in understanding the Vlasov-fluid model better, in providing analytic expressions for the eigenfrequency spectrum from zeroth through second order in the ion gyroradius, and in providing direction for future analytical work and improvements in methods for numerical evaluation of the Vlasov-fluid model.

3. Vlasov-Fluid Model for a Sharp-Boundary Equilibrium. When the Vlasov-fluid model is applied to an equilibrium with a sharp boundary, at which individual ions reflect specularly in the rest frame of the boundary, it is necessary to impose appropriate boundary conditions on the perturbed vector potential. The basic Vlasov-fluid equations do not provide the boundary conditions because the delta-function electric field at the boundary couples to the discontinuity in the perturbed magnetic field. The origin of the electric field is as follows. The electrons are massless, and are therefore tied to magnetic field lines. The ions, because of their finite gyroradii, try to expand beyond the region to which the electrons are confined, thereby generating a sheath whose thickness is on the order of an ion Debye length. In the sharp-boundary idealization the sheath thickness is assumed to be zero and so the sheath electric field must be taken as a delta function. It can be demonstrated that the correct magnetic boundary conditions at such a sharp boundary are that the normal component of the perturbed current density vanish and that the normal component of the magnetic field be continuous. Two consequences of the vanishing of the normal component of the current density appear to be significant in determining the physics contained in this sharp-boundary problem: (a) one of the expansion functions for the vector potential corresponds exactly to a state of the system in which all perturbed current flow only on the surface. (b) The dispersion function that determines the eigenfrequencies now has a form characteristic of a second-order differential equation in time such as a fluid equation of motion.

In addition to the question of magnetic boundary conditions there is the separate question of the appropriate form of the Vlasov equation when the system is enclosed by a moving, specularly reflecting boundary. This is related to the problem of the description of a gas by the Boltzmann equation when the gas is in a cylinder with a moving piston. We have found an elegant way of deriving the correct form of the Vlasov equation through making a time-dependent transformation of the phase space and perturbing about a time-dependent zeroth-order state that includes the equilibrium but also takes some effects of the moving perturbed boundary into account to first order. By the introduction of suitably defined new dependent variables to replace the perturbed vector potential and distribution function, the basic equations of the Vlasov-fluid model for a sharp-boundary equilibrium can be brought into a form that is very similar to the equations for a diffuse equilibrium.

4. Compressible MHD Growth Rates. The ideal MHD equations with an arbitrary compressibility γ were used for determining the eigenfrequency spectrum for a sharp-boundary screw pinch. Growth rates for various values of γ will be compared with growth rates determined from the Vlasov-fluid model.

5. Two-Fluid Model. A two-fluid model has been formulated for a sharp-boundary screw pinch as a possible phenomenological alternative to the Vlasov-fluid model for providing finite gyroradius corrections to MHD.

6. BGK Equilibria. A formulation of the linearized problem of electrostatic perturbations about an inhomogeneous equilibrium is being investigated which is analogous to the method being used with the Vlasov-fluid model. Specific problems are being studied from an analytical viewpoint. As with the Vlasov-fluid model, important features are that functions of position and velocity are expanded in eigenfunctions of the unperturbed Liouville operator, and that the expansion functions for the perturbed scalar potential are determined by the nature of the equilibrium inhomogeneity. A preliminary report on this work has been written (University of Wisconsin Plasma Studies Report PLP 573 by K.R. Symon).

7. General Vlasov Equilibria. A general approach has been developed for studying the linearized behavior of inhomogeneous equilibria in which one or more particle species are treated collisionlessly. The formulation is a generalization of the work underway on the Vlasov-fluid model and BGK equilibria. A previous restriction to equilibrium distribution functions that are functions only of the total energy has been removed, and we can now treat equilibrium distribution functions that are functions of all of the global constants of motion. Also, it is now possible to include a wide class of possible field operators whose eigenfunctions can be used as expansion functions for the perturbed potentials. This allows a desirably wide latitude for choosing the operator on physical grounds. In all cases the final equations to be solved are of a type that can be effectively treated numerically with techniques developed by Buzbee, Golub, and Lewis for the Vlasov-fluid model. It has been demonstrated that the eigenfunctions of the unperturbed Liouville operator that are used can be found analytically if there is at most one non-ignorable coordinate in the equilibrium. In that case the eigenvalues are always of the same form and an infinite sum over the eigenvalues can be performed in closed form. A preliminary report of this work has been written (University of Wisconsin Plasma Studies Report PLP 577 by K.R. Symon).

8. **Guiding-Center Model.** In an effort to elucidate further the numerical approach that is being applied to study the linear stability of Vlasov-fluid equilibria, we have applied an analogous approach to the simpler dynamics of single-species, inhomogeneous, two-dimensional guiding-center equilibria. Some particularly simple special cases have been found, and the initial-value problems for two of them have been solved in closed form. An interesting feature is that local density perturbations may grow and lead to spatial "clumping" even as a result of this linear analysis. Also, degenerate real eigenfrequencies can lead to growth of a peturbation.

R. Nonlinear Evolution of Vlasov Plasmas

The physically simplest Vlasov problem is the one-dimensional electrostatic problem. This has been considered as a model problem with the goal of finding more effective means of integrating the equations of motion. A significant feature of the motion is that the mapping from the phase plane at the initial time to the phase plane at any later time is measure preserving, i.e., the phase fluid is incompressible. It was conjectured that this property might be used to simplify the integration of the equations of motion.

Two aspects of this question have been considered. First, an attempt was made to simplify the exact equations of motion by the introduction of new variables which *a priori* reflect the measure-preserving property. A formalism for such a transformation is provided by the Hamiltonian formulation of the Vlasov equations. After a lengthy investigation it has been shown that it is not possible to canonically transform the exact equations in such a way that the new momenta are related to the measure preservation in any obvious way. This argument is based on a certain integrability condition which canonical transformations must satisfy. Thus, it seems unlikely that the exact equations may be simplified by imposing the measure-preserving constraint *a priori*.

A second approach is to derive approximate equations which reflect the measure preservation either exactly or to some order. An effort was made to find useful mappings which preserve measure. A number of references to this question were found in the literature, but none of these is appropriate to the Vlasov problem. If a sufficient number of degrees of freedom is retained, the algebraic relations between the variables become unmanageable.

The work to date will be summarized in a forthcoming paper which will tie together these results and indicate directions for further investigation.

S. Magnetic Field Diffusion Studies

Recent studies on the LASL toroidal Z-pinch have shown that the dominant effect limiting the containment time is the loss of initially favorable field profiles as a result of field diffusion. This has sparked interest in the properties of nonlinear anisotropic field diffusion.

A group of three 1-D codes solving for the field diffusion into a hollow cylinder were developed this year to study a classical ZT-1 type plasma. The first code solves for the diffusion of longitudinal and azimuthal fields for the case of constant conductivity and permeability. This code is a generalized version of our previous diffusion codes. The second code allows one to vary conductivity and permeability as functions of fields, (nonlinear case), radius and time.

The geometry for the 1-D anisotropic diffusion is illustrated by the drawing below.

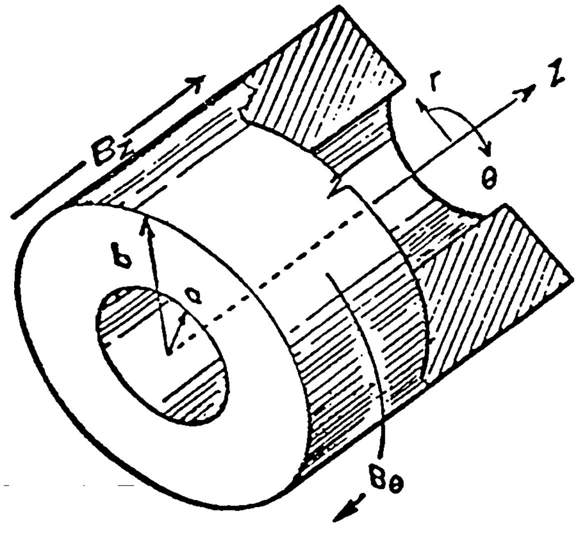

The equations that must be solved are:

$$\frac{\partial B_z}{\partial t} = \frac{1}{\mu r}\frac{\partial}{\partial r}\left[\eta_{\theta\theta} r \frac{\partial B_z}{\partial r} - \eta_{\theta z}\frac{\partial}{\partial r}\left(rB_\theta\right)\right]$$

$$\frac{\partial B_\theta}{\partial t} = \frac{1}{\mu}\frac{\partial}{\partial r}\left[-\eta_{z\theta}\frac{\partial B_z}{\partial r} + \eta_{zz}\frac{1}{r}\frac{\partial}{\partial r}\left(rB_\theta\right)\right]$$

$$\eta_{\theta\theta} = \frac{1}{\sigma_{\|}}\left[1 + \left(\frac{\sigma_{\|}-\sigma_{\perp}}{\sigma_{\perp}}\right)\left(\frac{B_z}{B}\right)^2\right]$$

$$\eta_{zz} = \frac{1}{\sigma_{\|}}\left[1 + \left(\frac{\sigma_{\|}-\sigma_{\perp}}{\sigma_{\perp}}\right)\left(\frac{B_\theta}{B}\right)^2\right]$$

$$\eta_{\theta z} = \eta_{z\theta} = -\frac{1}{\sigma_{\|}}\frac{\left(\sigma_{\|}-\sigma_{\perp}\right)}{\sigma_{|}}\frac{B_\theta B_z}{B^2}$$

where $\sigma_\perp$ and $\sigma_{\|}$ are the conductivities perpendicular and parallel to the field lines and μ is the total permeability.

These equations were solved by transforming our equation into a form that could use the linear multistep methods for solving ordinary differential equations.[32] Once the magnetic fields are obtained the current density $J=\hat{\theta}J_\theta + \hat{z}J_z$ is computed from $\nabla\times B=\mu J$ (we neglect displacement current). The electric fields then follow from

$$E=\eta\cdot J$$

where the resistivity diadic is

$$\hat{\eta}=\hat{\theta}\hat{\theta}\eta_{\theta\theta} + \hat{\theta}\hat{z}\eta_{\theta z} + \hat{z}\hat{\theta}\eta_{z\theta} + \hat{z}\hat{z}\eta_{zz}.$$

The solutions have been tested by flux and energy checks and verified with an analytical solution for a large radius case. Comparing results from these simple models with ZT-1 experiments showed that if the conductivity model is valid an anisotropic conductivity tensor must be used in the diffusion equation to explain the observed behavior of the poloidal and toroidal fields.

In particular if a scalar conductivity is used which is consistent with the observed rapid poloidal field diffusion to that of a uniform current in the pinch column, one calculates that the toroidal field will approach the vacuum field on the same time scale. The toroidal field is observed to remain peaked for the length of the experiment. This is explained by a higher conductivity along the field lines than normal to them. Theoretically the resulting peaked longitudinal field distribution for this anisotropic case persists to the steady state.

T. Mercier Localized Stability Criterion Dependence on Aspect Ratio

Our tests of stability for the toroidal Z-pinch use a discretization of δW. As a result the stability test is inherently subject to a finite resolution. To test highly localized modes we have included a separate calculation of the Mercier Q value[33] on each flux surface of the computed toroidal equilibrium. Axisymmetric toroidal equilibrium can be checked for localized, unstable ideal MHD modes by determining if $Q < 0$ on any flux surface. This test is analogous to the Suydam criterion for a cylindrical equilibrium. In fact the Mercier and Suydam criteria become equivalent as the toroidal aspect ratio approaches infinity.

Figure XI- shows how the Mercier Q value varies as a function of the aspect ratio of the device. (Aspect ratio is defined as mean radius of the torus/radius of the cross section of the conducting outer boundary.) This curve was calculated for the ZT-1 device for fixed pressure and poloidal current flux functions which are chosen to give a flat-topped reversed field profile. The peak value of plasma pressure was held fixed at a value where the straight machine is at the threshold of going Suydam unstable. The curve shows that as the aspect ratio is decreased the Mercier Q increases until the aspect ratio is about three; it then rapidly drops and the device is Mercier unstable for aspect ratios below about 2.4. While the Mercier Q value is not related quantitatively to growth rates, this curve indicates that there is an optimum aspect ratio where a device will hold the highest peak pressure without going unstable to the local modes. At the peak of the curve shown in Fig. XI-7 the device will hold 10% more plasma peak pressure before it reaches the Mercier stability threshold.

U. Automatic Experimental Data Processing

Our ultimate goal is to take experimental data from the Z-pinch experiments, digitize it and ship it to the CCF, fit the data so that it can be interpolated both in time and space, calculate quantities of interest, plot results, and display critical plots on a graphical terminal in time to help determine how the next shot should be fired. At the present time we have the codes running that fit the data with a spline and develop a plot of the data that is suitable for

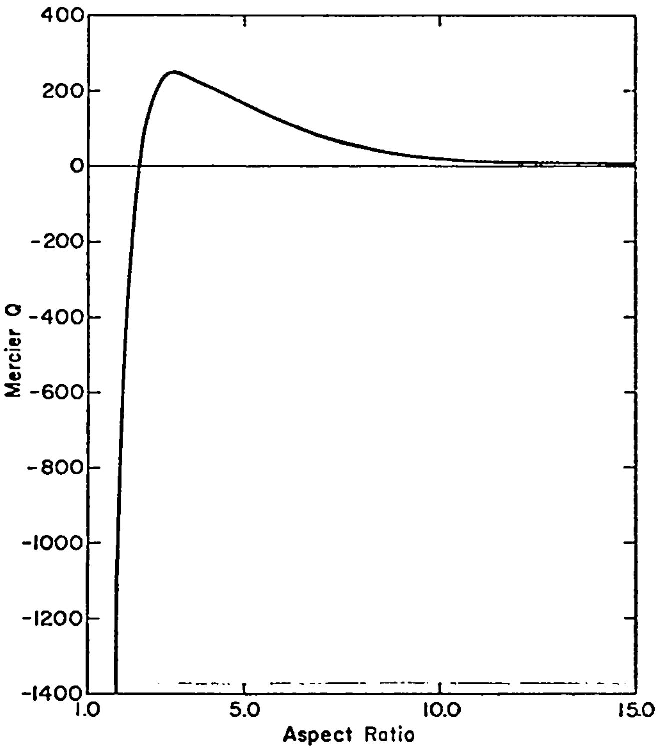

Fig. XI-7
Mercier Q value vs aspect ratio.

publication. We are planning to use the direct electronic fast scanning methods now under development to digitize the data. Provided money is available, a graphics terminal can be used advantageously with the experiment. This terminal would provide an interactive graphics capability as well.

V. Axisymmetric Toroidal MHD Equilibria and Stability Code

The following subroutines have been added to the equilibria portion of the present code.

(a) Energy subroutine which calculates the plasma energy, toroidal field energy, poloidal field energy and total field energy. This subroutine has been used to help design the new larger radius Z-pinch device.

(b) Electron velocity subroutine which calculates particle density, current density and electron velocity perpendicular and parallel to the magnetic field lines. The electron ion and thermal velocities are calculated based on input values of electron and ion temperature. This subroutine provides inputs for the toroidal case in the study of microinstabilities in ZT-1 discussed in Section M.

(c) The localized instabilities subroutine calculates the Mercier stability criterion which is a generalization to a torus of the Suydam criterion. The Mercier criterion for a large radius torus was compared with an independently coded Suydam criterion and good agreement was obtained. The ZT-1 geometry was found to be Mercier stable.

A resistive stability criterion developed at Princeton has been expressed in variables compatible with our code. We plan to have this test of localized resistive instabilities incorporated into the code soon.

W. ZT-S Design Calculations

A series of computer runs were made with our equilibrium code to aid in the design of the feed plates of ZT-S, the larger bore version of the ZT-1 experiment. The two parameters varied in this study were the half width of the plasma distribution and the poloidal beta β_p for the 4.8 aspect ratio of ZT-S.

We found that the ratio of poloidal field at the outermost major radius of the primary conductor to that at the innermost radius increased almost linearly with β_p. This ratio also increased as the half width decreased. There is a point for wide plasma distributions and low β_p where the outside field is lower than the inside field, see Fig. XI-8. The ZT-S is expected to run at a ratio ranging between 1.05 to 1.2.

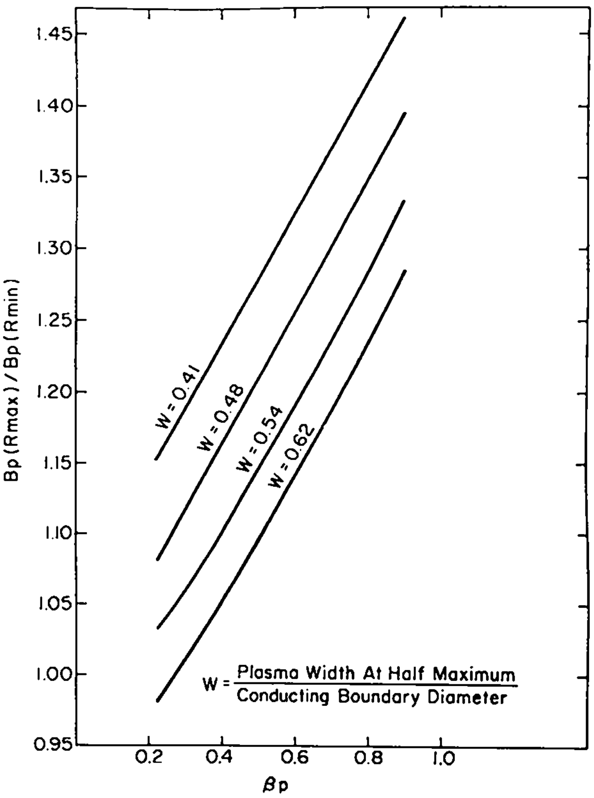

Fig. XI-8
Poloidal field ratio vs β_p.

References

1. C.W. Nielson and E.L. Lindman, "An Implicit, Two-Dimensional, Electromagnetic Plasma Simulation Code," Sixth Conference on Numerical Simulation of Plasmas (1973).

2. A.G. Sgro, CTR-6 Quarterly Progress Report, January 1, 1974 through March 31, 1974.

3. L. Spitzer, Jr., *Physics of Fully Ionized Gases, 1961* (John Wiley and Sons, New York).

4. C.G. Darwin, "The Dynamical Motions of Charged Particles," Phil. Magn. **39**, 537 (1920).

5. B.M. Marder and R.E. Siemon, "A Long Confinement Experiment (LCE) Proposal," Los Alamos Scientific Laboratory Report LA-5399-P (1973).

6. J.E. Thompson, F.C. Thames, C.W. Mastin, "Automatic Numerical Generation of Body-Fitted Curvilinear Coordinate System for Field Containing Any Number of Arbitrary Two-Dimensional Bodies," J. of Computation Physics **15**, 1974, pp. 299-319.

7. R.L. Morse and C.E. Nielson, "Numerical Simulation of the Weibel Instability in One and Two Dimensions," Phys. Fluids **14**, 830 (1971).

8. F.L. Ribe, "Proposed Experiments on Heating, Staging, and Stabilization of Theta Pinches," Los Alamos Scientific Laboratory Report LA-5026-P (1973).

9. K.S. Thomas, J.N. Downing, R.F. Gribble and R.K. Linford, "Experiments in the Staged Theta Pinch Experiment," Bull. Am. Phys. Soc. **19**, 904 (1974).

10. N.A. Krall and P.C. Liewer, "Low-Frequency Instabilities in Magnetic Pulses," Phys. Rev. A **4**, 2094 (1971).

11. K.N. Stepanov, "Stability of Ionic Cyclotron Wave in a Plasma," Soviet Phys. Tech. Phys. **9**, 1653 (1965).

12. J.B. McBride, E. Ott, J.P. Boris and J.H. Orens, "Theory and Simulation of Turbulent Heating by the Modified Two-Stream Instability," Physics Fluids **15**, 2367 (1972).

13. J.B. McBride and E. Ott, "Electromagnetic and Finite β_e Effects on the Modified Two Stream Instability," Physics Letters A **39**, 363 (1972).

14. G.S. Lakhina and A. Sen, "Electromagnetic and ∇B Effects on the Modified Two Stream Instability," Nucl. Fusion **13**, 913 (1973).

15. N.T. Gladd, "The Lower Hybrid Drift Instability and the Modified Two Stream Instability in High Density Theta Pinch Environments," submitted to Plasma Physics (1975).

16. M. Keilhacker, M. Kornherr and K.H. Steuer, "Observation of Collisionless Plasma Heating by Strong Shock Waves," Z. Phys. **223**, 385 (1969).

17. T.K. Fowler, "Thermodynamics of Unstable Plasmas," Advances in Plasma Physics (ed. A. Simon and W.B. Thompson) Vol. 1, p. 201 Interscience (1968).

18. P.C. Liewer and N.A. Krall, "Self-Consistent Approach to Anomalous Resistivity Applied to Theta Pinch Experiments," Physics Fluids **16**, 1953 (1973).

19. R.C. Davidson and N.T. Gladd, "Anomalous Transport Properties Associated with the Lower-Hybrid-Drift Instability," (to be submitted to Physics of Fluids).

20. D.A. Baker, L.C. Burkhardt, J.N. DiMarco, P.R. Forman, A. Haberstitch, R.B. Howell, H.J. Karr, J.A. Phillips, and A.E. Schofield, "Plasma Parameters and Stability of the ZT-1 Pinch Experiment," IAEA-CN-33/E3, Tokyo (1974).

21. R.A. Gerwin (to be published as Los Alamos Scientific Laboratory report).

22. D.A. Baker and R.B. Howell (private communication).

23. R.C. Davidson, R.A. Gerwin and N.T. Gladd (to be submitted to Phys. Rev. Lett.).

24. H. Grad, "Microscopic and Macroscopic Models in Plasma Physics," *Proceedings of the Symposium on Electromagnetics and Fluid Dynamics of Gaseous Plasma* Polytechnic Press, Brooklyn, New York, 1962.

25. E. Frieman, R. Davidson and B. Langdon, "Higher-Order Corrections to the Chew-Goldberger-Low Theory," Phys. Fluids **9**, 1475 (1966).

26. J.P. Freidberg, "Vlasov-Fluid Model for Studying Gross Stability of High-β Plasmas.

27. H.R. Lewis, "Linearized Variational Analysis of Single-Species, One-Dimensional Vlasov Plasmas," Phys. Fluids **15**, 103 (1972).

28. J.P. Freidberg, "Vlasov-Fluid Model for Studying Gross Stability of High-β Plasmas," Phys. Fluids **15**, 1102 (1972).

29. H.R. Lewis and J.P. Freidberg, "Application of the Vlasov-Fluid Model to High-Beta Stability," Bull. Am. Phys. Soc. **17**, 1013 (1972).

33. C. Mercier, "Critere Necessaire de Stabilite Hydromagnetique Un Plasma En Symetrie De Revolution," Nuclear Fusion **1**, 47-53 (1960).

30. H.R. Lewis and J.P. Freidberg, "Application of the Vlasov-Fluid Model to High-Beta Stability," paper 41 in Proceedings of the Fifth Conference on Controlled Fusion and Plasma Physics (Grenoble, France, August 21-25, 1972).

31. Progress Report, "LASL Controlled Thermonuclear Research Program for a 12-Month Period Ending December 1973," Los Alamos Scientific Laboratory Report LA-5656-PR (July 1974), pp. 93-4.

32. C.W. Gear, *Numerical Initial Value Problems in Ordinary Differential Equations* (Prentice-Hall, Englewood Cliffs, New Jersey 1971).

A.C. Hindmarsh, "Linear Multistep Methods for Ordinary Differential Equations: Method Formulation, Stability, and the Methods of Nordsieck and Gear," UCRL-51186.

XII. CTR ENGINEERING

E.L. Kemp, J.J. Banta, G.A. Barnes, K.J. Bickford, G. Boicourt, W.H. Borkenhagen, D.L. Call, R.S. Dike, W.D. Gutscher, R.A. Haarman, C.F. Hammer, K.W. Hanks, H.W. Harris, R.W. Kewish, K.J. Kutac, R.K. Linford, H.L. Maxwell, T.E. McDonald, J.G. Melton, G. Miller, W.C. Nunnally, L.S. Schrank, M.D. Wickham

A. System Design Construction and Operation

1. Scyllac Operation

a. Full-Torus Operation. Construction of the full Scyllac capacitor bank was completed by the end of 1973 and the three new racks of capacitors, which were constructed during full-torus conversion, were successfully fired in January 1974. Assembly of the compression coil and discharge tube was carried out during the day with system checkout being conducted in the evenings. The first full-torus plasma shot was achieved in April 1974. An overall view of the Scyllac full torus is shown in Fig. II-3.

Two-shift operation was begun in order to increase the total machine operating time. Bank voltage was normally 40 kV with a few shots taken at higher voltages. The full-torus experiments were operated for nearly eight months during which time a total of 822 shots were made with 543 of these being plasma shots. The full-torus experiment was completed in November 1974.

In the final weeks of the experiment a reverse B_0 field was applied to the full-torus plasma. The B_0 bank in each rack contains four 10-kV capacitors which were selected to total 721 μF. The B_0 field rose to a peak in 60 μs and was fired prior to the primary bank so the peak B_0 would coincide with the peak theta-pinch field. The B_0 bank voltage was varied to produce fields between 250 G and 1000 G.

b. System Modifications. When the full-torus Scyllac Experiment was put into operation the electrical noise level generated was larger than that experienced with earlier sector and linear experiments. This increased noise at primary bank time was sufficient to reset the master digital clock. This prevented the crowbar system from triggering.

To correct this problem the master clock, submaster delay chassis, slave delay units, and booster chassis were moved into the screen room leaving only the 8-kV pulsers in the high noise environment. In addition, a backup system was installed for the four crowbar pulse-charge circuits and the ten crowbar start circuits. For the normal shot this backup system had no effect; however, in the event the clock should stop or be reset after the main bank was fired the backup system fired the crowbar system 1.3 μs late.

Reliability of the crowbar system was improved by modifying the crowbar pulse-charge circuit. The original circuit used a single pulse-charge capacitor and a common inductor to fire as many as three master gaps; RG 17 DS cable was used to connect the inductor with the master gaps. High-voltage transients which occurred after the firing of the gaps caused frequent cable failures and resulted in master-gap failures. The circuit was modified by placing inductors between each master gap and the RG 17 DS cables. This change reduced the cable failures to an insignificant level.

c. Capacitor-Gap Failures. During full-torus operation (822 shots) 22 primary bank 1.85-μF, 60-kV capacitors failed. Fourteen of these capacitors shorted in service, a fifteenth unit was removed because it had a bulged can which indicates near end-of-life, and seven capacitors failed because their headers were broken due to gap malfunctions.

There were also five failures of the 0.7-μF, 75-kV capacitors which are used in the crowbar bank. Four of these were shorted and one had a broken header due to a gap failure.

A total of 176 spark gap units failed during the full-torus operation. Seven of the failures occurred in the P.I. bank, 14 in the crowbar bank, and 155 in the primary bank. The primary bank has 3150 capacitors with a start gap and crowbar gap assembled on the top of each capacitor. The losses caused by gap malfunctions made it necessary to remove 5% of the primary bank capacitor-gap units during the full-torus experiment. Table XII-1 gives the major causes of gap failure in the primary bank.

TABLE XII-1

SUMMARY OF THE CAUSES OF CAPACITOR GAP FAILURES

Cause	Quantity
RG 14/59 trigger cable, failed inside gap, destroying crowbar trigger jack	71
RG 17 DS trigger cable and RG 17/14 load cable failures and/or poor electrical connections of these cables inside the gap	26
Air line failures caused by low oil level inside the gap	21
Defective isolation resistor causing bank prefire and gap malfunction	18
Internal gap malfunction (Insulator failures, tracking)	12
Loose charge leads	4
Crowbar chimney current - joint arcing	3
	155

d. Other Component Failures. The majority of components in the Scyllac machine are very reliable and have failure rates too low to be statistically significant. However, there are three components having failure rates sufficiently high to warrant comment.

The most unreliable component in Scyllac is the RG 14/59 trigger cable that transmits the trigger pulse from the crowbar trigger capacitor to the primary-bank crowbar gap. It is underrated for this service and fails in the body of the cable as well as at the terminated ends as shown in Fig. XII-1. During the eight-month full-torus experiment over 225 have failed which is more than 7% of the total installed. Even worse, failures near the terminated end of the cable and inside the crowbar gap have been responsible for more than 45% of the gap malfunctions. Two improved cables have been designed. The first would fit the existing gap hardware while the second, which has a much higher reliability than the first, would require modifying the gap hardware at both ends. Both of these cables are being considered as suitable replacements for the RG 14/59.

The second Scyllac component having a high failure rate is a 300-Ω liquid-isolation resistor. These resistors are connected in series with the charge lead of each gap and are immersed in a mineral oil bath to prevent arcing around the resistor case. The liquid resistor is sealed with a neoprene seal at the top and bottom of the case. After approximately two years the neoprene seals deteriorate and permit oil to leak into the resistor itself. When sufficient oil has entered to surround the upper electrode the resistor becomes an open circuit. During the capacitor bank charge the difference in potential becomes great enough at 30-35 kV to produce an arc in the liquid resistor. The resulting voltage pulse causes the associated primary gap to prefire; the energy from the other 209 capacitors in the rack then discharges through the one gap. The resulting forces are often large enough to break the gap nylon insulators and even crack the capacitor header. Degraded liquid resistors that can be detected by visual inspection are replaced as part of a preventive maintenance program; however, even with these checks liquid resistor failures were the direct cause of 12% of the primary bank gap malfunctions during the Scyllac full-torus operation. Defective units are being replaced with a modified version which is expected to have increased life.

The third troublesome component is the spark plug in the primary-bank crowbar gap which has a limited life of about 2000 shots. At the time this component was developed it was believed that the Scyllac experiment would not see this many shots. Half of the gaps in racks 11 through 15 have 3620 shots. When crowbar trigger shots are included, the total is over 4000. Figure XII-2 shows the comparison of new spark plugs with spark plugs used more than 2000 shots. These worn spark plugs may be adversely affecting the quality of the crowbar in racks 11 through 15 and may need to be replaced before these racks are used again in a full-torus feedback experiment. Tests are being planned to determine the effect of worn spark plugs.

e. Modifications for the Feedback Sector Experiment. After the completion of the full-torus experiment on November 22, modifications were

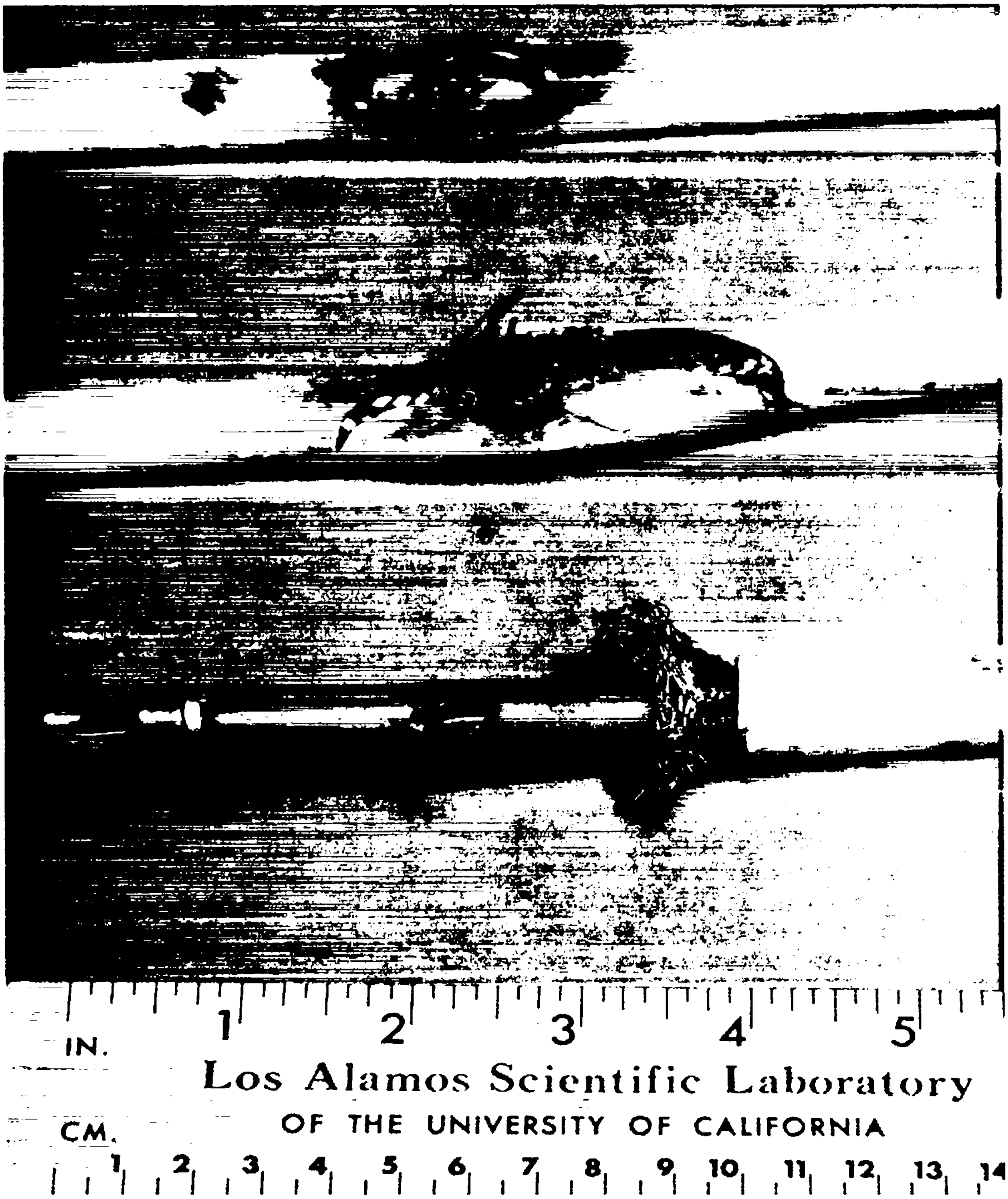

Fig. XII-2
Typical Failures of the RG 14/59 Scyllac Trigger Cable

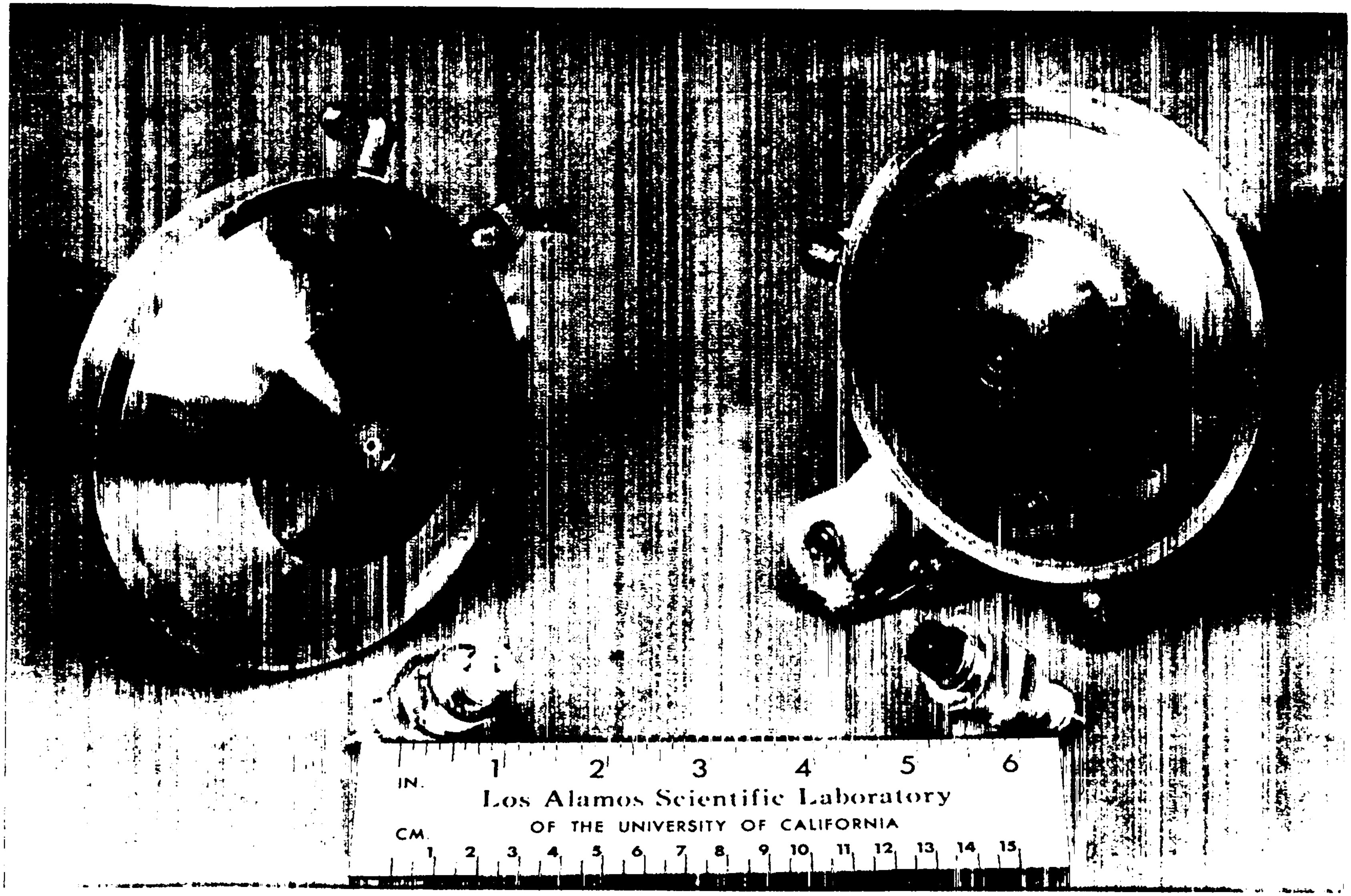

Fig. XII-3
Comparison of New and Old Scyllac Crowbar Gap Sparkplugs.

begun for the feedback sector experiment. This experiment will use racks 6 through 10 which were selected for ease of feedback module installation as well as to avoid putting additional shots on racks 11 through 15. Preventive maintenance activities were performed on the portion of racks 6 through 10 used in the feedback sector experiment. Maintenance included (a) replacement of 300-Ω liquid-isolation resistors with the modified units, which were described above, (b) restoration of liquid charge resistors to 20 kΩ, (c) installation of poly tubing over crowbar gap poly-flo nuts to prevent arcing between the metal nuts and the gap top plate, (d) restoration of oil level in all gaps.

2. Mechanical Engineering on Scyllac. The Scyllac load-coil parameters for the full torus experiment are given in Table II-1. The rather complex $\ell = 1,0$ helical flux surfaces were machined using a D'Andrea boring head with the cross sections of the coil being circular and each wavelength being made up of 330, 1.27-mm-wide machined steps. This procedure left the surfaces very rough.

The five-rack sector Scyllac Feedback Experiment requires a load coil having an average bore diameter of 24.0 cm and an $\ell = 0,1$ wavelength of 62.38 cm. The 4-m major radius is retained. Three of the existing coil sections make up a wavelength, thus, yielding 13 wavelengths for the sector with the end set of coils having an $\ell = 0$ feedback coil installed. The $\ell = 0$ feedback coils will be fabricated using RG 223 wire and terminated into a redesigned transformer unit with a plug-in cable geometry.

The load coils for the feedback experiment were machined with a new hydraulic tracing machine which was designed to bore coils with non-circular cross sections. The machine, which is shown in Fig. XII-3, has taken approximately one year to design fabricate, and make operational. The basic system consists of a male tracing template which was made on a digitally controlled milling machine, a hydraulic tracing unit which was modified extensively for the application, and a high-pressure, high-capacity oil pump. The elliptical cross section of the pattern requires a 2.5- to 5.0-cm side travel for 90° rotation of the pattern. Figure III-3 shows the helical $\ell = 1,0$ coil bore geometry for one rack of the coil system.

Design has also started on a quartz-forming machine which will form 5-, 10-, and 20-cm-diameter fused quartz tubes into helical $\ell = 1$ toroidal and linear configurations. The basic concept is adapted from a machine at the Garching laboratory in Germany, but this new design is substantially different. One machine will be utilized to form the three-diameter tubes, all with different wavelengths and helix radii. Initial operation of this machine should begin June 1975.

3. Feedback Stabilization System. The original system design of the Scyllac feedback experiment called for 60 power amplifiers to be installed on the Scyllac machine with five spares. The overall system was expected to have a delay-risetime of approximately 0.9 μs.

Construction of 65 power amplifiers was completed and 60 of the amplifiers were installed on the Scyllac machine by mid-1974. Three intermediate amplifiers with the associated position detectors were also installed and the complete system was operational by August 1974, driving dummy load coils. Noise tests were run on the feedback system under full operating conditions of the Scyllac bank. After solving some relatively minor cabling problems the noise levels at the output of the intermediate amplifiers were reduced to less than 100 mV which is less than 1% of the maximum intermediate amplifier output.

Measurements were made of amplifier risetime and frequency response. These measurements revealed some major unexpected problems with the feedback system. The problems are: (a) The delay-risetime of the system was found to be 2.1 μs instead of the expected 0.9 μs. (b) The saturation time of the intermediate transformer driving the output stage of the power amplifier was found to be approximately 15 μs instead of the expected 25 μs to 30 μs. (c) At less than full input to the power amplifier the 8618 output tube tended to arc.

The most serious of these problems is the increased delay-risetime of the overall system. In order to help relieve this difficulty the number of load coils being driven by a power amplifier was halved. Although this modification reduced the delay-risetime to 1.5 μs it also required that the number of modules be doubled. Further significant reductions will require more substantial design changes.

In order to solve the arcing problem and to reduce the delay-risetime a development bay is being constructed which will allow the necessary testing and redesign of the amplifiers to be made.

Because the required number of amplifiers has doubled, there is now an insufficient number of amplifiers to run the feedback experiment in the full-torus configuration. In addition, the increased delay-risetime means that the plasma cannot be as energetic as originally planned. As a result it has been decided to run the experiment on an approximate 120° sector of the torus with a lower

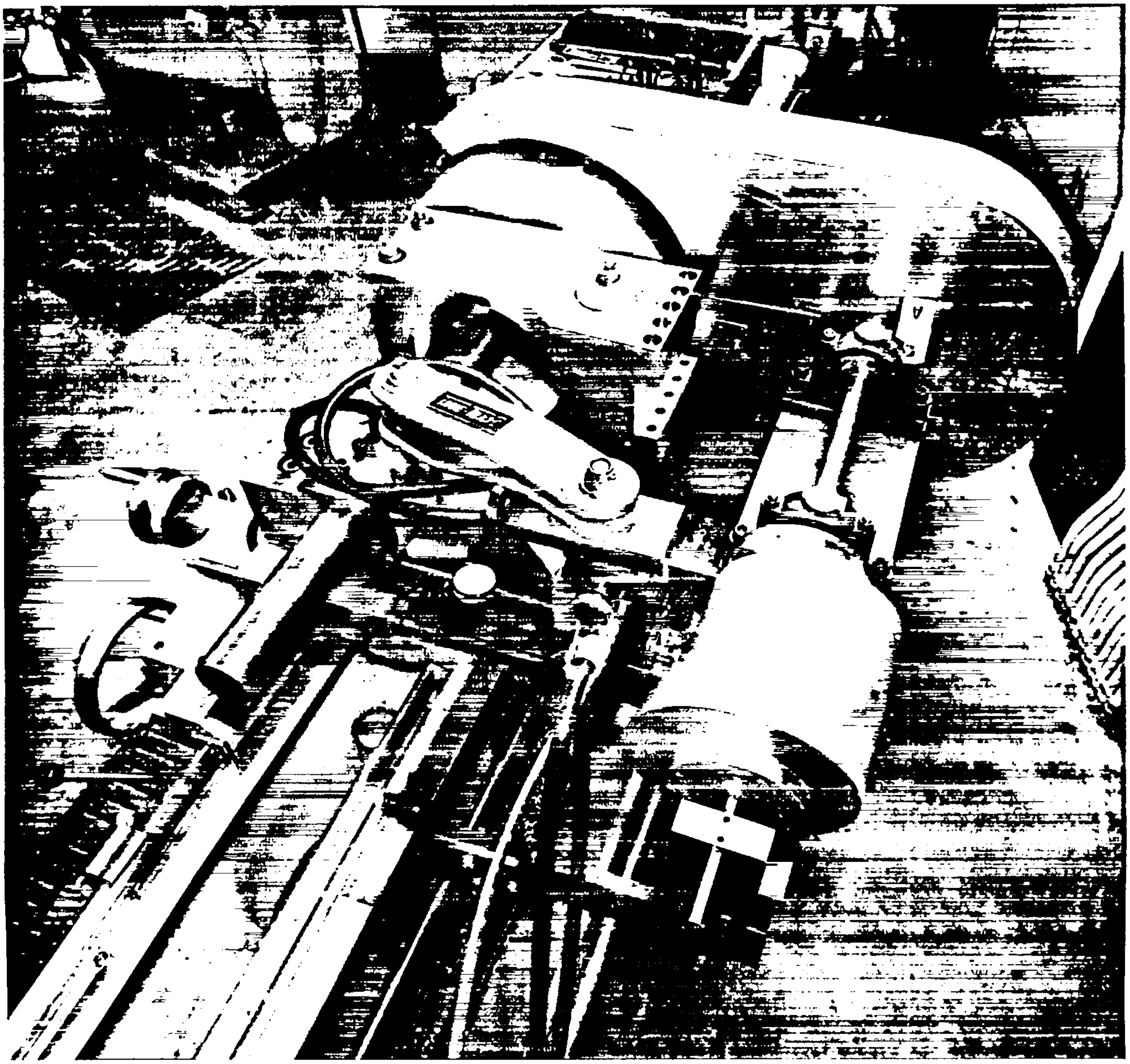

Fig. XII-4
Hydraulic Tracing Machine Used in Making Scyllac Load Coils

plasma temperature. The bore size of the machine load coils was also increased to reduce the load inductance of the feedback coils as much as possible.

Twenty-six amplifiers will be used on the sector experiment which required substantial modification of the water system, high-voltage cabling and filament wiring. As of the end of this reporting period the necessary modifications had been scheduled and were approximately 50% complete.

4. **Scylla IV-P Design and Installation.** Scylla IV-P is a 5-m linear theta pinch using 600, 1.85-μF, 60-kV capacitors in the crowbarred mode. It is designed primarily as a pulsed power supply which can be adapted to various experiments as required. Scyllac technology is being used for charging and triggering; however, rather than rack mounting the capacitors, modular mounting is being designed with 10 load capacitors and a crowbar trigger capacitor in each module.

Steel structure has been erected to divide the experimental area into three levels with the central or "B" level accommodating 200 capacitors and the collector-plate discharge tube assembly. The utilities tear-down required for the modifications has been completed and the new compressed air system is installed. The modified electrical system is designed.

Procurement of the capacitors, cables, collector plates, and gap parts is 90% complete. Available manpower is being used to assemble load gaps, shorting balls and the trigger system components while outside vendors are being employed to assemble load cables, master trigger cables, and crowbar trigger cables. The cables and load capacitors are being tested by LASL to eliminate the early failure modes.

Designs of the charging and triggering systems are 90% complete. Both systems are compatible with computer control using 5-V logic and solid-state switching where applicable. Computer control will give a degree of flexibility not previously available and will be employed at all levels of the operation. However, personnel safety is being assured by a conventional backup system which can override the computer, if required. This computer control is the major innovation in the Scylla IV-P experiment and the experience and knowledge gained in this system is expected to be valuable in future machines. The computer and most of the necessary interfacing are on hand and the 8 ft × 40 ft screen room which is required for the control system will be in place early in 1975.

5. **Toroidal Z Pinch.** The encouraging results obtained from the ZT-1 experiment during the past few years have prompted studies to be made to determine if a larger bore size could be installed within the limits of the present machine. These studies showed that an increase in bore size from 10.31 cm to 15.24 cm was possible while still using the existing iron cores and main drum headers. Figure XII-4 shows a comparison of the present ZT-1 bore and the increased bore size. New feed plates, primary castings and larger ceramic torus sections were designed and fabricated and are now being readied for the transitional installation. This larger geometry, known as the ZT-S, will provide the experimenter with many advantages which were not possible on the ZT-1 experiment.

The larger torus size, necessitating higher currents, has required new feed points designed for a double fuse capability and will use a special high-energy fuse package specifically developed for this purpose.[1] This package is a self-contained assembly and will provide for an inverted mounting arrangement with assurance that no sand or debris will be expelled into the collector plate region. Higher currents and larger bore size will also produce an improved magnetic field diffusion in the plasma which is expected to increase the plasma confinement time.

Peaking capacitor studies and experimentation are continuing using the existing header design and the Maxwell 0.08-μF, 100-kV capacitor.[1] While this particular arrangement is not considered ideal for future system designs of this type, it is nonetheless valuable to test the peaking capacitor concept while also testing various transfer switch geometries. Two types of switches are currently being tested. One is an enlarged version of the transfer switch used on the ZT-1 experiment. This switch is of the trigatron variety but has a specially contoured electrode and insulator designed in such a manner that prefire possibilities are reduced by assuring a compatability of electric field gradients within the gap. The second type switch is of the field distortion variety where its center electrode passes through the top electrode in an insulating fashion and is conveniently energized from the top of the gap geometry. Further tests on both switches are anticipated and actual plasma generation using this device will be performed.

Plans are being formulated for a new Z-pinch machine and some conceptual design and planning is now underway. This new concept, tentatively dubbed ZT-SP, again will have an increased bore

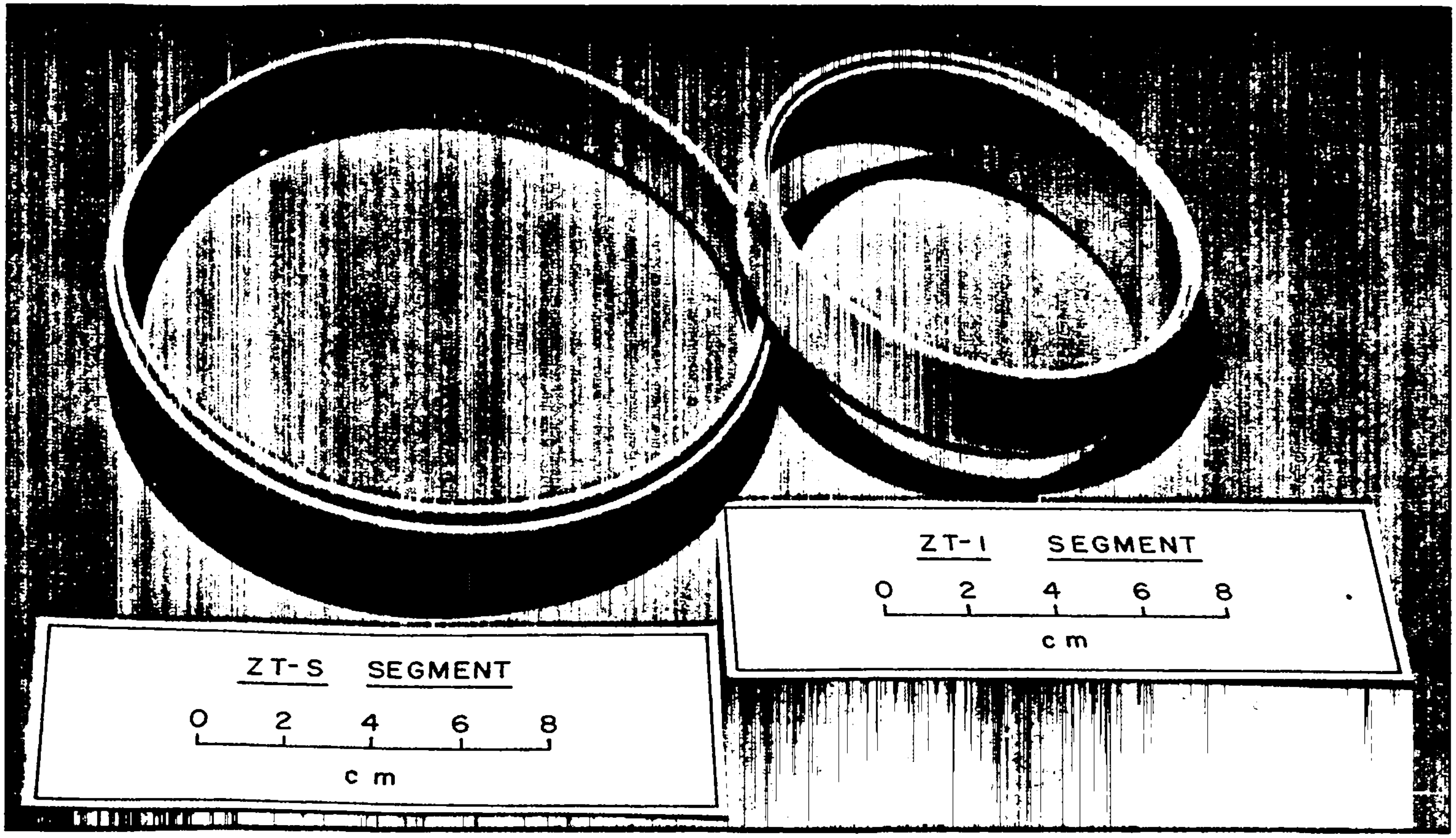
ZT-I SEGMENT
0 2 4 6 8
cm
ZT-S SEGMENT
0 2 4 6 8
cm

size with a minor diameter which is in the range of 25 to 30 cm. The major diameter will also increase but will be a function of feed point design, volume of iron required, and consideration of an appropriate aspect ratio. Improved peaking capacitor techniques will be included and other capacitors more suited to the constraints of this particular design will be employed.

B. Advanced Development

1. Scyllac Fusion Test Reactor (SFTR) Components

a. Crowbar Ignitron and 10-kV Capacitor Development. The Magnetic Energy Transfer Storage (METS) System of the proposed SFTR requires a large capacitor bank of approximately 200-MJ stored energy. The system also requires a crowbar that is capable of circulating 1000 C of charge and 60-kV pulsed operation. Prototype components for the crowbar and capacitors have been tested during the past year with a total of 85,000 full voltage shots being fired in the component test bay. The testing process involves discharging 10 parallel, 170-μF, 10-kV capacitors into a dummy load at full 10-kV charge and crowbarring the resultant 100 kA with an L/R decay of 4 ms.

The test capacitors have performed exceptionally well with eight of the original ten capacitors still in service after 200,000 shots. Variations of the basic 10-kV, 170-μF capacitor have been ordered from Aerovox Industries, Inc., General Electric Co., Maxwell Laboratories, Inc., and Sangamo Electric Co. for test and evaluation to develop a lower cost, more reliable capacitor for eventual use in SFTR.

The presently available size-D ignitron is being evaluated for use as the SFTR crowbar. The industry rating of the size D ignitron is 200 C; however, a total of 10 size-D ignitrons have been tested and 6 of the 10 have gone over 10,000 shots each at 400 C. The greatest single problem is the anode current joint which, it is felt, can be corrected quite easily. A new dummy load is now being installed to increase the L/R decay time of the circuit which will allow the ignitrons to be tested beyond the 400-C level now attainable. The size-D ignitron has demonstrated the capability of maintaining an 800-C charge for a few shots in the CTR-9, 300-kJ facility which indicates the potential for their use as the SFTR crowbar.

b. 60-kV High-Density Capacitor Development. A development program was started this past year to develop a high-density, 60-kV capacitor for use in Scyllac and future systems where a crowbarred application is required. The standard 1.85-μF, 60-kV capacitor was developed for an oscillatory discharge with 85% reversal, while in a crowbarred circuit, such a high-voltage reversal capacitor is not required. The high-density capacitor under development will store 5 kJ in the same size can as the present 3-kJ Scyllac capacitor. The ultimate goal of the program is to produce a 60-kV capacitor that is more economical than the 15 cents per joule, standard 60-kV capacitor.

A high-voltage test bay has been built to test four 60-kV capacitors simultaneously. The capacitors are charged to 60-kV and discharged into a crowbarred RG 17 cable load every 10 s. The first series of test capacitors were made with 0.9 gm/cm^3 paper which is somewhat less expensive than the 1.0 gm/cm^3 paper. Six capacitors were ordered from each of the manufacturers, Aerovox, Maxwell and Sangamo. These capacitors were made to the 1.85-μF, 60-kV specification so that the 0.9 gm/cm^3 paper could be evaluated against the well known 1.85-μF, 60-kV capacitor characteristics. Twelve capacitors (six each from Maxwell and Aerovox) have been tested to end-of-life with promising results but the capacitors from Sangamo have not yet been received.

A second series of six capacitors were ordered from the same companies for a 2.85-μF, 60-kV non-reversing capacitor. The order from Aerovox has been received and awaits testing.

2. Gap Development. In order to carry out staging in the Staged Theta Pinch (STP) Experiment a low-inductance, high-capacity spark gap is needed between the 50-kV high-energy capacitor bank and the PFN collector plates. To achieve the necessary low inductance a multichannel rail gap configuration was selected for the design. The basic requirements of the gap are:

Voltage Holdoff = 50 kV dc; 125 kV pulsed

Peak Current = 380 kA

L/R Decay Time = 30 μs

Total Charge = 11.5 C

Four prototype designs have been constructed and evaluated. All four designs used rails 15-cm long; however, different rail diameters and spacings were employed in the designs.

The first design uses rails which are approximately 2.5 cm in diameter with a 2-cm separation. It was found that the charge carrying capability of this design was inadequate due to the small volume of the gap chamber and a second design was made using the same rails but having a larger gap chamber volume with spring loaded end plates to relieve the overpressure. This design was able to carry 14 C; however, the chamber walls still cracked due to the shock wave of the discharge. In the third design rails having a 5-cm radius of curvature with a 1-cm separation were used and a stronger gap chamber was designed. The larger rails were chosen to distribute the shock from the discharge over a larger area of the chamber walls; however, tests showed that spring loaded end plates were still necessary due to the chamber over-pressure.

The third design was selected as being basically satisfactory. The parameters of the design are as follows:

Fill Pressure = 400 to 700 kPa of air

Peak Current = 380 kA

dc Voltage Holdoff = 50 kV

Pulse Voltage Holdoff = 125 kV (with ± 50 kV dc)

L/R Decay Time = 30 μs

Total Charge = 11.5 C

It has also been found that the gap has the ability to withstand occasional prefire conditions (single current channel operation). Successful operation of this gap, however, depends on a fast rising trigger pulse of approximately 15 kV/ns.

The design which will be used in the staged theta-pinch machine is basically the third gap design with some relatively minor modifications in the header and collector plate connections which provide a more convenient integration into the staged theta-pinch machine and also eliminates some troublesome oil splattering. As a result of the modifications a voltage holdoff problem now exists. This difficulty is expected to be solved by installing a solid epoxy-cast chamber in place of the present chamber. The present design has the following voltage ratings:

PFN Voltage	Maximum dc Bank Voltage
90	40 kV
110	25 kV
125	0

These conditions are acceptable for initial operation of the STP experiment. When the experiment has progressed to just the point that higher voltage operation is required, the gaps will be retrofitted with the new chamber. Figure XII-5 is a photograph of the final gap design mounted on a test stand.

C. Engineering Analysis

1. Cable Development

a. Semi-Emperical Design of Optimal Coaxial Cable. Coaxial cables are used extensively in CTR at voltages much higher than manufacturers' ratings. One reason is that the large number of cables needed to handle the current requires a minimum cable diameter so the cable bulk can be fitted into the space available. Heretofore, a number of cables have been designed, mainly by educated guess, and these cables have operated more or less successfully. It appeared that it might be possible to use the data obtained from testing and operating previous cable designs to design new cables and to design them in such a way that the cable diameter would be a minimum for a given operating voltage and inductance. Such an analysis has been carried out.

Three parameters were taken to be critical for CTR cable: the inductance, the peak operating voltage, and the maximum electric field. The inductance, L, is more critical in CTR than the cable impedance; moreover, in some cases it is vital that it be held below a given value. The peak voltage, V, is the maximum transient voltage that will be seen by the cable at any time during a normal operation in the projects application. Usually V will have to be computed using a circuit analysis code. The maximum electric field, E_m, is the most sensitive parameter in that it probably determines the life and failure rate of the cable. Suitable values of E_m can be estimated from the operations data on existing cables. Given these parameters and the additional condition that the cable diameter is to be a minimum, it can be shown that the inside radius of the cable dielectric satisfies the following transcendental equation:

$$V/E_m = r_i \ell n(\exp(2\pi L/\mu_o) - K/r_i)$$

where

$$K = (S_i + b_i/2) \exp(2\pi L/\mu_o) + (s_o + b_o/2).$$

Here s_i and s_o are the thicknesses of the inner and outer conducting screens and b_i and b_o are the thicknesses of the inner and outer conductors. This

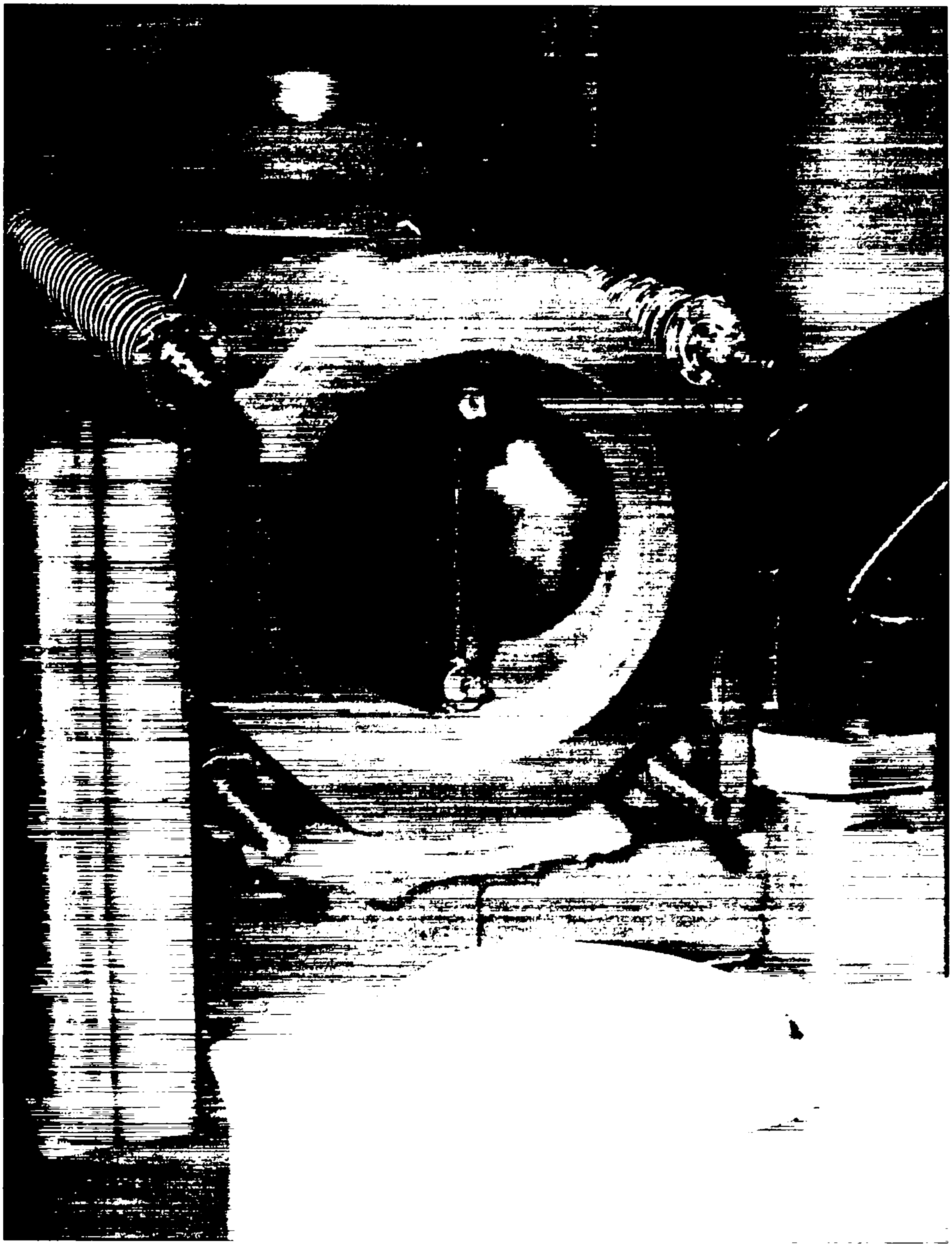

equation can be solved iteratively using the Newton-Raphson method. Once r_i is found, it is a straightforward matter to find all other necessary cable design values. Example curves of cable diameter versus inductance for constant V are given in Fig. XII-6 for a set of E_m values. It will be noted that these curves have a minimum. These minima represent the most economical designs for cable to operate at a given V and E_m provided the inductance is not important. A complete account of this work can be found in Los Alamos Scientific Laboratory report LA-5691, December 1974.

b. Cable Development Program. The pressing need for better high-voltage pulse cables has led to an extensive literature search to find methods for producing such cable. A number of promising approaches have been found and a report is being written detailing some results important for cable design and outlining a cable development program.

2. Computer Code Development

a. Electric Field Mapping. When designing components for high-voltage operation it is necessary to minimize, as much as possible, regions of high-electric field. In most instances this is done by guess or occasionally a proposed design is set up on a resistor board or in an electrolytic tank. Work with resistor boards and electrolytic tanks is tedious and time consuming.

Another method, which can be applied but is rarely used because it is difficult and also time consuming, is the numerical solution of LaPlace's equation with suitable boundary conditions using a digital computer. Numerical solutions by finite difference methods must usually be programmed individually for each problem and thus can be even more tedious and time consuming than resistor boards or electrolytic tanks. The introduction of multiple dielectrics only makes the situation worse.

A relatively new numerical method is available which can make the solutions of these problems easy and quick. This is the Finite Element Method. Finite element codes, while more complex to write initially, do not have to be altered to fit each new physical configuration and the inclusion of multiple dielectrics occurs naturally and easily. This means that a series of potential designs can be studied easily, quickly and cheaply.

The nucleus of a code to solve electric field problems has been written and tested. The finite elements used are eight-node isoperimetric quadrilaterals. These elements give considerably greater accuracy in fitting boundaries. Testing has shown that the code is quite accurate when checked against configuration for which an analytical solution is available.

Automatic data input and solution contour plotting routines are still required to make the code easy to use.

b. Inductance Calculations for dc Coils. Frequently it is necessary to design dc load coils for use in testing CTR components. The inductance of these coils must be fairly precise so that the components under test will operate at, but not over, specified ratings. Such coils must operate at high voltages and currents necessitating conductors having large interturn spacing and large cross sectional areas. Both these conditions cause the usual easy design formulas to break down. When this happens it is necessary to turn to a much more complex formula and, because it is not possiblle to solve backwards given the inductance required, one must iterate these formulas several times. Formulas such as given by Grover[2] are based on treating the currents in the conductor as being made up of multiple filamentary current. A computer program has been written which calculates the inductance of such dc coils for either square or round conductor cross section, with or without axial cooling channels in the conductor, and for any desired interconductor spacing. The program sets up a large number of current loops to simulate the conductors in the coil and then calculates the inductance contributions of each loop. The program was checked against Grover's formula for a Brooks coil and agreement to 0.0016% was achieved.

A second check was made of a Brooks coil and a round conductor. Here the solution attained was within 0.68% of that given by Grover's formula. Because there is no reason to believe that Grover's formula is any more accurate than the computer program for this geometry, it is felt that the computer program can be used when such coil calculations are required.

References

1. "LASL Controlled Thermonuclear Research Program for a 12-Month Period Ending December 1973," Los Alamos Scientific Laboratory report LA-5656-PR (July 1974).

2. Frederick W. Grover, *Inductance Calculations* (Dover Publications, Inc., New york 1946).

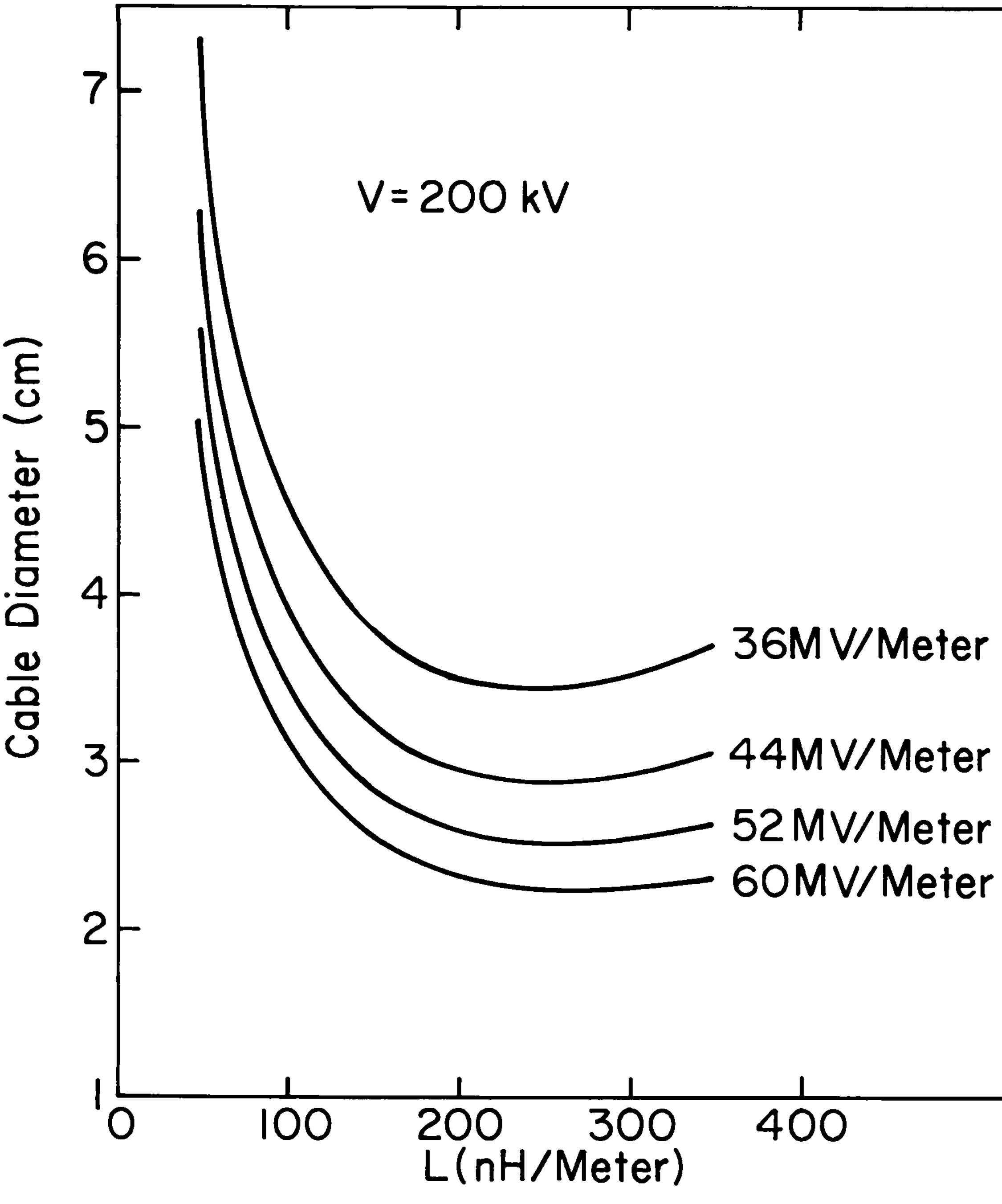
V= 200 kV
36MV/Meter
44MV/Meter
52MV/Meter
60MV/Meter
Cable Diameter (cm)
L(nH/Meter)
1
2
3
4
5
6
7
0
100
200
300
400

XIII. MAGNETIC ENERGY TRANSFER AND STORAGE (METS)

K.D. Williamson, A. Bailey, D.J. Blevins, E.G. Enderbrock, R.A. Haarman, C.R. Harder, C.G. Hoffman, J. Johnson, C.R. King, J. Lindsay, L.B. Lundberg, G.A. Miranda, R. Mjolsness, J.D. Rogers, W.F. Stewart, C.E. Swannack, W.C. Turner, D.M. Weldon, J.J. Wollan*

A. Summary

During the past year significant progress has been made toward the goal of providing superconducting magnetic energy storage for plasma compression in the next generation of θ-pinch experiments. The METS energy storage system will provide the primary energy for the compression coils in Scyllac Fusion Test Reactor (SFTR) and the staging energy requirements for the Experimental Power Reactor (EPR) torus and DEMO plant. In addition, this work will have application to other CTR programs such as ohmic heating in tokamak experiments and possible power supplies for laser flash lamps in the laser fusion program. The current program is developing the necessary components to accomplish this and will culminate in a demonstration METS-SFTR coupled superconducting prototype system. Highlights of the year include:

- A Ross Engineering Corporation interrupter was successfully operated at 12.7 kA and 41 kV. This performance exceeds the METS/SFTR requirement for a single interrupter (Section B).
- A superconducting industrial wire and coil program was initiated to provide low loss 300 kJ coils. Though progress has been slower than expected, significant information has been obtained on fabrication techniques for Nb-Ti wire (Section F).
- Two new facilities have become operable: The High Voltage Direct Current (HVDC) interrupter facility is being used to test interrupter components (Section B) and the high current test facility has been upgraded to permit testing of wire and cable up to currents of 50 kA (Section F).
- The LASL 300 kJ coil, interrupter facility and 300 kJ facility were combined for prototype METS transfer tests. Energy storage reached 250 kJ at 10 kA with 35 kV achieved during the transfer (Section B).
- Two new hardware items are under development: a cryogenic disconnect (Section H) and a flying disk interrupter (Section B). Both of these items are a result of the decision to use superconducting switches (Section E) as backup and not primary components of the METS transfer system.
- An order was placed for a 700 W, 4K ℓHe refrigerator for the prototype METS/SFTR system. Design of other major subsystems is in progress (Section H).
- A program has been initiated to measure dielectic strength, voltage tracking and arc-discharge shock-wave formation in cryogenic fluids (Section J).

B. HVDC Interrupter Facility

1. Facility. For the METS/SFTR application it was decided that an alternative was needed to replace the superconducting switch in order to reduce the load on the liquid helium refrigeration system. The most promising idea was a low resistance cryogenic disconnect to handle the charging current within the storage coil dewar, transferring the actual interruption operation to room temperature breakers through small cross section, pulsed current leads. The purpose of the facility is to provide experimental verification of successful current interruption using room temperature breakers and to test various components of the interrupter circuit.

The facility became operational in early November 1974. The first test breaker, a commercial Ross Engineering Corporation unit was operated at 12.7 kA and 41 kV without a single fault. No arc restrikes occurred. This performance exceeds the METS/SFTR requirement of 12.5 kA and 30 kV for a single interrupter. Other breakers made by Maxwell Laboratories and Avco Corp. have not yet been tested.

The system has experienced several high voltage arcing problems which have been eliminated, high

---

*Present address, General Atomics, San Diego, CA.

voltage noise triggering problems which have been suppressed, and multiple ground loop problems which are presently being isolated.

The dummy load coils used as the inductive current source for interruption have good voltage standoff but are mechanically marginal under the high current, high internal magnetic field stresses. Improved coils are planned.

The interruption facility was combined with the LASL 300 kJ coil and 300 kJ test facility to run experiments on the superconducting coil in a prototype METS/SFTR system. A knife switch paralleled the Ross Engineering breaker to allow a slow buildup of dc current in the storage coil without excessive heating of the breaker contacts. Two runs were conducted, each terminated by high voltage breakdown of the load-coil crowbar ignitrons. Before ignitron failure, energy storage reached 250 kJ at 10 kA with 34 kV achieved during the transfer.

2. Flying Disk Breaker. A LASL development program is in progress to make a fast breaker which opens under "no arc" conditions, with a gap opening velocity which exceeds the voltage rise waveform of the METS/SFTR circuit.

Hardware was devised and built to work out some of the mechanical problems associated with rapid opening and latching of the disks. This interrupter unit is shown schematically in Fig. XIII-1. The pulse coil is rapidly energized by capacitor discharge inducing several hundred kA of circulating eddy currents on the inside faces of the flying disks. The field rises to about 80 kG and the resultant magnetic pressure on the faces blows each Hisk away at $\sim 5 \times 10^4$ g acceleration.

As the disk piston unit moves to the travel limit of the cylinder, the highly compressed gas moves the valve, opening the relief port. As the gas cushion escapes, the piston head bottoms out on the valve and both move to and rebound off of the rubber bumper returning to the cylinder seal. All excess energy is dissipated in the valve wall and O-ring friction. The gas relief and heavy valve act as the dash pot.

The disk piston is vacuum latched to the valve face after the valve reseats on the cylinder. As the gas flows through the bleed-back channel to repressurize the cylinder, the disk piston slowly returns to the initial state. The pressure rises until the proper closed contact force is reached.

The opening time for the gap to reach one cm was 350 μs, with less than 5% jitter between test shots. Contact separation time is such that only a 10 μs current zero time need be applied to assure no-arc separation. A dash pot mechanism latches the breaker open for 25 milliseconds and allows a very slow closure rate to remove all mechanical shock degradation of the contacts and pulse coil. The magnetic coupling between the pulse coil and disks will be improved following initial tests of current interruption using the mechanical test prototype at low current and voltage levels.

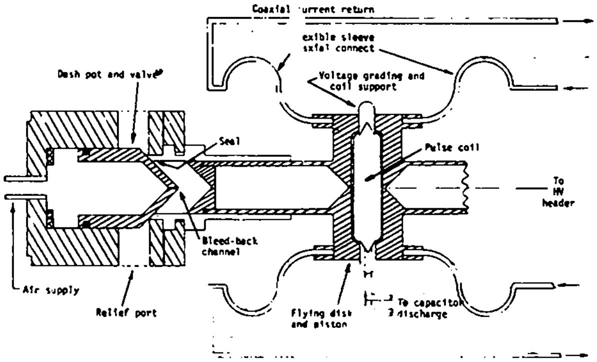

Fig. XIII-1
Flying Disk Breaker

C. 300 kJ Test Facility

The 300 kJ Test Facility became fully operationalin 1974 and has been used for testing the LASL 300 kJ storage coil (Section G) and superconducting switches (Section E). It will be used for testing the industrial 300 kJ coils as they become available. In addition, it will be combined with the interrupter facility for transfer tests involving the industrial coils. A discussion of major facility components follows.

1. Vapor Cooled High Current Leads. Vapor cooled leads for the 300 kJ coils supplied by American Magnetics Incorporated did not meet the design specifications of 12.5 kA dc current and 40 kV hold-off voltage. Two leads failed at 7 kA and 12 kA as a result of insufficient cooling, and a third failed at 10 kV. These have been replaced by leads of LASL design which have operated successfully at 12.5 kA and 35 kV.

2. Superconducting Switch Components. The high voltage trigger system used to drive superconducting switches normal is operating satisfactorily. A sensor to monitor the coil and switch voltage in order to detect accidental switch transitions to the normal resistance state was installed and is operational. This monitor drives the switch trigger on and forces the switch completely normal before localized damage can occur in the switch conductor.

3. 10 kA Homopolar dc Generator. This generator is used as the power supply for the 300 kJ facility. It was acoustically shielded with fire retardant material reducing the noise level from 85 dB to 67 dB. A severe brush problem exists above 6 kA dc current. Metallurgical analysis by CMB-6 followed by consultation with the electrical brush industry indicated that the brush composition was wrong for operation at the high altitude (0.78 atm ambient pressure) and in the dry environment of Los Alamos. A new set of brushes has been ordered.

4. Control Electronics, Data Acquisition Hardware, Screen Room. Several ground loops from the 300 kJ facility controller to the high current system, the switch trigger system and the screen room were removed to eliminate false noise triggering and to remove voltage baseline shifts in the oscilloscopes. In addition all data acquisition oscilloscopes have been isolated from each other and from ac power grounds. Each oscilloscope has one reference ground to the high current system. Baseline shifts of the current measuring scopes have been reduced to less than 5%.

5. 12 kA Rectifier Power Supply. A 12 kA, 20 V dc rectifier power supply was installed as a backup to the homopolar generator, and later will be used in parallel with the homopolar to develop the total 25 kA needed for testing prototype METS/SFTR storage coils. Several internal faults were found and repaired. The unit was reworked to improve the circuit. It now turns on at one volt open circuit, or at 50 mV and 250 A when the output bus is shorted.

6. Bolted Current Connectors. An extensive analysis has been carried out on the energy loss problems associated with the bolted current connectors to be used with the 300 kJ test coils. A code which evaluates the propagation problems associated with the transition to the normal state was written based on a model by Stekly.[1] It appears that for a discharge time equal to or faster than 10 msec the I^2R losses are less than 25 J. The heat conducted along the superconductor into the shrouded area is of the same magnitude.

7. Coil Shroud. A shroud for the 300 kJ coils was designed and is being procured. This shroud encloses a coil being tested in ℓHe and collects gas evolved by the coil thus giving a measure of the energy dissipated during discharge.

D. 30 kJ Energy Transfer System

The 30 kJ apparatus originally built to test superconducting switches and other components on a small scale was reactivated to study the energy required to completely switch superconducting switches to the normal state and to hold them normal long enough to begin the energy transfer. In addition the apparatus will be used to investigate energy transfer into resistive loads using different values of transfer capacitance and load resistance. Improved reproducibility and measurement accuracy were obtained from the apparatus by replacing the external electrolytic resistors with stainless steel units.

The relative merits of spark gaps and silicon control rectifiers (SCR) as high-current, high voltage, fast turn-on devices were investigated. It was concluded that the additional costs of an SCR system could not be justifiied.

Theoretical calculations of the current/time profiles for 30 kJ energy transfer were made for various capacitance values from 10 μF to 3.4 mF. The experimentally determined waveforms confirmed the calculations.

E. Superconducting Switch Development

During the year more than 20 different switches were designed, built, and tested. These switches generally fall into four basic types: (a) counterwound spiral or Ayrton-Perry, (b) bifilar wound pancakes or hairpin pancakes, (c) circular braid over an insulating tube or sleeve braided switch, and (d) stacked hairpins or accordion type switch. The essential characteristics of each type are as follows: Ayrton-Perry— low inductance, easily cooled, good voltage standoff, poor packaging density; hairpin pancake— low inductance, poor cooling, poor voltage standoff, excellent packaging density; sleeve braided switch— low inductance, good cooling, good voltage standoff, reasonable packaging density; hairpin accordion switch— low inductance, reasonable cooling, good voltage standoff, good packaging density.

Major emphasis has been placed upon the sleeve braided and accordion switches. Several of each of these types have been built and tested. Low voltage quenching currents of 1700 A and 2600 A have been achieved for sleeve braided and accordion switches respectively.

Five of the accordion switches were connected in parallel and operated at a current of 8000 amps in the 300 kJ test facility. A high voltage arc occurred at a void in the epoxy casting in one of the five modules which damaged the module. The parallel combination switch will be rebuilt and tested again on the 300 kJ storage coil. The superconducting switch development will be brought to a conclusion with the completion and testing of this switch and a parallel combination of circular braided switches.

Experiments were also performed to measure the switching speed of the superconducting wire used in the switches. The wire was switched from the superconducting to normal state by slowly increasing the current through the wire until it started to go normal. The resistance was measured as a function of time thus giving a propagation rate for the normal superconducting interface. Results of these measurements gave velocities of the order of 5000 cm/s at a time 1 ms after driving a point normal and velocities of the order of 50 m/s 25 ms later.

F. Superconducting Wire Development

1. Industrial Status. The performance specifications for the industrially fabricated 300 kJ energy storage coils require that the coils operate at 10 kA, be charged in 10 s, be discharged in 0.001 s without going normal and with a maximum energy loss per cycle of 0.3% or less of the stored energy. These specifications impose unusual requirements on the superconductor. Such a conductor must be multistrand cable or braid and possibly made of multifilament strands. To meet the large rate of change of field required without coupling between the individual Nb-Ti superconducting filaments, the superconducting filaments must be small, effectively isolated electrically and twisted or braided to yield low energy losses.

Wire production contracts were let to Magnetic Corporation of America (MCA) and Supercon, Inc. in April: MCA to produce wire for their 300 kJ coil and Supercon to produce wire for the Intermagnetics General Corporation (IGC) and Westinghouse coils (Section G). Each order is for eight four-inch billets.

The electrical coupling between filaments is minimized in the MCA coil wire by using 0.005-in. monofilament, Cu matrix wire that is cabled and braided into a 1215 strand conductor. The wire manufacturing by MCA was technically straightforward and has been completed. The braiding and cabling operations are now underway.

The electrical coupling between filaments is minimized for the IGC and Westinghouse wire by putting Cu-Ni resistance barriers between the filaments in each wire as well as by braiding and cabling. The manufacturing of such triple matrix (Cu-Ni, Cu, Nb-Ti) wire was not technically straightforward at the inception of these programs nor is it now although much progress has been made. During the past nine months these orders have generated significant information for determining the correct characterization and processing of Nb-Ti and for determining the process parameters for conventional extrusion. Unfortunately this progress has come as a result of Supercon's inability to produce satisfactory wire consistently, and at the expense of wire delivery delays.

Because of Supercon's inability to meet the original specifications on the Westinghouse wire, a design change was made in the coil. Consequently, the originally specified values of j_c and wire diameter were relaxed from 3×10^5 A/cm^2 and 0.020-in. to 2×10^5 A/cm^2 and 0.032-in. As a result of this change the coil will go normal during discharge; however, the losses are still expected to be less than 0.3%. Even at this lower specification only wire from one billet of the three processed so far has met the short sample requirement. The IGC j_c specification is 2×10^5 A/cm^2 at 30 kG for a 0.0165-in. diameter wire. All eight billets have been extruded and are in various stages of processing. Preliminary results indicate that only half of this wire meets specifications.

A backup program for the IGC wire was initiated at IGC in November 1974. Phase I of this program is to procure the necesssary materials for the total wire needed (260 pounds) and to processapproximately 20% into wire as a qualification program. In Phase II of the program the remaining material will be processed if needed.

2. Wire Evaluation Program. Evaluation of wire samples produced from the MCA and Supercon orders as well as other samples, is being done in three major areas: short sample critical current (< 1 kA) measurements, ac loss measurements, and metallurgical evaluation of extrusion crops and starting materials as well as wire.

The critical current measurements are done on bifilar wound coil samples approximately 1 meter in length. They provide data up to 500 A and 70 kG at wire resistivity values as low as 10^{-12} ohm-cm. The loss measurement apparatus is capable of measuring static hysteresis losses up to 30 kG and dynamic losses up to $\dot{B}$'s of 3×10^7 G/sec. The apparatus is presently being calibrated using a high purity Nb sample. When the calibration is completed, quantitative hysteresis measurements can be made routinely. Spurious imbalances and pick-up have now been reduced to the point that semi-quantitative pulsed losses can also be made.

The metallurgical evaluation includes the investigation of Cu-Ti interdiffusion, second phase precipitates in Nb-Ti, and hardness. These data are being correlated to process parameters and wire performance.

3. High Critical Current Testing Facility. The high current test facility has been upgraded from 25 kA to 50 kA with the addition of a new flux pump. A new dipole magnet is currently being designed which will accommodate large braided conductors and provide a field of up to 50 kG. This will be used to evaluate braided and cabled conductor manufactured as a result of our industrial wire and coil program.

4. LASL Wire Braiding. LASL capabilities for assembly of wire into conductor geometries increased during the year. A larger braider was purchased, has been set up, and is being checked out. A small braider was rebuilt and upgraded. A small cabling machine was purchased and is being rebuilt. A rig for insulating wire was built and is currently operational.

G. Coil Development Program

1. Industrial 300 kJ Coils. Three 300 kJ superconducting energy storage coils are being designed and fabricated by three industrial contractors: Intermagnetics General Corporation (IGC), Magnetic Corporation of America (MCA) and Westinghouse. These coils are the basis of an industrial qualification program to establish the expertise within industry for the production of some 800 coils for the SFTR facility. This work is also the foundation for the production of coils to be used in the EPR torus and DEMO plant. Each coil is unique in its basic wire design, the manner in which the wire is cabled and braided to form the conductor, and the manner in which the conductor is supported structurally in the coil. Wire for the MCA coil is being made by MCA and wire for the IGC and Westinghouse coils is being made by Supercon on separate contracts (Section F). All three organizations have produced, on schedule, satisfactory designs with novel features furthering the state-of-the-art. Predicted performance for the coils is well within LASL requirements.

All three manufacturers have encountered coil assembly delays as a result of wire fabrication, cabling and braiding difficulties. It is probably fair to say that everyone underestimated the magnitude of the conductor development work required to produce low loss coils. Best estimates for completion of the MCA, IGC and Westinghouse coils are now June, July, and September of 1975, respectively.

2. LASL 300 kJ Coil. In order to get experience in energy-storage coil construction and to have a coil available for facility checkout and transfer studies, a 300 kJ unit was constructed in house. This coil goes normal upon discharge and does not meet the low loss requirements of the industrial coils currently being fabricated.

The Los Alamos 300 kJ energy storage coil was successfully operated in the 300 kJ test facility. Field measurements along the axis of the coil were within 2% of the calculated value, peaking at 1.65 G/A at the center. At 12.5 kA the center field reached 20.6 kG, with a calculated maximum field of 22.7 kG on the conductor. The maximum current run in the coil was 12.5 kA with a corresponding stored energy of 386 kJ. Uniform magnet field tests on Kryo 210 wire from which this coil is fabricated indicate that the coil would go normal between 10.6 and 12.7 kA. The coil has not gone normal at currents as large as 12.5 kA.

The coil has been used to test superconducting switches up to 8 kA with no problems and has been operated in a prototype METS/SFTR circuit. The circuit was operated up to 10 kA corresponding to 250 kJ of stored energy, with a peak transfer voltage of 35 kV. No problems associated with the coil were noted. During transfer runs at 5 kA storage current the coil did not go normal when $\dot{B}$ reached 6.5×10^6 G/s at the coil conductor. At 8 kA current, when $\dot{B}$ reached 10^7 G/s, the coil went normal, and dissipated less energy than the calculated maximum value of 3 kJ.

H. SFTR Prototype METS System

Work is in progress on an experiment to study the behavior of energy storage and transfer from coupled superconducting coils into θ-pinch compression coils. This system will be based upon a three storage coil section of the SFTR and is to establish completeness of component development as well as engineering feasibility. Detailed progress on the various subsystems follows.

1. Cryogenic Disconnect. A mechanically actuated high current, very low resistance switch to replace the superconducting switches is being designed to operate in He. The apparatus for testing contact materials for the disconnect has been designed, procured and assembled.

If the disconnect is not staged, arcing would occur as the unit opens which in principle could generate a shock wave within the dewar. Theoretically such a shock wave would produce a pressure wave on the order of 50 to 100 psi. While not expected to be a major problem, since the disconnect can be staged, this will be investigated experimentally (Section H).

2. Cryogenic Refrigerator and Experimental Dewar. The refrigeration system for the prototype was ordered in June 1974 with delivery scheduled for January 1976. This is a major component of the prototype test facility and consists of a helium refrigerator, compressors, transfer lines, cold gas liquid helium storage dewar and a gas recovery system. A schematic drawing of this system is shown in Fig. XIII-2. The helium refrigerator will produce 290 liters/h of liquid helium when operated as a liquefier (no cold gas return). In actual practice it will operate as a hybrid refrigerator/liquefier providing 700 W at 4.5 K to the experimental dewar. The machine will utilize two gas bearing turbine expanders in series and will utilize a full flow purification system. The 375 kW compressor will be a nonlubricated two-stage, balanced, opposed-piston unit with a throughput of 680 kg/h. During times when the primary experiment is not operating, the refrigeration system will operate as a liquefier to provide an inhouse source of liquid helium for individual coil testing and other cryogenic experiments.

Two vacuum-jacketed fiberglass reinforced, epoxy dewars are to be custom-built since large dewars of this type are not standard commerical items. Design details have been completed for the first dewar which will be used to test single 490 kJ superconducting coils.

A LASL computer program called RASH was used to evaluate the mechanical and thermal stresses in both shells of this dewar. With overall dimensions of 1016 mm i.d. by 2590 mm high, this unit will be installed and evaluated in the existing 300 kJ facility. The second dewar, an SFTR prototype dewar, will be taller than the first dewar and will incorporate the best design features of the single module dewar. It will be used to test three prototype coils in the SFTR configuration.

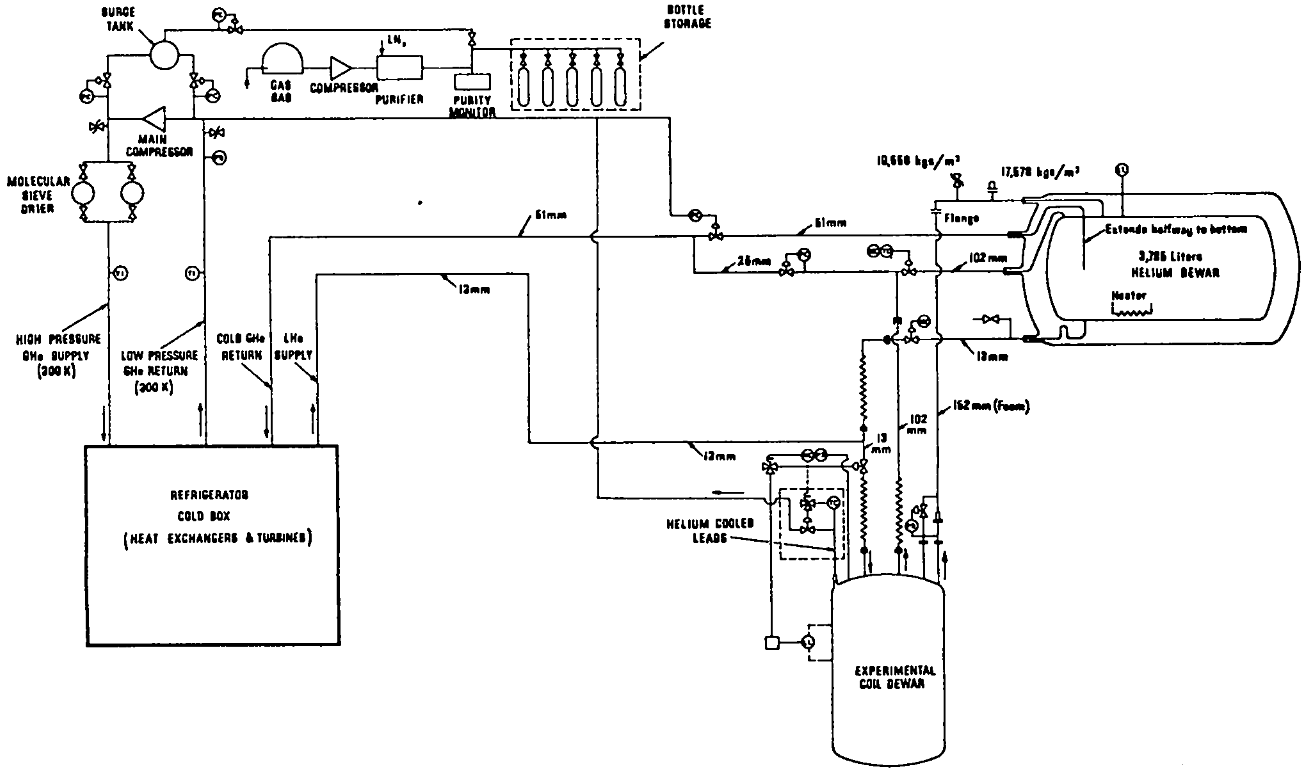

Fig. XIII-2
Schematic Drawing of the Refrigeration System

3. 60 kV, 25 kA Electrical Leads. Work is in progress to develop a pulsed electrical lead for use in the METS/SFTR applications. The ultimate goal of the development program is to design a pulsed lead that will carry the required 25 kA current pulse and allow a minimum of heat input to the cryogenic system.

The proposed lead is coaxial which offers the particular advantages of a single dewar penetration, limiting lead inductance and lessening of magnetically induced mechanical stress between leads. The lead uses the standard cooling technique of passing cold helium gas through and around the current carrying surfaces of the lead.

Two LASL computer programs have been used as aids in the design of the leads. OPTION is a steady state heat transfer and fluid flow code best suited for evaluating the temperature and pressure profiles in the continuous leads. AYER is also a heat transfer and fluid flow code and is easily adapted to the analysis of the transient temperature profiles which will occur in the pulse leads. A lead is presently under construction and will be tested in the CTR-4 high voltage research laboratory for voltage hold off characteristics.

I. SFTR Conceptual Design Study

A design has been made of the METS system as applied to the SFTR. Included are the magnetic energy storage coils, the plasma compression coil, vacuum breaker system, cryogenic leads, counter pulse system, transfer capacitor bank, dewars, cryogenic disconnects, refrigerator, and cabling. The design is virtually complete, but will require one more iteration based upon the final system parameters. Details on some of the subsystems follow:

1. Compression Coils. The basic design for the compression coil consists of several split pancake units connected together in parallel and energized by a single magnetic energy storage coil using the standard METS circuit (Fig. XIII-3). The major constraint on the compression coil design is that the peak voltage should not exceed 60 kV and the peak current should not exceed 25 kA. These constraints come from what is now thought to be presently attainable from superconducting and cryogenic technology. In addition, the coils are taken to be identical in length so that some constraint is placed on the design by the spacing of the shock heating system current feeds.

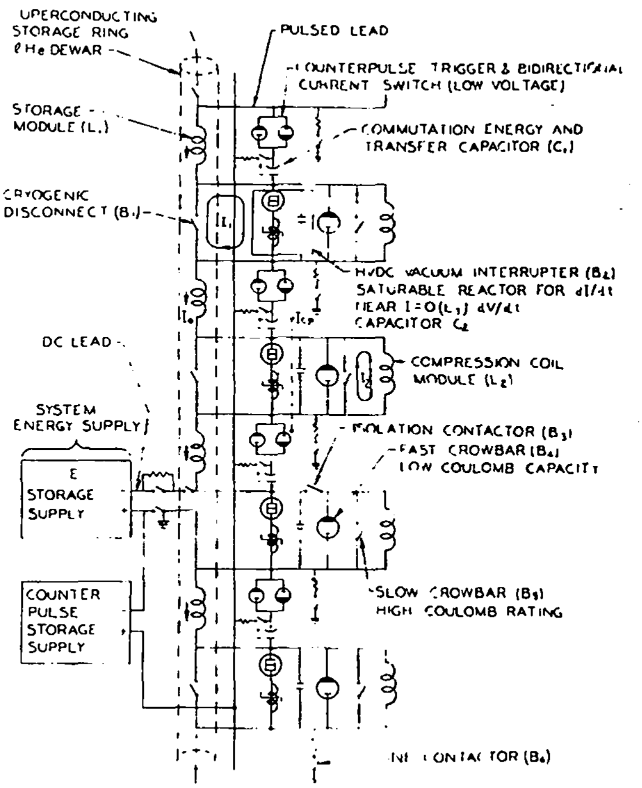

Fig. XIII-3
METS Electrical Circuit

Insulation of the coil has been assumed to be epoxy-fiberglass since the assumed radiation dose (10^7 Rad/year) is well within the range in which epoxy-fiberglass insulation has been successfully used in the particle accelerator field.

2. Modular Dewars with Storage Coils. For sometime the conceptual design of the magnetic energy storage system was a large toroidal coil made up of smaller submodules each energizing a section of the compression coil. The energy storage coil was to be placed in a single trough shaped dewar made of stainless steel but with a plastic lid. This arrangement has certain advantages in that stray fields are negligible, all coils are identical, and the large dewar can be mostly stainless steel for which a well established technology exists. The large disadvantage is that it is not easy to test subsections of the toroid before the entire dewar is constructed, and repair of any malfunction requires warming of the entire storage coil ring which is a lengthy procedure.

When the present layout of the SFTR experiment began to take shape, it became apparent that the spatial separation between the plasma compression coil and magnetic energy storage system would necessarily be quite large (approximately 18 meters) and the effect of stray fields from separate solenoidal storage systems would be much reduced. In addition the benefits of modularizing the storage system were thought to be sufficient to consider a METS system made of 80 cylindrical dewars positioned vertically. With the modularized dewar concept, refrigeration requirements are not increased because the additional coil charging electrical lead heat load is offset by the lower heat leak from the cylindrical dewars.

As envisioned, each of the vacuum jacketed, fiberglass reinforced, epoxy dewars will be a right circular cylinder approximately six meters in height and will accommodate ten storage coils each. The refrigerator will provide approximately 1700 kg/h of liquid helium and will have a total compressor input power of approximately 10 MW.

3. Interrupter Module. The interrupter module design was finalized early in the SFTR conceptual design study. Vacuum interrupter tests based upon this design proved that the approach was conservative. Further testing of commerical and LASL built breakers may lead to simplified designs which will only make the resulting module cheaper and smaller.

The mechanical layout minimizes the structural strength needed and the internal geometry minimizes the module inductance with a conservative spacing between low and high voltage components. The sub-master control electronics are located outside the shielded cabinet to alleviate arc and high voltage noise infiltration. Each of the ten modules within a cabinet can be removed and replaced rapidly. The electrical design of the module is shown in Fig. XIII-4.

Provision is made to assure equal current and voltage sharing in each interrupter unit. The saturable reactor lowers the dI/dt to a small value bracketing $I = 0$ to assure arc deionization during commutation, and the $\dot{V}$ capacitor holds the impressed voltage near zero during the 50 μs required for vacuum recovery. The damping resistor quenches all parasitic stray circuit oscillations which may be large enough to cause an arc hold-on voltage.

Voltage and current monitoring within the module will be used to detect malfunctions, and, if necessary, blow the triggerable fuse to isolate the interrupter.

4. 100 kJ Homopolar Transfer Capacitor. A computer study is in progress to analyze a small scale homopolar transfer capacitor. The capacitor is to store 100 kJ of energy using six disks in electrical series, capable of a rev-up and rev-down in one millisecond. The design of the homopolar capacitor is considerably different than for an energy storage homopolar. The steady state condition would be zero or near-zero rotation, which would imply use of a simple nonretractable electrical brush system. Energy storage and electrical circuit transfer losses make competing demands on material and geometry design parameters.

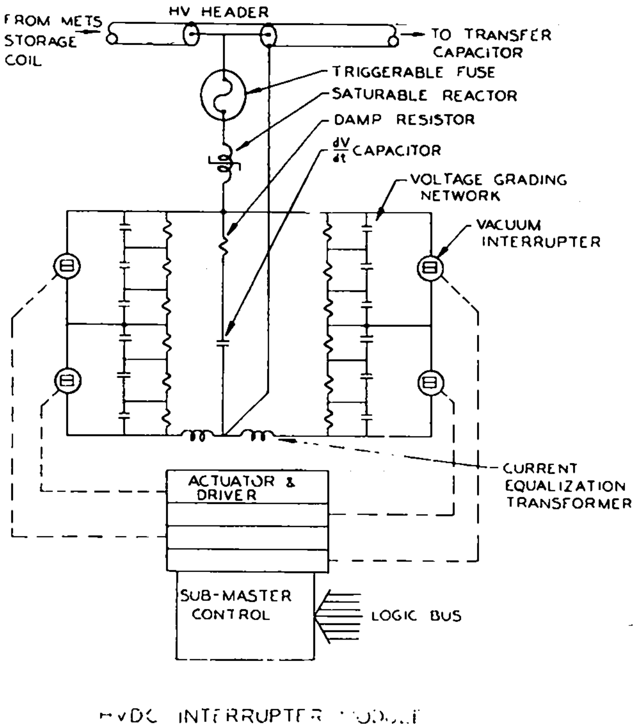

Fig. XIII-4
HVDC Interrupter Module

The big advantages of a homopolar transfer capacitor within a METS system or other similar LCL type systems would be several, and may be proved in detail by further work. This inertial energy storage system would have much higher energy density than conventional inductive storage systems and be an order of magnitude better than a capacitive storage system, thereby leading to more compact power systems. The cost per joule for even megajoule size packages should be less than 1 cent/joule.

5. Cryogenic Consultants, Inc. (CCI) Design Study. The CCI cryogenic system design study[2] for a toroidal, theta-pinch system was completed. This study utilized a single toroidal dewar as opposed to the current modular dewar concept consisting of 80 dewars. Many of the CCI design features and concepts have been carried over into the current modular dewar system.

J. Dielectric Strength, Voltage Tracking and Arc Discharge Studies

A program is in progress to study the dielectric strength of helium and nitrogen in both the liquid and gaseous state, voltage tracking along insulator surfaces in helium and nitrogen, and shock wave formation during arc discharges in liquid helium. The purpose of this work is to obtain engineering data to permit proper design of high voltage components (leads, cryogenic disconnect, etc.) for the SFTR system.

Some literature is available regarding low temperature helium and nitrogen dielectric properties, but the majority of the articles written are concerned with ac or dc application. It is difficult to extrapolate such data to the SFTR pulse voltage applications since dielectric breakdown is a function of many parameters including electrode size and shapes, dielectric pressure and temperatures, and applied voltage waveforms.

A test set-up consisting of a nitrogen shielded, stainless steel dewar with the capability of installing various electrode configurations within the dewar was built and installed in the CTR-4 high voltage research laboratory. An external high voltage circuit capable of providing a 60 kV pulse with 500 μs rise time is connected to the electrodes. The discharge current is limited by a resistor so that electrode damage is minimized. Electrode gap separation is adjusted external to the dewar with a micrometer and the breakdown characteristics are measured by oscilloscope with a high voltage probe and a Pearson current transformer.

Data are completed for air and nitrogen as the dielectric medium using sphere-sphere, plane-plane and point-point configurations. The data are presently being analyzed. Testing in helium is underway.

References

1. Stekly, Z.J.J., *Advances in Cryogenic Engineering,* 8, 585, Plenum Press (1963).

2. Vander Arend, P.C. West, J.E., Krishna, G.V., "Cryogenic System Design for a Toroidal, Separated Shock Theta-Pinch System," Reports of May 1, August 9 and November 14, 1974, Cryogenic Consultants, Inc., Allentown, PA.

XIV. FUSION TECHNOLOGY

R.A. Krakowski, L. Booth, G.E. Bosler, J.M. Bunch, F.W. Clinard, Jr., D.J. Dudziak, T. Frank, A.W. Gerstl, W.V. Green, G.M. Hale, D.R. Harris, J.G. Hoffman, D.W. Muir, T.A. Oliphant, D.M. Parkin, M.L. Simmons, P.D. Soran

A. Introduction

The Fusion Technology task assesses the long-range technological requirements of fusion power derived from high-β confinement concepts. The effort includes theoretical analyses and plasma engineering, neutronic studies, nuclear data assessment, electrical insulator and structural alloy research, and general engineering; progress within each of these areas is summarized herein. On the basis of a conceptual engineering design of a Reference Theta Pinch Reactor (RTPR)[1,2] an environmental impact study has been completed[3] and a technological assessment is near completion.[4,5] The Fusion Technology task has also supported engineering design activities for the Scyllac Fusion Test Reactor (SFTR, Sec. XV) in the areas of tritium handling, radiation shielding, materials, vacuum technology and environmental/safety analyses. Preliminary design studies of a Linear Theta-Pinch Hybrid Reactor (LTPHR) have commenced,[6] and more detailed design studies of this fission/fusion concept are proceeding.

B. Theoretical Analysis

Theoretical analysis and computational modeling efforts support many of the systems studies. Important highlights are reviewed below.

1. Neutral Gas Cooling Layers. The effectiveness of the neutral-gas layer in controlled cooling of the hot post-burn plasma has been analytically demonstrated in the steady state approximation.[7] The question of charge exchange occurring during the transient phase of the neutral gas blanket/plasma interaction and the ensuing wall damage has been addressed. The results of preliminary computations[8,9] are shown in Figs. XIV-1 and XIV-2 as radial density and temperature profiles at 200 μs after introduction of the neutral gas. A new and superior calculation is being developed, which treats the plasma dynamics and the nature of the incoming neutral atoms in more detail. The neutral gas is modeled with "simulation slabs", each of which has a well defined position and velocity component in the direction-of gas flow. The density and temperature dependence of both charge exchange and collisional rates are consistently and accurately taken into account by these new computational methods.

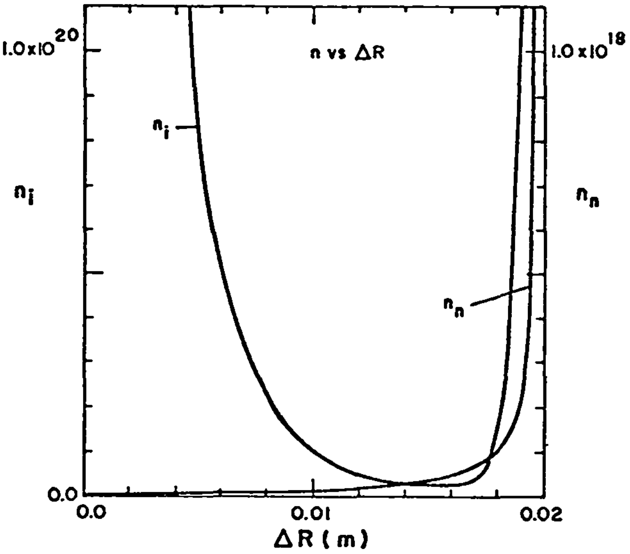

Fig. XIV-1

The ion density n_i and neutral gas density n_n are plotted vs the distance $\Delta\tau a R$ from the center of the diffuse plasma sheath at a time 200 μs after introduction of the neutral gas.

2. Thermonuclear Burn Calculations for LTPHR. A thermonuclear burn computer code has been written in which the dynamics of plasma compression is coupled to an external circuit analysis. These burn calculations provide input for the systems analysis of the LTPHR,[6] discussed in Sec. VIII.C.2. The circuit and its equations are illustrated

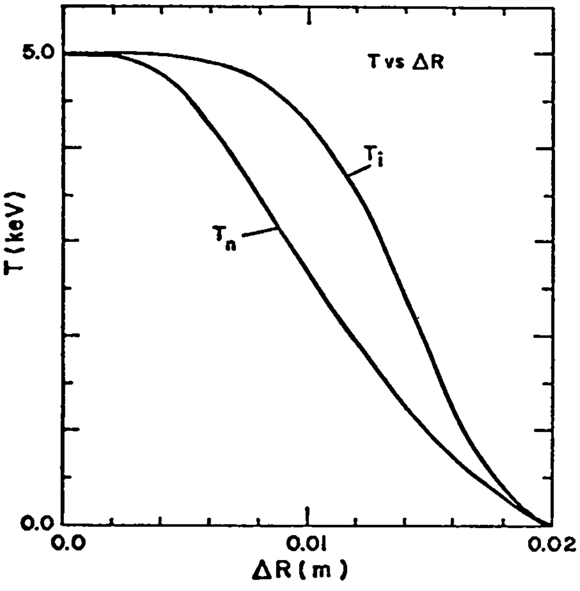

Fig. XIV-2
The ion temperature T_i and neutral gas temperature T_n are plotted vs the distance ΔR from the center of the diffuse plasma sheath at a time 200 μs after the introduction of the neutral gas.

in Fig. XIV-3; Fig. XIV-4 illustrates the calculated time dependence of ion temperature, plasma radius, and neutron yield. The simple bounce module[10] was used for the results of Fig. 4, but more sophisticated, mixed-bounce, snow-plow calculations[11] were also made. A comparison of these two models with Scylla IV experimental data[12] indicates that the simple bounce model adequately describes the implosion process. Hybrid calculations (i.e. a combination of analytical calculations with simulation calculations) are being formulated to model the implosion process, which may be computationally complicated by simultaneous compression.

3. Calculation of SFTR Operating Point. The thermonuclear burn code DTBURN[13] has been modified to monitor the plasma stability conditions and plasma Q (neutron energy/plasma energy) for a variety of input parameters. Figures XIV-5 through XIV-7 give computation results generated for theSFTR design. DTBURN has yielded a range of operating points for SFTR based on parameters determined by implosion-heating and stability-theory.

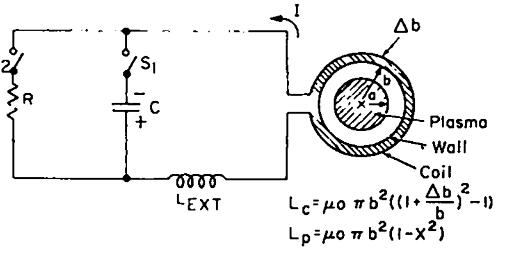

$$L_c = \mu o\, \pi b^2\left(\left(1+\frac{\Delta b}{b}\right)^2-1\right)$$

$$L_p = \mu o\, \pi b^2(1-X^2)$$

(a) Implosion/Compression Phase S_1 = Closed, S_2 = Open

$$\frac{1}{C}\int_0^t I\,dt-(L_{EXT}\cdot L_C+L_P)\frac{dI}{dt}=I\frac{dL}{dt}P$$

(b) Crowbar Phase S_1 = Open, S_2 - Closed

$$RI-(L_{EXT}+L_C+L_P)\frac{dI}{dt}=I\frac{dL}{dt}P$$

Fig. XIV-3
Circuit diagram used to model the thermonuclear burn for the LTPHR.

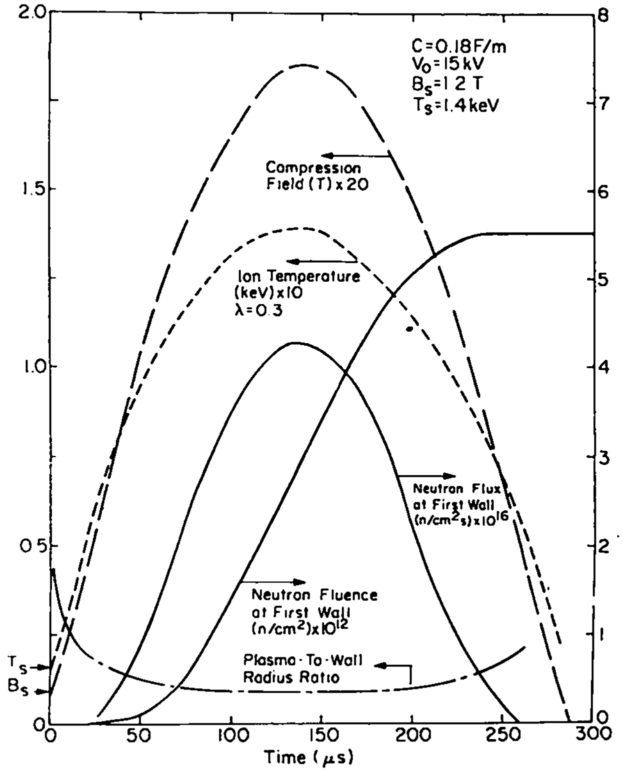

Fig. XIV-4
Typical results for the LTPHR thermonuclear burn for a simple, LC-ringing circuit.

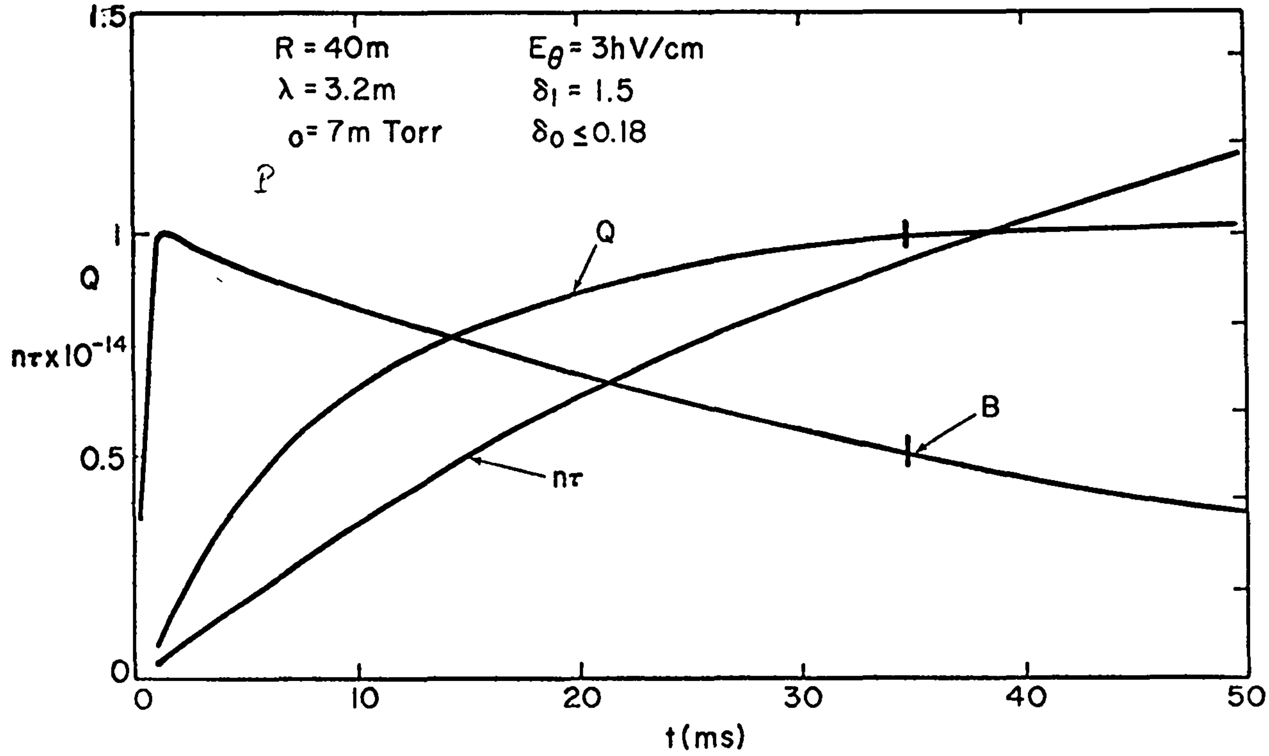

Fig. XIV-5
Time dependence of feasibility number Q, confining field B, and nτ during the burn.

4. Systems Analysis Code Development. The increased detail used to describe a given system has made it imperative to develop a generalized systems code. The development of the LASL fusion reactor systems code began with an ergodic analysis of the RTPR[14] (See XIV.C.1.a). Ultimately the system analysis code will provide a continuous update of the reactor concepts for RTPR, LTPHR, SFTR, as well as other (Z-pinch, high-β stellarator) fusion reactor concepts.

5. Theta-Pinch Coil Design Calculations. Work has progressed on general 3-D, distorted-mesh calculations of static magnetic fields. These calculations will impinge on almost every experimental project now being considered in CTR. The major steps taken over the past year are the development of a 3-D spline interpolator and the successful solution of 3-D magnetic scalar potential problems. The next steps are to develop a useful format for present applications and to extend the method to vector potential problems.

6. End-Loss Calculations. The effects of alpha-particle heating and adiabatic compression on end loss from a straight theta-pinch have been estimated. These calculations at present serve mainly to identify the direction to be taken by code development and will be pursued in collaboration with CTR-6. End-loss phenomena will eventually be incorporated into the thermonuclear burn computations for LTPHR.

7. Advanced Thermonuclear Burn Calculations. Calculations were made on the alteration to the shape of the reacting plasma surface as a result of the presence of alpha-particle reaction products. This analysis is continuing, and plans exist to develop more sophisticated transport theory for describing general spatial variation.

C. Reactor Design Studies

The systems analysis task at LASL assesses present technology, analytically identifies requirements, and forecasts research and development

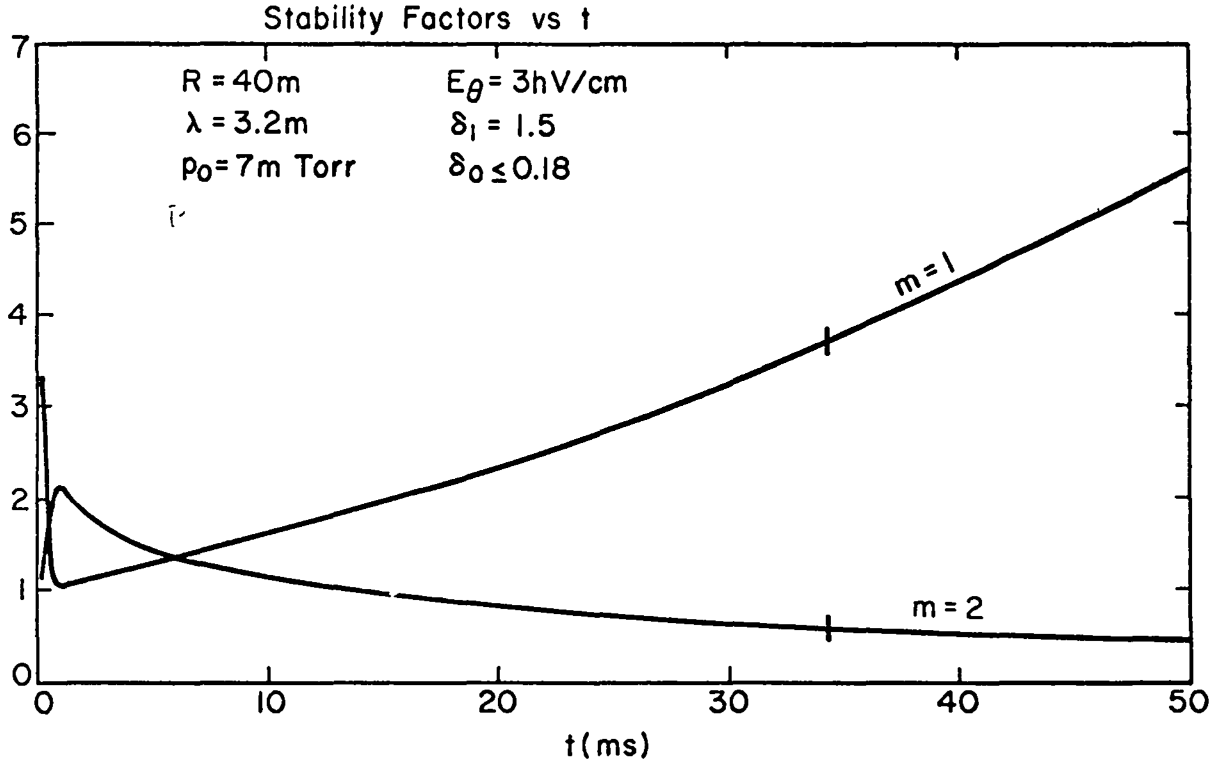

Fig. XIV-6
Stability criterion numbers for m = 1 and m = 2 stability vs burn time.

needed for fusion power systems. All reactor concepts being considered are based on high-β, pulsed-magnetic confinement schemes. Past efforts (1972-74) have focused on the engineering design of the RTPR,[1,2] shown in Fig. XIV-8. The focus of the CY 1974 effort in this area has been the environmental study,[3] the technological assessment,[4,5] and the resolution of problems revealed by these latter studies. Designs of fusion/fission reactors based on the linear theta-pinch concept are also underway. Progress in each of these areas is summarized below.

1. RTPR Studies

a. Technology Assessment. In an assessment of the RTPR design, technological problems and uncertainties were categorized into nine major areas:[4,5]

- **Plasma Physics.** The major areas of uncertainty associated with the plasma physics are stability/equilibrium, thermonuclear burn/energy balance, and neutral gas cooling.

Equilibrium/Stability: Freidberg and Ribe[15] have summarized the implications of toroidal equilibrium and MHD stability on the design of the SFTR. The final compression ratio selected for the RTPR is too large for effective wall stabilization of m = 1 modes during a major portion of the burn cycle, and feedback stabilization will be required.

Thermonuclear Burn/Energy Balance: The original RTPR design[1,2] did not consider the effects of impurities on the thermonuclear burn, the influence on the overall energy balance of the staging requirements, or the optimization of burn parameters (particularly under-compression vs over-compression). Subsequent analyses[14] have partially resolved these uncertainties.

Neutral Gas Cooling: Central to the operation of the RTPR is the need to cool the hot, (5-10 KeV), post-burn plasma by means of a neutral-gas blanket. Past analyses[1,7] assumed a quasi steady state, continuum model, which has subsequently been

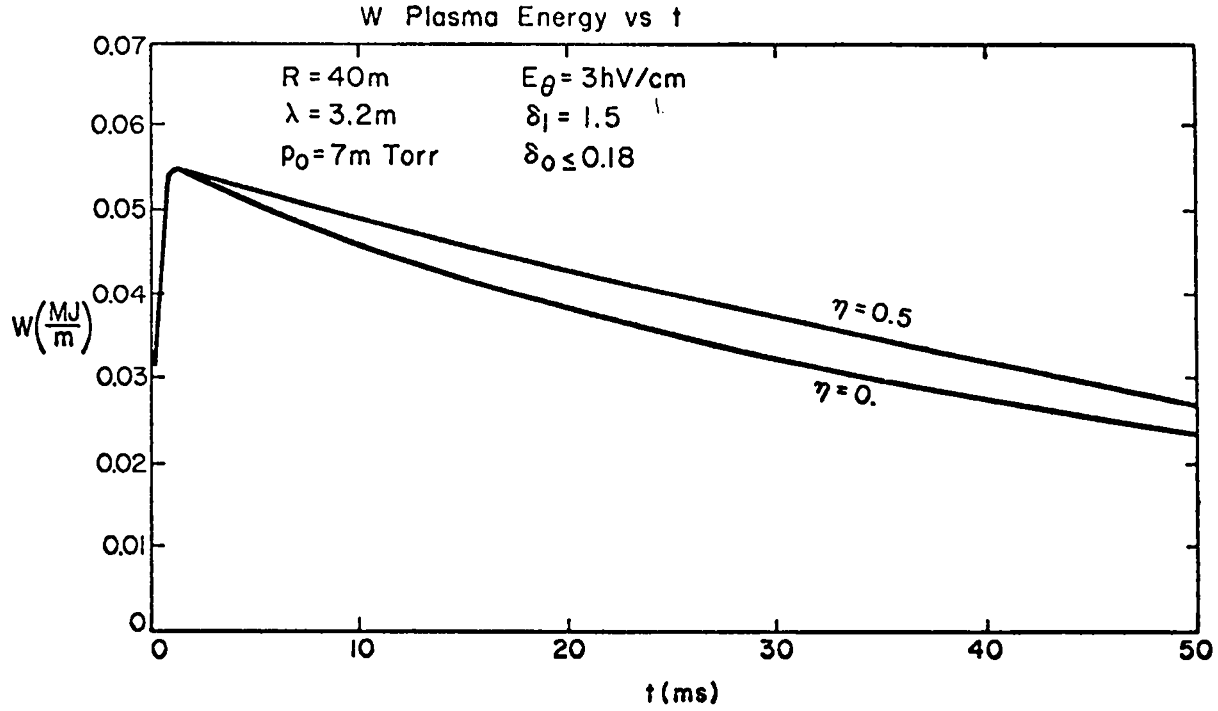

Fig. XIV-7
Plasma interval energy W(kJ/m) as a function of burn time for no alpha heating (η=0.0) and with alpha heating (η=0.5).

refined by Monte Carlo techniques.[7,8] Although the wall fluxes of charge-exchanged neutrals have been estimated,[8] more realistic, transient computations must be made and are now in progress.

- **Implosion and Compression Energy and Storage:** The RTPR design uses capacitive storage for implosion and staging, and reversible inductive storage (METS) for adiabatic compression. Energy-balance considerations demand METS transfer efficiencies of ~95%, and staging energies equal to and not much more than the implosion energy[14] are needed for an acceptable energy balance. The cost and efficiency of the compression energy storage was subsequently elucidated by an independent systems analysis.[16] On the basis of this study and the problems inherent to a purely capacitive/METS driven RTPR, on-going designs are considering capacitive implosion, METS staging, and a compression field driven by homopolar motor generator (HETS) sets.

- **Materials and Radiation Damage:** A materials assessment of the RTPR first wall and blanket[1,17,18] shows that the insulator/metal composite first wall presents the most crucial materials problem, from both a radiation-damage and a thermal stress viewpoint. New first-wall concepts, which include sacrificial "bumpers", purely ceramic first walls, and new geometric configurations, are being considered to reduce the radiation damage and thermal stress problems. Materials-related uncertainties associated with magnetic coils, molten lithium, tritium diffusion barriers, superconductors, molten-salt containment (in the tritium extractor), and blanket materials have been investigated.

- **Tritium Handling:** An RTPR operating at a 12 GWt power level must actively circulate 28.8 kg/d of tritium, most of which is transferred unburned through the vacuum and fuel injection/ recovery systems. Effective handling and containment of tritium is both an environmental and economic

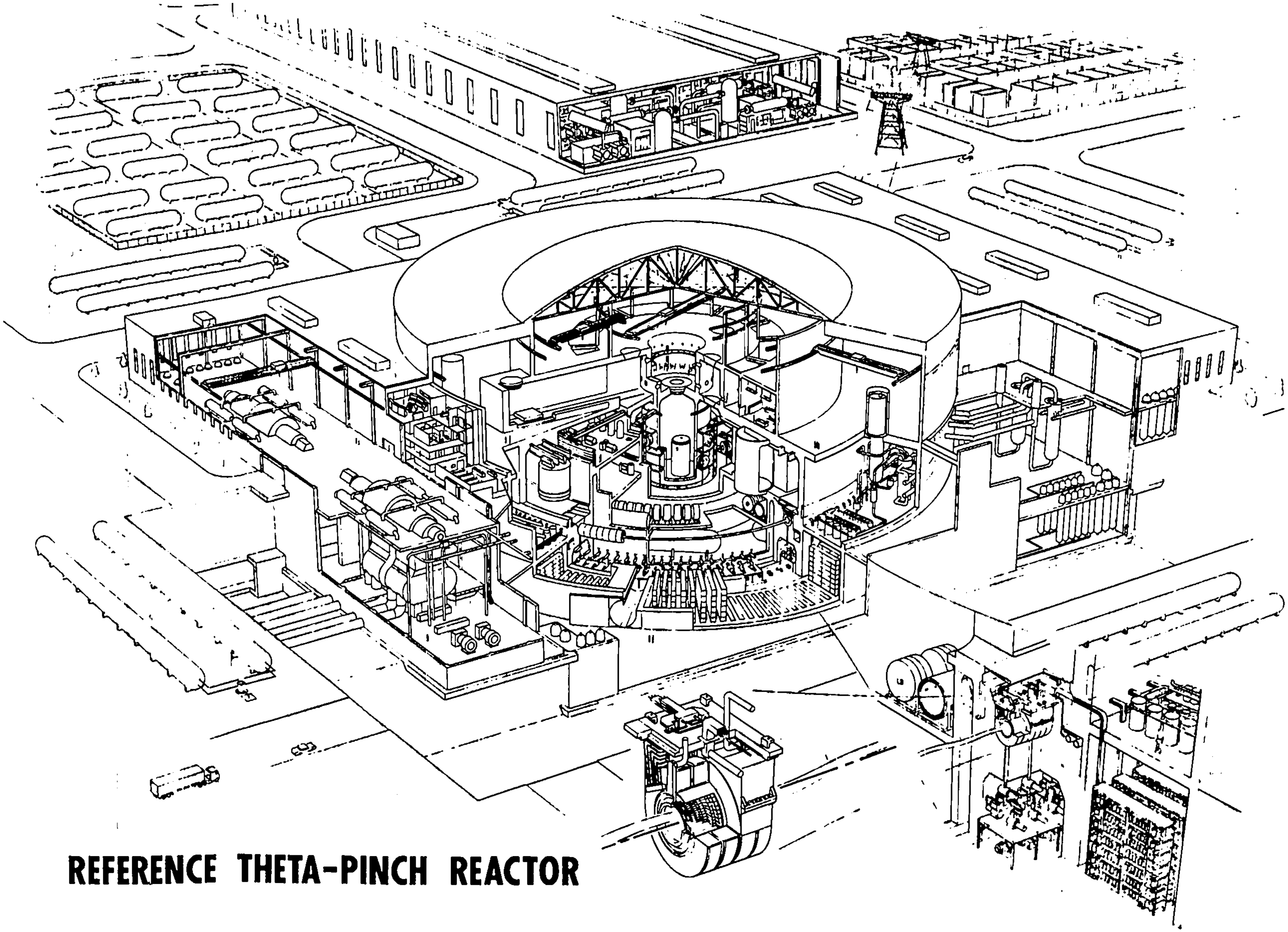

REFERENCE THETA-PINCH REACTOR

Fig. XIV-8
Cutaway view of the Reference Theta-Pinch
Reactor (RTPR)

necessity. The fuel supply/removal system and the isotope separation system do not appear to present severe design or economic demands. The molten-salt extraction system for tritium recovery from lithium is more uncertain from a physical-chemical viewpoint, although recent experimental results look encouraging.[19] Similarly, containment of tritium from the environment does not appear to present insurmountable problems.[3,20]

- **Blanket Neutronics:** Neutronic computations based on the results of the thermonuclear burn calculations yield neutron and gamma-heating rates, radioactivation, tritium breeding, radiation damage rates (dpa, He and H production, transmutations, etc.), radiation shielding requirements, and other important design parameters. These neutronic computations have been based on one-dimensional, time-independent models; although adequate for the purpose of conceptual reactor designs, neutronic techniques must be refined for more detailed studies. Although the neutronics is well in hand, areas where improvement appears desirable[21] are: (a) application of perturbation techniques to facilitate more rapid and far-ranging parametric systems studies; (b) optimization of blanket thickness vs tritium breeding rates and Be inventory; (c) detailed studies of the sensitivity of displaced atoms (dpa), breeding ratio, etc. to neutron cross sections; (d) time-dependent calculations (e.g. ^{6}Li burn-out); (e) two-dimensional, Monte Carlo computations to model critical regions of the segmented (axially and radially) RTPR blanket; and (f) more accurate modeling of the "deep-penetration" problem.

- **Construction, Operation and Maintenance:** In this category are the many engineering problems which are highly design-dependent and which determine the technological and economic viability of the RTPR. For instance, the interaction between duty cycle, first-wall loading (e.g. lifetime), and the feasibility of rapid module change-out will have a significant influence on the RTPR economics. Although the modular approach adopted by the RTPR design will facilitate rapid (i.e. short downtimes) replacement of the first-wall/blanket regions, much more engineering of the proposed remote-handling, maintenance, and repair schemes must be evolved before these ideas truly become credible. Details of construction, operation and maintenance problems are given in References 1 and 4.

Table XIV-I gives a synopsis of the above-described technology assessment. More detail is given in Vol. III of the RTPR design study.[5]

b. Environmental Assessment. The environmental assessment of the RTPR has been completed.[3] This study indicates that the environmental impact of theta-pinch fusion reactors would be minimal. In terms of radioactivity, material needs, and land despoilation, the anticipated advantages associated with the abundant fuel supply and less harmful reaction products appear to be without seriously offsetting disadvantages.

Several environmental aspects appear identical with other large energy sources (fossil, fissile). The waste heat from a fusion power plant, like all other power plants, is dependent on the maximum thermal conversion temperaure. If advanced (high-temperature) energy conversion cycles are used, the waste heat is reduced regardless of the specific heat source. The waste heat problem could, in principle, be worse for fusion reactors than for fissile or fossil fuel power plants because of the larger circulating power required by the former. This problem is reduced in the RTPR power plant by the direct conversion of ~9% of the total fusion energy.[1]

Land despoilment by fusion reactors appears to differ little from other heat sources. Presently, the likelihood of siting a fusion power plant in an urban setting and close to the load point appears to differ little from a fission or fossil power plant. The mining requirements for fuel and structural materials, although differing significantly in kind, do not appear to differ significantly between fusion, fission, or fossil power plants.

The major environmental effects of a fusion reactor that employs D-T fuel and magnetic confinement are associated with (a) the need to breed tritium (tritium inventories, lithium burnout), (b) the need to store large quantities of magnetic energy and the associated resource requirements on niobium, helium, copper, and steel, (c) the need to operate radioactive components as well as to transport and to store radioactive waste, and (d) the need to replace on a regular basis substantial quantities of radiation-damaged metals for a given amount of energy generated.

The RTPR power plant actively circulates 28.8 kg/d of tritium, passively stores 1.43 kg of tritium, and consumes 1.38 kg/d of tritium. Table XIV-II summarizes the RTPR tritium inventory. If a tritium partial pressure of 10^{-10} torr in the lithium coolant is assumed, and a copper diffusion barrier is placed in the primary heat exchanger, the leak rate of tritium to the environment (condenser water for the case of the present RTPR power plant design) amounts to 6 Ci/d. Table XIV-III gives the resulting radiation doses for three cooling water options.

Since 81% of the tritium breeding occurs in ^{6}Li, a total of 14,600 kg/y of natural lithium is consumed

TABLE XIV-I

SYMPOSIS OF THE RTPR TECHNOLOGY ASSESSMENT

Area	Problems, Uncertainties, and Needed Research/Development
PLASMA PHYSICS	
•Plasma Stability	*Achieve toroidal equilibrium with acceptably low $m=1$, $k=0$ ("fat" plasma) and $m \geq 1$, $k=0$ ("skinny plasma) growth rates for reasonable aspect ratios
	*Incorporation of $\ell=1,0$ perturbation onto blanket and coil flux surfaces
•Thermonuclear Burn/Energy Balance	*Optimize risetime, burntime, and compression field with respect to RTPR Q-value
	*Influence of impurities on energy balance
•Neutral Gas Cooling	*Cooling effectiveness and influence on maximum allowable burn intensity
	*Transient phase of gas cooling and influence of charge exchange
	*Effect of neutral gas cooling on energy balance (increased heating requirement)
IMPLOSION HEATING	*End-fed coil and electrical feedthrough design (low inductance)
	*L/R time constant of implosion/staging circuit and influence on Q-value
	*Large first-wall radius and fluting of ion sheath
	*Interaction of flowing neutral D-T gas with imploding plasma
	*Flux return path and related heating efficiency
	*Effects of $\beta < 1$ and impurities on implosion efficiency
	*Effects of desorbed gases $(D,T)_2$, O_2) on implosion heating
ADIABATIC COMPRESSION (METS)	*Staging of implosion field into compression field
	*Storage and transfer efficiencies $\geq$ 95% and acceptable cost
	*Development of storage/transfer system with high peak-power requirement. (Nested coils/transformer, homopolar generator, short-circuit ac generator-inverter system)
	*Generation of quench-and-hold field
	*Distribution of direct-conversion energy
	*Coil, leads, disconnect, circuit design
MATERIALS	*First-wall composite (neutron swelling, transmutations, He/H generation, sputtering, blistering, thermal shock and fatigue, chemical stability, dielectric strength and resistivity of insulators in a radiation field)
	*Radiation, chemical and thermal stability of blanket materials (Be, C, Li).
	*Magnetic coils fabrication, radiation damage, stress, fatigue
	*Development of fast-pulsed superconducting matrices
	*Materials transport in liquid-metal systems (Li and Na)
	*Tritium interactions and containment

TRITIUM HANDLING	
•Fuel Supply/Removal	*Development of high-capacity vacuum system (pumps and ducts)
	*Dynamics of a pulsed vacuum system which must supply both initial fuel charge and neutral gas blanket as well as remove spent fuel
•Isotope Separation	*Develop cryodistillation system which separates H, D, T, and He and has small hold-up time (inventory)
•Tritium Recovery from Lithium	*Better physical-chemical understanding of molten-salt extraction system
	*Find other extractants with higher partition coefficients
	*Understand effects of extractant solubility in lithium coolant on corrosion
•Tritium Containment	*Develop tritium barriers for high-temperature (heat exchanger, steam generator) containment
	*Develop low-temperature tritium barriers (glasses, He purge, rotating seals)
NEUTRONICS	*Perturbation techniques required for parametric systems analyses
	*Two-dimensional (Monte Carlo) calculations of neutron streaming and local heating
	*Sensitivity studies on tritium breeding, neutron heating, etc. to determine effects of cross section uncertainties
	*Enlarge and improve cross section data base
RADIOACTIVITY AND AFTERHEAT	*Influence of impurity activation on radwaste problem must be resolved
	*More detailed heat transfer calculation needed for loss-of-coolant accident
	*Use of low activation materials in blanket and magnetic coils
CONSTRUCTION, OPERATION, MAINTENANCE	*Develop a detailed systems analysis to determine interaction between duty cycle, materials, and economic constraints
	*More detailed design of module replacement scheme to assure a viable means to rapidly remove and replace first wall
	*Elucidate more the influence of pulsed operation of plant output, coolant pumping requirements (flow surges) and field/coolant interactions
	*A wide range of fabrication techniques (electron beam welding, plasma spraying, metal forming, etc.) must be extended to and developed for the RTPR
	*The complexity of "routine" operation of this power plant will require advancements in plant control, feedback, in situ system interrogation, and remote procedures to protect the large capital and energy investment as well as to assure an acceptable (80-85%) operating factor
RESOURCES	*If niobium is used, resource limitations will demand recycling of structural material. Remote reprocessing techniques must be developed
	*Unless a substitute for a neutron breeder is found, a substantial fraction (~50%) of the world Be resource will be used. The world resource of Be is not well known
	*Li usage is large

TABLE XIV-II

SUMMARY OF TRITIUM INVENTORY

Location	Inventory (g)
Reactor Blanket	53
Lithium Circuit (not including Tritium in Blanket)	404
Fuel-Ash Processing and Fuel Injection	1913
Sodium[a]	0.3
Steam	7
Storage	1426
Total	3804

[a] Based on 0.1 ppb concentration and 3.026×10^6 kg Na.

for a breeding ratio of 1.11. Approximately 1.0×10^6 kg of niobium and 1.3×10^6 kg of helium is required for inductive energy storage, and approximately 76,700 kg/y of radioactive niobium from the blanket must be handled (transported, stored, and reprocessed). An additional 1800 kg/y of low-level radioactive niobium must be processed as a result of lithium corrosion. The anticipated resource requirement for the RTPR is summarized on Table XIV-IV.

The quoted values of tritium losses, resource depletion, and radwastes are for the 12 GWt (4.0 GWe) RTPR power plant design described in Ref. 1. These effects are highly design-dependent. For instance, depending on the emphasis placed upon minimizing the tritium release rate and inventory, different coolant and breeding schemes can be adopted which, in principle, could reduce the 6 Ci/d tritium release rate to a level determined by the leak integrity of the helium purge system (0.01 to 0.1 Ci/d). The level of radwaste handled by the RTPR power plant could be reduced by the replacement of niobium in the blanket by metals which activate to a lesser extent. These examples serve to illustrate the variability of important environmental effects resulting from engineering design changes.

Structural and blanket material requirements, however, show little sensitivity to design change. For a given total energy output the neutron flux will produce a given number of displaced atoms in the surrounding structural material. The radiation-damaged material must be replaced at a rate (19.1 kg/MWe-y), which is roughly independent of the blanket design details. Hence, consumption of blanket materials is nearly proportional to the integrated thermal output of the fusion power plant.

A preliminary safety analysis for RTPR has been made. In the unlikely event that the total circulating tritium inventory were released to the atmosphere, the external radiation dose to the surrounding populace would amount to 7.6 rem at 600 m and 1.8 rem at 3 km from the release point. A liquid-metal fire could produce this kind of release, although the likelihood of an instantaneous and total release of all actively circulating tritium appears highly improbable. The losof-cooling accident (LOCA) appears more probable. However, if the LOCA is detected in time for the reactor to be shut down, the damage to the reactor should not be serious. None of the possible consequences of the LOCA should propagate outside the reactor containment.

Although other accident situations have been discussed in Ref. 3, more must be known about the details of plasma physics and the engineering design before conclusive remarks can be made. However, based on the tentative evidence accumulated thus far, the RTPR power plant appears to have an extremely low potential for a publicly hazardous accident.

c. RTPR Systems Code. The RTPR design effort has entered a "problem solving" phase whereby the aforementioned key uncertainties (energy storage, neutral gas blanket, insulating first wall, feedback stabilization, staging, etc.) are being more completely resolved by either more detailed analysis or design change. The focus of this effort is an integrated systems code, which analytically models all physics aspects of the RTPR burn cycle; other aspects of the RTPR (blanket neutronics, tritium handling, power conversion, etc.) are not incorporated into the LASL systems code. Evaluations will be made primarily on the basis of overall energy balances.

This code in a preliminary version was used in optimization studies of the RTPR burn cycle.[14] Figure XIV-9 illustrates the dependence of the overall Q-value (thermal energy deposited into blanket/recirculating energy) on the excess compression field ΔB above the minimum compression field $\check{B}_0$ required for plasma ignition. Four burn times τ_B are illustrated as is the propensity for plasma re-ignition after quench, as measured by the time rate of plasma temperature increase without neutral gas cooling. For the particular conditions shown on Fig. XIV-9, a minimum field $\check{B}_0 + \Delta B$ is required to obtain an economic Q-value for a given τ_B, whereas a maximum fieldis established by the desire to quench and cool the plasma after the burn is complete.

TABLE XIV-IIIA

SUMMARY OF ANNUAL INTEGRATED POPULATION (AIP) DOSE (MAN REM/YR) AT 6 Ci/DAY RELEASE RATE

	Cooling Case	Site 1 Baily (Lake, 5.8×10^6 People/ 50-Mile Radius)	Site 2 Oconee (River, 7.3×10^5 People/ 50-Mile Radius)
Case (1)	(Once-through cooling)	46 (Water)	1.7 (Water)
Case (2)	(Wet cooling tower)	12.7 (Water)	0.4 (Water)
Case (3)	(Dry cooling tower)	0.6 (Air)	0.5 (Air)
	Bkg/50-mile radius	13.3 (Total)	0.9 (Total)
	(125 mrem/yr)	9.9×10^5	9.1×10^4
	Fission plant (Prorated)	248	15.4

TABLE XIV-IIIB

MAXIMUM ANNUAL AVERAGE INDIVIDUAL DOSES FROM THE RELEASE OF 6 Ci/DAY OF TRITIUM (MREM/YR)

	Site 1 (Baily)		Site 2 (Oconee)	
	ICRP[a]	M&K[b]	ICRP[a]	M&K[b]
Case (1) (Once-through cooling)	0.064 (water)		0.064 (water)	
Case (2) (Wet cooling tower)	0.80 (water)		0.80 (water)	
	0.0059 (air)	0.12	0.027 (air)	0.18
	0.81 (total)	0.92	0.83 (total)	0.98
Case (3) (Dry cooling tower)	0.18 (air)	0.77	0.17 (air)	0.14

---

[a] Method of International Commission on Radiological Protection$^{(21)}$

[b] Method of Morley and Kennedy$^{(22)}$

Shown on Fig. XIV-10 is a diagram of the LASL systems code as it is presently being developed. In addition to a more refined energy balance that incorporates energy requirements of feedback stabilization, the thermonuclear burn subroutine DTBURN is coupled by means of a gas blanket model, GASBLK to the impurity emission rates from the first wall by the subroutine WALL and HTRANS. In addition to output in the form of energy balance quantities, the LASL systems code monitors the plasma stability/equilibrium condition, the plasma radius and temperature, and the conditions of the first wall. The task of each subroutine is to model accurately the response of the implosion (IMPL), staging (STG) and compression (COMP) phases of the RTPR cycle as well as the dynamic behavior of the plasma (DTBURN), gas blanket (GASBLK) and first wall (WALL).

1. Linear Theta-Pinch Hybrid Reactor (LTPHR) Studies. The overall energy balance for a linear theta pinch reactor can be improved by use of a fission-enhanced, energy-multiplying blanket. A study has been made[6] of constraints established by plasma physics, neutronics, energy balance, and economics on the design of a LTPHR; although

TABLE XIV-IV

RESOURCE REQUIREMENTS ANTICIPATED FOR THE RTPR

	12 GWt (4 GWe) RTPR			10^7 MWe from 2440 4 GWe RTPR's		Known Resources at Present Prices		Estimated Resources at Increased Prices	
Material	Const. (10^6 kg)	Oper. (10^6 kg/yr)	Requirement for 30 yr Plant Life (10^6 kg)	Const. (10^6 kg)	Oper. (10^6 kg/yr)	U.S. (10^6 kg)	World (10^6 kg)	U.S. (10^6 kg)	World (10^6 kg)
Niobium (Total)	3.608	0.0767	5.91	8,800	189	70^a	$6,000^a$	140^a	---
Blanket	0.383	0.0767^b				5.4^c	100^c	$7,800^c$	$17,200^c$
		0.011^d	0.33^d						
		6.76×10^{-6}			$26^{c,d}$				
Headers	0.356								
Manifolds	0.077								
Misc. Piping	0.352								
H Exch	0.812								
Li Processing	0.540								
Li Pumps	0.058								
METS	1.029								
Copper (Total)	9.304	1.7×10^{-3c}	9.355	22,700	4.15^c	$77,000^a$	$280,000^a$	$180,000^a$	$1,100,000^e$
Compression	5.582	1.7×10^{-3c}				20,000	100,000	100,000	300,000
Coil		1.3							
Leads	3.722		3.722						
Lithium									
Natural (Total)	1.58^h	0.016^h	2.06^h	3,8[illegible]0	39^h	$5,000^a$	$6-8,000^a$	$9,000^a$	$100,000^a$
Coolant Loop (Natural)	0.864					800^e	$1,000^e$	$2,700^e$	---
Blanket ^{7}Li	0.051	0.000238^c							
Blanket ^{6}Li	0.049	0.00119^c							
Blanket Natural Li	0.716^h		$0.48^{c,g}$						
Berylium	0.052	0.0104^b	0.3638^b	0.126	25.4^b	$26^{a,i}$	$380^{a,i}$	$72^{a,i}$	$1,000^{a,i}$
		6×10^{-4c}	0.018^c		1.46^c	18^e	---	250^e	280^e
Helium	1.253^n	0.0015^l	1.298	3.0[illegible]6	3,568	$1,200^{a,j}$	$1,300^{a,j}$	$5,000^{a,j}$	$29,000^{a,k}$
		0.002^m							
Carbon	0.68	0.136	4.76^b	1.659	332^b	500^a	$100,000^a$	---	---
			0.0074^c		0.697^c				
Tin	0.3	---	0.3	0.730	---	6^a	$4,000^a$	42^a	$7,000^a$
						0^e	$6,000^e$	100^e	$11,000^e$
Deuterium	0.003^o	0.0004	0.0162	---	---	---	---	---	---

---

[a] From Reference 23
[b] Assumes 5 year useful lifetime
[c] Transmutation
[d] Corrosion, sputtering products collected in cold trap
[e] From Reference 24
[f] Can be reprocessed
[g] 2.5×10^{14} kg in seas at 1.5 lb per 10^5 gallon
[h] One kg natural Li gives 0.074 kg ^{6}Li
[i] Little information available
[j] In the ground
[k] In the atmosphere
[l] Loss from purge
[m] Gain from transmutation of Be, ^{7}Li, ^{6}Li, T and D. Only about 50% may be captured.
[n] Superconductor in METS
[o] Equal storage for 10 day supply at 5% burnup

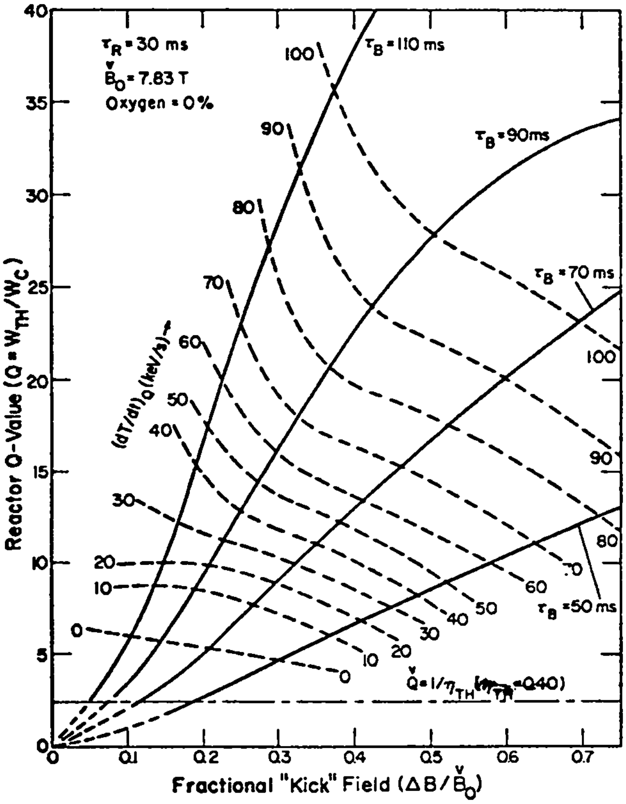

Fig. XIV-9
Dependence of the RTPR Q-value on $\Delta B/\hat{B}o$ *for various burntimes.*

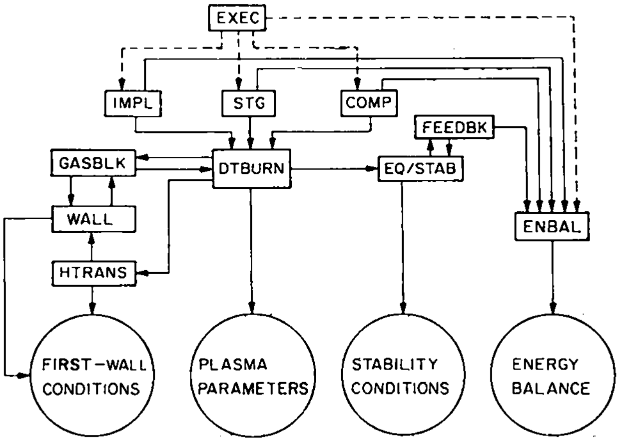

Fig. XIV-10
LASL systems analysis code for physics/technology studies.

preliminary, this study integrates these four important requirements in a consistent way. The $^{232}Th/^{233}U$ fuel cycle has been selected for this study on the basis of potential environmental advantages. Only well-understood technology is used for both the fission (HTGR) and fusion (Scylla) portions of the LTPHR. On the basis of a generalized energy balance developed for the fusion-fission symbiosis, as shown in Fig. XIV-11, favorable energy multiplication (Q_E = total electrical power/recirculated power ~5-10) results for theta-pinch systems which are below 1000 m in length and self-sufficient for tritium. Although some ^{233}U-enrichment of the blanket is shown to be necessary, the optimum blanket configuration has not been determined. An electro-technology based on LC-resonant circuits is proposed, and reversible transfer of magnetic energy with efficiencies >90% (including joule losses in the theta-pinch coil) will be required. Although a capacitive energy store will be required for the implosion heating phase, the energy for the compression field will be derived from a homopolar motor/generator set, which discharges slowly into a storage inductor; the homopolar motor/generator behaves electrically as a capacitive circuit element. The mix between fission and fusion energy production is not specified. Preliminary cost estimates of major portions of the "nuclear island" (power supplies, switches, blanket, prorated fission burner) indicate costs in the range of 600/KWe. A major portion of the cost (400-500/KWe) is associated with the capacitive power supply; alternative magnetic energy storage schemes will be explored.

A 1000 m long LTPHR which has a 18 kg/m ^{233}U loading gives an intrinsic doubling time of 14 y (0.72 tonnes/y ^{233}U production) for a first-wall, fusion neutron current equivalent to 1.0 MW/m^2. Table XIV-V summarizes the neutronic characteristics of a reference fission/fusion blanket, and Fig. XIV-12 gives a conceptual illustration of a "typical" LTPHR module. This system has a net tritium breeding gain, generates ~ 10 times its internal circulating power needs (for reversible transfer efficiency of 95%), and provides 7.38 MWe/m of electrical energy (12.8 MWe/m^3 of enriched seed or 2.44 kg ^{233}U/MWe) for a thermal conversion efficiency of 0.40. Approximately 10 GJ of stored energy will be required, which must be switched at a frequency of 2-4 Hz to maintain 1.0 MW/m^2 fusion-neutron wall loading. The design presented here in many ways is conservative, but these preliminary, favorable results warrant further exploration of the LTPHR concept.

D. Theta-Pinch Nucleonic Studies

1. Radioactivity and Afterheat. As part of the assessment of the RTPR, a comprehensive

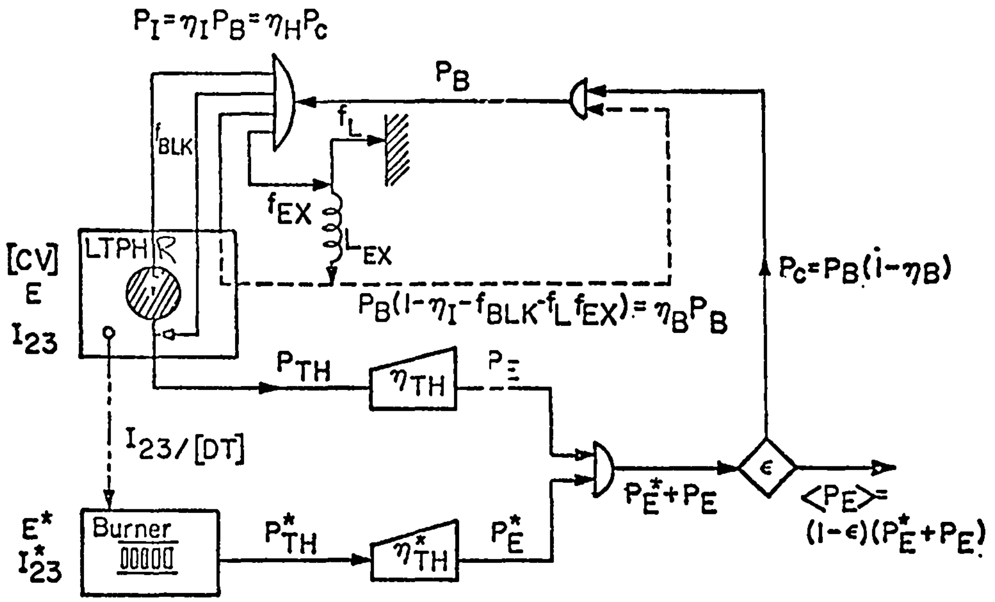

*All Power Expressed as MW/m

Fig. XIV-11
Schematic diagram of the LTPHR energy balance.

parameter study[33,34] was performed on induced structural radioactivity and afterheat. This parameter study varied the first-wall 14.1-MeV neutron current (0.2 to 6.7 MW/m^2), the reactor operating time (1 to 20 y), the time after shutdown (0 to 10^{12}s), and the blanket structural material (Nb1%Zr, V20%Ti). The variation of blanket radioactivity (Ci/Wt or Ci/Wt y), relative biological hazard (km^3/Wt), and nuclear afterheat (fraction of operating power) was investigated. A radioactivity burn-out effect shown in Fig. XIV-13 was demonstrated for the Nb1%Zr RTPR, whereby higher wall loadings lead to higher short-term radioactivity and lower long-term radioactivity. A comparison was made with other fusion reactor designs as well as with a typical fast fission reactor. Figure XIV-14 presents a summary of the relative biological hazard for several fusion reactor designs, as a function of shutdown time. Also shown are the fission product and actinide (plutonium) curves for a typical fast breeder fission reactor. Figure XIV-15 shows analogous curves for total afterheat power as a fraction of operating power.

Although calculations showed that ^{95}Nb ($t_{1/2}$=35 d) is a major source of afterheat in the RTPR, uncertainties in the cross section for the reaction ^{94}Nb (n,γ) $_5$Nb may introduce large errors in the calculated afterheat. This source of uncertainty has been examined in further detail.[35]

Target expense and radioactivity have limited ^{94}Nb cross section measurements, but several determinations of the thermal neutron capture cross section have been made, as well as two measurements of the capture resonance integral. The recommended values for these parameters are 13.6±1.5 b and 125±8 b, respectively; measurements of the energy dependence of the capture cross section are not available. Fortunately, reasonable estimates of the energy dependence can be made if the total cross section measurements are taken into account. This measurement, from which the capture cross section up to 50 eV can be inferred, revealed a large resonance at 11.6 eV and a much smaller one at 22.6 eV. The recommended resonance parameters account for 90±9 b of the 125 b capture resonance integral. The plausible assumption can therefore be made that the remaining 35±12 b results from resonances above 50 eV.

To determine the effect of the unknown distribution of resonances (above 50 eV) on the ^{94}Nb capture rate, the neutron energy spectrum has been examined. In the region (below 100 keV), where most captures occur, the spectrum in the RTPR (and most other fusion reactor blankets) follows a 1/E shape down to rather low energies (typically 1-100 eV). At lower energies, absorption becomes increasingly important and the spectrum becomes increasingly depleted relative to the pure 1/E spectrum used to

TABLE XIV-V

REFERENCE BLANKET CONFIGURATION AND PERFORMANCE

Region	Inner Radius (m)	Outer Radius (m)	Material
Plasma Chamber	0.0	0.100	Vacuum
Coil	0.100	0.115	Mo, 30 v/o He
Tritium Breeding	0.115	0.415	^{7}Li (99 a/o), 25 v/o He
Inner Enriched Seed	0.415	0.665	10 a/o ^{233}U, C/HM = 214, 25 v/o He
Outer Enriched Seed	0.665	0.865	4 a/o ^{233}U, C/HM = 214, 25 v/o He
Fertile Seed	0.865	1.215	C/^{232}Th = 214, 25 v/o He

PERFORMANCE CHARACTERISTICS

$[BR] = 1.35$

$[CV] = 0.233$ (including leakage)

$E = 413.5$ MeV/n

$E + E^* = 454.4$ MeV/n

^{232}Tn (n,Nn) = 0.0087/DT neutron

$I_{23} = 18.2$ kg/m

$E/I_{23} = 3.64 \times 10^{-18}$ MJ/kg per n/m

$(E + E^*)/I_{23} = 4.00 \times 10^{-18}$ MJ/kg per n/m

$R = 0.72$ (kg/m y) [^{233}U production at 1 MW/m^2 wall loading]†

---

†1 MW/m^2 of 14.1-MeV neutrons is equivalent to [illegible] = 4.44×10^{17} (n/m^2 s)

form resonance integrals. Hence, it is clear that the ^{94}Nb capture rate will be minimized if the available resonance integral is concentrated in low energy resonances. On the other hand it is entirely possible that the major resonances are concentrated above 200 eV, where the spectrum is not severely depleted. From these considerations, hypothetical cross section shapes were constructed, which tend to minimize or maximize the capture rate, while maintaining a 35 b resonance integral above 50 eV.

Low Capture: $\sigma_c(E)$ is assumed to be dominated above 50 eV by a single resonance at 55 eV.

Medium Capture: $\sigma_c(E)$ is assumed to have a 1/v shape from 50 eV to several MeV.

High Capture: $\sigma_c(E)$ is assumed to be zero from 50 eV to 200 eV, with a 1/v shape above that region.

To illustrate the sensitivity of RTPR afterheat and activity results to this effect, the total afterheat at time of shutdown was calculated, as well as the total ^{94}Nb activity, using the method described previously.[34] A wall loading of 2.0 MW/m^2 was assumed, and the reactor operating time was either 5, 20 or 50 y. The longer operating times are relevant to Nb recycle studies. The results of these calculations for the three operating times are given in Tables XIV-VI through XIV-VIII, respectively. All data are calculated at time of shutdown, and results are shown for each of the three cross section shapes discussed above. Shown for comparison are the results of a calculation using the ^{94}Nb capture cross section assumed in Ref. 34 (15 times the ^{93}Nb capture cross section at all neutron energies). From the results shown in Tables XIV-VI through XIV-VIII, the distribution effect should produce errors no greater than about 25% in RTPR afterheat and long-term radioactivity calculations.

2. RTPR Blanket Nucleonic Studies. Studies have continued on alternative materials and blanket thicknesses for the RTPR. Table XIV-IX illustrates a typical parameter study performed for the post-design assessment. Because of the large energy storage and transfer requirements of the RTPR a

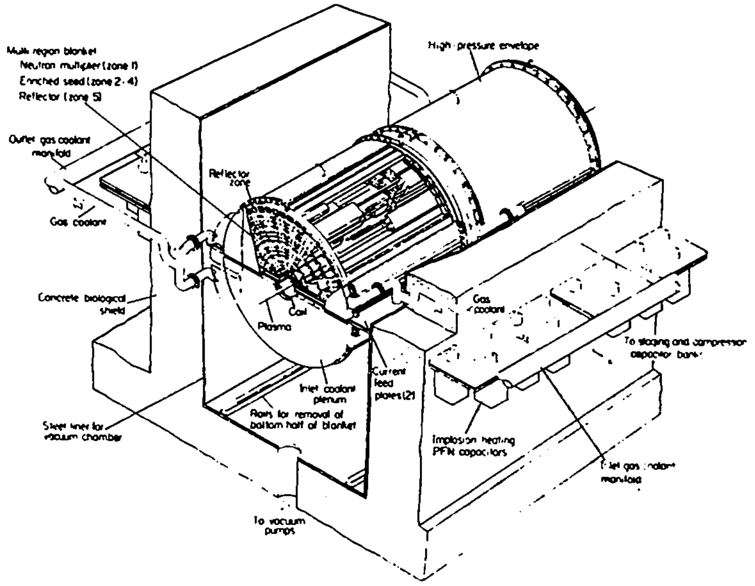

Fig. XIV-12
Conceptual illustration of a LTPHR blanket module.

strong incentive exists for minimizing blanket thickness. To a first approximation, as the blanket is thinned, the increased (radiation induced) waste heat in the coils is equal to the decreased recoverable heat in the blanket. Tritium breeding has been shown previously to be easily maintained at a value >1.0 by adjusting the beryllium region thickness. The recoverable and waste energies will both increase with increased beryllium thickness; e.g., a 10 mm increase in beryllium thickness provides a 1.1-MeV increase in recoverable energy per D-T neutron and a 0.07 increase in tritium breeding ratio. Radiation heating in the coil varies linearly with small (20 mm) changes in graphite thickness for a niobium structure. However, for molybdenum structures large changes of the graphite region were considered, and the effects were nonlinear (*cf.* Table XIV-IX). In general, application of perturbation theory by Gerstl[36] to moderate (10 to 20 mm) changes in beryllium and lithium regions of the RTPR, and to substitution of structural materials, has proven successful.

In further analysis it has been found that the outboard graphite region in a molybdenum RTPR blanket can be reduced in thickness by at least 60 mm, while maintaining an adequate breeding ratio. Over the range of 0 to 50 mm reduction in graphite, the parasitic absorption and (n,2n) reaction rates in the coils increase approximately linearly at 1.0% per mm and 1.2% per mm of reduction in blanket thickness, which does not impose serious limitations on reduction in blanket thickness. Rather, the ultimate reversal of tritium breeding ratio with decreasing blanket thickness limits the minimum blanket volume and hence the amount of stored magnetic energy.

Other neutronics studies concentrated primarily on a review and revision of source data used for the calculation of appropriate response functions. Table XIV-X summarizes the dpa values using two alternative displacement functions. Included are results for two neutron spectra, based on niobium or molybdenum structures. In each case dpa values were determined for three candidate structural materials (Nb, Mo, and V); i.e., it is implicitly assumed that the response is weakly dependent on the spectrum variation, an assumption which has been verified.

Analysis of transmutation and dpa in beryllium, graphite, and copper also reveals differences between molybdenum and niobium structures. A slight increase in transmutation rates generally results from using molybdenum because of the increased (n,2n) neutron production. Tritium breeding, however, is lower for a molybdenum structure because of increased low energy neutron capture (0.530 for Mo vs 0.378 for Nb), especially in the graphite regions. Sensitivity studies have shown that

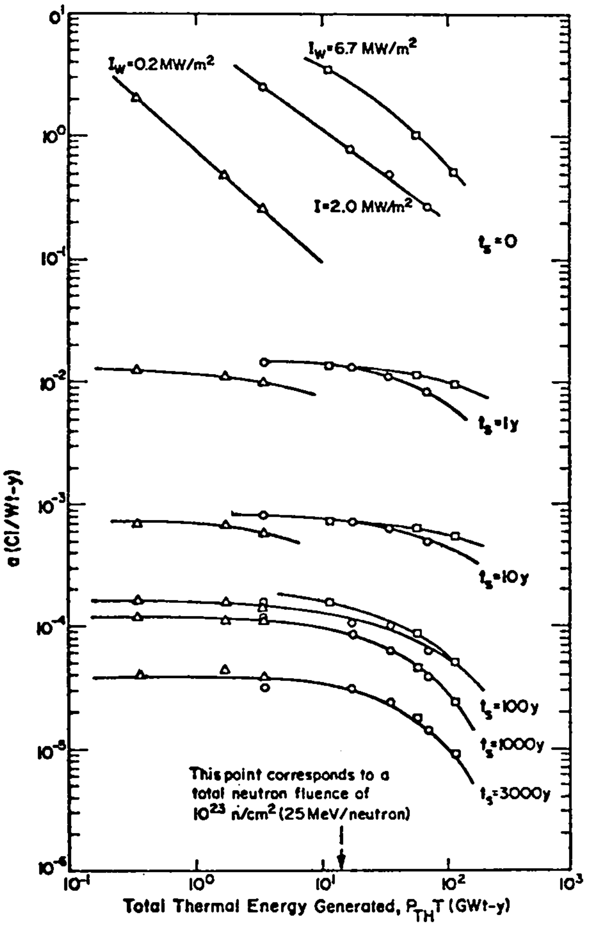

Fig. XIV-13

Dependence of a{Ci[W(th) yr]} on $P_{TH}T$ [GW(th) yr)] for various values of t_s.

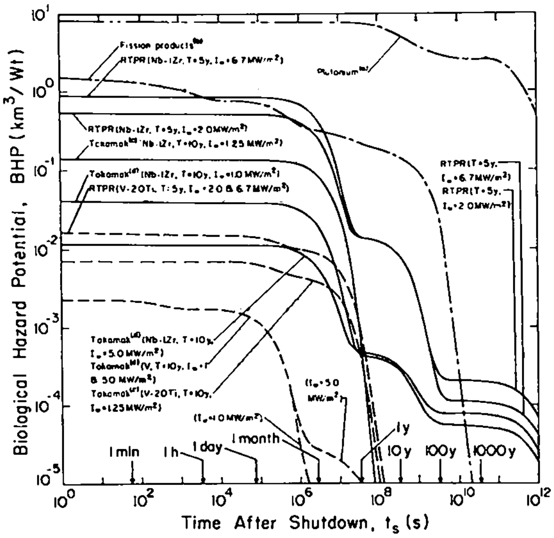

Fig. XIV-14

Intercomparison of BHP for various fusion and fission reactor concepts: (a) Ref. 26. (b) Ref. 27, (c) Refs. 28 and 29, and (d) Ref. 30.

decreasing the outboard graphite thickness, and hence total blanket thickness, by up to 60 mm *increases* tritium breeding ratio in a molybdenum structure RTPR by ~0.1% per mm of reduction. Similar studies for niobium show the opposite effect, because of the more predominant epithermal capture in niobium resonances.

Prediction of first-wall surface effects is complicated by two factors. First, the inner niobium surface is really the interface of a composite alumina-niobium structure, so the neutron sputtering or chunk injection effect is uncertain at this surface. Secondly, and perhaps more important, is the large range of uncertainty in 14 MeV neutron sputtering coefficients. To illustrate the range of values and their effect on erosion rates of the 1 mm niobium portion of the first wall, sputtering rates were computed using the coefficients of Kaminsky and Das[40] and of Behrisch.[41] The Kaminsky and Das 14 MeV sputtering coefficient of 0.25 atoms/neutron would lead to rapid (~0.27 mm/y) destruction of 1 mm niobium walls, while the alternative coefficient presents acceptably small (~10%) erosion over an estimated 5-y maximum wall lifetime. Hence, no definitive conclusions can be drawn regarding the effect of 14 MeV neutron sputtering until further experimental evidence establishes confirmed and repeatable sputtering coefficient values*

3. Resonance Self-Shielding in ^{93}Nb. A formalism to account for resonance self-shielding effects, the f-factor method, has been applied to the RTPR.[42,43] For a given material, the group self-shielding factor, f, is defined as the ratio of the resonance-shielded cross section to that for infinite dilution. Formally, f is a function of all the parameters (temperature, atom density, and resonance parameters), which define the total macroscopic cross section of the mixture. However, in practice the f-factors are specified as a function of temperature, T, and a single parameter, σ_0, which represents a conglomerate effect of the remaining parameters of the mixture. In essence the f-factors are used to account for flux depression in the vicinity of large resonances.

---

*The uncertainty in neutron sputtering coefficients is discussed further in Sec. VIII.F.2.c.

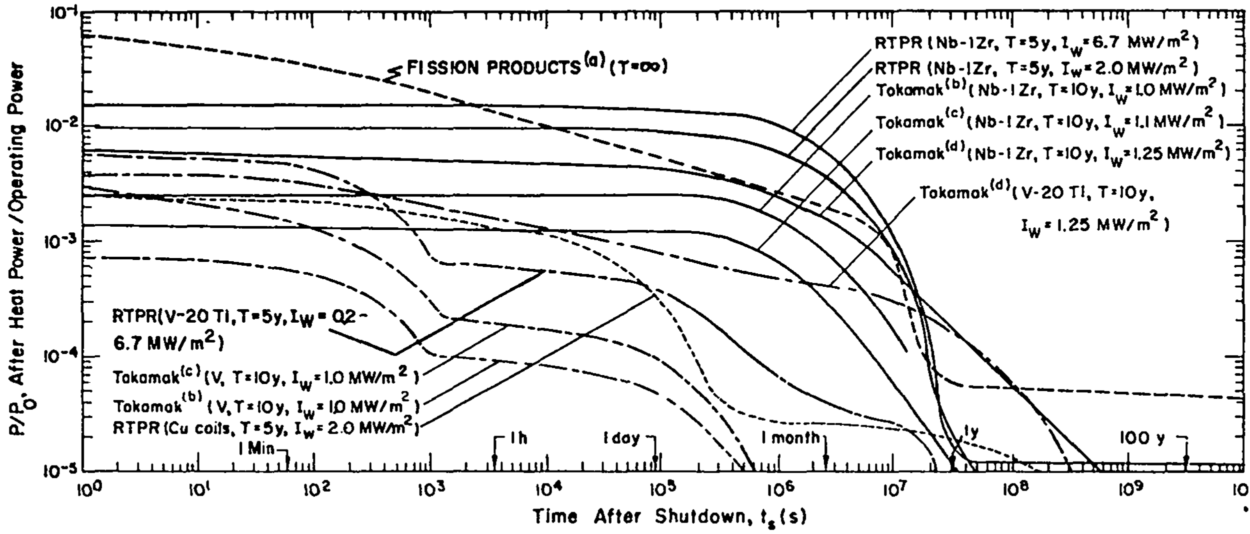

Fig. XIV-15

Comparison of nuclear afterheat, P/P_0, for the RTPR (Nb-1% Zr and V-20% Ti, I_w=2.0 and 6.7 MW/m², T=5 yr) with other fusion reactors and fission reactors: (a) Ref. 31, (b) Ref. 32, (c) Ref. 30, and (d) Ref. 29.

One material of special interest in the RTPR blanket is ^{93}Nb, for which the capture cross section exhibits a large number of resonances. Although Nb constitutes a small volume fraction of the blanket, its presence significantly affects the breeding potential, energy deposition, and radioactivity of the blanket.

Gerstl and Henryson[44] performed a detailed calculation of the resonance self-shielding in niobium using the MC^2-2 code, and σ_0 values averaged over the resolved energy region of Nb. Work at LASL employs f-factor tables which have been generated by the MINX code using ENDF/B-III data. After determining the proper σ_0 in each energy group and the corresponding temperature, self-shielded multigroup data sets were obtained and applied in RTPR blanket nucleonic calculations.

The results of the nucleonic calculations are presented in Table XIV-XI. All analyses were performed using the LASL CTR Nuclear Analysis Computation System.[21] Table XIV-XI verifies the assumption that resonance self-shielding will increase tritium breeding ratios by ~7% in the RTPR blanket. Additionally, niobium self-shielding will decrease blanket radioactivity, as well as total recoverable energy and magnet-coil heating. The net recoverable energy decreases by 0.37 MeV and the coil heating by 0.23 MeV (per D-T neutron) in going from the infinite dilution to the 1100 K, self-shielded cross sections. Temperature effects change these parameters by less than 2%. a024

4. TR3A and Other Code Development. Continuing studies of afterheat and radioactivity have led to modifications to the transport code post-processor TR3A. The principal modification was to the equations for ^{94}Nb, ^{95,95}Nb radioactivity. Whereas previously the assumed cross section behavior for ^{94}Nb(n,γ) reactions was implicit in the equations, the code now accepts input multigroup cross-section data. Modifications to compute biological hazard potentials (BHP) from input maximum permissible concentrations have also been made.

As part of the data assessment program the perturbation-theory code SENSIT has been modified to accept DTF-IV output and to improve several features of the code. For example, both design sensitivies and cross-section sensitivity profiles can be computed for simultaneous perturbations in all spatial regions, and automatic plotting options have been incorporated.

5. Fusion/Fission Hybrid Studies with ^{238}U/^{239}Pu. First scoping studies[45] of a linear theta pinch hybrid considered an LMFBR-blanket design as a fertile seed within the fusion reactor blanket. The fertile seed region was cooled by liquid lithium, which also served to breed tritium. Several studies were made for the ^{238}U blanket system. The requirement of placing the (copper) magnet coil as close as possible to the plasma seriously degrades the energy spectrum of the 14.1-MeV neutrons released

TABLE XIV-VI

RTPR ACTIVITY AND AFTERHEAT AT 5 YEARS

Case	A_{94}/P_0 (Ci/W)	A_{95}/P_0 (Ci/W)	P/P_0 (percent)
Times fifteen	4.10×10^{-4}	$1.31 \times 10^{+0}$	1.18
High capture	4.84×10^{-4}	5.67×10^{-1}	0.81
Medium capture	4.98×10^{-4}	4.09×10^{-1}	0.73
Low Capture	5.12×10^{-4}	2.52×10^{-1}	0.65

TABLE XIV-VII

RTPR ACTIVITY AND AFTERHEAT AT 20 YEARS (RECYCLE)

Case	A_{94}/P_0 (Ci/W)	A_{95}/P_0 (Ci/W)	P/P_0 (percent)
Times fifteen	8.44×10^{-4}	2.52	1.80
High capture	1.40×10^{-3}	1.61	1.34
Medium capture	1.56×10^{-3}	1.26	1.17
Low capture	1.74×10^{-3}	0.84	0.95

TABLE XIV-VIII

RTPR ACTIVITY AND AFTERHEAT AT 50 YEARS (RECYCLE)

Case	A_{94}/P_0 (Ci/W)	A_{95}/P_0 (Ci/W)	P/P_0 (percent)
Times fifteen	9.53×10^{-4}	2.56	1.82
High capture	2.04×10^{-3}	2.23	1.66
Medium capture	2.50×10^{-3}	1.96	1.52
Low capture	3.13×10^{-3}	1.47	1.27

in the D-T reactions. For coils of approximately 5 cm thickness, the neutron energy spectrum emerging from the coil has been softened considerably, reducing the probability of fast fissioning in ^{238}U and of the $^{7}Li(n,n'\alpha)T$ reaction; both reactions are important for neutron economy in that the ^{238}U fission reaction multiplies neutrons and the ^{7}Li reaction produces tritons without the loss of a neutron. Alternatives of increasing ^{239}Pu and ^{6}Li enrichments are possible, but not as desirable. Tritium breeding ratios greater than unity are possible for this system, but only for blankets which use fertile seeds enriched in ^{239}Pu.

Renewed studies of a LTPHR, employing the $^{238}U/^{239}Pu$ cycle have evolved from experience with the $^{232}Th/^{233}U$ cycle design (Sec. XIV.c.2). Blanket designs now consider much thinner coils made of molybdenum alloys, followed by a depleted ^{238}U multiplier (fast-fission) region. The fertile seed is also lithium cooled, but now uses carbide fuel technology being developed in the fission program, in the form of ^{238}UC or ^{232}ThC. No fissile (e.g., ^{239}Pu) loading of either multiplier or breeding portions of the seed is contemplated, except for the normal equilibrium fissile content caused by breeding during the fuel element lifetime.

TABLE XIV-IX

EFFECT OF GRAPHITE THICKNESS ON TRITIUM BREEDING, COIL HEATING, AND COIL TRANSMUTATION IN THE RTPR

Structure	Graphite (m)	T[a]	Coil[c] Heating (% change)	Cu(n,2n)[c] (% change)	Cu(n,γ)[c] (% change)
Nb[b]	0.1474	1.108	---	---	---
	0.1374	1.106	9	10	9
	0.1274	1.105	18	20	18
Mo	0.1474	0.924	---	---	---
	0.1274	0.943	20	22	19
	0.1074	0.961	42	50	40
	0.0874	0.979	69	83	66

(a) Including an estimated correction of 0.07 for resonance self-shielding.

(b) RTPR reference design case, for which waste heat (>99% in the coild and insulation) is 0.80 MW/m and recoverable heat is 9.6 MW/m.

(c) Relative to 0.1474-m thickness.

TABLE XIV-X

MAXIMUM ATOM DISPLACEMENT RATES AT FIRST WALL METAL AND IN GRAPHITE

$(I_w = 2.0\ \mathrm{MW/m^2})$

Structural Material (Spectrum)	Response Material	Location	Radius (m)	Original[a] (dpa/y)	Revised[a] (dpa/y)	ϕ_{TOT} ($m^{-2}s^{-1}$)	$\phi(E > 1\ \mathrm{MeV})$ ($m^{-2}s^{-1}$)
Nb	Nb	First Wall	0.500	36.2	18.2	9.02×10^{18}	3.95×10^{18}
Nb	Mo	First Wall	0.500	36.7	17.5	9.02×10^{18}	3.95×10^{18}
Nb	V	First Wall	0.500	54.7	26.0	9.02×10^{18}	3.95×10^{18}
Nb	C	Inner Graphite	0.605	--	11.7	6.13×10^{18}	1.72×10^{18}
Mo	Nb	First Wall	0.500	36.9	18.6	9.40×10^{18}	4.06×10^{18}
Mo	Mo	First Wall	0.500	37.5	17.8	9.40×10^{18}	4.06×10^{18}
Mo	V	First Wall	0.500	56.0	26.6	9.40×10^{18}	4.06×10^{18}
Mo	C	Inner Graphite	0.605	6.39	12.0	6.35×10^{18}	1.76×10^{18}

(a) The original calculations were performed with response functions for V, Nb, and Mo as given by Ref. 37, and for C as given by Ref. 38. Revised values are from Refs. 39 and 40, respectively, and are currently considered to be the best available values for the reference design.

TABLE XIV-XI

SELECTED NUCLEONIC EFFECTS IN A RTPR BLANKET AS A FUNCTION OF RESONANCE SELF-SHIELDING

Temperature (K)	σ_0	Breeding Ratio	Nb Abs.	Cu Abs.	^{6}Li(n,α)t	Total Neutron$^{(a)}$ Energy (MeV)	Total Gamma$^{(b)}$ Energy (MeV)	Gamma Energy in$^{(b)}$ Cu Coils (MeV)	Ci/Wt$^{(c)}$		P/Po$^{(c,d)}$
									^{94}Nb	^{95}Nb	
0	--	1.024	0.374	0.0966	0.862	14.60	9.90	1.65	0.00156	1.26	1.17
300	Variable	1.116	0.283	0.0970	0.953	15.07	8.99	1.43	---	--	--
1100	Variable	1.095	0.303	0.0969	0.933	14.98	8.92	1.42	0.00110	1.12	1.04

(a) Total neutron energy deposited in the blanket and coils, per D-T neutron.

(b) Gamma energy deposited per D-T neutron.

(c) Operating time is 20 y, representative of coil lifetime and recycled (~4 times) Nb structures, and shutdown time is zero. ^{94}Nb(n,γ) cross section is medium estimate (cf. section on ^{94}Nb Sensitivity Studies).

(d) Afterheat from Nb and Cu activation at shutdown as percentage of operating power.

E. Nuclear Data and Sensitivity Analysis

The effort to provide reliable nuclear data for the CTR program concentrated on the assessment of near-term nuclear data needs and expansion of the LASL/CTR multigroup data library.

1. Assessment of CTR Cross Section Needs. To coordinate with other laboratory programs, active participation has been maintained in the CTR Subcommittee of the U.S. Nuclear Data Committee, in the ASTM Neutron Dosimetry Standards Committee, and in the Cross Section Evaluation Working Group. Critical reviews of CTR-related nuclear data have been made, including cross sections for the D-T and T-T fusion reactions. Also, input was provided to the national nuclear data request list for new cross section measurements and evaluations required for CTR applications.

Work has begun on a program to determine quantitatively the cross-section requirements and highest priority areas for near-term nuclear data research and development for the national CTR program. This assessment takes into account the quality of currently available data, the sensitivity of important nuclear design parameters to these nuclear data, and the accuracy required in CTR design applications. The computational system used to perform these analyses employs forward and adjoint transport calculations to calculate sensitivities, and constructs covariance matrices from ENDF/B error files or other sources. A perturbation theory code combines the sensitivity information with the covariance matrices to obtain the uncertainties of calculated nuclear design parameters, which are then the quantitative basis for a judgment on the adequacy of cross sections. The capabilities of this approach were demonstrated with a sample calculation for the TFTR* design.[46] Subsequently, in close cooperation with Princeton Plasma Physics Laboratory and Westinghouse Research Laboratory, a more detailed assessment of nuclear data requirements for the TFTR design has been initiated.

An appropriate tool for studies of this type is perturbation theory. In this approximation, the standard deviation ΔR in a design parameter R can be written as follows:[47]

$$(\Delta R)^2 = \sum_{i,j} \frac{\partial R}{\partial X_i} \frac{\partial R}{\partial X_j} \mathrm{Cov}(X_i, X_j) \qquad (1)$$

In Eq. (1) X_i is the cross section for a particular nuclear reaction at a particular neutron energy. $\mathrm{Cov}(X_i,X_j)$ are the covariance matrix elements for cross sections X_i and X_j and contain the estimated errors, together with correlations, of existing cross-section sets. The quantities $\partial R/\partial X_i$ in Eq. (1) are sensitivity coefficients which result from a sensitivity analysis of the particular transport problem of interest.[48-50]

To illustrate results expected from this data assessment program, the methods outlined above were applied to the neutronics evaluation of the proposed TFTR.[46] As a critical design parameter we selected the production of the 5.3-y half-life cobalt-60 isotope from the ^{63}Cu(n,α)^{60}Co reactions in the copper coils was selected. The TFTR coils are shielded by a magnet shield consisting of commercial lead-loaded borated polyethylene. The effectiveness of this shield against high energy neutrons is derived largely from its hydrogen (2 w/o) and carbon contents (17 w/o). Therefore, it seemed appropriate for the sample case to evaluate the sensitivity of the ^{60}Co production in the coils to the carbon cross sections of the magnet shield.

The estimated uncertainties in the carbon cross sections for the TFTR shield,[47] together with calculated sensitivity coefficients, gave rise to the uncertainty of the ^{60}Co production calculation as shown in Table XIV-XIII. The overall uncertainty of 2.1% indicates that for this specific application the accuracy of the carbon cross sections is adequate.

To calculate sensitivity coefficients for secondary energy distributions, an extension of the usual perturbation approach has been developed. The main feature of this method is the introduction of a "sub-partial" reaction cross section $\hat{\sigma}$, which corresponds only to those events yielding high-energy secondary neutrons. The sensitivity coefficient for $\hat{\sigma}$ is calculated by an algorithm which allows the effect of uncertainty in the spectrum to be separated from uncertainty in the magnitude of the energy-integrated cross section. One important application of this method is to provide a quantitative basis for the assignment of priorities to measurements of neutron emission spectra.

2. The LASL/CTR Multigroup Library. One-hundred group neutron interaction cross sections have been prepared for vanadium and the results placed in the LASL/CTR processed nuclear data library described in Ref. 51. These cross sections were obtained by processing the ENDF/B-IV evaluation using the processing code MINX.[51] A multigroup data set for the analysis of fusion-fission hybrid reactors based on the ^{238}U cycle has been

---

*Tokamak Fusion Test Reactor, formerly Two Component Tokamak (TCT).

TABLE XIV-XII

ESTIMATED UNCERTAINTIES $\delta\Sigma/\Sigma$ FOR ^{12}C CROSS SECTIONS IN TFTR MAGNET SHIELD

Cross Section Type	Neutron Energy	
	5 to 9 MeV	9 to 15 MeV
Σ_T	0.03	0.04
$\Sigma_{Abs.}$	0.15	0.15
$\Sigma_{Scat.}$	0.05	0.15

TABLE XIV-XIII

PREDICTED UNCERTAINTY OF ^{60}Co-PRODUCTION IN TFTR COILS DUE TO CROSS SECTION UNCERTAINTIES SHOWN IN TABLE XIV-XIII

$\frac{\delta\Sigma_x}{\Sigma_x}$	$\frac{\delta R_x}{R}$	$\frac{\delta R}{R} = \left(\sum_x \left(\frac{\delta R_x}{R}\right)^2\right)^{1/2}$
Total	0.0059	0.021 overall uncertainty assuming no correlations between individual cross sections.
Abs.	0.0022	
Scat.	0.020	

prepared. A 25-group structure was formed as a subset of both the LASL/CTR and LASL/TD multigroup structures. A second group-collapsed data set was produced for the analysis of fusion-fission (hybrid) reactors based on the ^{232}Th-^{233}U cycle in a graphite lattice (thermal hybrids). This library consists of data in a 19-group format, including 3 upscatter groups. The previously reported portion of the multigroup library containing activation and transmutation cross sections has been revised and expanded. Resulting multigroup data (for 687 distinct nuclear reactions) are available on a BCD card-image tape for external distribution.

3. Cross Sections for Insulator Research. Spectrum-averaged transmutation cross sections have been calculated for Be, N, O, Al, and Si using the data in the multigroup library described above. These data allow predictions of the build-up of gaseous and metallic impurities in electrical insulators such as BeO, Si_3N_4, SiO_2, AlN, and Al_2O_3.

4. Cross-Section Library Utility Codes. Because of storage and running time requirements of various codes used in CTR nucleonic studies, conventional P_3, 100-neutron group, 21-photon group libraries used in previous studies are not always practical. To reduce the number of neutron energy groups, an existing LASL collapsing code was modified to additionally collapse neutron portions of photon-production matrices. At the option of the user, the 100-groups can be collapsed into subsets of any number ($\leq$100) and coupled neutron-gamma cross-section sets formed.

F. Insulator Studies

Emphasis was placed on problems associated with the first-wall liner of the RTPR; however, information from these studies is also applicable to other insulator uses in fusion reactors.

Experimental work was directed toward evaluation of electrical and structural behavior of insulators at elevated temperatures and under irradiation. Damage simulation experiments for 14 MeV neutron were also conducted. Calculations on sputtering, trannsmutation product generation rates, and ionization effects on resistivity were carried out. Dielectric strength of insulator-coated metal segments for possible use as an SFTR first wall was evaluated, and calculations made of anticipated water desorption from the SFTR first wall. Finally, a stockpile of ceramic materials for use by LASL and other CTR insulator laboratories was begun.

1. Electrical Properties Experiments

a. DC and Pulsed Voltage Dielectric Strength of Insulators at Elevated Temperatures. The insulating liner of the RTPR must withstand a pulsed voltage of 3 KV over a thickness of 0.3 mm (i.e., 100 kV/cm) at 800-1100 K. Measurements of the dielectric strength of a high-density polycrystalline Al_2O_3 as a function of temperature show that pulsed-voltage dielectric strength was much greater than that measured with dc voltage at elevated temperatures. The effect of electrode geometry has since been studied using diffuse-edge electrodes. This technique gives greater field uniformity than did measurements with point-contract electrodes used previously, and should more closely simulate breakdown conditions in fusion devices. Results obtained are shown in Fig. XIV-16; a significant increase in dielectric strength is realized with a diffuse-edge electrode.

An important variable in pulsed-voltage dielectric-strength measurements is the time required for electrical breakdown. This variable has been investigated experimentally for a vitreous enamel glass at 873 K and compared with theoretical breakdown models. Results obtained agree qualitatively with theory, in that the voltage vs time-to-breakdown curve shows the predicted shape in Fig. XIV-17. The results shown in this figure for Al_2O_3 at 973 K are explainable by assuming that characteristic breakdown times for this insulator are much longer than those for the enamel. Since the voltage induced during the implosion heating in a theta pinch will appear across the first wall insulator for less than one μsec, the higher dielectric strengths of Fig. XIV-17 should be applicable to the RTPR.

Earlier results on the dielectric strengths at 300 K and 873 K have been reported, for a number of insulators known to contain some porosity. The porosity is an important parameter, since high porosity can reduce breakdown strength. Work in this area has continued and more recent results are shown in Table XIV-XIV. Although the data are too sparse to permit detailed conclusions, the following indications seem evident: for porous materials little or

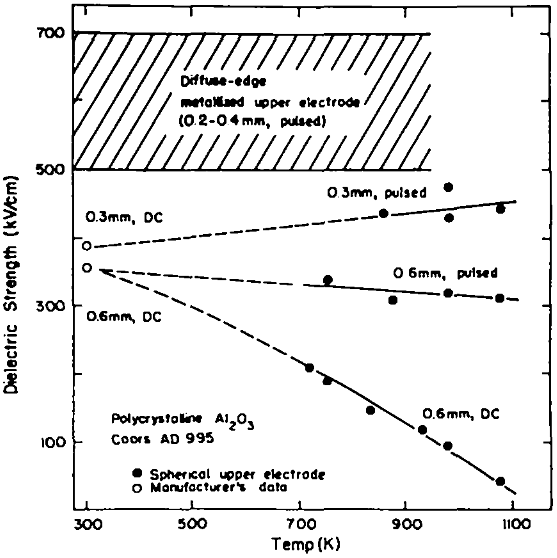

Fig. XIV-16
Pulsed dielectric strength of alumina as a function of temperature.

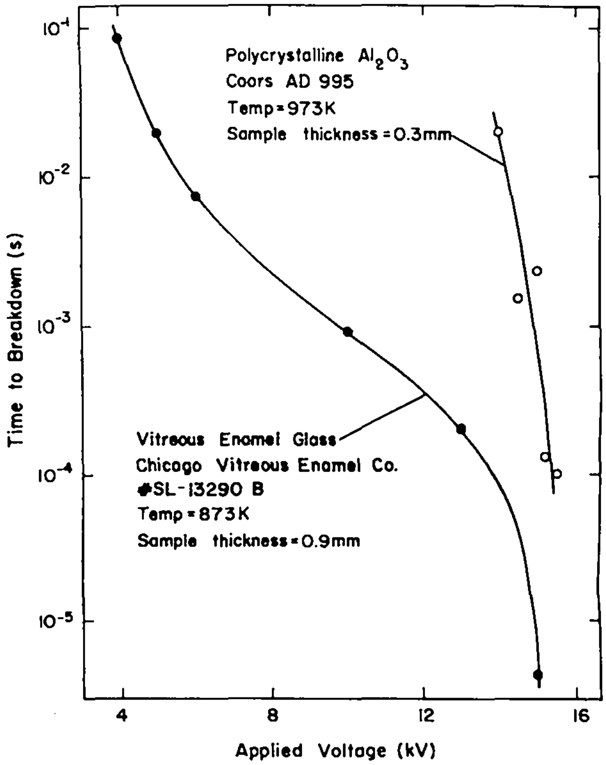

Fig. XIV-17
Time to breakdown vs applied voltage for alumina and vitreous enamel.

TABLE XIV-XIV

DIELECTRIC STRENGTH OF INSULATOR/METAL AND INSULATOR SAMPLES

Insulator[a]	Temperature, K	Dielectric Strength, kV/mm[b] dc Insulator/Metal[c]	Dielectric Strength, kV/mm[b] Pulsed Samples	Density, % of Theoretical	Remarks
Al_2O_3	300	28	30	85	plasma sprayed (LASL)
	873	11	9		
Al_2O_3	300	--	32	82	plasma sprayed
	873	—	20		(Plasmadyne)
Y_2O_3	300	25	32	—	plasma sprayed (LASL)
	873	~7	21		
Enamel[d]	300	27	--	—	0.8 mm thick LASL
	300	23	23		(LASL)
	873	<5	17	—	0.9 mm thick (LASL)
		Insulator Samples			
AlN	200	5	5	77	hot-pressed (MRC)
	873	12	13		
Si_3N_4	300	20	25	54	hot-pressed (MRC)
	873	12	16		
Si_2ON_2	873	~2	10	96	hot-pressed (Norton)
Y_2O_3-10% ThO_2	300	22	25	92	hot-pressed (LASL)
	873	13	15		
Y_2O_3	300	24	29	94	slip cast and sintered
	873	~5	10		(LASL)

[a] Insulator thickness 0.3-0.5 mm, unless otherwise specified.
[b] Spherical upper electrode.
[c] Metal substrates were austenitic stainless steel, Inconel, or Nb-1% Zr, ~1 mm thick; no effect of substrate composition on dielectric strength was observed.
[d] Chicago Vitreous Enamel Co. #SL-13290 B, applied by coating and firing.

no enhancement of dielectric strength with pulsed voltages is apparent, perhaps because breakdown is initiated in the pore gas on a time scale short compared with that for bulk thermal breakdown. Hence the dielectric stremgth for a porous material is lower than that for the same material near theoretical density.

b. Resistivity of Proton-Irradiated Glass. The RTPR first-wall insulator must exhibit a resistivity $\geq 10^6$ Ω-cm at 1073 K within 3-10 s, after irradiation by neutrons, charged particles, and photons (i.e., at the start of the next burn pulse). Preliminary measurements have been made of the effect of 6 MeV proton irradiation on electrical resistivity of a glass insulator at this temperature; for protons (6 MeV), both displacement damage and ionization damage resulted. Irradiation-produced defects are expected to decrease electronic conductivity, since they can serve as charge traps. However, enhanced ionic conductivity can result from displacements. Ionizing damage should increase conductivity by creating electron or hole charge carriers.

In these proton irradiation tests, SCB* glass (modified frit No. 1, of barium-aluminum-silicate composition) was irradiated. The incident protons passed through the 6×10^{-3} cm thick glass, losing 1 MeV to the specimen; the transmitted proton beam subsequently embedded in the bonding metal substrate. The 1.5 μA/cm^2 proton beam current gave a damage rate equivalent to that from an RTPR first-wall neutron flux of $\sim 10^{14}$ n/cm^2 s. Ionizing radiation was absorbed at a rate of $\sim 10^7$ rad/s. By comparison the ionizing radiation at the RTPR first wall during a pulse is estimated to be $\sim 4 \times 10^8$ rad/s.[1]

Typical results obtained are shown in Fig. XIV-18. During the first minute of irradiation, the glass exhibited a resistivity decrease of a factor of three; little additional change was noted during the remainder of the 5-m bombardment. After irradiation the SCB glass recovered its initial resistivity in roughly 1-m.

If the degradation of resistivity is assumed to have an electronic nature and to be a linear function of

---

*SCB is a designation of special glass originally developed as a hydrogen permeation barrier.

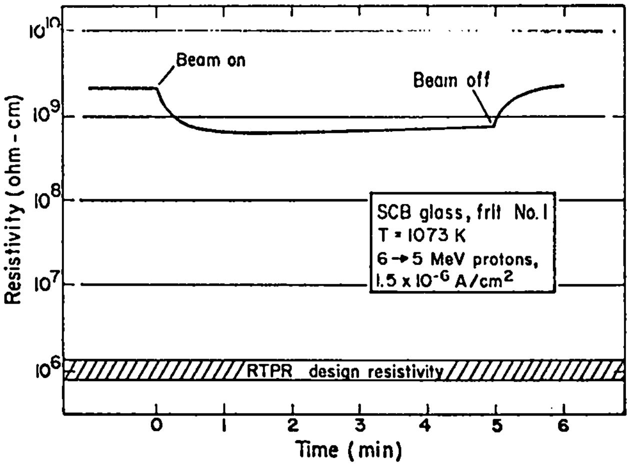

Fig. XIV-18

Effect of 5 MeV proton irradiation on the electrical resistivity of SCB glass insulators.

ionizing flux, the resistivity of this glass during irradiation at the RTPR first wall would be $\sim 10^7$ Ω-cm. The resistivity, therefore, would never be degraded to the minimum acceptable value of 10^6Ω-cm. The subsequent 10-s anneal would of course improve the resistivity before the next power cycle.

2. Structural Properties Experiments

a. Fission Neutron Damage to Al_2O_3 and Y_2O_3. A major problem for fusion reactor insulators will be radiation-induced swelling. Transmission electron microscopy was used to evaluate the damage structures of some potential first wall insulators after fission reactor irradiation at elevated temperatures. Al_2O_3 in three forms, Y_2O_3, and Y_2O_3, and Y_2O_3-10% ZrO_2 were irradiation at 723K, 873K, and 1023K in EBR-II to fluences of 3 to 6×10^{21} n/cm² ($E_n > 0.1$ MeV.)*

Macroscopic measurements showed that all three forms of Al_2O_3 (polycrystalline Lucalox, polycrystalline Coors AD 999, and monocrystalline TECO) swelled significantly (1 to 2%) after irradiation at 1023 K, while Y_2O_3 and Y_2O_3-10% ZrO_2 actually densified slightly. This densification may have resulted from sintering during the reactor exposure. Examination by transmission electron microscopy revealed a high density of irradiation-induced pores in all Al_2O_3 specimens irradiated at 873 K ($0.38T_m$) and 1023 K ($0.44T_m$). These pores were aligned, as shown in Fig. XIV-19 (Coors AD 999). Analysis of this photomicrograph shows the average pore diameter to be ~35Å and pore density to be $\sim 5 \times 10^{17}$/cm³ (assuming the foil thickness to be 1000Å). From these rough values a swelling of 1.1% can be calculated, which is in reasonable agreement with the macroscopic value of 2.0% measured for the sample as a whole. No pores were seen in Al_2O_3 irradiated at 723 K ($0.31 T_m$).

The Al_2O_3 pore orientation was determined in another foil by comparison of the photomicrograph with a corresponding electron diffraction pattern. Pore alignment was found to be parallel to the c-axis [0001] of the hexagonal structure, with the [1010] direction in the plane of the foil.

Irradiation-induced pores were occasionally seen in Y_2O_3 (Fig. XIV-20) as were "black spot" defects (unresolved damage) and dislocation loops (Fig. XIV-21). However, structural damage in the Y_2O_3 samples is not so severe as that in Al_2O_3, consistent with the low macroscopic swelling values observed for Y_2O_3. The good stability of Y_2O_3 under irradiation may result from its defect structure. This ceramic has a stable array of vacancies in the oxygen sublattice which may reduce pore formation by enhancing the recombination of irradiation-induced vacancies and interstitials.

b. Fission Neutron Irradiation Studies of Ceramics and Glasses. A new EBR-II irradiation experiment is planned and will encompass a large number of CTR candidate ceramics, glasses, and insulator/metal composites. Samples will be irradiated at 923 K and 1073 K at a flux roughly equivalent in calculated dpa to that expected at the RTPR first wall. Fluence will be comparable to a one year exposure at the RTPR first wall. After irradiation, samples will be evaluated for defect content, dimensional changes, dielectric strength, thermal conductivity, and interdiffusion effects with metal substrates. The experiment has received "Approval in Principle" from the Division of Reactor Research and Development, (ERA), and samples and irradiation capsules are being fabricated.

c. Evaluation of Chunk Sputtering from 14 MeV Neutron-Irradiated Al_2O_3. After it became known from the work of Kaminsky[41,58] that some materials suffer gross sputtering (removal of ~10 μm chunks) under 14 MeV neutron bombardment, a single-crystal Al_2O_3 sample used in optical absorption studies was examined for such effects. This sample had been irradiated to $\sim 10^{17}$ n/cm² with 14 MeV neutrons in room-temperature air. If chunk-type sputtering had occurred, the resultant holes left in

*Irradiations were conducted as part of another LASL project.[52]

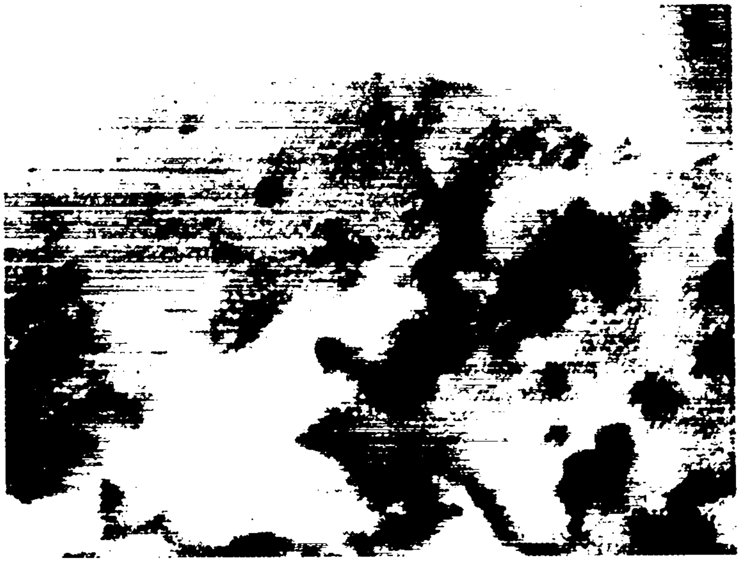

Fig. XIV-19

Al_2O_3

200,000X.

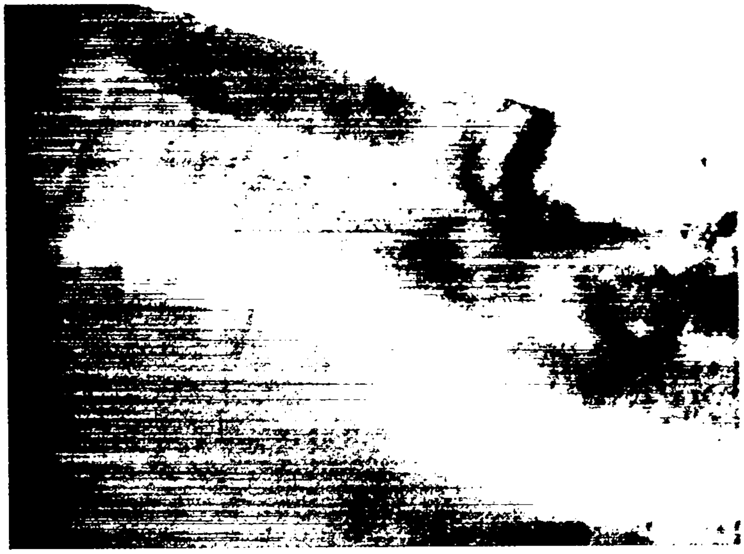

Fig. XIV-20

Y_2O_3-10% ZrO_2

120,000X.

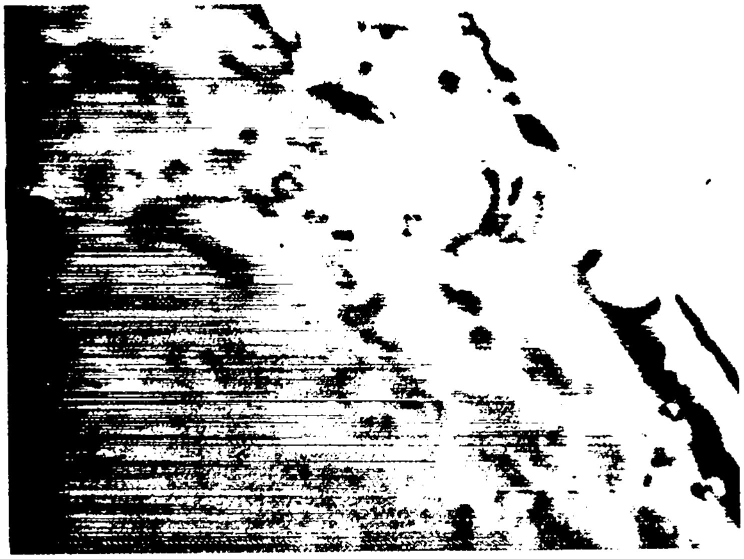

Fig. XIV-21

Y_2O_3

100,000X.

either front or rear surfaces should have been readily identified by the replica electron microscopy technique used (resolution ≈150Å). No evidence of any surface damage was found, even though the neutron fluence was ~20 times that utilized by Kaminsky.[42,60] Kaminsky has shown that the amount of chunk sputtering can be greatly reduced by polishing and annealing samples before bombardment and has postulated that internal strain is released by 14 MeV neutron bombardment, resulting in chunk emission. Since single-crystal Al_2O_3 should have a low internal strain content, the negative results for sapphire may be explainable by the same model. Generally, the nature of chunk sputtering is still in doubt; recent work by Thomas and Harling[54] failed to repeat the results of Kaminsky.

3. 14 MeV Neutron Damage Simulation Experiments

a. 14 MeV Neutron and High-Energy Proton Damage in Single-Crystal Al_2O_3. Insulators in fusion reactors will be irradiated with neutrons at energies up to 14 MeV. However, intense sources of 14 MeV neutrons are not available, so that fusion irradiation studies must be conducted with other damaging particles. Low-level damage from 14 MeV neutrons in single-crystal Al_2O_3 have been compared with that from 5 MeV protons, 15 MeV protons, and fission neutrons, to determine whether damage from protons and fission neutrons can simulate that from fusion neutrons. The fission neutron results were obtained by Levy.[55]

Damage was evaluated by measurement of irradiation-induced optical absorption. This technique is sensitive to low levels of damage, differentiates between different kinds of defects, and gives information primarily on isolated point defects which are expected to contribute to electrical effects.

Results obtained are given in Figs. XIV-22 and XIV-23. Figure XIV-22 shows the room temperature as-damaged optical absorption spectra, while Fig. XIV-23 presents the isochronal annealing curves for the three principle absorption peaks. The shapes of the damage spectra show that fission neutrons and 15 MeV protons can simulate 14 MeV neutron damage accurately, whereas incident 5 MeV protons are not simulated as successfully. The same conclusions can be drawn from evaluation of the annealing curves. These findings are consistent with the theoretical prediction by Logan[56] that for a niobium target 16 MeV protons should simulate 14 MeV neutrons. Calculations are being made for low-Z targets, such as Al_2O_3 to support experimental studies.

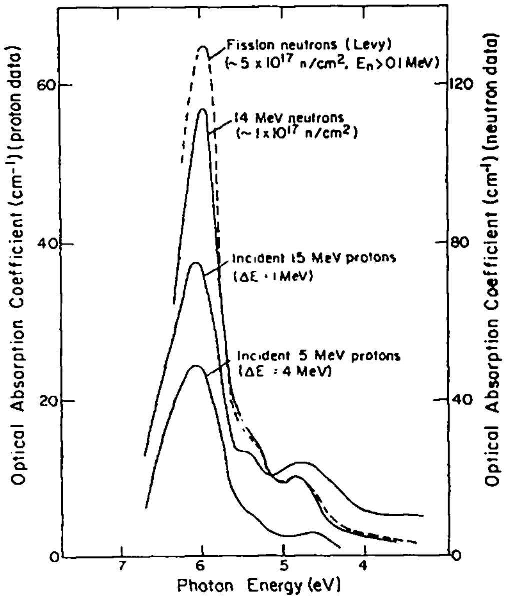

Fig. XIV-22
Optical absorption spectra for neutron and proton irradiated sapphire (alumina).

b. Simulation of 14 MeV Neutron Damage with Heavy Ions. Although ~15 MeV protons appear to produce damage which closely simulates that produced by 14 MeV neutrons, it is difficult to achieve proton fluences from available electrostatic accelerators high enough to produce in a short time structural damage equivalent to that from ~1 y exposure of the RTPR first wall. Irradiation with high energy heavy ions (He, Li, B, O, N, etc.) in theory would produce 100 to 1000 times more damage per incident particle; this approach is being explored for generating higher levels of damage. Two difficulties with this technique are:

(a) possible differences from neutrons (or high-energy protons) in details of the damage produced; and (b) the small penetration depths of heavy ions, leading to inhomogeneous damage and difficulties in interpreting experimental results in the case of electrical effects.

Calculations of heavy ion penetration depths and damage production have been carried out, and development of the necessary experimental techniques has begun.

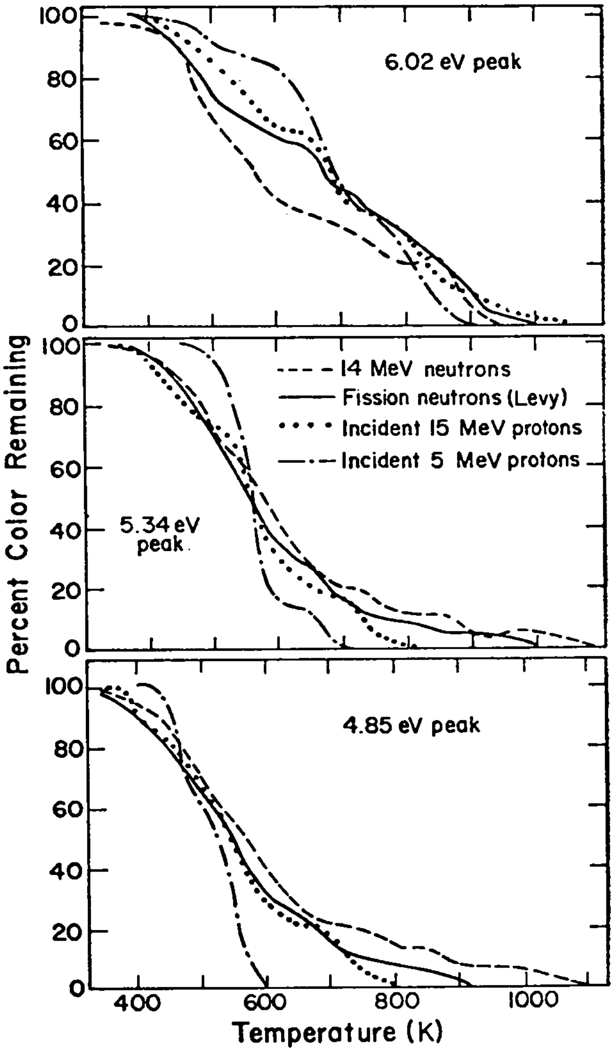

Fig. XIV-23
Isochronal annealing curves for proton and neutron irradiated sapphire (alumina).

4. Calculations on Radiation Effects

a. Physical Sputtering of the RTPR First Wall Insulator. A potential problem for the RTPR first-wall insulator is physical sputtering by D, T, He, and neutrons. Preliminary calculations on wall thinning by sputtering have been made, assuming different particle energies for monoenergetic impinging ions (i.e., different efficiencies of the gas blanket in degrading particle energies). Ion sputtering yields were taken from the literature and are not greatly dependent on target material. Yields for neutron sputtering are not well known, and so three calculations were made, each using different values which have been reported.

The calculational results are shown in Table XIV-XV. Wall thinning by ion sputtering is very much dependent on particle energy, with serious erosion predicted if ion temperatures are near those of the plasma. However, if the neutral gas blanket reduces these energies significantly, wall thinning will not be a problem. Sputtering by neutrons will be low, unless chunk sputtering by highest-energy neutrons occurs. For the latter case thinning will be a serious problem. It should be noted that these calculations address only physical sputtering, and do not include the effect of a distribution of ion energies.

b. Transmutation Rates of Insulator Elements. Knowledge of the rate at which insulator elements transmute under neutron bombardment to other elements is important to an understanding of insulator behavior in fusion reactors. Gaseous transmutation products can enhance swelling and degrade electrical properties, while metallic products can alter both structural and electrical behavior.

The generation rates of neutron-induced transmutation products in typical insulators at the first wall of the RTPR were computed (Sec. VIII.E). Calculated results are given in Table XVI, and for most isotopes both gaseous and metallic transmutation products are generated at the rate of about 500 to 2000 appm/y. Exceptions are ^{9}Be, which shows a high helium generation rate, and ^{15}N, which transmutes at a low rate. These results indicate that low-Z elements transmute relatively rapidly, and point to the importance of experimental studies to determine the effect of these impurities on insulator performance.

c. Effect of Ionizing Radiation on the RTPR First-Wall Insulator. During a thermonuclear burn the first wall insulator will absorb bulk ionizing radiation (bremsstrahlung), neutron-induced gamma rays), and the electrical conductivity will be increased. Concurrent displacement damage will probably reduce the conductivity, since defects can serve as traps for these charge carriers. Preliminary calculations have been made[57] of conductivity during irradiation at first-wall dose rate of $\sim 4\times10^{8}$ rad/s. Displacement damage effects were neglected. The resulting resistivity of $\sim 10^{7}$ Ω-cm, is above the minimum acceptable value of 10^{6} Ω-cm at the start of a burn. Furthermore, the 10 s annealing time between one pulse and the start of the next should result in significant recovery of the resistivity.

TABLE XIV-XV

Particle	Energy	Sputtering Yield (atoms/ion)	Thinning[a] (mm/yr)
D,T	3 keV	10^{-2}	0.5
	0.2 keV	10^{-4}	5×10^{-3}
He	4 keV	10^{-1}	0.1
	0.3 keV	10^{-2}	10^{-2}
Neutrons	1st wall spectrum	5×10^{-2}[b]	0.3
	1st wall spectrum	10^{-2}	6×10^{-2}
	1st wall spectrum	10^{-4}	6×10^{-4}

[a] initial insulator thickness = 0.3 mm

[b] assuming that 20% of the neutrons cause chunk sputtering with $x = 0.2$, and 80% cause atom-by-atom sputtering with $x = 10^{-2}$

TABLE XIV-XVI

TRANSMUTATION RATES (IN APPM/YR) OF SOME INSULATOR ISOTOPES
AT THE FIRST WALL OF THE RTPR

	Transmutation Products									
Isotope	He	H	C_{total}	^{14}C	Al	Li	B	N	Si	Mg
^{27}Al	852	1881							57	2078
^{16}O	2240	373	2240					111		
Si (natural)	1599	2254			541					1271
^{14}N	1322	1183	1220	638			1322			
^{15}N	162	359	308	108			34			
^{9}Be	10,328	400				442				

5. SFTR First-Wall Insulator Studies

a. Dielectric Strength of Composite Insulator/Metal Discharge Tubes. One design of the SFTR first wall envisages an assembly of insulator-coated metal trapezoids stacked into a cylindrical discharge tube. These trapezoids should be able to withstand high voltage across the thin insulator, and, therefore, high dielectric strength of a number of insulator-on-metal test disks, tubes, and trapezoids at room temperature have been measured. Insulators evaluated include a number of enamel glasses and plasma-sprayed Al_2O_3. Detailed results have been reported elsewhere.[58] The findings can be summarized as follows:

(1) Dielectric strength of the insulators when free of flaws is high.

(2) All as-fabricated insulators suffered degradation of dielectric strength due to the presence of flaws.

(3) Flaws in enamels were primarily isolated bubbles formed during the firing process.

(4) Flaws in plasma-sprayed Al_2O_3 were primarily interconnected pores formed during the spraying process.

(5) A judgment as to the effect of flaws on insulator performance in a discharge tube configuration should be based on tests in an existing fusion device, since conditions there will be different from those used in these dielectric strength measurements.

b. Evolution of Water From a Glass First Wall. Plasma contamination by impurities from the first wall is a potential problem for all fusion devices, including the SFTR. It is anticipated that the SFTR first-wall insulator will be a glassy material, and water will be the principal outgassing constituent. Calculations of water outgassing have, therefore, been carried out for such a material in the unirradiated condition. The glass was assumed to have outgassing characteristics similar to those of a soft lime glass for these calculations. This glass is well characterized and shows significantly greater outgassing than does a typical hard glass such as Pyrex or fused quartz. Calculations show that the quantity of loosely-bound surface moisture can be up to three times that of the D-T fuel and must be removed prior to system operation. A 673 K, 1 hr vacuum bakeout was then assumed, and this was found to remove the surface water and sufficiently dehydrate the material so that first-wall heating during a burn (assumed consevatively to be equivalent to 673 K for 1 m) would produce a negligibly small additional quantity of water from within the glass (mole fraction of water in the DT plasma would be 1.5×10^{-4}). Proper baking techniques should control the problem of plasma contamination by water desorption in SFTR.

6. CTR Insulator Materials Stockpile Insulator samples used in studies by different laboratories should be produced from a single source when possible, so that results obtained can be directly compared. Accordingly, a stockpile of insulators for use by the CTR insulator laboratories is being assembled. Materials obtained to date include monocrystalline and polycrystalline Al_2O_3, $Al_2O_3 \cdot MgO$, and Al_2O_3; and polycrystalline BeO, Si_3N_4, and AlN. Samples have been supplied to CTR insulator groups at Brookhaven National Laboratory, Argonne National Laboratory, and Pacific Northwest Laboratory.

G. Alloy Research

The objective of the alloy research task is to determine the limits of metals in future fusion power reactors. The intense neutron irradiation will displace atoms, produce hydrogen and helium and metal impurity atoms by nuclear reactions, and cyclic thermal stresses. Void formation induced by neutrons will cause high-temperature embrittlement. Facilities to simulate the combination of cyclic stress, elevated temperature, and neutron irradiation do not exist so effort has been focused on developing the appropriate facilities.

1. Cyclic Stress. The first wall of a theta-pinch reactor is a layered composite with an insulator facing the plasma and a metal backing facing the Li blanket structure. Cyclic tensile stresses will occur in the metal backing of the first wall. The life of metals under conditions of temperature (about 0.4 of the absolute melting temperature, T_m, of the candidate metals), neutrons irradiation (about 10^{19}n/m^{2}s) and cyclic stress will be limited by fatigue damage or the accumulation of pulses of thermal creep or by pulses of irradiation creep. The first step in establishing the metal life is to determine high-temperature strengths of candidate metals under cyclic stressing.

Initial results obtained on molybdenum were reported.[59] Deformation appeared to be dominated by pulses of thermal creep for all stresses at 1200 K with a 1 Hz stressing rate. Figure XIV-24 presents the cyclic stress results and compares them to the life under constant stress creep. Both published and new creep data are included, the creep data of Pugh[60] being obtained at a lower temperature. The new constant stress creep data fall along the same line as the cyclic stress data, whereas the data of Pugh at a different temperature fall along a parallel line. The displacement between these data reflects the strong temperature dependence of rupture life on temperature.

Figure XIV-25 shows the surface of a cyclicly stressed sample as revealed by scanning electron microscopy relative to interior microstructure of a constant stress tested molybdenum sample as revealed by light microscopy. Both show many intercrystalline cracks aligned transverse to their tensile axes. This failure mode is characteristic of high-temperature creep; transgranular cracking (few in number) is characteristic of fatigue.

The cycle stress testing reported to date utilized saw-tooth tensile stressing. The RTPR will generate square wave stressing of the metal structural components, and a creep machine was modified to more nearly simulate this waveform. Debugging was started and the first few cyclic stress tests completed.

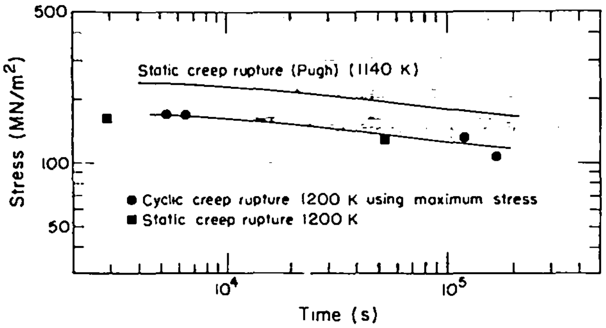

Fig. XIV-24
Cyclic stress curve for molybdenum.

Mechanical testing was initiated on molybdenum because it is an important candidate metal to the fusion reactor program; additionally, molybdenum requires less expensive vacuum systems for high-temperature testing than niobium or vanadium. Stainless steels are very radiation resistant and so would be less attractive for initial Los Alamos Meson Physics Facility (LAMPF) experiments than molybdenum.

In summary, saw-tooth cyclic stressing of molybdenum at 0.4 T_m leads to rupture life and fracture mechanisms that are equal to those produced by constant stress creep at the same stress as the maximum stress. The extensive creep data available in the literature can be used to predict life and ductility when neutron radiation is insufficient to produce voids.

2. Radiation Damage Analysis. The damage analysis program is directed toward the development of techniques for analyzing neutron spectral dependent radiation damage and applying these techniques to the design and analysis of experiments. This effort utilizes computer calculated radiation damage parameters based on damage models in the analysis. The first project for this year was to modify the computer program DON, which is used in the calculations, to run on the LASL computing system.[61]

In Table XIV-XVII damage energy cross sections normalized to the respective values in EBR-II row 7 are given for Al, Cu, Nb and Au in several neutron spectra. Since in the simple Kinchin-Pease type model currently used in radiation effects studies, the number of displacements is proportional to the damage energy, the normalized damage energy cross sections are equivalent to normalized displacement cross sections. The data in the upper part of Table XIV-XVII show that the relative radiation effects as measured by the number of displacements per neutron in the given spectra are similar for Cu, Nb and Au, whereas Al has quite a different behavior. In using damage energy or displacement cross sections in evaluating neutron spectra, such as those in Table XIV-XVII as fusion simulation spectra, it is necessary to consider the materials to be studied.

In the lower portion of Table XIV-XVII the damage energy cross sections have been divided by the corresponding (n,α) cross sections and normalized to that in a fusion reactor first wall spectrum (denoted Bench in Table XIV-XVII). Although the (n,α) cross section does not represent total helium production in all cases, such a ratio does give an indication of the number of defects produced per helium nucleus produced. This ratio can be thought of as a "CTR damage parameter". The results summarized in Table XIV-XVII show that only neutron-spectra with significant high-energy components have CTR damage parameters similar to that in a fusion reactor first wall.

The comparison of radiation effects for neutron spectra is not only dependent upon the material studied but also is a function of the model used and the type of radiation effect described. Normalized parameter cross sections for Nb using four models are given in Table XIV-XVIII. Each model describes a different aspect of radiation damage: number of displacements, total recoil energy, a hardening parameter which described the initial radiation hardening rate, and the number of free vacancies produced at about 500 K.[62] The free vacancy model was used by Doran *et al.* [62] to describe swelling. For example, approximately a factor of two difference between displacement and free vacancies at "14 MeV" is observed.

Table XIV-XIX shows the effect of using three models that describe the number of displacements. Model D is the damage energy Kinchin-Pease model used above; RT-B and RT-3 are based on the computer calculations of Robinson and Torrens.[63] In the first model (D) the damage energy per defect is constant, in RT-B the damage energy per defect is a weakly increasing function of recoil energy and in RT-3 it is a strong function of recoil energy. The results are essentially independent of the model for the two fission spectra, whereas, for the four spectra with high energy components as much as a factor of three variation is noted.

The data in Tables XIV-XVII, XIV-XVIII and XIV-XIX are average values integrated over the fast neutron flux above 0.5 eV, and show some of the characteristic properties of the radiation effects in these spectra. The spatial characteristics of defect production, however, are not adequately given by these integral data. Recoil energy and damage

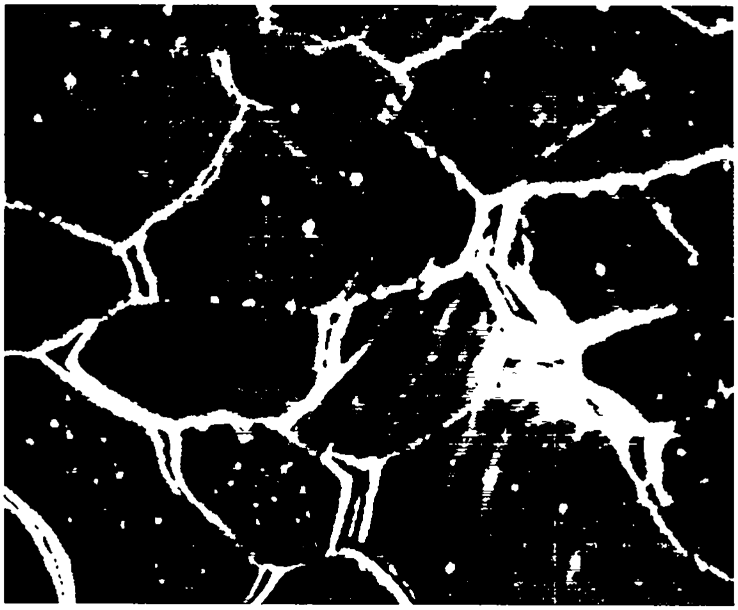

The surface microstructure of molybdenum after cyclic stressing at a rate of 1 Hz and a temperature of 0.4 T_m. Note grain boundary cracks and slip bands both common to constant stress creep.

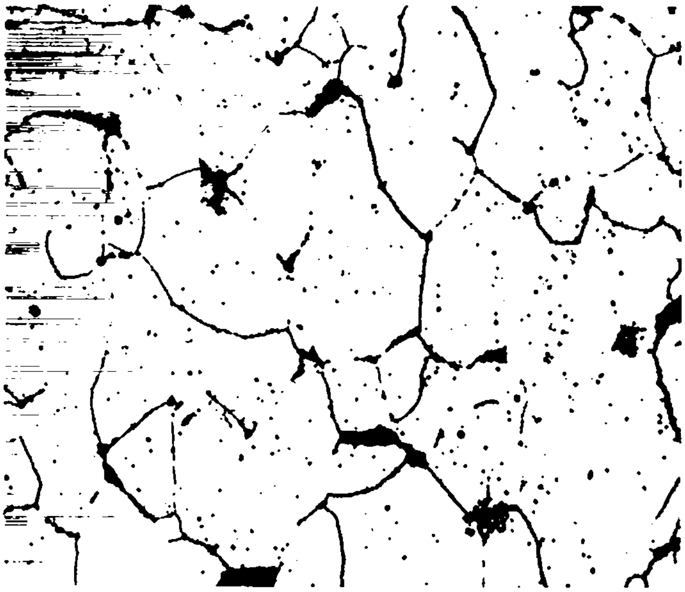

The interior microstructure of molybdenum after high temperature creep. Again note grain boundary cracks. (Slip bands are not observed on polished planes without special etching.)

Fig. XIV-25
Scanning electron micrograph of failed specimen.

TABLE XIV-XVII

NORMALIZED DAMAGE ENERGY CROSS SECTION

Spectrum	Al	Cu	Nb	Au
HFIR	0.6	0.7	0.8	0.8
EBRII-7	1.0 (51 bkeV)[a]	1.0 (32 bkeV)	1.0 (28 bkeV)	1.0 (18 bkeV)
M-LAMPF	1.2	1.9	2.0	2.2
BENCH	1.7	3.1	3.4	3.7
19 MeV Li	2.8	6.1	6.1	6.8
"14 MeV"	3.4	8.5	9.8	10.8
	NORMALIZED DAMAGE ENERGY CROSS SECTION/$\sigma_{n,\alpha}$			
HFIR	61	28	35	141
EBRII-7	239	94	116	-
M-LAMPF	7	3	3	0.4
BENCH	1.0	1.0	1.0	1.0
19 MeV Li	1.1	1.1	1.5	2.7
"14 MeV"	0.5	0.7	0.7	0.06

[a] Units of damage cross section in barn-keV

TABLE XIV-XVIII

NORMALIZED PARAMETER CROSS SECTIONS FOR Nb(1164)[a]

Spectrum	Displacements	Recoil Energy	Hardening	Free Vacancies
HFIR	0.76	0.79	0.85	0.61
EBRII-7	1.0	1.0	1.0	1.0
M-LAMPF	2.01	2.28	2.51	1.5
LLL	2.40	2.69	3.00	1.6
BENCH	3.38	3.86	4.36	2.16
24 MeV Be	7.02	8.15	9.39	3.9
"14 MeV"	9.67	11.5	13.4	5.24

TABLE XIV-XIX

NORMALIZED PARAMETER CROSS SECTIONS FOR Cu(1087)[a]

Spectrum	D	RT-B	RT-3
HFIR	0.7	0.7	0.6
EBRII-7	1.0	1.0	1.0
M-LAMPF	1.9	1.3	1.2
BENCH	3.1	2.8	1.6
19 MeV Li	6.1	5.5	2.9
"14 MeV"	8.5	7.5	3.0
	Al(1193)		
HFIR	0.6	0.6	0.5
EBRII-7	1.0	1.0	1.0
M-LAMPF	1.2	1.2	1.0
BENCH	1.7	1.6	1.1
19 MeV Li	2.8	2.6	1.4
"14 MeV"	3.4	3.1	1.4

[a] ENDF/B material number

energy spectra for Nb and Cu in three fission reactor spectra and two fusion spectra are given in Table XIV-XX. These data give a measure of the spatial and defect density distribution of radiation damage. Significant differences in the defects produced between these neutron spectra are shown, especially for the fast reactor (EBR-II), and the water-moderated reactor (HFIR) irradiations.

J. Weertman* made an analysis to resolve whether irradiation-induced fatigue crack growth could explain chunk formation observed by Kaminsky.[64] Growth of pre-existing cracks was considered as a possible cause of chunk formation. Bombardment by energetic neutrons would cause localized stresses that fluctuate both in time and position. It is not certain whether cracks will grow; the growth rate is at the threshold level measured in conventional fatigue experiments. The crack growth mechanism cannot explain chunk formation at the fluences used by Kaminsky.[41,60] If cracks do grow by the proposed mechanism, they may seriously limit the life of the first-wall material of fusion reactors.

Weertman also made an analysis of LCTR first-wall fatigue. Thermo-elastic stress pulses will start at the inner wall and move into the interior. The stress pulse magnitude is large enough to cause rapid crack growth. However, these short wavelength stress pulses may attenuate rapidly with distance. High-stress internal-friction measurements with and without radiation are necessary to establish suitable high damping materials.

3. LAMPF Neutron Irradiation Facility.

LAMPF is being developed as a neutron radiation effects facility with provision to heat and stress samples during irradiation. Both cyclic and constant stress testing will be possible. The neutron radiation damage cavity at LAMPF should be useful to the national fusion reactor radiation damage program.

a. Neutron Flux and Spectrum Calculations. Three Dimensional Monte Carlo neutron transport calculation and radiochemical dosimetry were utilized as independent evaluations of flux intensity. A detailed Monte Carlo calculation of the "as built" radiation effects facility at LAMPF was made with a minimum of geometric simplification so that neutron flux intensities and spectra could be directly related to a concurrent foil activation dosimetry program. The Nuclear Meson Transport Code (NMTC)[65] was used to transport all particles with energies greater than 20 MeV. Neutrons with energies less than 20 MeV were transported with the neutron Monte Carlo Code (MCN).[66] A delta-function proton pulse in time and energy (800 MeV) uniformly spread over a 50 mm-diameter spot located at the lower half of the copper beam stop[60] was used in the calculations to produce neutrons. This position will be that of the proton beam during LAMPF operation.

Figure XIV-26 gives a plot of neutron fluence per unit lethargy in a representative irradiation cavity, for a proton beam current of 1 mA. This will be the full beam current of LAMPF. In this case the total neutron flux is $2.38\times10^{17}/m^2s$ and the neutron flux above 1 keV is $2.19\times10^{17}/m^2s$. Neutron fluxes were also computed for other locations, using track length and surface estimates. The representative position is not the location of highest flux intensity; the flux intensity expected to exist at the furnace location of highest flux intensity will be at least twice as high.

Foil activation used (n,γ), (n,2n), (n,3n) and (n,4n) reactions in ^{197}Au, and (n,f) reactions in ^{235}U and ^{238}U. Radiochemical analysis yielded a full beam total neutron flux of $1.47\times10^{17}/m^2s$ with the

---

*Summer staff member, Los Alamos Scientific Laboratory, permanent position, Walter P. Murkly Professor of Materials Science and Professor of Geophysics, Departments of Materials Science and Geological Sciences, Northwestern University, Evanston, Illinois.

TABLE XIV-XX

RECOIL ENERGY AND DAMAGE ENERGY SPECTRA

Nb(1164)[a]

Recoil Energy keV	EBRII-2 %P(T)	EBRII-2 %E_D	EBRII-7 %P(T)	EBRII-7 %E_D	HFIR %P(T)	HFIR %E_D	BENCH %P(T)	BENCH %E_D	"14 MeV" %P(T)	"14 MeV" %E_D
0 - 0.1	2.2	0	3.8	0	57.2	0	4.4	0	0.3	0
0.1 - 1.0	15.8	1.0	22.8	2.1	11.4	1.1	20.6	0.5	2.9	0
1.0 - 5.0	36.9	12.4	40.3	18.8	12.1	7.7	30.3	3.9	11.0	0.4
5.0 - 10	19.1	17.0	16.4	20.8	6.4	10.9	13.2	4.6	10.1	0.9
10 - 50	24.0	53.3	15.9	48.5	11.0	50.7	19.8	18.1	21.4	4.8
50 - 100	1.7	12.1	0.7	7.3	1.6	21.2	2.9	8.9	6.2	4.9
100 - T_{max}	0.3	4.2	0.1	2.5	0.3	8.4	8.8	64.0	48.1	89.0

Cu(1087)[a]

Recoil Energy keV	EBRII-2 %P(T)	EBRII-2 %E_D	EBRII-7 %P(T)	EBRII-7 %E_D	HFIR %P(T)	HFIR %E_D	BENCH %P(T)	BENCH %E_D	"14 MeV" %P(T)	"14 MeV" %E_D
0 - 0.1	1.9	0	3.8	0	63.4	0.1	5.5	0	0.2	0
0.1 - 1.0	14.2	0.6	23.2	1.7	15.0	1.3	25.2	0.5	1.5	0
1.0 - 5.0	29.8	6.6	35.0	12.1	7.7	4.5	26.5	2.7	6.1	0.2
5.0 - 10	17.6	10.6	15.3	14.7	3.4	6.0	10.3	3.1	6.3	0.4
10 - 50	31.2	48.7	20.5	50.6	7.6	37.3	19.5	16.7	24.3	4.7
50 - 100	3.9	21.5	1.7	14.0	2.0	28.4	3.6	9.7	6.9	3.4
100 - T_{max}	1.4	12.0	0.5	6.9	0.9	22.4	9.4	67.3	54.7	91.3

[a] ENDF/B material number

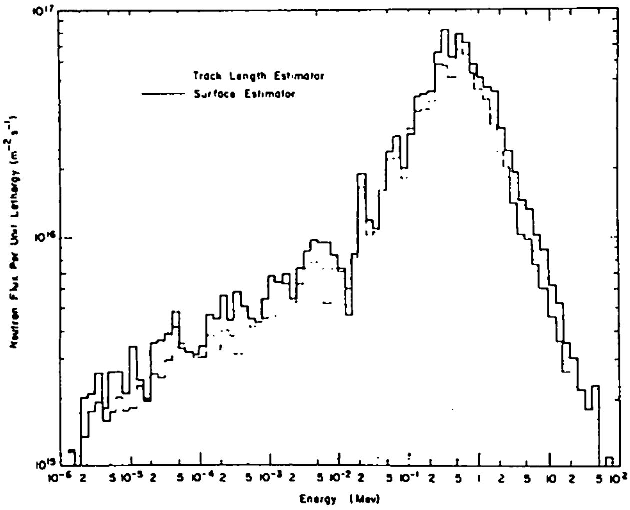

Fig. XIV-26
Neutron fluence per unit lethargy at the LAMPF Irradiation Facility for a 1 ma proton beam.

proton beam centered about 10 cm above the location considered in the Monte Carlo calculation. This beam position will be changed to the more desirable lower position during present accelerator modifications.

The 6 foil reactions considered were analyzed using spectrum unfolding techniques with good agreement to the Monte Carlo calculation results shown in Fig. XIV-26. The high energy data (E >20 MeV) are now available and show decreasing intensity with increasing energy.

b. Radiation Damage Calculation and Evaluation. The evaluation of LAMPF as a radiation effects facility and the relationship to other neutron irradiation facilities is being evaluated by both calculations and experiments. Results of these calculations are given in Tables XIV-XVII, XIV-XVIII and XIV-XIX. A review of these data indicates that the radiation effects expected in LAMPF will be intermediate between those in fission reactors and those expected in fusion reactors.

LAMPF has a "CTR damage parameter" similar to that for a fusion reactor first wall and hence has a significant advantage over fission spectra for fusion simulation. Experiments are being prepared for LAMPF that will enable direct comparisons of several forms of radiation damage in LAMPF to that observed in other neutron spectra. Some of these experiments are being prepared in cooperation with other laboratories including Brookhaven National Laboratory, Argonne National Laboratory, Lawrence Livermore Laboratory and Hollifield National Laboratory.

c. LAMPF Irradiation Facility Development. Development of the LAMPF radiation damage facility is proceding by two routes. The first route involves a system for attaching experiments on stringers which penetrate through the radiation shielding surrounding the beam stop. The second involves the development of an experimental tester which will heat and stress tensile bars in vacuum during neutron radiation. The stringers must provide cooling water, electric power, thermocouple control signals, and high- andlow-pressure gas to the tester. Neutron leakage past the stringer in its housing must be at an acceptable level. The testers are remote and miniaturized. Their design is based on proven "in reactor" test devices used in Canada.[67] LAMPF is presently undergoing modification for high-level beam operation, which involves the addition of more radiation shielding. The radiation damage stringers have been used to insert several dosimetry experiments. Improvements of the insertion and removal system and blockage of neutron leakage pathways are being made.

The first LAMPF furnace power supply and temperature controller system has been assembled and evaluation has been started. Miniaturized radiation resistant heaters are being evaluated.

H. Feasibility and Systems Studies of Applications of Laser Fusion

1. Introduction. Feasibility and systems studies are being done to assess the technical feasibility and the economic incentives of various commercial and military applications of laser fusion. Emphasis is placed on systems studies of the direct production of electricity in central-station power plants. The general objectives of these studies are: the conceptualization and preliminary engineering analyses of laser-fusion reactor and power-plant concepts, the development of parametric computer mooels of power-plant subsystems for economic and technology trade-off and comparison studies, and the identification of problems requiring long-term development efforts. Studies of such potential commercial applications of laser fusion as the production of fuel for fission reactors and providing high-temperature process heat are also included.

2. Pellet Microexplosions. Laser-fusion reactor concepts are based on the energy release characteristics of bare-DT fuel pellet microexplosions. The nominal pellet yield used as the basis for design considerations is 100 MJ. Theoretical calculations indicate that ~1 MJ of laser light will be required to heat and compress reference fuel pellets to conditions that result in a thermonuclear energy gain of 100. The characteristics of the energy-release mechanisms from a typical calculation for a 100 MJ fusion-pellet energy release are summarized in Table XIV-XXI.

The released energy must pass through or interact with the pellet material that was ablated during the pellet implosion-and-compression stage, must pass through or interact with any ambient gas in the cavity, and, finally, interact with the cavity wall and structure. The expansion dynamics are important because the temporal profiles determine the impulse on the cavity wall.

3. Laser-Fusion Reactor Concepts. Several reactor concepts are being considered for possible use in central-station power plants. Preliminary engineering analyses have been done for two concepts, the wetted-wall and the magnetically-protected designs, that may be attractive for this application.

The spherical cavity wall in the wetted-wall reactor concept, shown schematically in Fig. XIV-27, is protected against energy deposition by energetic particles from the pellet microexplosion by a film of liquid lithium on its interior surface. The energy of the alpha particles and the pellet debris and part of the x-ray energy is deposited in the lithium layer which is evaporated and ablated from the surface of the cavity wall. The lithium vapor is exhausted through a nozzle prior to the next pellet microexplosion.

Minimum cavity diameters for the wetted-wall reactor concept are determined by surface temperature increases due to x-ray energy deposition; the minimum niobium cavity diameter corresponding to 100 MJ pellet microexplosions is ~3.4 m. Conceptual blanket designs provide for the circulation of liquid lithium for the removal of heat and the breeding of tritium. Initial estimates indicate that acceptable tritium breeding ratios (1.07 to 1.40)

TABLE XXI

TYPICAL ENERGY RELEASE MECHANISMS FROM A 100-MJ PELLET MICROEXPLOSION

Mechanism	Fraction of Total Energy Release	Particles Per Pulse	Average Energy Per Particle	
X rays	0.01	----	~ 4 keV peak	
α particles that escape plasma	0.07	2.2×10^{19}	2 MeV	
Plasma kinetic energy	0.15			
α particles	----	1.3×10^{19}	0.6 MeV	(a)
Deuterons	----	1.2×10^{20}	0.3 MeV	
Tritons	----	1.2×10^{20}	0.4 MeV	
Neutrons	0.77	3.3×10^{19}	14.1 MeV	

(a) Total average energy per particle 0.37 MeV.

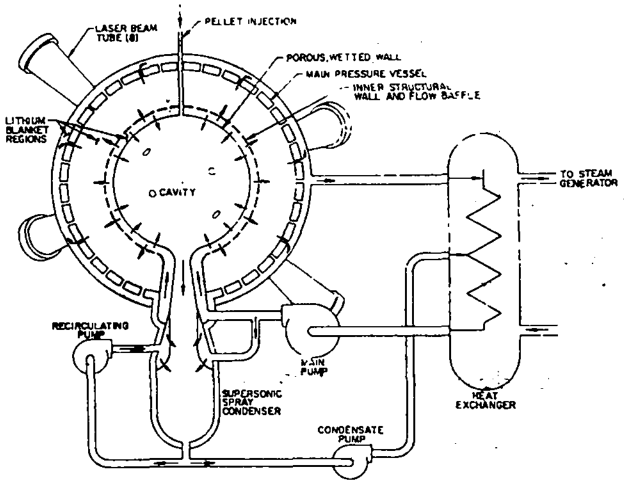

Fig. XIV-27
Wetted-wall laser fusion reactor concept.

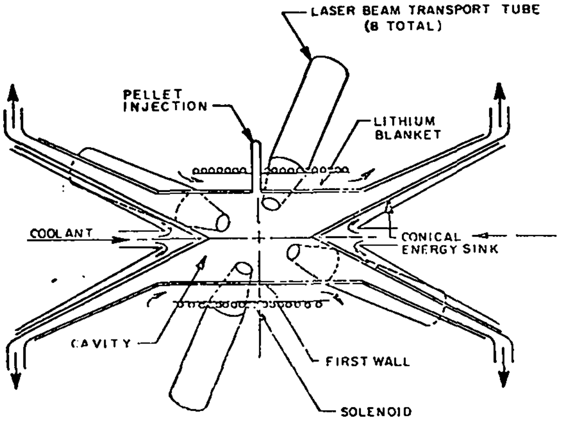

Fig. XIV-28
Magnetically-protected laser fusion reactor concept.

can be obtained from designs (~1 m thick) containing natural lithium, whose structural requirements are satisfied by either stainless-steel or refractory metal components.

The magnetically-protected reactor concept is shown schematically in Fig. XIV-28. The cavity is cylindrical with an impressed steady-state magnetic field produced by a solenoid concentric with and exterior to the cavity wall. Energetic charged particles resulting from fusion-pellet microexplosions are diverted by the magnetic field to conical energy sinks in the ends of the cylindrical cavity. Laser-beam transport tubes are arranged symmetrically about the axial and radial center of the cavity. The energy sinks are readily accessible for replacement without disturbing the lithium blanket, the laser-beam optics, or the fuel injection system. The minimum niobium cavity diameter for 100 MJ pellet microexplosions is ~5 m and is determined by surface heating due to x-ray energy deposition.

Estimates have been made of magnetic field strengths and field configurations necessary to divert charged particles to the energy sinks for theoretical fusion-pellet outputs ranging in yield up to 100 MJ. Maximum field requirements are ~0.3 T. Several solenoid concepts have been modeled for the systems analysis program, including the use of cryogenic superconducting coils as well as conventional copper coils. There is no apparent technical or economic advantage realized from the use of a particular concept.

4. Stress Analyses. Time-dependent, neutron- and gamma ray-transport calculations have been performed to determine the temporal and spatial dependence of energy deposition in the blanket region of a spherical laser-fusion reactor with niobium structural material. The results of these calculations were used to calculate pressure profiles in liquid lithium regions of the blanket due to thermal expansion. The responses of structural shells were then determined from these inputs in time-dependent, finite-difference, wave- propagation computer programs. From calculated stresses and materials property data, required structural wall thicknesses were determined. The wetted-wall concept with 100-MJ microexplosions and 0.9 m of natural lithium in the blanket requires two structural walls and an outer envelope. For a 2 m radius cavity, the structural walls are 0.03 m thick and the outer envelope is 0.02 m thick.

5. Lasers and Laser-Beam Transport Systems. A total laser-pulse energy of 1 MJ has been assumed for reference laser-fusion reactor design studies. It is anticipated that quasi-symmetrical illumination of fusion pellets by laser light will be required; thus, conceptual reactor designs provide for eight laser beams arranged symmetrically about the centers of reactor cavities.

The electron-beam sustained-discharge CO_2 laser system shows promise of achieving the required performance at reasonable cost and operating efficiency. Experimental CO_2 lasers at LASL provide the basis for designing larger systems. The reference power- amplifier design has an output of 0.125 MJ in a 1-ns-wide pulse and is expected to have an efficiency of 6 to 7%. It is pumped by an electric discharge, with ionization provided by an electron beam. Laser pulse repetition rates of from 35 to 50 per second appear to be desirable for power plant applications. For pulse rates in this range, circulation of laser gas for convective cooling will be necessary. At 35 pulses per second, the reference-design laser amplifier will require ~60 MW of cooling capacity, and because amplifier performance is significantly degraded by excessive temperatures, the waste heat is assumed dissipated to the environment.

The CO_2 laser systems model includes capacitive electrical energy storage and pulse-forming networks for power conditioning. In order to accomodate the high pulse rates and long lifetimes desired, the capacitors must be designed for low stress levels and convective cooling.

The HF chemical laser is also a viable contender for application in laser-fusion power plants and may be advantageous due to its relatively short wavelength (2.7 μm compared to 10.5 μm for CO_2), its relatively low capital cost, and its high operating temperature (permitting partial recovery of waste heat for conversion to electricity). The HF laser model adopted for systems analysis includes: the laser and associated optics, controls and gas supplies, an electric storage and power conditioning system, an HF electrolysis system, and a turbine-alternator for converting waste heat in the lasing media to electricity. The net efficiency of the laser system using nominal component efficiencies is ~10%.

Because the laser system represents a significant fraction of the capital investment of a laser-fusion power plant, it will apparently be economically advantageous to centralize components so that each laser system serves several reactor cavities. A centralized laser system requires rapid beam-switching from laser power amplifiers to selected cavity beam ports. Conceptual devices for this purpose include the use of rotating mirrors that direct laser beams sequentially to reactor cavities arranged in a circular pattern around a central laser system.

Beam-transport systems will consist of a large number of mirrors, windows and possibly lenses. For CO_2 laser beams, sodium chloride windows and lenses and bare metallic mirrors are used. Assumed laser-light fluence limits are 3 and 10 J per cm^2 per pulse for windows and mirrors, respectively. Sapphire windows and coated metallic mirrors are used to transport HF laser beams, and fluence limits are 10 J per cm^2 per pulse for both materials. Catoptric beam reflection systems are used to provide indirect beam paths through biological shielding surrounding reactor cavities.

6. Conceptual Laser-Fusion Power Plant. The preliminary design of nominal 1000-MWe laser-fusion power plants have been developed. Important considerations which led to design choices included component reliability, redundancy of essential components, access to components for service or replacement, and minimization of hazards from radioactive materials.

For power plants based on the wetted-wall reactor concept, twenty-four reactors are included in a 1000 MWe power plant; whereas, because of the higher pellet-microexplosion repetition rate, only three magnetically-protected reactors are required for this power level. The overall layout for a power plant that utilizes wetted-wall reactors is shown in Fig. XIV-29.

7. Systems Studies. Systems analyses of alternative laser-fusion power plants have been carried out to compare the following options: CO_2 or HF laser technology and wetted-wall or magnetically-protected reactor concepts. A serious attempt has been made to use a consistent set of cost data in the comparative economic analyses; however, because of rapidly changing costs and the difficulty of predicting future trends, the calculated costs of electric power and of plant capital costs were normalized to costs for a plant based on the wetted-wall reactor concept and CO_2 laser technology rather than being given in absolute values. Calculated power and capital costs are competitive with similar costs for other advanced power plants within the context of the cost data used.

The results of recent systems calculations with nominal values of systems parameters are given in Table XIV-XXII. Important figures of merit are given for each of several conceptual ~1000-MWe power plants. Variations of ~10% in the cost of electric power and of ~25% in plant capital costs were found among the various concepts considered. Current systems models predict substantial advantages in both net plant efficiency and circulating power fraction for plants based on HF laser technology compared to those based on CO_2 laser technology. Lower plant capital costs are associated with plant concepts based on the magnetically-protected reactor than with those based on the wetted wall reactor, but higher microexplosion repetition rates per reactor cavity result in higher maintenance and operating costs for the magnetically-protected design; thus, net power costs are essentially the same for these two reactor designs.

TABLE XXII

SUMMARY OF LASER-FUSION POWER PLANT SYSTEMS STUDIES

	Wetted-Wall Reactor Concept Nb First Wall			Magnetically-Protected Reactor Concept Nb First Wall		
	Stainless Steel Structure		Nb Structure	Stainless Steel Structure		Nb Structure
	CO_2 Laser	HF Laser	HF Laser	CO_2 Laser	HF Laser	HF Laser
Relative production costs per kWh	1.0	0.86	1.02	0.97	0.87	0.89
Relative capital cost per kWe	1.0	0.87	1.01	0.81	0.75	0.78
Net plant efficiency (%)	25	30	30	25	30	30
Net laser efficiency (%)	6.3	9.6	9.6	6.3	9.6	9.6
Net circulating power fraction (%)	38	25	25	38	25	25

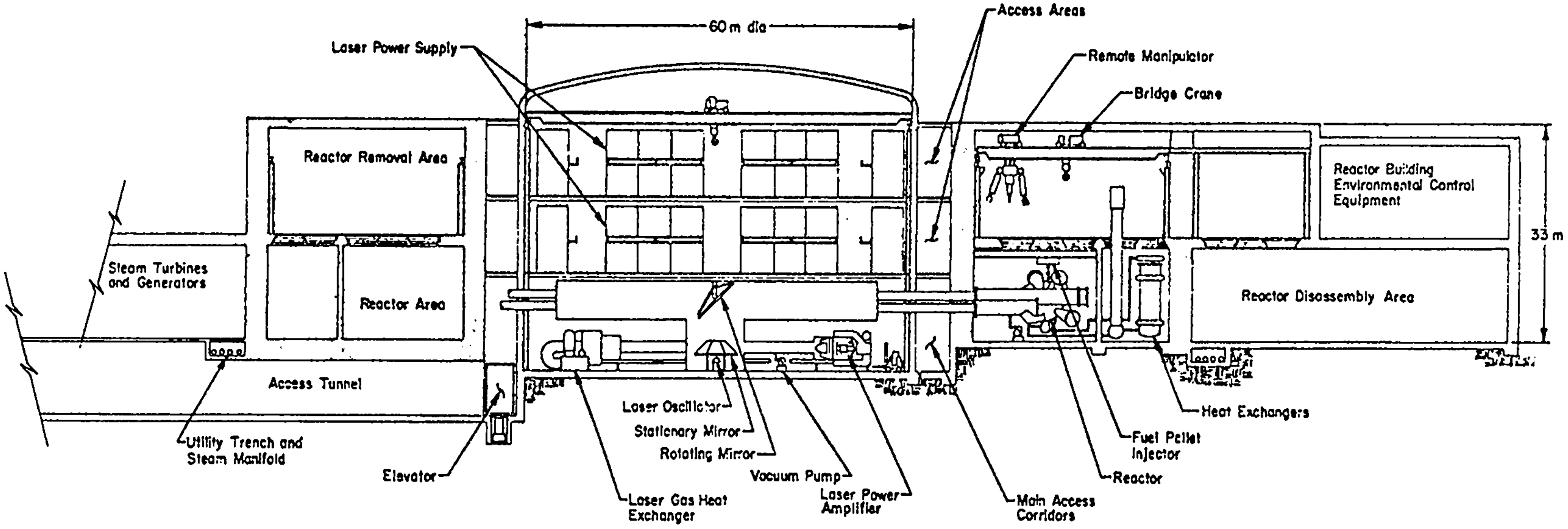

Fig. XIV-29
Conceptual design of a 1000 MWe laser fusion power plant.

References

1. R.A. Krakowski, F.L. Ribe, T.A. Coultas, A.J. Hatch, "An Engineering Design Study of a Reference Theta-Pinch Reactor (RTPR)", USAEC Rept. LA-5336/ANL-8019 (March 1974).

2. F.L. Ribe, R.A. Krakowski, K.I. Thomassen, T.A. Coultas, "An Engineering Design Study of a Reference Theta-Pinch Reactor (RTPR)," Nuclear Fusion, Special Supplement on "Fusion Reactor Design Problems," 1974.

3. T.A. Coultas, J.E. Draley, V.A. Maroni, R.A. Krakowski, "An Engineering Design Study of a Reference Theta-Pinch Reactor (RTPR) - An Environmental Impact Study," Vol. II, USAEC Rept. LA-5336/ANL-8019 (April 1975).

4. R.A. Krakowski, K.I. Thomassen, T.A. Coultas, "A Technological Assessment of the Reference Theta-Pinch Reactor (RTPR)", 8th Symp. on Fus. Tech., p. 623, Noordvijkerhaut, Netherlands, June 17-21, 1974.

5. R.A. Krakowski, K.I. Thomassen, R.J. Burke, T.A. Coultas, "An Engineering Design Study of a Reference Theta-Pinch Reactor (RTPR) - A Technological Assessment," Vol. III, USAEC Rept. LA-5336/ANL-8019 (to be published).

6. R.A. Krakowski, D.J. Dudziak, T.A. Oliphant, K.I. Thomassen, G.E. Bosler, F.L. Ribe, "Prospects for Converting ^{232}Th to ^{233}U in a Linear Theta-Pinch Hybrid Reactor (LTPHR),"United States Energy Research and Development Administration Report ERDA-4, pg. 249 (Dec. 1974).

7. T.A. Oliphant, "Plasma Cooling of a Pulsed Thermonuclear Reactor by Means of a Neutral Gas Layer," Nucl. Fus., **13**, 521 (1973).

8. T.A. Oliphant, "Monte Carlo Treatment of Heat Flow Through a Neutral Gas Layer," J. Nucl. Mater., **53**, 62, 1974.

9. T.A. Oliphant, "Heat Transfer Through a Reference Theta-Pinch Reactor (RTPR) Cooling Layer," Proc. of First Topical Meeting on the Technology of Controlled Nuclear Fusion, p. 677, April 16-18, 1974, San Diego, California.

10. J.P. Freidberg, R.L. Morse, F.L. Ribe, "Staged Theta Pinches with Implosion Heating," Texas Symp. on Technol. of Controlled Fusion Experiments and Egn. Aspects of Fusion Reactors, p. 812, Nov. 20-22, 1972.

11. T.A. Oliphant, "A Mixed Snowplow/Bounce Model Shock Heating in a Staged Theta Pinch," Nucl. Fus. **14**, 377 (1974).

12. E.M. Little, W.E. Quinn, G.A. Sawyer, "Plasma End Losses and Heating on the Low-Pressure Regime of a Theta Pinch," Phys. Fluids, **8**, 1168 (1965).

13. T.A. Oliphant, "Fuel Burn-up and Direct Conversion of Energy in a D-T Plasma," Proc. BNES Conf. on Nucl. Fus. Reactors, UKAEA Culham Lab., p.309, Sept. 17-19, 1969.

14. R.A. Krakowski, "Ergodic Optimization and Parameter Study on the RTPR Burn Cycle," First ANS Topical Meeting on the Technology of Nuclear Fusion, p. 112, April 16-18, 1974, San Diego, California.

15. J.P. Freidberg, F.L. Ribe, "Scaling of Wall Stabilized Scyllac Experiments," Comments on Plasma Physics and Controlled Fusion, **2**, 163 (1974).

16. R.E. Stillwagon (Principal Investigator), "Design Studies of Reversible Energy Storage and Transfer Systems for the Referennce Theta-Pinch Reactor," Westinghouse Elec. Corp. Rept. EM-4620, Sept. 1974.

17. J.M. Bunch, F.W. Clinard, D.J. Dudziak, W.V. Green, R.A. Krakowski, "An Evaluation of Major Material Problems Anticipated for the Reference Theta-Pinch Reactor (RTPR)," 5th Symposium on Engineering Problems of Fusion Research, Princeton, NJ, Nov. 6-9, 1973.

18. R.A. Krakowski, F.W. Clinard, F.L. Ribe, T.A. Coultas, "Surface Effects at the First-Wall of the Reference Theta-Pinch Reactor (RTPR)," J. Nucl. Mater., **53**, 54, (1974).

19. V.A. Maroni, personal communication, ANL (1974).

20. J.E. Draley, V.A. Maroni, T.A. Coultas, R.A. Krakowski, "An Engineering Impact Study of a Reference Theta-Pinch Reactor (RTPR)," First ANS Topical Meeting on the Technology of Controlled Nuclear Fusion, p. 564, April 16-18, 1974, San Diego, CA.

21. Donald J. Dudziak, "Fusion Reactor Nuclear Analysis Methods and Applications," 8th Symposium on Fusion Technol., p. 915, Noorwijkerhaut, Netherlands, June 17-21, 1974.

22. ICRP Publ. No. 2, "Recommendations of the International Commission on Radiological Protection," Pergamon Press, (1959).

23. F. Morley, J.W. Kennedy, "Fusion Reactors and Environmental Safety," BNES Nuclear Fusion Reactor Conference, p. 54, Culham Laboratory, (Sept. 1969).

24. Fusion Power:An Assessment of Ultimate Potential," USAEC Rept. WASH-1239 (Feb. 1973).

25. G.L. Kulcinski, Univ. of Wisconsin, private communication (1973).

26. "Final Reort, Project Definition Phase, 4th Round Demonstration Plant Program," Vol. I, Westinghouse Electric Corp. (Dec. 1970).

27. W.B. Cottrell and A.W. Savolainen, "U.S. Reactor Containment Technology," ORNL-NSIC-5, p. 4.2, U.S. Atomic Energy Commission (1965).

28. W.F. Vogelsang, G.L. Kulcinski, R.G. Lott, and T.Y. Sung, "Transmutation Effects in CTR Blankets," Trans. Am. Nucl. Soc., **17**, 138 (1973).

29. B. Badger,*et al.*, "UWMAK-I, A Wisconsin Toroidal Fusion Reactor Design," UWFDM-68, Vol. 1, U.S. Atomic Energy Commission (1973).

30. D. Steiner, "The Nuclear Performance of Vanadium as a Structural Material in Fusion Reactor Blankets," ORNL-TM-4353, Oak Ridge National Laboratory (1973).

31. K. Shure and D.J. Dudziak, "Calculating Energy Released by Fission Products," Trans. Am. Nucl. Soc., 4, 30 (1961); also, WAPD-T-1309, U.S. Atomic Energy Commission.

32. D. Steiner and A.P. Fraas, "Preliminary Observations on the Radiological Implications of Fusion Power," Nucl. Safety, **13, 5,** 353 (1972).

33. Donald J. Dudziak and R.A. Krakowski, "A Comparative Analysis of D-T Fusion Reactor Radioactivity and Afteheat," Proc. First Top. Mtg. Technology of Controlled Nucl. Fusion, San Diego, CA, 16-18 April 1974.

34. Donald J. Dudziak and R.A. Krakowski, "Radioactivity Induced in a Theta-Pinch Fusion Reactor," Nucl. Technol. **25, 32** (1975).

35. D.W. Muir and Donald J. Dudziak, "Sensitivity of RTPR Afterheat and Radioactivity to Nb-94 Cross Section Uncertainty," Trans. Am. Nucl. Soc. **19,** 465 (1974).

36. S.A.W. Gerstl, "Blanket Design Sensitivity Calculations Based on Perturbation Methods," Proc. First Top. Mtg. Technology of Controlled Nucl. Fusion, San Diego, CA, 16-18 April 1974. (CONF-74-0402).

37. D.G. Doran and G.L. Lukcinski, U. of Wisconsin, personal communication, July 1972.

38. W.J. Gray and W.C. Morgan, "Projection of Graphite Behavior in the LASL Reference Theta-Pinch Reactor," Pacific Northwest Laboratory Report BNWL-B-289 (1973).

39. W.C. Morgan, Battelle Northwest Laboratory, personal communication, 1973.

40. M. Kaminsky and S.K. Das, "Particle Release from Solids under 14-MeV Neutron Impact," Conf. Surface Effects in Controlled Thermonuclear Fusion Devices and Reactors, ANL, 10-12 January 1974.

42. R. Behrisch, R. Gähler, J. Klaus, "Sputtering Yields of Au by 14 MeV Neutrons and Emission of Recoils from (n,2n) Reactions in Au and Nb," J. Nucl. Mater., **53,** 183 (1974).

42. Patrick D. Soran and Donald J. Dudziak, "Bondarenko Formalism Applied to Theta-Pinch Reactor Nucleonics," Trans. Am. Nucl. Soc. **19,** 468 (1974).

43. Patrick D. Soran and Donald J. Dudziak, "Application of Bondarenko Formalism to Fusion Reactors," Proc. Conf. on Nucl. Cross Sections and Technology, Washington, DC, 3-7 March 1975.

44. S.A.W. Gerstl and H. Henryson, "The Effect of Resonance Self-Shielding in Niobium Structures on Tritium Breeding in CTR Blankets," Trans. Am. Nucl. Soc. **18,** 25 (1974).

45. Gerald E. Bosler, Donald J. Dudziak and William R. Ellis, "A Preliminary Appraisal of a Fusion/Fission (HYBRID) Reactor Based on the Linear Theta Pinch," Proc. Ninth Intersociety Energy Conversion Engineering Conference, San Francisco, CA, 26-30 August 1974.

46. "TCT — Two-Component Torus," joint conceptual design study, performed by Princeton Plasma Physics Laboratory, Princeton, NJ and Westinghouse Electric Corporation, Pittsburgh, Pa., Vol. II, Section 6.1 (1974).

47. D. Steiner, Coordinator, "The Status ofNeutron-Induced Nuclear Data for Controlled Thermonuclear Research Applications: Critical Reviews of Current Evaluations," Oak Ridge National Laboratory report USNDC CTR-1 (1974).

48. S.A.W. Gerstl, "Second-Order Perturbation Theory and Its Application to Sensitivity Studies in Shield Design Calculations," Trans. Am. Nucl. Soc. **16,** 342 (1973); S.A.W. Gerstl and W.M. Stacey, Jr., "A Class of Second-Order Approximate Formulations of Deep Penetration Radiation Transport Problems," Nucl. Sci. Eng. **51,** 339 (1973).

49. S.A.W. Gerstl, "The Application of Perturbation Methods to Shield and Blanket Design Sensitivity Analyses," AP/CTR/TM-28, Applied Physics Division, Argonne National Laboratory (1974).

50. D.E. Bartine, E.M. Oblow, and F.R. Mynatt, "Radiation-Transport Cross Section Sensitivity Analysis - A General Approach Illustrated for a Thermonuclear Source in Air," Nucl. Sci. Eng. **55,** 147 (1974); M.J. Katz, (ed.), "LASL Controlled Thermonuclear Research Program," Los Alamos Scientific Laboratory report LA-5656-PR (1974).

51. D.R. Harris, R.J. LaBauve, R.E. MacFarlane, P.D. Soran, C.R. Weisbin, and J.E. White, "MINX, A Modular Code System for Processing Multigroup Cross Sections from Nuclear Data in ENDF/B Format," Los Alamos Scientific Laboratory report LA-UR-1766 (Jan. 1973).

52. W.A. Ranken, "Quarterly Report on the Space Electric Power R&D Program," USAEC Rept. LA-5113-PR, (Nov. 1972).

53. M. Kaminsky, J.H. Peavey, and S.K. Das, "Particle Release from Niobium Irradiation with 14 MeV Neutrons," Phys. Rev. Lett. **32,** 599 (1974).

54. M.P. Thomas and O. Harling, results presented at the 21st National Vacuum Symposium of the AVS, Anaheim, CA, October 1974.

55. P.W. Levy, "Color Centers and Radiation-Induced Defects in Al_2O_3," Phys. Rev. **123.** 1226 (1961).

56. C.M. Logan, "Proton Simulation of Displacement Effects Induced in Metals," USAEC Rept. UCRL-51224 (1972).

57. V.A.J. van Lint, personal communication, LASL, (1974).

58. Contribution to the LASL CTR Technology and Development Quarterly Report for the Period April 1 - June 30, 1974.

59. R.A. Yeske, W.V. Green and E.G. Zukas, "The Tensile Fatigue Behavior of Molybdenum at 1153K," Proceedings of the First Topical Meeting on the Technology of Controlled Nuclear Fusion, p. 456 San Diego, CA, April 16-18, 1974, (1974).

60. J.W. Pugh, "The Tensile Properties of Molybdenum at Elevated Temperatures," Trans ASM **47,** 984 (1955).

61. D.M. Parkin and A.N. Goland, "A Computational Method for the Evaluation of Radiation Effects Produced by CTR-Related Neutron Spectra," USAEC Rept. BNL 50434, (Sept., 1974.)

62. D.G. Doran, R.L. Simons, and W.N. McElroy, "Spectral Effects in Neutron and Charged Particle Irradiations," to be published.

63. M.T. Robinson and J.M. Torrens, "Computer Simulation of Atomic-Displacement Cascades in Solids in the Binary-Collission Approximation," Phys. Rev. **B9,** 5008 (1974).

64. M. Kaminsky and S.K. Das, "Particle Emission from Solids Under 14 MeV Neutron Impact, Proceedings of Surface Effects in Controlled Thermonuclear Fusion Devices and Reactors," Argonne National Laboratory, January 10-12, 1974.

65. W.A. Coleman and T.W. Armstrong, "The Nucleon-Meson Transport Code MNTC," Oak Ridge National Laboratory report ORNL-4606 (1970).

66. E.D. Cashwell, J.R. Neergarrd, W.M. Taylor and G.D. Turner, "MCN:A Neutron Monte Carlo Code," Los Alamos Scientific Laboratory Report LA-4751 (1972).

67. B. Fidleris, I.R. Emmerton, R.D. Delaney, "An In-Reactor Creep Machine for High Flux Application," J. of Phys. E., Sci. Inst., Vol. 5, p. 442, 1972.

XV. SCYLLAC FUSION TEST REACTOR DESIGN

D.J. Dudziak, S.A. Gerstl, D.L. Houck, R.A. Jalbert, R.A. Krakowski, R.K. Linford, T.E. McDonald, J.D. Rogers, K.I. Thomassen

A. Introduction

In August 1974 the overall conceptual design of a large-radius toroidal theta pinch was initiated. The machine, which is designated as the Scyllac Fusion Test Reactor (SFTR)*, is designed for D-T operation to achieve Q=1, i.e. the total neutron energy (at 20 MeV/n) is equal to the internal energy of the plasma. The machine has a major radius of 40 m, a minor (first-wall) radius of 0.1 m, and an $\ell=1$ (helical) wavelength of approximately 3.2 m. The SFTR will be wall stabilized with the possibility of requiring a modest feedback system for long-term stability. Figure XV-1 is an illustration of the SFTR, showing the plasma chamber and implosion-heating capacitors in a concrete cell having 1.5-m thick walls. The dewars for the superconducting coils of the METS system are placed immediately outside the cell with the refrigeration system shown on the left of the facility. The tritium handling system is shown on the lower right of the facility. The SFTR is being designed for 1000 D-T plasma discharges per year and a repetition rate of a discharge every 15 min.

B. Project Organization

The SFTR design project covers a wide range of disciplines and requires extensive interaction among experts throughout the Laboratory. K.I. Thomassen (CTR-DO) has overall responsibility for the project with the following assignments made to coordinate the effort in specific areas:

1. J.D. Rogers: Cryogenic energy storage and transfer.

2. R.A. Krakowski: First wall, vacuum systems, tritium handling, CMB-liaison, radiation shielding.

3. T. Oliphant: Theoretical aspects of implosion, compression, burning, stability, and equilibrium.

4. T.E. McDonald: Electrical systems and controls, alternative energy storage and charging system.

5. W.A. Bradley: Overall engineering coordination, scheduling and cost estimating.

Over 30 persons have contributed to the proposal in areas of materials development and fabrication, electrical design, cryogenic engineering, facilities design and layout, radiation activation studies, shielding design, and health and safety studies. Table XV-1 is a list of the principal contributors.

C. General Design

The design effort has been divided into the following areas: (a) first wall and implosion-heating system; (b) tritium handling and vacuum system; (c) radiation shielding system; (d) magnetic energy storage system [METS]; (e) instrumentation and control; and (f) general facilities design. In addition to these design categories, work is also being done on the environmental and safety aspects as well as the quality assurance program.

The designs of the majority of the SFTR subsystems have progressed through at least one preliminary conceptual design and for some subsystems through several conceptual designs. The specific design of the first wall and implosion-heating circuit has presented a difficult problem. Although the basic operation is known, it is anticipated that further iterations of the implosion-heating hardware design will be required.

Tables XV-2 and XV-3 give the major parameters for the SFTR. Table XV-2 lists the parameters of the machine while Table XV-3 lists the plasma and field parameters immediately after implosion heating and at peak compression.

A typical cross section of the SFTR is shown in Fig. XV-2. The plasma chamber and implosion-heating system are shown inside a concrete cell which is a secondary neutron shield and also provides a secondary containment for tritium. The primary neutron shield is placed immediately

---

*previously denoted Fusion Test Reactor (FTR)

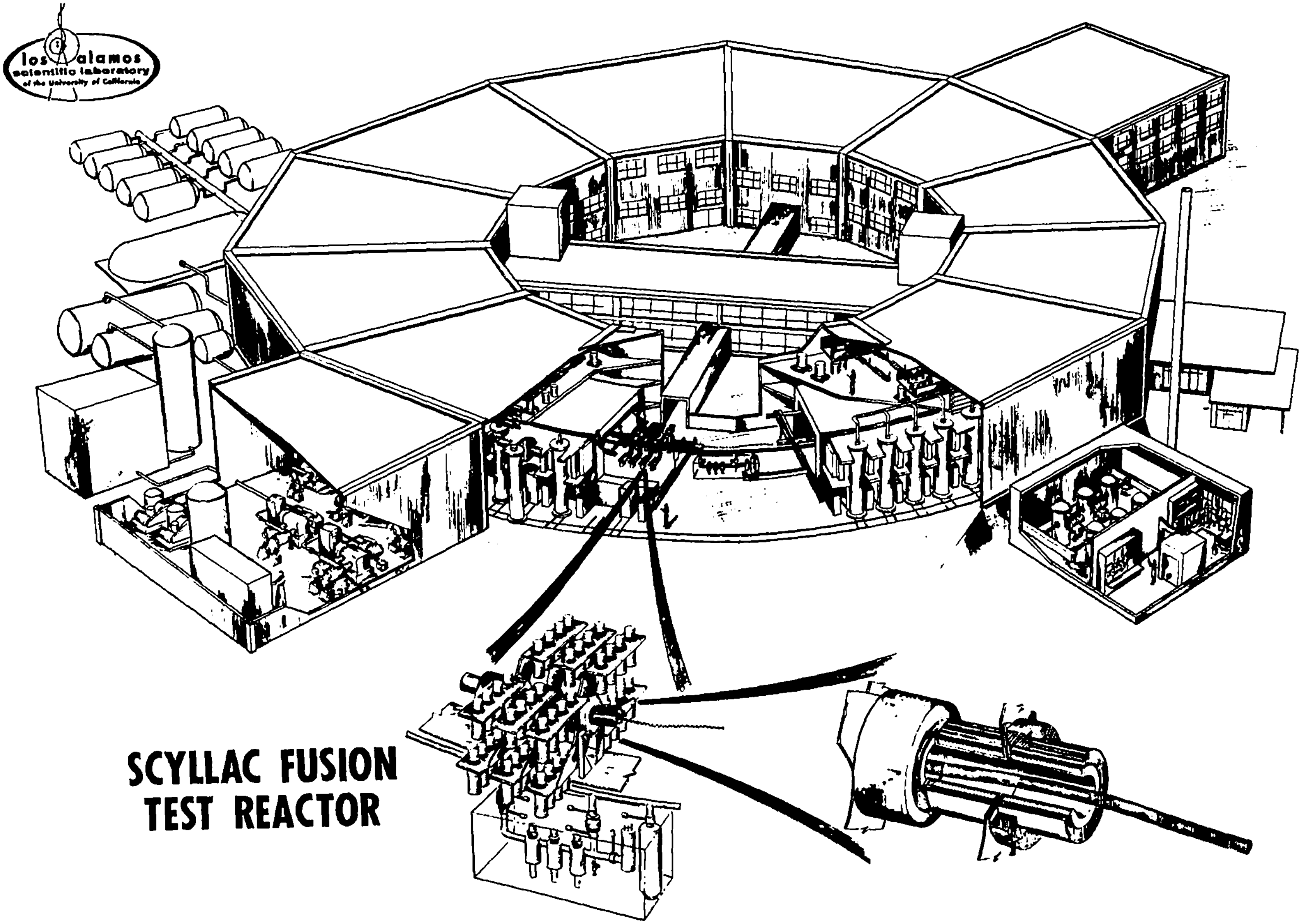

Fig. XV-1
Scyllac Fusion Test Reactor

TABLE XV-1

CONTRIBUTORS TO FTR DESIGN

Implosion and Burn Calculations

T. Oliphant, CTR-7
R. Linford, CTR-7

Marshall Coil and First Wall

R. Linford, CTR-7
K. Hanks, CTR-4
D. Sandstrom, CMB-6
J. Dickinson, CMB-6

Tritium Handling and Vacuum

R. Krakowski, CTR-7
J. Anderson, CMB-3
D. Vier, CMB-3

Diagnostics and Instrumentation

F. Jahoda, CTR-8
R. Siemon, CTR-8

Magnetic Energy Storage

J. Rogers, CTR-9
K. Williamson, CTR-9
D. Weldon, CTR-9
C. Swannack, CTR-9
H. Vogel, E-DO
R. Bartholomew, ENG-7

Facilities Design

D. Houck, ENG-9
R. Turner, ENG-9
J. Rand, ENG-7
D. Kirby, ENG-7
V. Starkovich, ENG-7

Capacitor Bank Design

E. Kemp, CTR-4
R. Häarman, CTR-4
L. Hansborough, CTR-4

Shielding Design and Neutronics

D. Dudziak, T-1
S. Gerstl, T-1

Safety

R. Jalbert, H-1

Quality Assurance

E. Brazier, ENG-DO-QA

Scheduling and Estimating

T. McDonald, CTR-4
W. Bradley, ENG-7
D. Orr, ENG-8

TABLE XV-2

SFTR MACHINE PARAMETERS

Plasma Chamber		
Major Radius	R	40 m
Minor Radius	b	0.1 m
Wavelength	λ	3.2 m
L=1 Perturbation	δ_1	1.5
Module Length	ℓ	0.2 m
Implosion System		
Capacitance/Module	C	0.12 µf
Capacitor Voltage	V	270 kV
Induced E-Field	E_θ	3.8 kV/cm
System Energy Storage		4.4 MJ
Compression System		
B-Field Risetime	τ_R	0.7 ms
B-Field Decay Time	$\tau_{L/R}$	250 ms
System Energy Storage		488 MJ
Plasma		
Time at Q-1	τ_B	120-170 ms
	$n\tau$	$>1.5\ (10)^{14}$ s/cm^3
Filling Pressure	p	4.5 mtorr

TABLE XV-3

SFTR PARAMETERS AFTER IMPLOSION AND AT PEAK COMPRESSION

		Implosion	Compression
Normalized Plasma Radius	a/b	0.8	0.33
Ion Temperature	T_i	2.5 keV	7 keV
Electron Temperature	T_e	1.2 keV	5 keV
Magnetic Field	B	8.3 kG	35-55 kG

around the plasma chamber. The primary radiation shield prevents neutron damage to the implosion-heating capacitors and limits the personnel radiation exposure inside the cell. The shielding is sufficient to allow unlimited personnel access inside the cell when the machine is not in operation and personnel access adjacent to the outside of the cell during operation.

Four cryogenic vacuum pump stations are equally spaced around the machine and are located inside the cell. The vacuum is maintained in a toroidal manifold located immediately below the plasma chamber and is connected to the plasma chamber by a series of downcommers. In case of an accidental tritium release to the cell, cell air is circulated through manifolds, which are routed through the bottom of the cell, to the main tritium cleanup facility. The air is then either recirculated back to the cell or, when the tritium concentration is low enough, vented to the atmosphere.

The pulse charging and trigger systems are located on top of the cell with cable feeds through the cell top. The METS system is located on the outside of the toroid next to the cell with cable feeds from the

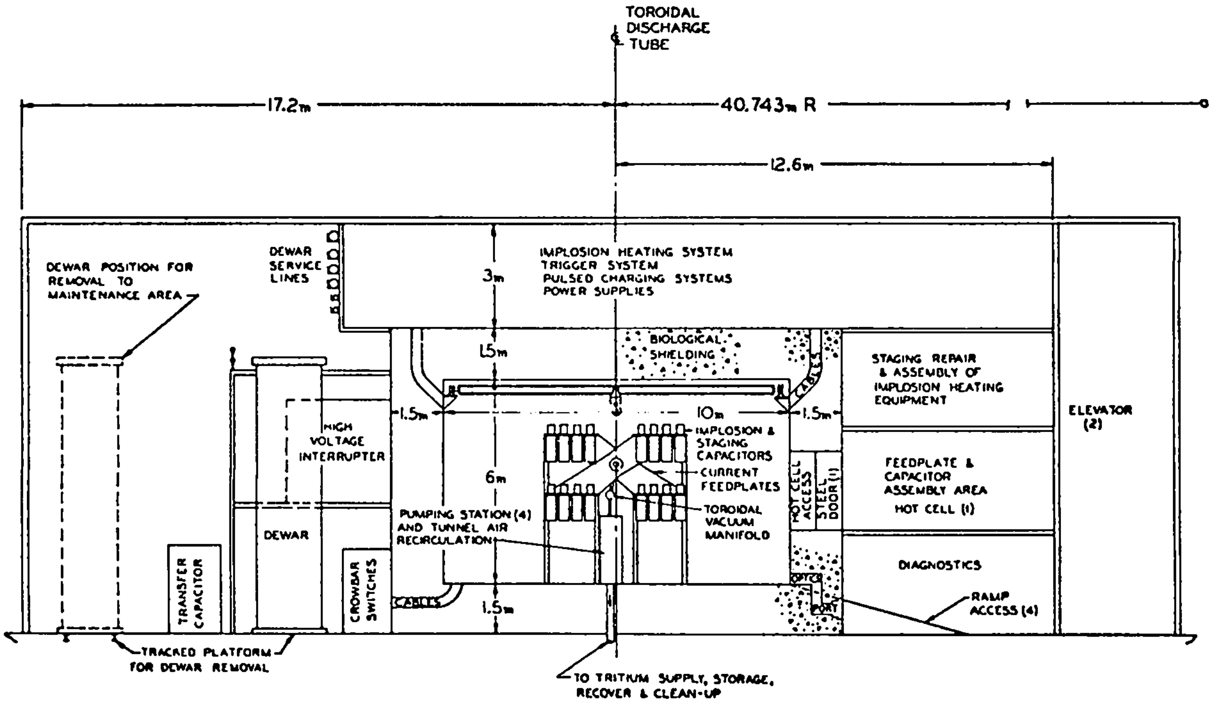

Fig. XV-2
Typical Cross Section SFTR

crowbar switches to the compression coils through the cell bottom. The diagnostics area is located on the inside of the toroid adjacent to the cell with optical ports being placed through the cell to provide access for optical diagnostics.

D. Implosion-Heating System

The implosion heating system is a high-voltage low-inductance capacitor bank feeding a load coil which provides a fast-rising magnetic field for shock heating the plasma. The energy capacity of the implosion-heating capacitor bank is approximately 5 MJ.

One possible implosion-heating circuit is shown in Fig. XV-3. In this concept the pulse-forming network employs voltage levels in the range of 270 kV to provide magnetic fields which rise to about 11 kG in 100 ns for shock heating. The fields are then sustained by the 60-kV staging bank and crowbar until the compression field can be raised. The ion temperature after the shock is approximately 2.5 keV. The concept of wall stabilization requires that the radius of the plasma column be at least 35% of the radius of the implosion-heating load coil. As a result, the radius of the plasma column must be as large as possible after shock heating to avoid over compression and loss of wall stabilization during the compression and burn phase. Work is now under way to determine the most efficient circuit for producing the proper implosion-heating field so that a large radius plasma will be produced.

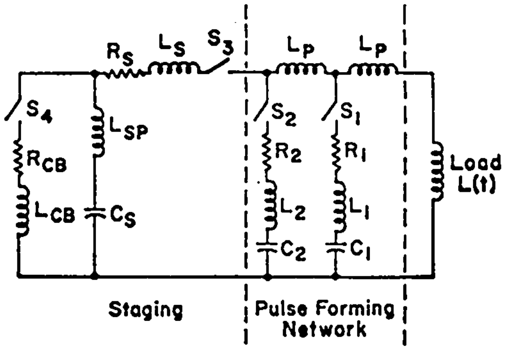

Fig. XV-3
Implosion Heating Network

The implosion-heating load coil is in the form of a Marshall coil, which is illustrated in Fig. XV-4. This configuration has low inductance and produces the desired Z directed magnetic field while allowing a compression load coil to be placed around the plasma chamber. The Marshall coils will be placed back-to-back to form modules as shown in Fig. XV-5. Weld joints are made between modules to allow

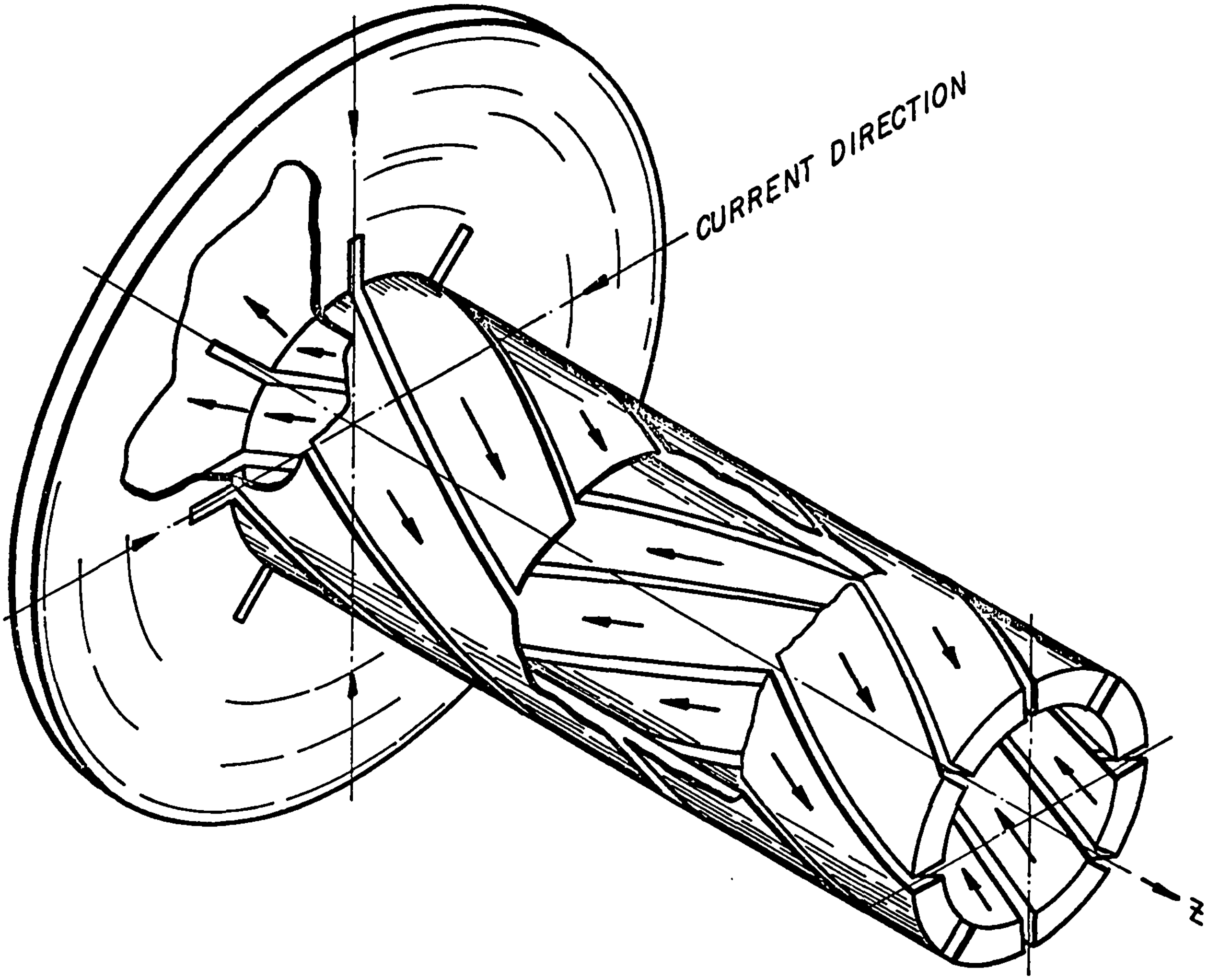

Fig. XV-4
Marshall Coil for Implosion Heating

removal for maintenance. The compression coils are placed around the Marshall coils with a magnetic material between the two to reduce the amount of energy required in the implosion system.

E. Compression System (METS)

Approximately 488 MJ of energy is required for the compression field which is in the range of 50 kG. This energy will be stored in the form of current flowing in a series of superconducting coils. Upon firing of the machine the current will be switched from the superconducting storage coil into the compression coil and crowbarred.

The basic METS circuit is shown in Fig. XV-6. The energy is stored in the superconducting coil by closing the interrupter switch and building up a current flow through the superconducting storage coil and interrupter; the current is transferred into the compression coil by opening the current interrupter. The current resonates with the transfer capacitor bank into the compression coil and the crowbar switch is then closed. The transfer capacitor bank is necessary to prevent losing half the energy in the interrupter switch and must have half the energy storage capacity of the superconducting coil.

A typical graph of the build up of the magnetic field produced by the implosion-heating and compression systems is shown in Fig. XV-7. The current reaches its peak in the compression coil in approximately 750 μs and decays with an L/R time of 250 ms.

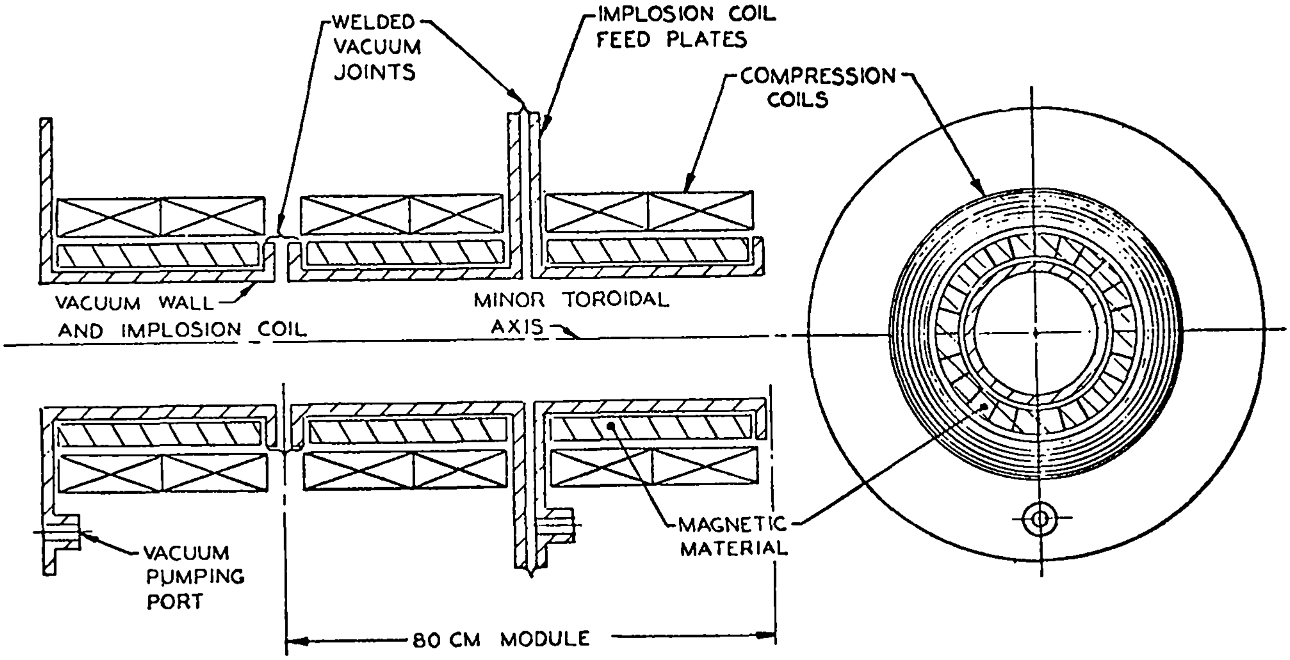

Fig. XV-5
Module of the 80M Diameter FTR Torus

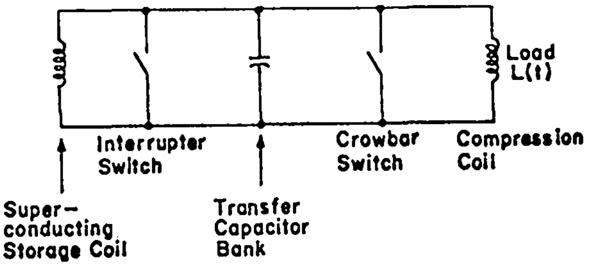

Fig. XV-6
Compression Circuit

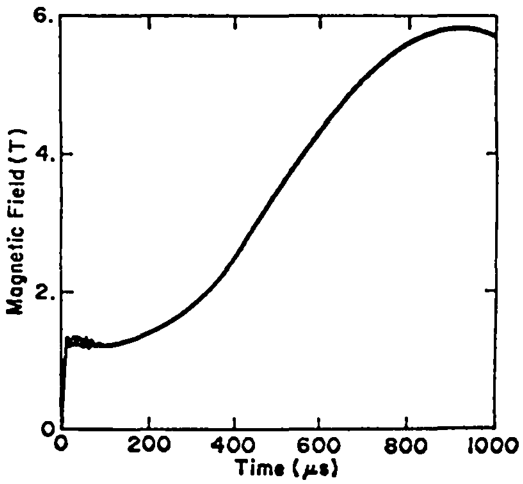

Fig. XV-7
Magnetic Field vs Time

F. Tritium Handling and Vacuum System

The major functions of the tritium handling system are: (a) to provide precisely measured D-T mixtures to the SFTR discharge tube in preparation for a D-T discharge; (b) to recover and/or to account for all unburned tritium after a D-T discharge; (c) to provide safe storage of gram quantities of tritium; (d) to monitor and to control the chronic release of tritium; and (e) to present safeguards and cleanup capabilities in the event of a significant accidental release of tritium. The major subsystems that comprise the tritium handling system are:

- Passive Storage Facility (PSF) Vault
- Tritium Injection System (TIS)
- Tritium Recovery System (TRS)
- FTR Vacuum System

- Tritium Waste Treatment (TWT) Facility
- Cell Cleanup Facility (CCF)

Figure XV-8 depicts schematically the interrelationship between components of the tritium handling system. In addition to the functions of storage, injection and recovery, the overall system also includes the SFTR vacuum system, D-T impurity control, and post- discharge gas analyses.

The interface between the major subsystems are multifarious and diffuse; for instance, the vacuum system *per se* plays important roles in both tritium injection and recovery and to some extent impinges upon the design of the TWT and CCF.

The tritium injection will use standard volumes and vacuum transfer techniques. A uranium bed will supply clean tritium to the injection system and used $(D,T)_2$ gas will be recovered at the cryogenic vacuum pump station and then stored on a second uranium bed. In addition to metal hydride storage of tritium, a vault will be used for more permanent and secure storage of gaseous tritium. Chronic tritium releases are expected to occur at the vacuum pump stations (four stations are located within the SFTR cell) and at the locations of major tritium handling components, e.g., cleanup units, uranium beds, etc. Such components will be located in ventilation hoods, and tritium released during routine maintenance of these components will be carried to a small 7 ℓ/s (15 cfm) cleanup unit. A larger 4700 ℓ/s (10 kcfm) cleanup unit will be provided to remove tritium from the air in the SFTR cell should a tritium release occur within the cell.

The tritium system described above is designed to provide for 1000 D-T discharges/week, each discharge requiring on the average 15 mg of T_2. On the basis of 20 D-T discharges/week, a total tritium supply of 0.3 g (one week's supply) will be stored as uranium hydride and 2.0 g (two month's supply) will be in gaseous form.

G. Shielding and Activation of the Scyllac Fusion Test Reactor (SFTR)

Initial analysis of the radiation problems of the SFTR has concentrated on (a) air activation in the cell; (b) doses to organics in the compression load coils and in the implosion-heating capacitors [castor oil]; (c) activation of the implosion-heating and compression coils; and (d) activation of the implosion-heating capacitors. Exploratory calculations were made under the assumption of no primary shield. The results of these calculations are given in the graph in Fig. XV-9 and show that possibly damaging doses of 15 Gy/pulse (1.5 [10]^3 rad/pulse) would occur in the capacitors. Also, activation of coils and capacitor structures without a primary shield would cause doses in the tunnel of greater than 1 rem/h for several hours after each pulse, precluding routine access for maintenance, and adjustment.

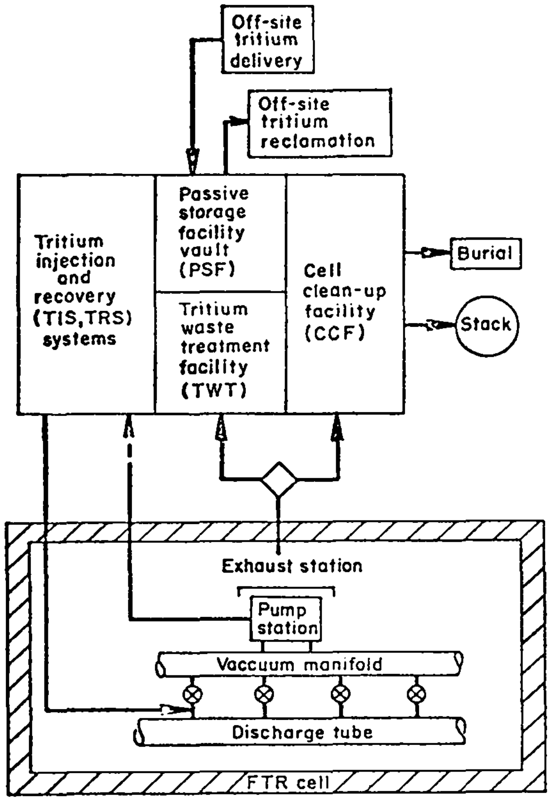

Fig. XV-8
Schematic Diagram of the Tritium Handling System

A primary shield was, therefore, provided to protect the capacitor insulation, minimize air and other activation throughout the chamber, and shield against activated coils and other magnetic materials. A 0.5-m thick annular shield around the coils consisting of laminated aluminum, graphite, and borated-lead polyethylene will reduce the maximum neutron dose in the capacitors to a negligible value and cell gamma-ray doses from the coils to ~1 mrem/h. Air activity consists primarily of short-lived ^{13}N and ^{16}N, 1.83-h ^{41}Ar, 260-y ^{39}Ar, and 5 730-y ^{14}C. Calculations, however, show that the air activities are within allowed occupational levels even before dilutions.

The 1.5-m-thick concrete cell walls provide sufficient secondary shielding to reduce the total

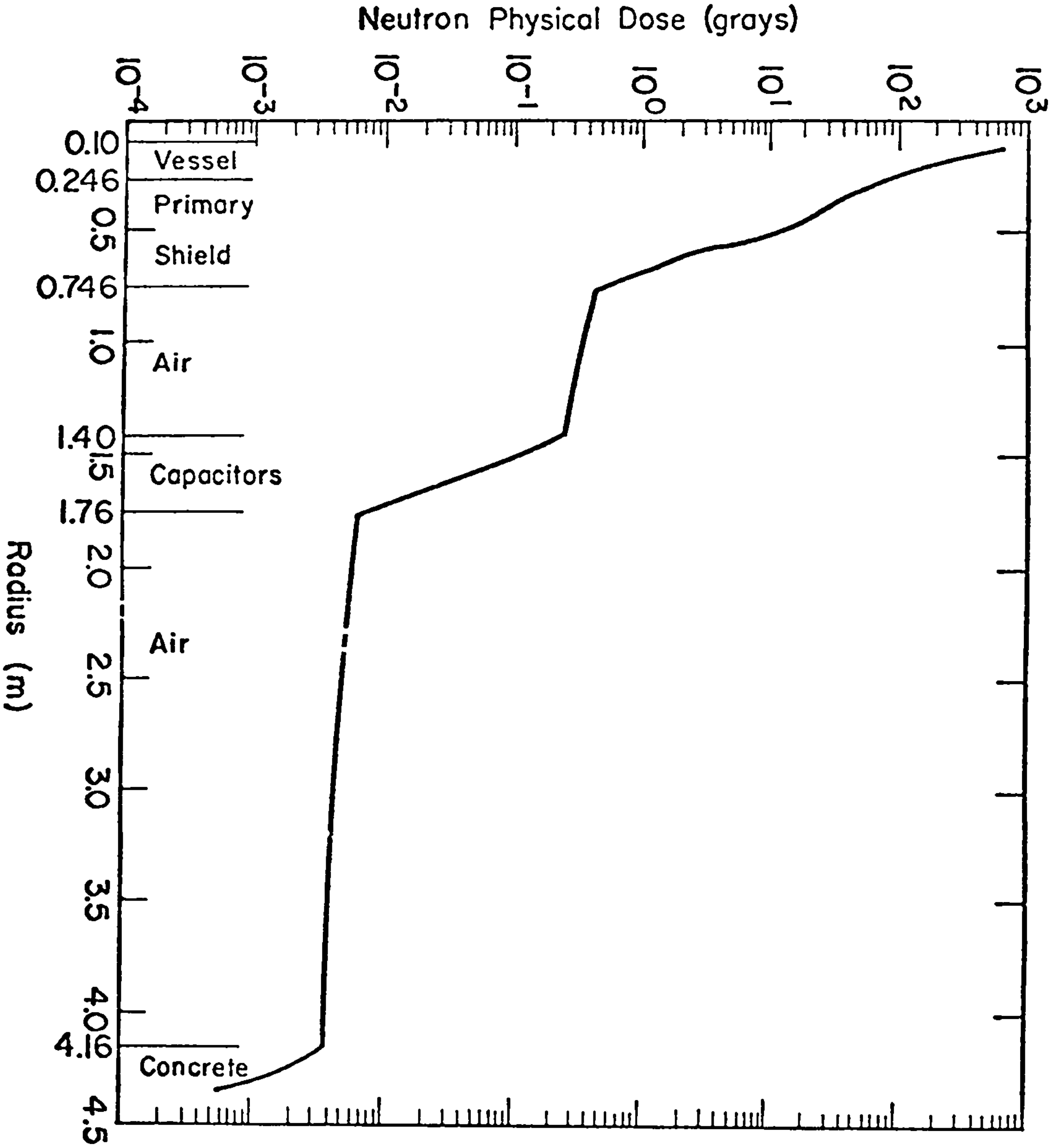

Fig. XV-9
Radiation Levels vs Coil Radius

biological dose on the outside of the cell to less than the design value of 0.5 rem/yr.

The neutron transport calculations have been based upon a conservatively assumed source of 1.8×10^{16} n/m per D-T discharge and 1000 discharges per year. Equivalently, the time-averaged 14.1-MeV neutron wall loading is 2.0 W/m^2. Maximum neutron plus gamma-ray energy densities in the load coils are ≤ 1 MJ/m^3 per pulse, so temperature rises will be <1 K. Transmutation effects in the coils (copper or aluminum) or the Fe-Ni alloy will be minor at the SFTR fluence levels; namely, <1 ppm/yr. Likewise, maximum dpa value in the Fe, Ni, Al, or Cu is $\sim 2\times10^{-8}$ per pulse, or 2×10^{-5} per year which is a negligible value.

H. Safety and Environmental Aspects

Key safety and environmental problems anticipated with the SFTR design have been identified and quantified. H-Division personnel with expertise in the areas of radiology, hydrology, geology, meteorology, and industrial hygiene have been identified for contribution to the safety and environmental aspects of the SFTR early in the conceptual design phase. The major effort thus far has been in the area of tritium control, structural and air activation by neutrons, radiation shielding, and chemical/radiation waste. All calculations have been of a preliminary, scoping nature and have served primarily a feedback function in the engineering design process. All safety and environmental considerations will be quantified once the SFTR design becomes firm.

References

1. K.I. Thomassen, "A Theta-Pinch Fusion Test Reactor," Trans. Am. Nucl. Soc. **20** (1975).

2. Code of Federal Regulations, Title 10, Part 20, "Standards for Protection Against Radiation," Appendix B (Jan. 1, 1975).

3. R. Jalbert, Los Alamos Scientific Laboratory, personal communication, January 1975. (MPC for ^{39}Ar is conservative, based upon lens of the eye and skin as critical organs.)

JOURNAL ARTICLES

J.P. Adams F.K. Wohn W.L. Talbert, Jr. W.E. Schick, Jr. J.R. McConnell	Internal Coefficient Measurements for Transitions in ^{140}Xe	Phys. Rev. C 10, 1467 (1974)
D.A. Baker J.A. Phillips	Pressure Balance Limitations in Z Pinches with Diffusion Heating	Phys. Rev. Lett. 32, 202 (1974)
D.I. Brown S.J. Gitomer H.R. Lewis	The Two-Stream Instability Studied with Four One-Dimensional Plasma Simulation Models	J. Computat. Phys. Vol. 14, No. 2 (1974)
J.H. Brownell H. Dreicer R.F. Ellis J.C. Ingraham	Influence of Intense AC Electric Fields on the Electron-Ion Collision Rate in a Plasma	Phys. Rev. Lett. 33, 1210 (1974)
J.M. Bunch F.W. Clinard, Jr.	Damage of Single-Crystal Al_2O_3 by 14 MeV Neutrons	J. Am. Ceram. Soc. 57, 279 (1974)
G.H. Carlson W.L. Talbert, Jr. J.R. McConnell	Decays of Mass-Separated ^{138}Xe and ^{138}Cs	Phys. Rev. C 9, 283 (1974)
D.J. Dudziak R.A. Krakowski	Radioactivity Calculations for the Reference Theta-Pinch Reactor (RTPR)	Nucl. Technol. 25, 32 (1975)
D.J. Dudziak M.L. Simmons G.J. Russell	Neutron Flux Distribution Calculations for the LAMPF Radiation Effects Facility	Trans. Am. Nucl. Soc. 19, 465 (1974)
W.R. Ellis	CTR Applications of the High Density Linear Theta Pinch	Nucl. Fusion 15, 2 (1975)
W.R. Ellis F.C. Jahoda R. Kristal W.E. Quinn F.L. Ribe G.A. Sawyer R.E. Siemon	Plasma Equilibrium and Stability in the Scyllac Toroidal Sector Experiments	Nucl. Fusion 14, 841 (1974)
J.P. Freidberg F.H. Haas	Kink Instabilities in a High-β Tokamak with Elliptic Cross Section	Phys. Fluids 17, 440 (1974)

J.P. Freidberg B.M. Marder H. Weitzner	Stability of Diffuse High Beta Helical Systems	Nucl. Fusion 14, 809 (1974)
J.P. Freidberg H. Weitzner	Endloss from a Linear θ Pinch	Nucl. Fusion (To be published)
R.A. Gerwin	Energy Loss of a Relativistic, Finite Electron Beam in a Plasma	Phys. Fluids (To be published)
W.V. Green J. Weertman	Increased Efficiency of a Dislocation Line as a Sink for Vacancies when it Oscillates	Radiat. Eff. 22, 9 (1974)
R.F. Gribble R. Kristal	Multifringe Electro-Optic Phase Modulator	Rev. Sci. Instr. 45, 520 (1974)
D.W. Hewett	Numerical Simulation of a Radially Inhomogeneous Cylindrical Plasma	J. Computat. Phys. 16, 49 (1974)
D.W. Hewett T.P. Armstrong	Nonlinear Landau Damping in a Radially Inhomogeneous Cylindrical Plasma	Phys. Fluids 17, 595 (1974)
R.A. Krakowski D.J. Dudziak	Radioactivity Induced in a Theta-Pinch Fusion Reactor	Nucl. Technol. (To be published)
R.A. Krakowski F.W. Clinard, Jr. F.L. Ribe T.A. Coultas	Surface Effects at the First-Wall of the Reference Theta-Pinch Reactor (RTPR)	J. Nucl. Mater. 53, 54 (1974)
R. Kristal	Pulsed HF Laser Holographic Interferometry	Appl. Opt. 14, 628 (1975)
H.R. Lewis C.W. Nielson	A Comparison of Three Two-Dimensional Electrostatic Plasma Simulation Models	J. Computat. Phys. 1, 17 (1975)
B.M. Marder	Kink Instabilities in the Belt Pinch	Phys. Fluids 17, 447 (1974)
B.M. Marder	Kink Instabilities in Arbitrary Cross-Section Plasmas	Phys. Fluids 17, 634 (1974)
B.M. Marder	GAP - A PIC-Type Fluid Code	Mathematics of Computation (To be published)
D. Montgomery L. Turner G. Joyce	Fokker-Planck Equation for a Plasma in a Magnetic Field	Phys. Fluids 17, 954 (1974)

D. Montgomery G. Joyce L. Turner	Magnetic Field Dependence of Plasma Relaxation Times	Phys. Fluids 17, 2201 (1974)
K.F. McKenna R. Kristal K.S. Thomas	Measurements of Plasma Density Distribution and Current-Sheath Structure in the Implosion Phase of a Theta-Pinch Discharge	Phys. Rev. Lett. 32, 409 (1974)
K.F. McKenna T.M. York	Transient Flow and Expansion of a Pinch Discharge Plasma in Self-Induced Magnetic Magnetic Fields	Plasma Phys. 17, 1 (1975)
G. Miller	Motion of a Plasma Column in a Perturbing Magnetic Field	Phys. Fluids (To be published)
D.W. Muir D.J. Dudziak	Sensitivity of RTPR Afterheat and Radioactivity to Nb-94 Cross Section Uncertainty	Trans. Am. Nucl. Soc. 19, 465 (1974)
T.A. Oliphant	A Mixed Snowplow Bounce Model for Shock Heating in a Staged Theta Pinch	Nucl. Fusion 14, 377 (1974)
T.A. Oliphant	Monte Carlo Treatment of Heat Flow Through a Neutral Gas Layer	J. Nucl. Mater. 53, 62 (1974)
D.M. Parkin A.N. Goland	Recoil Energy Distributions in CTR-Related Neutron Spectra	Trans. Am. Nucl. Soc. 19, 23 (1974)
W.G. Price D.J. Dudziak	D-T Fusion Reactor Activation and Afterheat	Trans. Am. Nucl. Soc. 19, 459 (1974)
F.L. Ribe R.F. Post	Fusion Reactors as Future Energy Sources	Science, 186, 397 (1974)
A.G. Sgro	The Collision of a Strong Shock With a Gas Cloud: A Model for Cassiopia A	Astrophys. J., Vol. 197, May 1975 (To be published)
R.E. Siemon	Polychrometer with Extreme Rejection of Stray Light	Appl. Opt. 13, 697 (1974)
P.D. Soran D.J. Dudziak	Bonarenko Formalism Applied to Theta-Pinch Reactor Nucleonics	Trans. Am. Nucl. Soc. 19, 468 (1974)
K.S. Thomas H.W. Harris F.C. Jahoda G.A. Sawyer R.E. Siemon	Plasma Experiments on the Linear Scyllac Theta Pinch	Phys. Fluids 17, 1314 (1974)

K.I. Thomassen D.J. Dudziak R.A. Krakowski	Prospects for Converting Th-232 to U-233 in a Linear Theta Pinch	Trans. Am. Nucl. Soc. 19, 6 (1974)
K.I. Thomassen T.A. Oliphant	First Wall Fluxes in a Theta-Pinch Feasibility/D-T Experiment	J. Nucl. Mater. 53, 48 (1974)
L. Turner	Image Effects in Bounded Plasmas	Phys. Fluids 17, 369 (1974)
J. Weertman	Theory of Irradiation Growth of Fatigue Cracks	J. Nucl. Mater. (To be published)
J.M. Williams T.G. Frank	Laser-Controlled Thermonuclear Reactor Materials Requirements	Nucl. Technol. 22, 360 (1974)
D. Winske E.A. Jackson	Partial Trapping of a Beam in a Cold Collisional Plasma	Phys. Fluids 18, 389 (1975)
J.J. Wollan K.W. Haas J.R. Clem D.K. Finnemore	Phase Transition at H_{c1} for Superconducting Nb and V	Phys. Rev. B 10, 1874 (1974)

FIFTH IAEA CONFERENCE ON PLASMA PHYSICS AND CONTROLLED NUCLEAR FUSION RESEARCH

Tokyo, Japan
November 1974

D.A. Baker L.C. Burkhardt J.N. DiMarco P.R. Forman A. Haberstich R.B. Howell H.J. Karr J.A. Phillips A.E. Schofield	Plasma Parameters and Stability of the Programmed Pinch Experiment ZT-1	Paper IAEA-CN 33/E3
J.H. Brownell H. Dreicer R.F. Ellis J.C. Ingraham	Hot Electron Production, Anomalous Absorption and Effect of Intense Electromagnetic Fields on Inverse Bremsstrahlung Absorption Near the Electron Plasma Frequency	Paper CN-33/H-4-2
E.L. Cantrell W.R. Ellis H.W. Harris F.C. Jahoda R. Kristal M.D. Machalek J.R. McConnell W.E. Quinn F.L. Ribe G.A. Sawyer F.T. Seibel R.E. Siemon	Plasma Experiments in the Scyllac Toroidal Theta Pinch	Paper CN-33/E1-2
J.P. Freidberg J.P. Goedbloed W. Grossmann F.A. Haas	Stability of Kink Modes in High Beta Tokamaks	Paper CN-33/A13-4
N.T. Gladd D.W. Hewett C.W. Nielson T.A. Oliphant A.G. Sgro	Theoretical and Numerical Studies of High-Beta Implosion Heating	Paper CN-33/E8-3

R.A. Krakowski R.K. Linford T.A. Oliphant F.L. Ribe K.I. Thomassen	Engineering Deisgn of a Fusion Test Reactor (FTR) and Fusion Engineering Research Facility (FERF) Based on a Toroidal Theta Pinch	Paper CN-33/G3-3 (A Joint LASL/ANL paper)
K.S. Thomas R.F. Gribble R.K. Linford I. Henins J. Marshall A.R. Sherwood J.E. Hammel F.C. Jahoda R. Kristal K.F. McKenna	Implosion Heating Studies in the Scylla 1B, Implosion Heating, and Staged Theta Pinch Experiments	Paper CN-33/E-8-4

MEETING OF THE AMERICAN PHYSICAL SOCIETY

Chicago, Illinois
February 1974

F.L. Ribe	Physics Problems of Thermonuclear Reactors	Bull. Am. Phys. Soc. 19, 85 (1974)
K.S. Thomas	Scyllac Theta-Pinch Experiments	Bull. Am. Phys. Soc. 19, 99 (1974)

MEETING OF THE AMERICAN PHYSICAL SOCIETY

Salt Lake City, Utah
June 1974

D.A. Baker L.C. Burkhardt J.N. DiMarco P.R. Forman R.B. Howell H.J. Karr J.A. Phillips A.E. Schofield	Improved Stability of the ZT-1 Toroidal Pinch by Programming	Bull. Am. Phys. Soc. 19, 642 (1974)
D.A. Baker L.W. Mann	Equilibria and MHD Studies for a High-Beta Tokamak	Bull. Am. Phys. Soc. 19, 642 (1974)

EIGHTH SYMPOSIUM ON FUSION TECHNOLOGY

Noordwijkerhout, The Netherlands
June 1974

Proceedings Published as Euratom Report EUR 5182e (1974)

D.J. Dudziak	Fusion Reactor Nuclear Analysis Methods and Applications
R.A. Krakowski K.I. Thomassen T.A. Coultas	A Technological Assessment of the Reference Theta-Pinch (RTPR)

1974 APPLIED SUPERCONDUCTIVITY CONFERENCE

Argonne National Laboratory, Oakbrook, Ill.
September 1974

Proceedings Published in IEEE Transactions on Magnetics
Mag. 11, No. 2 (1975)

J.D.G. Lindsay D.J. Blevins H.L. Laquer G.A. Miranda J.D. Rogers C.E. Swannack D.M. Weldon	Development of A Superconducting Switch for Magnetic Energy Storage Systems	p. 594
G.A. Miranda J.D. Rogers	Adjacent Conductor Field Corrections to High Critical Current Short Sample Measurements	p. 582
M.C. Ohmer J.J. Wollan J.C. Ho	Improved Superconducting Properties of Multifilamentary Niobium Carbonitride Wire	p. 159
D.M. Parkin A.R. Sweedler	Neutron Irradiation of Nb_3Sn and NbTi Multifilamentary Composites	p. 166
C.E. Swannack D.J. Blevins C.R. Harder J.D.G. Lindsay J.D. Rogers D.M. Weldon	10 kA 800 kJ Magnetic Energy Transfer and Storage (METS) Test Facility	p. 504

CONFERENCE ON ENERGY STORAGE, COMPRESSION AND SWITCHING

Torino, Italy
November 1974

Proceedings to be Published

L.C. Burkhardt R.S. Dike J.N. DiMarco J.A. Phillips R.A. Haarman A.E. Schofield	The Magnetic Energy Storage System Used on ZT-1
R.F. Gribble R.K. Linford K.I. Thomassen	Implosion and Staging Systems for a Theta-Pinch Fusion Test Reactor
J. Hammel I. Henins J. Marshall A. Sherwood	High-Voltage Low-Impedance Electrical System for Driving a Theta-Pinch Implosion-Heating Experiment

76TH ANNUAL MEETING OF THE AMERICAN CERAMIC SOCIETY

Chicago, Ill.
April 1974

Am. Cer. Soc. Bull., Vol. 53, No. 4

F.W. Clinard, Jr.	Ceramics for CTR Systems	p. 314
F.W. Clinard, Jr. J.M. Bunch	Electrical Insulator Studied for the Theta-Pinch Fusion Reactor	p. 364

16TH ANNUAL MEETING, DIVISION OF PLASMA PHYSICS
AMERICAN PHYSICAL SOCIETY

Albuquerque, NM
October 1974

Abstracts published in Bulleting of the American Physical Society
Series II, Vol. 19, No. 9 (October 1974)

N.E. Abt T.R. Jarboe W.B. Kunkel A.F. Leitzke G.H. Rankin	Investigation and Control of Flute-Like MHD Modes in Laser Plasmas from Pellets
D.A. Baker L.C. Burkhardt J.H. DiMarco H.J. Karr	Magnetic Field Programming in ZT-1
D.A. Baker L.C. Burkhardt J.N. DiMarco A. Haberstich H.J. Karr	Stability of the ZT-1 Toroidal Z Pinch at Reduced Toroidal Currents
D.A. Baker L.C. Burkhardt J.N. DiMarco A. Haberstich H.J. Karr J.A. Phillips	Energy and Pressure Balance Considerations in Z-Pinches
D.C. Barnes V.H. Weston	Stability of a Toroidal Theta Pinch
G. Berge J.P. Freidberg	Equilibrium and Stability of $\ell=1$ Helically Symmetric, Finite β, Diffuse Plasmas
J.U. Brackbill	A Numerical Study of the Rotating Theta Pinch
E.L. Cantrell R. Kristal M.D. Machalek J.R. McConnell W.E. Quinn	Plasma Column Motion in the Scyllac Torus
J.N. DiMarco P.R. Forman R.B. Howell H.J. Karr	Temperature Measurements on ZT-1
W.R. Ellis K.B. Freese R.E. Siemon	Beta-Dependence of Axial and Radial Plasma Equilibrium in the Scyllac Torus
K.B. Freese M.R. Mross J.E. Walsh	Electron Heating and High Energy Tail Formation in a Turbulent Beam-Plasma System
J.P. Freidberg W. Grossman	Toroidal Kink Mode Stability of a Finite β, Arbitrary Cross Section, Tokamak Plasma
D.A. Freiwald R.A. Axford	Approximate Spherical Blast Theory with Source Mass
N.T. Gladd	Effects of Finite β and Temperature Anisotropy on the Modified Two Stream Instability

J.P. Goedbloed	The MHD Spectrum of Axially Symmetric Systems
R.F. Gribble R.K. Linford G.P. Boicourt	Shock Heating and Staging Circuit for FTR Test Module
J.E. Hammel I. Henins T.R. Jarboe J. Marshall A. Sherwood	The LASL Implosion-Heating Experiment
D.W. Hewett C.W. Nielson	Two-Species Vlasov Confinement Equilibria
J.Y. Hsu G. Joyce D. Montgomery L. Turner G. Vahala	Thermal Relaxation of a Plasma in a Uniform Magnetic Field
F.C. Jahoda R. Kristal J.W. Lillberg F.T. Seibel	C.W. Laser Density Measurements on Scyllac
T.R. Jarboe W.B. Kunkel A.F. Lietzke	Formation Process of Isolated Laser-Produced Pure Deuterium Plasma Clouds
R. Kristal	Holographic Interferometry on Scyllac
H.R. Lewis K.R. Symon	Stability Analysis of Inhomogeneous Plasma Equilibria
A.F. Lietzke T.R. Jarboe W.B. Kunkel	Early Stages of Expansion of Isolated Deuterium Plasma Clouds in a Magnetic Field
R.K. Linford K.E. Thomassen K.W. Hanks	Theta Pinch FTR Test Module
M.D. Machalek E.L. Cantrell W.R. Ellis P.C.T. van der Laan	I_z Current Measurements in the Scyllac Torus
K.F. McKenna R. Kristal E. Zimmermann	Radial Plasma Structure of the Scylla 1-B Theta Pinch Implosion: Flute Instabilities
K.F. McKenna T.M. York	Estimation of Laser-Plasma Interactions in the Scylla 1-C Theta Pinch
G. Miller R. Kristal K.J. Kutac R.F. Gribble	Scyllac Feedback Stabilization System
C.W. Nielson H.R. Lewis	An Inductive Model for Multidimensional Plasma Simulation
W.E. Quinn	The Scyllac Full Torus Experiment
G.H. Rankin T.R. Jarboe W.E. Kunkel A.F. Lietzke	Plasma-Magnetic Field Interchange Observed in Laser Plasmas from Pellets

F.L. Ribe H.W. Harris E.L. Kemp W.E. Quinn G.A. Sawyer	The Design of the Scyllac Toroidal Theta-Pinch Experiment
A.G. Sgro C.W. Nielson T.A. Oliphant	A Hybrid Simulation of Pinch Implosions
R.E. Siemon G.I. Chandler J.W. Lillberg F.T. Seibel	Thomson Scattering on Scyllac
K.R. Symon H.R. Lewis	Stability Analysis of BGK Waves
K.S. Thomas J.N. Downing R.F. Gribble R.K. Linford	Experiments in the Staged Theta Pinch Experiment

MISCELLANEOUS MEETINGS

G.E. Bosler D.J. Dudziak W.R. Ellis	A Preliminary Appraisal of a Fusion/Fission (hybrid) Reactor Based on the Linear Theta Pinch	Proc. Ninth Intersociety Energy Conversion Engineering Conference, San Francisco, CA, 26-30 Aug 1974
G.P. Boicourt J.E. Hammel	NET Applications in CTR Engineering	Cube Symposium Livermore, CA, Oct. 1974, USAEC Report CONF 74001 (1974)
W.V. Green R.A. Yeske	Materials Problems in Magnetically Confined Pulsed Fusion Reactors	Proc. 14th Annual Symposium of Engineering for the Materials/Energy Challenge, Albuquerque, NM, Mar. 1, 1974
R.A. Krakowski F.W. Clinard F.L. Ribe T.A. Coultas	Surface Effects at the First Wall of the Reference Theta-Pinch Reactor (RTPR)	Proc. Conference on Surface Effects in Controlled Thermonuclear Fusion Devices and Reactors, Argonne National Laboratory, Jan. 10-12, 1974
M.C. Ohmer J.J. Wollan L.O. Lawson	Experimental Hysteretic Loss for a Series of Superconducting Filamentary NbTi	
F.L. Ribe R.A. Krakowski K.I. Thomassen T.A. Coultas	An Engineering Design Study of a Reference Theta-Pinch Reactor (RTPR)	Workshop at Culham Laboratory, UK, Jan. 19-Feb. 15, 1974 (To be published in Nuclear Fusion)
K.I. Thomassen	Reversible Magnetic Energy Transfer and Storage Systems	Texas Symp. on the Technology of Controlled Thermonuclear Fusion Experiments and the Engineering Aspects of Fusion, Univ. of Texas, Austin, Nov. 20-22, 1972 (1974). USAEC Report CONF 721111 (1974)

F. L. Ribe	The Theta-Pinch Toroidal Reactor	International School of Fusion Reactor Technology, Pulsed Reactor Course, Erice, Sicily, September 1974
F. L. Ribe	Thermonuclear Reactor Systems	Conference on Advanced Energy Systems, Denver, Colorado, June 21, 1974

OTHER REPORTS

R.A. Krakowski D.J. Dudziak	Prospects for Converting Th-232 to U-233 in a Linear Theta-Pinch Hybrid Reactor (LTPHR)	USERDA Report ERDA 4 (1975)
D.M. Parkin A.N. Goland	Computational Method for the Evaluation of Radiation Effects Produced by CTR-Related Neutron Spectra	Brookhaven National Laboratory Report BNL-50434 (1974)

LOS ALAMOS SCIENTIFIC LABORATORY REPORTS

M. Katz, editor	Annual Progress Report on LASL Controlled Thermonuclear Research Program for a 12-Month Period Ending December 1974	LA-5656-PR (1974)
W.R. Ellis	Scaling Laws for the Linear Theta Pinch, II: Circulating Power in a High-Field Reactor	LA-5499-MS (1974)
W.R. Ellis J.P. Freidberg W.E. Quinn	Supplement to Proposal for the Construction of a Scylla IV-P Confinement Studies Theta Pinch	LA-5474-P, Suppl. (1974)
W.R. Ellis R.F. Gribble C.R. Harder	Preliminary $\ell_{1,0}$ Feedback Force Experiments on Scylla IV-3	LA-5788-MS (1974)
J.P. Freidberg J. Marshall A.R. Sherwood	High-Beta Tokamak	LA-5476 (1974)
D.A. Freiwald	Approximate Spherical Blast Theory and Laser Initiated Pellet Microexplosions	LA-5641-MS (1974)
D.A. Freiwald	Laser Fusion for Laymen	LA-5706-MS (1974)
D.A. Freiwald R.A. Gerwin	On CTR Breakeven Including Energy Transfer and Recovery Efficiencies	LA-5640-MS (1974)
F.C. Jahoda R. Kristal W.E. Quinn	Toroidal Mode Structure in the Scyllac Full Torus	LA-5853-MS (1975)
K.F. McKenna T.M. York	Laser-Plasma Interactions in the Scylla 1-C Experiment: Preliminary Analysis	LA-5957-MS (1975)
G. Miller	Calculation of Magnetic Fields with Given, Nearly Cylindrical, Conducting Walls	LA-5779-MS (1974)
J.A. Phillips J.N. DiMarco F.C. Jahoda	The Present Status and Future Program of the ZT-1 Experiment	LA-5530-SR (1974)
J.D. Rogers C.E. Swannack K.T. Thomassen D.M. Weldon	Magnetic Energy Transfer and Storage (METS) Program Schedules for Fusion Test Reactor	LA-5748-MS (1974)
J. Weertman	Potential Fatigue Problems in First-Wall Laser-Controlled Fusion Reactors	LA-5664-MS (1974)

D.M. Weldon J.D.C. Lindsay	Methods of Energy Transfer from a Magnetic Energy Storage System Using a Transfer Capacitor and a Superconducting Switch	LA-5631-MS (1974)
J.M. Williams T.G. Frank	Laser Controlled Thermonuclear Reactor Systems Studies	LA-5718-MS (1974)

☆ U.S. GOVERNMENT PRINTING OFFICE: 1975—677-343/19